

Springer Series in MATERIALS SCIENCE

Editors: R. Hull R. M. Osgood, Jr. J. Parisi H. Warlimont

The Springer Series in Materials Science covers the complete spectrum of materials physics, including fundamental principles, physical properties, materials theory and design. Recognizing the increasing importance of materials science in future device technologies, the book titles in this series reflect the state-of-the-art in understanding and controlling the structure and properties of all important classes of materials.

- | | |
|---|---|
| <p>71 Dissipative Phenomena
in Condensed Matter
Some Applications
By S. Dattagupta and S. Puri</p> <p>72 Predictive Simulation
of Semiconductor Processing
Status and Challenges
Editors: J. Dabrowski and E.R. Weber</p> <p>73 SiC Power Materials
Devices and Applications
Editor: Z.C. Feng</p> <p>74 Plastic Deformation
in Nanocrystalline Materials
By M.Yu. Gutkin and I.A. Ovid'ko</p> <p>75 Wafer Bonding
Applications and Technology
Editors: M. Alexe and U. Gösele</p> <p>76 Spirally Anisotropic Composites
By G.E. Freger, V.N. Kestelman,
and D.G. Freger</p> <p>77 Impurities Confined
in Quantum Structures
By P.O. Holtz and Q.X. Zhao</p> <p>78 Macromolecular Nanostructured
Materials
Editors: N. Ueyama and A. Harada</p> | <p>79 Magnetism and Structure
in Functional Materials
Editors: A. Planes, L. Manósa,
and A. Saxena</p> <p>80 Ion Implantation
and Synthesis of Materials
By M. Nastasi and J.W. Mayer</p> <p>81 Metallopolymer Nanocomposites
By A.D. Pomogailo and V.N. Kestelman</p> <p>82 Plastics for Corrosion Inhibition
By V.A. Goldade, L.S. Pinchuk,
A.V. Makarevich and V.N. Kestelman</p> <p>83 Spectroscopic Properties of Rare Earths
in Optical Materials
Editors: G. Liu and B. Jacquier</p> <p>84 Hartree-Fock-Slater Method
for Materials Science
The DV-X Alpha Method for Design
and Characterization of Materials
Editors: H. Adachi, T. Mukoyama,
and J. Kawai</p> <p>85 Lifetime Spectroscopy
A Method of Defect Characterization
in Silicon for Photovoltaic Applications
By S. Rein</p> <p>86 Wide-Gap Chalcopyrites
Editors: S. Siebentritt and U. Rau</p> |
|---|---|

Volumes 20–70 are listed at the end of the book.

Y. Fukai

The Metal–Hydrogen System

Basic Bulk Properties

Second, Revised and Updated Edition

With 287 Figures and 55 Tables

 Springer

Professor Yuh Fukai, D.Sc.
Chuo University
Department of Physics
Kasuga, Bunkyo-ku, Tokyo 112., Japan
E-mail: yuh.fukai@m8.dion.ne.jp

Series Editors:

Professor Robert Hull
University of Virginia
Dept. of Materials Science and Engineering
Thornton Hall
Charlottesville, VA 22903-2442, USA

Professor R. M. Osgood, Jr.
Microelectronics Science Laboratory
Department of Electrical Engineering
Columbia University
Seeley W. Mudd Building
New York, NY 10027, USA

Professor Jürgen Parisi
Universität Oldenburg, Fachbereich Physik
Abt. Energie- und Halbleiterforschung
Carl-von-Ossietzky-Strasse 9-11
26129 Oldenburg, Germany

Professor Hans Warlimont
Institut für Festkörper-
und Werkstofforschung,
Helmholtzstrasse 20
01069 Dresden, Germany

ISSN 0933-033X

ISBN-10 3-540-00494-7 Springer Berlin Heidelberg New York

ISBN-13 978-3-540-00494-3 Springer Berlin Heidelberg New York

Library of Congress Cataloging-in-Publication Data

This work is subject to copyright. All rights are reserved, whether the whole or part of the material is concerned, specifically the rights of translation, reprinting, reuse of illustrations, recitation, broadcasting, reproduction on microfilm or in any other way, and storage in data banks. Duplication of this publication or parts thereof is permitted only under the provisions of the German Copyright Law of September 9, 1965, in its current version, and permission for use must always be obtained from Springer. Violations are liable to prosecution under the German Copyright Law.

Springer is a part of Springer Science+Business Media.
springeronline.com

© Springer-Verlag Berlin Heidelberg 2005
Printed in Germany

The use of general descriptive names, registered names, trademarks, etc. in this publication does not imply, even in the absence of a specific statement, that such names are exempt from the relevant protective laws and regulations and therefore free for general use.

Typesetting by the editors
Production: PTP-Berlin Protago-TeX-Production GmbH, Berlin
Cover concept: eStudio Calamar Steinen
Cover production: *design & production* GmbH, Heidelberg

Printed on acid-free paper SPIN: 10906514 57/3141/du 5 4 3 2 1 0

Preface

Ten years after I wrote the first Edition of this book, the situation surrounding hydrogen is dramatically changed. A growing consensus on the possible role of hydrogen in future energy technology has incited worldwide efforts for the development of new hydrogen-storage materials and their application to rechargeable batteries and fuel cells.

Meanwhile, research in the basic properties of metal-hydrogen systems which this book addresses has also been advanced, more quietly but significantly. High-pressure experiments have unraveled new features of elemental hydrogen (a number of different quantum phases of solid H_2 and metallization of liquid H_2) as well as of many metal-hydrogen systems (superabundant vacancy formation, phase diagrams over wide p - x - T ranges). The quantum character (the quantum atomistics) of interstitial hydrogen atoms has come to be more thoroughly elucidated, and culminated in the complete description of quantum diffusion over the whole temperature range.

In order to incorporate these new developments in a consistent way, the previous Edition has been revised substantially, both in depth and breadth, especially in regard to high-pressure experiments and quantum-atomistic properties. Thus, many new critically evaluated data have been included, and some 300 references are added. Also, very recent topics, just looming out in this and closely related areas, are added as Appendices. It is my belief that this revised Edition should help envisage the cleanest picture of the metal-hydrogen system presently available, and arouse a renewed interest of the readers in this ever fascinating field.

The revision of this book has been supported by many colleagues and friends; K. Aoki for hydrogen-induced amorphization, D.K. Ross for neutron scattering, H. Wipf and R. Kadono for diffusion, P. Vajda for rare-earth hydrides and hydrogen-defect interactions, P. Herzog for the theory of rare-earth hydrides, and S. Tsuneyuki for the theory of elemental hydrogen, just to name a few. Above all, I have been greatly benefited by the kind assistance of P. Vajda, who has devoted the labors of reading all the chapters, one after another, and provided valuable comments and advice. I wish to express my sincere thanks to all these colleagues, with whose assistance this book has been brought to the present form.

Tokyo, September 2004

Yuh Fukai

Preface to the First Edition

I think it is expedient here to clearly specify the readership for whom this book is intended. Some readers might infer from the title that this is a data book convenient for occasional reference purposes. Most of the data on the bulk properties and a comprehensive list of publications are indeed compiled here, and will be found useful as they are. The primary purpose of the book is, however, rather to provide a coherent and consistent description of the basic bulk properties of the metal–hydrogen system, ranging from macroscopic properties such as solubilities and phase diagrams to microscopic properties such as atomistic states and diffusion. The emphasis has been placed on the physics of how these properties actually come about. This structure of the book is considered to be useful, and even necessary, not only for physicists but also for researchers interested in the materials-science aspects of the system. Who could have anticipated that the solubility of hydrogen in iron reaches a level as high as $[H]/[Fe] \approx 1$ under a hydrogen pressure of 10 GPa; who could have anticipated that the diffusivity of hydrogen in metals increases at low temperatures; who could unravel the mechanism of “cold” fusion (if this indeed exists), without a basic understanding of the metal–hydrogen system? Obviously, these problems are not only of academic interest but also have profound technical implications.

To be more specific, this book covers the following topics: phase relations of the metal–hydrogen system over wide ranges of pressures (up to several hundred GPa), temperature (up to ~ 2000 K), and composition (from pure metal to pure hydrogen); the site preference and quantum-mechanical states of interstitial hydrogen atoms; diffusion behaviors and mechanisms due to quantum-mechanical tunneling. A brief description is also given of the electronic structure that underlies these properties.

The manuscript was completed and sent to the publisher for review, but was later revised to a large extent to include the referee’s comments and the developments made in this area since then. Some of them, for example, the metallization of elemental hydrogen, have been included in the text, but others are given in the Addenda at the end of Chap. 5.

Although our knowledge of the metal–hydrogen system is constantly increasing, this book should provide a sound basis for understanding future developments for many years to come and should serve as a lasting and useful

VIII Preface to the First Edition

guide for scientists and engineers interested in the fundamentals and/or applications of the system.

I dedicate this book to those of my colleagues who have actively participated in this area of research. Also, I thank H. Sugimoto for his critical reading, Y. Saito for his assistance in the preparation of the manuscript and, finally, the Iketani Science and Technology Foundation for its financial support during some phases of the work.

Tokyo, March 1992

Yuh Fukai

Contents

1	Hydrogen	1
1.1	Molecules	1
1.2	Description as an Ideal Gas	5
1.3	Some Characteristic Properties of Hydrogen	6
2	Phase Diagrams and Statistical Thermodynamics of Binary M–H Systems	9
2.1	Introduction to Phase Diagrams	9
2.2	Formation of Solid Solutions	14
2.2.1	Low Concentrations: Ideal Solution	14
2.2.2	High Concentrations: Effects of Interactions Between H Atoms	21
2.3	Spinodal Decomposition	27
2.4	Formation of Hydrides	30
2.4.1	Structure of Hydrides	30
2.4.2	Thermodynamics of Hydride Formation	36
2.4.3	Terminal Solubility	42
2.5	Effects of Hydrogen on the Relative Phase Stability	50
3	Hydrogen in Alloys	55
3.1	Effects of Alloying on the Solubility	55
3.2	Effects of Alloying on the Terminal Solubility	59
3.3	Hydrogen–Solute Interaction: Trapping and Blocking	63
3.4	Hydrogen in Ordered Alloys	68
3.5	Hydrogen in Amorphous Alloys	71
3.5.1	Thermodynamical Properties of Hydrogen in Amorphous Alloys	72
3.5.2	Site-Energy Distribution	74
3.5.3	A Structural Model of Hydrogen Absorption in Amorphous Alloys	79
3.5.4	Amorphization Induced by Hydrogenation	84

4 Metal–Hydrogen System

Under Extended p, T Conditions	91
4.1 Hydrogen Under High Pressures	91
4.1.1 High-Pressure Phases	91
4.1.2 Equation of State and Thermodynamical Quantities ..	96
4.2 Volume of Hydrogen in Metals	104
4.3 Solubility Enhancement	
Under High Hydrogen Pressures–Calculations	113
4.4 Phase Relation	
Under Extended p , T Conditions–Experiments	121
4.4.1 Transition Metal – Hydrogen Systems; Individual Cases	121
4.4.2 General Features of Phase Relations	135
Appendix 4A. Iron–Water Reaction Under High p , T Conditions, and Its Implication for the Evolution of the Earth	140

5 Atomistic States of Hydrogen in Metals 147

5.1 Site Location by the Channeling Method	148
5.2 X-ray Bragg and Diffuse Scattering	152
5.3 Neutron Diffraction–Elastic Neutron Scattering	159
5.4 Inelastic Neutron Scattering	164
5.4.1 Optic-Mode Vibration of Hydrogen Atoms	165
5.4.2 Local Potential Field for Hydrogen	175
5.4.3 Determination of Hydrogen Wave Functions by Inelastic Neutron Scattering	181
5.4.4 Band-Mode Vibration of Hydrogen Atoms	183
5.5 Stress-Induced States	187
5.6 Trapped States	193
5.6.1 Mutual Trapping–Hydrogen Pairs in Some Rare-Earth Metals	194
5.6.2 Trapping by Impurity Atoms	197
5.6.3 Trapping by Defects	202
5.6.4 Formation of Superabundant Vacancies	216
5.7 Theory of the Atomistic State of Hydrogen in Metals	229
5.7.1 Theory of Self-Trapped States–Empirical Potential Approach	231
5.7.2 Theory of β Phase of the Vanadium–Hydrogen System	244
5.7.3 Theory Based on Non-Empirical Potentials	249
5.8 Tunneling States	258
5.8.1 Two-Site and Four-Site Tunneling of Hydrogen Atoms	259
5.8.2 Theory of Tunneling States in Metals	274
Appendix 5A. Formation of Entangled States of Hydrogen in Metals	283
Appendix 5B. Enhanced Electron Screening in d-d Fusion Reactions in Metals	294

6	Diffusion	303
6.1	Introduction	303
6.1.1	Diffusion Coefficients	303
6.1.2	Diffusion of Interstitial Hydrogen in Metals	307
6.2	Experimental Methods	311
6.2.1	Nuclear Magnetic Resonance and Related Methods ...	312
6.2.2	Quasi-Elastic Neutron Scattering	320
6.2.3	Other Methods.....	324
6.3	Experimental Results on Diffusion Coefficients	326
6.4	Experimental Results on the Diffusion Mechanism	336
6.4.1	Elementary Jumps	336
6.4.2	Effects of Interaction Between Hydrogen Atoms	350
6.4.3	Atomic Jumps Over Inequivalent sites	360
6.5	Theoretical Considerations on the Diffusion Mechanism	373
6.5.1	Overview	373
6.5.2	Diffusion Mechanisms in the Low Temperature Region: Tunneling in the Polaron Band	374
6.5.3	Diffusion Mechanisms in the High Temperature Region: Phonon-Assisted Tunneling	382
6.6	Critical Analysis of the Experimental Data in Terms of the Quantum Theory of Diffusion	387
6.6.1	Diffusion of Positive Muons and Hydrogen Isotopes at Low Temperatures: Tunneling in the Polaron Band .	387
6.6.2	Diffusion of Positive Muons and Hydrogen Isotopes at High Temperatures: Phonon-Assisted Processes ...	389
	Appendix 6A. Tunneling Chemical Reaction in Solid Hydrogen ...	395
	Appendix 6B. A Muonium Atom in the Bloch State	397
7	Electronic Structure	401
7.1	Hydrogen-Induced Changes in the Electronic Structure of Metal Hydrides	401
7.2	Energies of Hydride Formation	407
7.2.1	Band-Theoretic Calculation.....	407
7.2.2	Effective-Medium Theory.....	410
7.3	Hydrogen–Metal Interaction Potential.....	412
7.4	The Metal-Insulator Transition in Rare-Earth Hydrides	415
7.5	Electronic Structure of Hydrogen Under High Pressures	421
7.5.1	Solid Hydrogen at Low Temperatures	421
7.5.2	Fluid Hydrogen at High Temperatures	426
7.5.3	Superconductivity	432

XII Contents

References	439
List of Symbols	479
List of Abbreviations	485
Index	487

1 Hydrogen

There are three isotopes of hydrogen: protium, deuterium, and tritium. Some of the fundamental properties of these isotopes, including nuclear, atomic, and molecular ones, are listed in Table 1.1 [1.1–1.5] for convenience of later reference.

The elemental hydrogen exists in several different forms; as a monatomic gas at low densities, diatomic molecules under ordinary conditions, a metallic conductor at high pressures, and as an ionized plasma at very high temperatures. All these states are realized in different places in the Solar System, but on Earth, the elemental hydrogen usually exists only as molecules. In this chapter, we deal exclusively with the molecular form of elemental hydrogen.

1.1 Molecules

Molecular hydrogen is a very stable entity. Its electronic ground state, the singlet state $^1\Sigma_g^0$ has an energy lower than two atoms by $E_0 = 4.748\text{ eV}$ (the binding energy), and the equilibrium separation is very short, being $r_0 = 0.7416\text{ \AA}$. The electronic energy as a function of internuclear separation r (the adiabatic potential) and energy levels of the stretching vibration are shown in Fig. 1.1 [1.6].

For an H_2 molecule, the zero-point vibration energy is $E_v^0 = 0.372\text{ eV}$, and accordingly, the dissociation energy is

$$E_d = E_0 - E_v^0 = 4.476\text{ eV} . \quad (1.1)$$

The dissociation energy becomes isotope-dependent due to the isotope dependence of E_v^0 . The energy of rotation along the two axes perpendicular to the molecular axis is smaller in comparison.

Due to large excitation energies of the stretching vibration, most of the molecules are in the ground state ($n_v = 0$) at ordinary temperatures ($T \leq 2000\text{ K}$), and its partition function can be approximately written as

$$Z_v = \sum_{n_v=0}^{\infty} e^{-E_v^{n_v}/kT} \cong e^{-E_v^0/kT} \quad (1.2)$$

The partition function for the rotational motion

Table 1.1. Some properties of hydrogen isotopes

	H	D	T
Nucleus			
Nuclear mass [M_p]	1.000	1.998	2.993
Nuclear spin	1/2	1	1/2
Nuclear moment [μ_B]	2.7928	0.8574	2.9788
Atom ($1s^1$)			
Ionization energy [eV]	13.5989	13.6025	13.6038
Molecule ($^1\sum_g^+$)			
Binding energy E_0 [eV]	4.748	4.748	—
Dissociation energy E_d [eV]	4.478	4.556	4.59
Vibrational energy ^a E_v^0 [eV]	0.5160	0.3712	0.3402
Rotational energy ^a B_r [eV]	7.32×10^{-3}	3.70×10^{-3}	—
Gas-liquid (normal)			
Critical point			
Temperature [K]	32.98	38.34	40.44
Pressure [MPa]	1.298	1.649	1.906
Boiling point at 0.1 MPa			
Temperature [K]	20.41	23.67	25.04
Latent heat [J mol ⁻¹]	913	1235	1394
Gas-liquid-solid (normal)			
Triple point			
Temperature [K]	13.96	18.73	20.62
Pressure [kPa]	7.20	17.15	21.60

^aCalculated from lowest excitation energies.

$$Z_r = \frac{1}{2} \sum_{J_r=0}^{\infty} (2J_r + 1) e^{-E_r^J/kT} \quad (1.3)$$

$$E_r^J = B_r J_r (J_r + 1) \quad J_r = 0, 1, 2, \dots \quad (1.4)$$

can be approximately given by

$$Z_r \cong \frac{kT}{2B_r} = \frac{4\pi^2 I_r kT}{h^2} \quad (1.5)$$

where $I_r = \frac{1}{2} M r_0^2$ is the moment of inertia of the molecule.

One important issue regarding the rotational motion is the existence of two distinct states, ortho(o)- and para(p)-states. The distinction comes from the requirement that the wave function of a molecule must be antisymmetric

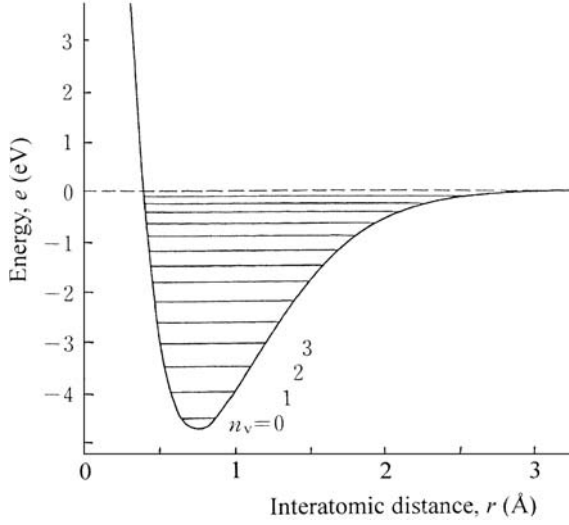


Fig. 1.1. Adiabatic potential and energy levels of the stretching vibration of H_2 molecule [1.6]

with respect to the interchange of the space coordinates of the two constituent fermions, and symmetric for interchange of bosons. Since the wave functions of the electronic ground state and vibrational states are symmetric with the interchange of the two nuclei, the symmetry requirement must be satisfied by the product of rotational and nuclear wave functions. In the case of protons and tritons (fermions) with nuclear spin $I = 1/2$, antisymmetric (odd J_r) and symmetric (even J_r) rotational states must be coupled with symmetric and antisymmetric nuclear states, respectively. These two groups of molecules are called o- H_2 (o- T_2) and p- H_2 (p- T_2), respectively. In the case of deuterons (bosons) with nuclear spin $I = 1$, on the other hand, they must be coupled with antisymmetric and symmetric rotational states, respectively. The energies and wave functions of rotational states of an H_2 molecule are shown in Fig. 1.2. Note, in particular, that hydrogen molecules do not always look like dumbbells; molecules in the $J_r = 0$ rotational state, the ground state of p- H_2 (p- T_2) and o- D_2 , are spherically symmetric.

As there are $(2I+1)(I+1)$ symmetric and $(2I+1)I$ antisymmetric states for nuclear spin I , the population ratio of o- H_2 (o- T_2) and p- H_2 (p- T_2) in thermal equilibrium is given by

$$\frac{N_o}{N_p} = \frac{(I+1) \sum_{J_r=\text{odd}} q_r^J}{I \sum_{J_r=\text{even}} q_r^J}, \quad (1.6)$$

$$q_r^J = (2J_r + 1) e^{-E_r^J/kT}. \quad (1.7)$$

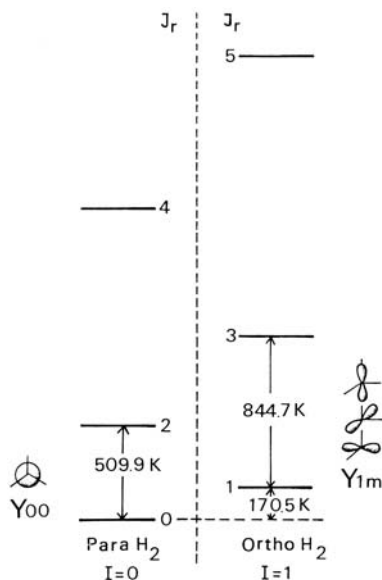


Fig. 1.2. Energy and wave functions of rotational states of para-H₂ and ortho-H₂ molecule. I , the total nuclear spin, is 0 or 1, J_r , the rotational quantum number is 0, 1, 2, ... [1.2]

As a function of temperature this ratio starts from zero at $T = 0$, and increases monotonically to $(I + 1)/I$ at high temperatures (already 2.990 at 300 K). In the case of D₂, the corresponding expression becomes

$$\frac{N_p}{N_o} = \frac{I \sum_{J_r=\text{odd}} q_r^J}{(I + 1) \sum_{J_r=\text{even}} q_r^J}, \quad (1.8)$$

and approaches 0.5 at high temperatures (0.4999 at 200 K). Thus, at room temperature and above, H₂ (T₂) gas can be regarded as a 3:1 mixture of o-H₂ (o-T₂) and p-H₂ (p-T₂), and D₂ gas as a 2:1 mixture of o-D₂ and p-D₂. These mixtures are called normal hydrogens (n-H₂, D₂, or T₂).

Under ordinary circumstances, conversion between ortho and para states is so slow that the ortho-para ratio can be regarded to be constant during cooling to low temperatures. This slow ortho-para conversion acts as an internal heat source that causes evaporation of hydrogen at low temperatures. In order to attain the thermal-equilibrium population in the course of cooling, a gas mixture must be placed in contact with some catalyst, such as charcoal or nickel-silica.

In view of the apparent simplicity of the hydrogen molecule, it may come as a surprise to learn that the complete assignment of the energy-level structure was achieved rather recently – in 1970s. Since then, however, molecular

hydrogen has been the prototype for the investigation of the electron–nuclear coupling, namely, how electronic energy is converted to the nuclei’s vibrational and rotational energy, and vice versa. The study of these intramolecular interactions provides a physical basis for the chemical reactions involving hydrogen. The recent advances of the molecular physics of hydrogen were described by Dehmer [1.7].

1.2 Description as an Ideal Gas

The molecular hydrogen exists in three different states, gas, liquid and solid, as shown in Fig. 1.3 [1.8]. The triple point is located at $T_t = 13.96$ K and $p_t = 7.20$ kPa, and the gas–liquid critical point at $T_c = 32.98$ K and $p_c = 1.298$ MPa.

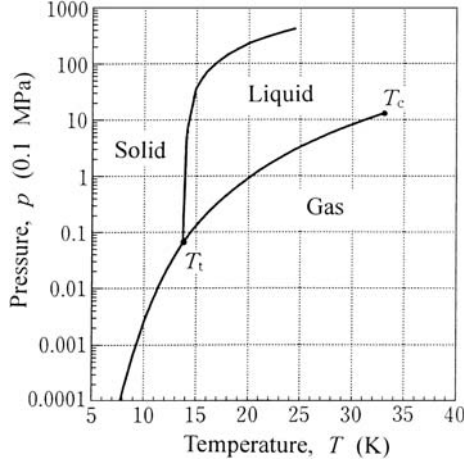


Fig. 1.3. p – T phase diagram of hydrogen. T_t and T_c signify the triple point and the critical point, respectively [1.8]

Under ordinary conditions adopted for the investigation of M–H alloys ($T > 300$ K, $p < 10$ MPa), hydrogen can be described reasonably well as an ideal gas. The chemical potential (per molecule) is given by

$$\mu^g = kT \ln \frac{p}{p_0(T)} - E_d \quad (1.9)$$

$$p_0(T) = \frac{(4\pi M kT)^{3/2} kT \cdot 4\pi^2 I_r kT}{h^5} . \quad (1.10)$$

Here, the energy has been measured from two dissociated H atoms. Then, the enthalpy and entropy of gaseous hydrogen per molecule can be obtained as

$$h^g = \frac{7}{2}kT - E_d \quad (1.11)$$

$$s^g/k = \frac{7}{2} - \ln \frac{p}{p_0(T)} . \quad (1.12)$$

It is often convenient to isolate the pressure dependence of μ^g and s^g , and express these quantities by taking the gas of pressure $p_0 = 0.1$ MPa (1 atom) as standard. Thus,

$$\mu^g - \mu^{g0} = -T(s^g - s^{g0}) = kT \ln \frac{p}{p_0} \quad (1.13)$$

$$\mu^{g0} = -kT \ln \frac{p_0(T)}{p_0} - E_d \quad (1.14)$$

$$s^{g0}/k = \frac{7}{2} + \ln \frac{p_0(T)}{p_0} . \quad (1.15)$$

For convenience, we may write

$$\frac{p_0(T)}{p_0} = \left(\frac{T}{T^*} \right)^{7/2} ; \quad T^* = 9.20 \text{ K} . \quad (1.16)$$

It must be recognized that deviations from the ideal-gas behavior, though small, may not be totally negligible for some purposes. At 300 K and 10 MPa, the actual volume V is larger than the ideal-gas volume V_{id} by 6.0%, which leads to the increase of the chemical potential

$$\Delta\mu = \int_0^p (V - V_{id}) dp \quad (1.17)$$

by 1.1% over the ideal-gas value (see Table 4.1). Thermodynamical properties of molecular hydrogen under more extended p , T conditions are described in Chap. 4.

1.3 Some Characteristic Properties of Hydrogen

Hydrogen as an element has various unique features, including in particular its reactivity with many different elements, even at very low temperatures in some cases. The anomalous dependence of the reactivity and various other properties on temperature and isotope mass have been taken to be the evidence that some quantum tunneling processes are involved. In broad terms, these unique features can be ascribed to (a) a medium value of the electronegativity, (b) a small atomic size, and (c) a small nuclear mass. In the following, these points are discussed in slightly more detail to bring out some of the most characteristic features of the M–H system.

(a) The Medium Electronegativity

The electronegativity describes the degree of easiness of attaching an electron to and/or difficulty of detaching an electron from a neutral atom, and serves as a useful measure for predicting the type of bonds to be formed between a pair of elements. Thus, if $\chi_A < \chi_B$ holds for the electronegativity of elements A and B, one electron will be transferred from A to B to form A^+B^- . If, instead, $\chi_A \approx \chi_B$, a chemical bond without a charge transfer, either a covalent bond or a metallic bond, is likely to form.

The fact that hydrogen has a medium value of the electronegativity [1.9] indicates that it may form various kinds of chemical bonds with various elements. An implication of this fact to the M–H system is discussed in the introduction to Chap. 2.

(b) The Small Size

One might consider intuitively that a hydrogen atom should be small in size because it has only a small number of electrons around. The situation is in fact not so simple. Of the three charged states of hydrogen, an H^- ion has an ionic radius of 2.1 Å, which is large and comparable to heavy halogens (1.95 Å for Br^- and 2.16 Å for I^-). The size of a neutral atom H^0 as measured by the Bohr radius is $a_B = 0.529$ Å. For an H^+ ion, the ionic radius of Shannon and Prewitt is $-(0.18 \sim 0.38)$ Å depending on the number of surrounding anions [1.10,1.11]. Considering that an H^+ ion is in fact a bare proton, it may appear strange to speak about its size, especially its negative value. What this actually implies is that the presence of a proton causes contraction of the neighboring bonds by the effect of hydrogen bonding.

When a hydrogen atom is placed in a metallic environment, conduction electrons screen the proton charge at short distances to make it appear as a neutral atom. Electronic calculations performed for hydrogen in transition metals have shown that 1s-like orbitals around the proton are strongly hybridized with d-orbitals of surrounding M-atoms to form bonding states (see Chap. 7). Thus, the apparent small size of an H atom, that allows it to enter narrow interstitial sites in metal lattices, is due in part to the flexibility of surrounding electronic states. A small positive charge on a proton leaves the surrounding electrons easily adaptable to given circumstances.

(c) The Small Nuclear Mass

In a molecular form, a small nuclear mass combined with strong binding forces makes the vibrational energy levels widely spaced and isotope dependent. Thus, the isotope dependence manifests itself in the heat of dissociation and many other thermodynamical properties, as shown in Table 1.1.

In alloys comprising M- and H-atoms of large mass differences, the frequency distribution of the coupled oscillator system comes to be separated into a low-frequency component (acoustic-mode vibrations) very similar to

the lattice vibration of the host metal, and a high-frequency component (optic-mode vibration) of interstitial H atoms. In comparison to typical vibration energies of M-lattices, the vibration energies of interstitial H atoms are usually much higher, being $50 \sim 200$ meV (see Chap. 5). These values are an order of magnitude smaller than in a molecule but, being comparable to thermal energies at ordinary temperatures, affect the stability of phases and/or the preference of the type of interstitial sites.

Another important aspect of the H vibration is the finite extension of its wave functions. In the adiabatic approximation, where an H atom is viewed as executing a vibrational motion in the potential field of slowly moving M atoms, the H atom may be described, approximately, by wave functions of harmonic oscillators. The ground-state wave function has a spatial variation of $e^{-(x/x_0)^2}$, where x_0 is given by $h/\sqrt{2\pi M \Delta E}$. Substituting the proton mass and the excitation energy $\Delta E = 0.1$ eV, we obtain $x_0 = 0.29$ Å. This value is comparable to the spatial extension of the H-1s orbital $a_B = 0.529$ Å, and by convolution, leads to an effective size of ~ 0.8 Å.

These estimates of the spatial extension of the wave function immediately point to the possibility of tunneling of an H atom between interstitial sites. In bcc metals, in which the spacing between neighboring tetrahedral sites is ~ 1.0 Å, evidence of tunneling processes was indeed observed. The tunneling of H atoms is believed to become much more important on the surface of metals where the undulation of potentials is believed to be much smaller. The occurrence of tunneling processes is one of the most important consequences of the light mass of H.

A quantum-mechanical description of interstitial H atoms in metals is one of the central issues of this book, and elucidated in Chaps. 5–6.

2 Phase Diagrams and Statistical Thermodynamics of Binary M–H Systems

Hydrogen reacts with many different elements to form various compounds, which can be classified conveniently according to the type of chemical bonds involved. With alkali and alkali-earth elements, which have small electronegativities, hydrogen forms ionic compounds (M^+H^- and $M^{2+}H_2^-$) called saline hydrides. To atoms or radicals having large electronegativities, such as halogens, some chalcogens, OH, NO_3 , SO_4 , etc, hydrogen donates its electron to become H^+ , and forms hydrogen-bonded molecular crystals (or liquids). Elements of electronegativities comparable to hydrogen are divided into three groups: Most of Group III–V non-metallic elements, as well as light simple metals of Group I–IV, form covalently bonded molecules or crystals, whereas most heavy simple metals do not form any compounds with hydrogen.

There still remain a large number of elements having comparable electronegativities, namely, d-band metals, lanthanides and actinides, which form metallic hydrides. It is these transition metal hydrides that we address exclusively in this book. Properties of the other types of metal hydrides have been elucidated in a number of literatures [2.1–2.3].

Metallic hydrides, by nature of metallic bonding, commonly exist over extended ranges of nonstoichiometric compositions. These hydrides can be called interstitial alloys, where interstitial sites of metal lattices are occupied by hydrogen (H) atoms, randomly at high temperatures and in some regular ways at lower temperatures. Frequently, metal lattices themselves undergo structural changes to accommodate a larger number of H atoms interstitially. Thus, a variety of phases can exist in M–H binary alloys.

It is intended in this chapter to elucidate the basic thermodynamic properties of the M–H system that determine the phase diagrams. Although many (most) of the phase diagrams of binary M–H systems are given at appropriate places for illustrative purposes, the reader is referred to more extensive compilations [2.3–2.5] for details of individual cases.

2.1 Introduction to Phase Diagrams

Some examples of phase diagrams are shown in Figs. 2.1–2.4. In these diagrams, the composition is written as a ratio of the number of H atoms to the number of M atoms, $x = [H]/[M]$, as is usually convenient for interstitial

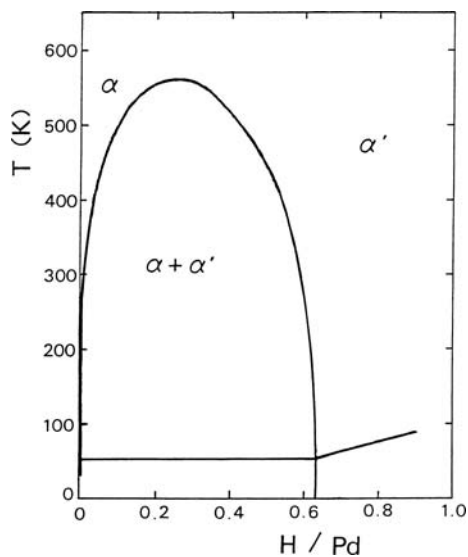


Fig. 2.1. Phase diagram of the Pd-H system [2.6,2.9,2.141]. The two-phase boundary in the Pd-D system is very similar. At low temperatures and high H concentrations, the linear phase boundary with a positive slope was recently established by specific-heat measurements [2.141]. No proper name has been given to the low-temperature phase. Occurrence of two different ordered structures along the line was also reported [2.7-2.9]

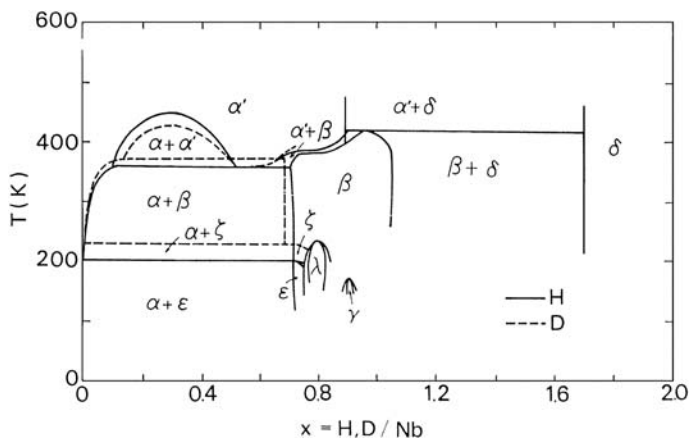


Fig. 2.2. Phase diagrams of Nb-H and Nb-D systems [2.10-2.12]

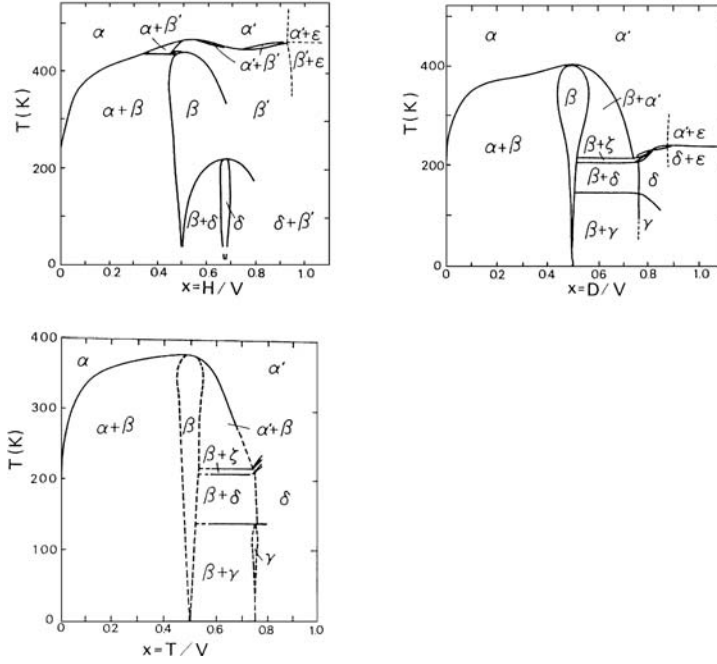


Fig. 2.3. Phase diagrams of V-H, V-D, and V-T systems [2.9,2.13,2.14]

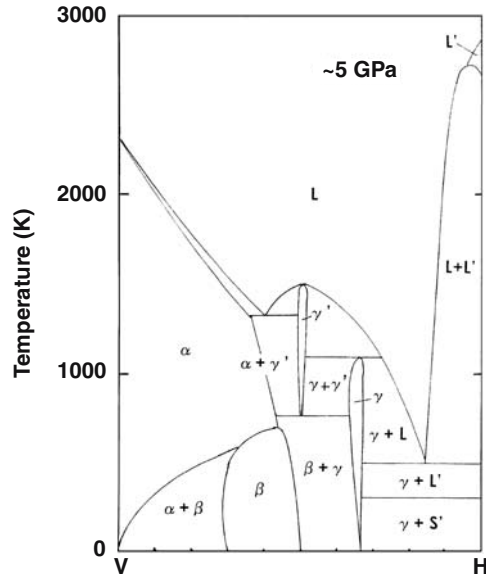


Fig. 2.4. Phase diagram of the V-H system under high pressure (~ 5 GPa) [2.15]

alloys; hence, we call them x - T diagrams. Characteristic features of these diagrams include: (1) the spinodal decomposition in Pd-H and Nb-H, D systems; (2) the occurrence of many ordered structures at lower temperatures; (3) the isotope dependence most conspicuous in V-H, D, T systems; and (4) the lowering of the melting point observed in the V-H system.

Before going into a discussion of these features, it may be appropriate here to make the following comments on the implication and use of x - T diagrams. Unlike the case of binary alloys formed between solid elements, under ordinary circumstances, we cannot change the temperature of a hydride specimen without causing concomitant changes in composition. We must recognize that the exchange of hydrogen between a specimen and the surrounding atmosphere is of crucial importance in treating M-H systems. The equilibrium concentration of hydrogen in a specimen is, in fact, a unique function of the temperature and pressure of the surrounding H_2 gas.

Thus, in constructing the phase diagram of the Pd-D system (Fig. 2.1), for example, we must make a series of isothermal measurements of the equilibrium composition of a specimen as a function of the pressure of the surrounding D_2 gas, and plot the result in the form of Fig. 2.5, which we call the p - x - T diagram. A phase boundary can be drawn by connecting the inflection points of different isotherms. In order to appreciate the meaning of the diagram, let us follow the isotherm of, say, 200°C . The concentration of D atoms in the specimen is increased gradually with increasing pressure of D_2 gas, except in the region of average concentrations between 0.1 and 0.5, where the absorption proceeds without a noticeable increase of the gas pressure. The appearance of a plateau in the isotherm implies that two hydride (deuteride) phases coexist in this region. The Gibbs phase rule states that in two-component systems existing in three different phases simultaneously (two hydride phases and D_2 gas), only one parameter (say, temperature) is left at our disposal and all the rest, including the hydride composition(s) and gas pressure, are determined uniquely. When hysteresis effects are observed in repeated heating and cooling cycles, as in Fig. 2.5, desorption branches are usually taken to represent the equilibrium condition more closely.

In most other transition metals, surface states impermeable to hydrogen are readily formed on exposure to air and help to confine hydrogen in the interior of the specimens. It is only after heating a specimen to some specific temperatures in vacuum or H_2 gas (activation treatment) that the surface becomes permeable to hydrogen. This means that, in these hydrides, the original composition of a specimen can be maintained in the course of temperature variation, which makes x - T diagrams practically more useful. If, conversely, one wishes to measure p - x - T relations in these hydrides, one has to make sure that the solid-gas equilibrium is attained.

A common practice for activating powder specimens is to repeat heating-cooling cycles to 400 – 500°C a sufficient number of times (see, e.g., [2.16]). In the case of bulk specimens, it is more convenient to cover the surface with a

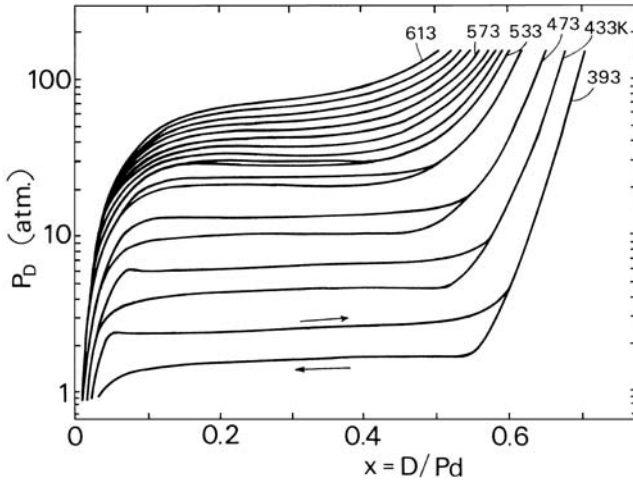


Fig. 2.5. Pressure–composition isotherms of the Pd–D system. The isotherms above 533 K are at 10 K intervals. Note the disappearance of hysteresis above the critical temperature, $T_c = 536 \pm 1$ K [2.6]

hydrogen-transparent Pd layer. Three different methods have been employed for this purpose: sputter-coating (ion-plating) of a clean activated surface (e.g., [2.17]), electrodeposition and subsequent annealing [2.18], and welding of a thin Pd foil [2.19].

Since the bulk diffusion of hydrogen proceeds rather rapidly, the kinetics of solid–gas equilibrium is usually determined by penetration through surface barriers. The equilibrium distribution inside a specimen can be achieved more easily. The mechanism of absorption kinetics and the nature of hydrogen-impermeable surface states are not yet thoroughly understood.

It may be added that the phase diagram shown in Fig. 2.4 was obtained by sealing specimens in some solid medium under such a high pressure that all the H atoms could remain confined to within the specimens even at elevated temperatures. As the pressure here is more than three orders of magnitude higher than in the experiment shown in Fig. 2.5, the effect of pressure itself on the relative phase stability is no longer negligible. This can be readily observed by comparing Fig. 2.4 with Fig. 2.3.

In the following Sects. 2.2–3.5, various factors determining the relative phase stabilities are described largely on a macroscopic, phenomenological level. Discussions based on statistical thermodynamics are made, but only to the extent that no detailed knowledge of the atomistic structures of the individual cases is needed. Thus, the problem of site occupancy which underlies the determination of the configurational entropy is only briefly touched on. A more detailed description of it is deferred to Chap. 5. Likewise, interatomic interactions are introduced as parameters for describing phase relations; their physical origin will be discussed more fully in Chap. 7. A detailed account of

the phase relation at high pressures and temperatures encompassing a wide composition range is given in Chap. 4, including the results recently obtained in our laboratory. In so doing, it is attempted to place hydrogen, a common end member of M–H systems, in its proper perspective.

2.2 Formation of Solid Solutions

2.2.1 Low Concentrations: Ideal Solution

At a given temperature the solubility of hydrogen in a metal increases with increasing pressure of H_2 gas. Figure 2.6 shows the p – x – T relation for the V–H system. At low hydrogen concentrations all isotherms have a common slope, showing that the relation

$$x \propto \sqrt{p} \quad (2.1)$$

holds¹. This relation, called Sieverts law, is known to hold for many other M–H systems as well. As shown immediately below, the square-root dependence on pressure comes from the fact that H_2 molecules are dissociated into atoms while getting dissolved in metals. Since the temperature dependence of the solubility shows a thermal-activation type of behavior, the overall expression for the solubility takes the form

$$x = \sqrt{\frac{p}{p_0}} e^{\Delta S_s/k} e^{-\Delta H_s/kT}. \quad (2.2)$$

ΔS_s is called the entropy of solution referred to the H_2 gas of pressure p_0 and temperature T , and ΔH_s the enthalpy (heat) of solution. Some selected values of ΔH_s and ΔS_s are given in Table 2.1. The values listed are those obtained from the Arrhenius plot of the solubility data at low H concentrations, and are labeled as ΔH_s^0 and ΔS_s^0 . A more extensive compilation was made by *Mueller et al.* [2.3], *Fromm and Gebhardt* [2.20], *Fromm and Hörz* [2.21], *Wenzl* [2.22], and, more recently, by *Griessen and Riesterer* [2.25]. Roughly speaking, ΔH_s and ΔS_s signify the change of enthalpy and entropy, respectively, of an H atom in entering a metal lattice from the gas phase. The values of ΔH_s listed in Table 2.1 vary systematically across the Periodic Table (see also Fig. 7.7), which suggests that ΔH_s is determined by the gross electronic structure of the host metal. This point will be discussed in more detail in Sect. 7.2. Regarding ΔS_s , by far the major contribution is expected to come from the vanishing of the entropy of a gas, which, at $T = 300\text{ K}$ and $p = 0.1\text{ MPa}$, becomes $\Delta S_s \approx -s^g/2 = -7.8k$ (from (1.15)). Table 2.1 shows that the experimental values of ΔS_s are always close to this expectation.

¹ This relation is often written in the form $\sqrt{p} = K_s x$, and K_s is called the Sieverts constant.

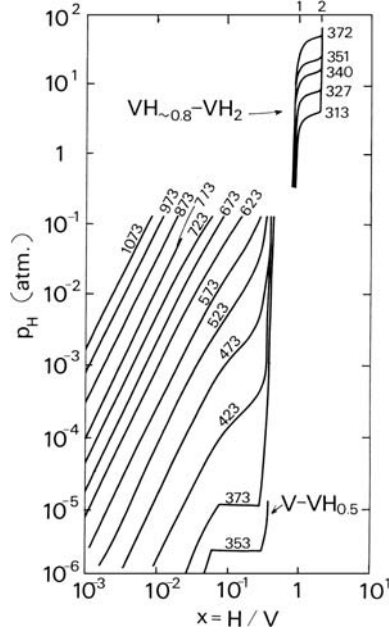


Fig. 2.6. Pressure–composition isotherms of the V–H system [2.16, 2.20]

In order to make clear the physical implication of the Sieverts law, let us consider the condition of thermal equilibrium between a solid solution and H_2 gas,



The condition is given by the equality of the chemical potential of hydrogen in the two phases,

$$\frac{1}{2}\mu^g = \mu^\alpha. \quad (2.4)$$

where μ^g is the chemical potential of gaseous hydrogen per molecule as defined in the previous section, and μ^α is that of hydrogen in the solid solution per atom. (A more rigorous treatment of the equilibrium condition should consider the equality of the chemical potentials of the metal species, as described in Sect. 2.4.2)

For a solid solution, the Gibbs free energy of a crystal containing n hydrogen atoms can be written as

$$G^\alpha = H^\alpha - TS^\alpha, \quad (2.5)$$

$$S^\alpha = S^{nc} + S^c, \quad (2.6)$$

$$S^c = k \ln \frac{N!}{n!(N-n)!}, \quad (2.7)$$

Table 2.1. Enthalpy and entropy of solution of hydrogen in metals, in the low-concentration limit

Metal	ΔH_s^0 [eV per atom]	$\Delta S_s^0/k$	T [°C]	Reference
Li	−0.54	−7	200–700	[2.22]
Mg	+0.22	−4	500	[2.20, 2.21]
Al	+0.70	−6	500	[2.22]
Sc	−0.94	−7	—	[2.23]
Y	−0.85	−6	—	[2.20, 2.21]
La (fcc)	−0.83	−8	—	[2.20, 2.21]
Ce (fcc)	−0.77	−7	—	[2.22]
Ti (hcp)	−0.55	−7	500–800	[2.22]
Ti (bcc)	−0.62	−6	900–1100	[2.22]
Zr (hcp)	−0.66	−6	500–800	[2.22]
Zr (bcc)	−0.67	−6	860–950	[2.22]
Hf (bcc)	−0.38	−5	300–800	[2.20, 2.21]
V	−0.28	−8	150–500	[2.20–2.22]
Nb	−0.35	−8	> 0	[2.22–2.24]
Ta	−0.39	−8	> 0	[2.22]
Cr	+0.60	−5	730–1130	[2.20, 2.21]
Mo	+0.54	−5	900–1500	[2.20, 2.21]
W	+1.1	−5	900–1750	[2.20, 2.21]
Fe (bcc)	+0.25	−6	< 900	[2.20, 2.21]
Ru	+0.56	−5	1000–1500	[2.20, 2.21]
Co (fcc)	+0.33	−6	1000–1492	[2.20, 2.21]
Rh	+0.28	−6	800–1600	[2.20, 2.21]
Ir	+0.76	−5	1400–1600	[2.20, 2.21]
Ni	+0.17	−6	350–1400	[2.20, 2.21]
Pd	+0.10	−7	−78–75	[2.20, 2.21]
Pt	+0.48	−7	—	[2.20, 2.21]
Cu	+0.44	−6	< 1080	[2.22]
Ag	+0.71	−5	550–961	[2.20, 2.21]
Au	+0.37	−9	700–900	[2.20, 2.21]
U(α)	+0.10	−6	< 668	[2.20, 2.21]

where S^c is the configurational entropy for distributing n atoms over N interstitial sites, and S^{nc} the non-configurational part of the entropy comprising vibrational and electronic contributions. We shall here separate the configurational entropy, and write

$$G^\alpha = G^{\alpha\text{nc}} - TS^c. \quad (2.8)$$

The chemical potential of a dissolved H atom is then obtained as

$$\mu^\alpha = \frac{\partial G^\alpha}{\partial n} = \frac{\partial G^{\alpha\text{nc}}}{\partial n} - T \frac{\partial S^c}{\partial n} \quad (2.9a)$$

$$= \mu^{\text{anc}} + kT \ln \frac{x}{r-x} \quad (2.9b)$$

$$= h^\alpha - Ts^{\text{anc}} + kT \ln \frac{x}{r-x}, \quad (2.9c)$$

where h^α is the partial enthalpy, s^{anc} the non-configurational part of the partial entropy of hydrogen in the solid solution, and r the number of interstitial sites per M atom, $r = N/N_0$.

The exact definition of the heat of solution, namely, the enthalpy change when one H atom is dissolved from the gas phase into a metal, should be

$$\Delta h_s = h^\alpha - \frac{1}{2}h^g. \quad (2.10)$$

The entropy of solution, on the other hand, is usually defined as the entropy change minus the term $-k \ln x$, i.e.,

$$\Delta s_s = s^{\text{anc}} + k \ln r - \frac{1}{2}s^g \quad (2.11)$$

for $x \ll r$.

The heat of solution thus defined can be determined by calorimetric measurements, as actually done for a number of systems [2.26–2.30].

In the determination of thermodynamical quantities from the pressure dependence of the solubility, the pressure-dependent term in the equilibrium condition has to be isolated:

$$\ln \frac{x}{r-x} = -\frac{\mu^{\text{anc}} - \frac{1}{2}\mu^g}{kT} \quad (2.12a)$$

$$= \frac{1}{2} \ln \frac{p}{p_0} - \frac{\mu^{\text{anc}} - \frac{1}{2}\mu^{g_0}}{kT}. \quad (2.12b)$$

A comparison of this expression with (2.2) leads to

$$\Delta H_s - T\Delta S_s = \mu^{\text{anc}} - \frac{1}{2}\mu^{g_0} - kT \ln r \quad (2.13)$$

for $x \ll r$. Thus, as long as the temperature dependence of the right-hand side can be written as $a - bT$, at least approximately, the Arrhenius plot of the equilibrium pressure should lead to $\Delta H_s = a$ and $\Delta S_s = b$. The quantities thus obtained do not necessarily have the meaning of enthalpy or entropy changes. A linear temperature-dependent term in the enthalpy, if it exists, cannot be distinguished from entropy. This statement applies not only to p - x - T but also to electrochemical measurements [2.31–2.33].

On the other hand, from the temperature dependence of solubility, the enthalpy and the entropy of solution can be determined separately. Under constant pressure, differentiation of the equilibrium condition (2.4) leads to

$$T \left(\frac{\partial \mu^\alpha}{\partial x} \right)_{p,T} \left(\frac{\partial x}{\partial T} \right)_p = T \left(s^\alpha - \frac{1}{2} s^g \right) \quad (2.14a)$$

$$= h^\alpha - \frac{1}{2} h^g . \quad (2.14b)$$

At low hydrogen concentrations, $x \ll r$,

$$\left(\frac{\partial \mu^\alpha}{\partial x} \right)_{p,T} = \left(\frac{\partial h^\alpha}{\partial x} - T \frac{\partial s^{\text{anc}}}{\partial x} \right)_{p,T} + kT \left(\frac{1}{x} + \frac{1}{r-x} \right) \quad (2.15a)$$

$$\approx \frac{kT}{x} , \quad (2.15b)$$

we obtain the relation

$$\Delta h_s = - \left(\frac{\partial \ln x}{\partial (1/kT)} \right)_p . \quad (2.16)$$

Once Δh_s is known, Δs_s can be obtained from

$$\frac{\Delta s_s}{k} = \frac{\Delta h_s}{kT} + \ln x . \quad (2.17)$$

These relations mean that Δh_s and Δs_s at a given temperature can be determined from the slope and intercept, respectively, of the tangential line of the Arrhenius plot of the solubility at that temperature.

An example of the Arrhenius plot of solubility data for H and D in Pd is shown in Fig. 2.7. [2.34, 2.35]. The apparent curvature that exists at higher temperatures indicates that both Δh_s and Δs_s are temperature-dependent.

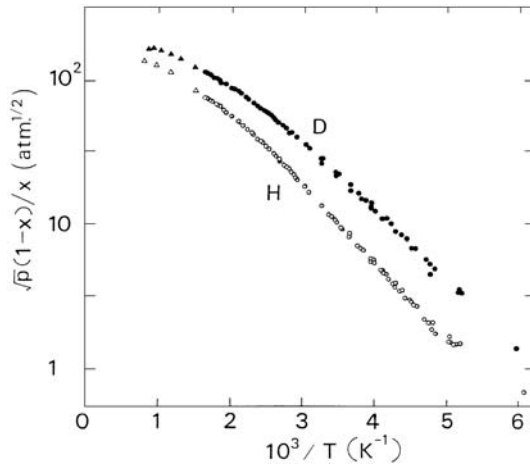


Fig. 2.7. Arrhenius plots of $\sqrt{p}(1-x)/x$ for H and D in Pd. Circles: [2.34]; triangles: [2.35]

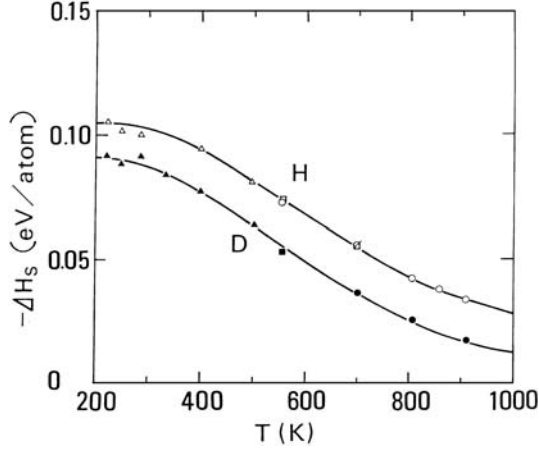


Fig. 2.8. Temperature dependence of the enthalpies of solution (ΔH_s^0) of H and D in Pd [2.29, 2.30]. Values refer to the limit of infinite dilution

Values of Δh_s determined by the slope of the Arrhenius plot exhibit the temperature dependence shown in Fig. 2.8. The data obtained from calorimetry [2.29, 2.30] are also included. Note that the overall temperature dependence is fairly large in this case, and the data from the two different experiments join smoothly at ~ 500 K.

Let us here examine briefly the origin of the temperature dependence of the enthalpy of solution. The discussion can be made conveniently in terms of the temperature derivative of Δh_s , which is equal to the difference in the specific heat per H atom under constant pressure:

$$\Delta c_p = \left(\frac{\partial \Delta h_s}{\partial T} \right)_p \quad (2.18)$$

$$= c_p^\alpha - \frac{1}{2} c_p^g. \quad (2.19)$$

The specific heat per H atom in the solid solution consists of three terms, arising from optic-mode vibrations of an H atom, changes in the acoustic-mode vibrations of M atoms, and changes in the electronic specific heat, viz.,

$$c_p^\alpha = c_{op} + \Delta c_{ac} + \Delta c_{el}, \quad (2.20)$$

$$c_{op} = k \sum_{i=1}^3 \frac{(\theta_{E\alpha(i)}/T)^2 e^{\theta_{E\alpha(i)}/T}}{(e^{\theta_{E\alpha(i)}/T} - 1)^2}, \quad (2.21)$$

$$\Delta c_{ac} = \frac{\partial c}{\partial \theta_D} \frac{\partial \theta_D}{\partial x}, \quad (2.22)$$

$$\Delta c_{el} = \frac{\partial \gamma_e}{\partial x} T, \quad (2.23)$$

where $\theta_{E\alpha(i)}$ is the Einstein temperature for the vibration of mode i , c is the specific heat, θ_D the Debye temperature, and γ_e the coefficient of the electronic specific heat of the host metal.

The specific heat of the gas, on the other hand, can be written as

$$\frac{1}{2}c_p^g = \frac{7}{4}k, \quad (2.24)$$

as long as the stretching vibration of molecules can be neglected.

In Fig. 2.9, the experimental values of $\frac{1}{2}c_p^g$ are compared with c_{op} and $c_{op} + \Delta c_{el}$ calculated for interstitial H in Pd using the values $\theta_{E\alpha(i)} = 650$ K, $\partial\gamma_e/\partial x = -1.2 \times 10^{-3} k$. We find that the major source of the temperature dependence of h^α is the optic-mode vibration of an H atom, c_{op} , and that the values of $c_{op} + \Delta c_{el}$ are rather close in magnitude to $\frac{1}{2}c_p^g$ over the temperature range of interest. Thus, these terms cancel with each other to a large extent in their contribution to Δh_s [2.30, 2.31]. This cancellation effect leaves only a modest temperature dependence of Δh_s , allowing us to define a single value of ΔH_s , approximately, over the whole temperature range. The contribution of Δc_{ac} appears to be negative, but not so large as to affect this cancellation effect significantly [2.36]. This point has been discussed in greater detail for H in Pd [2.28–2.30] and H in V [2.37].

In the case of H in V, Nb, and Ta, no sign of curvature was observed in the Arrhenius plot of p - x - T data [2.38], and no comparison between the p - x - T data and the calorimetric data [2.26] as reliable as in the case of Pd can be made.

In closing this section, we add some general comments on Sieverts' law. Sieverts law holds in the region where gaseous hydrogen can be regarded as

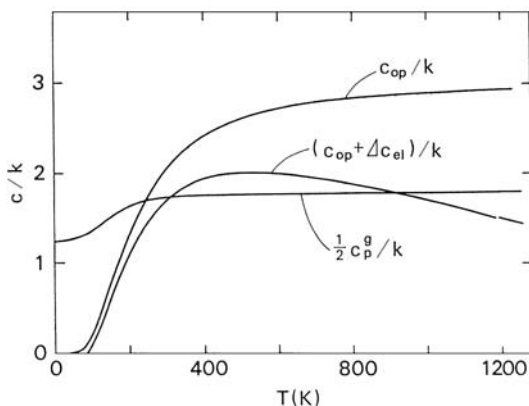


Fig. 2.9. Specific heats as a function of temperature. Specific heat of hydrogen in the gaseous state ($\frac{1}{2}c_p^g$), in solution in Pd arising from optic-mode vibration (c_{op}) and with electronic contribution added ($c_{op} + \Delta c_{el}$). Values are in units of k per H atom

an ideal gas. At high pressures, a deviation from ideal-gas behavior makes the chemical potential for given p , T higher and, consequently, the solubility larger than the Sieverts law predicts. For example, the solubility at room temperature under 5 MPa of H_2 gas is enhanced by $\sim 3\%$ due to deviation from ideal-gas behavior. At still higher pressures, the chemical potential of gaseous (fluid) hydrogen steeply increases, and gives rise to a very large enhancement of the solubility. This will be treated in Sect. 4.3.

2.2.2 High Concentrations: Effects of Interactions Between H Atoms

The heat of solution is, in general, a function of H concentration. The experimental values listed in Table 2.1 are, in fact, those of infinite dilution, ΔH_s^0 . Results obtained so far on the concentration dependence of ΔH_s are shown in Fig. 2.10. In all these cases, ΔH_s decreases initially, followed by an increase at higher concentrations.

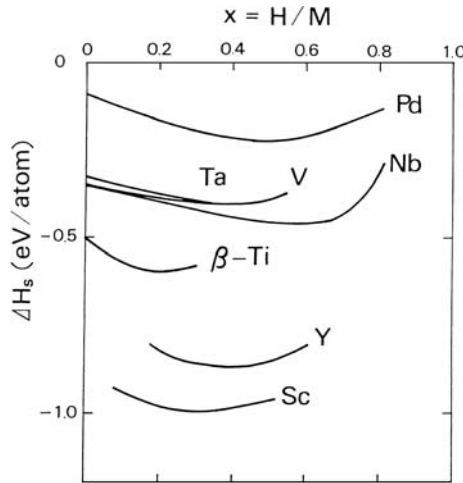


Fig. 2.10. Dependence of the enthalpy of solution on hydrogen concentration. Data taken from [2.39–2.41] for Pd, [2.42] for Nb, [2.24] for V and Ta, [2.43] for β -Ti, [2.44] for Y, and [2.33] for Sc

In brief, we may say that the concentration dependence of ΔH_s should be the consequence of interactions between the dissolved H atoms. The statistical thermodynamics including the pairwise H–H interaction was first formulated by *Lacher* [2.45,2.46], and was pursued further by several investigators. However, their treatment remained largely phenomenological because no clear physical picture was available at that time for the origin of H–H interactions.

An important step was made by *Alefeld* [2.47] as he recognized that the average elastic interaction should make an important contribution to the heat of solution. As shown by *Eshelby* [2.48], the presence of point defects in a bounded elastic medium should induce, in addition to local distortion, an average volume change in order to keep the external surface free of stress. Thus, interstitial H atoms produce, on an average, lattice dilatation, which in turn interacts with the stress field of each H atom, and lowers the heat of solution in proportion to the H concentration. This average elastic interaction, which does not depend on the local configuration of H atoms, can be called a mean-field contribution. The mean-field theory of the elastic interaction based on the discrete nature of the lattice has been worked out subsequently by *Wagner* and *Horner* [2.49, 2.50].

Before making quantitative discussions on the volume dependence of the heat of solution, we must recognize that the following two empirical relations hold for the volume increase due to H atoms.

First, the volume per M atom, v , increases linearly with H concentration:

$$v = v_0 + xv_{\text{H}} \quad (2.25)$$

where v_0 is the atomic volume of the pure host metal, and v_{H} is the volume increase per H atom that assumes a value between $2 \sim 3 \text{ \AA}^3$ (Table 4.2).

Second, the H-induced volume v_{H} satisfies the relation

$$v_{\text{H}} = \left(\frac{\partial h^\alpha}{\partial p} \right)_T + T \left(\frac{\partial v_{\text{H}}}{\partial T} \right)_p. \quad (2.26)$$

This can be obtained by subtracting from the thermodynamical relation for the solid-solution phase,

$$\begin{aligned} V^\alpha &= \left(\frac{\partial G^\alpha}{\partial p} \right)_T = \left(\frac{\partial H^\alpha}{\partial p} \right)_T - T \left(\frac{\partial S^\alpha}{\partial p} \right)_T \\ &= \left(\frac{\partial H^\alpha}{\partial p} \right)_T + T \left(\frac{\partial V^\alpha}{\partial T} \right)_p, \end{aligned} \quad (2.27)$$

the corresponding relation for the pure host metal, and differentiating with respect to the number of H atoms.

Noting that the pressure dependence of h^α essentially determines that of ΔH_{s} , and that the second term, being much smaller than the first term, can be neglected for most purposes, we have

$$v_{\text{H}} \approx \left(\frac{\partial \Delta H_{\text{s}}}{\partial p} \right)_T. \quad (2.28)$$

In examining the dependence of ΔH_{s} on the H concentration, we try to isolate the volume-dependent contribution, viz.,

$$\frac{\partial \Delta H_{\text{s}}}{\partial x} = \left(\frac{\partial \Delta H_{\text{s}}}{\partial V} \right)_x \frac{\partial V}{\partial x} + \left(\frac{\partial \Delta H_{\text{s}}}{\partial x} \right)_V. \quad (2.29)$$

(Hereafter, the subscript T on the partial derivative will be dropped for the sake of simplicity.) The first term, called the elastic contribution, can be calculated as

$$\begin{aligned} \left(\frac{\partial \Delta H_s}{\partial V} \right)_x \frac{\partial V}{\partial x} &= \left(\frac{\partial \Delta H_s}{\partial p} \frac{\partial p}{\partial V} \right)_x \frac{\partial V}{\partial x} \\ &\cong -K_0 \frac{v_H^2}{v_0} \\ &\equiv -u_{\text{els}} , \end{aligned} \quad (2.30)$$

using (2.25, 2.27, 2.28). Thus, the elastic contribution to ΔH_s can be written as $-u_{\text{els}}x$, with the factor u_{els} depending only weakly on the H concentration. The origin of this contribution is the decrease in the pv_H term in the enthalpy when a negative pressure (an image force) is produced by the presence of H atoms. Calculations based on the elasticity theory of the effect of finite sample size, i.e. the origin of the “image force” required for satisfying the free-surface condition [2.48], and a need to exclude the “self-energy” part from ΔH_s [2.47, 2.51], have led to a correction factor γ in (2.30), viz.

$$\left(\frac{\partial \Delta H_s}{\partial V} \right)_x \frac{\partial V}{\partial x} = -\gamma K_0 \frac{v_H^2}{v_0} \quad (2.31)$$

where

$$\gamma = \frac{2(1 - 2\sigma)}{3(1 - \sigma)} , \quad (2.32)$$

σ being the Poisson’s ratio. In practice, this correction factor is difficult to estimate. The values estimated from isotropically averaged Poisson’s ratio, which range between $\gamma = 1/4 \sim 1/2$ (Table 2.2), are most probably underestimated. Whereas the derivation of (2.31, 2.32) assumes the linear (isotropic) elasticity theory to hold up to the immediate vicinity of H atoms (the core region), numerous point-defect calculations have shown that atomic displacements in the core region are nearly twice as large as those extrapolated from large distances (the elastic region). Thus, the correction factor may well be twice as large, i.e. $\gamma = 1/2 \sim 1$.

The second term of (2.29), including all volume-independent contributions, can be called briefly as the “electronic” contribution. This is a contribution coming mainly from the extra electrons brought into the lattice by H atoms. We may expect that the electronic contribution consists of a term that depends only on the total number of extra electrons and acts uniformly over the crystal, and the rest that depends on local electronic states and becomes effective at shorter distances. For example, if we were to adopt a simple band-filling picture that the sole action of extra electrons is to fill the states at the Fermi level E_F of a rigid band of a host metal, the mean-field contribution to ΔH_s can be written as $\int_0^x N[(E_F)]^{-1} dx$, where $N(E_F)$ is the density of states (DOS) at E_F . The significance of this contribution will be examined later.

Table 2.2. Dependence of the heat of solution on hydrogen concentration. Values of the coefficient of the concentration-linear term $\Delta H_s - \Delta H_s^0 = -\bar{u}x = -(u_{\text{els}} + u_{\text{eln}})x$ are given

Metal	K_0 [GPa]	$\gamma(\text{calc})$	v_0 [Å ³]	$u_{\text{els}}(\text{calc})^{\text{a}}$ [eV per atom]	$\bar{u}(\text{obs})$ [eV per atom]		
					Heat of Solution ^b	Spinodal ^c	Gorsky Effect ^d
Sc	41.9	—	24.7	0.04	0.49	—	—
Y	43.9	0.47	38.9	0.05	0.39	—	—
Ti ^e	104.5	—	18	0.28	0.50	—	—
V	154.3	0.30	13.7	0.41	0.19	—	0.22
Nb	153.3	0.26	18.0	0.44	0.23	0.26	0.24
Ta	194.3	0.32	18.0	0.45	0.22	—	0.19
Ni	187.9	0.39	10.9	0.44	—	0.21	—
Pd	192.3	0.25	14.7	0.42	0.39	0.38	—

^aCalculated from $u_{\text{els}} = -K_0 v_{\text{H}}^2 / v_0$ with v_{H} taken from Table 4.2.

^bEstimated from Fig. 2.10.

^cSee Sect. 2.3.

^dSee Chap. 6.

^eDue to lack of pertinent data, K_0 for the hcp phase and $v_{\text{H}} = 3 \text{ Å}^3$ were adopted for estimating u_{els} .

We shall here write the electronic contribution as $-u_{\text{eln}}x$ by extracting a term proportional to H concentration. (The remaining contribution depending on higher powers of x is neglected for the time being.)

In order to assess the relative importance of the elastic and electronic contributions, the calculated values of $-u_{\text{els}}x$ are compared in Table 2.2 with the observed initial slopes of ΔH_s , viz.,

$$\Delta H_s - \Delta H_s^0 = -\bar{u}x = -(u_{\text{els}} + u_{\text{eln}})x, \quad x \ll 1. \quad (2.33)$$

The table also includes the values of \bar{u} obtained from two other sources: the spinodal decomposition and Gorsky effect (to be described in Sects. 2.3 and 6.2, respectively). The values obtained from different sources are mutually consistent. The fact that \bar{u} is invariably positive means that there are, in effect, long-range attractive forces acting between H atoms.

On a closer look at Table 2.2, we note that both u_{els} and $\bar{u}(\text{obs})$, and hence u_{eln} , vary systematically with the group number, rather than the period, of the host metal on the Periodic Table. Furthermore, $u_{\text{eln}} (= \bar{u}(\text{obs}) - u_{\text{els}})$ can assume either positive or negative values depending upon the group number of the metal. This is grossly at variance with the simple band-filling picture described above, which predicts that its contribution to ΔH_s is always positive. (For small H concentrations, $u_{\text{eln}} = -1/N(E_{\text{F}}^{\text{M}})$, E_{F}^{M} being the Fermi energy of a host metal, is always negative.) This comparison indicates clearly

that, for understanding the origin of the electronic contribution, more careful examination of the problem than a simple band-filling picture is needed.

Regarding the increase of ΔH_s at still higher H concentrations, *Griessen* [2.52] has shown that, in the case of Pd–H system, the concentration dependence can be explained reasonably well solely in terms of the band-filling picture. In this particular case, the filling of the high-DOS 4d band at low H concentrations leads to only small increases of E_F , but at higher concentrations ($x > 0.6$), when the 4d band is full, the filling of the low-DOS 5s band causes a rapid increase of E_F and, hence, of ΔH_s .

However, considering the generality of the increase of ΔH_s at high H concentrations, its origin cannot be sought in the shape of $N(E_F)$. It would be more reasonable to assume that there is, in addition, a short-range repulsive interaction between H atoms. Obviously, the interactions in question, either short-range or long-range ones, should be those acting between more than two H atoms. The total energy coming from any pairwise interactions should, on an average, be proportional to the square of the H concentration; accordingly, its contribution to ΔH_s should be contained in the $-\bar{u}x$ term.

The many-body character of the interaction at high H concentrations was noted by *Oates* and *Stoneham* [2.53], who showed that the short-range elastic interaction energy for clusters of H atoms cannot be written as a sum of pairwise interactions.

In what follows, we describe three other pieces of evidence that indicate the presence of this short-range repulsive interaction.

Firstly, we quote an empirical rule that H atoms do not come closer than 2.1 Å. This statement, originally put forward by *Westlake* [2.54] in a slightly more modest expression, seems to apply in most M–H systems, and is, therefore, believed to be a manifestation of the general character of the short-range repulsion between H atoms².

Secondly, reduction of the partial configurational entropy has been noted in solid-solution phases in comparison to what is expected for random distribution over all interstitial sites,

$$s^c = -k \ln \frac{x}{r - x} . \quad (2.34)$$

Intuitively, one may say that the configurational entropy is decreased because r is decreased by the mutual blocking of H atoms. More precisely, the mutual blocking becomes more important at higher concentrations; accordingly, r should decrease with increasing x .

Calculation of s^c in the presence of mutual blocking effects was first performed by *Oates et al.* [2.61] by the Monte Carlo method, and was made

² The only exception known so far is the hydrides of ternary intermetallic compounds LnNiIn (Ln = La, Ce, Pr, Nd), where H–H distances are as short as ~ 1.5 Å [2.58–2.60]. This is due to the rare combination of incipient ionicity in the bonding and peculiar geometry of H-sites. See after Sect. 3.4.

analytically later by *Boureau* [2.62, 2.63] from probability considerations. Boureau's expressions for the T-site occupancy in the bcc lattice are

$$s^c = -k \ln \frac{x(6-x)}{(6-4x)^2} \quad (2.35)$$

when the blocking extends to the second-nearest neighbors ($4+2=6$ atoms), and

$$s^c = -k \ln \frac{x(6-2x)(6-3x)}{(6-4x)(6-5x)^4} \quad (2.36)$$

when it extends to the third-nearest neighbors ($4+2+8=14$ atoms). (For the configuration of T sites in the bcc lattice, see Fig. 2.14). From a comparison of these calculations with the solubility data on H in bcc metals (β -Ti, β -Zr, V, Nb and Ta), it has been shown that the mutual blocking extends to the second nearest neighbors. The effect of mutual blocking on the configurational entropy is shown in Fig. 2.11. Analytic expressions for the case of T-site occupancy in the fcc lattice have also been worked out [2.64].

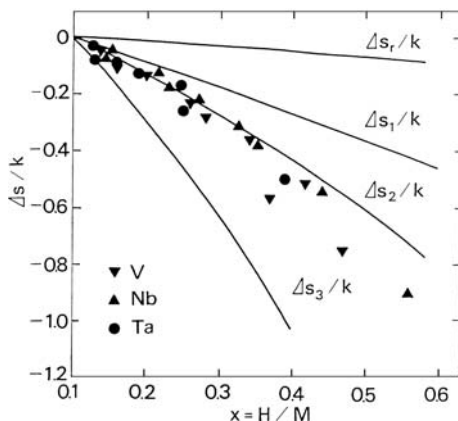


Fig. 2.11. Excess partial configurational entropy as a function of hydrogen concentration for T-site occupancy in a bcc lattice (in units of k). Values of $\Delta s = s - s_0$ ($s_0 = -k \ln x$) minus Δs at $x = 0.1$ are shown. s_r : random distribution on T sites; s_1 : occupancy of nearest-neighbor (n.n.) sites (4 sites) blocked; s_2 : up to second n.n. (6 sites) blocked; s_3 : up to third n.n. (14 sites) blocked. Calculated by Boureau's formula [2.62]

Thirdly, the formation of ordered structures in practically all M–H systems can also be regarded as evidence for the short-range repulsion. If H–H interactions were attractive, precipitation of H-rich phases should take place at low temperatures instead of formation of ordered arrangements. From the stability condition of the observed ordered structures, some constraints on major pairwise interaction parameters can be deduced (cf. the theory

of *Kanamori* and *Kakehashi* [2.65]). The short-range repulsion should also give rise to short-range order in seemingly disordered solid-solution phases and, consequently, to diffuse scattering in diffraction experiments. There is a method due to *Clapp* and *Moss* [2.66, 2.67] that allows the evaluation of interaction potential parameters between D atoms from diffuse scattering intensities of neutrons. This type of study performed by *Picton et al.* [2.68] for the Pd–D system indicates that major potential parameters between nearby D atoms are indeed positive, corroborating the repulsive nature of the interaction. The development of the overall understanding of the effect of H–H interactions on the thermodynamics of the Pd–H system has been described in a review paper by *Oates* [2.69].

In V [2.70] and Nb [2.71, 2.72], superlattice reflections reminiscent of low-temperature ordered phases were observed in the solid-solution phase, indicating a partial ordering of hydrogen atoms.

In some rare-earth metals, Sc, Y, Ho, Er, Tm and Lu, the ordering of H atoms in the seemingly solid-solution phase was found to occur in two steps: As the specimens are cooled from high temperatures, H atoms form pairs on next-nearest tetrahedral sites along the c axis, bridged by intervening M atoms; subsequently these pairs tend to form a chain-like structure along the c axis [2.73, 2.74] (see also Sects. 2.4.3 and 5.6.1).

As a result of these orderings, short-range or longer-range ones, further reduction of the configurational entropy can be expected. This has been observed in the calorimetric study of the V–H system [2.37].

2.3 Spinodal Decomposition

One of the important consequences of the long-range attractive H–H interaction is the spinodal decomposition, as observed in the Pd–H and Nb–H systems (Figs. 2.1, 2.2). In these phase diagrams, there exist regions labeled $\alpha + \alpha'$, where solid solutions of two different concentrations coexist.

The coexistence of these two phases cannot materialize as long as μ^α given by (2.9) is a single-valued function of x , but becomes possible when the concentration dependence of h^α makes μ^α a multivalued function of x .

The equilibrium condition for the two coexisting phases (with concentrations x_1 and x_2) is given by

$$\frac{1}{2}\mu^g = \mu^\alpha(x_1) = \mu^\alpha(x_2) \quad (2.37)$$

$$= \frac{1}{x_2 - x_1} \int_{x_1}^{x_2} \mu^\alpha(x) dx, \quad (2.38)$$

the so-called law of common tangent or an equal-area construction. [See after (2.51) for its physical implication.] The critical point can be determined from the condition

$$\frac{\partial \mu^\alpha}{\partial x} = 0 = \frac{\partial^2 \mu^\alpha}{\partial x^2} . \quad (2.39)$$

As a simple approximation for μ^α , let us introduce, as before, a linear term in the concentration dependence of h^α and write

$$\mu^\alpha = h_0 - \bar{u}x + kT \ln \frac{x}{r - x} . \quad (2.40)$$

The critical point can be easily obtained as

$$x_c = r/2, \quad T_c = r\bar{u}/4k . \quad (2.41)$$

In the Nb–H system, the critical point is located at $x_c = 0.31$ and $T_c = 444$ K [2.8], from which one obtains $r \approx 0.62$ and $\bar{u} \approx 0.26$ eV/atom. In the Pd–H system, $x_c \approx 0.25$ and $T_c \approx 565$ K [2.39]; hence, $r \approx 0.50$ and $\bar{u} \approx 0.39$ eV/atom. For Ni–H, $x_c \approx 0.5$ and $T_c \approx 630$ K [2.75]; hence, $r \approx 1.0$ and $\bar{u} \approx 0.21$ eV/atom. These estimates are in reasonable agreement with those obtained from other sources, as shown in Table 2.2. The small values of r deduced here in comparison to the total number of interstitial sites (Table 2.3) can be considered to be the result of the steep increase of h^α (and ΔH_s) near this concentration (Fig. 2.10). If one wishes to make better calculations, one has to take full account of the concentration dependence of h^α and the configurational entropy due to mutual blocking effects.

Table 2.3. Number and size of interstitial sites

Structure	fcc	and	hcp ($c/a = 1.633$)	bcc
Site ^a	O		T	O T
Number ^b	1		2	3 6
Size ^c	0.414		0.225	0.155 0.291

^aO: octahedral sites, T: tetrahedral sites.

^bNumber per M atom.

^cMaximum sphere radius to be accommodated in interstitial space formed by M-atom spheres. In units of M-atom sphere radius.

Among these types of calculation, the one performed by *Kuji* and *Oates* [2.76] on the Nb–H system can be regarded to be most successful. They performed very accurate measurements of the enthalpy and entropy of solution [2.12, 2.42], and constructed therefrom a phase diagram, as shown in Fig. 2.12. The agreement with the observations is quite satisfactory.

Generally speaking, the relative phase stability is determined by such small differences in free energies that very few measurements of thermodynamical quantities performed so far provide data with required accuracy. Judging from the success of *Kuji* and *Oate's* calculation, however, we may expect that the mechanism of spinodal decomposition is well described by

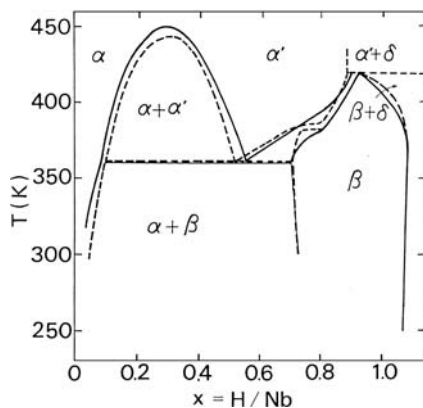


Fig. 2.12. Phase diagram of the Nb-H system. Comparison between calculation (—) [2.76] and observation (---) [2.10]

the foregoing treatment (a mean-field theory), and its dependence on temperature and composition can be predicted provided that the pertinent thermodynamical quantities are known with good precision.

The extremely long range character of elastic interactions gives a peculiar feature to the spinodal decomposition, namely, the shape dependence of spinodal boundaries [2.77, 2.78]. In the foregoing discussion, it was assumed implicitly that a sample could be neatly divided into two phases. In practice, a sample is not physically separated in the course of phase separation and, consequently, some elastic stress must build up. Thus, there are two limiting cases conceivable: coherent state and incoherent state, as shown schematically in Fig. 2.13. In the coherent case, since the stress introduced by H atoms depends on H concentration, certain modes of stress and concentration waves build up so as to satisfy the stress-free condition on the surface; in this way, the spinodal decomposition becomes dependent on sample shapes. In the incoherent case, on the other hand, the stress is relaxed on the boundaries of each of the small grains; accordingly, no shape dependence of the spinodal decomposition exists. *Zabel* and *Peisl* [2.77, 2.78] have shown that the coherent macroscopic density waves build up only when well-annealed samples of nearly critical concentrations are cooled slowly through the critical temperature. In most cases, samples can be considered to be in incoherent states, and the spinodal boundary observed corresponds to incoherent transitions. It must be borne in mind, however, that even in polycrystalline samples, the spinodal decomposition temperature can be suppressed to some extent (~ 20 K) due to partially coherent stress relaxation.

In contrast to the mean-field treatment of H-H interactions described above, an approach based on pairwise interactions between H atoms, a lattice-gas theory, was developed by *Wagner* and *Horner* [2.49, 2.50] and has been applied to the problem of spinodal decomposition in the Pd-H and

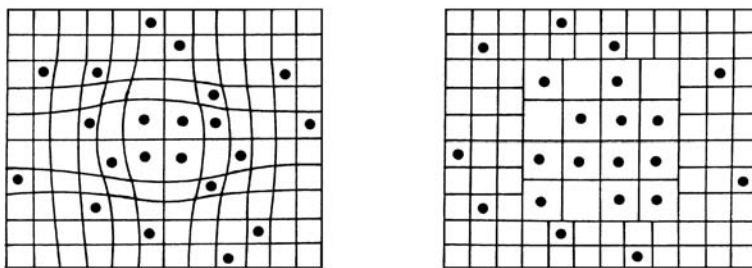


Fig. 2.13. Coherent and incoherent states

Nb–H systems. However, these calculations have been only partially successful so far, the main reason suspected being the inaccuracies in the interaction parameters. But, as long as spinodal decomposition is concerned, its major driving force is no doubt the long-range elastic force, which in turn can be well described by the mean-field theory. So, it suffices here to just mention the lattice-gas theory as an alternative approach.

The spinodal transition is accompanied by anomalous changes of many physical properties, including large-amplitude density fluctuations, the slowing-down of diffusion, and anomalous temperature dependence of the specific heat, etc. These aspects of spinodal transitions in metal-hydrogen systems have also been studied [2.79–2.85]. Some results on the anomalous diffusion will be described in Sect. 6.4.2.

2.4 Formation of Hydrides

2.4.1 Structure of Hydrides

The term hydride is a rather loosely defined one. In its narrow sense, the term is used only in cases where the structure of the metal lattice is changed by absorption of hydrogen. However, here we use it in a broader sense, including those cases in which the distribution of H atoms in the solid solution becomes ordered as the temperature is lowered. In short, we designate all the phases of metal-hydrogen systems other than a random interstitial solid solution as hydrides. It must also be mentioned at the outset that, owing to the metallic nature of hydrides, ordered structures described below are stable over certain ranges around stoichiometric compositions, the range being wider at higher temperatures. Thus, a certain degree of disorder usually exists in hydride phases.

In order to illustrate some typical structures of hydrides, interstitial sites in three principal crystal structures (fcc, hcp, and bcc) are shown in Fig. 2.14. Only two types of interstitial sites – octahedral (O) sites and tetrahedral (T) sites – are shown, because they are practically the only ones that are occupied by H atoms.

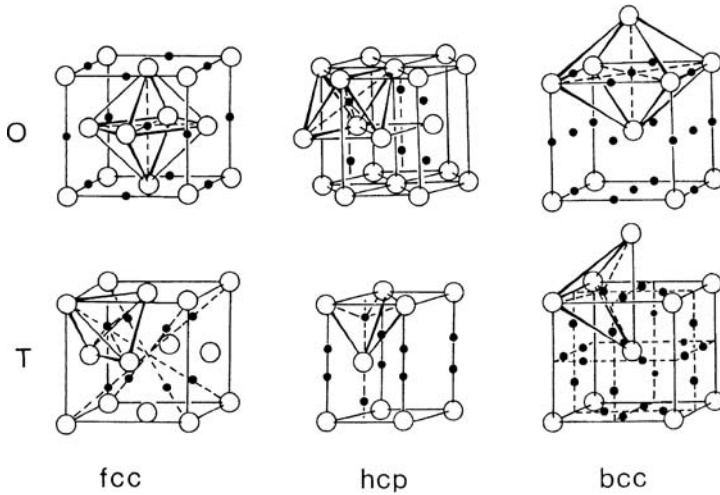


Fig. 2.14. Interstitial sites [octahedral (O) sites and tetrahedral (T) sites] in fcc, hcp, and bcc lattices

The number of interstitial sites per M atom and the space available for these sites are given in Table 2.3.

In the fcc lattice, T and O sites are surrounded by regular tetrahedra and octahedra, respectively, of M atoms. In the hcp lattice, the polyhedra formed by the nearest M atoms become distorted as the axial ratio deviates from the ideal value, $c/a = 1.633$. In the bcc lattice, an O site is surrounded by a heavily distorted octahedron, having two M atoms at a much closer distance than the remaining four atoms. Thus, O sites in the bcc lattice are further divided into O_X , O_Y , O_Z sites, depending upon the direction of the four-fold symmetry axis. Similarly, T sites in the bcc lattice are also divided into three groups, T_X , T_Y , T_Z , according to their symmetry axis.

In the structure determination of hydrides, X-ray diffraction has to be supplemented by neutron experiments (neutron diffraction or inelastic scattering) in order to locate the position of H atoms. In most cases, neutron diffraction experiments were performed on deuterides because the coherent scattering cross section is much larger and incoherent cross section much smaller in D than in H. However, the site location of H and D atoms in the corresponding hydride and deuteride phases may not necessarily be the same.

The structure and composition of hydrides can be written most concisely in the form $M^{\text{structure}}H_x^{\text{site}}$, where x is a rational number in completely ordered structures; a structure can be abbreviated as b (bcc), f (fcc), h (hcp) or dh (dhcp), and a site by t (tetrahedral) or o (octahedral). This is an adaptation of Lima-de-Faria's notation originally devised for expressing the structure of a wide variety of inorganic compounds [2.86, 2.87]. This notation is believed to be a useful convention to visualize the overall constitution of the structure.

Information not contained in this expression, for example, the ordering of H atoms on a certain sublattice of interstitial sites and a concomitant distortion of a metal lattice, has to be given separately. Details of crystallographic data of individual cases will be found in the following books [2.1–2.5].

For describing the systematics of hydride structures, it is expedient here to review briefly the structure of transition metals, as listed in Table 2.4 [2.4]. The general systematics is apparent. Complex allotropic transitions in Mn and Fe are due to the effect of magnetism. Among the trivalent lanthanide metals, Eu and Yb often behave differently from others because their ion cores prefer to be divalent due to the extreme stability of half-filled and completely-filled 4f-shell configurations. These structures occurring under normal pressure tend to become more compact ones under high pressures. For Fe, for example, dhcp and hcp structures appear above ~ 8 GPa (see Fig. 4.35).

Table 2.4. Crystal structure of transition metals. The structures are designated as b (bcc), f (fcc), h (hcp), dh (dhcp) or r (rhombohedral)³. The structures are given in the order of increasing temperature. Thus, for Mn, c* (complex cubic structures α , β) \rightarrow f (fcc) \rightarrow b (bcc) appearing at successively higher temperatures

Sc ^{h,b}	Ti ^{h,b}	V ^b	Cr ^b	Mn ^{c*,f,b}	Fe ^{b,f,b}	Co ^{h,f}	Ni ^f
Y ^{h,b}	Zr ^{h,b}	Nb ^b	Mo ^b	Tc ^h	Ru ^h	Rh ^f	Pd ^f
Ln ^a	Hf ^{h,b}	Ta ^b	W ^b	Re ^h	Os ^h	Ir ^f	Pt ^f

^aLanthanide metals.

La ^{dh,f,b}	Ce ^{f,dh,f,b}	Pr ^{dh,b}	Nd ^{dh,b}	Pm ^{dh,b}	Sm ^{r,h,b}	Eu ^b	
Gd ^{h,b}	Tb ^{h,b}	Dy ^{h,b}	Ho ^h	Er ^h	Tm ^h	Yb ^{h,f,b}	Lu ^h

The structure of hydrides depends on the matrix metal, hydrogen concentration, temperature and pressure. In cases where the solubility is limited, certain hydrides could be realized only under high hydrogen pressures. Here we focus attention solely on the structure and site occupancy of the hydrides attained so far, without regard to the condition of their synthesis. Individual high-pressure hydrides are described in Sect. 4.4. The observed structures of the hydrides are summarized in Table 2.5.

Starting from the right end of the table, fcc and hcp metals (including Co) absorb hydrogen in O-sites to form a continuous solid solution up to the monohydride composition $x = 1$. In some of these cases, substoichiometric hydrides are formed by the ordering of vacancies (Vacs) in the hydrogen

³ The stacking sequence of close-packed layers in usual notation is AB... for hcp, ABAC... for dhcp, ABC... for fcc. The rhombohedral structure of Sm is formed by stacking the close-packed layers in the order ABABCBCAC..., which is sometimes designated as 9H (9-fold hexagonal).

Table 2.5. Representative higher hydrides of transition metals. Structure of the metal lattice is indicated as f (fcc), h (hcp), dh (dhcp) or o (orthorhombic)

		$V^f H_{1-\alpha}$	$Cr^{h,f} H_{1-\alpha}$	$Mn^{h,dh,f} H_{1-\alpha}$	$Fe^{dh,f} H_{1-\alpha}$	$Co^{h,f} H_{1-\alpha}$	$Ni^f H_{1-\alpha}$
$Sc^f H_{2+\beta}$	$Ti^f H_{2\pm\beta}$	$V^f H_{2-\beta}$	$Cr^f H_{2-\beta}$				
$Sc^h H_{3-\gamma}$		$Nb^f H_{1-\alpha}$	$Mo^{h,f} H_{1-\alpha}$	$Tc^h H_{1-\alpha}$	$Ru^h H_{1-\alpha}$	$Rh^f H_{1-\alpha}$	$Pd^f H_{1-\alpha}$
$Y^f H_{2+\beta}$	$Zr^f H_{2-\beta}$	$Nb^f H_{2-\beta}$					
$Y^h H_{3-\gamma}$		$Ta^f H_{1-\alpha}$		$Re^h H_{1-\alpha}$			
$LnH_{2+\beta}^a$	$Hf^f H_{2-\beta}$	$Ta^f H_{2-\beta}$					
$LnH_{3-\gamma}^a$							
^a Lanthanide hydrides.							
$La^f H_{2+\beta}$	$Ce^f H_{2+\beta}$	$Pr^f H_{2+\beta}$	$Nd^f H_{2+\beta}$	$Sm^f H_{2+\beta}$	$Eu^o H_2$	$Gd^f H_{2+\beta}$	
$La^f H_{3-\gamma}$	$Ce^f H_{3-\gamma}$	$Pr^f H_{3-\gamma}$	$Nd^h H_{3-\gamma}$	$Sm^h H_{3-\gamma}$	—	$Gd^h H_{3-\gamma}$	
$Tb^f H_{2+\beta}$	$Dy^f H_{2+\beta}$	$Ho^f H_{2+\beta}$	$Er^f H_{2+\beta}$	$Tm^f H_{2+\beta}$	$Yb^{o,f} H_{2+\beta}$	$Lu^f H_{2+\beta}$	
$Tb^h H_{3-\gamma}$	$Dy^h H_{3-\gamma}$	$Ho^h H_{3-\gamma}$	$Er^h H_{3-\gamma}$	$Tm^h H_{3-\gamma}$		$Lu^h H_{3-\gamma}$	

sublattice. In the Pd-H system, for example, two such ordered structures [$I4_1/amd$ and $I4/m$ (H_4Vac in Ni_4Mo structure)] are known to occur at hydrogen concentrations higher than the spinodal region, at temperatures below about 50 K “50 K anomaly” [2.7–2.9, 2.88–2.90]. The fcc monohydride structure of O-site occupancy (NaCl type) was also observed in many other cases (V, Nb, Ta, Cr, Mo, Mn, Fe, Co), always as a high-temperature phase at high pressures (Sect. 4.4.1). In hcp metals with H atoms on O-sites (NiAs type), substoichiometric hydrides having anti- CdI_2 type structure were observed in Mn-H, Tc-H and Re-H systems, near the composition $[H]/[M] \sim 0.5$ (Sect. 4.4.1). It may be added that in noble metal Cu, a covalent monohydride of Wurtzite structure ($Cu^h H^t$) is formed by chemical synthesis in aqueous solution [2.3], whereas an fcc hydride, probably represented by $Cu^f H_x^o$, is formed under high hydrogen pressures (Sect. 4.4.1).

In bcc metals, H atoms at low concentrations occupy T sites randomly, but at high concentrations they tend to occupy certain sublattice(s) of interstitial sites at low temperatures, causing a small overall distortion of the lattice. In fact, this lattice distortion removes the degeneracy of the site energy in the original cubic lattice, allowing the occupancy of a certain interstitial sublattice among others. For example, in the β phase of the V-H(D) system (Fig. 2.3), one of the cube axes (Z axis) is elongated by about 10% by occupation of O_z sites, the energy of which has been lowered in turn by the overall tetragonal distortion. This particular example will be discussed more fully in Sect. 5.7.2. Hydrides in which H atoms are ordered on O sites in the bcc lattice include V_2H , V_3H_2 , and VH ($V_2^b H^o$, $V_3^b H_2^o$, and $V^b H^o$, respectively); those in

which they are ordered on T sites include Nb_4H_3 , NbH , Ta_2H , Ta_4H_3 , and TaH ($\text{Nb}_4^b\text{H}_3^t$, Nb^bH^t , Ta_2^bH^t , $\text{Ta}_4^b\text{H}_3^t$, and Ta^bH^t , respectively). Hydrides having these stoichiometric compositions can assume completely ordered structures. Note that, in spite of a large number of interstitial sites potentially available in the bcc lattice, the composition of these bcc-based hydrides is rather limited, namely, $x < 1$. This is a consequence of mutual repulsion operating between H atoms. The structure of hydrides of the bcc metals V, Nb, Ta is described in detail in a review article by *Schober* and *Wenzl* [2.10], and more recently in [2.5].

In the hcp solid solution of Ti [2.91], Zr [2.93] and rare-earth metals (Sc, Y and lanthanides), H atoms occupy T sites. Unlike the case of O-site occupancy in Group VI–VIII transition metals, terminal solubilities are rather limited, and further hydrogenation leads to the formation of dihydrides.

The dihydrides are formed in the CaF_2 -type structure, in which T sites in the fcc lattice are filled by H atoms (M^fH_2^t). All the dihydrides listed here except EuH_2 and YbH_2 have this structure. These two hydrides are, in fact, ionic compounds having the same structure as alkaline-earth dihydrides [2.3, 2.4]. The dihydrides of the CaF_2 structure are formed either from bcc or hcp metals. These dihydrides cannot be reached by successive filling of T sites of an fcc metal (with the only exception of Ce^f).

In Ti, Zr, and Hf, tetragonal distortion of the CaF_2 structure, in which one of the crystallographic axes is shortened, appears at H concentrations higher than the critical values, $x = 1.96$, 1.66 , and 1.86 , respectively, depending slightly on the temperature. The axial ratio c/a decreases with increasing H concentration, reaching 0.945 , 0.984 , and 0.887 , respectively, at $x = 2.0$ [2.1, 2.2].

Regarding the hydrides of rare-earth metals Sc, Y, and lanthanides, compilation of data by *Arons* [2.94, 2.97] was substantially updated in more recent review articles of *Vajda* [2.73] and *Vajda* and *Daou* [2.74]. These metals can be roughly classified into two groups according to the relative stability of different hydride phases. A schematic view of the phase diagrams of these systems is shown in Fig. 2.15. There is always a certain range of compositions where the fcc dihydride phase is stable. In lighter lanthanides, La, Ce and Pr, the fcc phase field extends to the trihydride composition. For heavier lanthanides, the fcc phase field becomes narrower; from $x \approx 2.5$ for Nd to $x \approx 2.03$ for Lu, and their trihydrides are formed in the hexagonal structure. A vertical solvus line in some of these cases, a consequence of the ordering of H atoms, will be discussed in Sects. 2.4.3 and 5.6.1.

The structure of cubic dihydrides can be written as $\text{M}^f\text{H}_2^t\text{H}_3^o$. The accommodation of excess D atoms ($x > 2$) in O sites was found by very early experiments of neutron diffraction on $\text{CeD}_{2.48}$ [2.92]. The generality of this result was questioned by subsequent experiments on various other systems, which suggested that the occupation of O-sites started in many cases before T-sites were completely filled. This question of site occupancy was clearly resolved

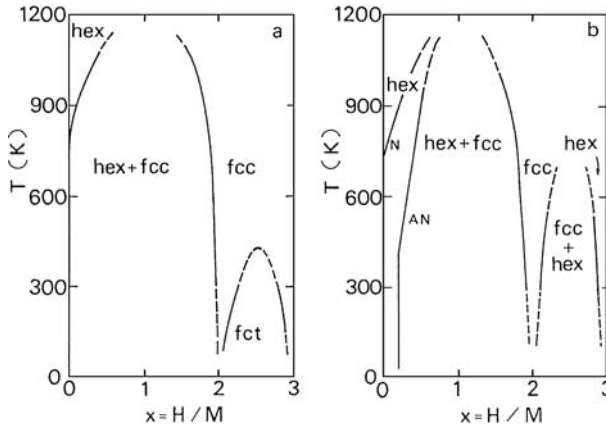


Fig. 2.15. Phase diagrams of rare-earth-metal-hydrogen systems classified into three groups: (a) light rare-earth metals forming cubic trihydrides (La, Ce, Pr); (b) light and heavy rare-earth metals (from Nd on ...) and Y forming hexagonal trihydrides, with further classification into a group showing normal terminal solubilities (Sm, Gd, Tb, Dy) and those showing anomalous (vertical) terminal solubilities (Ho, Er, Tm, Lu, Y, Sc), labeled N and AN, respectively

by more recent experiments of a French group [2.73, 2.74]. Taking sufficient care for the purity and perfection of samples, and noting that different site occupancies could be clearly discriminated by different equilibrium pressures, they showed unambiguously that in ideal situations H atoms occupy T-sites up to $x = 2.0$, and additional H atoms enter O-sites. In impure specimens, the total number of available T sites were less than $x = 2.0$, because a certain number of T sites were blocked by impurity atoms.

In many cases, a slight tetragonal distortion takes place as a result of ordering of H atoms on O sites (H^o). Thus the unit cell is doubled in the c direction in La, Ce and Sm dihydrides [2.98, 2.101], and in $TbD_{2.25}$ the H^o sublattice forms a DO_{22} (Ni_3Mo -type) structure [2.102, 2.104]. A few other tetragonal phases have been identified between the dihydride and trihydride phases of Ce [2.105].

The structure of cubic trihydrides, $M^fH_2^tH^o$, is sometimes referred to as BiF_3 structure. Note, however, that this structure cannot be formed in practice by successive filling of O sites in dihydrides ($M^fH_2^t$); a series of tetragonal phases must be traversed before reaching the trihydride phase. In Ce, the cubic trihydride phase starts at $x = 2.65$ at room temperature [2.105].

One peculiar feature of the cubic dihydride phase is that the volume decreases with excess H. This is believed to be the result of different bonding character of the H atoms on O sites and T sites (Sect. 7.4).

Hexagonal trihydrides are generally considered as having the structure $M^hH_2^tH^o$. Neutron diffraction experiments on HoD_3 have shown, however, that its structure is slightly different. The positions of H atoms are displaced

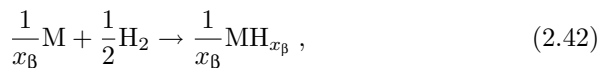
slightly from the original T and O sites, making the unit cell three times larger [2.106]. Other hexagonal trihydrides have also been believed to assume the HoD₃ structure, but more recent work on YD₃ suggested that its structure might be slightly different [2.107, 2.108]. In contrast to cubic trihydrides, the volume of hexagonal trihydrides is larger by 8 ~ 10% than the corresponding dihydrides.

Here we do not deal with hydrides of actinide elements, but briefly describe their general trend. Actinide elements are usually classified into the early-actinides (Ac, Th, Pa, U) and the late- (transuranium) actinides (Np, Pu, Am, Cm, Bk, Cf, etc.). In all the actinides studied so far, up to californium, fcc dihydrides MH_{2+β} are formed, and in the late-actinides up to berkelium hcp trihydrides MH_{3-γ} are formed. The site occupancy has not always been determined, but is believed to be the same as in rare-earth hydrides. The first two of the early-actinides, actinium and thorium, lacking 5f electrons, behave in many respects as an extension of trivalent Sc, Y and La, and tetravalent Ti, Zr and Hf, respectively. In protoactinium and uranium, delocalized 5f electrons having a broad energy band, dip below the Fermi level, and together with strongly hybridized s-d electrons contribute significantly to the bonding. The participation of 5f orbitals to the bonding leads to a diversity of hydride phases and structures in the early-actinides. In the late-actinides, as more electrons are added, narrowing of the 5f band proceeds through neptunium and plutonium, and is almost completed in americium. The 5f electrons are localized and no longer participate in the bonding. The situation is very similar to lanthanides, where inner-shell 4f electrons do not participate in the bonding. Thus many properties of the late-actinides follow the systematics of the lanthanides.

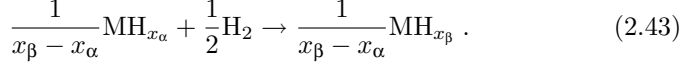
Now, a fairly large body of experimental data has been accumulated on actinide hydrides. For information on individual systems, the reader is referred to [2.1, 2.5]. There are many peculiar hydrides formed from actinide metals, Th₄H₁₅ being one of such examples. This hydride, having the highest H concentration among all the metallic hydrides, once attracted attention because of its superconducting properties [2.109, 2.110]. An interesting and useful comparison of actinide and lanthanide hydrides was made in the review paper by *Ward and Haschke* [2.111].

2.4.2 Thermodynamics of Hydride Formation

The stability of a hydride is measured by its heat of formation, usually defined as the enthalpy change due to the formation of the hydride from the reaction of 1 mol of H₂ gas with a metal. Here we prefer, for the consistency of description, to define it as per H atom. Thus, the heat of formation of a hydride MH_{x_β}, Δ*h*^β, is defined for a hypothetical reaction



where x_β takes a certain range of values around some rational numbers corresponding to stoichiometric compositions. Actually, a hydride is formed by the hydrogenation of a solid solution (α phase) through a reaction of the form



Writing the enthalpy and entropy changes in this reaction as $\Delta h^{\alpha \rightarrow \beta}$ and $\Delta s^{\alpha \rightarrow \beta}$, we may express the equilibrium condition as

$$\Delta h^{\alpha \rightarrow \beta} - T \Delta s^{\alpha \rightarrow \beta} = 0 . \quad (2.44)$$

Isolating, as before, the pressure dependence of $\Delta s^{\alpha \rightarrow \beta}$, this relation can be written approximately as

$$\Delta H^{\alpha \rightarrow \beta} - T(\Delta S^{\alpha \rightarrow \beta} + k \ln \frac{p}{p_0}) = 0 . \quad (2.45)$$

Thus, the values of $\Delta H^{\alpha \rightarrow \beta}$ and $\Delta S^{\alpha \rightarrow \beta}$, the enthalpy and entropy of hydride formation, can be determined from the Arrhenius plot of the plateau pressure.

Selected values of the enthalpy and entropy of formation of hydrides are given in Table 2.6. The most recent and extensive compilation of data, including those on hydrides of intermetallic compounds, was made by *Griessen* and *Riesterer* [2.25]. According to common practice, these values were determined from the desorption branches of p - x - T isotherms.

Comparing these values with heats of solution (Table 2.1), we note that $\Delta H^{\alpha \rightarrow \beta}$ and ΔH_s^0 for a given metal assume similar values, and their variation across the periodic table is also very similar. Thus, the electronic structure of a metal atom is more important than the crystal structure or the hydrogen content in determining these enthalpy values. Regarding the entropy, we immediately note that $\Delta S^{\alpha \rightarrow \beta}$ and ΔS_s also assume nearly the same value in all the cases, being essentially determined by the vanishing of the entropy of the H_2 gas.

In the following, we examine more closely the thermodynamics of the reaction (2.43), and show in particular how $\Delta h^{\alpha \rightarrow \beta}$ and $\Delta s^{\alpha \rightarrow \beta}$ are related to the enthalpy and entropy of formation, Δh^β and Δs^β , and how they can be determined from experiments.

In order to treat this problem, we need to develop a more general formalism applicable to binary interstitial solid solutions [2.112] than was adopted above in treating the case of solid solution and spinodal decomposition.

Consider a crystal consisting of N_0 metal atoms and n hydrogen atoms. The Gibbs free energy of the system, G , can be written in terms of the chemical potential of the metal species, μ_0 , and of hydrogen, μ :

$$G = N_0 \mu_0 + n \mu , \quad (2.46)$$

with

Table 2.6. Enthalpy and entropy of formation of hydrides

System	$\Delta H^{\alpha \rightarrow \beta}$ [eV per atom]	$\Delta S^{\alpha \rightarrow \beta}/k$	T [°C]	Reference
Li–LiH	−0.82	−8.1	600–900	[2.3]
Na–NaH	−0.59	−9.8	500–600	[2.3]
K–KH	−0.61	−10.1	288–415	[2.3]
Rb–RbH	−0.56	−10.2	246–350	[2.3]
Cs–CsH	−0.59	−10.2	245–378	[2.3]
Mg–MgH ₂	−0.39	−8.1	440–560	[2.3]
Ca–CaH ₂	−0.95	−8.4	600–800	[2.3]
Sr–SrH ₂	−1.03	−9.4	< 1000	[2.3]
Ba–BaH ₂	−0.91	−8.6	470–550	[2.3]
Sc–ScH ₂	−1.04	−8.7	> 600	[2.23]
Y–YH ₂	−1.18	−8.7	600–950	[2.44]
YH ₂ –YH ₃	−0.93	−8.3	250–350	[2.44]
La–LaH ₂	−1.08	−9.1	600–800	[2.3]
LaH ₂ –LaH ₃	−0.87	—	—	[2.3]
Ce–CeH ₂	−1.07	−8.9	600–800	[2.3]
CeH ₂ –CeH ₃	−1.24	—	—	[2.3]
Pr–PrH ₂	−1.08	−8.8	600–800	[2.3]
Nd–NdH ₂	−1.10	−8.8	650–840	[2.3]
Sm–SmH ₂	−1.16	−9.8	—	[2.3]
Gd–GdH ₂	−1.02	−7.9	600–800	[2.3]
Er–ErH ₂	−1.18	−9.4	—	[2.3]
Ti(hcp)–TiH ₂	−0.68	−6	< 300	[2.20, 2.21]
Zr(hcp)–ZrH ₂	−0.98	−9	400–550	[2.20, 2.21]
Hf–HfH ₂	−0.68	−6	600–900	[2.20, 2.21]
V–VH _{0.5}	−0.37	−6.5	0–100	[2.22]
V–VH ₂	−0.21	−9	50–120	[2.22]
Nb–NbH _{0.65}	−0.48	−8	0–80	[2.24]
Nb–NbH ₂	−0.21	−8	25	[2.22]
Ta–TaH _{0.65}	−0.41	−6	< 50	[2.22]
Mn(α)–MnH	−0.11	−7(assumed)	450–730	[2.22]
Ni–NiH	−0.30	−7(assumed)	20	[2.22]
Pd–PdH _{0.5}	−0.20	−5	−78–175	[2.20, 2.21]

$$\mu_0 = \left(\frac{\partial G}{\partial N_0} \right)_{p, T, n}, \quad (2.47a)$$

$$\mu = \left(\frac{\partial G}{\partial n} \right)_{p, T, N_0}. \quad (2.47b)$$

For interstitial solid solutions, it is convenient to express thermodynamical quantities per M atom, and the composition in terms of the atom ratio $x = [\text{H}]/[\text{M}]$. Thus, we define

$$g = \frac{G}{N_0} = \mu_0 + x\mu . \quad (2.48)$$

Both μ_0 and μ (and, hence, g) are functions of p , T and x (see the footnote⁴ below).

From (2.47b, 2.48), we obtain

$$\mu = \left(\frac{\partial g}{\partial x} \right)_{p,T} , \quad (2.49)$$

$$\mu_0 = g - x \left(\frac{\partial g}{\partial x} \right)_{p,T} . \quad (2.50)$$

In an x - g diagram for a given p , T condition, μ is the slope of the tangent to the $g(x)$ curve at a given x , and μ_0 is its intercept at $x = 0$.

The conditions to be satisfied for equilibrium between a solid solution MH_{x_α} , a hydride MH_{x_β} , and hydrogen gas are

$$\mu_0^\alpha(p, T, x_\alpha) = \mu_0^\beta(p, T, x_\beta) , \quad (2.51)$$

$$\mu^\alpha(p, T, x_\alpha) = \mu^\beta(p, T, x_\beta) , \quad (2.52)$$

$$= \frac{1}{2} \mu^g(p, T) . \quad (2.53)$$

For the gaseous state, the expression refers to the chemical potential per molecule as before. In the $x - g$ diagram, shown in Fig. 2.16, the condition for the equilibrium coexistence of α and β phases, (2.51, 2.52), is equivalent to the condition of a common tangent to $g(x)$ curves of the two phases. It can be easily verified that, when μ is expressed as a continuous function of x encompassing the α - and β -phase regions, the condition for the two-phase coexistence can be written as

$$\frac{1}{x_\beta - x_\alpha} \int_{x_\alpha}^{x_\beta} \mu(x) dx = \mu(x_\alpha) = \mu(x_\beta) = \frac{g(x_\beta) - g(x_\alpha)}{x_\beta - x_\alpha} ,$$

the so-called Maxwell's construction; see (2.37, 2.38). Because of the above three equations (2.51–2.53) only one of the four variables (p , T , x_α , x_β) can be considered to be independent. (Equivalently, the Gibbs' phase rule states that the number of degrees of freedom is $f = C - P + 2 = 2 - 3 + 2 = 1$). Thus, if we choose the temperature, T , as an independent variable, the other variables are uniquely determined as functions of T by the equilibrium conditions.

Suppose that the temperature is increased by dT , and the system reaches a new equilibrium state, accompanied by the corresponding changes of μ^α by $d\mu^\alpha$, etc. Thus, the following relations also hold:

⁴ In the literature of physical chemistry, it is customary to define these quantities per g-atom of the constituent elements, and call them partial molar quantities.

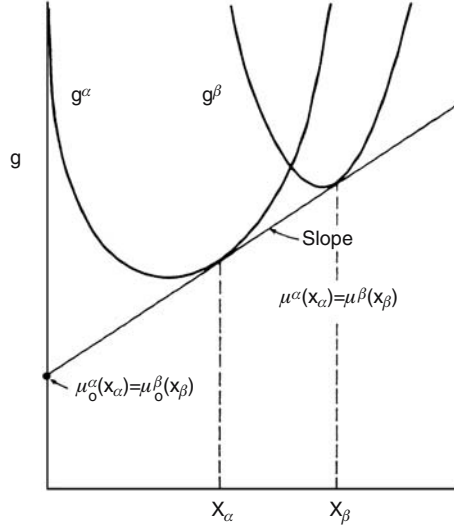


Fig. 2.16. Gibbs free energies of two phases, g^α and g^β , as a function of hydrogen concentration x (schematic)

$$\frac{d\mu_0^\alpha}{dT} = \frac{d\mu_0^\beta}{dT}, \quad (2.54)$$

$$\frac{d\mu^\alpha}{dT} = \frac{d\mu^\beta}{dT}, \quad (2.55)$$

$$= \frac{1}{2} \frac{d\mu^g}{dT}. \quad (2.56)$$

The quantities appearing in (2.54, 2.55) can be written in the following form:

$$\begin{aligned} \frac{d\mu_j^i}{dT} &= \left(\frac{\partial \mu_j^i}{\partial T} \right)_{p, x_i} + \left(\frac{\partial \mu_j^i}{\partial p} \right)_{T, x_i} \frac{dp}{dT} + \left(\frac{\partial \mu_j^i}{\partial x_i} \right)_{p, T} \frac{dx_i}{dT}, \\ &= -s_j^i + v_j^i \frac{dp}{dT} + \left(\frac{\partial \mu_j^i}{\partial x_i} \right)_{p, T} \frac{dx_i}{dT}, \end{aligned} \quad (2.57)$$

where $i = \alpha$ or β , j stands for M or H, and the standard thermodynamical relations

$$s_j^i = - \left(\frac{\partial \mu_j^i}{\partial T} \right)_{p, x_i}, \quad (2.58)$$

$$v_j^i = \left(\frac{\partial \mu_j^i}{\partial p} \right)_{T, x_i}, \quad (2.59)$$

have been used.

Using the notations

$$\bar{s}^i = s_0^i + x_i s^i, \quad (2.60)$$

$$\bar{v}^i = v_0^i + x_i v^i, \quad (2.61)$$

for the total entropy and volume, and noting the Gibbs–Duhem relation,

$$\left(\frac{\partial \mu_0^i}{\partial x_i} \right)_{p,T} + x_i \left(\frac{\partial \mu^i}{\partial x_i} \right)_{p,T} = 0, \quad (2.62)$$

we obtain from (2.57) the following relation:

$$\frac{d\mu_0^i}{dT} + x_i \frac{d\mu^i}{dT} = -\bar{s}^i + \bar{v}^i \frac{dp}{dT}, \quad (2.63)$$

where $i = \alpha$ or β .

Similarly, we have

$$\frac{d\mu^g}{dT} = -s^g + v^g \frac{dp}{dT}. \quad (2.64)$$

Using (2.63, 2.64) and (2.54–2.56), we obtain the expression for the entropy change in the reaction (2.43):

$$\Delta s^{\alpha \rightarrow \beta} = \frac{\bar{s}^\beta - \bar{s}^\alpha}{x_\beta - x_\alpha} - \frac{1}{2} s^g \quad (2.65)$$

$$= - \left(\frac{\bar{v}^\beta - \bar{v}^\alpha}{x_\beta - x_\alpha} - \frac{1}{2} v^g \right) \frac{dp}{dT}. \quad (2.66)$$

In a similar manner, by calculating $d(\mu_j/T)/d(1/T)$ and substituting (2.56) and

$$h_j^i = \left(\frac{\partial (\mu_j^i/T)}{\partial (1/T)} \right)_{p, x_i}, \quad (2.67)$$

we obtain

$$\Delta h^{\alpha \rightarrow \beta} = \frac{\bar{h}^\beta - \bar{h}^\alpha}{x_\beta - x_\alpha} - \frac{1}{2} h^g \quad (2.68)$$

$$= - \left(\frac{\bar{v}^\beta - \bar{v}^\alpha}{x_\beta - x_\alpha} - \frac{1}{2} v^g \right) T \frac{dp}{dT}, \quad (2.69)$$

where

$$\bar{h}^i = h_0^i + x_i h^i \quad (2.70)$$

is the total enthalpy for $i = \alpha$ or β .

From (2.66, 2.69), the equilibrium condition (2.44) can be seen to hold, as it should.

In examining the information obtained from p – x – T measurements, it is more useful to write the equilibrium condition in the form

$$\frac{1}{2} \ln \frac{p_{\text{eq}}}{p_0} = \frac{1}{kT} \left(\frac{\bar{g}^\beta - \bar{g}^\alpha}{x_\beta - x_\alpha} - \frac{1}{2} \mu^{\text{g}0} \right) \quad (2.71)$$

where p_{eq} is the equilibrium plateau pressure in the two-phase coexistence state,

$$\bar{g}^i = \mu_0^i + x_i \mu^i, \quad (2.72)$$

and the relations (1.13, 1.14) have been used. Substitution of the equilibrium conditions, (2.51, 2.52), leads to

$$\frac{1}{2} \ln \frac{p_{\text{eq}}}{p_0} = \frac{1}{kT} \left(\mu^\beta - \frac{1}{2} \mu^{\text{g}0} \right) \quad (2.73a)$$

$$= \frac{1}{kT} \left(\mu^\alpha - \frac{1}{2} \mu^{\text{g}0} \right). \quad (2.73b)$$

The implication of (2.71, 2.73a,b) is that the enthalpy and entropy changes of the reaction (2.43) that determine the plateau pressure are equal to the enthalpy and entropy of formation of the coexisting α and β phases, viz.,

$$\Delta h^{\alpha \rightarrow \beta} = \Delta h^\alpha(x_\alpha) = \Delta h^\beta(x_\beta), \quad (2.74)$$

$$\Delta s^{\alpha \rightarrow \beta} = \Delta s^\alpha(x_\alpha) = \Delta s^\beta(x_\beta). \quad (2.75)$$

Hereafter, the discussions follow closely the case of solid solutions described in Sect. 2.2.1. There is an intrinsic temperature dependence in h^i and s^i as well as in h^{g} and $s^{\text{g}0}$, and, in addition, h^i and s^i have to be evaluated at the phase boundary x_β , which is also temperature-dependent. However, thanks to the cancellation effect described in Sect. 2.2.1, $\Delta h^{\alpha \rightarrow \beta}$ and $\Delta s^{\alpha \rightarrow \beta}$ become nearly independent of temperature, and, to a good approximation, can be identified with $\Delta H^{\alpha \rightarrow \beta}$ and $\Delta S^{\alpha \rightarrow \beta}$ obtained from the slope and intercept of the Arrhenius plot. In fact, the linearity of the Arrhenius plots made so far has been as good as one can expect considering such uncertainties as hysteresis effects. The cancellation effects in the hydride formation have been discussed by *Flanagan* and *Lynch* [2.41] and *Flanagan* [2.113].

The absorption and desorption of H_2 gas in cooling–heating cycles, as a result of the formation and dissociation of hydrides, can be conveniently utilized for storage and supply of very pure hydrogen. The problem of hydrogen storage in hydrides is not treated in this book.

2.4.3 Terminal Solubility

The term terminal solubility means the maximum concentration of the solid-solution (α) phase in equilibrium with the coexisting hydride (β) phase. The phase boundary $\alpha - (\alpha + \beta)$, namely, x_α as a function of temperature, is called the solvus line.

For the experimental determination of the terminal solubility, the most commonly used techniques include measurements of the electrical resistivity

or the specific heat as a function of temperature for specimens with given concentrations of hydrogen. In some cases, internal-friction measurements have also been utilized for this purpose. Usually, the electrical resistivity increases with temperature, as dissolution of the hydride phase proceeds, because the resistivity is, in general, larger in disordered states than in ordered states. The positive anomaly in the specific heat with dissolution of the hydride means that the enthalpy of formation of the α phase is higher than that of the β phase. In internal-friction measurements, an extra energy loss, called the precipitation peak, is observed in the two-phase coexistence region. In all these experiments, hysteresis effects are usually observed: the point of complete dissolution in the heating run is higher than that corresponding to the beginning of precipitation in the cooling run. Since supercooling is commonly observed in the formation of an ordered phase from a disordered phase, the points determined in heating runs are believed to better represent the terminal solubility.

The situation is more complex in internal-friction measurements because the height and position of the precipitation peak change with thermal cycling. This is believed to be the effect of dislocations accumulated with repeated phase changes, to which the method is intrinsically very sensitive. Thus, the terminal solubility has often been determined in the first cooling run. However, as stated above, this procedure is not readily acceptable. No systematic comparison has been made so far between the terminal solubility obtained from internal-friction measurements and the results of resistivity and specific-heat measurements. Under these circumstances, the internal friction can at best be taken as a secondary measure for the determination of the terminal solubility, although the method is in some cases very sensitive to precipitation of the second phase, and is, therefore, potentially useful for this purpose in the very low concentration region [2.114].

Detailed discussions on the precipitation peak have been given by *Yoshinari* and *Koiwa* for V, Nb and Ta [2.115, 2.116], and Pd [2.117], where most other references can be found.

It must be borne in mind that these methods are applicable only to sealed specimens, namely, in cases where the equilibrium between the two solid phases can be established much faster than the solid-gas equilibrium. Thanks to the rapid diffusion of hydrogen in solid phases, this condition is usually well satisfied. In cases where the surface is easily permeable to hydrogen, such as Pd, the terminal solubility has to be determined in some other way, for example, by p - x - T measurements, or isothermal measurements of the resistivity, etc., as a function of hydrogen concentration.

Let us here briefly survey the experimental data available on the terminal solubility. In fcc metals, data are practically limited to Pd in the spinodal region, where two disordered phases coexist (Fig. 2.1). In bcc metals, numerous experiments have been performed on V, Nb, and Ta, and the results are reviewed in the article by *Schober* and *Wenzl* [2.10]. In these metals, a

solid solution coexists with a hydride of composition nearly independent of temperature: $x_\beta \sim 0.5$ for V and Ta, and $x_\beta \sim 0.7$ for Nb. In the Nb–H system, data are also available in the spinodal region (Fig. 2.2). For hcp metals, very peculiar features have been found regarding the terminal solubility in Sc, Y and some heavy rare-earth metals, in which a solid solution coexists with a dihydride phase. In this section, we deal with cases in which the α phase coexists with the β phase of nearly fixed composition, leaving aside the spinodal region, which has been treated in Sect. 2.3.

The thermodynamics for the terminal solubility is as follows. Note that, in the present problem, only the condition (2.52), $\mu^\alpha(x_\alpha) = \mu^\beta(x_\beta)$, has to be considered among the three equilibrium conditions (2.51–2.53). Besides, in view of small deviations from stoichiometry in the β phase in comparison to the α phase, the configurational entropy term for the β phase can be neglected. Hence,

$$h^\alpha - Ts^{\text{anc}} + kT \ln Z_\alpha = h^\beta - Ts^\beta, \quad (2.76)$$

where Z_α is usually written as $x_\alpha/(r - x_\alpha)$. Thus, we have

$$kT \ln Z_\alpha = -(h^\alpha - h^\beta) + T(s^{\text{anc}} - s^\beta) \quad (2.77)$$

$$= -\Delta H_{\text{solv}} + T\Delta S_{\text{solv}}, \quad (2.78)$$

where ΔH_{solv} and ΔS_{solv} are called the solvus enthalpy and entropy, respectively. We expect, therefore, that as long as ΔH_{solv} and ΔS_{solv} are independent of temperature, the Arrhenius plot of the terminal solubility should form a straight line. Actually, all the terms on the right-hand side of (2.77) are temperature-dependent, mainly due to the optic-mode vibration of hydrogen atoms, but the temperature dependence from the two phases are almost cancelled by each other when hydrogen atoms occupy the same type of sites in the two phases. Even when the site location is different, the cancellation is usually much better than in cases where solid–gas equilibria are involved.

Experimental values of ΔH_{solv} and ΔS_{solv} obtained for V, Nb, and Ta in the low-concentration region are: $\Delta H_{\text{solv}} = 0.14, 0.12, 0.15$ eV and $\Delta S_{\text{solv}}/k + \ln r = 1.63, 1.67, 3.73$, respectively [2.10]. At low concentrations, $\ln r \approx \ln 6 = 1.79$, and we note that ΔS_{solv} is very small, much smaller than ΔS_s or $\Delta S^{\alpha-\beta}$, for which the vanishing of the gas entropy played a decisive role. In fact, the entropy change of a few k is as much as we can expect for any solid-state phase changes.

Experiments become more difficult at lower temperatures as the terminal solubility becomes smaller. *Hanada et al.* [2.118] have shown, however, that in the case of H in Ta, the terminal solubility can be represented by a simple exponential form down to 70 K, where x_α is as small as a few ppm.

At higher temperatures, upward deviations from straight lines are observed in the Arrhenius plot, such as the one shown in Fig. 2.17 for H in V [2.119]. Points to be noted in analyzing the high-temperature data are as follows: First, at temperatures where x_β [the $(\alpha + \beta) - \beta$ boundary] becomes

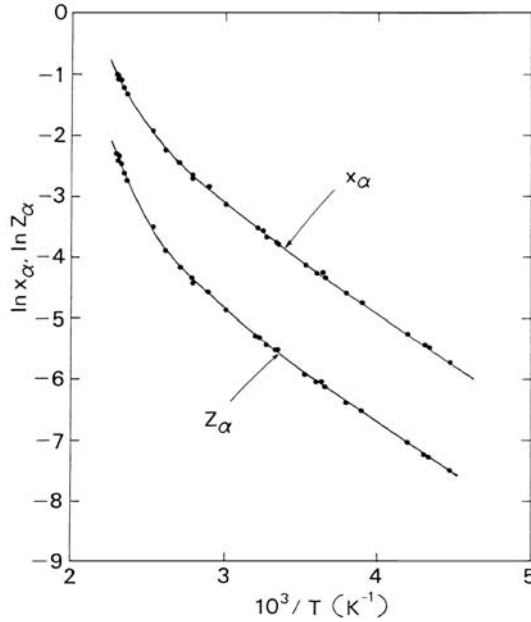


Fig. 2.17. Arrhenius plots of the solvus line $x_\alpha(T)$ [2.119] and $Z_\alpha(T) = x_\alpha(6 - x_\alpha)/(6 - 4x_\alpha)^2$ for the V-H system

dependent on temperature, h^β may also become temperature-dependent, and the above discussions based on the assumption of a constant reference state break down. Second, as x_α becomes of the order of unity, it becomes necessary to plot $\ln Z_\alpha$ instead of $\ln x_\alpha$. Such a plot using Boureau's expression (2.35), $Z_\alpha = x(6 - x)/(6 - 4x)^2$, is also included in Fig. 2.17. In this plot, the deviation at high temperatures becomes further accentuated.

The upward curvature of the Arrhenius plot might appear to indicate that the solvus enthalpy and entropy are both temperature-dependent. However, we point out here that the operational definition of ΔH_{solv} and ΔS_{solv} as slope and intercept of the tangent to the Arrhenius plot at each temperature leads to physically unreasonable results. Towards the high-temperature end of the plot shown in Fig. 2.17, both ΔH_{solv} and ΔS_{solv} become much larger than lower-temperature values, leading to ΔS_{solv} as large as $(10 \sim 15)k$. This value is quite unlikely for solid-state phase transitions; we would rather expect that ΔS_{solv} should be nearly independent of temperature.

There is an alternative method of analysis to the Arrhenius plot – in fact, a preferable one – in situations where the activation enthalpy and entropy depend on temperature [2.120, 2.121]. In this method, we plot $-kT \ln Z_\alpha$ as a function of T , instead of $\ln Z_\alpha$ vs. $1/T$. If there is no temperature dependence in ΔH_{solv} and ΔS_{solv} , the former can be obtained from the intercept and the latter from the slope of the plot. The data in Fig. 2.17 are replotted

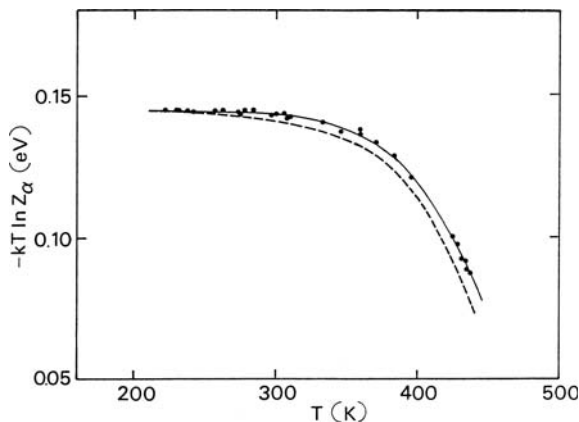


Fig. 2.18. Plots of $kT \ln Z_\alpha$ vs. T for the terminal solubility of the V–H system. Data from [2.119]

in this manner in Fig. 2.18. If we assume that ΔS_{solv} is independent of temperature, the downward bend at higher temperatures can be attributed to a gradual decrease of ΔH_{solv} , which can be obtained immediately as a function of temperature by subtracting the $T\Delta S_{\text{solv}}$ term on the graph. (This term, estimated from the low-temperature asymptote, is very nearly zero in this case.) It has been shown [2.119] that the gradual decrease of ΔH_{solv} observed at high temperatures can be explained largely in terms of the interaction between H atoms, as described in Sect. 2.2.2. The dashed line in Fig. 2.18 shows the deviation estimated by using the value $\bar{\mu} = 0.19$ eV/atom (Table 2.2) for the H–H interaction. (The best-fit value is $\bar{\mu} \sim 0.15$ eV/atom.)

A rationale for adopting this alternative method of analysis, which we call for the sake of convenience a straight- T plot or FF plot, is not simply that the Arrhenius plot is visually misleading because it is compressed in the high-temperature region [2.121], but, more importantly, that it can be physically misleading if combined with the operational definition of the activation enthalpy and entropy as slope and intercept of the tangent to the curved Arrhenius plot at each temperature.

It may be appropriate here to elucidate the physical implication of this statement. The point to be noted is that the right-hand side of (2.78), $\Delta S_{\text{solv}} = s^{\text{anc}} - s^\beta$, is not really the difference of entropies of the two states, because the configurational-entropy term of the α phase has been subtracted. Because of this, if we write as usual $\Delta G_{\text{solv}} = \Delta H_{\text{solv}} - T\Delta S_{\text{solv}}$, this quantity does not have the meaning of the difference of Gibbs free energies of the two states. The fact that ΔS_{solv} and ΔG_{solv} are not state variables invalidates the blind application of the thermodynamical relations such as $\Delta H_{\text{solv}} = [\partial(\Delta G_{\text{solv}}/T)\partial(1/T)]_p$, $\Delta S_{\text{solv}} = -(\partial\Delta G_{\text{solv}}/\partial T)_p$, $(\partial\Delta H_{\text{solv}}/\partial T)_p = T(\partial\Delta S_{\text{solv}}/\partial T)$. In the problem treated above, the temperature dependence of ΔH_{solv} is, in fact, balanced by the change in the configurational entropy, which is not included in ΔS_{solv} .

Exactly the same problem exists in the treatment of the formation of point defects in solids. The formation entropy, being defined as the total entropy change caused by a point defect minus the configurational entropy change, does not have the meaning of a thermodynamical state variable. Thus, all analyses assuming thermodynamical relations between the enthalpy and entropy of defect formation are incorrect.

A slightly different situation has been encountered in anomalous diffusion caused by second-order phase transitions, for example, ferromagnetic transition or order-disorder transition. On the Arrhenius plot, the diffusion coefficient D tends to increase steeply while approaching the transition temperature T_c from below, thereafter forming a straight line above T_c . If we write $D = D_0 \exp(-H_a/kT)$, the values of D_0 and H_a , obtained from the operational definition diverge at T_c , which is physically unreasonable. In such cases, data can be analyzed most simply by the FF plot, namely, by plotting $kT \ln D$ vs. T . Since D_0 can be considered to be nearly temperature-independent, H_a as a function of temperature can be obtained by subtracting $kT \ln D_0$ on the graph. H_a decreases progressively while approaching T_c from below, until it assumes a constant value at $T > T_c$. The temperature dependence of H_a in this case is a counterpart of the gradual change of the order parameter, or, equivalently, the configurational entropy in the ordered phase, which is not included in the activation entropy for individual atomic jumps and is, therefore, missing in D_0 .

The FF plot was adopted by *Fukai* and *Kazama* [2.120] in their analysis of anomalous diffusion of H in V across the $\beta_1 - \beta_2$ phase transition (Sect. 6.4.2) and its physical implication was discussed later in more general terms by *Fukai* [2.122, 2.123].

It has been found in the case of V that there is a fairly large isotope effect in the terminal solubility as a part of the isotope dependence of the phase diagram shown in Fig. 2.3. This quite exceptional observation can be understood as resulting from different site occupations in α and β phases. Since hydrogen atoms, including both H and D, occupy largely T sites in the α phase and O sites in the β phase, having correspondingly different optic-mode frequencies, the cancellation in $h^\alpha - h^\beta$ and $s^{\text{anc}} - s^\beta$ is no longer as complete, which gives rise to temperature and isotope dependence of these terms. This particular problem has been discussed by *Flanagan et al.* [2.119].

The terminal solubility in lanthanide metals increases with the atomic number. It is, e.g. at 500°C, ten times larger in Lu than in La (Sc and Y behaving like heavy lanthanides). This seems to be related with the lanthanide contraction; the lattice parameter becoming smaller and the melting point higher for heavier lanthanides.

The anomalous terminal solubility in rare-earth metals was discovered by *Daou* and *Bonnet* [2.116] in Lu and Tm, and is now known to be the common property of Sc, Y, and heavy rare-earth metals Ho, Er, Tm, and Lu [2.117–2.131].

As an example, a part of the phase diagram of the Lu–H system is shown in Fig. 2.19. As we follow the solvus line from high temperatures, it goes down almost vertically from $T_{\text{crit}} \sim 440$ K, allowing H atoms to remain in

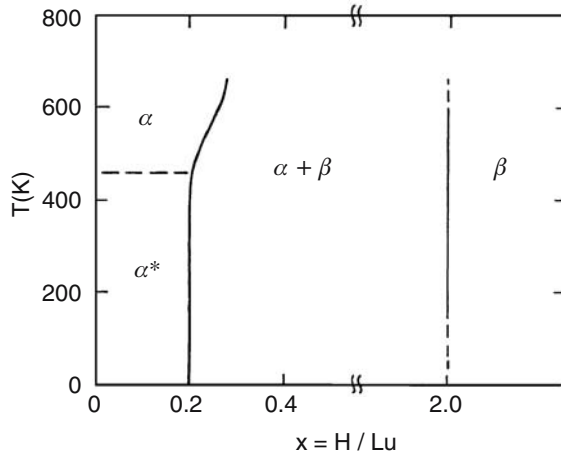


Fig. 2.19. Phase diagram of the Lu–H system [2.3, 2.125, 2.128]

solution up to the critical concentration, $x_{\text{crit}} \sim 0.20$, even at absolute zero of temperature. In addition, a resistivity anomaly was observed around 170 K, independent of H concentration. (Here we label the solid-solution phase below T_{crit} as α^*). The nature of these anomalies in the terminal solubility and resistivity has since been the subject of intensive studies.

The values of T_{crit} , x_{crit} and the temperature of resistivity anomaly, T_{anom} , are given in Table 2.7.

Table 2.7. Anomalies in solid-solution phase of rare-earth-metal–hydrogen systems

Metal	Sc	Y	Ho	Er	Tm	Lu
T_{crit} [K]	> 300	400 ^b	360 ^e	380 ^f	400 ^f	440 ^f
x_{crit}	0.35 ^a	0.19 ^c 0.20 ^d	0.03 ^e	0.06 ^g	0.11 ^h	0.20 ^{c,i}
T_{anom} [K] ^k	152.5 ^a	168 ^d	174 ^e	173 ^g	169 ^h	166 ^j

^a[2.127]; ^b[2.128]; ^c[2.125]; ^d[2.129]; ^e[2.130]; ^f[2.134]; ^g[2.131]; ^h[2.133]; ⁱ[2.128]; ^j[2.129]; ^kValues refer to H; those for D are about 5 K higher.

The effects of quenching and electron irradiation on the resistivity anomaly showed that, below T_{anom} , H atoms are in some kind of ordered state, giving smaller resistivity per H atom in comparison to the higher-temperature phase (α) [2.127–2.129, 2.131–2.134].

Neutron elastic (diffuse) and inelastic scattering experiments demonstrated that pairs are formed by H atoms on the next-nearest T sites along the c axis, bridged by intervening M atoms (T–M–T pairs) [2.132, 2.133]. As a result of the interaction between paired H atoms, the optic-mode vibration

of H atoms along the c axis is split into two modes having slightly different frequencies (doublets) [2.133, 2.134]. Results obtained for $\text{YH(D)}_{0.18}$ [2.133] showed that a proportion of the split component increased steadily as the temperature was lowered from 330 to 8 K, indicating that T–M–T pairs are in thermal equilibrium with isolated H atoms (forming singlets).

Subsequent diffuse neutron scattering experiments showed that, in addition to the pair formation, long-range ordering of T–M–T pairs took place at low temperatures. Based on the observation on the Lu–H system, a model was proposed that T–M–T pairs form zigzag chain segments along the c axis, which interact with each other to form a three-dimensional superstructure [2.132, 2.135]. This configuration was later confirmed in ScH_x [2.136] and YD_x [2.137].

Let us now examine the effect of the formation of T–M–T pairs and long-range order on the terminal solubility. We can readily see that the pair formation causes only small changes in the configurational entropy. If we assume that any M atom can serve as a mediator of a T–M–T pair, the number of possible sites for pairs amounts to one-half of the total number of T sites, and the number of pairs is, of course, reduced to one-half of the total number of H atoms. Thus, as long as blocking between neighboring pairs can be neglected, the configurational entropy is the same as that for the random distribution of single H atoms on T sites. The formation of long-range order, on the other hand, can be shown to cause a drastic reduction of the configurational entropy.

The fact that the anomalous terminal solubility sets in at a temperature where most of the H atoms are still singlets [2.132, 2.133] indicates that T_{crit} is not determined by entropy effects but, most probably, by the average decrease of ΔH_s as more pairs are formed in the α phase. Quantitatively, ΔH_{solv} for H in Y determined in the high-temperature region amounts to only 0.02 eV [2.117], which is so small that it can be easily reduced to zero if a certain proportion of H atoms in the α phase are lowered in energy by forming pairs. (We may even anticipate a retrograde behavior because ΔH_{solv} should be over-compensated at lower temperatures.) Then, the low-temperature anomaly which showed up in the resistivity can be naturally ascribed to the long-range order formation. Although the details of these anomalous behaviors are still under investigation, we may say at least that they are a consequence of the state changes of H atoms occurring in the solid-solution phase.

The reason why these anomalies do not occur in other hexagonal metals of T-site occupancy, such as Ti, Zr, and light rare-earth elements, all of which form dihydrides of CaF_2 type, is not yet understood. A close correlation of its appearance to electric and magnetic properties led Vajda to suggest that it originates from specific webbing features of the Fermi surface responsible for the occurrence of charge density waves [2.136]. More microscopic aspects of T–M–T pair formation are described in Sect. 5.6.1.

2.5 Effects of Hydrogen on the Relative Phase Stability

In metals having different allotropic forms, the relative stability of these phases is affected by dissolution of hydrogen. An example is shown in Fig. 2.20 for the Ti–H system [2.139, 2.140]. Here, the temperature of the transition hcp–bcc is lowered by dissolution of hydrogen, forming a very wide bcc (β) phase field that serves as a high-temperature phase of the eutectoid reaction between the hcp (α) phase and the fcc (δ) phase of CaF_2 structure. The fact that the bcc phase is stabilized relative to the hcp phase can be understood, at least qualitatively, by noting that the partial configurational entropy for a given hydrogen concentration is larger in the bcc phase because of the larger number of interstitial sites available. The phase diagrams of the Ti–H and Hf–H systems are very similar (see, e.g., [2.3]).

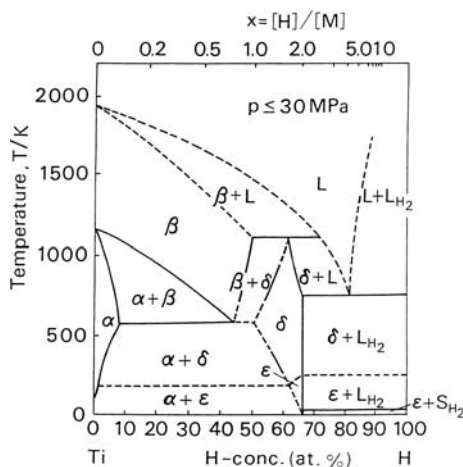


Fig. 2.20. Phase diagram of the Ti–H system. A key for this construction was an indication of the second phase occurring to the right of the δ -phase field between 400–800°C [2.193], which was later identified as a liquid phase [2.140]

Another case in which this explanation in terms of configurational entropy holds is the reduction of the melting point T_m by dissolution of hydrogen, as shown by our high-pressure determination of phase diagrams (Chap. 4). In V–H and Ti–H systems, for example, T_m is lowered by $\sim 1000 \text{ K}$, at a rate as large as $\Delta T_m / \Delta x = -(2 \sim 5) \times 10^3 \text{ K/H}$. This rate of reduction is nearly the same as those observed in other interstitial solute atoms in transition metals. The melting-point reduction is also indicated by the observed distribution coefficient, a ratio of the solubility in liquid (x_L) to that of solid (x_S), listed in Table 2.8. The fact that x_L/x_S is always larger than 1 indicates that T_m is lowered by dissolution of hydrogen.

Table 2.8. Distribution coefficient of hydrogen. The ratio of the solubility of hydrogen in liquid to that in solid at melting point under 1 atm of H_2 gas is given [2.20]

Metal	Al	Mn	Fe	Co	Ni	Cu	Ag	U
Distribution Coefficient	14.6	1.35	1.87	2.25	2.32	3.22	2.93	1.62

This lowering of the melting point can be explained in terms of the following model of interstitial solution for both solid and liquid states [2.139]. In this model, the usual expression of the Gibbs free energy for the solid is extended to the liquid state by assuming an appropriate number of interstitial sites N_L , viz.,

$$G_L = G_{L0} + nh - TS_L^c, \quad (2.79)$$

$$S_L^c/k = N_L \ln N_L - (N_L - n) \ln(N_L - n) - n \ln n. \quad (2.80)$$

In the corresponding expressions for the solid state, the letter L is simply replaced by S. In terms of the number of M atoms, N_0 (per volume), we define $r_L = N_L/N_0$, $r_s = N_S/N_0$, and $x = n/N_0$.

The condition of equilibrium coexistence of solid and liquid phases, the condition of a common tangent as illustrated in Fig. 2.21, reads

$$\left. \frac{\partial G_S}{\partial n} \right|_{x_S} = \left. \frac{\partial G_L}{\partial n} \right|_{x_L} \quad (2.81)$$

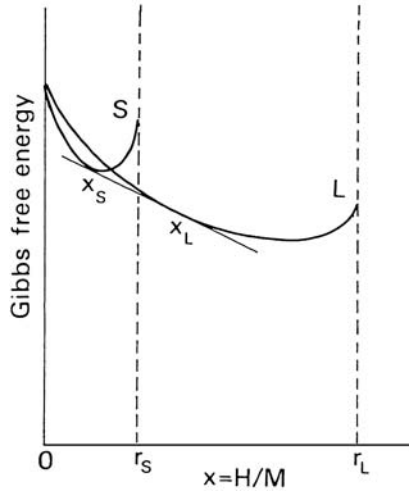


Fig. 2.21. Gibbs free energies of solid (G_S) and liquid (G_L) phases, giving the coexistence condition at compositions x_S and x_L [2.139]

$$= \frac{G_L(x_L) - G_S(x_S)}{N_0(x_L - x_S)} . \quad (2.82)$$

Equation (2.81) reduces to

$$\frac{x_L}{r_L} = \frac{x_S}{r_S} , \quad (2.83)$$

and, in terms of the heat of fusion ΔQ_m , (2.82) can be written as

$$\left(\frac{T_m}{T} - 1 \right) \frac{\Delta Q_m}{N_0 k T_m} = -(r_L - r_S) \ln \left(1 - \frac{x_S}{r_S} \right) . \quad (2.84)$$

The ratio $\Delta Q_m/N_0 k T_m$ is known to assume very nearly the same value in a large number of metals, viz.,

$$\Delta Q_m/N_0 k T_m \approx 1.15 . \quad (2.85)$$

Thus, the equilibrium compositions x_S and x_L can be obtained quite easily, provided that r_S and r_L are known.

Remembering that the coordination number of a metal is not much changed upon melting, we assume that the local configuration of interstitial sites is also reasonably well conserved, and that the same type of interstitial sites as in the solid state is preferred by H atoms for occupation. We assume

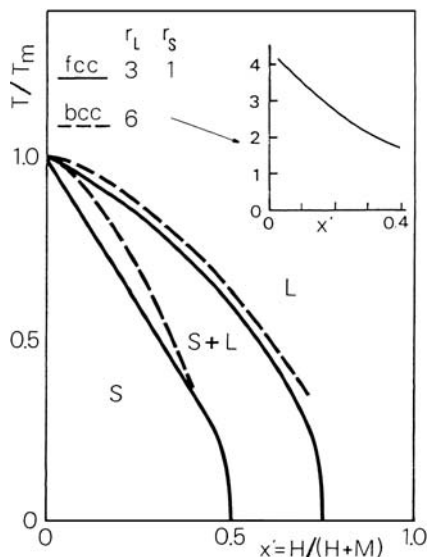


Fig. 2.22. Calculated variation of solidus and liquidus temperatures with composition of M-H alloys having fcc or bcc structures. The following values have been assumed for the number of interstitial sites: for fcc metals $r_L = 3$, $r_S = 1$; for bcc metals, $r_L = 6$, r_S variable with composition as shown in the inset [2.139]

furthermore that, in the liquid state, geometrical and elastic constraints of the lattice being removed, all the interstitial sites become available. Thus, we assume that $r_L = 3$ (O and T sites) for fcc metals and $r_L = 6$ (T sites) for bcc metals. In the solid state, the mutual blocking effect makes the number of available sites smaller (Sect. 2.2.2): $r_S = 1$ for fcc metals, and r_S decreases with composition in bcc metals (see the inset of Fig. 2.22).

The calculated solidus and liquidus lines, namely, the temperature dependence of the equilibrium compositions x_S and x_L , are shown in Fig. 2.22 for fcc and bcc metals. The good agreement of these calculated results with the observations in Ti-H and V-H systems indicates that the lowering of the melting point is simply a consequence of the increased number of sites for H atoms in the liquid as compared to the solid state.

It must be admitted that these simple entropy considerations can be valid only when the heat of solution does not vary much with hydrogen concentration.

3 Hydrogen in Alloys

Being composed of more than two kinds of atoms, the crystal lattice of alloy-hydrogen systems has, in general, a complex structure, containing different types of interstitial sites with different chemical as well as geometrical configurations of the surrounding atoms. In ordered alloys, the number of such types is relatively small, and at least countable, but in disordered alloys, there may well be a continuous distribution of local configurations and site energies.

In this chapter, we approach these systems in the following two steps. We start by examining the average effects of alloying on the solubility and the terminal solubility of hydrogen, and then proceed to develop a formalism that allows for the distribution of site energies for H atoms. This formalism is applied to the problem of trapping and blocking by solute atoms and, subsequently, to hydrogen in ordered and disordered alloys – ordered alloys including intermetallic compounds and disordered alloys including amorphous alloys.

3.1 Effects of Alloying on the Solubility

Effects of substitutional solute atoms on the solubility of hydrogen in metals have been studied from as early as the 1930s, mainly in connection with the practical applications of Pd alloys, but have not yet been given a clear physical picture. Here we try to survey the experimental results and make some inferences therefrom.

Let us start by examining the relative importance of the average electronic and elastic contributions.

Figure 3.1 shows the heats of solution at infinite dilution, ΔH_s^0 , obtained for substitutional alloys of Group IV–VI transition metals. The overall correlation between ΔH_s^0 and the average electron-to-atom ratio (e/a) is obvious. In contrast, scarcely any correlation was found between ΔH_s^0 and the lattice parameter change (not shown). Thus, in these cases, the electronic interaction is by far the more important factor in determining ΔH_s^0 than the volume effect.

In the case of Pd, the situation is reversed. No systematic variation exists between ΔH_s^0 vs. e/a , whereas a correlation is found between ΔH_s^0 and

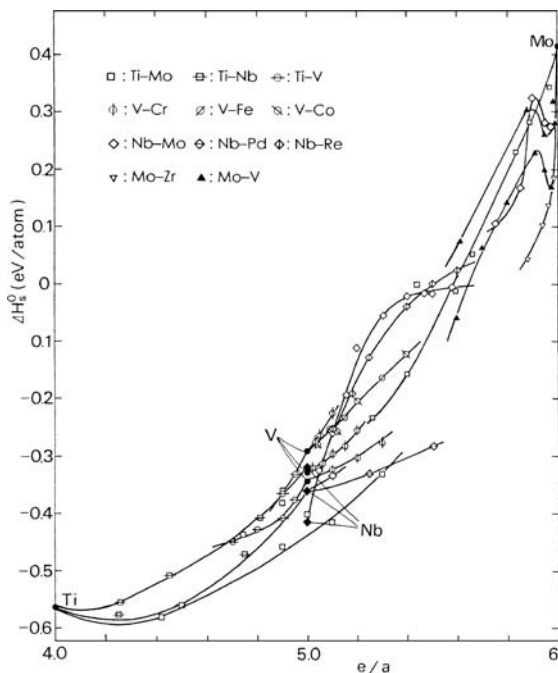


Fig. 3.1. Heats of solution of hydrogen at infinite dilution, ΔH_s^0 , in substitutional alloys as a function of electron-to-atom ratio, e/a [3.1–3.9]

the lattice parameter (Fig. 3.2). The correlation can be expressed, roughly, as $\partial \Delta H_s^0 / \partial V = -1.3 \pm 0.7$ eV/atom H. Within the scatter of data points, this agrees with the estimate obtained from the average elastic interaction between H atoms (2.31),

$$\frac{\partial \Delta H_s^0}{\partial V} = -\gamma K_0 v_H = -0.84 \text{ eV/atom H.}$$

The mutual consistency of these two estimates shows that in Pd-based alloys the volume effect is more important than the average electronic effect in determining ΔH_s^0 .

In an attempt to give a consistent description of the alloying effect on ΔH_s^0 , *Griessen* and *Riesterer* [2.25] developed a band structure model, and applied it to a wide range of alloy-H systems. In the case of Pd-alloys, the volume effect estimated from their model was

$$\frac{\partial \Delta H_s^0}{\partial V} = -3.1 \pm 0.7 \text{ eV/atom H.}$$

The agreement with observation is not so satisfactory as they claimed. (They compared their estimate with an average “experimental” value of -2.3 eV, based on a smaller number of data points.) Thus, the efforts made in the past

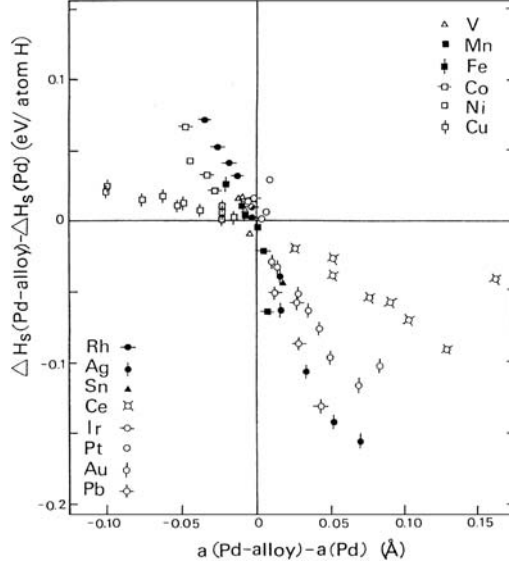


Fig. 3.2. Heats of solution of hydrogen at infinite dilution, ΔH_s^0 , in Pd alloys as a function of lattice parameter [2.25]

trying to correlate ΔH_s^0 with the average elastic and electronic interactions have met with only a limited success.

More insight into the alloying effect can be gained by examining the entropy of solution at the infinite dilution ΔS_s^0 . Figure 3.3 shows that, in Pd-based alloys, ΔS_s^0 decreases with solute concentration for all the solute species. This suggests that the number of available interstitial sites, r , is decreased with increase of the solute concentration, probably as a result of repulsive interactions between H and solute atoms. Similar observations have been made in Ti, V, and Nb alloys, as shown in Fig. 3.4. The only exception is the case of Ti in V metal, in which ΔS_s^0 increases with an increase of Ti concentration. This can be understood if Ti atoms in V act as traps for H atoms. (There are other pieces of evidence in support of this.) Thus we infer that the local configurational effects play an important role in determining the solubility of H in substitutional alloys.

The heats of solution at higher concentrations of hydrogen also support this inference. Figure 3.5 shows that the increase of ΔH_s at high H concentrations is shifted to lower concentrations as more solute atoms are added. This behavior can be naturally understood if some local repulsion operates between H and solute atoms. H atoms will be confined to a smaller number of interstitial sites and, consequently, the repulsive interaction between H atoms will become stronger on an average.

We are now faced with very complex problems of local configurational effects. As a result of the interaction with solute atoms, the energy of H

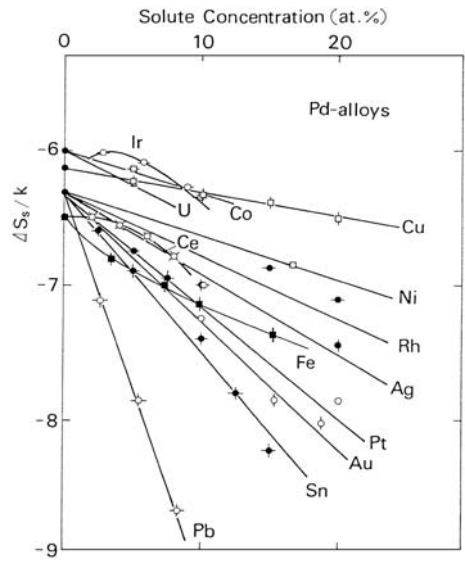


Fig. 3.3. Entropy of solution of hydrogen at infinite dilution, ΔS_s^0 , in Pd alloys as a function of solute concentration [3.10–3.22]

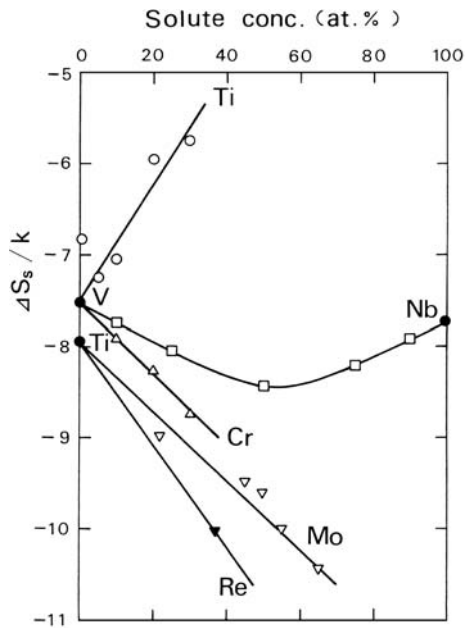


Fig. 3.4. Entropy of solution of hydrogen at infinite dilution, ΔS_s^0 , in some alloys: Ti–Mo, Re [3.1], V–Ti, Nb, Cr [3.7]

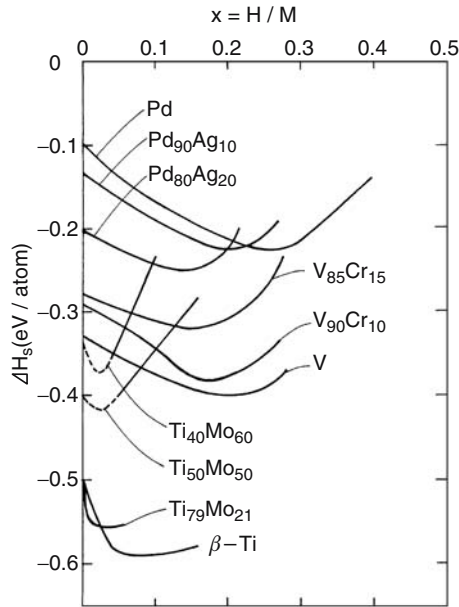


Fig. 3.5. Heats of solution of hydrogen ΔH_s in substitutional alloys as a function of hydrogen concentration: Ti–Mo [3.1]; V–Cr [3.6]; Pd–Ag [3.17, 3.23]

atoms should vary depending on their position relative to solute atoms. Thus, in order to understand the alloying effect, we have to know the strength of the solute–H interaction at a large number of sites around each solute atom, and perform complex probabilistic calculations on the distribution of the interacting atoms.

Calculations based on this approach have been pursued by *Hall et al.* on Nb–V, Mo alloys [3.24–3.26], and by *Griessen* on Pd–Ag alloys [2.52]. These calculations are believed to be important as theoretical approaches to random-field systems, but still appear to suffer from inaccuracies in the solute–H interaction strengths and difficulties in treating the local configurational effect and the average (mean-field) effect in a consistent way.

3.2 Effects of Alloying on the Terminal Solubility

In substitutional alloys, the terminal solubility of hydrogen (TSH) at low solute concentrations is affected in various ways depending on the solute species, but at high solute concentrations appears to be invariably increased. Here we try to provide a simple explanation for the increase of TSH based on solution thermodynamics originally due to *Oates* and *Flanagan* [3.27, 3.28], and then add a few words on more local effects, operating possibly at lower solute concentrations.

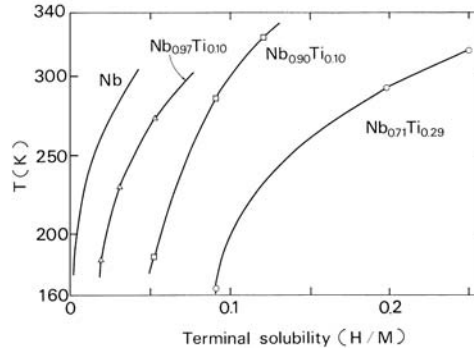


Fig. 3.6. Solvus line shifts in Nb-Ti-H alloys [3.30]

Figure 3.6 shows how the solvus line is shifted to higher H concentrations with increasing solute concentrations in Nb-Ti alloys. Similar results were also obtained for V and Mo in Nb [3.29, 3.30]. The variation of TSH over a wide range of alloy compositions can be seen in Fig. 3.7, in which the terminal solubilities at 250 K for Nb-V and Nb-Ta alloys are shown [3.29, 3.30]. In both cases, the observed TSH exhibits a pronounced maximum at a certain alloy composition. Since, in these alloys, most bulk properties such as the lattice constant, the electronic DOS at the Fermi energy, and the heat of solution of hydrogen vary monotonically with the alloy composition, this behavior of TSH appeared rather surprising before it was explained in a natural way in terms of solution thermodynamics.

Let us derive the equilibrium condition between the α and β phases of a pseudo-binary system MH_x , where $M = A_{1-y}B_y$. For the equilibrium between the solid-solution (α) and the hydride (β) phases to be attained, only H atoms are allowed to move between the two phases; A and B atoms are assumed to be frozen. This kind of equilibrium is called the para-equilibrium (PE), as distinct from the complete equilibrium (CE), in which all the component atoms are mobile and adjust themselves to attain the minimum total free energy. For the sake of simplicity, we assume that the hydride phase has a nearly fixed composition MH_a . Referring to Fig. 2.16, this means that the free-energy function g^β has a very sharp minimum, i.e.,

$$x_\beta \approx a, \quad (3.1)$$

$$g^\beta(x_\beta) \approx \text{const} \quad (3.2)$$

$$= \mu_0^\beta + a\mu^\beta = g_a. \quad (3.3)$$

For the α phase, writing

$$\mu^\alpha = \mu^{\text{anc}} + kT \ln \frac{x}{r-x}, \quad (3.4)$$

we obtain the following expressions:

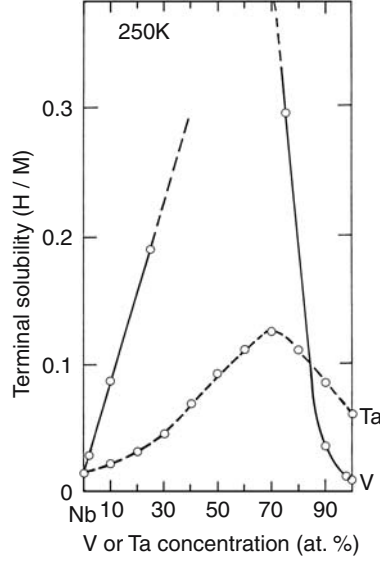


Fig. 3.7. Terminal solubilities for hydrogen at 250 K in Nb–V and Nb–Ta alloys [3.29, 3.30]

$$\mu_0^\alpha = \mu_0^{\text{anc}} + kTr \ln \frac{r-x}{r}, \quad (3.5)$$

$$g^\alpha = (\mu_0^{\text{anc}} + x\mu^{\text{anc}}) + kT[x \ln x + (r-x) \ln(r-x) - r \ln r]. \quad (3.6)$$

The equilibrium condition, the condition of common tangent, can be written as

$$\left(\frac{\partial g^\alpha}{\partial x} \right)_x = \frac{g_a - g^\alpha}{a - x}; \quad (3.7)$$

hence,

$$kT[a \ln x + (r-a) \ln(r-x) - r \ln r] = g_a - (\mu_0^{\text{anc}} + a\mu^{\text{anc}}). \quad (3.8)$$

Substituting

$$\Delta g^0(\text{MH}_a) = \left(\mu_0^\beta - \mu_0^{\text{anc}} \right) + a \left(\mu^\beta - \frac{1}{2} \mu^{\text{g}0} \right) \quad (3.9)$$

for the free energy of formation of the hydride MH_a in H_2 gas of standard state, and

$$\Delta \mu^\alpha = \mu^{\text{anc}} - \frac{1}{2} \mu^{\text{g}0}, \quad (3.10)$$

we finally obtain

$$kT[a \ln x + (r-a) \ln(r-x) - r \ln r] = \Delta g^0(\text{MH}_a) - a \Delta \mu^\alpha. \quad (3.11)$$

Note here that the left-hand side is an increasing function of x in the concentration range of interest: $0 < x < a$ when $a < r$, and $0 < x < r$ when $r < a$. The gist of Oates and Flanagan's explanation is that free energies of formation of alloy hydrides are expected to be higher in many cases than those of constituent metal hydrides, which, according to (3.11), makes the equilibrium H concentration of the α phase correspondingly higher. This expectation can be rationalized as follows. We assume that metals A and B are of the same structure, and form an ideal solution. As regards hydrides, we must recognize that the hydride AH_a , which coexists with α - AH_x , may not be isomorphous with the hydride BH_b , which coexists with β - BH_x . Let us consider here the effect of alloying A with B; the effect of alloying B with A must be treated in a similar way later. We regard the alloy hydride as being a solid solution of AH_a and BH_a . The hydride BH_a , which is isomorphous with AH_a , may not actually exist and may, therefore, be a hypothetical one. Noting that the entropy of mixing A and B atoms in the hydride, $-kT[y \ln y + (1-y) \ln (1-y)]$, is cancelled by the corresponding term in the alloy, we obtain the expression for the free energy of formation of the alloy hydride:

$$\Delta g^0(MH_a) = [(1-y)\Delta g^0(AH_a) + y\Delta g^0(BH_a) + g^m y(1-y)]. \quad (3.12)$$

It may be reasonable to assume that the hydride solid solution exhibits a positive deviation from ideality, viz., $g^m < 0$. The first term can either increase or decrease with y , but we may surmise that an increase is more plausible. This is so because the free energy of formation of a hypothetical hydride is expected to be generally higher than its counterpart actually existing in nature. There is no compelling reason to believe these arguments, but at least we may accept them as reasonable guesses. Thus, both terms of (3.12) are expected to increase with an increase of y , the concentration of B atoms.

Oates and Flanagan [3.27] attempted a realistic calculation of the TSH in the Nb-Ta system based on these ideas, and succeeded in reproducing the observation excellently. In particular, the sharp maximum in TSH, as seen in Fig. 3.7, was found to occur at an alloy composition to the left of which the hydride is β -Nb(Ta)H_{0.71} and to the right β -Ta(Nb)H_{0.47}, having different structures. They subsequently extended their calculation to the Nb-V system, and achieved comparable success [3.31].

Although a critical evaluation of their work is extremely difficult due to numerous fitting parameters involved, their conclusion that the seemingly anomalous TSH in concentrated alloys can follow naturally from solution thermodynamics of alloy hydrides is believed to be sound. Further implications of their work, for example, a connection between the paraequilibrium and the complete equilibrium, can be learned from their original papers [3.27, 3.28, 3.31].

Effects of small concentrations of impurity atoms on the TSH were first noticed as discrepancies of data from different investigators, especially in bcc metals at low temperatures. Subsequently, it was recognized that a heat

treatment in ultrahigh vacuum could remove the discrepancies [3.32, 3.33], and that gaseous impurities N and O in specimens caused the increase of TSH in proportion to their concentration (see, e.g., [3.34, 3.35]). The increase of TSH in these cases is now believed to be the result of trapping by these interstitial atoms, N and O, which prevent H atoms from precipitating as hydride. Trapping behaviors of these interstitial solutes have since been investigated in detail by using various techniques; for example, measurements of the electrical resistivity, internal friction, channeling, etc. (see Sects. 5.6.2 and 6.4.3).

The increase of TSH in dilute substitutional alloys has been observed in a limited number of cases. In the V–H system, the TSH is increased by Ti and Zr, but affected only slightly by Mo, Nb, Cr, Fe, and Cu [3.36, 3.37]. In the Nb–H system, the TSH is increased by Ti, V, and Mo, but unaffected by Ta [3.30]. The mechanism operating here is also believed to be the trapping of H atoms; direct evidence of trapping has been obtained for Ti and Mo in Nb, for which enhanced TSH takes place.

Admittedly, the occurrence of trapping itself does not automatically lead to the enhancement of TSH. We can only surmise that the lowering of energy by trapping should be more effective in the α phase, because in a hydride phase, the presence of solute atoms will also exert an adverse effect by partially destroying the ordered structure.

It is noteworthy that the mechanism operating here is distinctly different from what was described earlier. In dilute alloys, a local interaction between H and solute atoms in the α phase is responsible, whereas in concentrated alloys, average thermodynamical properties of a hydride phase are responsible for a change of TSH.

3.3 Hydrogen–Solute Interaction: Trapping and Blocking

In most of the foregoing treatment, it has been assumed that H atoms are distributed over interstitial sites having the same energy. In cases where local interactions between hydrogen and the solute atoms or between hydrogen atoms came into play, we assumed that a certain number of interstitial sites are disturbed by the interaction in such a way that H atoms are either completely excluded from these sites (blocking) or completely bound to these sites (trapping) before these sites are exhausted. Actually, the degree of blocking or trapping may vary with temperature, according to the relative magnitude of the energy difference between the disturbed and undisturbed sites in comparison to the thermal energy kT .

We shall present here a formalism – the so-called two-state model – that applies to the situation where interstitial sites comprise sites having two different energies. Extension to multiple or continuous site energies will be made in the next section.

Let us consider the case of two energy states: N_1 interstitial sites with energy E_1 and N_2 sites with energy E_2 . The distribution of H atoms is such that the number of ways of distributing n atoms over these sites becomes maximum for a given total energy. Statistical mechanics tells us that the Fermi–Dirac distribution applies in this case, namely,

$$\frac{N_1}{e^{(E_1-\mu)/kT} + 1} + \frac{N_2}{e^{(E_2-\mu)/kT} + 1} = n, \quad (3.13)$$

where μ , is the chemical potential of H atoms [3.38].

To be more specific, suppose there are impurity atoms which lower the original site energy e_0 by the binding energy e_b . Writing the total number of sites as N and the number of disturbed sites N_d , we can rewrite (3.13) as

$$\frac{N - N_d}{e^{(e_0-\mu)/kT} + 1} + \frac{N_d}{e^{(e_0-e_b-\mu)/kT} + 1} = n, \quad (3.14)$$

from which we obtain

$$e^{(e_0-\mu)/kT} = \frac{1}{2x} \{ (r - x - r_d - \theta x + \theta r_d) + [(r - x - r_d - \theta x + \theta r_d)^2 + 4x(r - x)\theta]^{1/2} \}. \quad (3.15)$$

Here, as before, the concentrations are written as ratios to the number of M atoms, $r = N/N_0$, $x = n/N_0$, $r_d = N_d/N_0$, and $\theta = \exp(e_b/kT)$. We may say that impurity atoms either trap or block H atoms according as $e_b > 0$ or $e_b < 0$.

Let us consider the two limiting cases: a strong trapping and a strong blocking. In the strong blocking case ($-e_b \gg kT$), the second term of (3.14) becomes small, and one obtains

$$\mu \approx e_0 + kT \ln \frac{x}{r' - x}, \quad (3.16)$$

where $r' = r - r_d$. In the strong trapping case ($e_b \gg kT$), all the H atoms will be trapped as long as $x < r_d$. In this case, the first term of (3.14) is small ($e_0 - \mu \gg kT$), and one obtains

$$\mu \approx e_0 - e_b + kT \ln \frac{x}{r_d - x}. \quad (3.17)$$

When $x > r_d$, H atoms fill the trapping sites, and the rest are distributed over undisturbed sites. In this case, the exponential term in the second term of (3.14) is small, and one obtains

$$\mu \approx e_0 + kT \ln \frac{r - r_d}{r' - (x - r_d)}. \quad (3.18)$$

It can be seen that, in comparison to the original host metal without containing solute atoms, the chemical potential is increased by blocking and decreased by trapping, as anticipated.

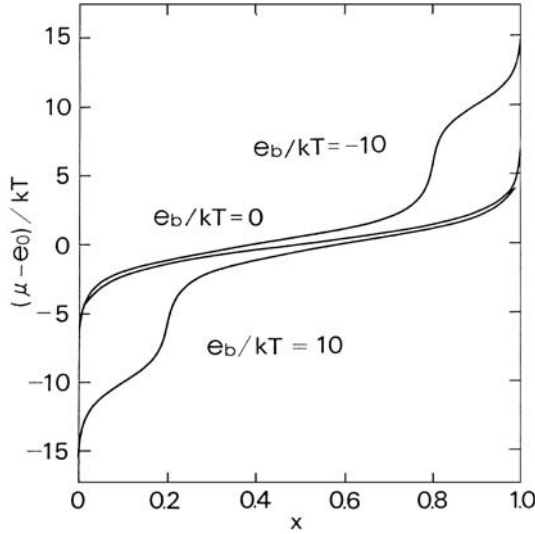


Fig. 3.8. Chemical potential as a function of hydrogen concentration in the presence of trapping or blocking: (a) with trapping sites of concentration $r_d = 0.2$ and the binding energy $e_b/kT = 10$; (b) without trapping or blocking; (c) with blocking sites of concentration $r_d = 0.2$ and the binding energy $e_b/kT = -10$

Variation of the chemical potential with hydrogen concentration is shown in Fig. 3.8. To avoid complexity, the curves are shown for only three cases: blocking ($e_b/kT = -10$); no interaction ($e_b = 0$); and trapping ($e_b/kT = 10$), with $r = 1$ and $r_d = 0.2$. When e_b/kT becomes larger in magnitude, the stages at e_0 and $e_0 - e_b$ become more clearly separated, making the approximation of complete blocking or trapping more justifiable.

It may be appropriate here to mention the conditions under which the Fermi–Dirac statistics are reduced to the more commonly used Boltzmann statistics. The two statistics become equivalent in the limit that the exponential terms in the denominators of (3.14) are much larger than 1, namely, that

$$e_0 - \mu \gg kT \quad \text{and} \quad e_0 - e_b - \mu \ll kT. \quad (3.19)$$

Then we have

$$[(N - N_d) + N_d e^{e_b/kT}] e^{(e_0 - \mu)/kT} = n, \quad (3.20)$$

and the ratio of the population of H atoms on disturbed and undisturbed sites becomes $N_d \exp(e_b/kT)/(N - N_d)$, as it should. This expression was used, for example, by *Hohler* and *Kronmüller* [3.39] in their analysis of hydrogen trapping by substitutional impurity atoms in Ni. Other approximate forms were also adopted in the past to describe the trapping phenomenon (see, e.g., [3.35, 3.40]). It must be noted that, with reference to Fig. 3.8, the conditions

(3.19) are satisfied only at very low concentrations of hydrogen, so that in most cases the analysis in terms of the Fermi–Dirac statistics appears to be necessary. A more general formulation based on the Fermi–Dirac statistics that allows for multiple trapping configurations was given by *Cannelli et al.* [3.41].

Experimental values of the binding energy between the solute and hydrogen atoms are compiled in Tables 3.1 and 3.2 for interstitial and substitutional solutes, respectively. The binding energies are in the range 0.1 ± 0.05 eV, large enough in comparison to thermal energies at ordinary temperatures to affect significantly the behaviors of hydrogen.

As regards the maximum number of H atoms, n_d , trapped by each solute atom, $n_d \approx 1$ was obtained for C and N in V [3.34] and N in Nb [3.35], and $n_d > 1$ for O in V [3.33, 3.42], and Ti in Nb [3.40, 3.41, 3.48]. In the case of H trapped by Ti in Nb, two distinct energy states were found and attributed to TiH and TiH₂ complexes. In the case of V–O–H, the presence of many kinds of higher complexes had to be introduced [3.34].

Table 3.1. Binding energies of interstitial solute–hydrogen pairs in bcc metals

Metal Pair	V				Nb			Ta
	C–H	N–H	O–H	O–D	N–H	O–H	O–D	N–H
Binding energy e_b [eV]	0.135 ^a	0.135 ^a	0.09 ^a	0.10 ^b	0.12 ^c	0.09 ^{e,f}	0.13 ^{e,f}	0.06 ^h
					0.1 ^d	$\langle 100 \rangle 0.1^g$ $\langle 111 \rangle 0.08$		

^a[3.34]; ^b[3.42]; ^c[3.35]; ^d[3.43]; ^e[3.44]; ^f[3.45]; ^g[3.46]; ^h[3.47].

Table 3.2. Binding energies of substitutional solute–hydrogen pairs

Metal	V	Nb		Ni					
Pair	Ti–H	Ti–H,D	Mo–H	Fe–H,D	Cu–H,D	Ti–H	Pd–H	Pt–H	V–H
Binding energy	0.15 ^a	0.10 ^{b,c}	0.09 ^d	0.08(H) ^f	0.095(H) ^f	0.12 ^f	0.05 ^f	0.085 ^f	0.056 ~ 0.097 ^f
e_b [eV]			$\approx 0.05^e$	0.11(D) ^f	0.11(D) ^f				

^a[3.36]; ^b[3.40]; ^c[3.48]; ^d[3.49]; ^e[3.50]; ^f[3.39].

Most of the values given above were deduced from the measurements of internal friction caused by the reorientation of solute–hydrogen pairs under stress. An analysis of the data was made in most cases by some approximate

methods based on the Boltzmann statistics, except in the case of Nb–Ti where a legitimate application of the Fermi–Dirac statistics was made even allowing for more than one disturbed energy state [3.41, 3.48].

Compared to trapping, it is more difficult to draw quantitative information on the blocking by solute atoms. *Watanabe* and *Fukai* [2.37] performed calorimetric studies of the vanadium–alloy–hydrogen system, and attempted to deduce a number of blocked sites around each substitutional atom by analyzing the observed entropy changes for the phase transition β_1 – β_2 in a series of alloys $V_{1-y}I_yH_{0.5}$. The values obtained are: $n_d = 14, 12, 5, 5, 3$ and 0 for Mo, Fe, Cr, Nb, Ti, and Zr, respectively. The structure of the β_1 and β_2 phases of the V–H system is body-centered tetragonal, in which the number of O_Z sites in the first, second, and third shells around a solute is 2, 4, and 8, respectively. The experimental values of n_d imply that Mo and Fe atoms block up to the third-nearest neighbor shells, Cr and Nb probably up to second shells, and Ti and Zr practically none.

More microscopic information can be obtained from the Mössbauer effect when appropriate probe nuclei are available. The isomer shifts and Zeeman splittings of the Mössbauer spectra allow the determination of the electron density and hyperfine fields, respectively, on the probe nuclei, and their changes induced by H atoms. (For the application of Mössbauer spectroscopy to M–H systems, see, e.g., [3.51–3.53].) As the effects of H atoms become more conspicuous when they enter the nearest interstitial sites of the probe nuclei, trapping or blocking by probe atoms can be studied by analyzing the observed spectra.

For ^{57}Fe in PdH_x ($x = 0.62 \sim 0.96$), *Pröbst et al.* [3.54] succeeded, by the application of a strong magnetic field at low temperatures, in resolving the spectrum into seven components corresponding to the configurations having $0 \sim 6$ H atoms as nearest neighbors. From the relative intensities of the individual components, binding energies were estimated to be between $e_b = -0.03$ eV and $-(0.1 \sim 0.15)$ eV for $1 \sim 6$ nearest-neighbor H atoms.

Mössbauer experiments were also made on substitutional atoms, Co, Ru, Rh, Os, Ir, Pt, Au, and Sn in PdH_x , for which suitable isotopes are available [3.55]. The resolution was not as good in these cases but allowed an approximate evaluation of the interaction energies. e_b was negative in all cases, indicating that blocking has taken place. The magnitude of e_b appears to be correlated with the position of the solute element in the Periodic Table: smallest (~ 0.02 eV) for Ru and Rh (4d-series elements, same as Pd), largest (> 0.15 eV) for Au and Sn (5d, B-group elements), and intermediate for others. It is interesting to note that Au and Sn cause strong blocking, but at the same time lower the heat of solution ΔH_s [3.18, 3.21]. Probably, these solute atoms make ΔH_s lower through average lattice expansions, although they repel H atoms locally by some short-range electronic interactions.

Evidence of blocking was also obtained from Mössbauer studies on Ru, Ir, and Au in NbH_x [3.56, 3.57] and VH_x [3.58], and also on Fe in NiH_x ($x \approx 1$) [3.59] and Ni–Cu alloys [3.60].

We next examine briefly how the spinodal decomposition is affected by alloying. This can be done by adding a term $-\mu x$ to the chemical potential in (3.15), or, (3.16) or (3.18) in the two limiting cases of strong trapping and strong blocking, respectively. Then the critical point can be easily calculated, with the following results:

$$\begin{aligned} \text{Strong trapping: } x_c &= (1 + r_d) x_{c0}, & T_c &= T_{c0}(1 - r_d), \\ \text{Strong blocking: } x_c &= (1 - r_d) x_{c0}, & T_c &= T_{c0}(1 - r_d), \end{aligned} \quad (3.21)$$

where the critical point in the pure host metal is represented by (x_{c0}, T_{c0}) and that of the alloyed specimen by (x_c, T_c) . The critical concentration is increased by trapping and decreased by blocking, but the critical temperature is lowered in both cases.

The lowering of the spinodal decomposition temperature has been observed in many systems. The most famous one is probably the case of a Pd–Ag alloy, in which the addition of ~ 30 at.% Ag lowers the spinodal to below room temperature and, thus, suppresses the failure of hydrogen-purifying membrane caused by the repeated precipitation and dissolution of the α' phase in the course of heating-cooling cycles. Although problems in concentrated alloys would be better described by a formalism that allows for distributed site energies, the physics of the suppression of spinodal decomposition is believed to be contained in the above discussion based on the two-state model.

3.4 Hydrogen in Ordered Alloys

Among various problems associated with hydrogen in ordered alloys (including intermetallic compounds), here we focus on their very basic aspects, i.e. the site occupancy and energy states.

The site location of H atoms has been determined by neutron diffraction on a large number of deuterided intermetallic compounds, and the results are compiled in the review paper of *Yvon* and *Fischer* [3.61]. There, interstitial sites are classified according to the number and composition of surrounding M atoms. In C15 type Laves compounds AB_2 , for example, there exist 17 T sites per formula unit, consisting of 12 $[\text{A}_2\text{B}_2]$ type, 4 $[\text{AB}_3]$ type and 1 $[\text{B}_4]$ type sites. H atoms on different types of sites have different energies, which we call site energies. In the course of hydrogenation, H occupation starts from those of the lowest site energy and proceeds successively to higher energy sites. Thus, the order of site energies can be learned from the order of site preference as a function of total H concentration. This information is listed in the review of *Yvon* and *Fischer* [3.61].

The distribution of H atoms over these sites is to be expressed by the Fermi–Dirac statistics,

$$N_0 \sum_i \frac{p_i}{e^{(E_i - \mu)/kT} + 1} = n, \quad (3.22)$$

where N_0 is the number of formula units (AB_2 , for example) in the sample, p_i and E_i the number and site energy of the interstitial site of type i , respectively, and n the total number of H atoms. The chemical potential μ is determined by this equation for a given number of H atoms. It increases gradually as H concentration is increased, leading to the occupation of higher-energy sites.

Experimentally, the assignment of energy states to different types of sites can be made by comparison of two separate experiments – site occupancy and energetics – as a function of H concentration. To illustrate such a procedure, the case of Laves phase compound ZrV_2 will be described in some detail. Determination of H energies was performed by thermal desorption spectroscopy (TDS) [3.62]. In this method, the rate of desorption of H into vacuum was measured in the course of linear ramping of temperature, repeatedly for different initial H concentrations. An example of such measurements is shown in Fig. 3.9 [3.62]. Three desorption peaks appeared consecutively as initial H concentration x_0 was increased. At lower initial concentrations ($x_0 < 1$), only a single peak A appears at high temperatures. At $x_0 \approx 1$, a shoulder appears on the lower temperature side and develops into peak B. Subsequently, at $x_0 \approx 2.6$, a second shoulder appears and develops into peak C. As no phase separation is known to occur above room temperature, these peaks can be assigned to desorption from different types of sites. On the other hand, neutron diffraction data on ZrV_2D_x showed that at room temperature only $[\text{Zr}_2\text{V}_2]$ type sites were occupied up to $x_0 \approx 2.5$. Above this concentration, the occupancy of this type of sites became slow and that of $[\text{ZrV}_3]$ type sites increased instead [3.61]. Thus, the peaks A and B can be ascribed to desorption from $[\text{Zr}_2\text{V}_2]$ sites, and peak C from $[\text{ZrV}_3]$ sites. The activation energies estimated for A, B, C peaks were 1.6 eV \sim 1.4 eV and 0.4 eV, respectively.

Note that the site occupancy starts from 1 out of 12 $[\text{Zr}_2\text{V}_2]$ sites, subsequently to another ~ 1.5 $[\text{Zr}_2\text{V}_2]$ sites, and turns to $[\text{ZrV}_3]$ sites leaving the remaining $[\text{Zr}_2\text{V}_2]$ sites empty. This is a consequence of mutual repulsion between H atoms, and self-organizing effect of H occupancy that makes a certain interstitial sublattice lower in energy than the rest. There are many such examples of the formation of H ordered sublattice in binary M–H alloys (Sect. 2.4.1).

Parenthetically, a word of caution will be given to the interpretation of TDS spectra. In the analysis described here [3.62], it was assumed that the desorption process is rate-limited by the recombination process $\text{H} + \text{H} \rightarrow \text{H}_2$ on the surface, and that H atoms on the surface are in thermal equilibrium

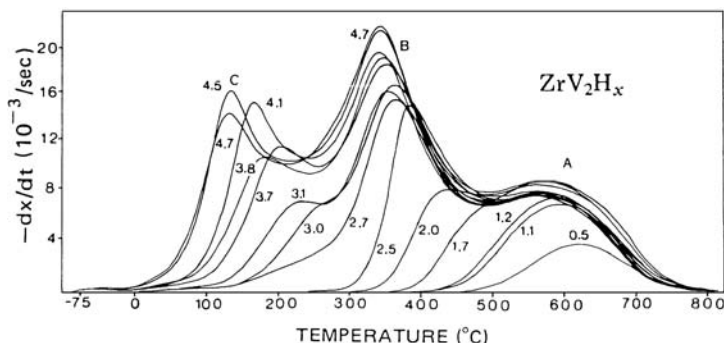


Fig. 3.9. The thermal desorption spectra of ZrV_2H_x . The numbers on the curves denote the initial H concentrations [3.62]

with those in the bulk. Thus, the activation energies observed should be equal to the site energies measured from the surface state. The validity of these assumptions was tested by comparing the calculated TDS curves with observed ones. An excellent agreement was obtained in this case for a wide variety of initial H concentrations.

Naturally, a rate-limiting step can be different in different circumstances. There are indeed cases where the diffusion to the surface is slower than the recombination process. Thus, in order to extract useful information from TDS data, we have to first identify the rate-limiting process, and adopt a method of analysis appropriate for the situation.

The method of thermal desorption spectroscopy was originally developed for investigating the adsorbed states on the surface, and later applied to the study of bulk properties. Such studies performed up to 1991 were critically reviewed by *Mintz et al.* [3.63].

Site energies can also be extracted from analysis of p - x - T relations. This method is more transparent in principle than TDS because it is based on thermal equilibrium properties free from kinetics. In the case of TiFeH_x , for example, two well-separated plateaux were observed, reflecting the presence of three different phases; α for $x \leq 0.06$, β for $x \approx 1.0$, and γ for $x \approx 2.0$. The activation energies determined from the desorption plateaux are $-(0.25 \sim 0.29) \text{ eV/H}_2$ for α/β and -0.35 eV/H_2 for β/γ [3.64, 3.65]. This implies that the site energies in β and γ phases are $(0.27 + H_s)/2 \text{ eV}$ and $(0.62 + H_s)/2 \text{ eV}$ lower, respectively, than in the α phase (H_s : heat of solution in eV/H_2). In terms of structure, TiFe has a cubic CsCl type structure, which becomes slightly distorted in β and γ phases. H atoms are accommodated in O sites; They enter $[\text{Ti}_4\text{Fe}_2]$ type sites in the α phase, fill them up in the β phase, and subsequently fill up the $[\text{Ti}_2\text{Fe}_4]$ sites in the γ phase [3.61]. The site energies derived above can be assigned, respectively, to these types of sites.

In this particular case, two plateaux appear well separated due to rather discontinuous changes in composition, but sloping plateaux due to multiple

site occupancy are more commonly observed. In these cases, too, appropriate analysis of p - x - T data can lead to reasonable estimates of the number and energy of the interstitial sites involved. For many other aspects of H atoms in intermetallic compounds, the reader is referred to the two volumes of books devoted to this subject [3.66, 3.67].

It may be added here that in intermetallic hydrides containing lanthanide atoms, peculiar properties sometimes show up. For example, in the hydrides of ternary intermetallic compounds LnNiIn ; $\text{Ln} = \text{La, Ce, Pr, Nd}$, the H-H separation is exceptionally short. (See, footnote 2 in Sect. 2.2.2.) A pair of H atoms occupying a face-sharing tetrahedra, with three Ln atoms forming a shared face, come as close as $\sim 1.5 \text{ \AA}$ [2.58–2.60]. These lanthanides, the most electropositive of all the lanthanides, are expected to donate some electrons to neighboring H atoms, and exert strong attractive forces towards the shared plane. The large volume expansion caused by hydrogenation is also consistent with this reasoning of charge transfer. (See Table 4.3 and discussions there.) The strong affinity of hydrogen to lanthanide atoms plays a crucial role in determining the local structure of amorphous alloys, as described in the next section.

3.5 Hydrogen in Amorphous Alloys

Most amorphous (glassy) alloys are formed by rapidly quenching the melt to room temperature or below at cooling rates of 10^4 K s^{-1} . Other techniques such as thermal evaporation, sputtering, electrodeposition, and ion implantation have also been adopted. In all these methods, samples are usually obtained in the form of thin film or foil. Amorphous alloys can also be fabricated by ball-milling elemental metal powders for $30 \sim 60 \text{ h}$ (mechanical alloying), or in some cases by simply hydriding the crystalline alloys. In these methods, powder samples are obtained.

Amorphous alloys are thermodynamically metastable, and decompose into multiple crystalline phases when heated to the crystallization temperature $T_{\text{cryst}} = 200 \sim 500^\circ\text{C}$, depending on the alloy species. Thus, in charging amorphous alloys with hydrogen, either by electrolysis or from the gas phase, care must be taken not to raise the temperature above T_{cryst} . We cannot activate the surface by heating in vacuum or H_2 gas, as is usually done in the case of crystalline samples, but content ourselves, in most cases, by simply abrading the surface with emery paper and cleaning ultrasonically in acetone and/or ether. Coating with a Pd overlayer after cleaning by argon-ion sputtering has also been known to be effective.

Several review papers have been written on amorphous-alloy-hydrogen systems by *Maeland et al.* [3.68] and *Maeland* [3.69–3.71].

In this section, we describe some of the characteristic thermodynamical properties of amorphous-metal-hydrogen systems and their explanation in

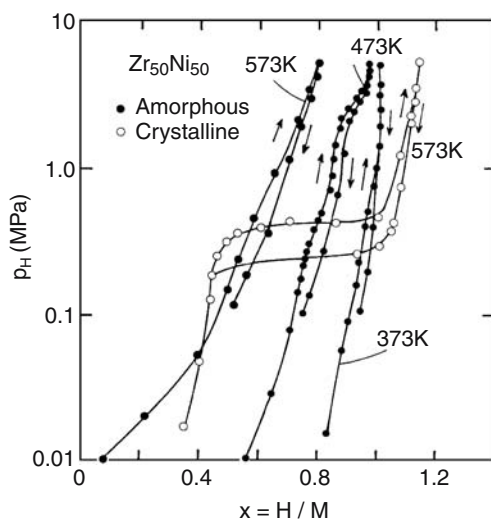


Fig. 3.10. Pressure–composition isotherms for hydrogen in amorphous and crystalline $\text{Zr}_{50}\text{Ni}_{50}$ [3.72]

terms of microscopic structural information. A brief description of hydrogen-induced amorphization is also given.

3.5.1 Thermodynamical Properties of Hydrogen in Amorphous Alloys

The amorphous alloys considered here are those having negative heats of solution of hydrogen. They can be roughly classified into three groups: (1) alloys of early transition metals (ETM: Ti, Zr, Hf) and late transition metals (LTM: Fe, Ni, Cu, Rh, Pd); (2) alloys of rare-earth metals (RE: Y, La ~ Er, excepting Eu) and LTM (Mn, Fe, Co, Ni); and (3) metals with metalloid elements (P, Si, etc.).

Typical p - x - T curves as measured for the Zr–Ni alloy are shown in Fig. 3.10 [3.72]. One of the most characteristic changes in going from crystalline to amorphous alloys is the disappearance of plateaux in the isotherms. In fact, in no case in amorphous-alloy–hydrogen systems has there been any sign of a plateau observed in p - x - T isotherms. It is the absence of plateaux and the concomitant absence of disintegration during absorption/desorption cycles that led *Spit et al.* [3.73, 3.74] to suggest the use of amorphous alloys for hydrogen storage, and inspired subsequent research activities along these lines.

Hysteresis effects, as seen in Fig. 3.10, have also been observed in other cases, but cannot be said to be a general property because they were not

observed for a Ti–Fe film sputter-deposited on Al foil [3.75]. The existence of hysteresis is quite unusual if there is no two-phase separation involved. It may be due, at least in part, to changes in the kinetics of absorption/desorption of hydrogen caused by changes in the surface compositions, but may also be due to some structural relaxation.

Figure 3.11 shows that the Sieverts' law is very strongly violated [3.72]. The positive deviation from the Sieverts' law at higher H concentrations has also been observed in other cases, and is believed to be a general feature of amorphous-alloy–hydrogen systems. The implication should be that there is a distribution of energy states in the amorphous structure, and H atoms enter successively higher-energy states.

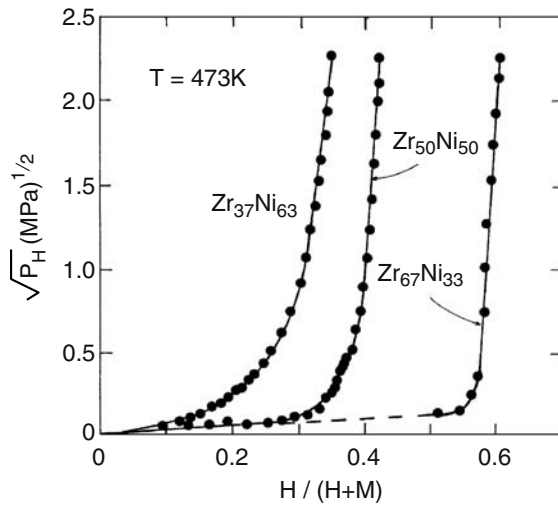


Fig. 3.11. Sieverts' law plots of the pressure–composition isotherms in amorphous Zr–Ni alloys [3.72]

In fact, evidence of distributed site energies has also been found from other experiments. Inelastic neutron scattering experiments have shown broad excitation spectra for optic-mode vibration of H atoms, and internal friction and NMR experiments have revealed distributed activation energies of diffusion (see Sects. 6.4.3). A description of the thermodynamical properties of amorphous-alloy–hydrogen systems in terms of site-energy distribution is given in the next section (Sect. 3.5.2).

It may be appropriate here to mention some aspects of the volume changes caused by hydrogenation of amorphous alloys. As in crystalline metals and alloys, hydrogenation causes volume expansion in most cases, with the volume increase per H atom being very similar to crystalline cases (see Sect. 4.2).

However, possible effects of elastic interaction between H atoms, namely, a linear decrease of the heat of solution with increasing H concentration and concomitant phase separation, have not been observed. Admittedly, observation of these effects should be hampered by the presence of site-energy distribution. One other observation about the volume change is that, in $\text{Pd}_{80}\text{Si}_{20}$ and $\text{Ni}_{34}\text{Pd}_{48}\text{P}_{18}$, a normal volume expansion with $v_{\text{H}} \sim 2.5 \text{ \AA}^3$ occurred at H concentrations larger than about 10^{-4} , but at lower concentrations a volume contraction with $v_{\text{H}} \approx -1.5 \text{ \AA}^3$ took place [3.76]. This implies that H atoms up to a concentration of 10^{-4} filled up deep traps, the nature of which is still unknown.

3.5.2 Site-Energy Distribution

The experimental evidence that H atoms in amorphous alloys are in distributed energy states can be naturally understood as being the consequence of the varying local environments around atomic holes available for hydrogen. There may be different types of sites with different coordination numbers, each with different combinations of M atom species and continuously varying geometrical configurations. In brief, we may say that, in amorphous alloys, a distribution of chemical as well as geometrical configurations leads to a continuous distribution of site energies for H atoms.

In order to describe this situation, *Kirchheim et al.* [3.77] introduced the site-energy distribution function $D(E)$ such that the number of sites having energies in the range $E \sim E + dE$ is given by

$$dN = D(E)dE , \quad (3.23)$$

and the total number of sites by

$$N = \int_{-\infty}^{+\infty} D(E)dE . \quad (3.24)$$

The number of H atoms occupying these sites can be written as

$$n = \int_{-\infty}^{+\infty} f(E)D(E)dE , \quad (3.25)$$

where $f(E)$ is the Fermi–Dirac distribution function

$$f(E) = \frac{1}{e^{(E-\mu)/kT} + 1} , \quad (3.26)$$

and the chemical potential μ is determined by (3.25) from the given number of H atoms. Forms of these distribution functions are shown schematically

in Fig. 3.12. When the site-energy distribution is sufficiently broad in comparison to kT , the Fermi–Dirac distribution may be approximated by a step function, yielding

$$n = \int_{-\infty}^{\mu} D(E) dE . \quad (3.27)$$

Thus, $D(E)$ can be determined by measuring μ as a function of H concentration $x(= n/N_0 = rn/N)$.

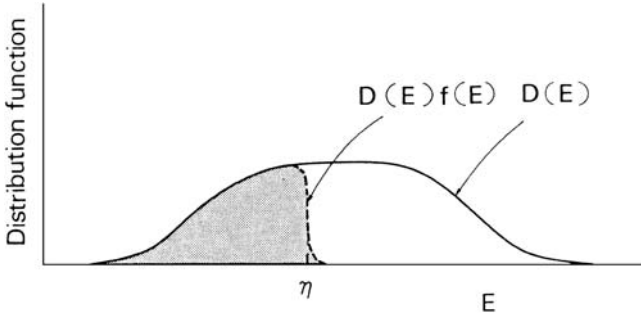


Fig. 3.12. Distribution functions (schematic): $D(E)$: site-energy distribution; $f(E)$: Fermi–Dirac distribution with the Fermi energy μ . The *shaded part* indicates the states filled by H atoms

Kirchheim et al. [3.77] showed that the adoption of a Gaussian function for the site-energy distribution gives an excellent description of the relation between the solubility and chemical potential observed in a number of amorphous alloys. The form they adopted is

$$D(E) = rN_0 \cdot \frac{1}{\sigma\sqrt{\pi}} \exp \left[- \left(\frac{E - e_0}{\sigma} \right)^2 \right] . \quad (3.28)$$

For $kT \ll \mu$, the integration of (3.27) gives

$$\frac{x}{r} = \frac{1}{2} \left(1 - 2 \operatorname{erf} \left| \frac{\mu - e_0}{\sigma} \right| \right) , \quad (3.29)$$

where x/r is the fraction of occupied sites, and the error function is defined as

$$\operatorname{erf}(z) = \frac{1}{\sqrt{\pi}} \int_0^z e^{-t^2} dt .$$

Hence, the relation between μ and x can be approximately written as

$$\mu = e_0 \pm \operatorname{erf}^{-1} |1 - 2x/r| , \quad (3.30)$$

with the + sign for $x > r/2$, the - sign for $x < r/2$, and erf^{-1} represents the inverse error function.

Figure 3.13 shows the measured chemical potentials plotted against $\text{erf}^{-1} |1 - 2x/r|$ for four different alloys (assuming $r = 1$) [3.77]. Experimental data obtained from electrochemical [3.77] and p - x - T measurements [3.73, 3.74] are included. In the electrochemical method, the chemical potential was obtained from the open-circuit e.m.f., and the H concentration from the total integrated current. (For details of the experimental procedure and evaluation, see [2.32, 2.33, 3.77]). From p - x - T data, the chemical potential was calculated using (1.13). Note that all the data points lie on straight lines, and in addition the slopes are nearly the same. This indicates that the Gaussian function with nearly the same width provides an excellent description of the situation.

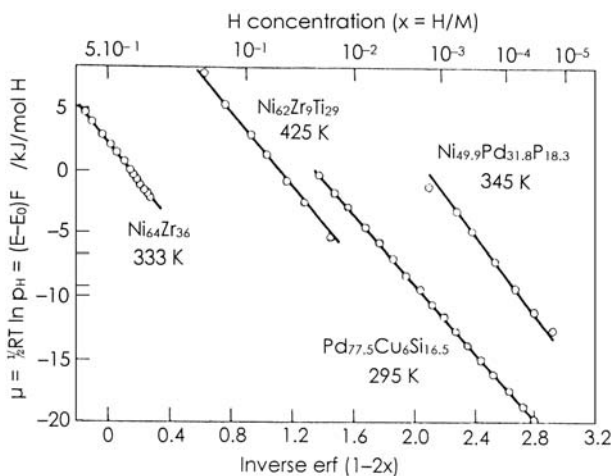


Fig. 3.13. Chemical potential vs. inverse error function $\text{erf}^{-1} |1 - 2x|$ for four amorphous alloys; Zr-Ni, Zr-Ti-Ni alloys [3.73, 3.74] and Pd-Cu-Si, Pd-Ni-P alloys. ($1 \text{ eV} = 96.5 \text{ kJ/mol H}$) [3.77].

Figure 3.14 shows a similar plot for amorphous $\text{Pd}_{82}\text{Si}_{18}$ alloys, including high-pressure data (i.e. high chemical potentials) [3.78]. For low H concentrations between $x = 10^{-4}$ and 0.1, the data points lie on a straight line, but shows a deviation at high H concentrations $x > 0.2$. It was shown that this deviation can be explained by assuming either that the number of interstices r is reduced from 1 to 0.45, or that the chemical potential contains a repulsive H-H interaction $\bar{u} \sim -0.12 \text{ eV}$. An analysis of the data on other compositions of Pd-Si alloys led to very similar conclusions.

The site-energy distribution of arbitrary form can also be determined by electrochemical measurements, namely, by a numerical differentiation of n

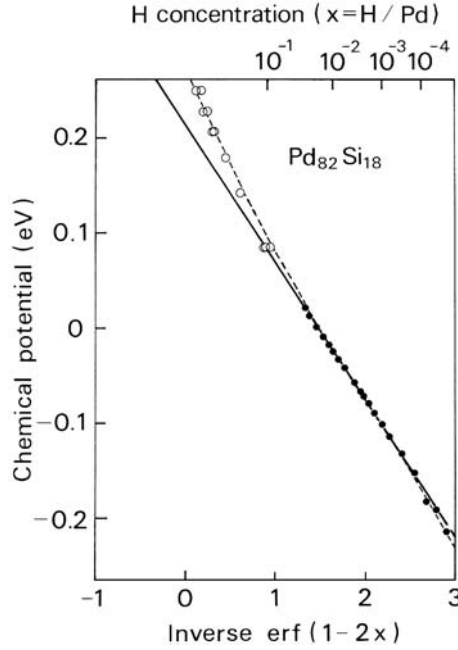


Fig. 3.14. Chemical potential of hydrogen in amorphous $\text{Pd}_{82}\text{Si}_{18}$ at 295 K vs. inverse error function $\text{erf}^{-1}|1 - 2x|$ [3.78]. ○: [3.78]; ●: [3.79]. The dotted curve corresponds to a chemical potential which contains an H-H interaction term 0.12 eV per H atom

with respect to μ ,

$$\frac{\partial n}{\partial \mu} = D(\mu), \quad (3.31)$$

which follows immediately from (3.27).

The site-energy distributions obtained in this way for amorphous $\text{Ti}_{65}\text{Ni}_{35}$ and $\text{Zr}_{50}\text{Ni}_{50}$ [3.80] are shown in Fig. 3.15. The appearance of maxima and minima in the $D(E)$ curves suggests that the curve consists of contributions from different types of sites, each having a Gaussian distribution. More detailed discussions on the form of $D(E)$ based on the amorphous structure will be made in the next section.

We can show that distributed site energies tend to suppress the spinodal decomposition. Assuming in the spirit of mean-field theory that the chemical potential contains an H-H interaction term $-\bar{u}x(= -\bar{v}c; c = x/r, \bar{v} = r\bar{u})$, we may obtain the condition for the occurrence of spinodal decomposition, just as in the crystalline case described in Sect. 2.3. We adopt, for the sake of simplicity, a square distribution function [3.81],

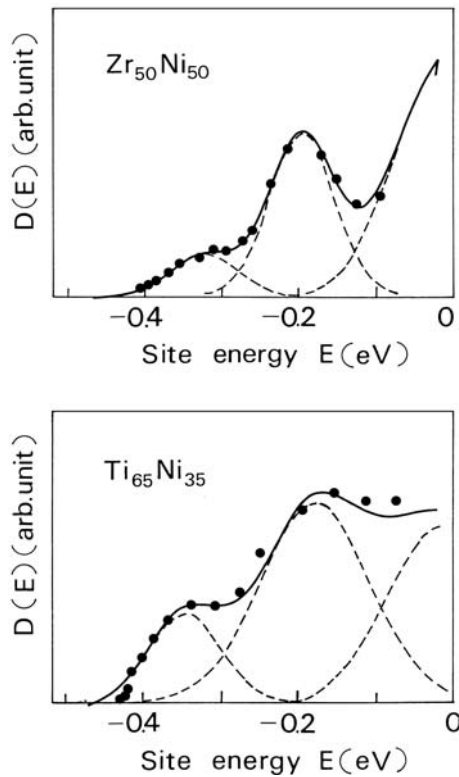


Fig. 3.15. Site-energy distribution function $D(E)$ for amorphous $\text{Zr}_{50}\text{Ni}_{50}$ and $\text{Ti}_{65}\text{Ni}_{35}$ alloys obtained by electrochemical measurements [3.80]

$$\begin{aligned} D(E) &= N/2\Delta \quad \text{for } e_0 - \Delta \leq E \leq e_0 + \Delta, \\ D(E) &= 0 \quad \text{otherwise.} \end{aligned} \quad (3.32)$$

The integration of (3.24) can be carried out analytically, yielding

$$c = \frac{kT}{2\Delta} \ln \frac{e^{-(e_0 - \Delta - \mu)/kT} + 1}{e^{-(e_0 + \Delta - \mu)/kT} + 1}, \quad (3.33)$$

where $c = n/N = x/r$. Hence, the following expression for the chemical potential results:

$$\mu = e_0 - \Delta + kT \ln \frac{e^{2\Delta c/kT} - 1}{1 - e^{-2\Delta(1-c)/kT}}, \quad (3.34)$$

In the limit $\Delta \rightarrow 0$, this reduces to

$$\mu \rightarrow e_0 + kT \ln \frac{c}{1 - c},$$

as it should.

The H–H interaction is introduced by adding a term $-\bar{v}c$ to the right-hand side of (3.34) [3.81].

From the condition $\partial^2\mu/\partial c^2 = 0$, the critical concentration is obtained as $c = 1/2$, and the expression for $\partial\mu/\partial c$ becomes

$$\frac{\partial\mu}{\partial c} = -\bar{v} + \frac{4\Delta}{\ln \left| \frac{\bar{v}+2\Delta}{\bar{v}-2\Delta} \right|} . \quad (3.35)$$

The condition for the occurrence of spinodal decomposition is that there is some positive value of T that makes $\partial\mu/\partial c = 0$. Thus, we obtain

$$\bar{v} > 2\Delta . \quad (3.36)$$

The critical temperature is obtained as

$$T_c = T_{c0} \frac{4\Delta/\bar{v}}{\ln \left| \frac{\bar{v}+2\Delta}{\bar{v}-2\Delta} \right|} , \quad (3.37)$$

with $T_{c0} = \bar{v}/4k$. The variation of T_c/T_{c0} as a function of $2\Delta/\bar{v}$ is plotted in Fig. 3.16 [3.81]. The figure shows that the broader the site-energy distribution, the lower the temperature of the spinodal decomposition. The figure also includes the result of the calculation by *Richards* [3.82], who developed an alternative approach, a lattice-gas theory, by treating site-by-site variation of energies more explicitly, and found in particular that the spinodal decomposition is indeed suppressed but not to the extent that the mean-field theory predicts. In any case, we may say roughly that T_c is reduced to less than one-half of T_{c0} , if 2Δ is greater than $(1 \sim 1.5)\bar{v}$.

A comparison of these predictions with experiments can only be semi-quantitative. In Pd–Si alloys, as \bar{v} is estimated to be zero or negative [3.78], the spinodal decomposition is expected to be completely suppressed. In other cases, if we assume \bar{v} to be of the same order of magnitude as that determined in crystalline cases, Table 2.2 with $r = 1$, the above condition for $T_c/T_{c0} \leq 1/2$ reads roughly as $2\Delta \leq 0.3 \text{ eV}$. Figure 3.14 shows that this condition is barely satisfied in Ti–Ni and Zr–Ni alloys.

3.5.3 A Structural Model of Hydrogen Absorption in Amorphous Alloys

Here we describe a structural model for H absorption in binary amorphous alloys A_yB_{1-y} , consisting of an ETM(A) and an LTM(B). In constructing a model, we regard amorphous alloys as being composed, predominantly, of packed, distorted tetrahedra. X-ray and neutron diffraction as well as neutron inelastic scattering experiments performed on a number of ETM/LTM amorphous alloys have shown that H atoms occupy fourfold coordinated sites, i.e. T sites located in these distorted tetrahedra [3.83–3.90].

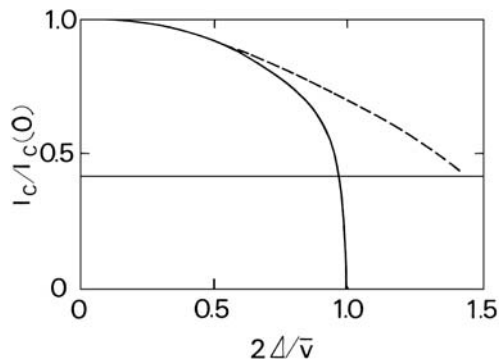


Fig. 3.16. Variation of the critical temperature of spinodal decomposition with width of site-energy distribution function. The width of square distribution 2Δ is measured by the strength of H-H interaction \bar{v} . The calculated results of mean-field theory (—) [3.81] and lattice-gas theory (---) [3.82] are shown

In A_yB_{1-y} alloys, there are five different types of tetrahedra ($[A_4]$, $[A_3B]$, $[A_2B_2]$ etc.), and the energy of H atoms in these tetrahedra should vary with the number of surrounding A atoms having larger affinities to H. Hence, $E^4 < E^3 < E^2 < E^1 < E^0$, where E^i is the energy of an H atom in an $[A_iB_{4-i}]$ site. A distribution of site energies about these mean values may be described by a Gaussian function. Thus, the overall site-energy distribution may be written as

$$D(E, y) = rN_0 \sum_i p_i d_i(E), \quad (3.38)$$

$$d_i(E) = \frac{1}{\sigma_i \sqrt{\pi}} \exp \left[- \left(\frac{E - E^i}{\sigma_i} \right)^2 \right], \quad (3.39)$$

where r is the effective number of sites available to H atoms per M atom. In chemically disordered alloys, the probability of finding a $[A_iB_{4-i}]$ type site varies with alloy composition as

$$p_i = \binom{4}{i} y^i (1-y)^{4-i}, \quad (3.40)$$

At low temperatures, the total H concentration is written in terms of the site-energy distribution function as

$$x = \frac{1}{N_0} \int_{-\infty}^{\mu} D(E, y) dE. \quad (3.41)$$

In the following, we apply this formalism to amorphous Zr-Ni alloys and examine the physical implications of the results.

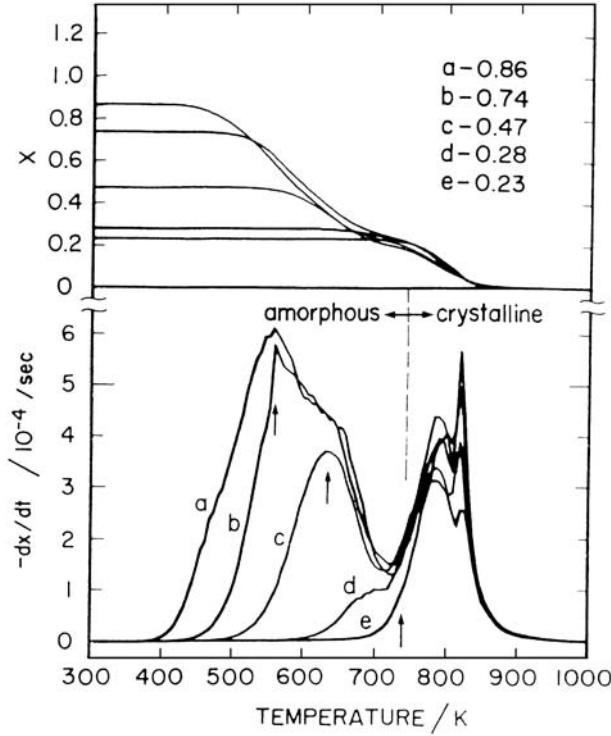


Fig. 3.17. TDS spectra for amorphous $\text{Zr}_{50}\text{Ni}_{50}\text{H}_x$ alloys, and the variation of H concentrations with temperature. Initial H contents are inscribed in the figure [3.91]

The site-energy distribution deduced from the electrochemical measurements on amorphous $\text{Zr}_{50}\text{Ni}_{50}$ alloys (Fig. 3.15) shows that in this particular case $[\text{Zr}_4]$ and $[\text{Zr}_3\text{Ni}]$ sites were completely filled and $[\text{Zr}_2\text{Ni}_2]$ sites only partially filled. The third peak was seen more clearly in $\text{Zr}_{65}\text{Ni}_{35}$ alloys where the total H concentration was higher, and $[\text{Zr}_2\text{Ni}_2]$ sites were filled to higher energies. Assuming a random-alloy formula for p_i (3.40), the authors determined the best-fit values of E^i (measured from E^2) and σ_i ; $E^4 - E^2 \approx -0.3 \text{ eV}$, $E^3 - E^2 \approx -0.2 \text{ eV}$, $\sigma_4 \approx \sigma_3 \approx \sigma_2 \approx 0.10 \text{ eV}$. The number of occupiable sites was $r \approx 1.3$ [3.80].

Information on the site-energy distribution in amorphous Zr–Ni alloys was also obtained from thermal desorption spectroscopy (TDS). *Araki et al.* [3.91] performed TDS measurements on three different compositions of $\text{Zr}_y\text{Ni}_{1-y}$ alloys ($y = 0.36, 0.50, 0.67$) pre-charged with H at $p_{\text{H}} = 1 \sim 2 \text{ MPa}$ and 473 K. Results obtained for amorphous $\text{Zr}_{50}\text{Ni}_{50}$ alloys are shown in Fig. 3.17. In this alloy, crystallization occurred at $T_x = 740 \text{ K}$. Nearly 3/4 of pre-charged H was desorbed in the amorphous phase, and the rest carried over to the crystalline phase was desorbed subsequently. Comparison of the three different

alloys showed that with the increase of Zr contents, peak temperatures were shifted upward (site energies shifted downward), whereas crystallization temperatures T_x were shifted downward. In consequence, in $\text{Zr}_{65}\text{Ni}_{35}$ alloys, desorption peaks for $[\text{Zr}_3\text{Ni}]$ and $[\text{Zr}_2\text{Ni}_2]$ sites were displaced above T_x to become unobservable.

They performed simulations of TDS spectra by assuming surface recombination to be the rate-limiting process and determined several parameters from the best fit to the observation. The best-fit spectra thus obtained for several different H concentrations in $\text{Zr}_{50}\text{Ni}_{50}$ alloys are shown in Fig. 3.18, together with the site-energy distribution. (In the simulation, effects of crystallization were not taken into account.) The agreement with the observed spectra was deemed satisfactory, and the three density peaks deduced were assigned, from low to high energies, to $[\text{Zr}_4]$, $[\text{Zr}_3\text{Ni}]$ and $[\text{Zr}_2\text{Ni}_2]$ type sites.

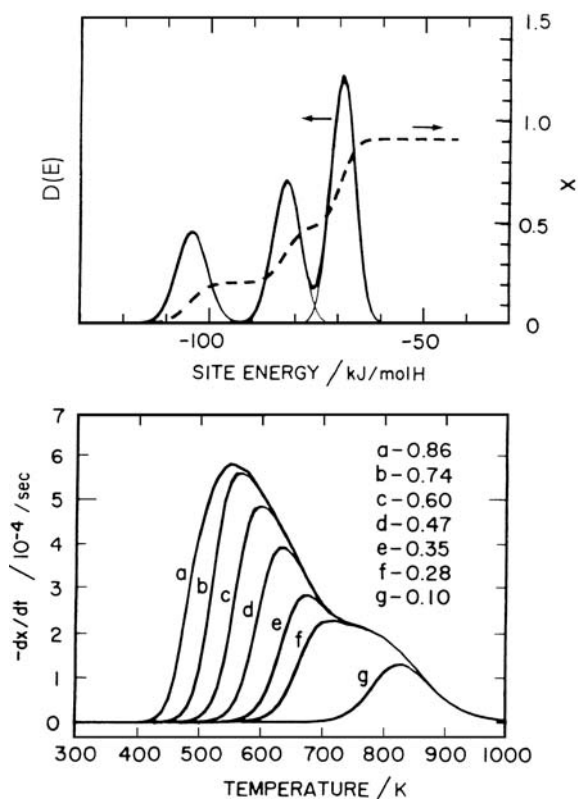


Fig. 3.18. Site-energy distribution function $D(E)$ and the corresponding TDS spectra for amorphous $\text{Zr}_{50}\text{Ni}_{50}\text{H}_x$ alloys obtained by the simulation. Effects of crystallization have not been taken into account. (1 eV/atom H = 96.5 kJ/mol H) [3.91]

Parameters determined for the three alloy compositions are listed in Table 3.3. The results are nearly consistent with the electrochemical data of Jaggy *et al.* [3.80], (except that the peaks are narrower.) Noteworthy here is the fact that the relative weight of the peaks vary systematically with alloy composition, especially the weight of $[\text{Zr}_4]$ sites. In comparison with the estimates based on random distribution, the contribution of sites of higher Zr coordination becomes relatively more important for higher Zr contents. These results suggest that the structure of the amorphous state is not simply random, but possesses a certain spatial correlation between different atom species (the chemical ordering). The depletion of $[\text{Zr}_4]$ sites in $\text{Zr}_{36}\text{Ni}_{64}$ alloys is particularly suggestive. As this alloy assumes the C15 Laves structure in the crystalline state, in which no $[\text{Zr}_4]$ sites exist, the observed depletion indicates that the short-range order reminiscent of the crystalline structure persists in the amorphous phase.

Table 3.3. Parameters in the site-energy distribution in amorphous $\text{Zr}_y\text{Ni}_{1-y}$ alloys. The energies of sites $[\text{Zr}_i\text{Ni}_{4-i}]$ ($i = 2, 3, 4$) are measured from the surface state [3.91].

Samples y	Type of Sites i	E^i (eV)	σ_i (eV)	rp_i	$p_i/\Sigma p_i$	
					(obs.)	(random distr.)
0.36	2	-0.61	0.08	0.40	0.733	0.730
	3	-0.78	0.08	0.14	0.256	0.240
	4	-0.99	0.10	0.01	0.011	0.030
0.50	2	-0.72	0.04	0.43	0.430	0.545
	3	-0.85	0.05	0.28	0.280	0.364
	4	-1.08	0.05	0.20	0.200	0.091
0.67	2	-0.75	0.05	0.38	0.271	0.329
	3	-0.99	0.01	0.57	0.407	0.445
	4	-1.00	0.01	0.45	0.320	0.226

The issue of H-induced changes in amorphous structure was also addressed by Rodmacq *et al.* in $\text{Ti}_{0.5}\text{Cu}_{0.5}$ alloys [3.92, 3.93]. They studied local structural changes by X-ray and neutron diffraction on specimens charged with H at room temperature, and discovered a phase separation into Cu and TiH_x regions on a microscopic scale of $10 \sim 15 \text{ \AA}$. This microstructure persisted up to 360°C , where a transition to a stable $\gamma\text{-TiCu}$ phase took place. The observed tendency for agglomeration of like atoms is in fact the opposite of what is expected from non-hydrogenated Ti-Cu amorphous alloys, where neutron scattering results showed the existence of chemical ordering with a preference for unlike neighbors [3.89, 3.94]. They demonstrated by computer simulation that successive permutations of neighboring Ti-Cu pairs over the

system could reproduce main features of the observed microscopic structure, but did not lead to reconstruction into the γ -phase.

In connection to these H-induced structural relaxations, an important point was made by *Jaggy et al.* [3.80]. They plotted the p - x - T data reported by various authors on amorphous Zr-Ni alloys on the same scale, and noted that the data near room temperature agree reasonably well with each other, but those above 400 K are significantly different. Referring to the work of *Rodmacq et al.* [3.92, 3.93], they suggested that this scatter of data should be the result of H-induced rearrangements of metal atoms, which lead to higher H solubilities in some cases depending on the annealing procedure.

Summing up, we have now convincing evidence that H-induced structural relaxation does take place in amorphous alloys at fairly low temperatures (\sim room temperature), and leads to microscopic chemical ordering that brings forth higher H solubilities than in random alloys, and probably also to hysteresis effects (Fig. 3.10 in Sect. 3.5.1). The observations cited above cast serious doubts on the validity of a random structural model proposed earlier by *Harris et al.* [3.95] and *Curtis et al.* [3.96]. They performed electrochemical measurements on amorphous Zr-Ni alloys, and noting that many features of their results could be reproduced by a random-alloy model, claimed that the state of H in a wide class of amorphous alloys could be described quantitatively by the random-alloy model. Probably, the reason why they overlooked the presence of chemical ordering was that, within the window of chemical potential accessible to their experiment, only a single density peak corresponding to $[\text{Zr}_2\text{Ni}_2]$ sites was observed, and their discussions were based critically on the population of H on this type of sites. However, as seen in Table 3.3, this quantity is not sufficiently sensitive to the occurrence of chemical ordering. In the first edition of this book, this section on the structure of amorphous alloy-H systems was based on the random-alloy theory of *Harris et al.* [3.95] but has been rewritten completely emphasizing the occurrence of H-induced chemical ordering. The strong effect of H to reorganize the metal lattice in its own favor is manifested most clearly in the H-induced amorphization of crystalline intermetallic compounds, which is the subject of the next section.

3.5.4 Amorphization Induced by Hydrogenation

In the late 1970s, sporadic observations were reported of the disappearance of Bragg peaks in XRD on hydrogenation of some intermetallic compounds, including several La-Ni alloys [3.97], CeFe_2 [3.98], GdNi_2 [3.99] and GdM_2 ($\text{M} = \text{Mn}, \text{Fe}, \text{Co}, \text{Ni}$) [3.100], and in some of these reports a possibility of amorphization was suggested [3.97, 3.99, 3.100]. However, the disappearance of Bragg peaks alone cannot be taken as evidence of amorphization, because it also results from disintegration into fine powder, as frequently experienced in hydriding intermetallic compounds. The first confirmation of the amorphous phase formation upon hydrogenation was made by *Yeh et al.* in 1983 in Zr_3Rh

[3.101]. They measured XRD, density and superconducting properties, and confirmed that samples prepared by hydrogenation of a crystalline phase at $\sim 200^\circ\text{C}$ exhibited the same properties as those prepared by hydriding rapidly quenched amorphous alloys of the same composition. It appeared to be a quite peculiar phenomenon that equilibrium crystalline alloys transformed to a metastable amorphous structure, in the direction opposite to ordinary amorphous-to-crystalline transition.

This phenomenon, called hydrogen-induced amorphization (HIA), has since been studied extensively by *Aoki et al.* [3.102–3.123], and in the meantime, a large number of intermetallic compounds have been shown to be amorphized. Materials so far amorphized by HIA are listed in Table 3.4 [3.112, 3.118, 3.123]. The mechanism of HIA has also been clarified from their systematic studies of C15-type Laves phase compounds AB_2 . The following description closely reproduces their line of work.

Table 3.4. Intermetallic compounds in which hydrogen-induced amorphization has been observed [3.112, 3.118, 3.123]

Composition (Structure)	B \ A														
		La	Ce	Pr	Nd	Sm	Gd	Tb	Dy	Ho	Er	Y	Ti	Zr	Hf
$\text{AB}_2(\text{C15})$	Mn						O		O						
	Fe		O			O	O	O	O	O	O	O			
	Co		O	O	O	O	O	O	O	O	O	O			
	Ni	O	O	O	O	O	O	O	O	O	O	O			
$\text{AB}_2(\text{C14})$	Mn				O										
AB	Al	O	O	O	O	O									
$\text{A}_2\text{B}(\text{C23})$	Al			O	O	O	O	O	O	O		O			
$\text{A}_2\text{B}(\text{B8}_2)$	Al													O	
	In	O	O	O	O	O	O	O	O	O	O				
A_3B (L1_2 or fcc)	Al													O	
	Ga					O	O								
	In	O	O	O	O	O								O	
	Rh													O	
$\text{A}_3\text{B}(\text{DO}_{19})$	Al	O	O	O	O								O	O	O
	Ga	O		O	O	O							O		
	In												O		

O: observed.

The structure of C15 AB_2 Laves compounds is made up of close packed spheres, with the atomic size ratio $r_A/r_B = 1.225$ for the ideal close packing. In practice this packing condition is rather flexible, and a large number of compounds of this structure are formed, over the range $r_A/r_B = 1.05 \sim 1.68$. Nearly half of them have been known to undergo HIA.

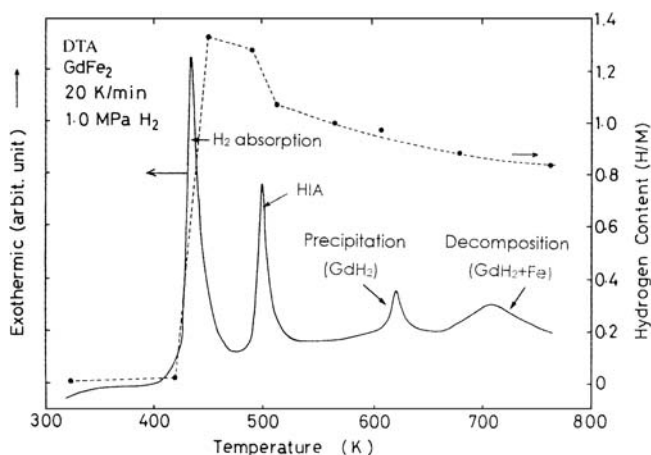


Fig. 3.19. Differential thermal analysis of GdFe_2 under 1.0 MPa H_2 . The H content in samples heated to distinct stages is given on the *right-hand* scale [3.113]

From their compilation of data, *Aoki et al.* found that for the occurrence of HIA, the ratio of the Goldschmidt radii R_A/R_B should be larger than 1.37. This empirical rule can be taken to imply that the crystal lattice should not be too stable; it must bear some inherent instability arising from the size mismatch. This limited stability is also manifested by the fact that the temperature of decomposition (or melting) of crystalline compounds is lower than 1650 K for HIA to occur [3.114].

The process of HIA was studied most intensively for a series of Laves phase compounds RFe_2 (R = rare-earth metals). An example of differential thermal analysis (DTA) of GdFe_2 in 1 MPa H_2 is shown in Fig. 3.19 [3.113]. There are four distinct exothermic peaks. The origin of these peaks was identified with the help of XRD, electron microscopy and diffraction, thermomagnetization, and Mössbauer spectra measured on specimens heated to several different temperatures, and the results are inscribed in the figure. The first peak is due to hydrogenation of the crystalline compounds ($c\text{-GdFe}_2 \rightarrow c\text{-GdFe}_2\text{H}_{4.2}$), the second peak due to amorphization of the hydride ($c\text{-GdFe}_2\text{H}_{4.2} \rightarrow a\text{-GdFe}_2\text{H}_{3.2}$), the third peak due to precipitation of GdH_2 ($a\text{-GdFe}_2\text{H}_{3.2} \rightarrow a\text{-GdFe}_2\text{H}_x + \text{GdH}_2$), and the fourth peak due to decomposition into GdH_2 and $\alpha\text{-Fe}^1$. The fact that the HIA peak is exothermic means that the enthalpy of

¹ The internal consistency of the thermometry can be checked by comparing the enthalpy of initial and final materials. Let us write the total reaction as $\text{Gd} + 2\text{Fe} + \text{H}_2 \rightarrow c\text{-GdFe}_2 + \text{H}_2 \rightarrow \text{GdH}_2 + 2\text{Fe}$, omitting the intermediary stages in the second reaction. Then, the sum of the formation enthalpy of the $c\text{-GdFe}_2$ (-35 kJ/mol Gd) and the observed heat release (-81 kJ/mol Gd) [3.115] should be equal to the formation enthalpy of GdH_2 ($-101 \sim 107 \text{ kJ/mol Gd}$ [3.124, 3.125]). The agreement is reasonably good, probably made better by

the amorphous hydride is lower than the crystalline hydride. The origin of this lowering of the enthalpy on amorphization is of crucial importance for understanding the mechanism of HIA.

Table 3.5. The interatomic distance r and coordination number N_c in H-induced a -GdFe₂H_{3.0}, a -GdFe₂ and c -GdFe₂. The corresponding values for c -GdH₂ are also given for comparison [3.115]

Alloys	Fe-Fe		Fe-Gd		Gd-Gd	
	r (Å)	N_c	r (Å)	N_c	r (Å)	N_c
c -GdFe ₂	2.60	6	3.05	6	3.18	4
a -GdFe ₂	2.54	6.3 ± 0.5	3.07	3.3 ± 0.3	3.47	6 ± 1
a -GdFe ₂ H _{3.0}	2.58	6.7	3.13	1.3	3.81	11.4
c -GdH ₂					3.75	12

In this regard, measurements of the structure factor $S(Q)$ to large Q values proved particularly useful. The X-ray structure factor measured on a -GdFe₂H_{3.0} prepared by HIA revealed the following features [3.115]. First, oscillations in $S(Q)$ persisted to higher Q values than in c -GdFe₂. This was also observed earlier in Zr₃Rh [3.101], and indicates the presence of short-range order in the amorphous structure, i.e. the presence of species with definite bond lengths and angular relations. Second, the distribution of interatomic distances changed in a specific way. To facilitate comparison between the structures of a -GdFe₂H_{3.0} prepared by HIA, a -GdFe₂ and c -GdFe₂, the bond lengths and coordination numbers were estimated from the radial distribution function (calculated by standard methods from $S(Q)$), with the results listed in Table 3.5. The most conspicuous change in a -GdFe₂H_{3.0} is the Gd-Gd distance and its coordination number. The expansion of the Gd-Gd distance, selectively, on hydrogenation should imply that H atoms have entered the sites surrounded by Gd atoms. The large coordination number for the Gd-Gd pairs in a -GdFe₂H_{3.0} as compared with c -GdFe₂ implies that rearrangements of Gd atoms have taken place during the HIA. It is interesting to note that the local environment of H atoms in a -GdFe₂H_{3.0} prepared by HIA is very similar to that in GdH₂, both in terms of Gd-Gd distance and its coordination number.

More detailed information on the local environment of hydrogen atoms was obtained from the measurements of XRD and ND structure factors on TbFe₂D_x [3.122]. The interatomic distance and coordination number deduced are listed in Table 3.6. The M-M correlation deduced from XRD shows that both the atomic distance and the coordination number for Tb-Tb pairs

taking account more properly of a gradual heat absorption (buried in the background) accompanying the gradual desorption of H.

increase on HIA, the same trend noted above for α -GdFe₂H_{*x*}. One additional feature here is that the average coordination number for Fe–Fe pairs is also increased on HIA. This indicates the tendency of segregation of the two metal species, which was absent in α -GdFe₂H_{*x*}. The coordination numbers deduced from ND show the difference between crystalline and amorphous hydrides more clearly: whereas D atoms enter [Tb₂Fe₂] sites in c -TbFe₂D_{3.8}, the average configuration in α -TbFe₂D_{*x*} is close to [Tb₃Fe]. The fact that the average number of Tb–Fe pairs is larger for lower D concentrations indicates that [Tb₄] (and probably [Tb₂Fe₂] sites as well) are also occupied in the amorphous phase.

Table 3.6. The interatomic distance r and coordination number N_c in c -TbFe₂, c -TbFe₂D_{3.8}, and hydrogen-induced α -TbFe₂D_{*x*}. a) M–M correlation deduced from XRD, and (b) D–M correlation deduced from ND [3.122]

(a) M–M correlation deduced from XRD

Alloys	Fe–Fe		Fe–Tb		Tb–Tb	
	r (Å)	N_c	r (Å)	N_c	r (Å)	N_c
c -TbFe ₂	2.60	6	3.05	6	3.18	4
c -TbFe ₂ D _{3.8}	2.90	6.07	3.36	5.98	3.49	3.92
α -TbFe ₂ D _{3.0}	2.51	8.61	3.05	2.44	3.62	8.00
α -TbFe ₂ D _{2.0}	2.48	8.41	3.00	2.38	3.57	7.62

(b) D–M correlation deduced from ND

Alloys	D–Fe		D–Tb		Tb–Tb
	r (Å)	N_c	r (Å)	N_c	$N_c(\text{D–Fe}) + N_c(\text{D–Tb})$
c -TbFe ₂ D _{3.8}	1.72	2.05	2.21	2.01	4.06
α -TbFe ₂ D _{3.0}	1.73	0.98	2.23	3.03	4.01
α -TbFe ₂ D _{2.0}	1.72	0.62	2.23	3.33	3.95

These changes in the local environment of interstitial H atoms are believed to be the origin of the lowering of the enthalpy going from the crystalline to the amorphous hydride. Whereas the hydride of C15 Laves compound c -RM₂H_{*x*} accommodates H atoms in T sites surrounded by 2R + 2M and 1R + 3M, α -RM₂H_{*x*} holds them predominantly in 3R + M and/or 4R-type T sites. The formation of a greater number of stable R–H bonds lowers the enthalpy of the amorphous state.

The fact that the amorphous hydride transforms successively by exothermic reactions to reach the final product RH₂ + M indicates that the amorphous phase is metastable, arrested in this structure due to restricted interdiffusion of metal atoms at low temperatures. It is at higher temperatures where the interdiffusion becomes sufficiently fast to allow chemical segregation that

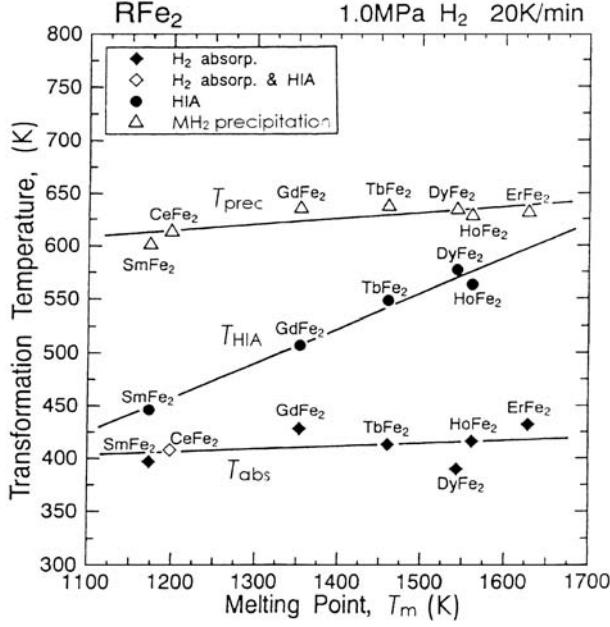


Fig. 3.20. The temperature of H absorption (T_{abs}), H-induced amorphization (T_{HIA}), and precipitation of RH_2 (T_{prec}) plotted against the melting point (T_m) of a series of C15-type compounds RFe_2 [3.118]

transformation to more stable states – a partial precipitation of RH_2 and eventual decomposition – can take place.

This reasoning can be substantiated by looking into the systematics of transition temperatures shown in Fig. 3.20. It is significant to note that the temperature of amorphization T_{HIA} , when normalized to the melting point T_m , assumes nearly the same value $T_{HIA}/T_m \approx 0.38$ across the series [3.118]. This is a clear indication that HIA is controlled kinematically by the migration of constituent metal atoms. As the activation energy of atomic jumps generally scales with the melting point of metals, the reduced temperature being the same implies that the amorphization starts when the jump frequency reaches a certain value to allow short-range atomic migration².

² As a crude measure, let us assume that successive interchange of neighboring atoms by 50 times causes HIA. Taking the elementary jump distance $d \approx 3 \text{ \AA}$, we obtain the migration distance l after 50 jumps as $l \approx d\sqrt{50} \approx 20 \text{ \AA}$. The jump frequency at the temperature of HIA estimated from $\nu \approx 10^{11} e^{-e_m/kT} \text{ s}^{-1}$, with empirical relations $e_m \text{ (eV)} \approx 6 \times 10^{-4} T_m \text{ (K)}$ and $T_{HIA}/T_m \approx 0.38$, is $\nu \approx 10^3 \text{ s}^{-1}$, and the time spent for 50 jumps is $\Delta t \approx 5 \times 10^{-2} \text{ s}$. At decomposition temperatures where $T_{dec}/T_m \approx 0.5$, the migration distance during the same time interval becomes an order of magnitude larger.

Details of the process of HIA are different in different materials depending on the relative stability of relevant phases. Whereas the Co-based C15 compounds RCo_2 behave similarly to RFe_2 , Ni-based compounds RNi_2 behave very differently [3.102,3.115]. There, HIA occurs simultaneously with H absorption at room temperature, and the end product consists of $\text{RH}_2 + \text{RNi}_5$ instead of $\text{RH}_2 + \text{Ni}$. The formation of different end products affects the energetics of the HIA process. In Zr_3Rh , a metastable compound of L1_2 structure transforms directly to the amorphous state on hydrogenation at $\sim 200^\circ\text{C}$, which then transforms to the E9_3 structure upon heating to $\sim 400^\circ\text{C}$ [3.101].

One of the biggest advantages of investigating the RFe_2 series was that, unlike the cases quoted above, the state changes occur successively at different temperatures, and allow to assess the implication of the individual process. The RFe_2 series of compounds serve as a prototype of the material amenable to HIA. The systematic studies of this material by *Aoki et al.* have laid a firm basis for understanding the mechanism of the HIA process in general.

4 Metal–Hydrogen System Under Extended p , T Conditions

In this chapter, we treat M–H systems over the entire composition range, including elemental hydrogen, over much wider ranges of p , T . Recent progress in high-pressure technology has allowed the study of M–H systems under very high hydrogen pressures, making it possible in consequence not only to dissolve a larger amount of hydrogen but also to retain it in solution at high temperatures. Thus there is compelling reason to describe the thermodynamical properties of the M–H system under such extended conditions.

4.1 Hydrogen Under High Pressures

4.1.1 High-Pressure Phases

As described in Chap. 1, a gas–liquid boundary of the elemental hydrogen vanishes at the critical point, $p_c = 1.30$ MPa and $T_c = 33.0$ K. Above this point, where a distinction between gas and liquid no longer exists, it is more appropriate to use the term “fluid”.

A liquid–solid boundary on a p – T diagram, the melting curve, was determined for both n-H₂ and n-D₂, as shown in Fig. 4.1 [4.1]. At a given temperature, the melting pressure of D₂ is lower than that of H₂ by about 4%. More recent knowledge on the melting curve and its implications are given in Sect. 7.5.3.

Hydrogen having a substantial fraction of spherically symmetric $J_r = 0$ molecules, including n-H₂ and n-D₂, solidifies in the close-packed hcp structure and remains so down to lowest temperatures [1.2]. This phase, called phase I, transforms to high-pressure phases, called phase II and III, as shown in Fig. 4.2 [4.2, 4.3]. These phase boundaries were determined by infrared spectroscopy under static compression in diamond anvil cells (DACs), mainly from observed changes in the stretching vibration of molecules (called vibrons in solids). *Loubeyre et al.* [4.4] found that vibron signals remained observable to 316 GPa at 100 K, but at room temperature the sample became completely opaque to visible light at 320 GPa. The earlier report of solid hydrogen being transparent to 342 GPa [4.5] thus came to be seriously questioned. From these observations, they concluded that solid hydrogen remained an insulator under these conditions and its electronic band gap should close at ~ 450 GPa.

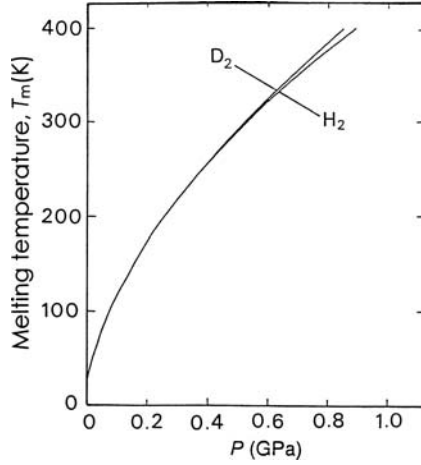


Fig. 4.1. Melting curves for n-H₂ and n-D₂ [4.1]

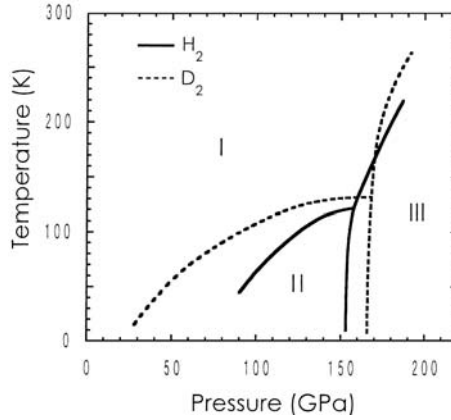


Fig. 4.2. The p - T diagram of H₂ and D₂, with three phases I, II and III [4.2,4.3]

XRD measurements performed to 25.6 GPa at 300 K [4.6] were later extended to ~ 120 GPa in the phase I region of n-H₂ and n-D₂ [4.7]. In the latter experiment, a very ingenious device of growing a single crystal in He was employed. The molar volume and the axial ratio of hcp n-H₂ as a function of pressure are shown in Fig. 4.3 The compression curve (EOS) is very well represented by the Vinet function

$$p = 3K_0 \frac{1-y}{y^2} e^{\eta(1-y)}, \quad y = (V/V_0)^{1/3} \quad (4.1)$$

with $V_0 = 25.43 \text{ cm}^3 \text{ mol}^{-1}$, $K_0 = 0.162 \text{ GPa}$, $K'_0 = 6.813$ and $\eta = 3/2(K'_0 - 1)$ for n-H₂ [4.7]. The volume of n-D₂ was only slightly smaller (by $\sim 0.4\%$). As can be seen in the figure, solid molecular hydrogen is a highly

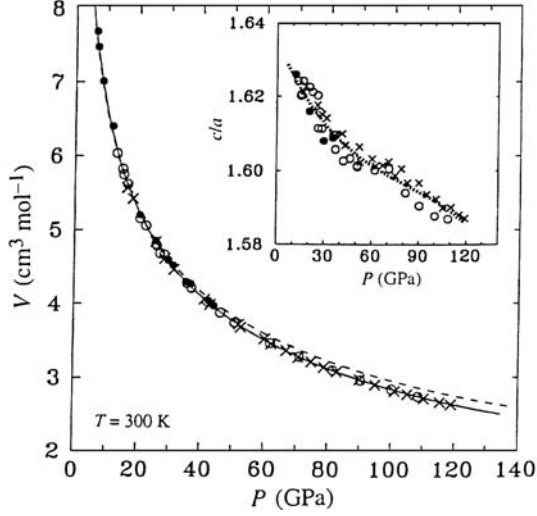


Fig. 4.3. Pressure dependence of the volume of hydrogen isotopes at 300 K. H_2 in circles and D_2 in crosses. The *solid line* is a fit of the H_2 data to the Vinet function (see text). Pressure dependence of the axial ratio c/a is shown in inset [4.7]

compressible substance. The zero-pressure volume is reduced by nearly an order of magnitude at ~ 150 GPa. The axial ratio c/a , which assumes nearly the ideal value of 1.633 at zero-pressure, decreases with increasing pressure. The origin of the apparent break at ~ 40 GPa is not known. More recent experiments on $n\text{-D}_2$ at 15 K, between 15 \sim 57 GPa encompassing both phase I and II, showed that the center of molecules in phase II is also located on the hcp lattice, and the EOS is well represented by the Vinet function with $V_0 = 19.93 \text{ cm}^3 \text{mol}^{-1}$, $K_0 = 0.386(23)$ GPa, $K'_0 = 6.83(10)$ without any discontinuity at the I–II phase boundary [4.8,4.9]. The axial ratio as a function of pressure is close to the observation at 300 K shown in Fig. 4.3.

The large isotope dependence of the phase diagram (Fig. 4.2) immediately shows that the phase transition should be quantum-mechanical in origin. In short, these phase transitions at high pressures are caused by changes in the rotational and vibrational states of molecules as intermolecular interactions become stronger for shorter distances. A more detailed description on solid molecular hydrogen is given in Chap. 7.

In comparison to the static compression results at low temperatures, properties of hydrogen revealed by dynamic compression experiments are distinctly different both in regard to compressibility and electrical conductivity. As substantial heating occurs inevitably during shock compression, temperature becomes an implicit parameter in each data point (~ 3000 K at 10 GPa and higher at higher pressures). Hydrogen is now in the fluid state, and molecular dissociation becomes an important issue.

In Fig. 4.4 are compiled available single-shock and double-shock compression (Hugoniot¹ data on D_2 [4.10–4.14, 4.16, 4.17] and reverberating-shock data on H_2 and D_2 [4.15]. The low-temperature static compression data (Fig. 4.3) are also included for comparison². It can be seen that, under single-shock compression, hydrogen is much less compressible than in static compression, and tends to approach some limiting compression at high pressures. This is because the increase of temperature that accompanies the increase of shock pressure inhibits further compression.

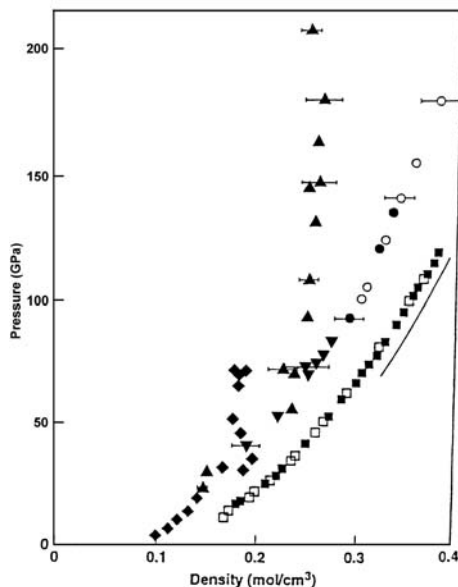


Fig. 4.4. Pressure–density curves for H_2 (*open symbols*) and D_2 (*solid symbols*) obtained by different techniques: Gas-gun experiments under single shocks (*diamond*; ≤ 20 GPa, ≤ 4800 K [4.10, 4.11], 30–70 GPa [4.12, 4.13]), double shocks (*downward triangle*; 3800–5200 K [4.10, 4.14]), *reverberating shocks* (*circles*; 1670–3090 K). Single shocks by pulsed laser (*upward triangles*; 4500–50000 K [4.16, 4.17]). Static compression by DAC (*squares*; 300 K [4.7])

Unfortunately, there is at present a big discrepancy between two groups of single-shock data – those obtained by high explosives [4.10–4.12] and by magnetic compression using a pulsed-current Z-machine [4.13] on one hand

¹ The locus of final p , V states obtained by a series of single-shock experiments with different shock velocities starting from the same initial condition is called the Hugoniot.

² Instead of plotting the volume against pressure as in Fig. 4.3, here the pressure is plotted as a function of density, according to the common practice in the shock-wave community.

(Group A), and a pulsed-laser radiation using Nova laser [4.16, 4.17] on the other (Group B). The discrepancy amounts to $\sim 50\%$ at high pressures, well above the stated error limits. Results of recent intensive scrutiny appear to be in favor of the Group A data. This problem is discussed in more detail in Chap. 7. In any case, the compression under reverberating shocks is much larger than in single shocks, and rather close to the static compression data. This is because of lower average shock temperatures due to longer experimental lifetimes (~ 100 ns in reverberating shocks in comparison to ~ 10 ns in single shocks).

Earlier single-shock data of *Grigor'ev et al.* [4.18, 4.19], which indicated much higher compressibilities (0.46 mol cm^{-3} at 300 GPa and 0.83 mol cm^{-3} at ~ 800 GPa), are seriously questioned of their accuracy, and therefore not included in the figure.

Another feature of shock-compression results is that the electrical resistivity of liquid hydrogen decreases with pressure. Figure 4.5 shows the results obtained by single-shock experiments below 20 GPa [4.11] and those of reverberating-shock experiments above 83 GPa [4.15, 4.21]. The gap between the two sets of data is believed to be due to different shock temperatures. The gradual decrease of the resistivity followed by a break at 140 GPa (and ~ 3000 K) was interpreted by the authors as an indication of the transition from semiconducting to metallic state. More discussions on the mechanism of electrical conduction in the shocked state are given in Chap. 7.

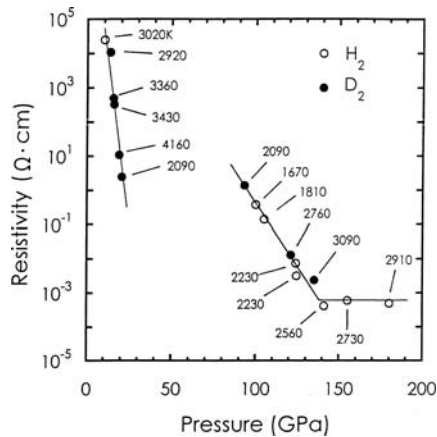


Fig. 4.5. Electrical resistivity of H₂ (open circles) and D₂ (solid circles) plotted against pressure. Temperatures estimated for measured data points are inscribed. The data points below 20 GPa were obtained by single-shock experiments [4.11], and those above 83 GPa by reverberating-shock experiments [4.15, 4.21]. The abrupt slope change at 140 GPa indicates the transition from semiconducting to metallic fluid

4.1.2 Equation of State and Thermodynamical Quantities

In treating M–H alloys, we are primarily interested in the equation of state (EOS) and thermodynamical properties of hydrogen at reasonably high temperatures, where hydrogen is in the fluid state. All the thermodynamical quantities can be obtained once the EOS is known. The Gibbs free energy and entropy can be obtained by integration,

$$G(p, T) = G(p_0, T) + \int_{p_0}^p V dp, \quad (4.2)$$

$$S(p, T) = S(p_0, T) - \int_{p_0}^p \left(\frac{\partial V}{\partial T} \right) dp, \quad (4.3)$$

by substituting ideal-gas values for $G(p_0, T)$ and $S(p_0, T)$ for the reference isobar ($p_0 = 0.1$ MPa). Other thermodynamical quantities can be readily calculated.

Values of the chemical potential of hydrogen were calculated by *Hemmes et al.* [4.22] making use of all the experimental data available at that time on the EOS (Fig. 4.6 [4.22–4.25]), and physically better-founded fitting procedures to allow extrapolation to still unexplored ranges of p, T . They found that an EOS of Benedict type, a polynomial expression of V and T with non-integer powers formerly adopted by *Mills et al.* [4.24], gave physically unrealistic results when extrapolated to high p, T ; instead, the available data could be well reproduced by a van der Waals type equation if appropriate modifications were made. Thus, they adopted a form

$$\left[p + \frac{a(p)}{V^\zeta} \right] [V - b(p)] = RT, \quad (4.4)$$

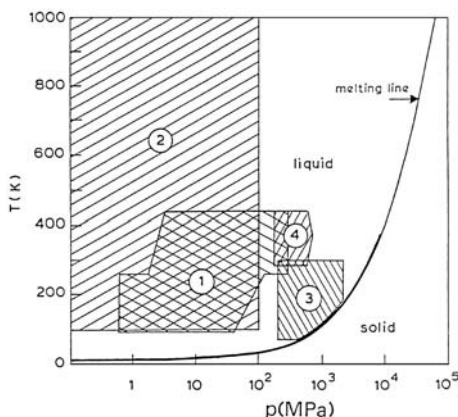


Fig. 4.6. Data sets adopted for constructing the EOS of H_2 [4.22], (1) *Michels et al.* [4.23], (2) *Vargaftik* [1.1], (3) *Mills et al.* [4.24], (4) *Tsiklis et al.* [4.25]

where $b(p)$ is a pressure-dependent excluded volume, $a(p)$ a pressure-dependent interaction term, and ζ is close to 2 but weakly temperature dependent. (A similar and slightly simpler modified van der Waals type EOS was later proposed by *Tkacz* and *Litwiniuk* [4.26].) In this way, they calculated the EOS and other thermodynamical quantities in the range $p \leq 100$ GPa and $100 \leq T \leq 1000$ K. Their calculation was extended by *Sugimoto* and *Fukai* [4.27] to higher temperatures, $T \leq 2000$ K, because with the progress in high-pressure experiments, a knowledge of the chemical potential of hydrogen at higher temperatures became indispensable.

The numerical values of V , H , S , and G calculated in the range 0.1 MPa $\leq p \leq 100$ GPa and $100 \leq T \leq 2000$ K are given in Table 4.1. To conform to a common practice, the values refer to one mole of molecular hydrogen, and the zero of energies is taken at the energy of isolated molecules at $T = 0$. Hence, G and H per molecule are greater than μ_f and h_f by E_d .

Table 4.1. The volume V , enthalpy H , Gibbs free energy G and entropy S of n-H₂ at selected temperatures ($T = 100$ – 2000 K) and pressures ($p = 0.1$ MPa– 100 GPa, i.e., $1 - 10^6$ bar). The quantities p , V , G , H , and S are given in units of bar [0.1 MPa], $\text{cm}^3\text{mol}^{-1}$, $[\text{J mol}^{-1}]$, $[\text{J mol}^{-1}]$, and $[\text{J mol}^{-1}\text{K}^{-1}]$, respectively. These quantities refer to 1 mole of hydrogen, and the zero of energies is taken at the energy of isolated molecules. Thus, G per molecule is greater than μ_f by E_d . The values for 100–400 K are taken from [4.22] and those for 400–2000 K from [4.27]. (The 400 K values are duplicated for the sake of comparison.) For conversion of units, 1 eV per molecule = $96.49 \text{ kJ mol}^{-1}$

p	100 K				200 K			
	V	H	G	S	V	H	G	S
1	8314.34	2999	−7072	100.71	16628.68	5687	−18184	119.36
2	4151.30	2994	−6496	94.90	8322.82	5686	−17031	113.59
5	1658.57	2980	−5736	87.16	3335.01	5685	−15505	105.95
10	828.37	2960	−5161	81.21	1672.73	5683	−14347	100.15
20	414.02	2921	−4587	75.08	841.91	5682	−13184	94.33
50	167.16	2818	−3827	66.44	343.99	5685	−11628	86.56
100	87.42	2689	−3237	59.26	178.62	5703	−10415	80.59
200	50.89	2595	−2591	51.86	96.63	5775	−9133	74.54
500	31.23	2872	−1448	43.21	48.46	6131	−7175	66.53
1000	24.21	3639	−97	37.36	32.53	6887	−5239	60.63
2000	19.65	5218	2057	31.62	23.80	8461	−2509	54.85
5000	15.43	9586	7186	24.00	17.09	12828	3382	47.23
10000	12.25	15128	14023	11.04	13.75	19251	10957	41.47
20000	10.41	25974	25219	7.55	11.14	30346	23205	35.71
50000	8.19	52947	52505	4.42	8.28	55507	51250	21.29
100000	6.75	89669	89350	3.19	6.78	91808	88367	17.20
200000	5.49	149945	149687	2.57	5.50	151746	148873	14.36
500000	4.10	289881	289656	2.25	4.10	291410	288950	12.30
1000000	3.22	469762	469546	2.16	3.22	471195	468873	11.61

(continued)

Table 4.1. (*continued*)

p	300 K				400 K ^a			
	V	H	G	S	V	H	G	S
1	24943.02	8506	-30724	130.77	33257.36	11402	-44237	139.10
2	12485.87	8507	-28994	125.00	16644.02	11403	-41930	133.33
5	5003.08	8510	-26704	117.38	6666.88	11407	-38878	125.71
10	2508.87	8515	-24968	111.61	3341.20	11413	-36565	119.95
20	1261.83	8526	-23224	105.84	1678.39	11427	-34244	114.18
50	513.73	8560	-20895	98.18	680.77	11467	-31150	106.54
100	264.51	8620	-19091	92.37	348.30	11536	-28767	100.76
200	140.09	8747	-17210	86.52	182.15	11678	-26304	94.96
500	65.78	9176	-14454	78.77	82.63	12129	-22776	87.26
1000	40.98	9954	-11924	72.93	49.34	12916	-9664	81.45
2000	27.96	11529	-8615	67.15	32.12	14493	-15777	75.67
5000	18.75	15896	-1962	59.53	20.42	18860	-8362	68.06
10000	14.58	22319	6189	53.77	15.41	25283	365	62.29
20000	11.56	33414	19013	48.00	11.97	36378	13766	56.53
50000	8.64	60517	48402	40.39	8.80	63481	43916	48.91
100000	6.84	94585	86094	28.31	6.93	97784	82755	37.57
200000	5.52	154070	146981	23.63	5.56	156862	144174	31.72
500000	4.10	293183	287378	19.35	4.11	295373	285090	25.71
1000000	3.23	472676	467424	17.51	3.23	474429	465384	22.61

p	400 K ^b				500 K			
	V	H	G	S	V	H	G	S
1	33257.36	11402	-44230	139.08	41571.70	14311	-58474	145.57
2	16641.07	11415	-41922	133.34	20797.48	14327	-55590	139.84
5	6666.87	11420	-38870	125.73	8330.00	14332	-51776	132.22
10	3340.29	11428	-36556	119.96	4171.93	14340	-48886	126.45
20	1679.09	11443	-34236	114.20	2095.24	14357	-45989	120.69
50	680.92	11489	-31138	106.57	847.42	14407	-42128	113.07
100	348.81	11566	-28752	100.80	432.31	14489	-39164	107.31
200	182.50	11722	-26284	95.01	224.38	14654	-36115	101.54
500	82.85	12195	-22746	87.35	99.68	15148	-31808	93.91
1000	49.43	12998	-19628	81.56	57.82	15965	-28106	88.14
2000	32.12	14579	-15738	75.79	36.28	17550	-23637	82.38
5000	20.41	18946	-8323	68.17	22.08	21918	-15461	74.76
10000	15.41	25369	406	62.41	16.24	28341	-6155	68.99
20000	11.97	36464	13805	56.65	12.39	39436	7820	63.23
50000	8.80	63571	43961	49.03	8.97	66543	38738	55.61
100000	6.89	97959	82735	38.06	7.14	103215	78291	49.85
200000	5.56	157244	144022	33.05	5.60	160207	140644	39.13
500000	4.12	295574	285069	26.26	4.13	297939	282441	31.00
1000000	3.23	474275	465512	21.91	3.24	475967	463398	25.14

Table 4.1. (*continued*)

p	600 K				700 K			
	V	H	G	S	V	H	G	S
1	49886.04	17221	-73305	150.88	58200.38	20131	-88622	155.36
2	24953.91	17240	-69844	145.14	29109.29	20153	-84586	149.63
5	9992.30	17245	-65269	137.52	11654.79	20158	-79248	142.01
10	5002.92	17254	-61802	131.76	5833.85	20166	-75204	136.24
20	2511.04	17270	-58328	126.00	2926.65	20183	-71155	130.48
50	1013.70	17321	-53705	118.38	1179.87	20233	-65770	122.86
100	515.52	17404	-50165	112.62	598.64	20317	-61653	117.10
200	266.00	17571	-46539	106.85	307.56	20484	-57451	111.34
500	116.36	18071	-41468	99.23	132.99	20985	-51618	103.72
1000	66.16	18893	-37188	93.47	74.48	21809	-46761	97.96
2000	40.43	20481	-32141	87.70	44.59	23397	-41138	92.19
5000	23.74	24848	-23203	80.09	25.40	27764	-31438	84.57
0000	17.07	31271	-13321	74.32	17.90	34187	-20980	78.81
20000	12.80	42366	1230	68.56	13.22	45282	-5852	73.05
50000	9.13	69473	32910	60.94	9.30	72389	26590	65.43
100000	7.22	106146	73039	55.18	7.31	109062	67295	59.67
200000	5.64	163362	136576	44.64	5.77	169299	131568	53.90
500000	4.15	300597	279235	35.60	4.17	303484	275464	40.03
1000000	3.25	477984	460839	28.58	3.26	480298	457817	32.12

p	800 K				900 K			
	V	H	G	S	V	H	G	S
1	66514.72	23039	-104357	159.25	74829.05	25947	-120456	162.67
2	33265.73	23065	-99744	153.51	37421.63	25975	-115267	156.94
5	13317.31	23070	-93644	145.89	14980.13	25980	-108405	149.32
10	6664.80	23078	-89024	140.13	7495.59	25988	-103209	143.55
20	3342.50	23095	-84399	134.37	3757.98	26005	-98007	137.79
50	1345.93	23145	-78251	126.75	1512.21	26055	-91097	130.17
100	681.77	23229	-73559	120.98	764.89	26139	-85829	124.41
200	349.10	23396	-68780	115.22	390.65	26306	-80474	118.64
500	149.62	23897	-62185	107.60	166.24	26807	-73117	111.03
1000	82.80	24721	-56752	101.84	91.11	27631	-67108	105.27
2000	48.74	26309	-50553	96.08	52.90	29220	-60332	99.50
5000	27.06	30677	-40091	88.46	28.73	33587	-49108	91.88
10000	18.73	37100	-29056	82.69	19.56	40010	-37497	86.12
20000	13.64	48194	-13352	76.93	14.05	51105	-21217	80.36
50000	9.46	75301	19852	69.31	9.63	78212	12749	72.74
100000	7.39	111974	61133	63.55	7.47	114885	54606	66.98
200000	5.81	172212	125983	57.79	5.86	175122	120032	61.21
500000	4.20	306508	271116	44.24	4.22	309706	266267	48.27
1000000	3.27	482819	454295	35.65	3.28	485579	450333	39.16

(continued)

Table 4.1. (*continued*)

p	1000 K				1100 K			
	V	H	G	S	V	H	G	S
1	83143.39	28852	−136879	165.73	91457.73	31755	−153592	168.50
2	41577.02	28883	−131113	160.00	45734.72	31789	−147250	162.76
5	16642.55	28888	−123490	152.38	18305.66	31794	−138865	155.14
10	8327.21	28897	−117717	146.61	9158.24	31802	−132516	149.38
20	4173.74	28913	−111939	140.85	4589.41	31819	−126162	143.62
50	1678.26	28964	−104267	133.23	1844.38	31869	−117728	136.00
100	847.99	29047	−98423	127.47	931.14	31953	−111308	130.24
200	432.22	29215	−92491	121.71	473.77	32120	−104799	124.47
500	182.86	29716	−84372	114.09	199.47	32621	−95919	116.85
1000	99.43	30539	−77787	108.33	107.75	33445	−88758	111.09
2000	57.06	32128	−70435	102.56	61.22	35033	−80829	105.33
5000	30.39	36495	−58449	94.94	32.05	39401	−68081	97.71
10000	20.40	42918	−46262	89.18	21.23	45824	−55317	91.95
20000	14.47	54013	−29406	83.42	14.88	56919	−37885	86.19
50000	9.80	81120	5322	75.80	9.96	84026	−2395	78.56
100000	7.56	117793	47756	70.04	7.64	120699	40615	72.80
200000	5.90	178030	113758	64.27	5.94	180936	107194	67.04
500000	4.25	313179	261077	52.10	4.32	320846	255483	59.42
1000000	3.30	488671	446073	42.60	3.31	492264	441749	45.92

p	1200 K				1300 K			
	V	H	G	S	V	H	G	S
1	99772.07	34653	−170570	171.02	108086.41	37548	−187789	173.34
2	49889.33	34690	−163651	165.28	54046.80	37588	−180294	167.60
5	19968.89	34695	−154505	157.67	21629.96	37593	−170386	159.98
10	9988.56	34704	−147579	151.90	10820.02	37601	−162884	154.22
20	5005.09	34721	−140649	146.14	5420.84	37618	−155377	148.46
50	2010.67	34771	−131453	138.52	2176.63	37668	−145419	140.84
100	1014.30	34854	−124456	132.76	1097.41	37752	−137847	135.08
200	515.30	35022	−117372	126.99	556.83	37919	−130186	129.31
500	216.11	35523	−107729	119.38	232.71	38420	−119781	121.69
1000	116.06	36347	−99992	113.62	124.37	39244	−111468	115.93
2000	65.37	37935	−91487	107.85	69.53	40832	−102386	110.17
5000	33.72	42302	−77978	100.23	35.38	45200	−88115	102.55
10000	22.06	48725	−64637	94.47	22.89	51623	−74199	96.79
20000	15.30	59820	−46629	88.71	15.71	62717	−55614	91.02
50000	10.13	86927	−10376	81.09	10.30	89824	−18599	83.40
100000	7.72	123600	33209	75.33	7.81	126497	25562	77.64
200000	5.98	183838	100365	69.56	6.02	186735	93294	71.88
500000	4.34	323747	249416	61.94	4.36	326644	243106	64.26
1000000	3.33	496846	437817	49.19	3.34	502432	434493	52.26

Table 4.1. (*continued*)

p	1400 K				1500 K			
	V	H	G	S	V	H	G	S
1	116400.75	40436	-205231	175.48	124715.09	43317	-222879	177.46
2	58205.56	40479	-197160	169.74	62357.85	43363	-214232	171.73
5	23294.16	40484	-186490	162.12	24956.08	43368	-202800	164.11
10	11650.90	40492	-178411	156.36	12482.33	43376	-194145	158.35
20	5836.76	40509	-170329	150.60	6252.51	43393	-185486	152.59
50	2342.89	40559	-159608	142.98	2509.00	43443	-174003	144.96
100	1180.51	40643	-151460	137.22	1263.68	43527	-165279	139.20
200	598.42	40810	-143222	131.45	639.94	43694	-156465	133.44
500	249.34	41311	-132056	123.83	265.97	44195	-144537	125.82
1000	132.68	42135	-123167	118.07	141.00	45019	-135072	120.06
2000	73.68	43723	-113508	112.31	77.84	46607	-124837	114.30
5000	37.04	48091	-98476	104.69	38.70	50975	-109043	106.68
10000	23.72	54514	-83982	98.93	24.55	57398	-93973	100.91
20000	16.13	65609	-64822	93.16	16.55	68493	-74236	95.15
50000	10.46	92716	-27045	85.54	10.63	95600	-35697	87.53
100000	7.89	129389	17693	79.78	7.97	132272	9617	81.77
200000	6.06	189626	86001	74.02	6.11	192510	78501	76.01
500000	4.37	329536	236576	66.40	4.39	332420	229838	68.39
1000000	3.36	510536	433051	55.35	3.37	521352	433891	58.31

p	1600 K				1700 K			
	V	H	G	S	V	H	G	S
1	133029.44	46190	-240720	179.32	141343.77	49052	-258739	181.05
2	66515.06	46238	-231495	173.58	70673.86	49104	-248939	175.32
5	26618.21	46243	-219302	165.97	28280.09	49109	-235983	167.70
10	13312.86	46252	-210070	160.20	14144.04	49117	-226175	161.94
20	6668.12	46269	-200836	154.44	7083.54	49134	-216364	156.18
50	2675.11	46319	-188591	146.82	2841.25	49184	-203357	148.55
100	1346.77	46402	-179290	141.06	1429.88	49268	-193481	142.79
200	681.47	46570	-169900	135.29	723.09	49435	-183514	137.03
500	282.59	47071	-157210	127.68	299.21	49936	-170062	129.41
1000	149.32	47894	-147168	121.91	157.63	50760	-159445	123.65
2000	82.00	49483	-136357	116.15	86.15	52348	-148057	117.89
5000	40.36	53850	-119801	108.53	42.03	56716	-130739	110.27
10000	25.38	60273	-104155	102.77	26.21	63139	-114516	104.50
20000	16.96	71368	-83842	97.01	17.38	74234	-93628	98.74
50000	10.79	98475	-44541	89.38	10.96	101341	-53564	91.12
100000	8.06	135148	1349	83.62	8.14	138014	-7098	85.36
200000	6.15	195385	70809	77.86	6.19	198251	62939	79.60
500000	4.41	335295	222908	70.24	4.42	338161	215799	71.98
1000000	4.21	534226	431056	64.48	4.22	537092	424524	66.22

(continued)

Table 4.1. (*continued*)

p	1800 K				1900 K			
	V	H	G	S	V	H	G	S
1	149658.11	51903	−276927	182.68	157972.45	54740	−295273	184.22
2	74831.16	51957	−266550	176.95	78981.77	54798	−284319	178.48
5	29943.65	51962	−252832	169.33	31605.27	54803	−269840	170.86
10	14975.14	51971	−242448	163.57	15806.13	54811	−258879	165.10
20	7499.31	51988	−232061	157.80	7914.97	54828	−247916	159.34
50	3007.63	52038	−218292	150.18	3173.74	54878	−233385	151.72
100	1512.97	52121	−207839	144.42	1596.17	54962	−222356	145.96
200	764.64	52289	−197296	138.66	806.21	55129	−211236	140.19
500	315.83	52790	−183083	131.04	332.44	55630	−196261	132.57
1000	165.94	53613	−171889	125.28	174.26	56454	−184491	126.81
2000	90.31	55202	−159925	119.51	94.46	58043	−171951	121.05
5000	43.69	59569	−141845	111.90	45.35	62410	−153109	113.43
10000	27.04	65992	−125046	106.13	27.87	68833	−135734	107.67
20000	17.79	77087	−103581	100.37	18.21	79928	−113693	101.91
50000	11.13	104194	−62755	92.75	11.29	107035	−72105	94.28
100000	8.22	140867	−15714	86.99	8.31	143708	−24487	88.52
200000	6.23	201104	54900	81.22	6.27	203946	46704	82.76
500000	4.44	341013	208521	73.61	4.46	343855	201087	75.14
1000000	4.23	539944	417822	67.85	4.24	542786	410964	69.38

2000K				
p	V	H	G	S
1	66286.78	57564	−313767	185.67
2	83138.58	57624	−302238	179.93
5	33268.64	57629	−286997	172.31
10	16636.96	57638	−275459	166.55
20	8331.04	57655	−263920	160.79
50	3339.95	57705	−248627	153.17
100	1679.21	57789	−237022	147.41
200	847.75	57956	−225326	141.64
500	349.05	58457	−209589	134.02
1000	182.57	59280	−197243	128.26
2000	98.62	60869	−184126	122.50
5000	47.02	65236	−164523	114.88
10000	28.71	71160	−146571	109.12
20000	18.62	82754	−123954	103.35
50000	11.46	109861	−81603	95.73
100000	8.39	146534	−33410	89.97
200000	6.31	206772	38357	84.21
500000	4.47	346681	193502	76.59
1000000	4.25	545612	403956	70.83

^a[4.22]; ^b[4.27].

Regarding the reliability of these values, *Hemmes et al.* [4.22] stated that their calculation could reproduce the observed values to within 0.2% on the reference isobar of 0.1 MPa, and generally within the stated experimental errors of volume (of the order of 1%). This gives a rough idea of the possible errors involved in these values. The calculation of *Sugimoto* and *Fukai* confirmed most of the results of *Hemmes et al.* In the solid phase, however, the entropy values of *Hemmes et al.* were found to be too large (by 3.2% at 400 K and 7.6% at 1000 K under 100 GPa); concomitant discrepancies in the enthalpy values were negligibly small. A more detailed table of the thermodynamical quantities of solid hydrogen is given in [4.28].

One last note about the table: not all the digits of the values presented are significant. The extra digits are for interpolation purposes only.

Figures 4.7–4.9 show the overall dependence of the thermodynamical quantities, G , H , and S on pressure and temperature. The variation of G (Fig. 4.7) and H (Fig. 4.8) is nearly that of an ideal gas up to approximately 0.1 GPa, whereupon they start to increase rapidly and their temperature dependences become weaker. This steep increase of G of fluid H_2 at high pressures has an important implication for the dissolution process in metals, as described in Sect. 4.3. Figure 4.9 shows that the behavior of the entropy is like that of an ideal gas up to the pressure of solidification, the slope of S in the fluid phase being equal to the gas constant $N_A k$.

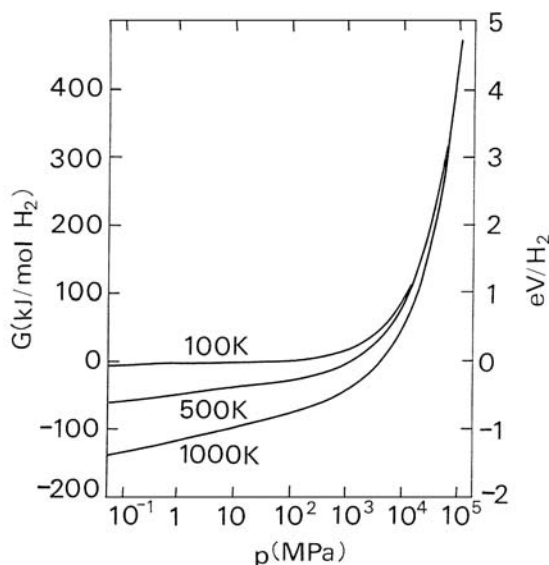


Fig. 4.7. Molar Gibbs free energy of H_2 as a function of p , T [4.22]

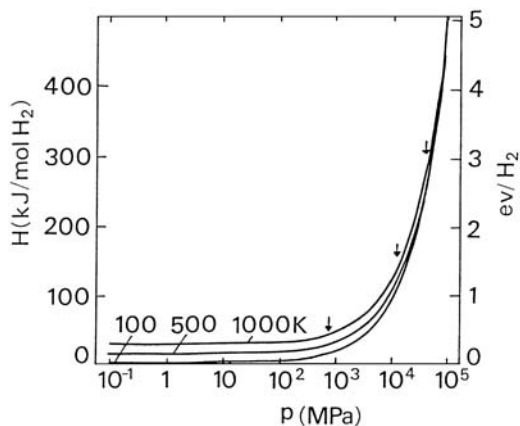


Fig. 4.8. Molar enthalpy of H_2 as a function of p, T [4.22]

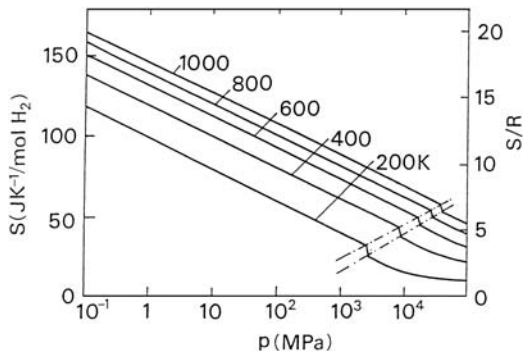


Fig. 4.9. Molar entropy of H_2 as a function of p, T [4.22]

4.2 Volume of Hydrogen in Metals

Since *Baranowski et al.* [4.29] pointed out that the volume expansion caused by a hydrogen atom assumes nearly the same value ($v_H \approx 3 \text{ \AA}^3$ per H atom) in the fcc metals Ni, Pd and their alloys, a large amount of data on v_H have been accumulated, and its near constancy has proved to hold in many different kinds of metals and alloys (see, e.g., [4.30, 4.31]). In this section, we present a compilation of existing data, and try to examine the extent to which the hydrogen-induced volume depends on site location, structure and chemical species of the host metal. Also, by comparison of the compression behavior of the volume of interstitial hydrogen with that of elemental hydrogen, we draw attention to the fact that a specific volume of hydrogen in metallic environment can be fairly well defined.

Table 4.2 gives the values of the hydrogen-induced volume v_H in metals, classified according to the structure of the metal lattice and site location

Table 4.2. Volume of interstitial hydrogen in metals. (The values refer to low concentrations of hydrogen, unless otherwise specified)

Structure	Site	Metal/Hydride	$v_H[\text{\AA}^3 \text{ per H atom}]$	Reference, Comment
bcc	T	V	2.64	[4.30]
		Nb	3.13	[4.30]
		Ta	2.80	[4.30]
	O	α' -VH _{0.013}	2.33	[4.32, 4.33], Under stress
		β -VH _{0.5-0.7}	2.23	[4.34, 4.35]
		κ -NbH _{0.75}	2.2	[4.36], 30–60 GPa
		Ti _{0.75} V _{0.25}	2.0	[4.37]
		Ti _{0.5} Nb _{0.5}	2.3	[4.38]
hcp	T ^a	Y	2.79	[2.70]
		Tb	4.72	[4.39]
		Dy	3.93	[4.39]
		Ho	3.54	[4.39]
		Er	3.39	[4.40]
		Lu	3.61	[4.41]
			2.51	[2.116]
	T–M–T ^b	Sc	1.97	[2.70, 4.42, 4.43]
		Y	3.07	[2.117]
		Er	3.87	[2.117]
		Tm	3.35	[2.117, 4.41]
		Lu	3.25	[2.116, 2.117]
	O	ϵ -CrH _{1.0}	$\sim 1.7^c$	[4.44, 4.45], 3–5 GPa
		ϵ -MnH _{1.0} , D _{>0.6}	1.66	[4.46–4.48]
		ϵ' -FeH _{1.0}	2.6	[4.49, 4.50]
		ϵ -CoH _{<0.6}	1.82	[4.48]
		ϵ -MoH _{1.0}	1.8	[4.45, 4.51]
			$\sim 1.7^c$	[4.45, 4.52], 3–5 GPa
		TcH _{0.45}	1.86	[4.51]
		ReH _{0.23}	2.19	[4.51]
		ReH _{0.5}	$\sim 1.6^c$	[4.53], 10–20 GPa
			$\sim 1.7^c$	[4.54], 10–20 GPa
fcc	T	ScH ₂	2.23	[2.2, 4.45]
			2.36	[2.2, 4.55]
		TiH ₂	2.83	[2.2, 4.45]
			2.78	[2.2, 4.55]
		VH ₂	3.29	[2.2, 4.45]
		YH ₂	2.38	[2.2, 4.45]
			3.07	[2.2, 4.55]
		ZrH ₂	2.60	[2.2, 4.45]
			3.11	[2.2, 4.55]
		NbH ₂	2.83	[2.2, 4.45]

Table 4.2. (*continued*)

Structure	Site	Metal/Hydride	$v_{\text{H}}[\text{\AA}^3 \text{ per H atom}]$	Reference, Comment
fcc		LaH ₂	4.25	[2.2, 4.45]
		CeH ₂	4.48	[2.2, 4.45]
		HfH ₂	2.90	[2.2, 4.45]
		TaH ₂	$\geq 2.3^c$	[4.45, 4.56], 4 GPa
	O	γ -CrH _{1.0}	$\sim 2.3^c$	[4.44, 4.45], 3–5 GPa
		γ -MnD _{0.41}	1.85	[4.57]
		(Fe,Mn,Ni) ^d H _{0.95}	1.9	[4.58]
		γ -CoH _{1.0}	1.9	[4.59]
		NiH _{1.0}	2.20	[4.51]
			$\sim 2.21^c$	[4.60]
		(Ni,Mn) ^e H _{<0.85}	2.3	[4.61]
		(Ni,Fe) ^f D _{1.0}	2.15	[4.62]
		γ -MoH _{1.0}	$\sim 2.3^c$	[4.45, 4.52], 3–5 GPa
		PdH _{1.0}	2.47	[4.63]
		RhD _{1.0}	2.40	[4.51]

(a) Measured at high temperatures where T–M–T pairs, if any, are dissociated.

(b) Measured at room temperature. (c) H concentration assumed, (d) Fe:Mn:Ni = 65:29:6, (e) Ni:Mn = (100 – y): y ; y = 5 – 37, (f) Ni:Fe = 80:20.

of hydrogen. In deriving v_{H} , the volume of a hydride has to be compared with that of a corresponding host metal having the same structure. This is because the atomic volume of metals is, in general, different in different structures, and the differences (as observed in allotropic phase transitions) can be a sizeable fraction of hydrogen-induced volume changes. Thus, for d-band metals which do not assume the fcc structure in nature, the volume of fcc reference states was taken from theoretical calculations [4.45, 4.55]. Possible errors due to uncertainties in the calculated reference volume can be assessed by comparison of the two sets of values listed for dihydrides of d-band metals. For Fe, in which ϵ' -FeH_{1.0} having the dhcp structure was prepared by high-pressure synthesis and examined by X-rays after quenching to normal pressure [4.49], hypothetical hcp Fe at normal pressure was chosen as a reference state, and its volume was estimated from that of α -Fe (bcc) at a normal pressure and a volume change at the $\alpha \rightarrow \epsilon$ (hcp) transition at high pressures ($\Delta\Omega = -0.63 \text{\AA}^3$ [4.50]). Similarly, for hcp and fcc monohydrides of Cr and Mo synthesized under pressure, the reference volume was assumed to be larger than the bcc volume by 0.4\AA^3 based on the calculation of *Korzhavyi et al.* [4.45], $\Delta\Omega$ (bcc \rightarrow fcc) $\approx 0.4 \text{\AA}^3$ for these metals.

It may be noted that ND experiments were made on deuterides instead of hydrides. But, in most cases, the isotope dependence of the volume expansion scarcely exceeds the possible error limits, and is, therefore, negligible for most purposes.

In Table 4.2, we note the following general features. First, the hydrogen-induced volume v_H is larger in lanthanide metals than in d-band metals. Second, in d-band metals, v_H is larger for T-site occupancy ($v_H = 2.9 \pm 0.3 \text{ \AA}^3$) than for O-site occupancy ($v_H = 2.2 \pm 0.3 \text{ \AA}^3$).

Let us start by examining some problems in d-band metals. There, the case of O-site occupancy in the fcc lattice deserves special considerations. Figure 4.10 shows the hydrogen-induced volumes in a series of fcc metals and alloys [4.29, 4.64, 4.65]. One peculiar feature is that most data points lie on a straight line only up to $x \leq 0.7$, and bend off thereafter. The slope gives $v_H = 2.8 \text{ \AA}^3$ for $x \leq 0.7$, and $v_H = 0.3 - 0.7 \text{ \AA}^3$ for $x \geq 0.7$. *Baranowski et al.* were the first who noted this anomalous bend in Pd and its alloys [4.29], and the Russian group discovered subsequently that in Ni and its alloys the lattice expansion shows the same anomaly and continues on to the H concentration of ~ 1.2 , well above the stoichiometric limit of the O-site occupancy ($x = 1$) [4.48].

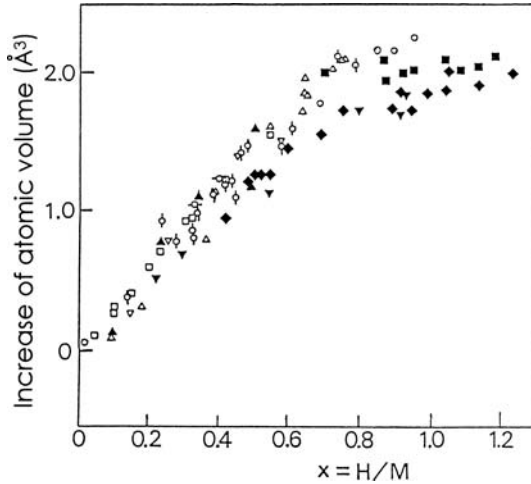


Fig. 4.10. Volume increase due to H in fcc metals and alloys. o: Pd, ×: Pd-Cu, +: Pd-Ag, □: Pd-Au, ▽: Pd-Ir, △: Pd-Pt, ▲: Cu-Ni [4.29]; ■: Ni, ◆: Ni-Fe, ▼: Fe-Ni-Mn [4.64]

Fukai et al. [4.66, 4.67] proposed that for these features the formation of superabundant metal-atom vacancies (SAVs) up to ~ 10 at % should be responsible. The SAV formation, which occurs most prominently in fcc hydrides of high H concentrations, should induce lattice contraction and create extra sites for H occupancy. (See Sect. 5.5.4.)

However, there are cases where such an anomaly was not observed. *Krukowski and Baranowski* reported that in Ni-Mn alloys, the lattice expands linearly with H concentration and approaches the limiting value of

the other anomalous cases at $x \rightarrow 1$ [4.61]. Recently, *Antonov et al.* [4.62] re-examined this problem on $\text{Ni}_{0.8}\text{Fe}_{0.2}\text{H}_x$ and concluded that the inhomogeneous H distribution in samples – higher near the surface and lower in the interior – should be responsible for the apparent anomaly. The presence of such a large concentration fluctuation may well be anticipated in the supercritical region, i.e. above the critical point of the spinodal decomposition, where the samples were prepared. They demonstrated that the apparent anomaly showed up because the lattice parameter was determined by XRD in the near-surface region ($\leq 15\text{ }\mu\text{m}$), and was plotted as a function of average H concentration. No such anomalies were manifested by the ND experiment which probed the whole sample volume, and in addition, the XRD and ND results agreed with each other at high concentrations where critical fluctuations should be suppressed. As all the systems included in Fig. 4.10 exhibit spinodal decomposition, very similar situation should be expected in all these cases. In view of these possible errors in the intermediate concentration region, the values listed in Table 4.2 for O-site occupancy in fcc metals have been obtained, whenever possible, from high-concentration data.

The large volume expansion in $\epsilon\text{-FeH}_x$ is believed to be the result of magnetism: The magnetostriction increases the volume by ca. $0.9\text{ }\text{\AA}^3$ [4.68, 4.69]; (See the discussions at the end of this section). The small v_{H} in Sc, on the other hand, may be related to the small atomic volume ($12.5\text{ }\text{\AA}^3$ in comparison to $14.8\text{--}18.8\text{ }\text{\AA}^3$ for lanthanide metals) and large elastic anisotropy of the hcp phase.

The physical origin of this empirical rule of hydrogen-induced volume in d-band metals lies in a very similar electronic process of hydrogen dissolution. There, H atoms enter the lattice by forming local bonding states with surrounding M atoms (by hybridization of H 1s and metal d states), with a resultant depletion of anti-bonding states, which in effect produces outward displacements of the surrounding lattice (Chap. 7).

As regards lanthanide metals, the large v_{H} is believed to be the consequence of charge transfer from metal to hydrogen atoms. Hydrogen atoms bear some negative charges and become larger in size. The fact that v_{H} is largest in La and decreases along the series is coherent with the variation of the electronegativity, and corroborates this reasoning. The importance of charge transfer effects in lanthanide hydrides has been recognized in relation to their electronic band structure, and still remains as one of the central issues (Chap. 7). The most spectacular exception to these empirical rules of hydrogen-induced volume change (not included in the table) is the case of superstoichiometric dihydrides of lanthanides, $\text{LnH}_{2+\beta}$, where excess H atoms on O sites cause contraction, instead of expansion, of the lattice (for a review, see [3.67]). This occurs as the bonding character changes from metallic to covalent (see Chap. 7).

The data of volume expansion in intermetallic compounds are given in Table 4.3, and those on amorphous alloys in Table 4.4. In these cases, the

Table 4.3. Volume of hydrogen in intermetallic compounds

Compound	Metal atom structure	$v_H[\text{\AA}^3 \text{ per H atom}]$	Reference
β -TiFeD _{1.0}	CsCl (deformed)	2.97	[3.61]
γ -TiFeD _{1.94}	CsCl (deformed)	2.43	[3.61]
ZrV ₂ D _{4.9}	MgCu ₂	2.12	[3.61]
ZrCr ₂ D ₃₋₄	MgCu ₂	2.72	[3.61]
TiCr _{1.9} D _{2.9}	MgCu ₂	2.51	[4.70]
HfV ₂ H ₄	MgCu ₂	2.22	[4.70]
TaV ₂ H _{1.8}	MgCu ₂	2.09	[4.70]
CeRu ₂ D ₅	MgCu ₂	3.99	[4.70]
Nb ₃ SnH	Cr ₃ Si	2.12	[3.61]
Pd ₃ P _{0.8} D _{0.15}	Fe ₃ C	2.26	[3.61]
Zr ₃ V ₃ OD _{4.93}	Ti ₂ Ni(filled)	2.07	[3.61]
ErMn ₂ H ₄	MgZn ₂	3.05	[3.61]
ZrMn ₂ D ₃	MgZn ₂	3.21	[3.61]
LaNiD _{3.7}	CrB	3.79	[3.61]
β -LaNi ₅ D _{6.7}	CaCu ₅ (deformed)	3.21	[3.61]
LaNiInD _{0.48}	ZrNiAl	4.93	[2.57]
LaNiInD _{1.22}	ZrNiAl	4.69	[2.57]
CeNiInD _{0.48}	ZrNiAl	2.77	[2.57]
CeNiInD _{1.24}	ZrNiAl	4.73	[2.57]
NdNiInD _{0.55}	ZrNiAl	4.20	[2.57]
NdNiInD _{1.19}	ZrNiAl	4.05	[2.57]

Table 4.4. Volume of hydrogen in amorphous alloys [3.70]

Alloy	$v_H[\text{\AA}^3 \text{ per H atom}]$
Pd _{0.82} Si _{0.18} H _{0.02}	2.7
Zr ₂ PdH _{2.73}	2.8
Zr ₃ RhH _{5.56}	2.6
Zr _{0.36} Ni _{0.64} H _{0.19}	2.0
Zr _{0.67} Ni _{0.33} H _{1.40}	2.7
Zr _{0.11} Ni _{0.89} H _{0.20}	4.7
Zr _{0.76} Ni _{0.24} H _{1.72}	2.7

scatter of the values is admittedly larger, reflecting the wide varieties of chemical as well as geometrical configurations around interstitial H atoms. Nevertheless, the general trend that v_H is larger in lanthanide-containing alloys can be clearly seen. In CeRu₂, the effect of valence change from Ce⁴⁺ to Ce³⁺, induced by hydrogenation [4.71,4.72], should also add to the increase of v_H .

It may be added here that previous discussions on the hydrogen-induced volume, put forward by *Griessen* and *Feenstra* [4.73], were apparently based on values estimated by comparison of hydrides and original host metals

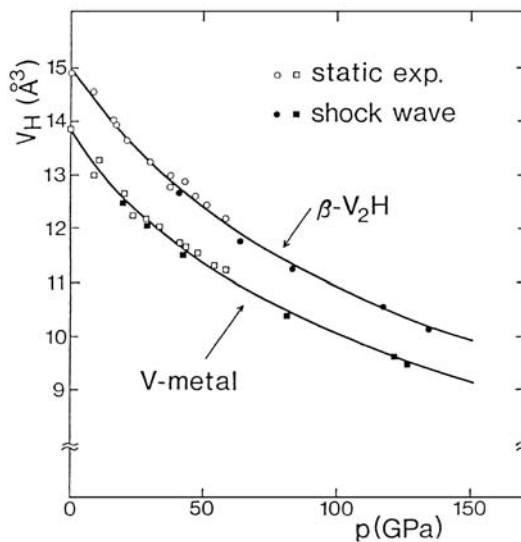


Fig. 4.11. Compression curves of V_2H , V_2D and V , including static-compression data (V_2H (\circ) and V (\square) [4.36]) and shock-compression data (V_2H , V_2D (\bullet) and V (\blacksquare) [4.74])

without paying sufficient attention to their structures, and, therefore, should be taken with some reservations.

The pressure dependence of hydrogen-induced volume was investigated in $VH(D)_{0.5}$ (Fig. 4.11 [4.36, 4.74]), $NbH_{0.75}$ (Fig. 4.12, [4.36, 4.75]) and $TaH_{0.5}$ (Fig. 4.13 [4.75]). The compression curve observed for $NbH_{0.75}$ (Fig. 4.12) clearly shows a decrease of v_H going from the low-pressure phase, β (bcc), to the high-pressure phase, κ (bct), as a consequence of site change from T to O_Z . The structure of this high-pressure phase of Nb hydride is realized under normal pressure in $\beta-VH(D)_{0.5}$, in which no pressure-induced transition was observed up to 135 GPa (Fig. 4.11).

The pressure dependence of v_H derived from these experiments on V , Nb and Ta is shown in Fig. 4.14, along with the data obtained for Fe and Ni . Also included for comparison are the observed compression curves of elemental hydrogen (reproduced from Fig. 4.3 [4.7, 4.76]). We note that, at all pressures, the volume of interstitial hydrogen in metals is much smaller and much less compressible than in the elemental molecular state, but rather close to the calculated volume of metallic hydrogen [4.77, 4.78]. This suggests that the volume of hydrogen in metallic environment follows a fairly universal behavior. As the calculated curve of *Chakravarty et al.* [4.78] can be fitted to a Vinet-type formula (4.1) with $V_0 = 2.96 \text{ \AA}^3$, $K_0 = 99.2 \text{ GPa}$ and $\eta = 4.47$, the compression curve of the interstitial hydrogen can be expressed to a good approximation by substituting an appropriate initial volume for V_0 .

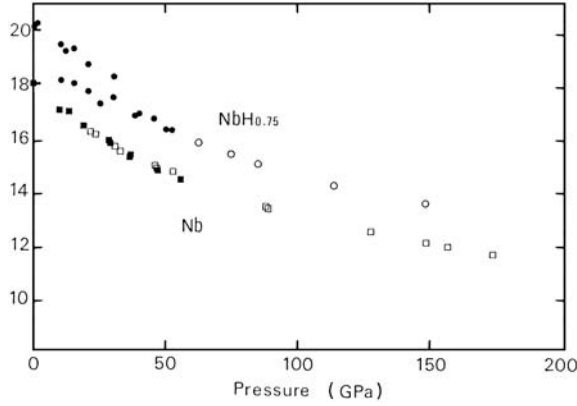


Fig. 4.12. Compression curves of $\text{NbH}_{0.75}$ and Nb, including static-compression data ($\text{NbH}_{0.75}$ (●) and Nb (■) [4.36]) and shock-compression data ($\text{NbH}_{0.75}$ (○) and Nb (□) [4.75])

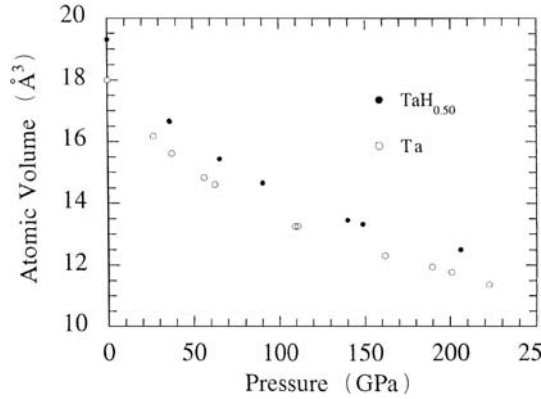


Fig. 4.13. Shock-compression data on $\text{TaH}_{0.50}$ (●) and Ta (○) [4.75]

The effect of magnetism on the H-induced volume deserves special comments. As the appearance of magnetism is in general accompanied by volume expansion (volume magnetostriction), it gives an additional contribution to v_{H} . The volume is increased when the magnetism appears upon hydrogenation of non-magnetic metals, and decreased when the magnetism disappears upon hydrogenation. Unfortunately, the absolute magnitude of volume magnetostriction is difficult to obtain accurately from experiments; The ordinary method of integrating the magnetic contribution to thermal expansion appears to grossly underestimate the total volume expansion. Thus we have recourse to theoretical calculations, which in themselves involve uncertainties due to various approximations adopted. Within these limitations, however, it

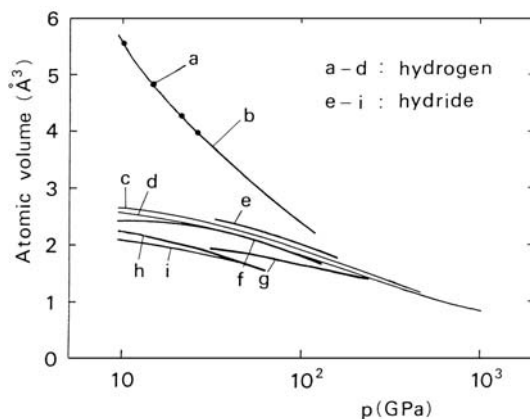


Fig. 4.14. Compression curves of hydrogen in elemental form (observed: a [4.76], b [4.7]), calculated: c [4.77], d [4.78]) and in interstitial sites in V (e [4.36, 4.74]), Nb (f [4.36, 4.75]), Ta (g [4.75]), Fe (h [4.79, 4.81]) and Ni (i [4.61])

is possible to illustrate the effect of magnetism on v_H in a few representative cases.

In the case of Fe, a nearly stoichiometric dhcp hydride ϵ' -FeH_x appears above 3.5 GPa at room temperature, and its compression curve was measured by *Badding et al.* to 62 GPa [4.79], and more recently by *Hirao et al.* to 80 GPa [4.80]. In comparison with the EOS of ϵ -Fe [4.81], they found that in ϵ' -FeH_x, the H-induced volume is much more compressible; $v_H = 2.6 \text{ Å}^3$ at 3.5 GPa and 1.6 Å^3 at 60 GPa, as shown in Fig. 4.14. This anomalous compression behavior is believed to be associated with magnetism. Unlike ϵ -Fe which is non-magnetic, ϵ' -FeH_x is a ferromagnet, in which magnetic moments on Fe atoms are fairly large, only 20% smaller than those in α -Fe, and decrease with increasing pressure [4.82, 4.83]. The volume magnetostriction calculated by *Elsässer et al.* [4.68, 4.69], amounts to $0.9 \pm 0.4 \text{ Å}^3$ under normal pressure, which makes the non-magnetic part of the H-induced volume at 3.5 GPa $2.6 - (0.9 \pm 0.4) \approx 1.7 \pm 0.4 \text{ Å}^3$. The value is consistent with other cases of O-site occupancy in the hcp lattice (Table 4.2). The calculation of *Elsässer et al.* could reproduce the observed EOS reasonably well up to 60 GPa [4.69].

In the case of Ni, the situation is reversed. The ferromagnetism of Ni disappears in NiH; thus the effect of magnetism, if any, should make v_H smaller. In fact, theoretical calculations unanimously predicted very small volume magnetostriction ($0 \sim 0.15 \text{ Å}^3$ under ambient pressure [4.45, 4.55]), and therefore its contribution to v_H can be regarded to be sufficiently small. On the experimental side, accurate XRD data using DACs are available for both Ni and NiH up to 50 GPa (shown in Fig. 4.14) [4.60]. Beyond this pressure, the DAC experiments on NiH were extended to 120 GPa, and yielded highly compressible v_H with reference to shock-compression data on Ni; $v_H = 1.16 \text{ Å}^3$

at 120 GPa (not shown in Fig. 4.14) [4.60]. Regarding the reference volume, detailed re-analysis confirmed that corrections for shock-heating effects are negligibly small (0.02 and 0.04 Å³ at 60 and 120 GPa, respectively [4.84,4.85]), but the volume of NiH derived from a single weak diffraction line can at best provide only a crude measure. Thus the data above 50 GPa cannot be treated on the equal footing. In any case, up to 50 GPa, the absence of any anomaly in v_{H} is consistent with a small magnetostriction in Ni.

The Co-H system exhibits intermediate properties. The ferromagnetism of Co is tenacious in the hcp phase; the magnetic moment per Co atom is decreased only weakly by hydrogenation, from $1.7\mu_{\text{B}}$ in ϵ -Co to $1.5\mu_{\text{B}}$ in ϵ -CoH_{0.5} [4.48]. It is therefore expected that the volume magnetostriction in ϵ -Co and ϵ -CoH _{x} should cancel each other out, leaving v_{H} unaffected. In the fcc phase, on the other hand, the magnetism is quickly lost by hydrogenation, which in effect should make v_{H} smaller. As the calculated values of volume magnetostriction in fcc Co are in the range $0.43 \sim 0.44 \text{ Å}^3$ [4.45,4.55], the non-magnetic part of v_{H} in γ -CoH_{1.0} is estimated at $\sim 2.3 \text{ Å}^3$. This value appears more coherent with other cases of O-site occupancy in the fcc lattice.

Not much is known about magnetic rare-earth hydrides.

4.3 Solubility Enhancement Under High Hydrogen Pressures—Calculations

The treatment of the solubility of hydrogen in metals described in Sect. 2.2 is valid only at reasonably low pressures ($p \leq 1 \text{ MPa}$), where hydrogen behaves very much like an ideal gas. In this section, we extend our calculations to high hydrogen pressures.

It may be readily anticipated that a very steep increase of the chemical potential of fluid hydrogen, μ^{f} , at high pressures, such as the one shown in Fig. 4.7, should result in a drastic enhancement of the solubility. Indeed, according to the calculation of *Sugimoto* and *Fukai* [4.27], the solubility enhancement amounts to many orders of magnitude in easily accessible pressure ranges. Therefore, it is believed that the solubility enhancement is a generally important consideration for high-pressure experiments, especially so because it may cause embrittlement and lowering of the melting point of host metals (Sect. 4.4).

In view of its importance and usefulness for high-pressure experimentalists, we have performed an improved calculation of the solubility under high pressures of hydrogen for some selected metals that have small solubilities under normal pressures [4.27], and reproduce the results here.

Under high pressures, both μ^{f} and the chemical potential in the solid solution (μ^{α}) that constitute the equilibrium condition

$$\mu^{\alpha} = \frac{1}{2}\mu^{\text{f}} \quad (4.5)$$

assume forms different from those at low pressures. We write μ^α in the form

$$\mu^\alpha = \mu_{\text{vib}} + h^{\alpha'} - Ts^{\alpha\text{nc}} - Ts^{\alpha\text{c}} , \quad (4.6)$$

where μ_{vib} is the vibrational contribution

$$\mu_{\text{vib}} = kT \sum_{i=1}^3 \ln[1 - \exp(-\theta_{\text{E}\alpha(i)}/T)] , \quad (4.7)$$

and

$$h^{\alpha'} = h^{\alpha 0} + pv^{\text{f}} - \bar{u}x + \bar{w}x^3 . \quad (4.8)$$

Here h^α is a value of $h^{\alpha'}$ for low concentrations of hydrogen at low pressures, and $-\bar{u}x$ and $\bar{w}x^3$ come from long-range and short-range interactions, respectively, between H atoms (Sect. 2.2.2); $s^{\alpha\text{nc}}$ is a nonconfigurational part of the partial entropy, and the configurational part can be written as

$$s^{\alpha\text{c}} = -k \ln Z_\alpha , \quad (4.9)$$

with $s^{\alpha\text{c}}$ given by (2.35) or (2.36). Then, the equilibrium condition can be written as

$$Z_\alpha = \exp \left(- \frac{(\mu_{\text{vib}} + h^{\alpha'} - Ts^{\alpha\text{nc}}) - \frac{1}{2}\mu^{\text{f}}}{kT} \right) \quad (4.10)$$

$$= \prod_{i=1}^3 [1 - \exp(-\theta_{\text{E}\alpha(i)}/T)]^{-1} \exp \left(- \frac{(h^{\alpha 0} - Ts^{\alpha\text{nc}}) - \frac{1}{2}\mu^{\text{f}}}{kT} \right) . \quad (4.11)$$

In order to extract necessary information from low-pressure data, we adopt the following procedure. At low pressures, μ^{f} can be identified with the ideal-gas formula (1.13–1.16)

$$\mu^{\text{f}} = kT \ln \frac{p}{p_0} - \frac{7}{2}kT \ln \frac{T}{T^*} - E_{\text{d}} \quad (4.12)$$

and Z_α can be written at low H concentrations as

$$Z_\alpha = \frac{x}{r - x} \approx \frac{x}{r} . \quad (4.13)$$

Then, (4.11) is reduced to

$$x = \sqrt{\frac{p}{p_0}} \frac{(T^*/T)^{7/4}}{\prod_{i=1}^3 [1 - \exp(-\theta_{\text{E}\alpha(i)}/T)]} \text{re}^{s^{\alpha\text{nc}}/k} \exp \left(- \frac{h^{\alpha 0} + \frac{1}{2}E_{\text{d}}}{kT} \right) . \quad (4.14)$$

Values of $h^{\alpha 0} + \frac{1}{2}E_{\text{d}}$ and $s^{\alpha\text{nc}}$ can be determined, approximately, by fitting this expression to the Sieverts formula (2.2) with tabulated values of

ΔH_s and ΔS_s . In the second factor of (4.14), the temperature dependence of the numerator and denominator is largely cancelled, and the weak temperature dependence that remains can be absorbed in the Sieverts formula by choosing a slightly different ΔH_s from $h^{\alpha 0} + \frac{1}{2}E_d$. The values of $\theta_{E\alpha(i)}$ were chosen to approximately reproduce the observed vibration energies: 120 and 170 meV for singlet and doublet modes in bcc metals, and 60 meV for a threefold degenerate mode in fcc metals (Table 5.4). In addition, we put $r = 6$ and 1 for bcc and fcc metals, respectively. Values of $h^{\alpha 0} + \frac{1}{2}E_d$ and s^{anc} obtained from the reported values of ΔH_s and ΔS_s [2.20] are listed in Table 4.5. The values of $h^{\alpha 0} + \frac{1}{2}E_d$ and ΔH_s are not much different, as a consequence of the cancellation effect mentioned above.³

Table 4.5. Enthalpy and non-configurational part of the entropy of solution excluding the vibrational contribution ($h^{\alpha 0} + \frac{1}{2}E_d$ and s^{anc}/k) obtained by fitting (4.14) to the Sieverts law [4.27]. The values of ΔH_s and ΔS_s are taken from [2.20]

Metal	ΔH_s [eV per H atom]	$\Delta S_s/k$	$h^{\alpha 0} + \frac{1}{2}E_d$ [eV per H atom]	s^{anc}/k
Al	0.66	-5.8	0.65	0.98
Ni	0.17	-5.9	0.15	0.65
Pt	0.48	-6.7	0.49	0.26
Cu	0.44	-5.5	0.48	1.55
Ag	0.72	-5.1	0.69	1.41
Au	0.37	-9	0.35	-2.4
γ -Fe	0.31	-5.5	0.27	0.88
α, δ -Fe	0.35	-4.8	0.41	2.35
Cr	0.60	-5	0.64	3.64
Mo	0.55	-5.5	0.57	1.47
W	1.05	-4.7	1.07	2.14

For the parameters of H-H interactions, we choose $\bar{u} = 0.35$ eV and $\bar{w} = 0.5$ eV so that they describe reasonably well the existing data on the concentration dependence of ΔH_s (Fig. 2.10). The volume increase caused by an H atom in solution is regarded as being the same in all cases ($v_H = 2.5 \text{ \AA}^3$ per H atom), and at all pressures. From what has been described in the foregoing section, these simplifications can be considered sufficient for the present purpose. Finally, as regards the configurational entropy, an expression appropriate for a random solution (2.34), with $r = 1$ is used for fcc metals,

³ Note that the value of s^{anc} for Au is anomalous. This apparently arises from large experimental errors due to the limited temperature ranges of the measurements. As the actual data points lie rather close to those of Al and Ag, for which more accurate data are available, the actual values of $h^{\alpha 0} + \frac{1}{2}E_d$ and, s^{anc} and hence the solubilities, in Au are expected to be similar to these metals.

whereas, for bcc metals, the expression (2.36) appropriate for T-site occupancy with second-nearest-neighbor blocking is adopted.

Thus, we have all the necessary ingredients for determining the solubility from the equilibrium condition (4.5). When this condition is satisfied by more than one value of x , that is, when the spinodal decomposition takes place, the phase boundary has to be determined by Maxwell's equal-area construction. The calculation has been performed for nine metals, including the fcc metals Al, Ni, Pt, Cu, Ag, γ -Fe, and the bcc metals α , δ -Fe, Cr, Mo, W, up to a maximum pressure of 100 GPa. The results of the calculation are shown in Figs. 4.15–4.24, in which the boundary of the two-phase region is marked by a dotted line.

It can be seen that the solubility enhancement is really appreciable in this pressure range. The pressure effect works in such a way that, as the hydrogen pressure is increased, the slope of the isobars becomes smaller. Physically, this arises from the fact that the volume of an H atom is smaller in metals than in the fluid state; therefore, the term $p(v_H - 1/2v^f)$ at large values of p tends to offset positive heats of solution. Comparison of Figs. 4.15–4.24 indicates that the enhancement is effective up to several tens of GPa, and approaches saturation at pressures of ~ 100 GPa, independent of temperature, as the case of W (Fig. 4.24) clearly shows. This is a consequence of the pressure dependence of v^f . As can be seen in Table 4.1, the volume per H atom ($1/2v^f$) approaches v_H at $p \geq 100$ GPa, independent of temperature.

For approximate evaluation of the solubility at high hydrogen pressures from the tabulated values of ΔH_s^0 and ΔS_s^0 (Table 2.1) and G (Table 4.1), it is convenient to use the following expression;

$$\frac{x}{1-x} \approx e^{\Delta S_s^0/k - \Delta H_s^0/kT} F(p, T), \quad (4.15)$$

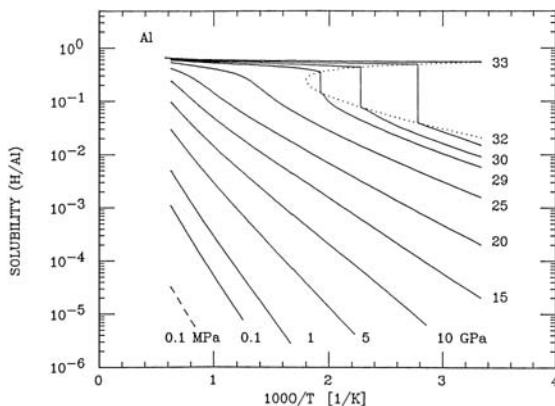


Fig. 4.15. The solubility of H in Al as a function of temperature and hydrogen pressure [4.27]

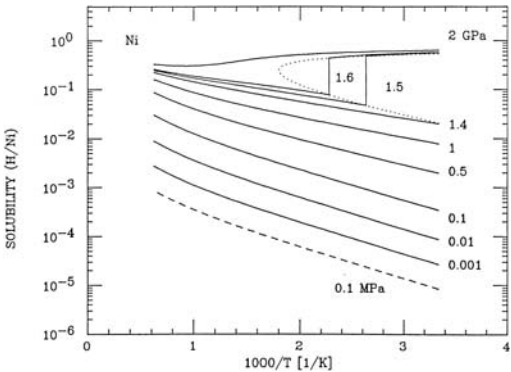


Fig. 4.16. The solubility of H in Ni as a function of temperature and hydrogen pressure [4.27]

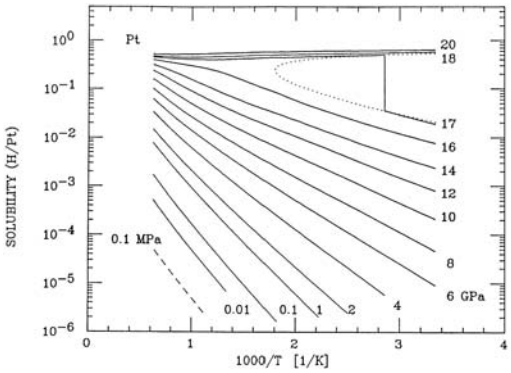


Fig. 4.17. The solubility of H in Pt as a function of temperature and hydrogen pressure [4.27]

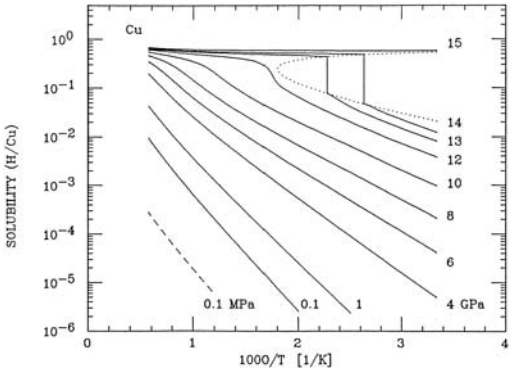


Fig. 4.18. The solubility of H in Cu as a function of temperature and hydrogen pressure [4.27]

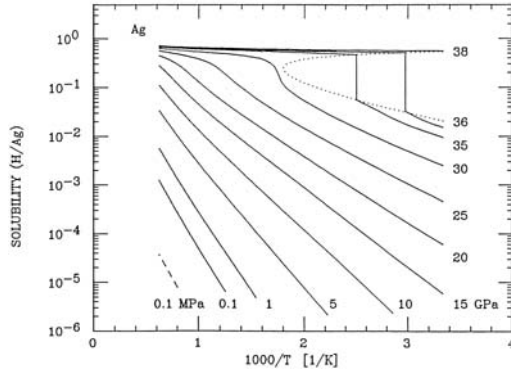


Fig. 4.19. The solubility of H in Ag as a function of temperature and hydrogen pressure [4.27]

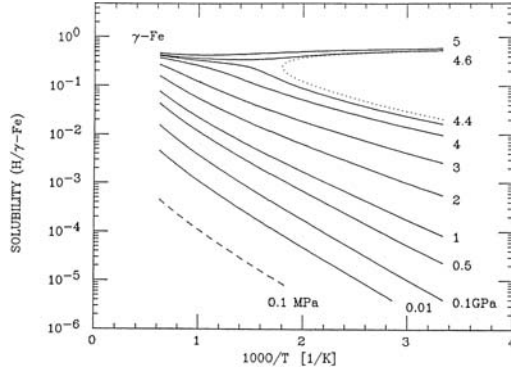


Fig. 4.20. The solubility of H in γ -Fe as a function of temperature and hydrogen pressure [4.27]

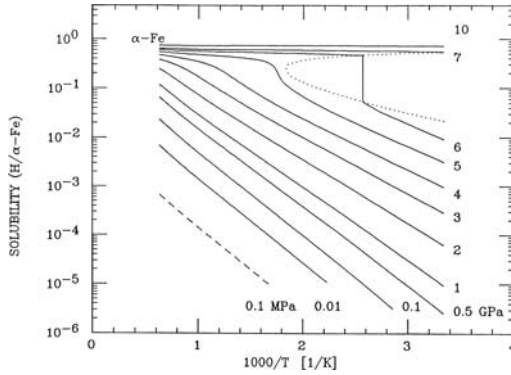


Fig. 4.21. The solubility of H in α , δ -Fe as a function of temperature and hydrogen pressure [4.27]

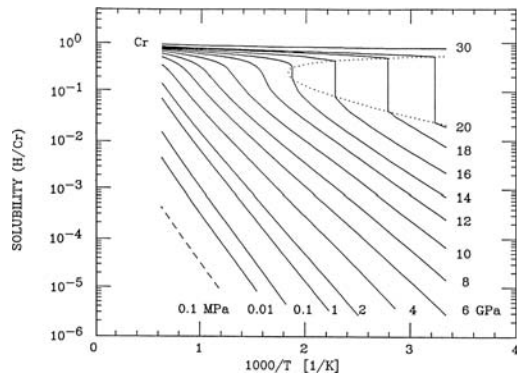


Fig. 4.22. The solubility of H in Cr as a function of temperature and hydrogen pressure [4.27]

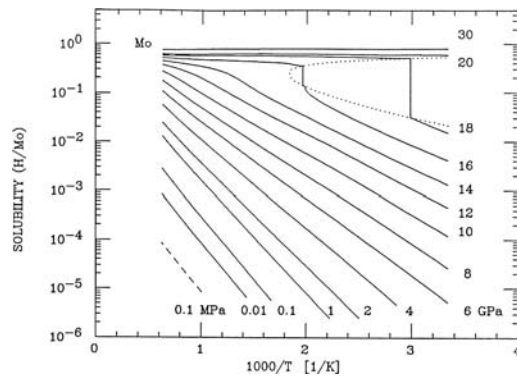


Fig. 4.23. The solubility of H in Mo as a function of temperature and hydrogen pressure [4.27]

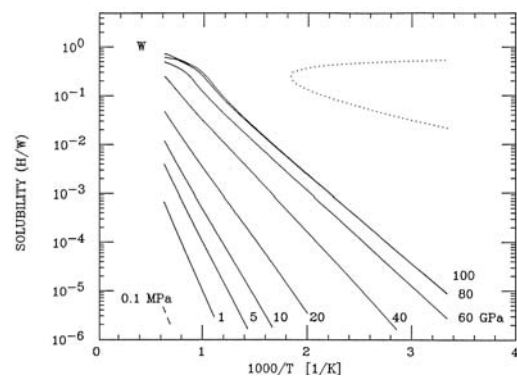


Fig. 4.24. The solubility of H in W as a function of temperature and hydrogen pressure [4.27]

$$F(p, T) = e^{-(\mu^f - \mu^{g0})/kT} \quad (4.16a)$$

$$= \left(\frac{T}{T^*} \right)^{7/4} e^{G/2kT}, \quad (4.16b)$$

where $\Delta H_s^0/kT = 1.16 \times 10^4 \Delta H_s^0 \text{ (eV)}/T(\text{K})$, $T^* = 9.20 \text{ K}$, $G/2kT = G(\text{kJ mol}^{-1})/16.63T(\text{K})$, and $r = 1$ has been assumed. In describing the deviation from the ideal-gas behavior by $F(p, T)$, the different choice of the zero of energies (by E_d) has been properly included.

Driessen et al. [4.86] have performed similar calculations of the solubility under high pressures of hydrogen for metals having large positive heats of solution. For those metals where the heats of solution are not known, they made estimates based on the semiempirical model of *Griessen* and *Driessen* [4.87]. The values of the heat of solution (for $x = 0.5$) and the equilibrium plateau pressure for spinodal decomposition at 300 K are given in Table 4.6. It can be seen that some of the metals listed here have such large heats of solution and high plateau pressures that they are hardly susceptible to hydrogen effects and are therefore useful for high-pressure experiments. The result of their calculation for Ni is compared with observations in Fig. 4.25. The satisfactory agreement gives a good measure of the reliability of the calculation.

Table 4.6. Heat of solution $\Delta H_s(x = 0.5)$ and the plateau pressure calculated [4.86]

Metal	$\Delta H_s(x = 0.5)$ [eV per H atom]	Plateau pressure [GPa]
Be	0.29	12
Cu	0.12	4.3
Zn	0.65	>100
Ru	0.27	11
Ag	0.49	31
Cd	0.16	5.9
In	0.07	2.9
Sn	0.68	>100
Sb	2.28	>100
W	0.23	8.9
Re	0.26	10.5
Os	0.68	>100
Ir	0.84	>100
Pt	0.57	44
Au	0.74	>100
Hg	0.29	12.5
Tl	0.87	>100
Pb	1.27	>100
Bi	1.27	>100

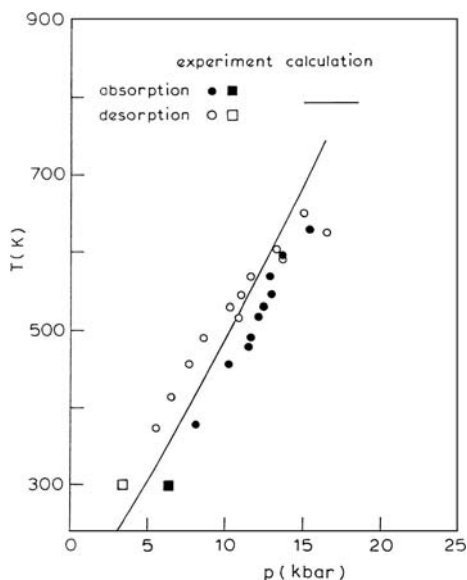


Fig. 4.25. Comparison of calculated and observed plateau pressures in the Ni-H system. Calculations from [4.86] and experimental data from [4.88, 4.89]

In practice, high hydrogen pressures often induce structural changes, with abrupt increases of the hydrogen concentration. The solubilities calculated above are meaningful only within the region of original structures. For more realistic evaluation of hydrogen effects at high pressures, knowledge of the constitution of phase diagrams thus becomes the necessity.

4.4 Phase Relation Under Extended p, T Conditions—Experiments

4.4.1 Transition Metal – Hydrogen Systems; Individual Cases

Two different types of high-pressure experiments have been performed on M-H alloys. In the first type of experiments, a high pressure is applied on a hydride sample prepared in advance under normal conditions. In this seal-off type experiment, the effect of pressure on the relative stability of different phases is studied for each prescribed hydrogen concentration. The intrinsic pressure effect here arises primarily through the pv_H term in the chemical potential. For $v_H = 2.9 \text{ \AA}^3$ per H atom and $p = 1 \text{ GPa}$, pv_H becomes 0.18 eV^4 , which is certainly an important contributor to the chemical potential. Thus, under high pressures, hydrogen tends to prefer sites with smaller volume

⁴ A convenient conversion formula is $p(\text{GPa}) v_H(\text{\AA}^3) = 0.00624 pv_H (\text{eV})$.

expansion. In the second type of experiments, where a metal sample is placed under high hydrogen pressures, the exchange of hydrogen between the interior and the exterior of the specimen takes place. The hydrogen concentration as well as the structure of phases vary as a function of p , T . Hereafter, in order to distinguish the hydrogen pressure in the second type of experiments, it is denoted by p_{H} .

Results of the second type of experiments are usually given in the form of equilibrium $p_{\text{H}}-T$ diagrams with hydrogen concentration x as an implicit variable; if they are given in the form of $x-T$ diagrams, the equilibrium hydrogen pressure assumes different values at different points on the diagram. High hydrogen pressures cause large enhancements of the solubility, and allow the investigation of M-H systems in hitherto unattainable ranges of temperature and hydrogen concentrations, in addition to intrinsic pressure effects on the phase stability.

Studies of the equilibrium $p_{\text{H}}-T$ conditions for hydride formation were initiated by a Polish group in the 1960s. They compressed hydrogen in a piston-cylinder-type apparatus, and attained ~ 3 GPa at room temperature and ~ 1.5 GPa at $T \leq 450^\circ\text{C}$ in a volume of ~ 1 cm³. For details of their experiments, see [4.89]. Subsequently, a Russian group developed a technique of producing higher hydrogen pressures in a somewhat smaller volume by thermal decomposition of some hydrogen-containing material inside an externally compressed sample cell. With the help of this method, they investigated phase changes by measuring the electrical resistance. Also, by developing a technique to recover specimens from the high-pressure cell by cooling to liquid nitrogen temperature before decompression, thus preventing the specimen from decomposition, they determined the structure and hydrogen concentrations of hydrides synthesized under high pressures. Their p_{H} , T conditions ranged between $p_{\text{H}} \leq 9$ GPa and $-150 \leq T \leq 500^\circ\text{C}$ (see e.g. [4.48, 4.90]), and more recently up to $p_{\text{H}} \leq 3$ GPa and $T \leq 900^\circ\text{C}$ [4.91]. The results of their systematic investigation of the phase diagrams of 3d-, 4d-metal-hydrogen systems are reviewed by *Antonov* [4.92].

High-pressure techniques using a multi-anvil press in combination with solid pressure transmitting medium have been developed in Japan [4.93, 4.94], and applied to the studies of M-H systems. Typically, a fairly uniform pressure of $2 \leq p \leq 10$ GPa can be generated over a sample volume of ~ 1 mm³, and temperature can be raised to $\sim 2000^\circ\text{C}$. This method is usually adopted for the sealed-off-type experiments, but it can also be used for equilibrium $p_{\text{H}}-T$ measurements by the introduction of some internal hydrogen source. The design of a sample cell assembly developed for this purpose by our group is described in [4.95].

Recent developments of the diamond-anvil cell technique have opened a possibility of greatly extending p , T conditions, $p \leq 300$ GPa, $1 \leq T \leq 600$ K, though necessarily in a rather limited volume ($\sim 10^{-4}$ mm³). Difficulties exist,

however, in raising the temperature: The maximum temperature is limited by the incipient damaging effects of hydrogen on diamond.

Both the multi-anvil and diamond-anvil press allow in situ determination of the crystal structure; in many cases by XRD [4.93] and in some cases by neutron diffraction [4.96].

In the following, the results of high-pressure studies of equilibrium phase relations of transition metal–hydrogen systems are described, arranged in the order of group number III–VIII on the Periodic Table.

Some recent results on noble metal Cu are also added at the end.

Group III Metal–Hydrogen Systems

A quest for the systematics of hydride formation in rare-earth metals was completed by the high-pressure synthesis of the trihydrides of Sc by *Bashkin et al.* – $\text{ScH}_{2.65}$ at $p_{\text{H}} = 1.0 \text{ GPa}$ [4.97].

As described in the previous section (Sect. 4.2), the atomic volume of the cubic dihydride phase tends to decrease with additional hydrogen, but ν_{H} increases abruptly in the hcp trihydride phase. From this observation, the following prediction can be made. (a) For metals having a limited cubic phase field (Nd and beyond, Fig. 2.15), the limiting H concentration should increase with increasing (mechanical) pressure. (b) Cubic hydrides having non-stoichiometric composition should undergo decomposition into a pure metal (or into the α^* solid solution of the respective concentration, if existing) and a cubic hydride of maximum H concentration. (c) At sufficiently high pressures, hcp trihydrides should transform to the fcc structure (BiF_3 type) [4.98]. This last prediction was recently confirmed in ErH_3 [4.165] and YH_3 [4.166]; in both cases the transition to the fcc structure was observed at $\sim 15 \text{ GPa}$.

Group-IV Metal–Hydrogen Systems

The phase diagrams (x – T diagram) of the Ti–H system at 5 GPa is shown in Fig. 4.26 [4.99]. Most of the phase boundaries were determined by seal-off type experiments, by in situ measurements of the electrical resistance and/or XRD. In comparison to the phase diagram determined at low pressures ($\leq 30 \text{ MPa}$; Fig. 2.20), two high-pressure phases are to be noted. The occurrence of trihydride was inferred from comparison of the results with and without surrounding hydrogen. Without an internal hydrogen source, the atomic volume of $\text{TiH}_{1.8}$ increases monotonically with temperature, whereas with hydrogen a reversible volume change takes place between the two fcc structures at $\sim 500^\circ\text{C}$, as shown in Fig. 4.27. The state of smaller atomic volume realized in the higher temperature region is believed to be the trihydride having the BiF_3 -type fcc structure.

Another feature is the appearance of a new phase (ζ) at H concentrations of $40 \sim 44 \text{ at\%}$ ($[\text{H}]/[\text{Ti}] = 0.67 \sim 0.77$) [4.99]. The structure is bct with $c/a = 1.2$ at 300°C . The occurrence of this phase as a function of pressure had

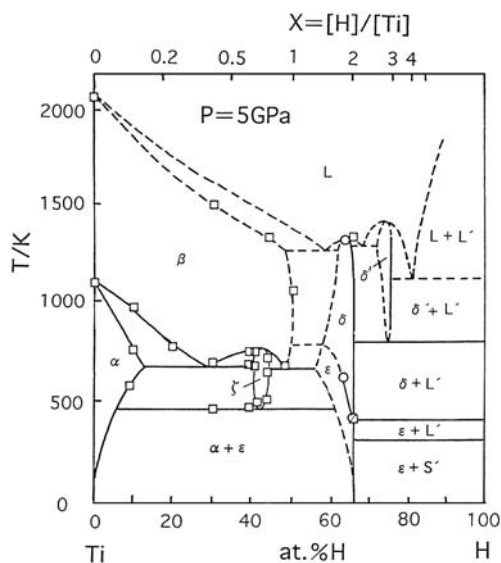


Fig. 4.26. The composition–temperature (x – T) diagram of the Ti–H system [4.99]

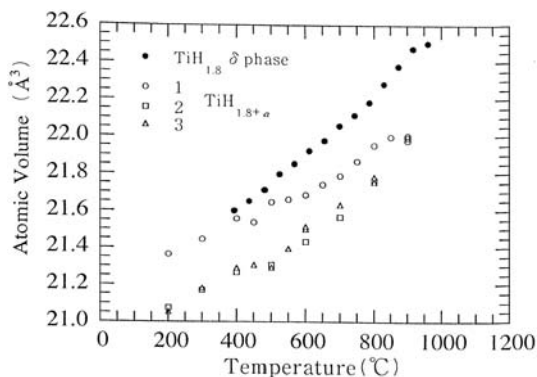


Fig. 4.27. Variation with temperature of the atomic volume of $\text{TiH}_{1.8+y}$ coexisting with fluid H_2 at 5 GPa; heating (1) \rightarrow cooling (2) \rightarrow heating (3). Data for δ - $\text{TiH}_{1.8}$ without fluid H_2 are shown for comparison [4.99]

been investigated by the Russian group, with the results shown in Fig. 4.28 [4.100–4.102]. A large isotope dependence is to be noted. These features – the bct structure and the isotope effect – are the clear indication that this high-pressure phase (ζ) is isomorphous with β - $\text{V}_2\text{H(D)}$ where H(D) atoms occupy O_Z sites. Evidence in support of O-site occupancy was also provided by low vibrational frequencies of H observed in this structure [4.103].

In both Ti–H and Zr–H systems, occurrence of many metastable phases after quenching in terms of pressure and temperature makes the determination

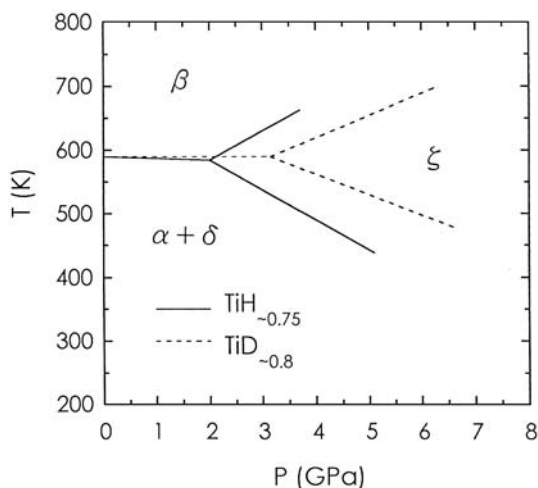


Fig. 4.28. The p - T diagram of $\text{TiH}_{\sim 0.75}$ and $\text{TiD}_{\sim 0.8}$, showing the occurrence of the bct high-pressure phase (ζ). For the sake of clarity, only the results for heating runs are shown; in cooling runs the transition temperatures were 50 ~ 100 K lower [4.100–4.102]

of equilibrium phase diagrams rather difficult. These problems will not be treated here [4.103, 4.104].

Group V Metal–Hydrogen Systems

For the V–H(D) system, the pressure dependence of the β - α transitions was investigated by in situ resistometry, with the result shown in Fig. 4.29 [4.105]. The large isotope effect observed under ambient pressure gradually vanishes, and the transition temperatures increase with pressure. As discussed in more detail later (Sect. 5.7.2), this isotope dependence of the β - α transition is a consequence of the site change of H atoms across the transition. For the V–D system, the x - T diagram varies with pressure as shown in Fig. 4.30 [4.106].

The x - T diagram of the V–H system at ~5 GPa was determined by combination of various seal-off type experiments, including in situ XRD and resistometry, and microscopic observation of recovered specimens. The results are shown in Fig. 2.4 [2.15]. One of the peculiar features here is the occurrence of a high-pressure phase (γ'), which is a monohydride of NaCl type, existing in a narrow composition range up to very high temperatures. This phase had been overlooked in our previous studies, which led us to a topologically rather different phase diagram [4.107].

In the Nb–H system, a room-temperature compression of β - $\text{NbH}_{0.75}$ manifested a transition to a bct phase (κ) at 20 GPa (Fig. 4.12 [4.36]). The tetragonality increased from $c/a = 1.12$ at 20 GPa to 1.16 at 60 GPa. This structure is believed to be isomorphous with β - VH_x and ζ - TiH_x . A similar structural

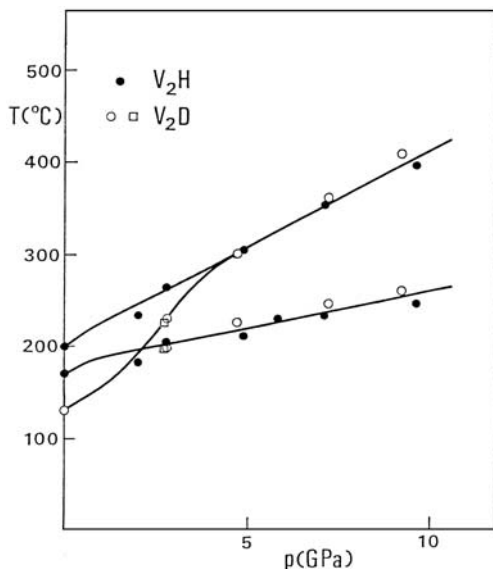


Fig. 4.29. The p - T diagram for the β - α transition in $VH_{0.5}$ and $VD_{0.5}$ [4.105]

change was observed in $TaH_{0.50}$ between 10 ~ 30 GPa [4.75]. A monohydride phase of NaCl type and dihydride phase of CaF_2 type were formed in the Nb-H and Ta-H systems under ~5 GPa and 1000°C [4.56].

In contrast to the V-H system, the phase diagrams of Nb-H and Ta-H systems do not exhibit noticeable isotope effects under normal pressure, and its pressure dependence is small up to ≤ 5 GPa. This is because H atoms retain the T-site occupancy in most phases except the high-pressure bct phase (see Sect. 5.7.2).

Group VI Metal-Hydrogen Systems

The p_H - T phase diagram of the Cr-H system is shown in Fig. 4.31. The α (bcc)- ϵ (hcp) boundary determined by resistometry in isothermal decompression processes [4.48, 4.108] agrees reasonably well with the results of in situ XRD [4.44]. The H concentration estimated from the unit-cell volume is $x = [H]/[Cr] \leq 0.03$ for the α (bcc) phase, and nearly stoichiometric ($x \approx 1$) for the ϵ (hcp) and γ (fcc) phases. These hydrides of hcp and fcc structures were also synthesized by electrolytic methods [4.109-4.111]. A drastic reduction of the melting point with dissolution of hydrogen should also be noted.

The phase diagram of the Mo-H system is very similar, as shown in Fig. 4.32 [4.52]. In this case, too, the H concentration is very small in the α (bcc) phase, and nearly stoichiometric ($x \approx 1$) for the ϵ (hcp) and γ (fcc) phases. Difference from the Cr-H system is that the ϵ - γ boundary is shifted to lower temperatures, whereas the melting point of the γ -hydride was always higher than 1200°C and was therefore inaccessible.

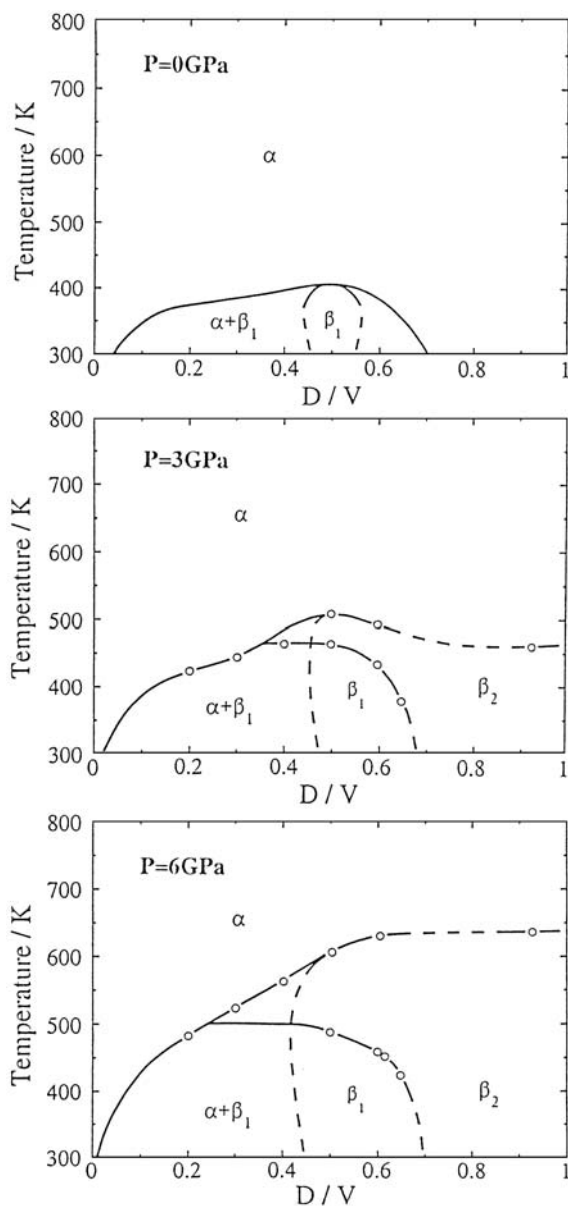


Fig. 4.30. Composition–temperature (x – T) diagrams of the V–D system at several different pressures [4.106]

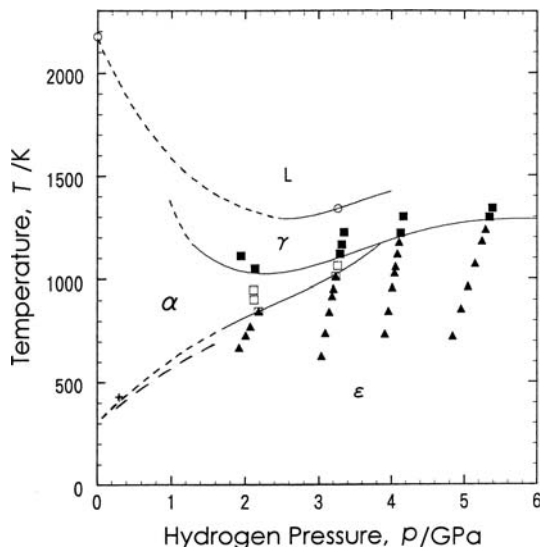


Fig. 4.31. The p_H - T diagram of the Cr-H system [4.44]. The α - ϵ boundary determined earlier in the lower p_H , T region [4.48, 4.108] is also inscribed

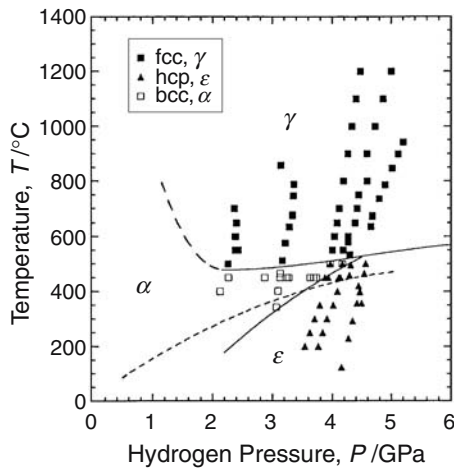


Fig. 4.32. The p_H - T diagram of the Mo-H system [4.52]. The α - ϵ boundary determined earlier in the lower p_H , T region [4.48] is also inscribed

In W, no noticeable solubility was observed in the bcc phase at $T \leq 400^\circ\text{C}$ and $p_H \leq 9$ GPa [4.48], consistent with the calculation of *Sugimoto* and *Fukai* [4.27], (Fig. 4.24), but a transition to the hcp structure was recently observed at $p_H = 24$ GPa with an abrupt increase of the atomic volume of $\sim 1.6 \text{ \AA}^3$ [4.167].

Group VII Metal–Hydrogen Systems

Manganese metal undergoes allotropic transitions; α (complex cubic)– β (complex cubic)– γ (fcc)– δ (bcc)–melt, and all the transition temperatures are simply shifted upward with pressure [4.112]. Under high H_2 pressures, ϵ (hcp) hydride is formed below $\sim 350^\circ\text{C}$, and the stability field of the fcc structure (γ) is extended to lower temperatures [4.113]. The phase diagram determined by *Antonov et al.* [4.114] by quench-recovery experiments, together with the results of *Filipek et al.* [4.115] showed that α - and β -Mn structures are destabilized below 0.7 GPa and transformed to γ or ϵ hydride depending on p_H, T conditions.

The p_H – T diagram determined subsequently by our group by in situ XRD over a wide range of p_H, T conditions is shown in Fig. 4.33 [4.116], including the phase boundaries determined earlier below 4.5 GPa. The results of the two groups are consistent with each other except the presence of the intervening phase ϵ' having the dhcp structure. This is because the ϵ – ϵ' transition is very fast and reversible, unlike ϵ, ϵ' – γ transitions, and was therefore unquenchable in the experiments of *Antonov et al.* [4.114].

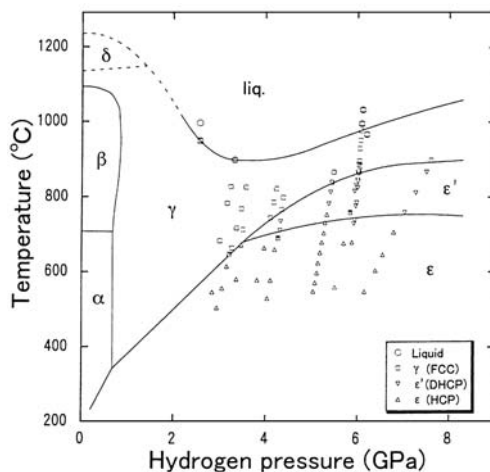


Fig. 4.33. The p_H – T diagram of the Mn–H system [4.116], supplemented by the phase boundaries below 4.5 GPa determined earlier [4.113, 4.114]

In the α and β phases, the H concentration is low, $x \leq 0.1$, whereas in ϵ and γ hydrides the concentrations are high and increase with pressure; $x = 0.35 \sim 0.5$ in the γ -phase and $x = 0.8 \sim 0.95$ in the ϵ -phase in the p_H, T range investigated.

Hydrogen atoms occupy O sites in both γ and ϵ phases, with an indication of ordering into the anti- CdI_2 type structure in ϵ - $\text{MnH}_{0.46}$, where every other O-site layers perpendicular to the c -axis are occupied [4.117].

In the Tc-H system, the hcp structure of Tc metal is retained on dissolution of hydrogen. The average H concentration as a function of H_2 pressure measured at 300°C increased in two steps; the first plateau of $x \approx 0.5$ realized between 0.5 ~ 1 GPa and the second one of $x \approx 0.8$ at ≥ 1.5 GPa [4.118, 4.119]. The structure of the former may be identified to be the anti-CdI₂ type, and the latter the defect-NiAs type where O sites are occupied randomly [4.120].

The Re-H system also retains the original hcp structure on dissolution of hydrogen. The O-site occupancy of hydrogen is established by neutron diffraction [4.51]. Early studies of the Russian group showed that the solubility increased with pressure; $x = 0.13$ at 9 GPa and 250°C, increasing to $x = 0.22$ at 170°C [4.121, 4.122]. More recent investigation using DACs showed that at room temperature the increment of the unit-cell volume from that of Re metal increased with H_2 pressure to $p_H \sim 9$ GPa, and remained constant thereafter, at least up to ~ 20 GPa [4.53, 4.54]. This is a clear indication that a stable hydride having a fixed composition was formed. A careful scrutiny of the XRD data revealed superlattice reflections arising from the modulation of lattice spacing along the c -axis, from which the formation of anti-CdI₂ structure was concluded [4.54]. Assuming $x = 0.5$ above $p_H \sim 9$ GPa, we obtain the H-induced volume of $v_H = 1.6 \sim 1.7 \text{ \AA}^3$, which is coherent with other cases of O-site occupancy in the hcp lattice.

Group VIII Metal-Hydrogen Systems

Figure 4.34 shows the p_H - T diagram of the Fe-H system. The data of *Fukai et al.* [4.123] has been supplemented by the earlier data of the Russian group in the lower p_H , T region [4.124], and a few other works from Japan in the high p_H , T region [4.125, 4.126]. There are three different solid phases, α (bcc), γ (fcc) and ϵ' (dhcp), which join at a triple point, 5 GPa and 260°C.

The p - T phase diagram of Fe is shown in Fig. 4.35 for comparison [4.127]. Note the difference in the pressure scale. In view of its implication for the state of the Earth's core, the phase relation has been studied over the wide range of p , T conditions. There are four solid phases; α (bcc), γ (fcc), ϵ (hcp) and ϵ' (dhcp). The ϵ' phase field has not been determined accurately so far, but its existence was confirmed by *Saxena et al.* [4.128]. The melting curve (the ϵ -liquid boundary) at high pressures agrees reasonably well with other reports [4.129-4.131]. The γ - ϵ -liquid triple point is located at $2200 \pm 200^\circ\text{C}$ and 50 ± 10 GPa [4.127].

Comparison of the two phase diagrams reveals the following differences: (1) The dissolution of hydrogen causes a drastic reduction of the melting point below $p_H \leq 3$ GPa. (2) It makes the dominant high-pressure phase dhcp instead of hcp. (3) ϵ' -FeH _{x} is ferromagnetic in contrast to ϵ -Fe which is non-magnetic. The effect of magnetism on the atomic volume was mentioned in the foregoing section. Regarding the H concentration, a large positive heat of solution limits the solubility in the α phase rather low ($x \approx 0.06$ at 2 GPa,

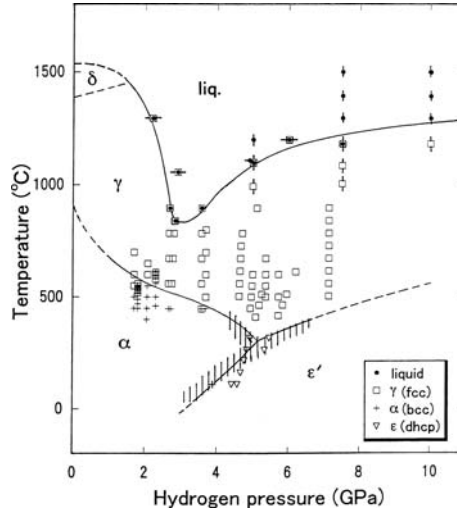


Fig. 4.34. The p_H - T diagram of the Fe-H system [4.123]. The dashed area represents the region of data points of [4.124]. At high temperatures, data points with horizontal bars are those from [4.125], those with vertical bars from [4.126]

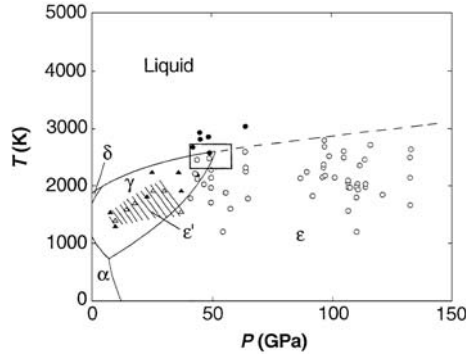


Fig. 4.35. The p - T diagram of Fe [4.127]

400 ~ 550 C), whereas the ϵ' -FeH $_x$ is nearly stoichiometric ($x = 1.05 \pm 0.03$ at 4 ~ 9 GPa, 350°C). The x - T diagram of the γ -phase region is shown in Fig. 4.36 [4.132]. The fact that the dissolution process changes from exothermic to endothermic between $p_H = 4$ and 5 GPa is a feature characteristic of supercritical anomaly. Concentration fluctuations large in amplitude and extremely sluggish in time, another feature of supercritical anomaly, were also observed in XRD measurements in this p_H , T range. The critical point is thus roughly located at $p_c = 4.5$ GPa and T_c near the ϵ - γ boundary. The situation is very similar to the Co-H system as described below. In the ϵ' -phase, H atoms are distributed randomly over O-sites [4.48].

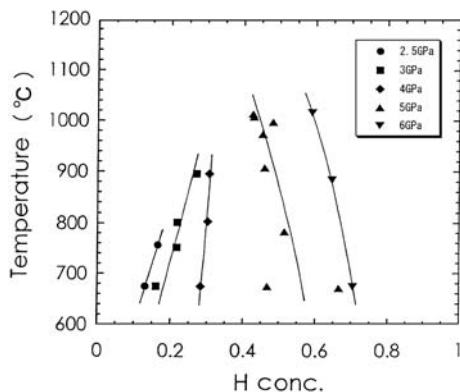


Fig. 4.36. The composition-temperature (x - T) diagram of γ -Fe [4.132]

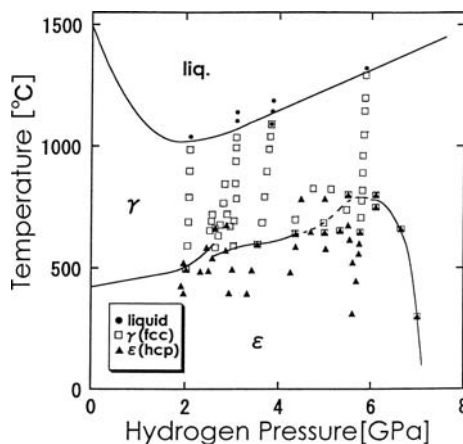


Fig. 4.37. The p_H - T diagram of the Co-H system [4.133]

In Co metal, as in Mn, the temperature of the allotropic transition $\epsilon(\text{hcp})$ - $\gamma(\text{fcc})$ simply increases with pressure, at a rate of 40 K/GPa [4.112]. In the p_H - T diagram of the Co-H system (Fig. 4.37 [4.133]), the ϵ - γ boundary is also shifted upward with pressure, but goes through a small hump indicated by scattered data points and drops almost vertically at $p_H \sim 7$ GPa. The H concentration measured at 350°C increased with pressure to $x = 0.55$ in the ϵ -phase, and jumped up to $x \approx 1$ on crossing the ϵ - γ boundary at 7 GPa. Thus it was suggested that the anomalous drop of the phase boundary should be the consequence of a rapid increase of the solubility in the γ -phase relative to the ϵ -phase [4.134]. In their subsequent experiment using samples alloyed with 0.2 at% Fe, *Antonov et al.* [4.59] succeeded in suppressing the ϵ - γ transition and observed the metastable γ -phase in the ϵ -phase field. There, the H concentration in the γ -phase at 325°C increased steeply but continuously

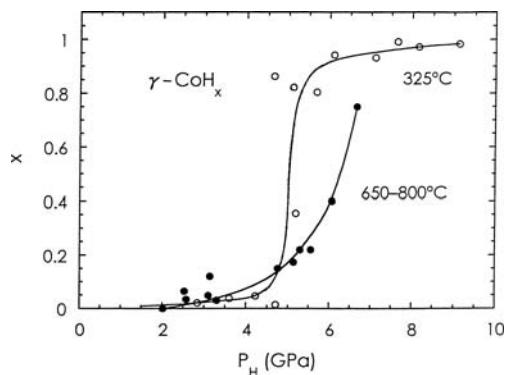


Fig. 4.38. The p_H – x diagram of fcc CoH_x [4.59, 4.133]. The data at 325°C were taken by suppressing the ϵ – γ transition by alloying with 0.2 at % Fe [4.59]

in a narrow pressure interval between 4.5 and 5.5 GPa (Fig. 4.38). A hypothetical critical point of the γ -phase was thus located at 5.5 ~ 6.0 GPa and $\leq 300^\circ\text{C}$. Later experiments showed that, at higher temperatures, the increase of the solubility with pressure became more gradual (Fig. 4.38) and a transition from endothermic to exothermic process, a characteristic feature of the supercritical anomaly, took place between 5 and 7 GPa [4.133].

The neutron diffraction on ϵ - CoD_x showed that D atoms occupy O sites; every third base layer at $0.26 < x < 0.38$, and every second layer at $x \geq 0.38$ [4.135].

For the Ni–H system, a nearly stoichiometric fcc hydride of NaCl type was synthesized both by electrochemical and high-pressure techniques [4.89, 4.136]. The p_H – T phase relation determined by resistometry in a series of isothermal decompression runs is shown in Fig. 4.39(a) [4.88, 4.138]. The

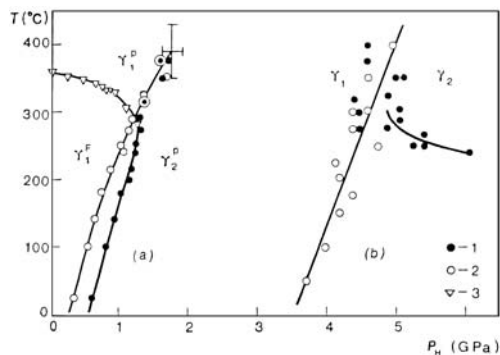


Fig. 4.39. The p_H – T diagram of the Ni–H system (a; [4.88, 4.137, 4.138]) and the Rh–H system (b; [4.140])

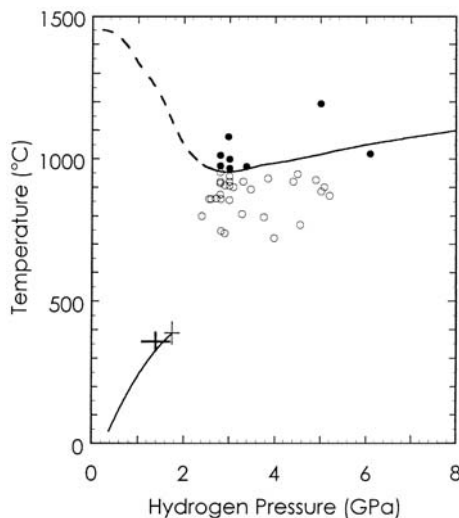


Fig. 4.40. The $p_{\text{H}}-T$ diagram of the Ni-H system over wider temperature ranges [2.72, 4.139]

critical point was located at $p_{\text{c}} \sim 1.75$ GPa and $T_{\text{c}} \sim 390^{\circ}\text{C}$ by extrapolation from a series of data on Ni-Fe-H alloys [4.137].

The $p_{\text{H}}-T$ and $x-T$ diagrams of the Ni-H system subsequently obtained by our in situ XRD is shown in Fig. 4.40 and 4.41 [2.72, 4.139]. The reduction of the melting point is similar to other cases and amounts to $\sim 600^{\circ}\text{C}$. The H concentration was estimated from the observed volume expansion assuming $v_{\text{H}} = 2.2 \text{ \AA}^3$ for the H-induced volume⁵. The critical point here is located at a slightly lower position; $p_{\text{c}} \approx 1.4$ GPa and $T_{\text{c}} \leq 360^{\circ}\text{C}$. The small discrepancy may well be attributed to possible uncertainties in the resistometric method, especially near the critical point: A large concentration change in a narrow temperature region above the critical point (in Run C2 in Fig. 4.41, for example) should be accompanied by resistance anomalies, hardly discernible from those due to phase boundaries.

The $p_{\text{H}}-T$ diagram of the Rh-H system constructed by resistometry is similar; only shifted to higher pressures (Fig. 4.39(b), [4.140]). The critical point has not been determined yet. The structure is always fcc and a nearly stoichiometric hydride is formed at room temperature [4.141].

⁵ In the original paper of *Shizuku et al.* [4.139], the maximum H concentration was estimated at $x \approx 0.8$ by adopting the H-induced volume of $v_{\text{H}} = 2.8 \text{ \AA}^3$ [4.88]. However, as shown by *Antonov et al.* later [4.62], there is reason to believe that $v_{\text{H}} = 2.2 \text{ \AA}^3$ should be the correct value (see Sect. 4.2), and the diagram has been revised accordingly. The revised diagram is more consistent with the observation that at room temperature only the nearly stoichiometric hydride ($x \approx 1$) could be formed.

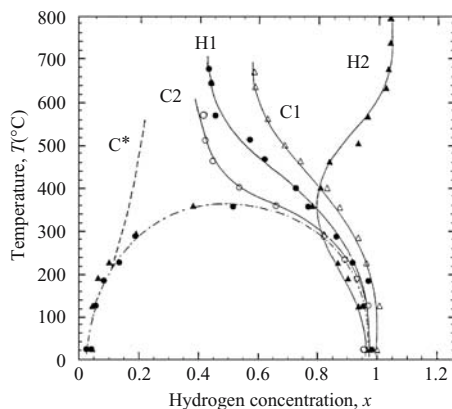


Fig. 4.41. The composition-temperature ($x - T$) diagram of the Ni-H system. Cooling runs C1($p_H = 1.5 \sim 2.4$ GPa), C2(1.1 \sim 2.1 GPa), heating runs H1(1.9 \sim 2.2 GPa), H2(4.3 \sim 5.4 GPa). C* is an isopiestic line expected for $p_H \sim 1$ GPa [2.72, 4.139]

The Pd-H system has been studied for more than a century, and its phase relation was elucidated in [4.142], for example. As shown in Fig. 2.1 and 2.5, the spinodal decomposition takes place, with a critical point located at $p_c = 19.7 \pm 0.2$ GPa, $T_c = 292 \pm 2^\circ\text{C}$, and $x_c = 0.250 \pm 0.005$. The p_H - T diagram looks similar to that of the Ni-H system, only shifted to the lower p_H , T region.

Among the remaining Group VIII metals, only Ru absorbs a measurable amount of hydrogen; $x \approx 0.03$ at $p_H = 9$ GPa and 250°C . The electrical resistance isotherms measured at 250°C are shown in Fig. 4.42 [4.48]. The effect of H dissolution was isolated from direct pressure effects by reference measurements in an inert medium. A slight increase of the resistance can be seen in Os, but practically no changes in Pt and Ir.

Noble-Metal – Hydrogen Systems

Recently, the formation of a substoichiometric hydride of composition $\text{CuH}_{\sim 0.4}$ was found at room temperature at $p_H \geq 14.4$ GPa [4.168].

4.4.2 General Features of Phase Relations

There are two general features of p_H - T diagrams to be noted; the reduction of the melting point T_m with increasing hydrogen pressure and the appearance of hydride phases having close-packed structures. As the increase of the hydrogen pressure is accompanied simultaneously by the increase of the mechanical pressure and hydrogen concentration, the assessment of the relative importance of these two factors is necessary. For this purpose, the p - T phase

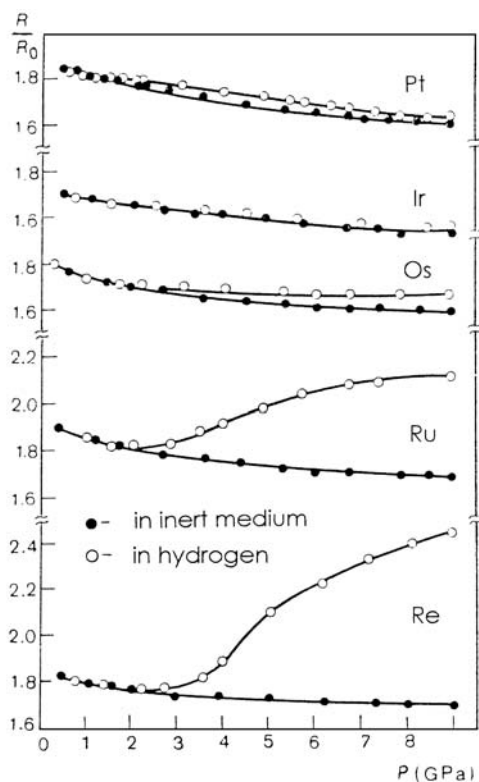


Fig. 4.42. The pressure dependence of the electrical resistance of Pt, Ir, Os, Ru and Re at 250° C measured in hydrogen (○) and in an inert atmosphere (●) [4.48]

diagrams of Mn [4.112], Fe [4.127–4.131] and Co [4.112], metals showing allotropic phase transitions, are helpful. In all the cases (except in the α - γ transition in Fe), the transition temperature is increased with pressure, in consequence of the larger specific volume of the higher-temperature phase. (In the exceptional case of the α - γ transition in Fe, this order is reversed.) Thus the reduction of T_m at $p_H \leq 3$ GPa should be ascribed primarily to the effect of dissolution of hydrogen. The effect of mechanical pressure is manifested in the gradual increase of T_m at higher pressures where the hydrogen should have approached the limiting composition.

The appearance of the close-packed structures is also the effect of hydrogen dissolution. The solubility of hydrogen is generally much higher in these close-packed phases than in low-pressure phases. The sequence of phase transitions in the close-packed phases with temperature, hcp \rightarrow dhcp \rightarrow fcc is in fact quite general. The whole sequence is realized in Mn-H and Fe metal at high pressures, and the transition dhcp \rightarrow fcc in many more cases including La, Ce, Am metals [4.143] and Fe-H (Fig. 4.34) at high pressures. This

indicates that after the limiting hydride composition has been approached, the relative stability of hydride structures simply follows the known trend in pure metallic structures.

The x – T diagram of the Ni–H system deserves special attention. Here, the dissolution process of hydrogen changes from endothermic ($\Delta H_s > 0$) at ≤ 2 GPa to exothermic ($\Delta H_s < 0$) at ≥ 5 GPa, passing through the two-phase region existing between these hydrogen pressures. This form, which is very different from the familiar case of the Pd–H system (Fig. 2.5) where the dissolution process is always exothermic on both sides of the two-phase region, was in fact predicted to occur in some metals having a positive heat of solution [4.27].

One important consequence of this form of the phase diagram is that the supercritical region becomes much wider than in the case of, say, the Pd–H system. Our experience with the Ni–H system indeed showed this; in situ XRD measurements were severely hampered by the sluggishness and large fluctuations in approaching the equilibrium concentration, over the wide supercritical region. There is evidence that γ -FeH $_x$ behaves similarly [4.123, 4.132]. The heat of solution changes from positive to negative between $p_H = 4$ and 5 GPa, accompanied by large concentration fluctuations. The actual occurrence of the two-phase region in this case was disrupted by transition to the ϵ' phase, however. The situation in γ -CoH $_x$ appears very similar. *Antonov et al.* [3.96] succeeded in suppressing the $\gamma \rightarrow \epsilon$ transition by alloying with 0.2 at% Fe, and inferred that the (hypothetical) critical point of γ -CoH $_x$ is located at $T_c \leq 325^\circ\text{C}$, $p_c \approx 4$ –6 GPa. In the pure Co–H system, this critical point is unobservable because it lies in the ϵ -phase field. As described in the foregoing section (Sect. 4.2), *Antonov et al.* [4.62] also demonstrated that a large concentration fluctuation persisted in the quenched samples of Ni $_{0.8}$ Fe $_{0.2}$ hydride and inferred that the well-known anomaly in the H-induced volume in fcc metals should be the consequence of inhomogeneous hydrogen distribution.

In closing this section, we try to make some heuristic predictions regarding the general forms of the phase diagram of M–H systems over the entire composition range, including elemental hydrogen. Here, just as in the ordinary phase diagrams of binary alloys, the composition should be written in terms of the atomic ratio of hydrogen, $x' = [\text{H}]/([\text{H}] + [\text{M}])$. The external pressure is supposed to be in the range 5–10 GPa. This raises the melting point of the transition metals by 200–300 K [4.112], and the melting point of molecular hydrogen to ~ 300 K.

A tentative phase diagram for the fcc (Ni, Pd, Rh, etc.) metal–H systems is shown in Fig. 4.43. It is assumed that the highest concentration in the solid-solution phase, designated as α (and α'), does not exceed appreciably $x' = 0.5$, and no higher hydrides are formed. Appropriate values are used for the rate of melting-point reduction and the distribution coefficient. On the right end of the diagram, the solubility of metallic elements in molecular hydrogen

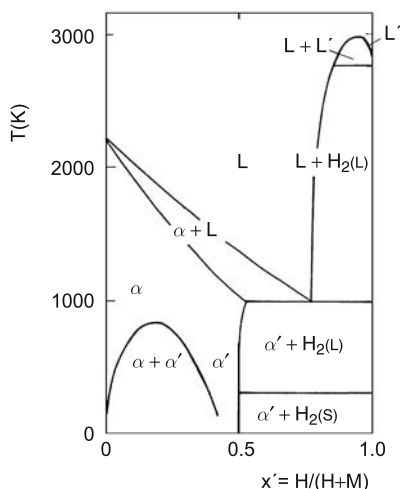


Fig. 4.43. Tentative phase diagram for the fcc-metal-H system ($p \sim 5$ GPa)

is believed to be negligibly small. The molecular and metallic phases will be nearly completely immiscible, even in the liquid state. It is only at sufficiently high temperatures, where the number of thermally ionized molecules exceeds some critical value to induce the molecular-to-metallic transition, that finite amounts of metallic elements become soluble and the liquid immiscibility disappears.

In bcc and hcp metals, which form dihydrides of fluorite structure, a phase diagram would look like Fig. 4.44a or 4.44b, depending upon the relative magnitude of the melting-point reduction of the solid-solution phase and the melting point of the dihydride. In the solid-solution phase at lower temperatures (the shaded areas), several ordered structures are expected to form. In cases where trihydrides are formed, the phase diagram is expected to assume forms as in Fig. 4.45. Here, the melting point of a (semiconducting) trihydride is assumed to be higher than that of a (metallic) dihydride. It may be mentioned in this regard that the volume expansion in forming dihydrides of CaF_2 structure from bcc or hcp metals amounts to about 2.0 \AA^3 per H atom, and becomes even smaller than this value when trihydrides are formed. Therefore, it is very probable that lower hydrides of these metals decompose under high pressures into a dilute solid solution of hydrogen in these metals and dihydrides or trihydrides.

In metals with different allotropic phases, the phase diagrams are obviously expected to become more complex, as actually observed in Ti.

It can be seen that the lowering of the melting point and the immiscibility of metallic and molecular phases make the hydrogen-rich side of phase diagrams very nearly identical in many M-H systems. This opens the possibility that metallic hydrogen in the liquid state can be realized more easily under

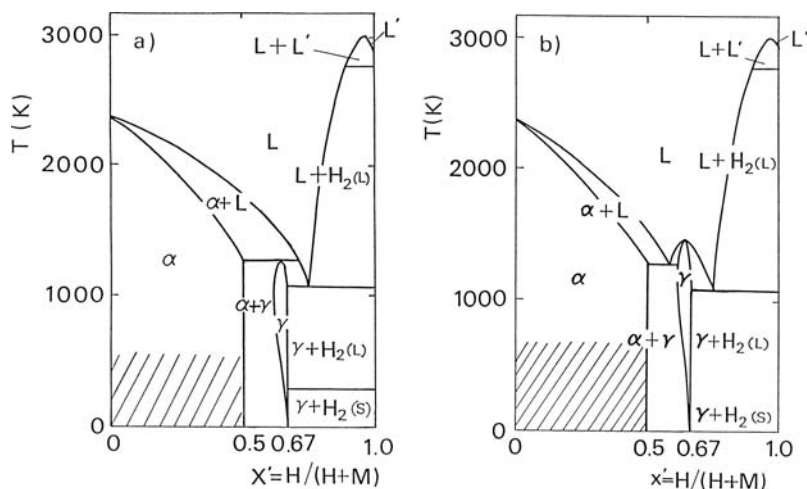


Fig. 4.44. a and b. Tentative phase diagrams for bcc- and hcp-metal-H systems with a CaF_2 -type (fcc) dihydride phase ($p \sim 5$ GPa)

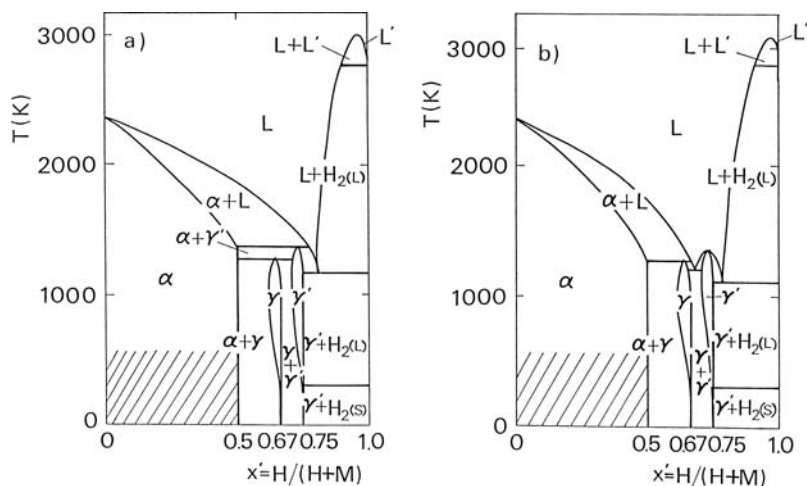


Fig. 4.45. a and b. Tentative phase diagrams for bcc- and hcp-metal-H systems with dihydride and trihydride phases ($p \sim 5$ GPa)

moderate conditions by alloying with some transition metals than the ordinary method of compressing to extremely high pressures. At sufficiently high temperatures, there is always a continuous path to approach the pure metallic-hydrogen state. Although the tenacity of H_2 molecules is expected to sustain the immiscibility to rather high pressures, the addition of transition metals may possibly incite molecular dissociation. Also interesting are the properties of liquid hydrogen alloys to be realized at reasonably low

temperatures, at a dip of the liquid-phase field on the invariant line, and at pressures of the order of only several GPa. The constitution and properties of hydrogen alloys with hydrogen as a major constituent are the area of research just emerging.

One final comment regarding the implication of the phase diagrams presented above. Contrary to what is generally accepted, these phase diagrams are not equilibrium diagrams. As discussed in detail in Sect. 5.4, thermodynamically the most stable structures of metal hydrides are defect structures containing a large amount of M-atom vacancies. These defect structures are, however, usually not realized because the introduction of vacancies by diffusion requires long-time holding at high temperatures without loss of hydrogen, which is a condition very difficult to realize in ordinary hydrogenation procedures. It is for this reason that the phase diagrams presented above are useful in practice, but it is important to recognize that most (all) the phase diagrams of M–H systems reported heretofore are in fact metastable ones.

Appendix 4A. Iron–Water Reaction Under High p , T Conditions, and Its Implication for the Evolution of the Earth

A direct reaction with hydrogen is not the only way for hydrogenating metals. Some metals more electropositive (having smaller electronegativity) than hydrogen react with water to form oxides, and the hydrogen that evolves may form hydrides when they are stable. For rare-earth metals, Ti and Zr, for example, this hydride-forming reaction proceeds under ordinary conditions. For Fe, the condition for its occurrence is marginal and requires high p , T s.

The first observation of such a reaction was made with Fe and $\text{Al}(\text{OH})_3$ at 6.4 GPa and 900°C [4.144]. The reaction product, after recovery, consisted of Al_2O_3 , FeO and Fe, as a consequence of a series of reactions; $2\text{Al}(\text{OH})_3 \rightarrow \text{Al}_2\text{O}_3 + 3\text{H}_2\text{O}$, $\text{Fe} + \text{H}_2\text{O} \rightarrow \text{FeO} + \text{H}_2$, $\text{Fe} + \frac{1}{2}x\text{H}_2 \rightarrow \text{FeH}_x$ at high p , T s, and $\text{FeH}_x \rightarrow \text{Fe} + \frac{1}{2}x\text{H}_2$ after recovery to the ambient condition. A subsequent experiment using Fe powder and complex hydroxides, talc ($\text{Mg}_3\text{SiO}_{10}(\text{OH})_2$) and brucite ($\text{Mg}(\text{OH})_2$), revealed interesting features [4.145]. Figure 4A.1 shows a picture of the reaction products after a heat treatment at 5.3 GPa, 1200°C for 20 min. Original Fe particles of irregular shape, $\leq 30\text{ }\mu\text{m}$ in size, agglomerated into lustrous balls of $\sim 300\text{ }\mu\text{m}$ in diameter, embedded in a silicate (Mg, Fe) SiO_3 matrix. This is a clear indication that the Fe– H_2O reaction had taken place. The resulting oxide was dissolved in a molten magnesium silicate to form the mixed silicate, and the resulting hydride caused the melting-point reduction of Fe of at least 500°C (from 1700°C at 5.3 GPa in Fe to less than 1200°C). Subsequently, the formation of FeH_x was confirmed directly by in situ XRD under high p , T s, using synchrotron-radiation X-rays [4.146].

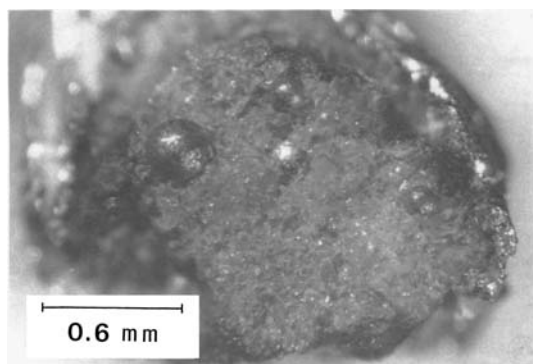


Fig. 4A.1. Photomicrograph of a recovered specimen after the reaction at 5.3 GPa, 1200°C for 20 min. The starting material consisted of 5Fe + Talc + 2Brucite, and the run product Fe (ball) + silicates (olivine + pyroxene) [4.145]

The incentive of these high p , T experiments on the Fe–silicate reaction was, in fact, to simulate the evolution process of the Earth in a laboratory – specifically the formation process of the core, in connection to its chemical composition. Lacking direct methods for determination, the core composition has to be inferred in such a way as to be consistent with various observational facts – the constraints. Among them, two major ones are the natural abundance of the elements learned from the frequency and composition of meteorites which are the remainders of the planetary evolution of the solar system, and the density of the core determined from seismological data. The purpose of the simulation experiments was to impose a third constraint based on materials reactions during the thermal history of evolution.

According to our current understanding, the Earth started from the aggregates of small bodies called planetesimals, composed mainly of mixed silicates with dispersed Fe powder (formed in the high-temperature (HT) region of the solar system), and a small fraction containing hydrated and hydroxide minerals (formed in the low-temperature (LT) region). From comparison with the abundance of the elements in the present mantle, the ratio of HT to LT components in the primordial material was estimated to be 9:1 [4.147, 4.148]. Table 4A.1 lists the composition of the primordial material constructed on these bases [4.149]. The fraction of metallic elements (Fe + Ni) in this hypothetical primordial material agrees with the mass fraction of the core estimated from seismological data (33%, according to the Earth model called PREM [4.150]). Detailed analysis of seismological data revealed, however, that the density of the core is nearly 10% lower than Fe or Fe–Ni alloy under corresponding p , T conditions (Fig. 4A.2) [4.81, 4.150], the fact which suggested the presence of some light elements dissolved in the core. Note that the total H₂O content (including hydroxides) amounts to ~2%.

Table 4A.1. Composition of high-temperature (HT) and low-temperature (LT) components of the primordial material. A mixture of HT:LT = 9:1 has been assumed [4.149]

	High-temperature Component*	Low-temperature Component**
Fe	34.5	0
Ni	2.0	0
SiO ₂	34.5	21.74
MgO	24.9	15.24
Al ₂ O ₃	2.4	1.59
CaO	1.7	1.18
FeO	0	22.86
NiO	0	1.19
S	0	5.65
C	0	2.99
H ₂ O	0	19.19

* Derived from the average of 11 meteorites belonging to the type called E-chondrite. The amount of SiO₂ has been reduced to fit the solar-system ratio of Mg/Si, and all the volatiles have been removed.

** Composition of a meteorite Orgueil, belonging to the type called C1 chondrite.

These observations brought us to the recognition that the whole problem had to be reexamined, focusing attention on possible chemical reactions that Fe particles should have undergone during the process of core formation.

The presently accepted scenario of the Earth’s evolution is shown in Fig. 4A.3 [4.149]. As the primordial Earth grew in size by continual accretion of planetesimals, the heat was accumulated by the concomitant liberation of

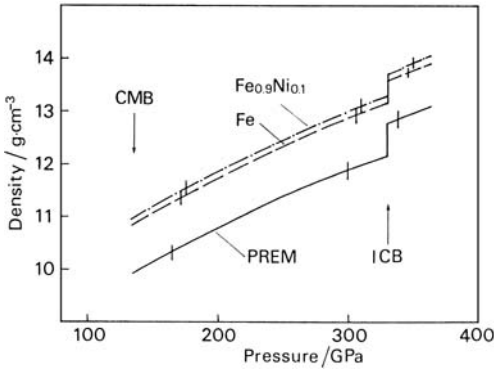


Fig. 4A.2. Density profile of the Earth’s core. The density deduced from observations (PREM [4.150]) is compared with those of Fe and Fe_{0.9}Ni_{0.1} alloy [4.150]. CMB = core-mantle boundary, and ICB = inner-core boundary [4.151]

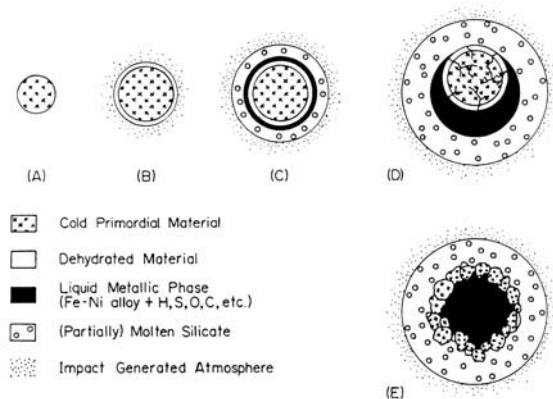


Fig. 4A.3. Schematic picture of the scenario of Earth' evolution. (A) The proto-Earth starts as a cold body of primordial material. (B) As it grows in size, the velocity of infalling planetesimals is increased, and the primordial material is dehydrated by impact heating to form the water vapor atmosphere. (C) Due to the greenhouse effect, the surface temperature is raised, the silicate becomes partially molten, and a layer of Fe–Ni alloy builds up. At a certain instant, (D) spontaneous asymmetry occurs, and after overturn, the proto-core is formed (E). After this, the proto-core grows continuously until the accretion comes to the end. The overall temperature is gradually lowered and the water atmosphere becomes condensed on the surface to form the proto-sea [4.149]

the gravitational energy (impact heating), which in time led to overall melting of the silicates called magma ocean. A partial decomposition of hydroxide minerals should have formed a water vapor atmosphere and helped confining the heat by the greenhouse effect. A careful analysis of the process showed that nearly 100% of hydrogen in the primordial material was retained in solution in molten silicates in the form of H_2O , leaving only a small fraction in the atmosphere [4.152,4.153]. The core formation proceeded in the meantime.

The elementary process of Earth's core formation is the separation of Fe particles out of a fine mixture with silicates, and concomitant partitioning of the elements in the primordial material into metallic and silicate phases. Sulfur and carbon, for their large affinity to metallic phase and their depletion in the present mantle compared with the primordial material, were unanimously thought to have entered the core [4.154]. Then oxygen was added to the list because its solubility in Fe was found to increase at very high p , T s, and its dissolution to a limited extent was considered probable in the deep interior of the magma ocean [4.155, 4.156]. Finally, the significance of the Fe– H_2O reaction in supplying H to the core came to be realized [4.157].

Let us examine what happened to Fe particles during the process of core–mantle separation. In contact with molten silicates containing H_2O at high p , T s, they should have reacted with H_2O to form FeH_x . Molten FeH_x particles

sunk towards the bottom progressively faster as they grew in size by agglomeration. As the pressure is estimated to be rather high in most part of the magma ocean (≥ 2 GPa at ≥ 50 km deep from the surface in the final stage of accretion), the H concentration in the FeH_x droplets is also expected to be rather high.

More quantitative discussions can be made by looking into the materials budget during the evolution process [4.149]. According to the mass-flow diagram shown in Fig. 4A.4, the role of $\text{Fe-H}_2\text{O}$ reaction is twofold; while H gets dissolved in the core, another reaction product FeO goes into the mantle. In fact, the FeO contained in the LT component of the primordial material (2.3%) amounts to only a smaller fraction of FeO in the present mantle (5.3%); a larger fraction should have come from the $\text{Fe-H}_2\text{O}$ reaction. The reaction of all the water in the LT component could produce 7.7% FeO, which should have been partitioned into the mantle (3.0%) and the core (4.7%). If we assume, in addition to this amount of O, all the H produced by the reaction entered the core, the overall core composition becomes $\text{FeH}_{0.41}\text{C}_{0.05}\text{O}_{0.13}\text{S}_{0.03}$.

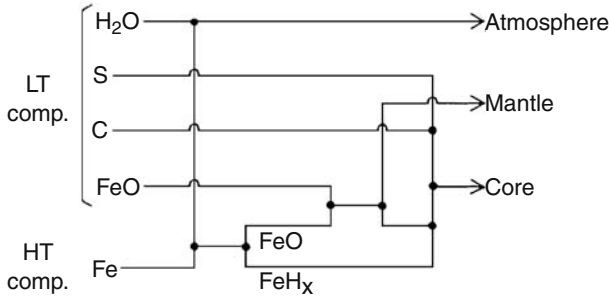


Fig. 4A.4. Mass-flow diagram of the evolutionary process of the Earth. For the sake of clarity, SiO_2 and other non-volatile oxides, all of which go to the mantle, have been omitted from the figure [4.149]

The density change due to dissolution of these solute elements can be estimated by using the expression [4.151]

$$-\Delta\rho/\rho_0 = \frac{\sum x_i \left(\frac{V_i}{V_0} - \frac{M_i}{M_0} \right)}{1 + \sum x_i \frac{V_i}{V_0}}, \quad (4A.1)$$

where x_i is a concentration of the i -th solute (in atomic ratio), V_i/V_0 and M_i/M_0 are the ratios of the volume and the atomic weight of the solute and Fe (or Fe–Ni alloy), respectively, and $\rho_0 = M_0/V_0$. Using available EOS for Fe [4.81], O [4.156, 4.158, 4.159], S [4.158] and H [4.160], and approximating the compression behavior of C by that of O, we obtain $-\Delta\rho/\rho_0 = 0.113$

at the core–mantle boundary (135 GPa). This agrees reasonably well with the observed density deficit (9.6% in comparison to $\text{Fe}_{0.9}\text{Ni}_{0.1}$), but slightly too large. To bring them into agreement, we have to assume that nearly 60% of H was actually dissolved in the core. The core composition becomes $\text{FeH}_{0.25}\text{C}_{0.05}\text{O}_{0.13}\text{S}_{0.03}$, and hydrogen accounts for 30% of the density deficit.

This is the story of the Fe– H_2O reaction that should have occurred 4.5 billion years ago in the proto-Earth. At the time when this proposal was made [4.157], the general consensus of Earth scientists was that most H contained in the primordial material should have been lost in the evolution process because it is too volatile and too light to remain trapped in the Earth’s gravitational field. But, as explained above, subsequent studies of materials properties pointed otherwise. Hydrogen supplied to the Earth in the form of hydrous minerals could be retained as such to rather high temperatures [4.152, 4.153], and even after decomposition ($\sim 700^\circ\text{C}$), the resulting H_2O could remain in solution in molten silicates up to very high temperatures. Thus practically all the H was preserved in the proto-Earth in the form of H_2O , and after the Fe– H_2O reaction 40% of which left the magma ocean in a gaseous form and eventually lost into space. The amount of H thus retained in the core is 50 times more abundant than in sea water, which is a condensate of the vapor around the proto-Earth⁶.

This scenario has since been actively pursued and substantiated by several earth scientists, by a number of more detailed experiments, including, for example, the determination of the p , T dependence of the Fe– H_2O reaction [4.162], the solubility of H in molten Fe [4.162], the surface tension of Fe blobs in molten silicates [4.163], and is now widely accepted. Any reasoning over the planetary ages could only be meaningful when it is firmly based on the properties of relevant materials – the interplay between Fe and silicates in the case of the Earth. In outer giant planets, including Jupiter, Saturn, Uranus and Neptune, which consist mainly of hydrogen, the interior is believed to be metallic with some rocky minerals dissolved [4.164]. Thus, for the constitution of the outer giant planets, properties of H-based alloys at high p , T s play the key role.

Hydrogen is a unique entity not only for its physical and chemical properties, but also for its position in the Planets, and more specifically, in our Earth. Here, after describing macroscopic properties of the M–H system in detail, I have tried to turn the eyes of the readers to the outside world, hoping to incite them to the exploration of its possible implications in other fields of science.

⁶ These estimates depend on the reliability of the compression behavior of solute atoms. If we adopt for the atomic volume of oxygen the value deduced from V–O alloys [4.161] instead of EOS of elementary oxygen [4.158, 4.159], we have to assume 80% retention of hydrogen to reproduce the density deficit. The core composition becomes $\text{FeH}_{0.33}\text{C}_{0.05}\text{O}_{0.13}\text{S}_{0.03}$, the hydrogen in the core accounts for 40% of the density deficit, and amounts to 70 times that in the sea water.

5 Atomistic States of Hydrogen in Metals

The atomistic state of interstitial hydrogen in metals is characterized by the location, the wave function, and the energy of vibrational motion. Several different techniques are utilized for its investigation, for example, X-ray diffraction and scattering, neutron diffraction and scattering, and ion channeling.

The ion channeling technique makes use of the channeling motion of ions in a metal lattice and their reaction with hydrogen nuclei, viz., $H(^{11}\text{B}, \alpha)\alpha\alpha$ or $D(^3\text{He}, p)\alpha$. In relatively simple structures, the location of hydrogen nuclei can be determined by measuring the reaction yields for several different directions of the incident ion beam.

X-rays are scattered by the electrons in a system. Therefore, hydrogen atoms are hardly visible to X-rays; only metal atoms are. Thus, X-ray diffraction and scattering provide structural information on the metal lattice, i.e., the structural changes and/or lattice distortion caused by the hydrogen atoms.

Neutrons are scattered by nuclei, rather strongly by hydrogen isotopes among others. The diffraction of coherently scattered neutrons allows one to determine the lattice location of hydrogen even in complex structures and, furthermore, to delineate the density distribution (i.e., the wave function) of hydrogen nuclei in the metal lattice.

Here, caution must be exercised to discriminate between the wave function of vibrational states and the nuclear wave function itself. Each nuclear reaction or scattering event occurs only when an incoming particle comes within the range of internuclear interaction with a hydrogen nucleus (i.e., the range of nuclear wave functions), typically $\sim 10^{-3}$ Å. What is measured by channeling or neutron diffraction experiments is the sum of a great number of such events that have taken place in a specimen, which, in consequence, portrays the wave function of vibrational states.

The vibrational energy levels, on the other hand, can be determined from the inelastic scattering of neutrons, namely, by measuring the energy gain or loss of neutrons as they pass through the sample and exchange energies with hydrogen nuclei. Jump processes of hydrogen nuclei can also be investigated by quasi-elastic neutron scattering, i.e., scattering with small energy transfers.

Thus, the atomistic properties of interstitial hydrogen can only be described in terms of quantum mechanics. Important is the fact that an H atom, while being much heavier than an electron, is much lighter than any M atom of interest here. Accordingly, electrons can respond quickly enough to any motion of H and M atoms, providing in effect the interaction potential between these atoms, and H atoms to any motion of M atoms. Therefore, H atoms can be considered to move in the instantaneous potential field of interaction with the surrounding M atoms.

In this chapter, we present a review of the experimental data obtained so far on the atomistic properties and, subsequently, try to construct a consistent quantum-mechanical picture of interstitial hydrogen based on these observations.

5.1 Site Location by the Channeling Method

The phenomenon of channeling of fast ions in a crystalline lattice, discovered in the early sixties, has proved to be an extremely useful tool in a wide range of problems in materials science. Various aspects of the channeling phenomenon have been described in several review articles and books (e.g., [5.1–5.4]), and its application to site-location studies of hydrogen in metals in [5.5].

As this phenomenon may not be so familiar to the readers as X-ray or neutron diffraction, we present here a brief description of its physics, which we believe is necessary for understanding and evaluating the experimental results for the determination of interstitial sites of hydrogen atoms.

When a beam of ions accelerated to energies of the order of MeV is injected into a crystal, the ions are scattered repeatedly by lattice atoms in the near-surface region and, eventually, either stopped in the lattice or backscattered out of the lattice. The fraction of back-scattered ions is greatly reduced and the average penetration depth is greatly increased when the ion beam enters the lattice at glancing angles ($< 1^\circ$) with the low-index crystal axes or planes. This phenomenon, called ion channeling, occurs as the ions moving through channels in a lattice are steered by focusing collisions with the surrounding lattice atoms. Intuitively, the potential field acting on a fast-moving ion should have a minimum at the channel center, and, by the action of this potential field, the originally uniform distribution of the incident ions gradually becomes peaked at the center. The situation is similar to the passage of light through an optical fiber, in which graded indices of reflection act to confine the light by total reflection.

The potential as seen by the fast-moving ions can be expressed to a good approximation by a “string potential”, which is an average of the potentials of interaction with the lattice atoms (e.g., of the Thomas–Fermi type) along the channel [5.6, 5.7]. Then the flux distribution in the channel can be calculated either by assuming a statistical equilibrium or by following the trajectories of many ions in the channel by simulation.

In the application of a channeling method for the site location of interstitial hydrogen atoms, signals emitted as incident ions hit the hydrogen in channels are registered as a function of the tilt angle. For the site location of protons, we make use of the $\text{H}(^{11}\text{B}, \alpha)\alpha\alpha$ reaction, which occurs at a resonance energy of 1.79 MeV, and detect α particles of energies 1–4 MeV. For deuterons, we utilize the $\text{D}(^3\text{He p})\alpha$ reaction, which occurs at a resonance energy of 0.645 MeV, and detect α particles of 2–5 MeV and/or protons of 12–14 MeV. The reaction yield measured as a function of the tilt angle for a number of different channel orientations allows an unambiguous determination of hydrogen sites.

Naturally, channeling experiments can be done only on single crystals, and those of very high quality, without a mosaic angular spreading of $> 0.01^\circ$ or any appreciable internal stress to avoid dechanneling of the incident ion beams. As the beam energy is usually chosen to be a little higher than the resonance energy of the nuclear reaction [~ 2 MeV for the $\text{H}(^{11}\text{B}, \alpha)\alpha\alpha$ reaction and 0.7–0.8 MeV for the $\text{D}(^3\text{He p})\alpha$ reaction], the incident ions travel about 0.1–1 μm before they attain the resonance energy and react with the hydrogen atoms. In site-location experiments, detailed measurements of the angular profiles must be made for several different channel configurations, and practical limits on the hydrogen concentration, usually set by machine-time considerations, are $[\text{D}]/[\text{M}] \sim 10^{-2}$ and $[\text{H}]/[\text{M}] \sim 10^{-1}$.

For T-site and O-site occupancies in simple crystal lattices, the reaction-yield profiles obtained by scanning the tilt angle of the crystal with respect to the incident beam can be understood, at least qualitatively, from the projections of these sites, as shown in Figs. 5.1–5.3, for fcc, bcc, and hcp metals, cf. Fig. 2.14.

Typical experimental data are shown in Figs. 5.4–5.6, including D in Pd (O-site occupancy in fcc) [5.8], D in Ta (T site in bcc) [5.9], and D in $\beta\text{-VD}_{0.5}$ (O_Z site in bct) [5.10].

It can be seen that the reaction yield shows a dip at $\psi = 0$ when the D atoms are shadowed by the lattice atoms, and a peak when they are located near the center of a channel. When a part of the D atoms are located in a channel whereas the others are shadowed by the lattice atoms, a peak is superposed on a dip. The T-site and O-site occupancies can be easily distinguished by these considerations.

Similar experiments have been performed on D in V [5.11], Nb [5.5, 5.12], and Ta [5.13], and on H in V [5.14, 5.15], Nb [5.16], and Ta [5.17, 5.18], and T-site occupancies established in all these cases.

In all the experiments cited above, hydrogen was introduced from the gas phase. Other experiments were reported which could determine the location of hydrogen implanted in metals of low hydrogen solubilities. In such experiments, the implantation could not be made without producing defects such as vacancies and interstitials of the lattice atoms; accordingly, the interaction

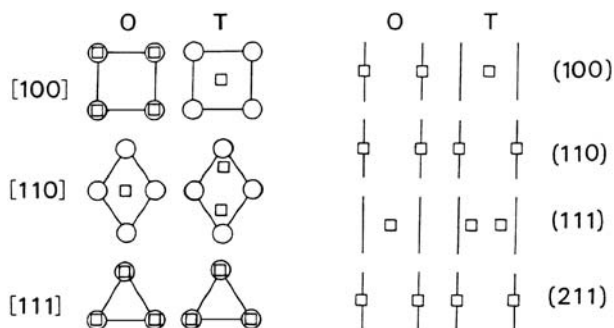


Fig. 5.1. Projections of octahedral (O) and tetrahedral (T) sites along the main crystal axes and planes of an fcc lattice

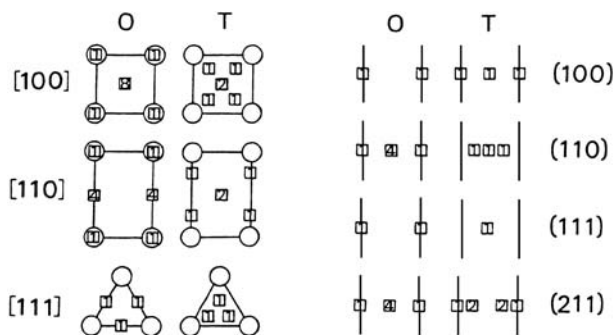


Fig. 5.2. Projections of octahedral (O) and tetrahedral (T) sites along the main crystal axes and planes of a bcc lattice. Relative weights are inscribed in the *squares*

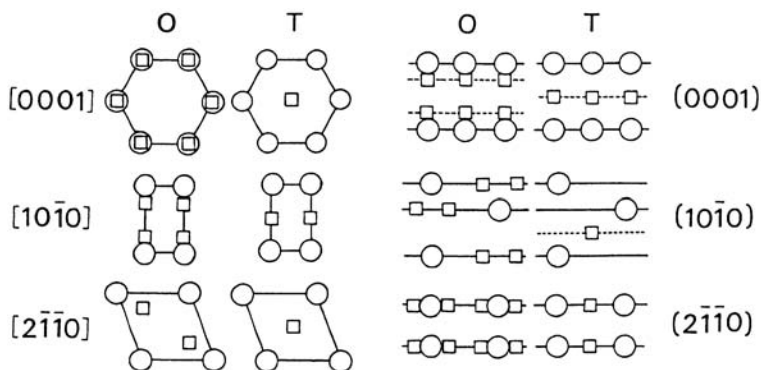


Fig. 5.3. Projections of octahedral (O) and tetrahedral (T) sites along the main crystal axes and planes of an hcp lattice

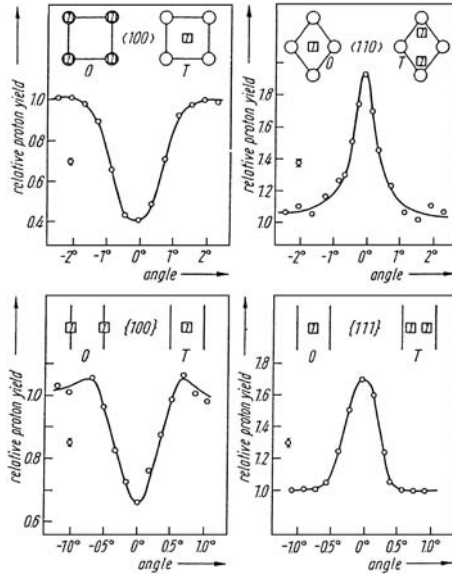


Fig. 5.4. D in Pd-yield profiles of the $D(^3\text{He}, p)\alpha$ reaction from angular scans across the axes and planes indicated in the figure ($750\text{ keV } ^3\text{He}^+$, $\text{Pd}_{0.007}$, 295 K) [5.8]

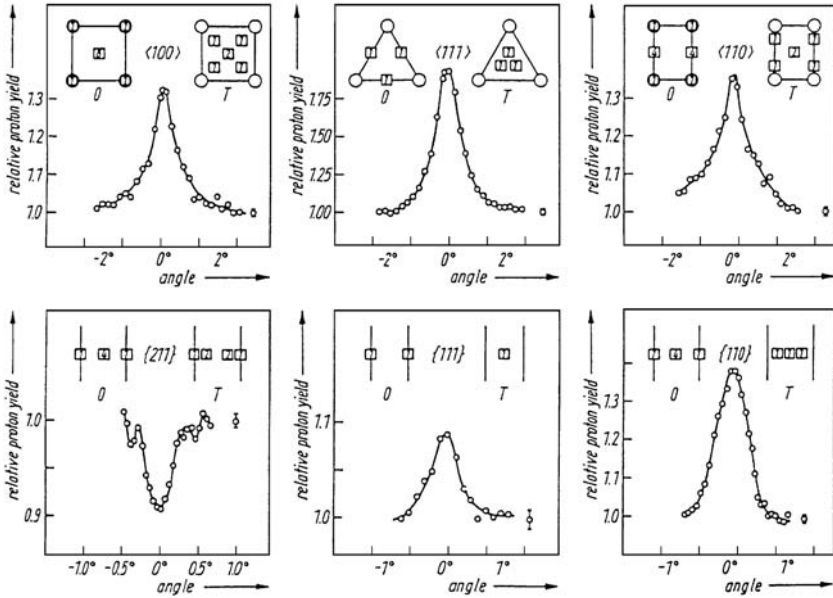


Fig. 5.5. D in Ta-yield profiles of the $D(^3\text{He}, p)\alpha$ reaction from angular scans across the axes and planes indicated in the figure ($750\text{ keV } ^3\text{He}^+$, $\text{Ta}_{0.067}$, 295 K) [5.9]

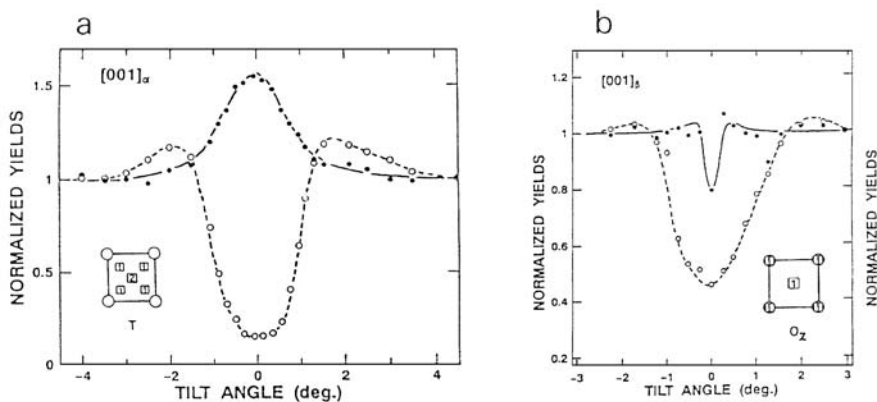


Fig. 5.6. **a** and **b.** D in α -VD_{0.5} and β -VD_{0.5}—yield profiles of the D(³He, p) α reaction for scans through the $\langle 001 \rangle$ axis, measured at 423 K (**a**) and 300 K (**b**), respectively [5.10]. The change in site occupancy from T sites in the α phase to O_z sites in the β phase can be clearly seen. \circ : V-backscattering yield and \bullet : D-yield

of implanted hydrogen with such defects was unavoidable. These problems are described in detail in Sect. 5.6.3.

It may be appropriate to mention here that in more detailed studies of lattice location, which become necessary for hydrogen atoms interacting with defects, one has to specify in which direction the crystal is tilted while measuring the axial channeling. This point is clearly illustrated in Fig. 5.7, in which the angular profiles for the $\langle 110 \rangle$ axial channeling assume very different shapes for different scanning directions [5.19]. Apparently, a “random” direction frequently used in axial channeling experiments is not a well-defined geometry. This point has to be well recognized in performing site-location experiments, and detailed simulation calculations appear to be necessary for the analysis of such experiments [5.20].

5.2 X-ray Bragg and Diffuse Scattering

A hydrogen atom entering an interstitial site in a metal lattice produces a strain field which decreases with distance as $1/r^3$, and in order that the stress-free condition on the surface be satisfied, the lattice expands itself more or less uniformly. In actual systems, the superposition of the strain fields from a large number of hydrogen atoms results in an overall lattice distortion, consisting of both uniform and non-uniform components. These components of strain can be studied by X-ray scattering.

A convenient way of describing the action of a point defect to produce lattice distortion is in terms of a set of virtual forces (Kanzaki forces) [5.21] that act on the surrounding lattice atoms to yield the same lattice distortion

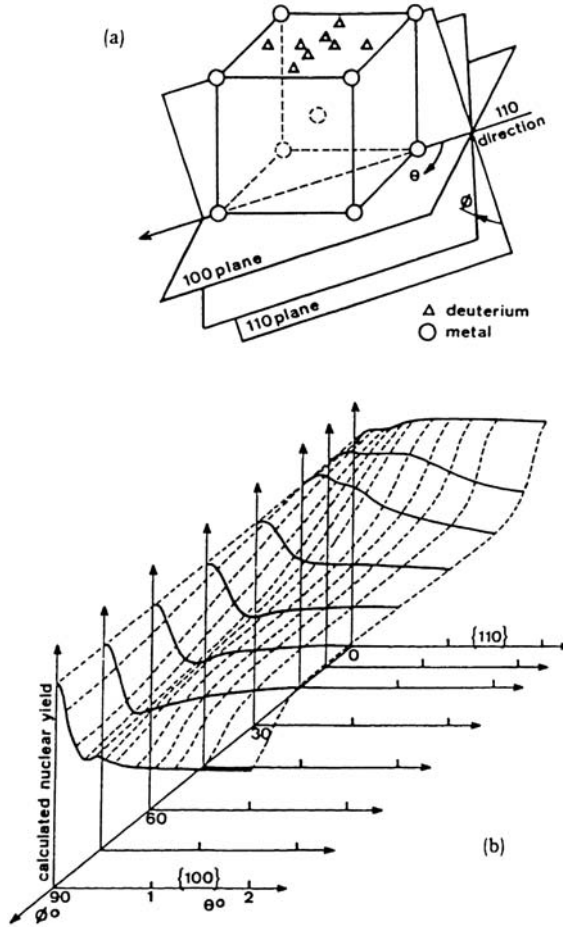


Fig. 5.7. Detailed calculation of yield profiles for D in V [5.19]. (a) Schematic view showing that channeling along the $\langle 110 \rangle$ axis can be obtained through scans (θ) along different planes. The D atom is supposed to occupy a displaced tetrahedral site (0.36 \AA towards the O site), (b) Angular scans of the nuclear-reaction yield of $D(^3\text{He}, p)\alpha$ calculated for vanadium, when the $\langle 110 \rangle$ axis is scanned along different planes defined by the angle ϕ . The curves $\phi = 0$ and $\phi = 90^\circ$ correspond to a scan along the $\langle 110 \rangle$ and $\langle 100 \rangle$ planes, respectively

as the defect (see, e.g., [5.22]). In most cases, the stress field can be written more simply in terms of a force-dipole tensor \tilde{P} , with components

$$P_{ij} = \sum_m f_i^m r_j^m, \quad (5.1)$$

defined in terms of the moments of the Kanzaki force \mathbf{f}^m acting on atom m located at \mathbf{r}^m from the defect. Alternatively, a defect can be described by a

strain tensor $\tilde{\lambda}$, having the components

$$\lambda_{ij} = \frac{1}{v_0} \sum_{k,l} S_{ijkl} P_{kl} , \quad (5.2)$$

where S_{ijkl} are the elastic compliance constants, and $1/v_0$ is equal to the total number of metal atoms in a unit volume.

These tensors reflect the symmetry of the defect site as well as of the lattice. Let us consider here hydrogen atoms only on T and O sites in cubic crystals, fcc, and bcc. In an fcc lattice, as the point symmetry of both T and O sites is cubic, the second-rank tensors \tilde{P} , and $\tilde{\lambda}$, are isotropic. Hence,

$$\tilde{P} = \begin{pmatrix} A & 0 & 0 \\ 0 & A & 0 \\ 0 & 0 & A \end{pmatrix} \quad (5.3)$$

and

$$\tilde{\lambda} = \begin{pmatrix} \lambda_0 & 0 & 0 \\ 0 & \lambda_0 & 0 \\ 0 & 0 & \lambda_0 \end{pmatrix} . \quad (5.4)$$

In a bcc lattice, the point symmetry around T and O sites is tetragonal; therefore, \tilde{P} and $\tilde{\lambda}$ tensors are axially symmetric. For a hydrogen atom on an O_X site, for example, these tensors can be written as

$$\tilde{P}_X = \begin{pmatrix} A & 0 & 0 \\ 0 & B & 0 \\ 0 & 0 & B \end{pmatrix} \quad (5.5)$$

and

$$\tilde{\lambda} = \begin{pmatrix} \lambda_1 & 0 & 0 \\ 0 & \lambda_2 & 0 \\ 0 & 0 & \lambda_2 \end{pmatrix} . \quad (5.6)$$

The components of these tensors are related to each other as

$$\lambda_1 + 2\lambda_2 = \frac{1}{v_0} \frac{A + 2B}{c_{11} + 2c_{12}} , \quad (5.7)$$

$$\lambda_1 - \lambda_2 = \frac{1}{v_0} \frac{A - B}{c_{11} - c_{12}} , \quad (5.8)$$

where c_{11} and c_{12} are the elastic stiffness constants. The expressions for O_Y and O_Z sites are obvious. The tensors for hydrogen atoms on T sites (T_X , T_Y , T_Z sites) in a bcc lattice take the same form.

Let us consider what happens when X-rays are incident on a crystal containing point defects (like hydrogen atoms). X-rays are scattered by these defects and lattice atoms displaced from their original positions, with the resultant intensity

$$I_d(\mathbf{Q}) \propto \left| \sum_d f_d(\mathbf{Q}) e^{i\mathbf{Q} \cdot \mathbf{r}^d} + \sum_m f_m(\mathbf{Q}) e^{i\mathbf{Q} \cdot (\mathbf{r}^m + \mathbf{u}^m)} \right|^2, \quad (5.9)$$

where $f_d(\mathbf{Q})$ and $f_m(\mathbf{Q})$ are the scattering amplitudes of a defect and a host metal atom, respectively, \mathbf{u}^m is the displacement of the m th host atom (originally at \mathbf{r}^m) produced by defects located at \mathbf{r}^d . For interstitial hydrogen, $f_d(\mathbf{Q})$ is negligibly small and the whole effect arises from deviations of the host atoms from the regular sites.

A uniform component of the strain causes shifts of Bragg peaks, whereas a nonuniform component gives rise to diffuse scatterings close to the Bragg peaks (Huang scattering) and between the peaks (Zwischenreflexstreuung). As a result of the diffuse scattering, the intensity of the Bragg peaks is attenuated. All these aspects of X-ray diffraction and scattering can be utilized for investigating the lattice distortion caused by the hydrogen atoms.

Let us start with lattice parameter changes. In a bcc metal containing hydrogen, MH_x , distributed equally over three types of T(O) sites, a fractional change in the atomic volume (and in the lattice parameter) can be written as

$$\frac{\Delta v_0}{v_0} = 3 \frac{\Delta a}{a} = \frac{x}{3} \text{Tr}\{\tilde{\lambda}_X + \tilde{\lambda}_Y + \tilde{\lambda}_Z\} = x(\lambda_1 + 2\lambda_2). \quad (5.10)$$

When the populations of hydrogen atoms on different types of these sites are different, the overall lattice parameter change becomes anisotropic. For example, in the β phase of VH_x , where the populations on O_Z and $\text{O}_{X,Y}$ sites are in the ratio $p_Z : (1 - p_Z)$, the changes in the lattice parameters a and c are given by

$$\frac{\Delta v_0}{v_0} = \frac{\Delta(2a + c)}{a_0} = x(\lambda_1 + 2\lambda_2), \quad (5.11)$$

$$\frac{c - a}{a_0} = \frac{3}{2} \left(p_Z - \frac{1}{3} \right) x(\lambda_1 - \lambda_2), \quad (5.12)$$

where a_0 is the lattice parameter of the host metal V without hydrogen. Thus, the two components of the tensor (and \tilde{P}) can be obtained provided the population p_Z is known. The variation of the lattice parameters a and c in $\beta\text{-VH}_x$ as a function of hydrogen concentration is shown in Fig. 5.8 [5.23, 5.24]. Assuming that all hydrogen atoms occupy O_Z sites ($p_Z = 1$), we obtain $\lambda_1 = 0.205$ and $\lambda_2 = -0.020$, and substituting $c_{11} = 237 \text{ GPa}$, $c_{12} = 122 \text{ GPa}$, and $v_0 = 13.70 \text{ \AA}^3$ into (5.7) and (5.8), we have $A + 2B = 6.80 \text{ eV}$ and $3(A - B)/(A + 2B) = 0.98$. The strongly anisotropic strain can be easily understood because a hydrogen atom on an O_Z site should exert strong repulsive forces on a pair of nearest-neighbor metal atoms along the Z axis.

As the quantity $\Delta v_0/x$ is what we called the hydrogen volume v_H in the preceding chapter, values of the dilatation $\lambda_1 + 2\lambda_2$ for bcc metals (and $3\lambda_0$ for fcc metals) can be readily obtained from Table 4.2 by dividing the listed

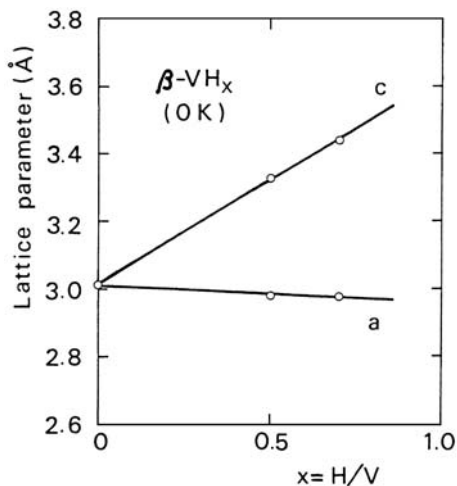


Fig. 5.8. Lattice parameters as a function of hydrogen concentration in $\beta\text{-VH}_x$ (body-centered tetragonal) [5.23, 5.24]

values of v_H by the respective atomic volumes. As noted there, hydrogen atoms on O sites in a bcc lattice produce smaller lattice expansion and, therefore, have smaller values of $\lambda_1 + 2\lambda_2$ than those on T sites (see also Table 5.2).

The theory of diffuse scattering by point defects in crystals has been worked out by *Krivoglaz* [5.25], *Trinkaus* [5.26, 5.27], and *Dederichs* [5.28]. The gist of the theory is to calculate the spectrum of Fourier components of the displacement field in the reciprocal space by taking an appropriate average of (5.9).

The Huang diffuse scattering (HDS) intensity is

$$I_{\text{HDS}} = \frac{x}{v_0} \left(\frac{F}{V_c} \right)^2 |\mathbf{Q} \cdot \tilde{\mathbf{u}}(\mathbf{q})|^2, \quad (5.13)$$

where F and V_c are the scattering amplitude and the volume of the unit cells, respectively, and \mathbf{q} is the deviation of the scattering vector \mathbf{q} from the nearest reciprocal lattice vector \mathbf{G} : $\mathbf{q} = \mathbf{Q} - \mathbf{G}$. The Fourier transform of the displacement field $\tilde{\mathbf{u}}(\mathbf{q})$ is mainly given by that of a single hydrogen atom and, hence, in terms of \tilde{P} -tensor components. For hydrogen atoms in a bcc metal (5.13) can be written in the form

$$I_{\text{HDS}} = \frac{2x}{3} \left(\frac{F}{V_c} \right)^2 \left(\frac{G}{q} \right)^2 \Pi. \quad (5.14)$$

The factor Π contains the \tilde{P} -tensor components and the elastic constants, and depends on the orientation of \mathbf{G} and \mathbf{q} . As shown in Table 5.1, the values of A

Table 5.1. Values of Π (5.14) for $(hh0)$ reciprocal lattice points in three high-symmetry directions of \mathbf{q} , $\Xi = \sum_{i>j} P_{i,j}^2$

Direction of \mathbf{q}	$[110]$ (radial)	$[\bar{1}\bar{1}0]$ (angular)	$[001]$ (angular)
Π	$\frac{(A + 2B)^2 - B^2 + 2\Xi}{(c_{11} + c_{12} + 2c_{14})^2}$	$\frac{(A - B)^2}{(c_{11} - c_{12})^2}$	$\frac{\Xi}{2c_{44}^2}$

and B can be determined from the scattering intensity distribution around an $(hh0)$ reciprocal lattice point. The intensity along the $[001]$ direction, which is determined by the off-diagonal elements of the \tilde{P} tensor $\Xi = \sum_{i>j} P_{i,j}^2$, gives a measure of the possible deviation from tetragonality, and the intensity along the $[\bar{1}\bar{1}0]$ direction depends on the magnitude of the tetragonality $(A - B)^2$ and, in combination with that along the $[110]$ direction, allows one to determine A and B .

An example of such an experiment is shown in Fig. 5.9 for H in Ta [5.29]. A comparison of the data along the $[001]$ and $[\bar{1}\bar{1}0]$ directions, with and without hydrogen, shows clearly that both Ξ and $(A - B)^2$ are very nearly zero. Thus, we have $A \approx B = 3.36 \pm 0.16$ eV. These values agree excellently with those derived from lattice parameter changes, 3.44 eV [5.30].

The expressions for Π given in Table 5.1 have been derived on the assumption of incoherent scattering, namely, that the phase of the scattered waves from different hydrogen atoms is randomly distributed. If, instead, scattered waves are assumed to be interfering with each other, somewhat different expressions follow [5.31].

The reported values of \tilde{P} -tensor components for hydrogen in V, Nb, and Ta are compiled in Table 5.2. Included here are data obtained by three

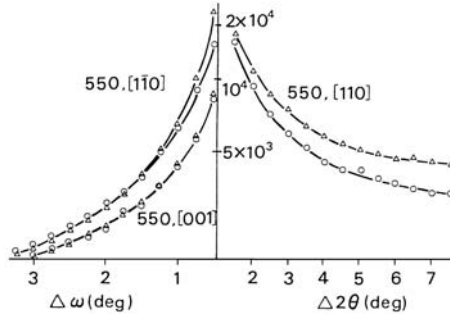
**Fig. 5.9.** Diffuse scattering intensity from Ta doped with H, near the (550) $\text{MoK}\alpha_1$ reflection, in the $[\bar{1}\bar{1}0]$, $[001]$, and $[110]$ directions. \circ : pure Ta; \triangle : $x(\text{H}/\text{Ta}) = 0.111$ [5.29]

Table 5.2. Reported values of \tilde{P} -tensor components for hydrogen atoms in V, Nb, and Ta

Metal	Isotope	Phase (site)	$A + 2B$ [eV]	$\frac{3(A-B)}{A+2B}$	Method	Reference
V	H,D	$\beta(\text{O})$	6.85	0.98	$\Delta a/a^a$	[5.23, 5.24]
	H } D }	$\alpha(\text{dis-T})^b$	6.79 6.66	0.54 0.51	HDS, $\Delta a/a^b$	[5.31]
	H } D } H,D }	$\alpha(\text{T})$	7.45 7.25 7.71	0.30 0.30 —	HDS, $\Delta a/a^b$	[5.31]
					$\Delta L/L$	[5.32]
Nb	H } H,D }	$\alpha(\text{T})$	10.1 ± 0.3 9.99 ± 0.3 9.63	≈ 0.06 — —	HDS	[5.33]
					$\Delta a/a$	[5.30]
					$\Delta L/L$	[5.32]
Ta	H } H } D } H,D }	$\alpha(\text{T})$	10.1 ± 0.5 10.3 ± 0.2 9.5 ± 0.3 9.95	≈ 0.06 — — —	HDS	[5.29]
					$\Delta a/a$	[5.30]
					$\Delta L/L$	[5.32]

^aEvaluated at 0 K by extrapolation. All other values were obtained from room-temperature data.

^bEvaluated under compressive stress allowing for the occupancy of two types of sites: ordinary T sites and stress-induced displaced T sites (dis-T) described in Sect. 5.5.

different methods: measurements of the Huang diffuse scattering (HDS), the lattice parameter change ($\Delta a/a$), and the length change ($\Delta L/L$).

The following features may be noted:

- (1) The distortion around a T site is nearly isotropic in Nb and Ta, but weakly anisotropic in V.
- (2) The distortion around an O site is strongly anisotropic.
- (3) The distortion does not depend on isotopes.

The fact that the values of $A + 2B$ from $\Delta a/a$ and $\Delta L/L$ agree with those from the Huang scattering is significant. This implies that the electronic interaction, which depends on volume but not on the local configuration of M atoms plays a minor role in producing lattice dilatation. Also significant is the nearly isotropic displacements for T-site occupancies in the bcc lattice. If we try to reproduce the nearly isotropic distortion by central forces acting on the nearest and next-nearest metal atoms, we have to make a specific assumption for the ratio of these forces [5.34]. In view of this, *Dosch et al.* [5.35] suggested that what one observes as diffuse scattering of X-rays and neutrons from H and D in Nb is in fact a temporal average of the fluctuating distortion fields caused by rapidly jumping H, D atoms over adjacent T sites. *Elsässer et al.* [5.36] showed, however, by electronic calculations that short-range forces

around an H atom on T site in Nb do indeed produce a nearly isotropic distortion field, yielding $3|A - B|/(2A + B) \sim 0.1$. Thus, the small anisotropy of the force-dipole tensor in Nb is explainable solely in terms of static forces, and therefore does not serve as evidence in support of the dynamical model of *Dosch et al.* [5.35].

Large atomic displacements close to hydrogen atoms cause diffuse scatterings into angles widely separated from Bragg peaks (Zwischenreflexstreuung). This scattering was first measured with neutrons for D in Nb, and a set of forces acting on the first-nearest- and second-nearest-neighbor metal atoms was deduced [5.34].

The decrease of Bragg intensities caused by diffuse scattering is usually described in the form of a static Debye–Waller factor, $\exp(-2W_D)$ [5.25, 5.37].

For a random distribution of hydrogen atoms,

$$W_D = x \left(1 - \frac{x}{x_{\max}} \right) \left\langle \sum_m (\cos \mathbf{Q} \cdot \mathbf{u}^m - 1) \right\rangle. \quad (5.15)$$

Metzger et al. [5.38] have noticed that, in the case of H in Nb, W_D is essentially ($\geq 95\%$) determined by the displacement of nearest-neighbor Nb atoms, u_1 , viz.,

$$W_D \approx \frac{2}{3} x Q^2 u_1^2, \quad (5.16)$$

and deduced $u_1 \approx 0.100 \pm 0.007 \text{ \AA}$. Thus, the measurement of the static Debye–Waller factor provides a unique possibility of determining the local distortion of the lattice.

5.3 Neutron Diffraction–Elastic Neutron Scattering

Neutron diffraction has been a very useful technique for structural studies of metal hydrides because, quite unlike X-rays, neutrons are scattered strongly by hydrogen nuclei. Thus, many complex structures of metal hydrides have been determined by this technique, including the positions of hydrogen atoms. We shall not be concerned here with structure determinations but rather with the fact that, by careful measurements of the diffraction intensities from single-crystal specimens, we can go a step further from site location of hydrogen to its density distribution in the lattice. (For fundamentals of neutron scattering and diffraction, see, e.g., [5.39–5.41].)

In neutron diffraction experiments, one measures the elastic scattering function $S(\mathbf{Q})$, which is the Fourier transform of the time-averaged density distribution, viz.,

$$S(\mathbf{Q}) = \frac{1}{2\pi\hbar} \int \rho(\mathbf{R}) e^{i\mathbf{Q} \cdot \mathbf{R}} d\mathbf{R}, \quad (5.17)$$

$$\rho(\mathbf{R}) = \int G(\mathbf{R}, t) dt, \quad (5.18)$$

$$G(\mathbf{R}, t) = \frac{1}{N} \sum_{j \neq j'} \left\langle \delta(\mathbf{R} - \mathbf{R}^j(t) + \mathbf{R}^{j'}(0)) \right\rangle, \quad (5.19)$$

where $\hbar\mathbf{Q}$ is the momentum change of a neutron on scattering, $\mathbf{R}^j(t)$ is the instantaneous position of atom j at time t , and the summation runs over all atom pairs in the crystal consisting of N atoms. The intensity of the diffracted neutrons is proportional to the coherent cross section σ_{coh} of the system, which is determined by an average of the scattering lengths of the constituent nuclei. Neutrons are also scattered incoherently, forming an undesirable background for diffraction signals. Scattering cross sections of some selected nuclei are given in Table 5.3. As the incoherent cross section of the proton is very large, the deuteron is more easily accessible for diffraction work; most of the structural studies on metal hydrides have, therefore, been performed on deuterided samples.

Table 5.3. Cross section for coherent scattering (σ_{coh}) and incoherent scattering (σ_{inc}) of neutrons by some selected isotopes [10^{-28}m^2] [5.41]

Isotope	σ_{coh}	σ_{inc}
H	1.758	79.7
D	5.597	2.0
N	11.0	0.46
O	4.23	<0.02
Ti	1.43	2.7
V	0.019	4.79
Y	7.75	0.15
Pd	4.5	0.09
Zr	6.2	0.1
Nb	6.24	0.0063
Ta	6.0	0.02

The density distribution $\rho(\mathbf{R})$ can be obtained from the diffraction data by Fourier reconstruction,

$$\rho(\mathbf{R}) = \frac{h}{(2\pi)^3} \int S(\mathbf{Q}) e^{-i\mathbf{Q} \cdot \mathbf{R}} d\mathbf{Q}, \quad (5.20)$$

provided that $S(\mathbf{Q})$ is measured over a sufficiently wide range in the reciprocal space.

Examples of such measurements are shown in Fig. 5.10 for D in $\text{VD}_{0.79}$ and Fig. 5.11 for D in $\text{NbD}_{0.73}$ [5.42]. In the latter, the contribution of Nb nuclei has been subtracted; no such procedure is necessary for the former because

of the small σ_{coh} of V. In both cases, the D density is localized around T sites, consistent with channeling results. Very similar results were obtained for H in TaH_{0.20} [5.42]. On a closer look at Fig. 5.10, we find a small density maximum at the center (O site) in addition to the density maxima on T sites. In Nb and Ta, there is no such indication of partial O-site occupancy. This problem will be examined later in Sect. 5.5. It may be appropriate here to remind the reader of the fact that the Fourier-reconstructed density map can provide only the time average; these figures (Figs. 5.10, 5.11) do not imply that four adjacent T sites are occupied simultaneously.

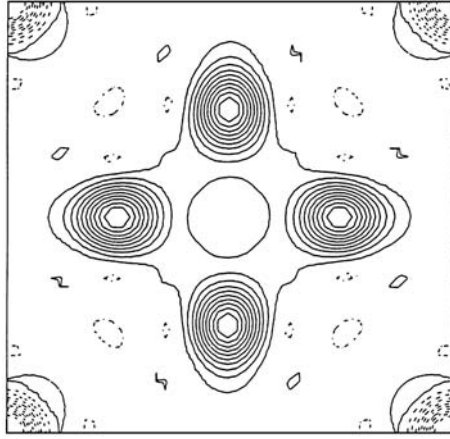


Fig. 5.10. Deuteron density contour maps in VD_{0.79} at 70°C, Fourier-reconstructed from neutron diffraction data [5.42]

Another example is shown in Fig. 5.12 for D in β -VD_{0.51} [5.43]. In this structure, D atoms occupy one of the two sublattices of O_Z sites (labeled O_{Z1}) in the bct structure of V atoms. Here, the extension and the anisotropy of the individual D-atom distributions is more conspicuous. It must be recognized, however, that short-wavelength components in the density map may not be well reproduced because the diffraction data for large Q values are difficult to obtain experimentally.

Figure 5.13 illustrates the density map constructed from the same data, but supplementing the high- Q diffraction data by an appropriate extrapolation method [5.44]. The difference between these two figures (Figs. 5.12, 5.13) gives a measure of this kind of cutoff errors.

The density distribution obtained in this way reflects the form of the wave functions of hydrogen in the potential field of the surrounding metal atoms, and, in some cases, even suggests the possible jump paths of hydrogen atoms. In β -VD_{0.51}, for example, the density distribution is extended along the line connecting the neighboring O_{Z1} sites, indicating that the potential

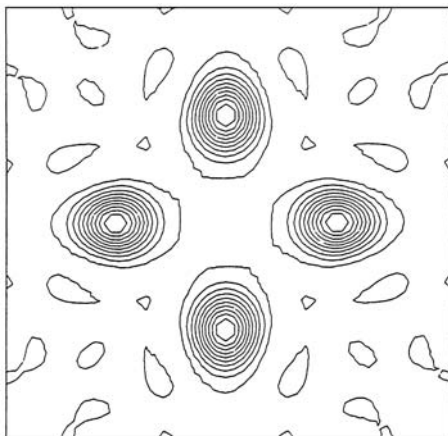


Fig. 5.11. Deuteron density contour maps in NbD_{0.73} at 14°C, Fourier-reconstructed from neutron diffraction data [5.42]

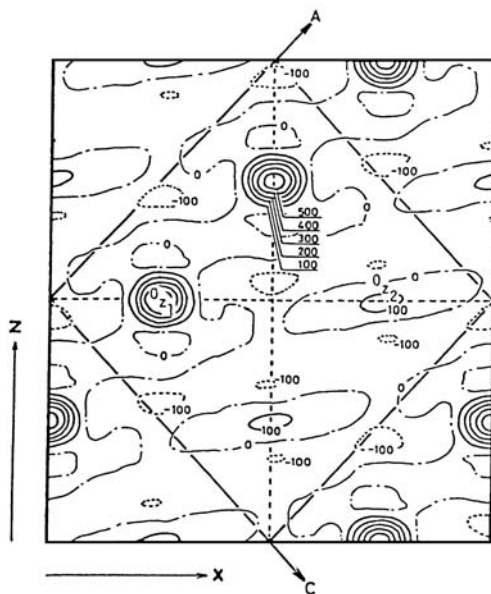


Fig. 5.12. Deuteron density contour map of β-V₂D. Fourier projection on the (010) plane. Contours are drawn at equal intervals in arbitrary units: *full*, *dotted*, and *broken lines* indicate positive, negative, and zero contours, respectively [5.43]

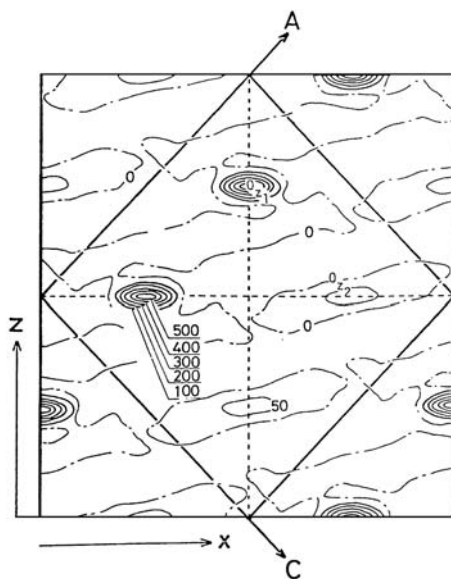


Fig. 5.13. Deuteron density contour map of β -V₂D. Same as Fig. 5.12, except that higher-order reflections buried in noise in the neutron diffraction spectra have been supplemented by an appropriate extrapolation method [5.44]

has a valley along this line, probably allowing a rapid motion of hydrogen along this path.

One conventional way to quantify the density distribution is in terms of the occupation fractions (populations) of prespecified interstitial sites. A set of populations and temperature factors of (anisotropic) atomic vibrations are so determined as to best reproduce the observed set of diffraction intensities.

In Fig. 5.14a–5.14c, the density of D atoms in VD_{0.51} is shown at three different temperatures, and in Fig. 5.15 the same result is expressed in terms of occupation fractions [5.43]. As the β_1 – α transition is approached from below, the density distribution around O_{Z1} sites gradually becomes more extended, and some occupation of T sites becomes visible at 403 K (just below the transition, $T_c = 406$ K). According to Fig. 5.15, the occupation fraction of T sites here amounts to as much as 0.7, which, however, does not appear to correctly represent the situation seen in the density map. In effect, the gradual broadening of the density distribution around O_{Z1} sites is here described by the increased population on the nearby T sites. We must recognize that this is a consequence of a purely mathematical convention. As the wave function of interstitial hydrogen atoms has a certain intrinsic extension, it is physically meaningless to dissect it into pieces or construct it by superposition of, say, O_{Z1}- and T-site contributions. It might possibly be that the gradual broadening of the density distribution noted above is

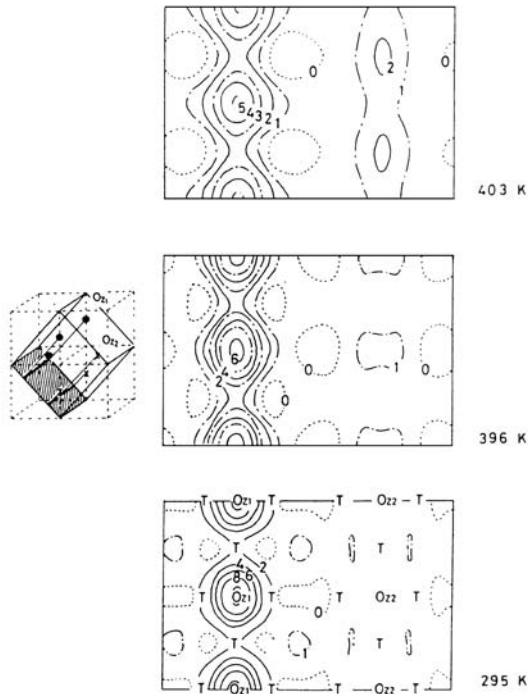


Fig. 5.14. Changes in the D-density distribution on the (100) plane of $\beta\text{-VD}_{0.51}$ at three different temperatures [5.43]

a result of thermal excitation to higher-energy states having more extended wave functions. These problems will be examined in Sect. 5.7.

In experiments using powder specimens, the information available is necessarily more limited. At best, one can determine the type of site occupied by hydrogen atoms by trying to reproduce the observed set of diffraction lines.

5.4 Inelastic Neutron Scattering

When monoenergetic neutrons pass through a crystal, they exchange energy with lattice vibrations and emerge with a certain distribution of energy – the phenomenon called the inelastic neutron scattering (INS). Thus, by measuring the energy spectra of the originally monoenergetic neutrons, the distribution of vibrational energy states can be studied.

The incoherent scattering function can be written in a one-phonon approximation as

$$S_{\text{inc}}(\mathbf{Q}, \omega) = \frac{\hbar}{2M|\omega|} \left(\bar{n} + \frac{1}{2}(1 \pm 1) \right) Q^2 g(\omega) e^{-Q^2 \langle u^2 \rangle}, \quad (5.21)$$

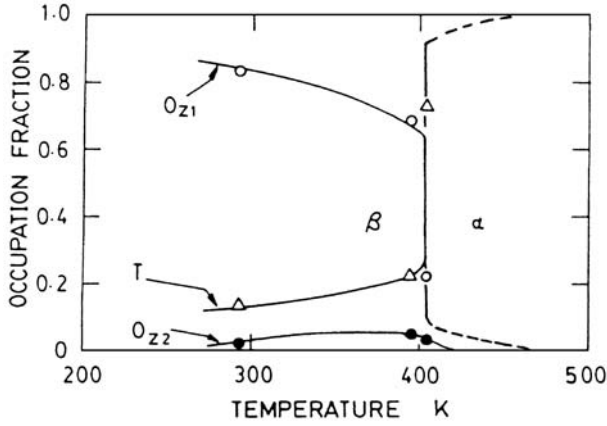


Fig. 5.15. Occupation fractions of deuterium at the O_{Z1} , O_{Z2} , and T-sites in the β - α transition of $VD_{0.51}$, determined by the least-squares fitting of neutron diffraction intensity [5.43]

where $\hbar Q$ and $\hbar\omega$ are, respectively, the momentum and the energy transferred from a neutron by scattering, $\hbar Q = \hbar(\mathbf{k}_i - \mathbf{k}_f)$ and $\hbar\omega = E_i - E_f$, with i and f signifying states of the neutron before and after the scattering, \bar{n} is the average number of phonons at temperature T :

$$\bar{n} = [\exp(\hbar\omega/kT) - 1]^{-1}, \quad (5.22)$$

where the $+$ ($-$) sign refers to neutron energy loss (gain), and $g(\omega)$ is the phonon density of states. Thus, the vibrational energy states can be studied by means of both energy-loss and energy-gain spectroscopies, the latter being feasible only at reasonably high temperatures, where many phonons are available in the excited states.

The significance of this type of experiments for our purpose is that it provides microscopic information on the state of existence of interstitial hydrogen atoms in metals – not only their vibrational energies but their wave functions and the local potential field in which they are placed. These problems are explained here taking some typical examples of fcc, bcc and hcp metals. For more details, the reader is referred to a number of review papers [5.45, 5.46], especially the most recent and comprehensive one by Ross [5.47]. Inelastic neutron scattering experiments on two-site tunneling states are described separately in Sect. 5.8.1.

5.4.1 Optic-Mode Vibration of Hydrogen Atoms

An example of the phonon dispersion relation, i.e., the phonon frequency as a function of wave number, is shown in Fig. 5.16 for $PdD_{0.63}$, where D atoms occupy O sites in the fcc lattice [5.48]. The presence of dispersion

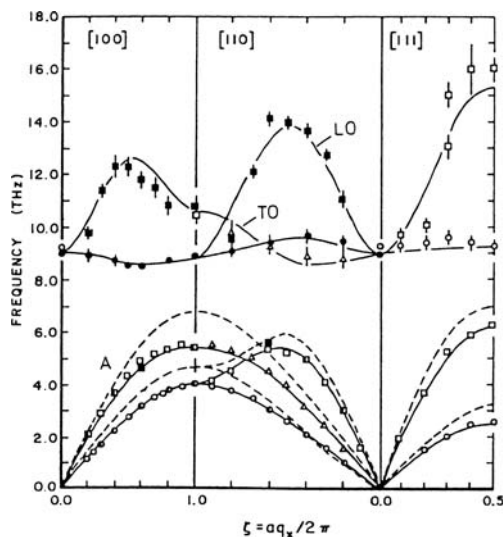


Fig. 5.16. Dispersion curves for $\text{PdD}_{0.63}$. Filled and open symbols represent data taken at 150 and 295 K, respectively. The dashed line is for pure Pd [5.48]. 1 THz = 4.15 meV

is a manifestation that the vibration of constituent atoms bears some wave-like character and propagates in the crystal lattice. The labels on each branch signifies the mode of vibrations; O signifies the optic-mode vibration (Pd and D atoms vibrating 180° out of phase), A the acoustic-mode vibration (Pd and D atoms vibrating in phase), L the longitudinal mode in which the direction of vibration is parallel to the direction of wave propagation, and T the transverse mode, perpendicular to it. Because of the lower mass of D in comparison to Pd atoms, the optic-mode vibrations have frequencies distinctly higher than the acoustic-mode vibrations. The magnitude of dispersion in optic-mode vibrations is a measure of the strength of the interaction between hydrogen atoms. Due to interactions between neighboring hydrogen atoms, the local oscillations are coupled with each other and bear some wave-like character, which gives rise to dispersion.

A dispersion of similar magnitude was observed in $\text{CeD}_{2.72}$, as shown in Fig. 5.17 [5.49]. There are two different groups of optic-mode vibrations; one centered around 21 THz and the other around 11 THz. The latter group did not exist at lower D concentrations $\text{CeD}_{2.12}$, from which it was concluded that the former originates from D atoms on T sites in the fcc lattice, and the latter from those on O sites.

Figure 5.18 shows the dispersion curves of Ta-D alloys where D atoms occupy T sites in the bcc lattice [5.50]. In contrast to the case of Pd and Ce hydrides, practically no dispersion can be seen for the optic-mode vibrations. This is known to be the common trend for hydrogen atoms occupying T sites

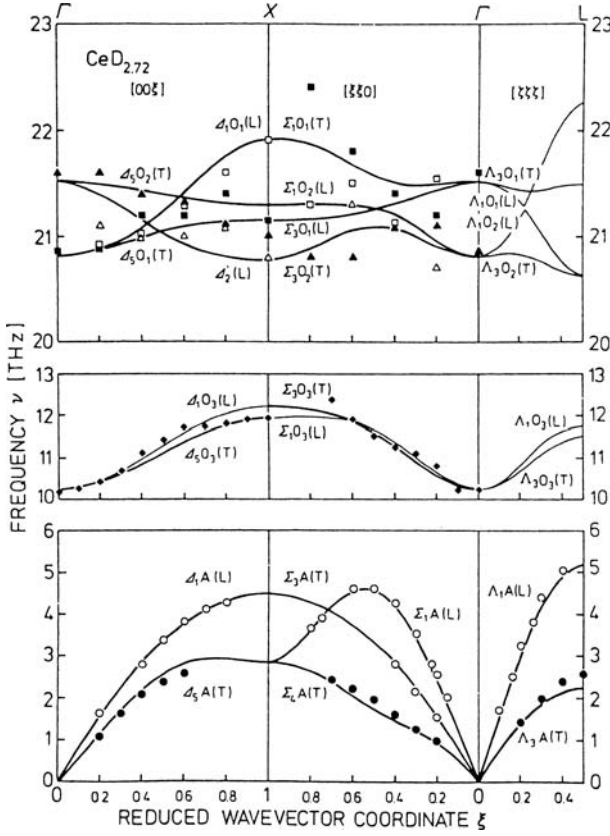


Fig. 5.17. Dispersion curves for $\text{CeD}_{2.72}$. From *top to bottom*, the optic-mode vibration originating from D atoms on T sites, those from D atoms on O sites, and the acoustic-mode vibrations, respectively [5.49]. 1 THz = 4.15 meV

in bcc metals. The absence of dispersion means that each hydrogen atom is oscillating independently in the local potential field of the surrounding metal atoms.

Hereafter, for the sake of simplicity, we shall focus on optic-mode vibrations, and regarding the dispersion to be reasonably small, treat hydrogen atoms as three-dimensional Einstein oscillators in isolated potential wells. Then, in the harmonic approximation, the energy eigenvalues are given by

$$e_{lmn} = \left(l + \frac{1}{2}\right) \hbar\omega_X + \left(m + \frac{1}{2}\right) \hbar\omega_Y + \left(n + \frac{1}{2}\right) \hbar\omega_Z, \quad (5.23)$$

$l, m, n = 0, 1, 2, \dots$

When the local symmetry of the hydrogen site is cubic, the oscillators along the three principal axes become degenerate; hence,

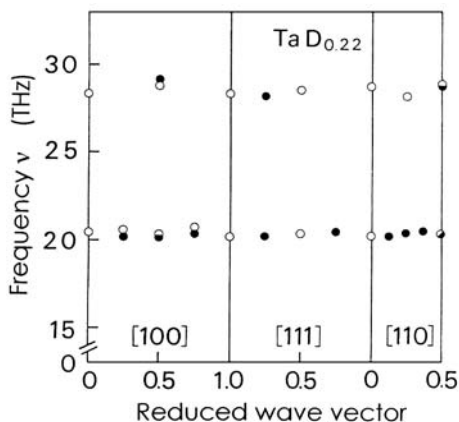


Fig. 5.18. Dispersion curves of $\text{TaD}_{0.22}$ [5.50] for different directions of polarization. ○: longitudinal polarization; ●: transverse polarization. 1 THz = 4.15 meV

$$e_{lmn} = \left(l + m + n + \frac{3}{2} \right) \hbar \omega_0 . \quad (5.24)$$

This is the case with T and O sites in the fcc lattice. In T and O sites in the bcc lattice, where the local symmetry is tetragonal, we have

$$e_{lmn} = (l + m + 1) \hbar \omega_1 + \left(n + \frac{1}{2} \right) \hbar \omega_2 . \quad (5.25)$$

In INS experiments performed on polycrystalline (or powder) samples, measured energy spectra are the average of dispersion curves over all crystal orientations. Figure 5.19 shows the vibration energy spectra of stoichiometric PdH measured at 200 K [5.51]. The position of the peak and a tail on the higher-energy side appear consistent with the dispersion curves obtained with a single crystal of PdD shown in Fig. 5.16 (when the energies are scaled by $\sim\sqrt{2}$ according to the mass ratio). Higher-order transitions are also visible, though obscured to some extent by phonon contributions. A peculiar feature of this higher-energy tail is that it persists to very low H concentrations (down to $x = 0.002$) without any change in shape, as shown in Fig. 5.20 [5.52]. If this really indicates the extremely long-ranged H–H interaction is a question worth pursuing further. This problem will be resumed in Sect. 5.7.3.

The INS spectra for $\text{NiH}_{1.05}(\text{fcc})$, $\text{CrH}_{1.00}(\text{hcp})$ and $\text{MoH}_{1.2}(\text{hcp})$ measured at 15 K are shown in Fig. 5.21 [5.53]. Hydrogen atoms occupy O sites in all these cases. Each of these spectra consists of three peaks arising from transitions to the first, second and third excited states. The similarity of these spectra to those shown in Figs. 5.19 and 5.20 indicates that the environments of H atoms in all these cases are very similar. These features are determined essentially by the position of octahedrally coordinated M atoms.

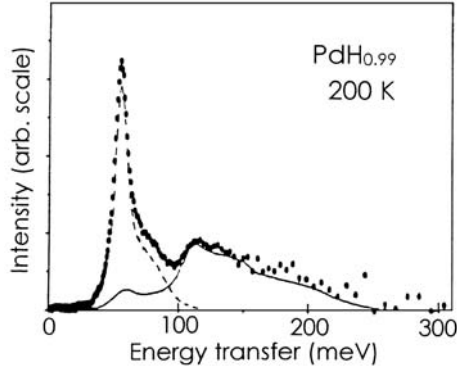


Fig. 5.19. Vibration energy spectrum of $\text{PdH}_{0.99}$ measured at 200 K. The measured curve is separated into one-phonon (---) and multi-phonon (—) components [5.51]

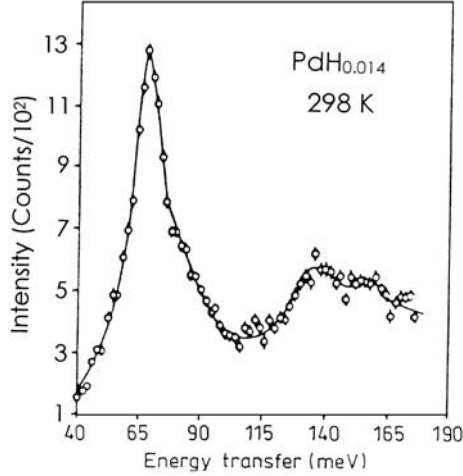


Fig. 5.20. Vibration energy spectrum of $\text{PdH}_{0.014}$ measured at 298 K [5.52]

The same conclusion was reached from close comparison of observed INS spectra in $\epsilon\text{-MnH}_{0.86}(\text{hcp})$ [5.51] and $\gamma\text{-MnH}_{0.41}(\text{fcc})$ [5.54]. The observed spectra agreed with each other both in shape and position, indicating that the local potential field was very nearly the same. The origin of the higher-energy tail, a common feature of all these cases, will be discussed later (Sect. 5.7.3).

Recently, detailed INS measurements were made on a highly oriented foil sample of $\text{PdH}_{0.99}$ [5.55], subsequently on a single-crystalline sample of $\text{PdH}_{0.85}$ up to ~ 380 meV [5.56], and close comparison with theoretical calculations was made in regard to the orientation dependence of the energy and intensity of the excitation. This will be described in Sect. 5.7.3.

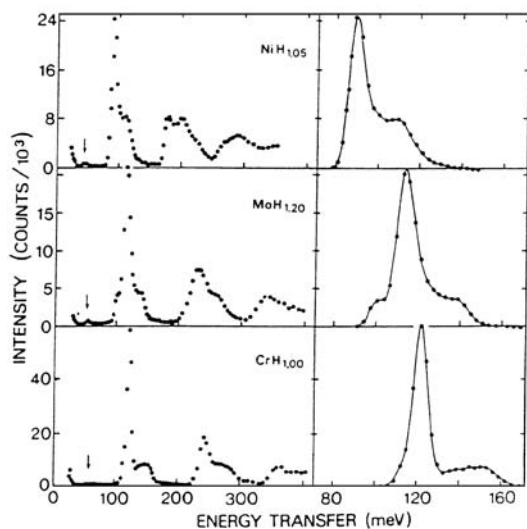


Fig. 5.21. Vibration energy spectra of $\text{NiH}_{1.05}$, $\text{MoH}_{1.20}$, and $\text{CrH}_{1.00}$ measured at 15 K [5.53]

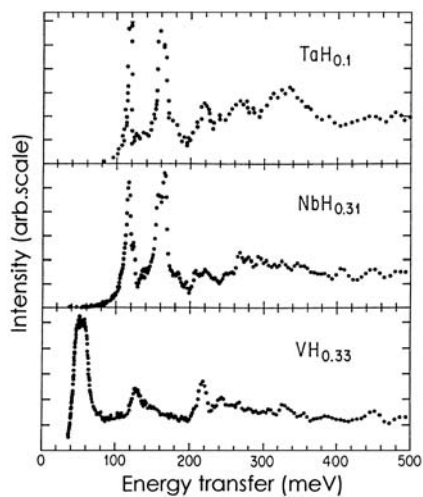


Fig. 5.22. Vibration energy spectra observed in $\text{VH}_{0.33}$, $\text{NbH}_{0.31}$, and $\text{TaH}_{0.1}$ at 30 K. The actual phases under observation are $\beta\text{-VH}_{0.5}$, $\epsilon\text{-NbH}_{0.7}$, and $\beta\text{-TaH}_{0.5}$, respectively [5.57]

Owing to the lack of dispersion in bcc metals, the INS spectra measured with polycrystalline specimens exhibit well-resolved peaks. Thus, as shown in Fig. 5.22 [5.57], in addition to two sharp peaks due to excitation to the first excited states, excitation to a multitude of states extending to ~ 1000 meV

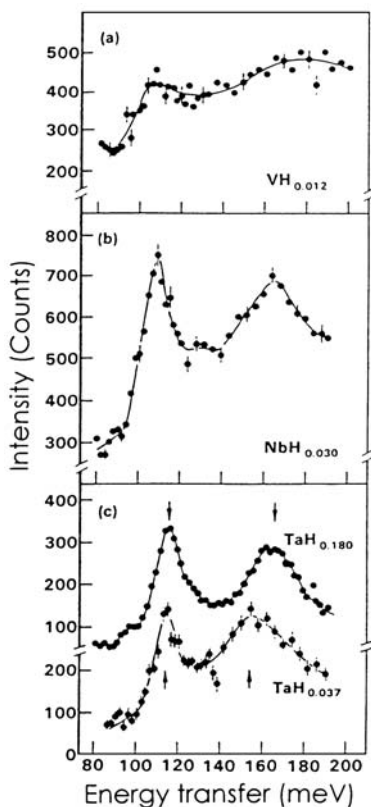


Fig. 5.23. a–c. Vibration energy spectra of low concentrations of H in V, Nb, and Ta measured at room temperature [5.58]

could be resolved in Nb–H and Ta–H alloys. (These spectra observed at 30 K in fact refer to the precipitated phases ϵ -NbH_{0.7} and β -TaH_{0.5}.) The two prominent peaks observed in the solid-solution phase of V–H, Nb–H and Ta–H alloys, with intensities in the ratio 1:2 at energies about 120 and 170 meV for H (nearly scaled by $1/\sqrt{2}$ for D), are assigned to fundamental excitations in the non-degenerate and doubly degenerate modes of vibration, respectively, of the hydrogen atoms on T sites.

The spectra taken at very low hydrogen concentrations (in the disordered phase) are shown in Fig. 5.23 [5.58]. The higher-energy peak is broader than the lower-energy peak, and the peaks in V are much broader than those in Nb and Ta. The origin of this extreme broadening has not been fully understood so far; see Sect. 5.5.

In β -VH_{0.5}, with H atoms occupying O_{Z1} sites in the bct lattice (Sects. 5.1–5.3), the shape of the spectrum is very different from that with H atoms on T sites in Nb and Ta (Fig. 5.22). An unambiguous assignment of the peaks was

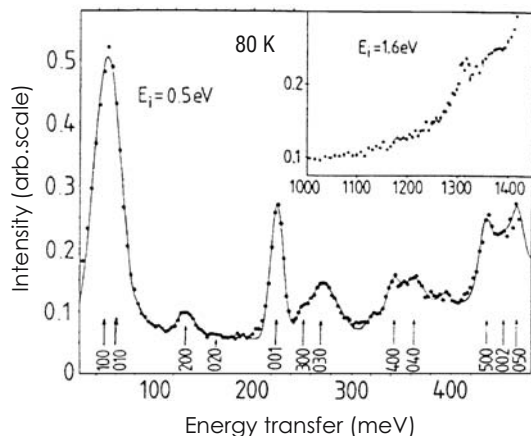


Fig. 5.24. Inelastic neutron scattering spectra from β -V₂H at different incident neutron energies E_i . The indices l, m, n mark assignments for the different transitions [5.59]

made by experiments using a single-crystal specimen [5.59]. The spectrum observed is shown in Fig. 5.24. As the transition probability between the ground state (0) and the excited state (α), $|\langle 0 | \exp(i\mathbf{Q} \cdot \mathbf{R}) | \alpha \rangle|^2$, depends on the momentum transfer, the symmetry of the excited state can be learned by choosing appropriate directions of \mathbf{Q} with respect to the crystal axis. In the experiment shown, the 50 meV transition was excited by the component of \mathbf{Q} along the a axis, the 58 meV peak by that along the b axis, and the 223 meV peak by that along the c axis, thus allowing an identification of the excited states as those having wave functions extending in the a , b , and c directions, respectively. In addition to the mode assignment, the authors also succeeded in observing higher harmonics, up to the fourth in the c direction, and up to the 14th in the a - b plane. A more detailed analysis of the spectrum will be given later.

Similar mode assignments were also made for hydrogen atoms in the hcp metals Sc [5.60,5.61], Y [2.133], and Lu [5.62], and more recently on Re [5.63].

Figure 5.25 shows the observed spectrum for TiH₂ [5.64]. A series of peaks, nearly equally spaced, indicate that H atoms are behaving as isotropic three-dimensional harmonic oscillators. This is consistent with the known occupancy of T sites in the fcc lattice of Ti. In addition, the sharpness of the peaks indicates the absence of any appreciable dispersion in this system. The spectrum observed in ZrH₂ was very similar [5.64].

Some of the excitation energies obtained so far are listed in Table 5.4. A more complete listing on rare-earth metals is given in the review paper by Vajda [2.70]. The formation of hydrogen pairs in some rare-earth metals is described in the next section.

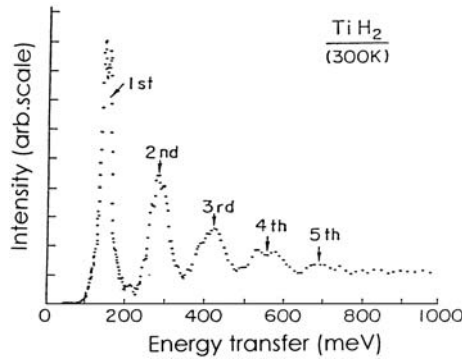


Fig. 5.25. Vibration energy spectrum of TiH_2 measured at 300 K [5.64]

Table 5.4. Vibrational excitation energies of interstitial hydrogen in metals. The values have been obtained from the observed peaks of inelastic neutron scattering experiments using polycrystalline (powder) specimens. The presence of dispersion in fcc and some hcp metals detracts to some extent from the physical significance of these values

Structure	Site	Sample	Excitation Energy [meV]		Temperature [K]	Reference
fcc	O	$\text{MnH}_{0.41}$	111		2	[5.54]
		$\text{CoH}_{1.0}$	101		5	[5.65]
		$\text{NiH}_{1.05}$	89		15	[5.53]
		$\text{PdH}_{0.002}$	68.5(2)		77	[5.66]
		$\text{PdH}_{0.014}$	69.0(5)		295	[5.52]
		$\text{PdH}_{0.63}$	56(2)		80	[5.67]
		$\text{PdH}_{0.99}$	56.0		15	[5.51]
			56.0		200	[5.51]
		$\text{PdD}_{0.014}$	46.5(5)		295	[5.52]
		$\text{PdD}_{0.63}$	37.6		80	[5.68]
fcc	T	TiH_2	145.2		300	[5.64]
		YH_2	127			[5.69]
		YD_2	90			[5.69]
		$\text{LaH}_{1.94}$	103			[5.70]
		$\text{ZrH}_{1.41}$	143.8		300	[5.64]
fcc	T+O	$\text{LaH}_{2.18}$	109(T)	73(O)	298	[5.71]
		$\text{LaH}_{2.98}$	127(T)	61(O)	298	[5.71]
		$\text{LaD}_{2.98}$	93(T)	43(O)	298	[5.71]
		$\text{CeH}_{1.98}$	93(T)	43(O)	300	[5.51]
		$\text{CeH}_{2.96}$	128(T)	63(O)	298	[5.71]
		$\text{CeD}_{2.97}$	92(T)	47(O)	298	[5.71]

continued

Table 5.4. (*continued*)

Structure	Site	Sample	Excitation Energy [meV]		Temperature [K]	Reference
bcc	O	VH _{0.5}	50.2 ^a	223 ^b	80	[5.59]
			56	230	80	[5.72]
			54	220	295	[5.72]
		VD _{0.5}	39	164	80	[5.72]
			47		295	[5.72]
		VT _{0.5}	36		295	[5.72]
bcc	T	TiH _{0.14}	120(2) ^b	171(2) ^a	998	[5.73]
		VH _{0.012}	106	~170	300	[5.58]
		VH _{0.51}	113	180	498	[5.74]
		VD _{0.5}	82(3)	123(7)	425	[5.75]
		NbH _{0.03}	107	163	300	[5.58]
		NbH _{0.7}	116.0(7)	167.0(15)	10	[5.76]
		NbD _{0.85}	86(1)	120.0(15)	10	[5.76]
		NbT _{0.7}	72(1)	101(1)	10	[5.76]
		TaH _{0.037}	114	154	300	[5.58]
		TaH _{0.08}	114.0(6)	163.5(8)	300	[5.77]
		TaH _{0.5}	121.3(2)	163.4(4)	10	[5.76]
		TaD _{0.09}	84.4(6)	116.0(6)	300	[5.77]
		TaD _{0.5}	88.4(4)	118.7(6)	10	[5.76]
hcp	O	CrH _{1.0}	121		15	[5.53]
		MnH _{0.86}	111		100	[5.51]
		FeH _{1.0} ^c	105		90	[5.78]
		CoH _{0.05}	118		5	[5.65]
		CoH _{0.5}	110		15	[5.65]
		MoH _{1.2}	113		15	[5.53]
		ReH _{0.09}	100, 130		5	[5.63]
hcp	T	ScH _{0.34} ^d	103.5(2) ^b	147.5(1) ^a	8	[5.60]
		ScD _{0.34} ^d	79.0(1)	107.3(1)	4	[5.60]
		YH _{0.18} ^d	100.1(2)	134.2(5)	80	[2.133]
		YD _{0.18} ^d	75.8(1)	96.3(1)	80	[2.133]
		LuH _{0.19} ^d	102.8(3)	143.5(1)	4	[5.62]
		LuD _{0.19} ^d	76.2(1)	101.7(1)	4	[5.62]
		TiH _{0.05}		141(1)	588	[5.73]
		TiH _{0.07}	105.5(20)	162.0(25)	599	[5.79]
		TiD _{0.09}		108.4(12)	601	[5.79]
		ZrH _{0.05}		143.1(6)	873	[5.79]
		ZrD _{0.05}		105.0(10)	765	[5.79]

^a doubly degenerate mode^b non-degenerate mode^c dhcp structure^d single-crystal data.

5.4.2 Local Potential Field for Hydrogen

One of the most natural ways to go beyond the harmonic approximation is to introduce the anharmonicity in the potential as a perturbation (see, e.g. [5.46]). Thus, for a site of cubic symmetry, such as T and O sites in the fcc lattice, we may write the local potential field approximately in the form

$$U(X, Y, Z) = c_2(X^2 + Y^2 + Z^2) + c_4(X^4 + Y^4 + Z^4) + c_{22}(X^2Y^2 + Y^2Z^2 + Z^2X^2), \quad (5.26)$$

and the energy eigenvalues in the first-order perturbation theory as

$$e_{lmn} = \sum_{j=l,m,n} \left[\hbar\omega_0(j + \frac{1}{2}) + \beta(j^2 + j + \frac{1}{2}) \right] + \gamma [(2l+1)(2m+1) + (2m+1)(2n+1) + (2n+1)(2l+1)], \quad (5.27)$$

where l, m, n are the quantum numbers of the vibration in Z, X, Y directions, respectively, and

$$\omega_0 = \sqrt{\frac{2c_2}{M}}, \quad \beta = \frac{3\hbar^2 c_4}{4Mc_2}, \quad \gamma = \frac{\hbar^2 c_{22}}{8Mc_2}. \quad (5.28)$$

The lowest excitation energies $\varepsilon_{lmn} = e_{lmn} - e_{000}$ are given by

$$\begin{aligned} \varepsilon_{100} = \varepsilon_{010} = \varepsilon_{001} &= \hbar\omega_0 + 2\beta + 4\gamma \quad (\text{fundamental vibration}) \\ \varepsilon_{200} = \varepsilon_{020} = \varepsilon_{002} &= 2\hbar\omega_0 + 6\beta + 8\gamma \quad (\text{first overtone}) \\ \varepsilon_{110} = \varepsilon_{011} = \varepsilon_{101} &= 2\hbar\omega_0 + 4\beta + 12\gamma \quad (\text{combination vibration}) \end{aligned} \quad (5.29)$$

Analysis based on this formalism was made on α -PdH_x [5.52]. As shown in Fig. 5.20, INS peaks were observed at 69 meV, 138 meV and 156 meV. In view of the expected intensities 2:1 for ε_{110} and ε_{200} peaks, these peaks were identified, respectively, as ε_{100} , ε_{110} and ε_{200} . This assignment led to $\hbar\omega_0 = 50$ meV, $2\beta = 19 \pm 4$ meV, and $|\gamma| \leq 0.4$ meV. $\gamma \approx 0$ indicates that the vibrations in the three directions can be regarded independent. The positive β (and hence c_4) means that the potential is well-like – more steeply varying than a parabola, (whereas a negative β means that the potential is trumpet-like – more open at high energies than a parabola).

The potential field appropriate for the symmetry of T sites in bcc metals can be written in the form

$$U(X, Y, Z) = c_{2X}(X^2 + Y^2) + c_{2Z}Z^2 + c_{4X}(X^4 + Y^4) + c_{4Z}Z^4 + eZ(X^2 - Y^2) + fX^2Y^2 + gZ^2(X^2 + Y^2). \quad (5.30)$$

The excitation energies $\varepsilon_{lmn} = e_{lmn} - e_{000}$, where l, m, n refer to vibrational excitations in Z, X, Y directions, respectively, can be calculated by the first-order perturbation theory, and some of their expressions in terms of potential parameters were listed by *Eckert et al.* [5.80].

If we assume that the coupling terms are small ($e, f, g \approx 0$), we are left with two anharmonic oscillators with frequencies

$$\omega_{01} = \sqrt{\frac{2c_{2X}}{M}} \quad (\text{doubly degenerate}), \quad \omega_{02} = \sqrt{\frac{2c_{2Z}}{M}} \quad (\text{non-degenerate}), \quad (5.31)$$

and the anharmonicity parameters

$$\beta_1 = \frac{3\hbar^2 c_{4X}}{4Mc_{2X}}, \quad \beta_2 = \frac{3\hbar^2 c_{4Z}}{4Mc_{2Z}}. \quad (5.32)$$

This simplified expression is valid for O sites in bcc metals having the tetragonal symmetry.

There are two useful relations for extracting the degree of anharmonicity from observed excitation energies. We shall here measure the anharmonicity by

$$\Delta E^H = \varepsilon_{200} - 2\varepsilon_{100} = 2\beta \quad (5.33)$$

for H. Due to the mass dependence of β , the corresponding quantities for other isotopes should satisfy the relation

$$\Delta E^H = 2\Delta E^D = 3\Delta E^T, \quad (5.34)$$

as long as the potential field remains the same.

Another useful relation for the isotope dependence of the fundamental transition energies reads

$$(1 - 1/\sqrt{2}) \Delta E^H = \hbar\omega_0^H - \sqrt{2}\hbar\omega_0^D \quad (5.35)$$

for D, and $\sqrt{2}$ replaced by $\sqrt{3}$ for T. Values of ΔE^H deduced from these two methods are listed in Table 5.5 for O-site and T-site occupancies in fcc and bcc (bct) lattices.

We note immediately that $\Delta E^H > 0$ for O-site occupancy, and $\Delta E^H < 0$ for T-site occupancy, for both fcc and bcc lattices. This implies that, as a consequence of larger volume of O sites, an H atom does not experience strong repulsion from surrounding M atoms over a certain central region around the O site. In the case of V_2H , the vibration is strongly anharmonic in the doubly degenerate X - Y direction, whereas it is closely harmonic in the Z direction having nearest-neighbor M atoms at much shorter distances. In addition, we note that the anharmonicity parameter deduced from the two methods agree reasonably well with each other. This is an indication that the isotope dependence of the potential is small, if at all present [5.76].

In some rare-earth metals where both T and O sites in the fcc lattice are occupied at high hydrogen concentrations ($H/M > 2$), the anharmonicity parameter bears a negative sign, as listed in Table 5.6. Qualitatively, it is because H atoms already existing on T sites exert additional repulsion, and makes the available volume of O sites smaller.

Table 5.5. Anharmonicity parameters for hydrogen atoms occupying O and T sites in fcc and bcc lattices

Structure	Site	Sample	Anharmonicity Parameter ΔE^H [meV]	Deg- eneracy	Method	Tempe- rature	Reference
fcc	O	MnH _{0.41}	8	3	a	5	[5.54]
		NiH _{1.05}	16	3	a	15	[5.53]
		PdH _{0.014}	19	3	a	295	[5.52]
		PdH _{0.85}	25	3	a	80	[5.56]
		PdH _{0.99}	23	3	a	80	[5.56]
		Pd(H,D) _{0.6~0.7}	9.7	3	b	80	[5.68]
		Pd(H,T) _{0.6~0.7}	9.1	3	b	80	[5.68]
bcc	O	V ₂ H	≈0	1	a	80	[5.59]
			21	2	a	30	[5.57]
			22	2	a	80	[5.59]
			18	2	a	80	[5.72]
		V ₂ D	18	2	a	80	[5.72]
		V ₂ T	12	2	a	295	[5.72]
fcc	T	TiH ₂	-4.8	3	a	30	[5.64]
		ZrH _{1.41}	-7.0	3	a	30	[5.64]
bcc	T	NbH _{0.78}	-10	1	a	78	[5.80]
		NbH _{0.92}	-13	1	a	78	[5.80]
		NbD _{0.80}	-15	1	a	78	[5.80]
		NbD _{0.7}	-14	1	a	10	[5.76]
		Nb(H,D) _{0.8}	-19	1	b	10	[5.76]
		Nb(H,T) _{0.8}	-21	1	b	10	[5.76]
		Nb(H,D) _{0.8}	-10	2	b	10	[5.76]
		Nb(H,T) _{0.8}	-19	2	b	10	[5.76]
		TaH _{0.71}	-15	1	a	78	[5.80]
			-16	1	a	10	[5.76]
			-18	1	a	77	[5.76]
			-13	1	b	77	[5.76]
			-14	2	b	77	[5.76]
			-14	2	b	77	[5.76]

a. Comparison of fundamental and first overtone.

b. Comparison of fundamentals of different isotopes.

Table 5.6. Anharmonicity parameter ΔE^H for hydrogen atoms in higher hydrides of rare-earth metals; the case of dual occupancy of T and O sites in the fcc lattice. ΔE^H in meV

Sample	Site		Method	Temperature [K]	References
	O	T			
YD ₂		-1.2	a	10	[5.62]
Y(H,D) ₂		-0.9	b	373	[5.69]
LaD _{2.25}	- 0.8		a	8	[5.83]
La(H,D) _{2.98}	-0.1	-15.4	b	298	[5.71]
Ce(H,D) _{2.96}	-11.8	-7.1	b	298	[5.71]

- a. Comparison of fundamental and first overtone.
- b. Comparison of fundamentals of different isotopes.

In hexagonal metals, three-fold local symmetry along the *c*-axis around the T sites can be described conveniently in terms of spherical harmonics. The energy eigenvalues and wave functions can be calculated by the perturbation theory formally equivalent to the calculation of crystal-field splitting of atomic energy levels. Such calculations were performed by *Bennington et al.* [5.84–5.86], and all necessary coefficients are tabulated.

An example of such analysis on α -YH_{*x*} is shown in Fig. 5.26. The six observed peaks (1a through 2d) were assigned to transitions from the ground state (*nlm*) = (000) (1s state) to the excited states, as listed in Table 5.7. The quantum states are labeled by ordinary spectroscopic notations, and the assignment was made based on the orientation dependence of the intensities in single-crystal data. Choosing appropriate values for four potential parameters, they calculated the energies and wave functions (and hence intensities) of six transitions, the result of which is shown in Fig. 5.26 for comparison. The agreement with observation is satisfactory. The general shape of third-order transitions, not well resolved experimentally, is also fairly well reproduced by

Table 5.7. Vibrational energy levels of α -YH_{*x*}, A spectroscopic notation is used to describe the final quantum states [5.86]

Peak	Energy Levels Observed [meV]	Final state	Energy Levels Calculated [meV]
1a	100.0 ± 0.2	2 <i>p</i> ₀	100.0
1b	134.4 ± 0.1	2 <i>p</i> _{±1}	134.4
2a	185 ± 5	$\frac{2}{3}3d_0 + \frac{1}{3}3s$	185.3
2b	237.0 ± 0.5	$\frac{1}{3}3d_0 + \frac{2}{3}3s$	245.7
2c	253.0 ± 0.3	$\frac{1}{2}3d_1 + \frac{1}{2}3d_{\pm 2}$	253.0
2d	267.8 ± 0.2	$\frac{1}{2}3d_{\pm 1} + \frac{1}{2}3d_{\pm 2}$	267.8

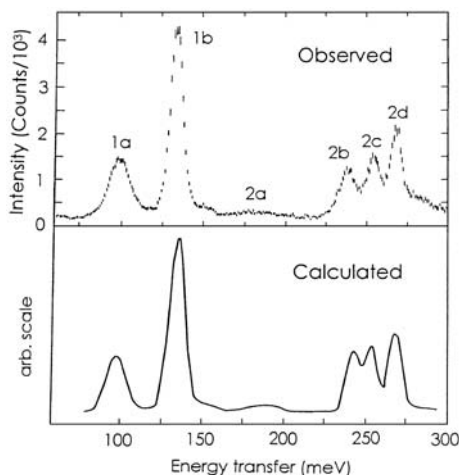


Fig. 5.26. Vibration energy spectrum of α -YH_x [5.84]. A spectrum calculated by Bennington and Ross [5.86] is shown for comparison

the calculation. High-resolution measurements showed fact that the 1a peak was split due to H–H interactions along the c -axis. The extreme broadening of the 2a peak suggests the H–H interactions extending to much longer distances. This problem, the formation of H–M–H pairs in the c -direction, will be discussed in more detail in Sect. 5.6.1.

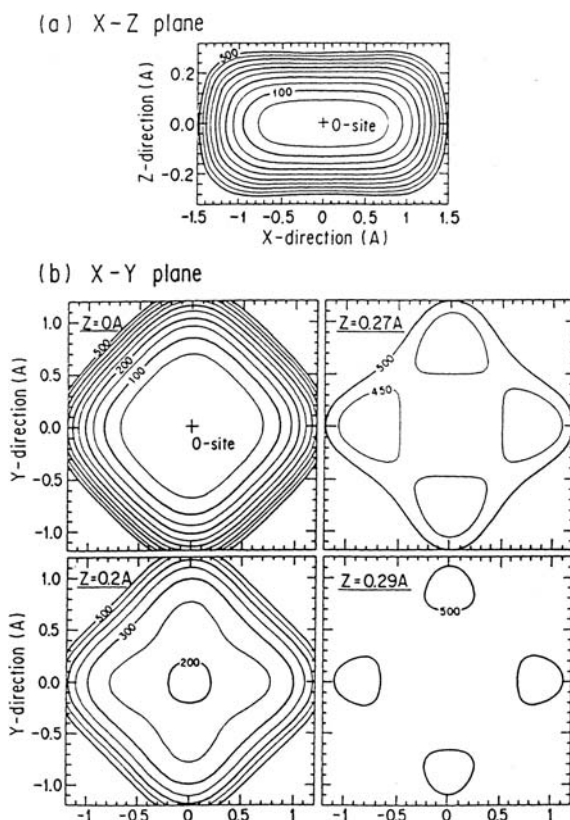
More about the potential field has been disclosed as more data have become available on higher excitation energies. For example, *Eckert et al.* [5.80] introduced a perturbing potential having the point symmetry of a T site in the bcc lattice (5.30), and determined some of the potential parameters from the observed (one or two) higher-harmonic excitations in the ordered phases of NbH_x, NbD_{0.80}, and TaH_{0.71}.

A more detailed analysis was made by *Ikeda and Watanabe* [5.58] of their data on NbH_{0.31} and VH_{0.33} (hereafter referred to as ϵ -NbH_{0.7} and β -VH_{0.5}, respectively, the actual phases under observation.) They adopted a potential of the form of (5.30) plus one additional term $c_6 Z^6$, and $e = 0$ for the O_Z site in β -VH_{0.5}. The potential parameters determined by using six observed vibration energies are listed in Table 5.8. For the remaining 3 ~ 5 observed transitions, the agreement between the experimental and the calculated values was reasonably good.

A contour map of the potential for H in β -VH_{0.5} is shown in Fig. 5.27 The potential has a rather flat bottom in the X – Y plane, but is very strongly compressed along the Z axis (note the difference in scales). The wave functions of hydrogen can also be calculated in the first-order perturbation as linear combinations of the harmonic-oscillator wave functions. The result for the ground state of H in β -VH_{0.5} has a strong anisotropy, consistent with the density maps shown in Figs. 5.12, 5.13.

Table 5.8. Potential parameters for H determined by fitting to the observed vibrational energies [5.58]

Parameter	β -VH _{0.5}	ϵ -NbH _{0.7}
$\hbar\omega_X$ [eV]	0.0152	0.147
$\hbar\omega_Z$ [eV]	0.218	0.130
e [eV \AA^{-4}]		1.246
f [eV \AA^{-4}]	0.565	30.77
g [eV \AA^{-4}]	-1.438	-4.23
C_{4X} [eV \AA^{-4}]	0.092	1.373
C_{4Z} [eV \AA^{-4}]	9.032	-3.807
C_{6Z} [eV \AA^{-6}]		2.272

**Fig. 5.27.** a and b. Contour maps of the potential for H in β -VH_{0.5} deduced from the observed vibration energies. Note that in (a) the scale in the Z direction (along the tetragonal axis) is enlarged by three times [5.58]

Hempelmann et al. [5.60] analyzed their data on β -VH_{0.5} in terms of a simple model potential. By noting that vibrational excitations in the X - Y plane as well as those in the Z direction are repeated regularly to high energies, they regarded these three modes as independent oscillators. Whereas the vibration in the Z direction can be regarded as a simple harmonic oscillator with $\hbar\omega_0 = 223$ meV, the ones in the X , Y plane exhibit a deviation from harmonic behavior at low excitation energies ($\beta > 0$). In order to model a harmonic potential with a flattened bottom, they added a small Gaussian function in the X , Y directions, and succeeded in reproducing the observed energy deviation. Roughly speaking, the potential in the X - Y plane has a comparatively flat bottom over distances of about 0.6 Å, whereas it is much more steeply varying in the c direction.

Rush et al. [5.72] later made comparative measurements of the vibration energies of V₂H, V₂D and V₂T, and examined the validity of this empirical potential of *Hempelmann et al.* [5.60]. The excitation energies predicted by the model for other isotopes were grossly at variance with observed values, especially for V₂T, from which they questioned the Hempelmann's ad hoc method of constructing the potential. We must note, however, that whereas most other data were taken at low temperatures, the V₂T data were taken only at room temperature where, being rather close to the β - α transition, the axial ratio c/a should be much smaller than at low temperatures. Thus a straightforward comparison between different isotopes may not be warranted. The extreme sensitivity of the potential in V₂H to the c/a ratio was demonstrated by the calculation of *Sugimoto* and *Fukai* [5.87] and *Sugimoto* [5.88] (see Sect. 5.7.2).

The large anharmonicity of the potential deduced for many cases (Tables 5.5, 5.6) questions the validity of the perturbation theory, and strongly indicates the necessity to treat the problem in more general terms. Such approaches based on detailed quantum-mechanical description will be given in Sect. 5.7. The neutron scattering results for hydrogen atoms trapped at impurity atoms are described in Sect. 5.6.2.

5.4.3 Determination of Hydrogen Wave Functions by Inelastic Neutron Scattering

Inelastic neutron scattering experiments can also be utilized for mapping out the wave functions of interstitial H atoms.

The intensity of the inelastic scattering of neutrons from state \mathbf{k}_i to \mathbf{k}_f ($\mathbf{Q} = \mathbf{k}_i - \mathbf{k}_f$), accompanying the vibrational excitation of H atoms from the ground state Ψ_0 to the excited states Ψ_α (with excitation energies near ΔE_m), is given by

$$I(\mathbf{Q}; E_m) = n \sum_{\alpha} \left\langle \left| \int \Psi_{\alpha}^*(\mathbf{R}) e^{i\mathbf{k}_i \cdot \mathbf{R}} V_{\text{int}} \Psi_0(\mathbf{R}) e^{-i\mathbf{k}_f \cdot \mathbf{R}} d\mathbf{R} \right|^2 \right\rangle \quad (5.36a)$$

$$= AP(\mathbf{Q}; E_m), \quad (5.36b)$$

$$P(\mathbf{Q}; E_m) = \sum_{\alpha} \left\langle \left| \int \Psi_{\alpha}^*(\mathbf{R}) e^{i\mathbf{Q} \cdot \mathbf{R}} \Psi_0(\mathbf{R}) d\mathbf{R} \right|^2 \right\rangle, \quad (5.36c)$$

where $A = nV_{\text{int}}^2$ is the strength of the neutron-H interaction V_{int}^2 times the number of H atoms n in the specimen. Thus, by measuring the \mathbf{Q} -dependence of the intensity of vibrational excitations, direct information on the wave functions of H atoms can be obtained. The temperature should be kept low enough to avoid the possible effects of vibrations of the host lattice.

Ikeda et al. [5.89] performed this type of experiment on ZrH_2 and $\text{NbH}_{0.7}$ at 20 K and obtained the following results.

In ZrH_2 , three peaks were observed at 147, 294, and 441 meV, at nearly equal intervals, and were considered to be due to transitions to the first, second, and third excited state in an isotropic harmonic potential. The \mathbf{Q} -dependence of the intensities for harmonic wave functions is given by

$$P^h(\mathbf{Q}; E_m) = C_m Q^{*2m} \exp(-Q^{*2}/2), \quad (5.37a)$$

$$C_1 = 1/2, \quad C_2 = 1/8, \quad C_3 = 1/48. \quad (5.37b)$$

with $Q^* = Q/\sqrt{M\omega/\hbar}$.

In Fig. 5.28, three solid curves have been calculated from (5.37) with $\hbar\omega = 147 \text{ meV}$ and $A_{\text{Zr}} = 12.5$. The agreement with observations is excellent.

In $\text{NbH}_{0.3}$, three peaks observed at 115, 220, and 161 meV were identified as corresponding, respectively, to the first and second excitations along the symmetry axis (Z) and the first excitation along the perpendicular

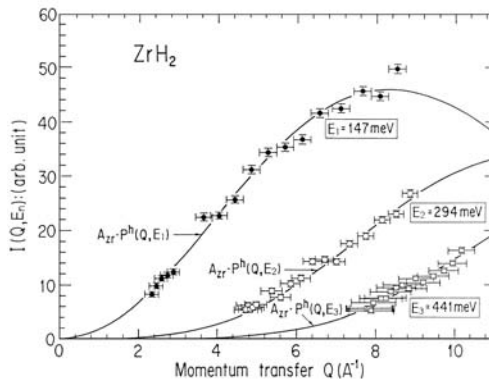


Fig. 5.28. Neutron scattering intensity $I(\mathbf{Q}; E_m)$ of ZrH_2 at 20 K [5.89]. Filled circles, open circles, and open squares show the observed values of $I(\mathbf{Q}; E_m)$ for $E_m = 147, 294$, and 441 meV , respectively. The curves have been calculated by assuming harmonic wave functions, with $A_{\text{Zr}} = 12.5$

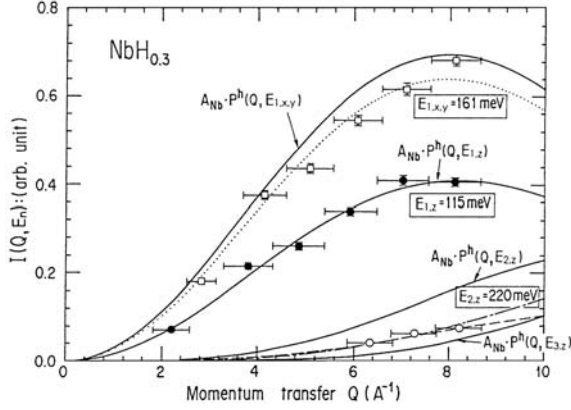


Fig. 5.29. Neutron scattering intensity $I(\mathbf{Q}; E_m)$ of $\text{NbH}_{0.7}$ at 20 K [5.89]. Filled circles, open squares, and open circles show the observed values of $I(\mathbf{Q}; E_m)$ for $E_m = 115$, 161, and 220 meV, respectively. The curves have been calculated by assuming harmonic wave functions, with $A_{\text{Nb}} = 36$

directions (X , Y). Following the results of their previous work [5.57], the ground-state wave function was approximately written as a product of harmonic wave functions in the three directions with two kinds of normal vibrations, $\hbar\omega_Z = 130$ meV and $\hbar\omega_X(\hbar\omega_Y) = 147$ meV (Sect. 5.4.2). The \mathbf{Q} -dependence of the intensity calculated in this way is shown in Fig. 5.29. The result agrees excellently with the observation for the ΔE_1^Z transition, but is slightly smaller for the $\Delta E_1^{X,Y}$ transitions, and appreciably smaller for the ΔE_2^Z transition. The discrepancy can be largely removed if the calculated values for the $\Delta E_1^{X,Y}$ and ΔE_2^Z transitions are multiplied by 0.92 and 0.47, respectively (dotted and broken lines). This reduction of intensities can be ascribed to the fact that the wave functions of the excited states are not totally confined to a single potential well but partially extended to neighboring interstitial sites (see, e.g., Fig. 5.72).

In these experiments, information on the excited-state wave functions was obtained from the \mathbf{Q} -dependence of the intensity by assuming a harmonic wave function for the ground state. Conversely, information on the ground-state wave function can be obtained by observing transitions to final states of sufficiently high energies well describable by plane waves. This type of experiment was also undertaken by Ikeda [5.90] on H and D in Pd, and revealed a significant isotope dependence of the ground-state wave functions.

5.4.4 Band-Mode Vibration of Hydrogen Atoms

In addition to optic-mode vibrations, there exists another mode of vibration of hydrogen atoms in the frequency range of acoustic phonons of a host lattice.

The first observation of such modes of vibrations was made by *Shapiro et al.* [5.91] on $\text{NbH}_{0.84}$ and $\text{NbD}_{0.85}$. Figure 5.30 shows the dispersion curves measured along the three symmetry directions [100], [110], and [111] in the α' phase (160°C) and β phase (20°C). Also shown for comparison are the measurements for pure Nb [5.92] and $\text{NbD}_{0.45}$ [5.93]. Two dispersionless excitations located at 10.8 and 18.4 meV are the new features observed in the presence of deuterons. These peaks are narrow (resolution-limited) in the ordered phase β but considerably broadened in the disordered phase α' . In contrast to optic-mode vibrations, these excitation energies are isotope-independent.

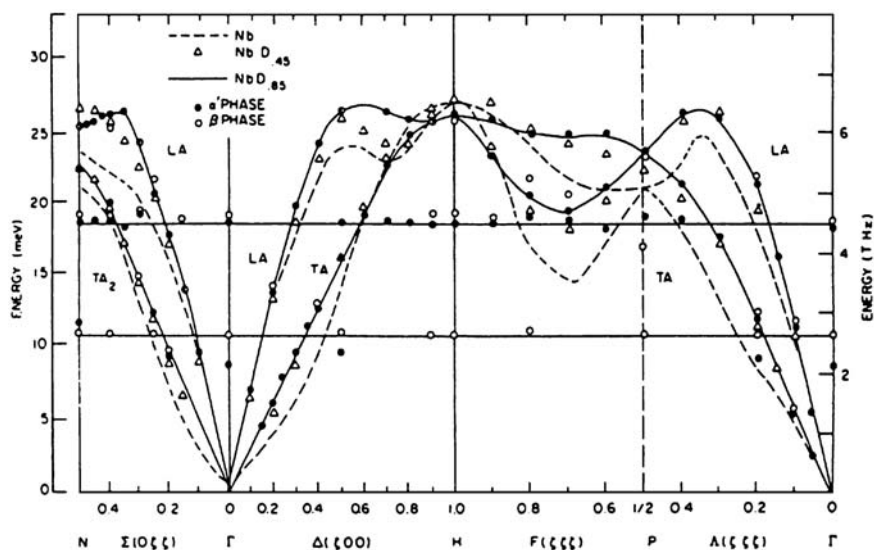


Fig. 5.30. Dispersion curves of $\text{NbD}_{0.85}$ in the α' phase (160°C) and the β phase (20°C) [5.91] compared with the results for pure Nb [5.92] and $\text{NbD}_{0.45}$ [5.93]

Subsequent work of *Lottner et al.* [5.94] also revealed a similar excitation peak at 15.7 meV in a dilute specimen of $\alpha\text{-NbH}_{0.005}$, which they interpreted as being a resonant-like motion of H atoms in phase with acoustic-mode vibrations of the host atoms [5.94, 5.95]. The frequency spectrum of the hydrogen vibration was calculated by Green's function technique for the following two models of coupling force constants. Model I considers only a longitudinal coupling with nearest metal atoms, adjusted to local-mode frequencies. Model II considers both longitudinal and transverse couplings, so chosen as to reproduce the long-range displacement field and the changes in the elastic constants.

Figure 5.31 shows the spectra of H vibrations, in the direction shown in the inset, calculated by these two models, together with the respective host spectra. In order to facilitate comparison in terms of vibration amplitude,

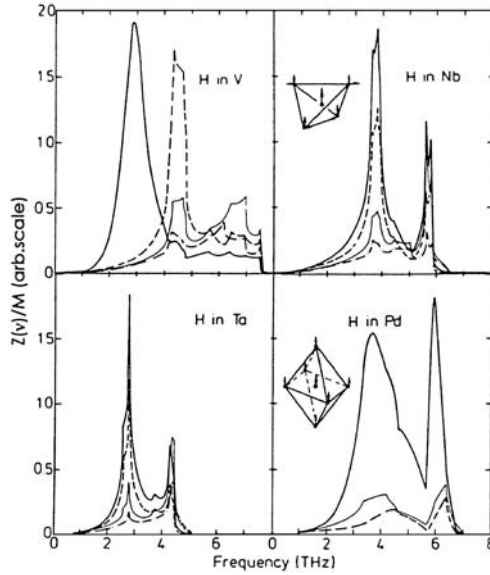


Fig. 5.31. Comparison of band-mode spectra of hydrogen with the host spectrum. —: model I ($\parallel Z$). ---: model II ($\parallel Z$). · - · - ·: model II ($\parallel X$). —: host spectrum [5.95]. 1 THz = 4.15 meV

hydrogen and host spectra have been divided by the respective masses. Although only a small fraction of the hydrogen vibration appears in the acoustic region, the low mass of hydrogen makes its amplitude comparable to (or even larger than) the host vibration. As can be seen in the inset, the displacement of a hydrogen atom is assisted by the outward displacement of a pair of metal atoms in front. There are two pronounced peaks, mirroring the host spectrum, located at 15.7 and 24.1 meV in Nb. *Lottner et al.* [5.94] and *Schober* and *Lottner* [5.95] calculated a vibrational spectrum by these two models, and found excellent agreement with observations (Fig. 5.32).

Due to the presence of the band modes, the total vibration amplitude of hydrogen atoms becomes much larger than what would result from optic-mode vibrations alone. The mean-square displacements consist of contributions from the localized and the band modes, $\langle u^2 \rangle^H = \langle u^2 \rangle_{\text{loc}}^H + \langle u^2 \rangle_{\text{band}}^H$, and each of these contributions can be calculated separately. The result of such calculations for H in V, Nb, Ta, and Pd is shown in Fig. 5.33. The band-mode contribution is very large and strongly temperature-dependent, and brings the calculation into good agreement with observations [5.96–5.98]. The strong temperature dependence comes from the low frequency of band-mode vibrations. This allows a classical treatment at ordinary temperatures, yielding a linear temperature dependence, $\langle u^2 \rangle_{\text{band}}^H \sim kT \langle \omega^{-2} \rangle_{\text{band}}^H$.

A possible implication of the band-mode vibrations in the migration process of H atoms has also been discussed [5.95].

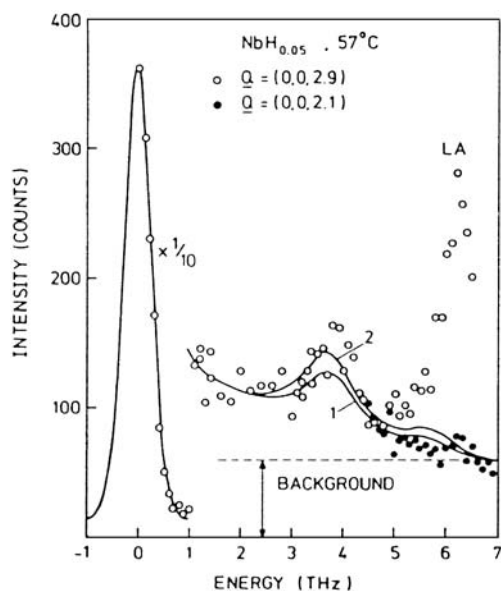


Fig. 5.32. Measured scattering intensity of $\text{NbH}_{0.05}$ compared with the theoretical values for model I (curve 1) and model II (curve 2) [5.94]

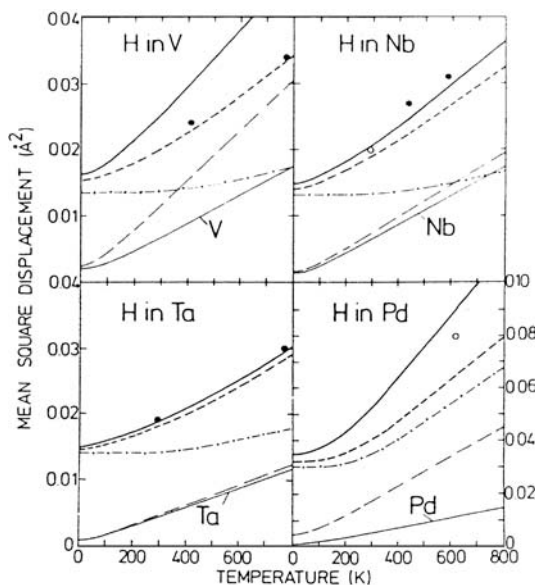


Fig. 5.33. Mean-square displacements. —: $\langle u^2 \rangle^{\text{H}}$ model I. ---: $\langle u^2 \rangle^{\text{H}}$ model II. ---: $\langle u^2 \rangle^{\text{H}}_{\text{band}}$ model I. ···: $\langle u^2 \rangle^{\text{H}}_{\text{loc}}$ model I. —: $\langle u^2 \rangle^{\text{H}}_{\text{host}}$ [5.95]. Experimental values: ● [5.96], Nb ○ [5.97], Pd ○ [5.98]

5.5 Stress-Induced States

Koike and *Suzuki* [5.99] discovered in their electron-microscopic studies of crack propagation in dilute V–H alloys (~ 0.1 at%) that H atoms were accumulated in the crack-tip region and induced a small tetragonal distortion of the lattice ($c/a \approx 1.02$). Later this stress-induced state was produced, reversibly, by application of a tensile stress of ~ 30 MPa (3 kg mm^{-2}) along the [001] crystal axis, and concomitant lattice distortion was measured [5.100]. The force-dipole tensor of this stress-induced state had intermediate features between the O-site and T-site occupancies, both in terms of dilatation and tetragonality (Table 5.2) [5.31].

Subsequent work of *Yagi et al.* [5.14, 5.15] established the configuration of this stress-induced state by the channeling method. The result of their first experiment is shown in Fig. 5.34a–c. When hydrogen was introduced from the gas phase at 150°C to form a solid-solution $\alpha\text{-VH}_{0.1}$ (the virgin α state), a channeling profile characteristic of T-site occupancy was observed, as shown in Fig. 5.34a. The profile changed after cooling the specimen to room temperature (b), and reheating it to 150°C (c). The observed site change is believed to be due to the internal stress introduced by thermal cycling, caused by precipitation and redissolution of the β phase. From the broadening of the X-ray diffraction line, the r.m.s. strain existing in the β -redissolved α phase was estimated at 2.6×10^{-4} , which corresponds to a stress of $\sim 4 \text{ kg mm}^{-2}$, consistent with the observation of *Suzuki et al.* [5.100]. The channeling profile (Fig. 5.34c) shows that, in the stress-induced state, H atoms are displaced from ordinary T sites towards O sites. From the position of the two small peaks in Fig. 5.34c, the displacement was estimated to be 0.44 \AA , which,

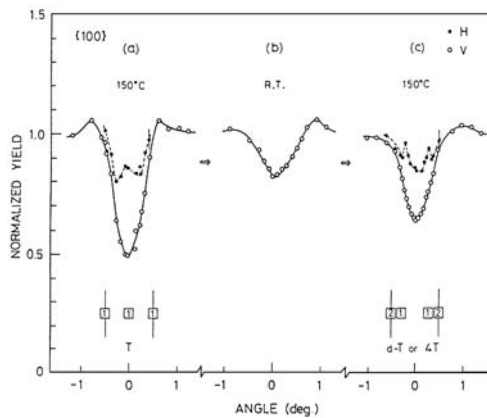


Fig. 5.34. a–c. A change of (100) angular profiles of α -particle and backscattered- ^{11}B yields in **a** the virgin α state (150°C), **b** the β -precipitated state (room temperature), and **c** the β -redissolved α state (150°C). The incident energy of the $^{11}\text{B}^{2+}$ beam is 2.02 MeV [5.14]

in comparison to the T–O distance of 0.76 \AA , means that the position of maximum density is closer to O sites than to T sites.

More precisely, the following two configurations are possible: a) an H atom confined to a single T site but displaced towards the nearest O site (displaced T, or dis-T), b) an H atom distributed symmetrically around a single O site, with density maxima localized around four positions located between the O site and the four nearest T sites (4T). The channeling experiment cannot distinguish between the dis-T and 4T configurations.

Subsequently, *Yagi et al.* [5.15] performed channeling experiments on $\alpha\text{-VH}_{0.010-0.015}$ under a compressive stress of 7 kg mm^{-2} , and again observed profiles characteristic of dis-T (4T) configurations which, after removal of the stress, recovered the original T-site form. The observed profiles are shown in Fig. 5.35. The profiles observed under the [001] compressive stress along the Z axis are consistent with dis-T or 4T configurations around $O_{X,Y}$ sites, shown schematically in Fig. 5.36; both (001) and (010) profiles consist of a dip and

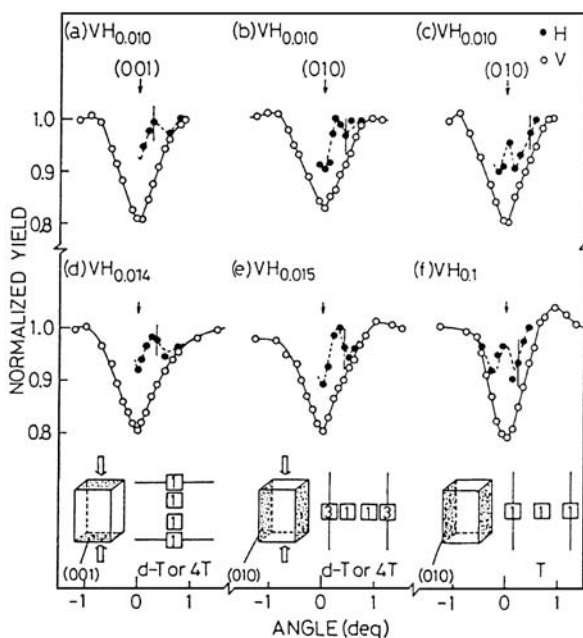


Fig. 5.35. a-f. (001) and (010) channeling angular profiles of backscattered ^{11}B and α -particle yields under the [001] compressive stress $\sigma = 1 \text{ kg mm}^{-2}$ (a, b, d, and e) or after releasing the stress (c) in $\text{VH}_{0.010}$, $\text{VH}_{0.014}$, and $\text{VH}_{0.015}$ (room temperature). The (010) angular profiles in virgin $\alpha\text{-VH}_{0.1}$ at 150°C under $\sigma = 0$ are shown in f. The full curves and the dashed curves have been drawn to guide the eye. The insets indicate the projections of T sites and displaced-T (dis-T) or 4T configuration onto the plane perpendicular to the (001) or (010) planar channel [5.15]

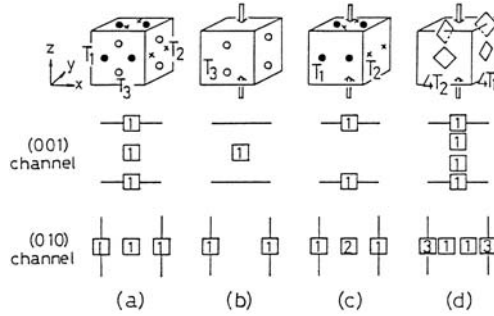


Fig. 5.36. a-d. Tetrahedral sites (a, b, and c), displaced-T or 4T configuration (d) and their projections onto the plane perpendicular to the (001) or (010) planar channel, without stress (a) and under the [001] compressive stress (b, c, and d) [5.15]

two subsidiary peaks superposed on it, and the (001) dip is shallower than the (010) dip.

Qualitatively, a continuous movement of the equilibrium position of hydrogen from a T site towards an O site under stress has been predicted by theoretical calculations [5.88] (Sect. 5.7.2), but the mechanism of how such small stresses could induce drastic site changes is hard to understand. The sharpness of the two subpeaks in Fig. 5.34 indicates that the stress-induced state has a well-defined configuration in spite of the possible inhomogeneous distribution of internal stress. Thus, it appears that the stress triggers a transition between the two well-defined configurations T and dis-T (4T).

In order to investigate the energetics of the stress-induced site changes, adiabatic calorimetry experiments were performed [5.101], in which transient temperature changes were measured on application and removal of the tensile stress. As shown in Fig. 5.37, hydrogen-induced temperature changes were observed, which started at about 10 MPa and nearly reached saturation at 40 MPa. The stress-induced change was found to be an exothermic reaction, indicating that hydrogen atoms transformed into a state of lower enthalpy (and entropy). The enthalpy change was, however, found to be very small, amounting to only $4.0 \text{ J (mol H)}^{-1}$ on an average, much smaller than the thermal energy of 2.4 kJ mol^{-1} at room temperature.

The following two interpretations were suggested for this small enthalpy change: First, in order that the two states differing in energy by $\delta E = 4 \text{ J (mol H)}^{-1}$ ($x\delta E = (\text{mol M})^{-1}$ for MH_x) can exist as two distinct states at a finite temperature, the fluctuation of the total energy of the system should be smaller than $x\delta E$, i.e.,

$$c_v k N_A T^2 / N \ll (x\delta E)^2, \quad (5.38)$$

where N is the number of M atoms in the system, and $c_v \approx 3kN_A$. From this, a criterion for the minimum number of M atoms contained in the system is

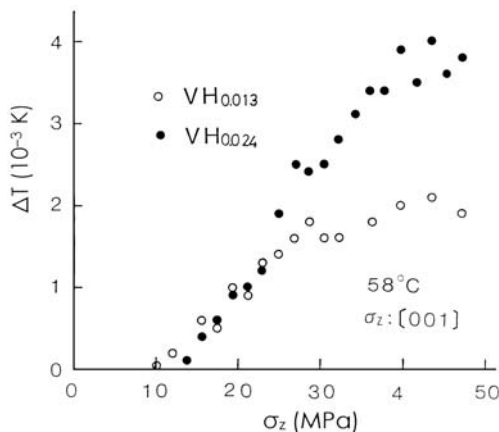


Fig. 5.37. Hydrogen-induced temperature changes on adiabatic stretching of single-crystal $VH_{0.013}$ and $VH_{0.024}$ along the $[001]$ axis at room temperature [5.101]

obtained as $N \gg 3(kN_A/x\delta E)^2 \approx 10^{10}$. This means that the stress-induced state is caused by some long-range cooperative transition, a so-called ferroelastic transition [5.102, 5.103], and the coherence length of the transition extends to about $0.5 \mu\text{m}$.

Second, there is a possibility that only a part of the H atoms went through site changes under the action of stress. If we assume that the conversion into the stress-induced state occurred only in the near-surface region probed by the channeling experiment, the actual enthalpy change per H atom participating in the transition should be obtained by dividing the observed value by the fraction of these H atoms. If the depth of the near-surface region is assumed to be $\sim 0.2 \mu\text{m}$, the actual enthalpy change per H atom becomes about 2 kJ mol^{-1} , quite a reasonable value for ordinary site changes of H atoms. As the lattice relaxation is expected to be easier in the near-surface region than in the bulk [5.104, 5.105], the possibility of the stress-induced state formed only in this region cannot be totally discarded.

Evidence of stress-induced site changes has also been obtained for D in V. *Takakusaki et al.* [5.106] examined the D density distribution in $VD_{0.3}$ by neutron diffraction, under application of elastic stress along $\langle 001 \rangle$ and $\langle 111 \rangle$ directions. The density redistribution caused by stress was clearly observed, but, due to the limited validity of their method of analysis, i.e. the population analysis of T and O sites fixed in their geometrical positions (Sect. 5.3), their density maps cannot be literally accepted as such. The importance of this experiment is that the density redistribution observed is the average over the whole sample, which indicates strongly that the formation of stress-induced states is not limited to the near-surface region but occurs in the bulk.

Subsequently, channeling experiments were also performed to investigate the stress-induced state of D in V. *Carstanjen* [5.5] observed distinct changes

in the (110) planar channeling profiles under application of compressive and tensile stress along the [001] axis, and showed that the observed profiles could be reproduced by assuming redistribution of D atoms between three types of T sites. However, this interpretation is not unique. The lower resolution of their experiment does not allow such detailed characterization of the stress-induced state as for H in V. Recently, we performed D-channeling experiments on the isotope-mixture samples of VH_xD_y and observed a site change in β -redissolved α -phase, closely similar to the case of H in V (Fig. 5.34) [5.107].

The formation of stress-induced states of H and D in V provides reasonable explanations for some peculiar observations made in the past on these systems.

Early neutron diffraction experiments on powder samples of $\text{VD}_{0.5}$ and $\text{VD}_{0.8}$ indicated that $\sim 10\%$ D atoms occupy O sites [5.108, 5.109]. But, this may well have been a convention to describe the dis-T (4T) configuration induced by the internal stresses. Specimens of V-H, D systems, if not very carefully annealed or if once subjected to thermal cycling which causes a precipitation of the β phase, should inevitably contain internal stresses large enough to convert the hydrogen site from T to dis-T (4T).

The excess specific heat due to H, D atoms in V can also be understood in terms of stress-induced states. In Fig. 5.38 the observed excess specific heats are shown as a function of temperature and compared with those calculated from the known vibrational energies of H, D atoms on O and T sites in V [5.110]. Here, a major contribution to the excess specific heat comes from the thermal excitation to higher vibrational states of H (D) atoms. (Changes in the lattice specific heat and the electronic specific heat are much smaller in

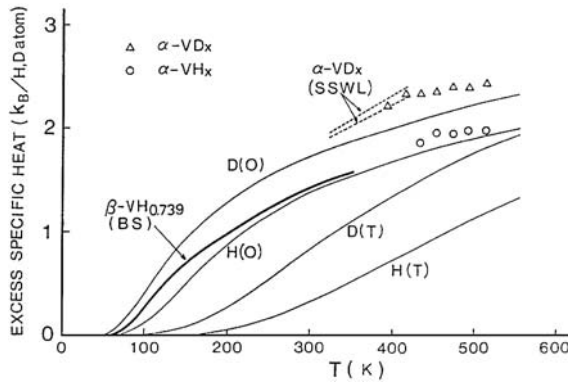


Fig. 5.38. Temperature dependence of the excess specific heat due to H, D atoms in VH_x and VD_x . Experimental data include those on $\alpha\text{-VH}_x$ (\circ) and $\alpha\text{-VD}_x$ (Δ) by Watanabe and Fukai [5.110], on $\alpha\text{-VD}_x$, by Sotzek *et al.* [5.111] (SSWL: dashed line), and on $\beta\text{-VH}_{0.739}$ by Bieganski and Stalinski [5.112] (BS: thick line). Curves labeled H(T) and D(T) are calculated by the Einstein model using INS data on T-site occupancy, and those labeled H(O) and D(O), on O-site occupancy

comparison.) The experimental data differ distinctly from the calculation for H, D atoms on T sites, but agree reasonably well with the calculated curves for O-site occupancy, with regard to their magnitude as well as temperature dependence. The isotope dependence is also nearly correctly reproduced. Stated more precisely, what one needs for explaining the excess specific heat of H, D atoms is that the excitation energies of the two (degenerate) modes are low (≤ 50 meV) and that of the remaining one is high (> 200 meV). This situation can be realized for the occupancy of O sites or dis-T (4T) sites close enough to O sites.

Actually, the inelastic scattering peaks observed in the α phase of V-H samples were much broader in width and weaker in intensity than those in the β phase, and the corresponding ones in the α phase of Nb-H and Ta-H systems (Fig. 5.23). This observation suggests that in α -VH_x only a small fraction of H atoms enter T sites, and their energies are rather widely distributed. Early experiments by *Rush* and *Flotow* [5.113] indicated that as the temperature was raised from the β -phase to the α -phase region for VH_{0.2} and VH_{0.4} samples, low-energy excitations below 30 meV were increased appreciably at the expense of the 50 meV peak characteristic of O-site occupancy in the β phase. Perhaps, these low-energy excitations, overlapping with the vibrational energies of the metal lattice, are those required for the explanation of the excess specific heat, and characteristic of the stress-induced state of H atoms in V.

The extreme sensitivity of the state of hydrogen to stress is a phenomenon peculiar to V. No such phenomena have been detected by channeling experiments on Nb or Ta in the course of thermal cycling and concomitant precipitation and redissolution of the hydride phase [5.16, 5.18]. Neutron diffraction experiments revealed, however, that very small (barely detectable) density redistribution was induced in NbD_{0.2} by straining the specimen to $\leq 2 \times 10^{-4}$ [5.114].

In order to determine the threshold stress for site changes, *Koike* and *Kojima* [5.115] performed resistivity measurements on VH_{0.0103}, NbH_{0.0369} and TaH_{0.0789} under the application of stress. Results they obtained are shown in Fig. 5.39. The measurements were made for three principal directions, a tensile stress applied along the [001], [110] and [111] axis, and the applied stress along the $\langle 110 \rangle$ and $\langle 111 \rangle$ directions has been divided by $\sqrt{2}$ and $\sqrt{3}$, respectively, to convert them into equivalent $\langle 001 \rangle$ tensile stresses. A threshold tensile stress can be located at ~ 10 MPa for V, ~ 25 MPa for Nb and ~ 20 MPa for Ta. For H in V, this value agrees with the result of calorimetry (Fig. 5.37). These results indicate that the stress-induced state change does take place in Nb and Ta as well, but at threshold stresses much higher than in V, and with magnitudes (fractions of H atoms undergoing the state change) much smaller for a given concentration of hydrogen. These results are consistent with our experience (described above) in the relative stress sensitivity of these metals.

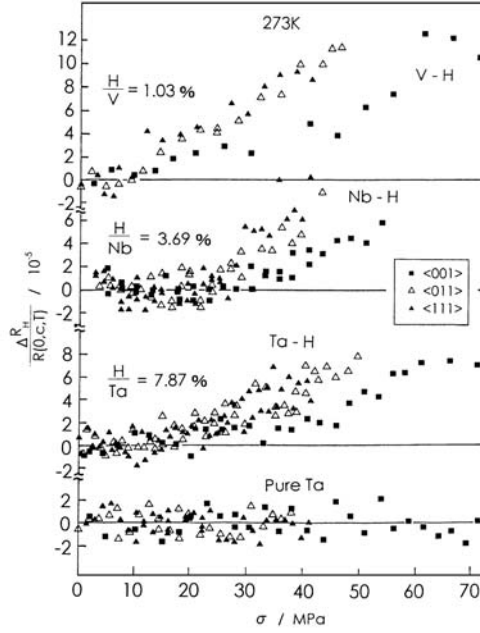


Fig. 5.39. Resistivity increment as a function of tensile stress along the [001] axis in $\text{VH}_{0.0103}$, $\text{NbH}_{0.0369}$ and $\text{TaH}_{0.0789}$, measured at 273 K. Tensile stress was applied along the [001] axis (\blacksquare), [110] axis (\triangle) and [111] axis (\blacktriangle), and the stress in the latter two cases has been divided by $\sqrt{2}$ and $\sqrt{3}$, respectively, to convert them into equivalent [001] tensile stress [5.115]

The stress sensitivity of these metals is believed to be closely related to the general trend in the site preference that O sites become more easily accessible in metals having smaller atomic volumes. The fact that a bct structure isomorphous to $\beta\text{-VH}_x$ occurs only under high pressures in NbH_x and TaH_x is also in line with the appearance of the stress-induced state (Sect. 4.4). The mechanism of $\text{bcc} \rightarrow \text{bct}$ transition will be discussed in more detail in Sect. 5.7.2.

5.6 Trapped States

Macroscopic, thermodynamical aspects of trapping have already been described in Sect. 3.3. In this section, we focus our attention on the atomistic configuration of hydrogen atoms – in the form of pairs between themselves, with impurity atoms or lattice defects, predominantly M-atom vacancies.

5.6.1 Mutual Trapping–Hydrogen Pairs in Some Rare-Earth Metals

As described in Sect. 2.4.3, some rare-earth metals exhibit anomalous terminal solubilities of hydrogen: they become independent of temperature and, therefore, appear vertical on the phase diagram. According to our present understanding, the origin of this anomaly is that hydrogen atoms in the α phase form pairs as the temperature is lowered below 400 K, and these pairs tend to form a long-range order at still lower temperatures (150 ~ 180 K).

A pairing of hydrogen atoms on the neighboring T sites, first proposed for an explanation of the resistivity anomalies in the α phase of these systems, was later rectified on the basis of diffuse neutron scattering experiments on $\text{LuD}_{0.19}$ [5.116] and $\text{YD}_{0.17}$ [5.117, 5.118] to be the pairing of two hydrogen atoms on the next-nearest T sites bridged by a metal atom along the c axis. Inelastic neutron scattering experiments on $\text{YH(D)}_{0.18}$ described below [2.133] have helped clarifying the mechanism of this pair formation.

Anderson et al. [2.133] measured the vibrational energies in single crystals of $\text{YH}_{0.18}$ and observed two prominent peaks at 100 and 138 meV, the former being observable only for the momentum transfer parallel to the c -axis and the latter perpendicular to the c -axis. Thus, these peaks were assigned unambiguously to the excitations of vibrational modes along the c -axis and in the basal plane, respectively. A similar observation and assignment was also made on $\text{YD}_{0.18}$.

These results were, in fact, quite unexpected because Y metal has an hcp structure with very nearly the ideal c/a ratio (smaller than 1.633 by less than 3%), and accordingly, the three vibrational modes are expected to be nearly degenerate. The smaller excitation energy along the c -axis than in the basal plane indicates that the potential around a T site is anisotropic, having a small curvature in the c direction, and allows hydrogen atoms to be displaced relatively easily along the c -axis.

Temperature dependence of the excitation along the c -axis provided clear evidence for the state change occurring in the α phase, as shown in Fig. 5.40 [2.133]. At 300 K, the spectrum is a single broad peak centered at 74 meV, which evolves at 240 K into a more complex shape and, finally, splits into two separate peaks at 73 and 77 meV at lower temperatures (200 and 8 K). The peak splitting is dependent on hydrogen concentrations; the splitting occurs only at high concentrations of hydrogen (Fig. 5.41) [5.119].

These results can be naturally interpreted in terms of pair formation. The central peak located at 74.7 meV corresponds to the vibration of isolated D atoms, while the remaining two peaks correspond to vibrational levels split by the interaction between D atoms in a pair. From the intensities of the peaks, the fraction of D atoms forming pairs at 240 K was estimated as ~33%, in good agreement with the result of diffuse neutron scattering [5.118].

The simplest phenomenological model for these observations is based on an elementary pair of coupled harmonic oscillators described by the potential

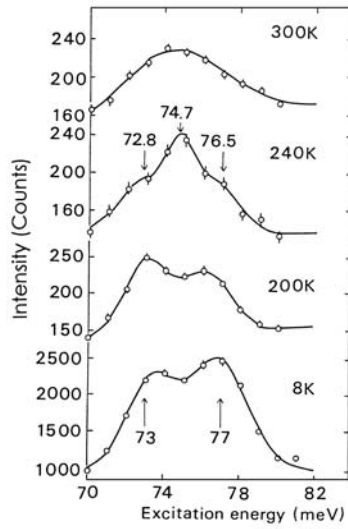


Fig. 5.40. Measured vibration spectra for polycrystalline $\text{YD}_{0.18}$ as a function of temperature [2.133]

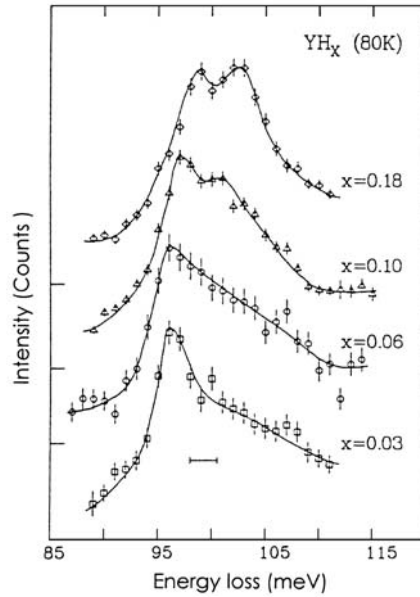


Fig. 5.41. Measured vibration spectra in YH_x as a function of hydrogen concentration [5.119]

function

$$U = \frac{1}{2}\kappa(Z_1^2 + Z_2^2) + \frac{1}{2}\kappa'(Z_1 - Z_2)^2, \quad (5.39)$$

where Z_1 and Z_2 represent the displacements of the two hydrogen atoms along the c axis. The presence of the second term causes splitting of the local optic mode from the local acoustic mode of vibration. Assuming $\kappa' \ll \kappa$, the two frequencies are obtained as $\omega_0 = \sqrt{\kappa/M}$ and $\omega_0(1 + \kappa'/\kappa)$. The splitting of the peaks gives a measure of the coupling strength.

Equation (5.39) can also be solved for a pair consisting of two different isotopes, say H and D, and many of the predictions of the model in this case were actually verified in subsequent isotope-mixture experiments [5.119].

Vibration energies measured in $\text{ScH}(\text{D})_x$, $\text{YH}(\text{D})_x$ and $\text{LuH}(\text{D})_x$ are summarized in Table 5.4. The ratio of excitation energies of c -parallel to c -perpendicular mode is nearly the same, but the splitting and width of the peak of c -parallel mode varies in the order $\text{Sc} \rightarrow \text{Lu} \rightarrow \text{Y}$. As shown in Fig. 5.42, the splitting increases, whereas the width decreases in this order [5.62]. This in fact agrees with the order of increasing lattice parameter and decreasing c/a ratio, but a possible implication of this fact has not been well understood so far.

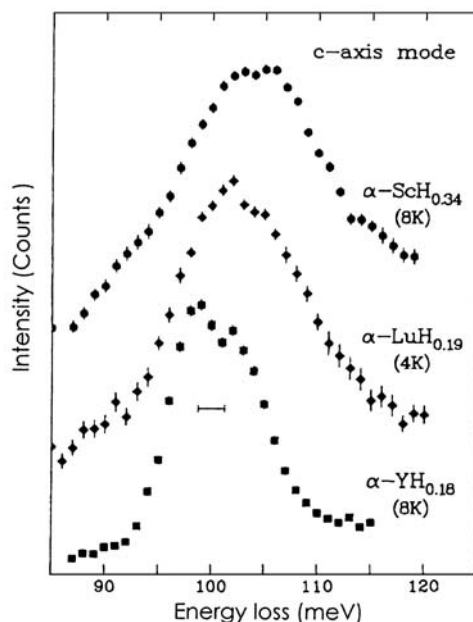


Fig. 5.42. Variation of the splitting and width of the peak of c -parallel mode in ScH_x , LuH_x and YH_x [5.62]

The configuration of H–M–H pairs, deduced from diffuse neutron scattering on LuD_x , is shown in Fig. 5.43 [5.120]. This alignment of pairs is believed to be a common feature of all the anomalous rare-earth metals, and its development into long-range order at low temperatures to be the cause of observed resistivity anomalies. The details of spatial correlation between adjacent chains are still under discussions, however [5.117, 5.121].

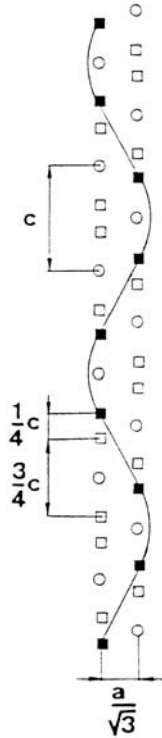


Fig. 5.43. Schematic representation of a chain structure of hydrogen pairs along the c -axis. ● M-atom, ■ T-site occupied by H-atom. □ empty T-site [5.120]

5.6.2 Trapping by Impurity Atoms

Interstitial impurities such as N and O are known to enter O sites in bcc metals, and trap hydrogen atoms in their vicinity. The first direct information on the configuration of this kind of complexes was derived by channeling experiments on the V–O–D system by *Ozawa et al.* [5.11]. They found that a channeling profile came to have O-site character when D atoms coexisted with interstitial O atoms, although the statistics of the data was not sufficient to elucidate the trapped configuration.

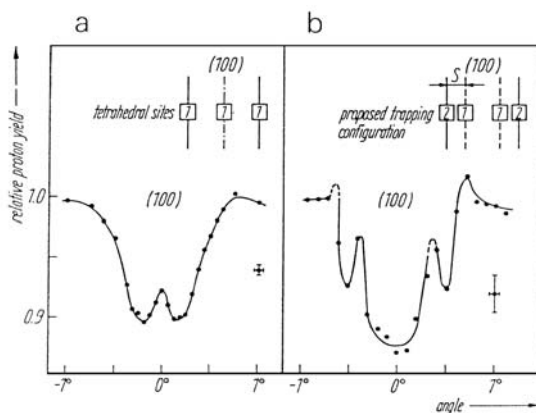


Fig. 5.44. **a** and **b.** Ta–D and Ta–N–D channeling yield profiles of the $D(^3\text{He}, p)\alpha$ reaction from the (100) planar scans: **(a)** $\text{TaD}_{0.067}$ at 295 K, with D atoms occupying T sites; **(b)** $\text{TaN}_{0.015}\text{D}_{0.005}$ at 83 K, with D atoms trapped by N atoms occupying displaced T sites [5.5]

Subsequently, channeling experiments on the Ta–N–D system revealed that D atoms are located at positions displaced from normal T sites [5.5]. The channeling profiles of D atoms observed in the absence and presence of N atoms in Ta are shown in Fig. 5.44. The profile for Ta–N–D is very similar to that observed for the stress-induced states of H in V (Figs. 5.35, 36), and suggests that D atoms occupy displaced T (dis-T) sites. The occurrence of the dis-T configuration is naturally understandable because an N atom on an O_Z site, say, causes a large local stretching of the lattice along the Z direction and, hence, tends to displace the equilibrium positions of T sites around the neighboring O_Z sites towards these O_Z sites.

X-ray measurements of Huang scattering and lattice parameter changes showed that the force-dipole tensor of an H atom in Nb is changed by trapping at an interstitial N atom: $A + 2B$ is reduced by 10–20% and the tetragonality parameter $3|A - B| / (A + 2B)$ is increased from ≈ 0.06 to 0.24 ± 0.06 [5.122]. Both these changes are characteristic of the transition from a T site to an O site through dis-T configuration. A comparison of this tetragonality parameter with that of O-site occupancy (Table 5.2) suggests that the trapped site should be closer to T sites than to O sites in this particular case.

Internal-friction experiments on O–H (and N–H) complexes in Nb showed that most of the complexes are directed along the [111] direction at low temperatures (≤ 80 K) [5.123, 5.124], whereas at higher temperatures (~ 200 K) other pairs directed along the [100] and [110] directions appear to exist [5.125]. Two distinct relaxation peaks were also observed in the temperature dependence of internal friction [5.126].

Inelastic neutron scattering experiments have shown that vibrational energy levels of H atoms when trapped at N or O in Nb [5.127] and N in Ta [5.128] are only slightly perturbed (Table 5.9). This implies that the local atomic configuration around H atoms in the trapped state is very nearly the same as in the ordinary state of T-site occupancy. The trapped H atoms should not be too close to the impurity atoms. Furthermore, specific-heat measurements and inelastic neutron scattering experiments performed at very low temperatures have revealed the formation of a tunnel-split state, formed from the ground states localized on two adjacent equivalent sites. The distance between the two sites, estimated to be $\sim 1 \text{ \AA}$, is consistent with the separation between the dis-T sites. (For details, see Sect. 5.8.1.)

Table 5.9. Vibrational energies of H atoms trapped by N and O in Nb [5.127] and N in Ta [5.128]

Sample	Vibrational Energies		T [K]
	[meV]		
NbN _{0.004} H _{0.003}	106 ± 1.0	157 ± 2.5	10
NbO _{0.011} H _{0.010}	108 ± 1.5	159 ± 3	4
α -NbH _{0.0055}	106	167	300
ε -NbH _{0.7}	117 ± 1	167 ± 2	78
TaN _{0.006} H _{0.003}	113 ± 1	163	1.4
α -TaH _{0.086}	113	163	295

These considerations lead to the following picture, shown in Fig. 5.45. An H atom trapped at an interstitial atom (O, N, C) in a bcc lattice occupies one of the tunnel-split states formed from pairs of equivalent dis-T sites. A pair a–a is considered to be energetically most favorable, as suggested in [5.127], but at least one of the other pairs appears to exist as well.

Regarding hydrogen atoms trapped at substitutional impurity atoms, microscopic information has been rather limited. *Yagi et al.* [5.129] performed first detailed lattice location studies on H atoms trapped at Mo in Nb by the channeling method. Their measurements were made on a specimen of Nb_{0.97}Mo_{0.03}H_{0.02} at room temperature, and on Nb_{0.97}Mo_{0.03}H_{0.05} at room temperature and 100°C (Points A, B, and B', respectively, in Fig. 5.46). It was found that, although A and B' are both located in the α -phase region, hydrogen atoms occupy different types of sites – a trapped site in A and an ordinary T site in B', and partitioned between these two types of sites in B. The configuration of the trapped hydrogen atom deduced from the angular profiles of the reaction-yield α particles is shown in Fig. 5.47. A hydrogen atom is attracted to a Mo atom by about one-third of their original separation. Strictly speaking, there is no way to determine directly the position of H atoms relative to Mo atoms. However, in view of the smaller size of a

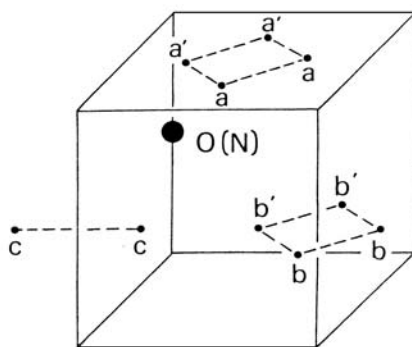


Fig. 5.45. Possible pairs of equivalent dis-T sites occupied by an H atom trapped at an interstitial O (N) atom in a bcc lattice; a-a, a'-a', b-b, b'-b' and c-c. A pair a-a is considered to be the most likely, but other pairs cannot be totally excluded

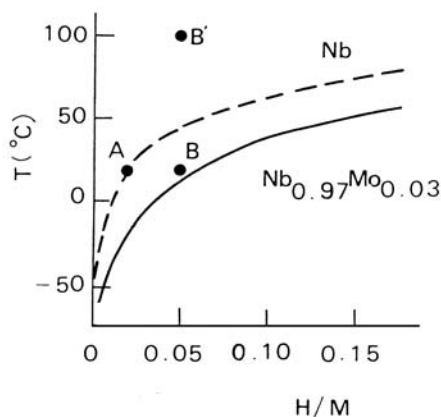


Fig. 5.46. Experimental conditions (A, B, B') in comparison to the terminal solubility of hydrogen in $\text{Nb}_{0.97}\text{Mo}_{0.03}\text{-H}$ and Nb-H systems [5.129]

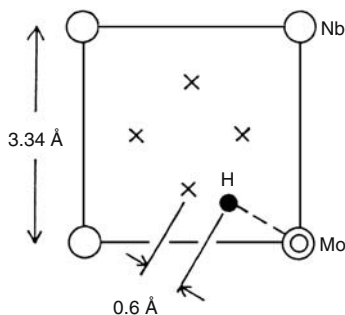


Fig. 5.47. Lattice location of an H atom trapped by a Mo atom in Nb [5.129]

Mo atom in comparison to a Nb atom, the configuration as shown, i.e. the nearest T site attracted to Mo, is believed to be most probable. The binding energy was estimated from this experiment to be about 0.05 eV, in reasonable agreement with the previous determinations by other techniques [5.130].

Vibrational states of H atoms trapped at substitutional impurities have been investigated for Ti, Cr [5.131], and V [5.132] in Nb. In $\text{NbTi}_{0.01}\text{H}_{0.009}$, two fundamental excitation energies were located at 105.0 ± 0.5 and 153.0 ± 2.0 meV, the latter being appreciably lower than those characteristic of ordinary T-site occupancy (106 and 163 meV). In the case of $\text{NbCr}_{0.009}\text{H}_{0.009}$, the lower fundamental excitation was located at 123.3 ± 0.8 meV, being appreciably higher than that for T-site occupancy. The fact that the excitation energies are significantly affected by trapping indicates that H atoms are located close to the impurity atoms.

A qualitatively different result was obtained for $\text{Nb}_{0.93}\text{V}_{0.07}\text{H}_{0.07}$. Excitation energies characteristic of T-site occupancy in α and β (hydride) phases were not affected by the presence of V atoms, but at low temperatures another state of H atoms, having excitation energies of 40 and 90 meV, was found to coexist with the β phase. From the temperature dependence of the population of H atoms in this state, the binding energy was estimated to be 10–20 meV. Probabilistic analysis has led to the conclusion that these low-energy excitations are due to H atoms on O sites associated with pairs of V atoms. A detailed configuration of this state is not known, however.

In more concentrated alloys, $\text{Nb}_{0.5}\text{V}_{0.5}$ [5.133], $\text{Ti}_{0.75}\text{V}_{0.25}$ [5.134], $\text{Nb}_{0.5}\text{Ti}_{0.5}$, and $\text{Ti}_{0.8}\text{Mo}_{0.2}$ [5.135], internal-friction experiments provided evidence for O-site occupancy of H atoms. In these alloys, a pronounced internal-friction peak was observed around 100 K, and was attributed to stress-induced reorientation (Snoek effect) of H atoms on O sites. The magnitude and anisotropy of the strain tensor deduced from these experiments are also consistent with the notion of O-site occupancy. The O-site occupancy of D was also observed in a concentrated Nb–Mo alloy (20 at% Mo) by the channeling method [5.136], in contrast to the T-site occupancy observed in a dilute alloy (3 at% Mo) [5.129]. Taken altogether, these observations appear to suggest that in bcc alloys, the site occupancy changes in the order $\text{T} \rightarrow \text{dis-T} \rightarrow \text{O}$ with increase of solute concentrations.

A systematic investigation of site changes with alloy composition has been pursued by Yagi *et al.* on Nb–Mo alloys up to the composition of 26 at% Mo [5.137–5.139]. For low H concentrations ($[\text{H}]/[\text{M}] \leq 0.06$) at room temperature, a fraction of H atoms in the trapped state (described above) was $\sim 100\%$ for 3 at% Mo, but decreased to 40 \sim 60% in 10 at% Mo, and became vanishingly small in 20 at% Mo alloy. The rest of H atoms were on T sites. The O-site occupancy became visible at 20 at% Mo (20 \sim 30%), but this also diminished with increasing Mo concentration, and returned to $\sim 100\%$ T-site occupancy in the 26 at% Mo alloy.

Recognizing that Mo atoms are smaller in size and have less chemical affinity to H than Nb atoms, *Yagi et al.* proposed the following explanations for the observed site changes [5.138]. The initial trapped state is realized by the elastic interaction – an attraction caused by undersized Mo atoms, but its configuration comes to be smeared with increasing solute concentrations due to overlapping distortions. Subsequently, a decrease of the average lattice parameter tends to favor the O-site occupancy, according to the general trend of site occupancy in bcc metals. At still higher Mo concentrations, the chemical effect overtakes the elastic effects: As the total number of $[\text{Nb}_4]$ sites is nearly twice as many as $[\text{Nb}_6]$ sites in 26 at% Mo alloy and even more in higher-Mo alloys, the fraction of T-site occupancy should increase with increasing Mo content.

In their more recent experiments, *Yagi et al.* [5.140] found that the occupancy of displaced T sites became dominant in a more concentrated (50 at%) Mo alloy. A dis-T site occupancy was also found to be dominant in a $\text{Nb}_{0.95}\text{Ta}_{0.05}$ alloy, in which the size misfit between the two metal species is small. The occurrence of dis-T site occupancy in these cases, in addition to the stress-induced case in V, suggests that the dis-T configuration is a very stable one realized under widely different conditions. The origin of this stability of the dis-T configuration has not been understood.

Thermodynamical consequences of site occupancies in alloys were discussed in Chap 3.

5.6.3 Trapping by Defects

It has been widely recognized that interstitial hydrogen atoms are trapped by various types of lattice defects – point defects, dislocations, grain boundaries, voids, etc. The trapping affects the solubility and diffusivity of hydrogen on one hand and properties of the traps on the other. Here we deal specifically with microscopic aspects of trapping by vacancies and their agglomerates (voids). Trapping by self-interstitials is usually much weaker, and the effects of trapping by dislocations are described in the following review articles [3.77, 5.141].

Effects of hydrogen on vacancy migration are manifested in the retardation of Stage III recovery process¹. *Schultz* [5.142] and *Kugler et al.* [5.143] measured the recovery process of the electrical resistivity of electron-irradiated Nb, and found that the temperature of Stage III in a hydrogen-free sample ($[\text{H}]/[\text{Nb}] < 1$ ppm), $T_{\text{III}} \approx 200$ K, was shifted to $T'_{\text{III}} \approx 350$ K in a sample containing 20 ppm of hydrogen. Similar observations were also made on Ta. For this shift of the recovery temperature, two alternative

¹ Point defects introduced at low temperatures by various techniques (quenching from high temperatures, electron or neutron irradiation, etc.), change their state and decrease in number in several stages on subsequent annealing. Stage III corresponds to the temperature where monovacancies start migrating.

interpretations are possible, namely that it is either due to the onset of migration of Vac-H complexes or of vacancies liberated by the dissociation of the complexes.

The positron annihilation spectroscopy (PAS) performed by *Hautojärvi et al.* on Nb and Ta provided more definitive information on the annealing process of vacancies introduced by electron and neutron irradiations [5.144, 5.145]. The lifetime spectroscopy allowed to isolate the positrons trapped at monovacancies and Vac-H complexes, and their variation in the annealing process. Thus in Nb, the onset temperature of Stage III was shifted from $T_{\text{III}} \approx 190$ K to $T'_{\text{III}} \approx 380$ K, and in Ta, from $T_{\text{III}} \approx 240$ K to $T'_{\text{III}} \approx 440$ K. Assuming that the shifted recovery temperature marks the dissociation of Vac-H complexes, we may estimate the Vac-H binding energy from the following approximate relation [5.146]

$$\frac{e_{\text{m}}^{\text{v}}}{T_{\text{III}}} \approx \frac{e_{\text{m}}^{\text{v}} + e_{\text{b}}}{T'_{\text{III}}}. \quad (5.40)$$

Substituting $e_{\text{m}}^{\text{v}} = 0.55$ eV for Nb and $e_{\text{m}}^{\text{v}} = 0.7$ eV for Ta [5.147], we obtain $e_{\text{b}} = 0.55$ eV for Nb and $e_{\text{b}} = 0.58$ eV for Ta.²

Similar estimation of the Vac-H binding energies by PAS was made on Al [5.148], Ni [5.149, 5.150], Cu [5.151] and Mo [5.149]. The results are listed in Table 5.10.

The positron annihilation spectroscopy is a technique particularly sensitive to vacancy-type defects, in which the lifetime of positrons is made longer by the reduced electron density and assumes values specific to the type of defect. The sensitivity is such that it detects the presence of monovacancies of concentrations of the order of 10^{-7} . There is, however, a problem in applying this method to Vac-H complexes. The trapping power of a vacancy should be weakened when it is preoccupied by H atom(s). Whether a Vac-H complex can trap positrons has to be examined in each case.

By far the more powerful technique for investigating the interaction of hydrogen with defects is the combination of ion implantation and channeling. Ion implantation was conveniently utilized for doping hydrogen in metals having low solubilities of hydrogen. However, with the growth of experimental data, it became clear that channeling experiments on implanted hydrogen atoms (D in most cases) did not give information on the intrinsic lattice location but, instead, on the configuration of D atoms trapped at implantation-induced defects. Evidence for trapping includes the following: a) The location of implanted D atoms is in many cases displaced from the ideal T- or O-site positions, being different from those introduced from the gas phase, b) Implanted D atoms stay in the near-surface region even at temperatures where, without trapping, they should be sufficiently mobile to diffuse out of the region.

² The assignment of *Hautojärvi et al.* [5.145] of the activation energy for T'_{III} in the hydrogen-containing sample to $e_{\text{m}}^{\text{H}} + e_{\text{b}}$ is not correct.

Table 5.10. Binding energies of hydrogen atoms with monovacancies and bubbles/voids, obtained by various methods; including ion implantation/channeling (I/C), positron annihilation spectroscopy (PAS), superabundant vacancy formation/thermal desorption spectroscopy (SAV/TDS). All energies are in eV

Metal	Vacancy	Bubble/Void	Method	Reference
Al	~0.52	≤ 0.52	I/C	[5.176]
	0.53		PAS	[5.148]
V	0.11		I/C	[5.177]
	0.23		I/C	[5.19]
Cr	0.89, 0.73		SAV/TDS	[4.44]
Fe	0.63, 0.43		I/C	[5.175]
Ni	0.44, 0.28	0.55	I/C	[5.163]
	0.58		PAS	[5.149]
	0.44		PAS	[5.150]
	0.43, 0.27		SAV/TDS	[5.178]
	0.45, 0.28		SAV/TDS	[5.179]
Cu	0.42, 0.22		I/C	[5.167]
	0.37, 0.23		SAV/TDS	[5.179]
Zr	0.28		I/C	[5.180]
Nb	0.55		PAS	[5.144, 5.145]
Mo	1.03, 0.80	1.15	I/C	[5.176]
	1.4		PAS	[5.149]
Pd	0.23, 0.15	0.31	I/C	[5.153, 5.181]
Ta	0.58		PAS	[5.145]
W	0.42	0.53	I/C	[5.182]
	1.43		I/C	[5.183]

Great effort has been devoted to investigate the properties of implanted hydrogen, because of its technological importance in nuclear fusion reactors. In present-day plasma machines, high fluxes of hydrogen isotopes are implanted into the first walls surrounding the plasma. The retention in the near-surface region, the diffusion into the bulk, and the re-emission of hydrogen in the plasma are of importance for the composition and temperature of the plasma, the mechanical properties of the wall, and the tritium inventory in future devices.

A number of review papers have been written on this subject, including those concerned with macroscopic aspects of trapping–detrapping kinetics [5.152–5.154], microscopic aspects like lattice locations and binding energies of trapped states [5.155, 5.156], and the most comprehensive reviews by *Myers et al.* [5.141, 5.157]. Here we focus on microscopic aspects of implanted D atoms after a brief description of the situation produced in actual implantation–channeling experiments.

Usually, samples are prepared by implanting D atoms at low temperatures (10–100 K), at an energy of 10–20 keV to a fluence of 10^{15} – 10^{16} D atoms

cm^{-2} . The implanted D atoms produce Frenkel defects (self-interstitials + vacancies), in the form of close pairs and/or isolated ones, as they collide with the lattice atoms before they come to rest in the lattice. As shown in Fig. 5.48, the distributions of the implanted D atoms and Frenkel defects overlap with each other, with a maximum located at $600 \sim 800 \text{ \AA}$ from the surface [5.152]. As interstitial atoms are much more mobile than vacancies, many Frenkel defects are annihilated below $\sim 100 \text{ K}$, leaving nearly one vacancy per incident D atom on average. A majority of incident ^3He ions which have passed the D-implanted region without causing the nuclear reaction come to rest at a depth of $\sim 1 \mu\text{m}$, and produce lattice defects with a distribution closely similar to that of ^3He ions. As the solubility of He is vanishingly small in all metals, the implanted ^3He atoms coagulate into bubbles as soon as they become mobile.

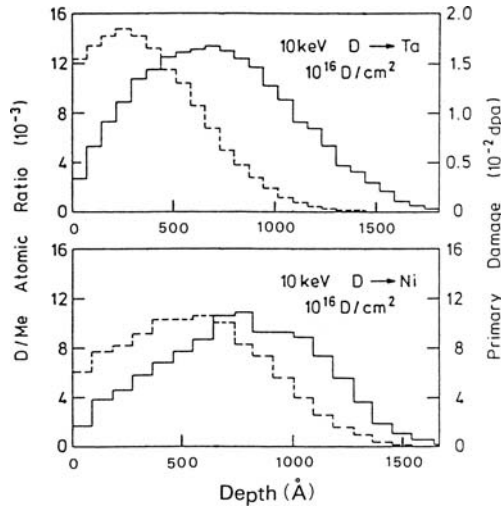


Fig. 5.48. Computer-simulated range (*solid lines*) and damage (*dashed lines*) distributions for 10 keV deuterons incident on Ta and Ni. The unit dpa is an abbreviation of “displacements per atom”, an average frequency of radiation-induced displacements per atom [5.152]

All the defects thus introduced, including interstitials, vacancies, and He bubbles, act as traps to hydrogen. Among them, the effect of trapping by He-induced bubbles, which is a nuisance in channeling experiments utilizing the reaction $\text{D}(^3\text{He}, \text{p}) \alpha$, was circumvented by restricting the fluence and shifting the position of the probing beam, and studied by separate experiments of pre-implantation of He ions.

In order to identify the type of these defects, a number of annealing experiments have been performed in which the location and the total number of D atoms retained in the lattice are measured after implantation at a low temperature and subsequent annealing at successively higher temperatures.

These experiments give us information on the characteristic temperatures where the defects in question or the trapped D atoms start migrating and find some new positions of lower energies.

Ligeon et al. [5.158] noted that a) the lattice location of D atoms is independent of the implanted dose for 10^{15} – 10^{16} D atoms cm^{-2} in fcc and $\leq 10^{17}$ D atoms cm^{-2} in some bcc metals, and b) the lattice location after implantation at 15–40 K and annealing at an elevated temperature T_a is the same as that observed by implantation at T_a .

The results of the annealing experiments are compiled in Fig. 5.49 for D atoms implanted in fcc, hcp, and bcc metals. Also inscribed in the figure are the characteristic temperatures where interstitials, vacancies, and D atoms start migrating short distances (~ 20 Å) within the annealing time (~ 15 min), designated, respectively, as T_i , T_v , and T_D . (A migration over longer distances (~ 600 Å) occurs at 1.26 times these temperatures.)

For Ni, implantation-annealing experiments were made by *Myers et al.* [5.157] and *Besenbacher et al.* [5.159–5.162]. In the process of annealing, the spatial distribution of D atoms changed, as shown in Fig. 5.50 [5.160]. The shift of the distribution of D atoms to smaller depths, caused by annealing at 250 K, indicates a short-range migration of the as implanted D atoms to implantation-induced defects, and the overall broadening and the decrease in number after annealing at 285 K indicates a long-range migration of D atoms after dissociation of the defect–D complexes. Correspondingly, the fraction of D atoms in the near-surface region remained nearly constant up to 250 K, and decreased to zero through two distinct stages as shown in Fig. 5.51 [5.160]. From this two-stage annealing process, they deduced two binding energies ($e_b = 0.24$ and 0.43 eV), which they attributed to two different trapped configurations around monovacancies. (Their later analysis accounting also for higher-temperature deviations led to 0.28 and 0.43 eV for monovacancies and $e_b = 0.55$ eV for bubbles and voids [5.163].)

The effects of isochronal annealing on the channeling angular profiles provide more useful information on the configuration of D atoms. Such data on Pt are shown in Fig. 5.52 [5.158, 5.164]. As implanted at 25 K, D atoms occupy O sites, but move to displaced O sites when the sample is annealed above 50 K, eventually decreasing in number after annealing above 275 K due to detrapping from defect–D complexes. Implanted D atoms in Pd behave in a very similar manner [5.164, 5.165].

An analysis of similar experiments on D in Ni led *Besenbacher et al.* [5.162] to conclude that the profiles observed for the as-implanted (at 25 K) D atoms can be fitted by assuming a regular O-site occupancy, whereas those observed after annealing at ≥ 200 K can be explained only by assuming a rather extended distribution of D atoms. A tentative model proposed for the profile after annealing at 270 K yields 87% occupancy of the displaced O sites (0.3 Å towards the vacancy) and 13% occupancy of the displaced T sites (0.2 Å towards the vacancy). Their subsequent experiments [5.166]

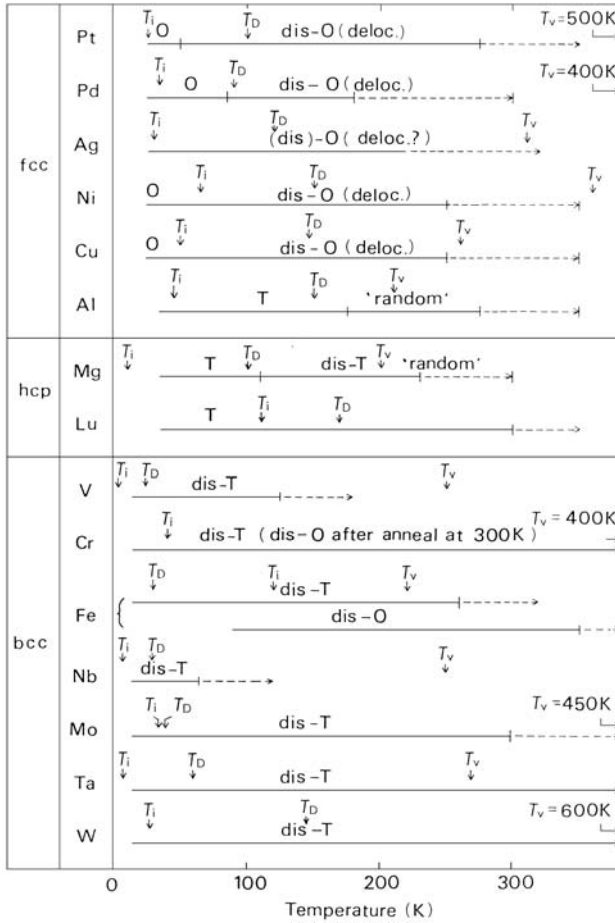


Fig. 5.49. Changes in the lattice location of D atoms implanted at low temperatures upon subsequent annealing. The temperatures where interstitials, vacancies and D atoms start migrating are designated, respectively, as T_i , T_v , and T_D . Lu is an exceptional case where T_D marks the temperature of the break-up of H-M-H pairs (Sect. 5.6.1). For the geometry of displaced-T (dis-T) and displaced-O (dis-O) configurations, see the text. A transition from *solid* to *dashed* line marks the temperature at which D atoms are released from the implanted region. For references, see the text

showed that the intensity of a small peak observed after annealing at 270 K depends on the measurement temperature (Fig. 5.53). The relative fraction of displaced-T site occupancy was found to obey the Arrhenius law with an activation energy of 3.3 meV. The significance of these observations, which reflect the local environment of D atoms trapped at monovacancies, will be examined in Sect. 5.7.3.

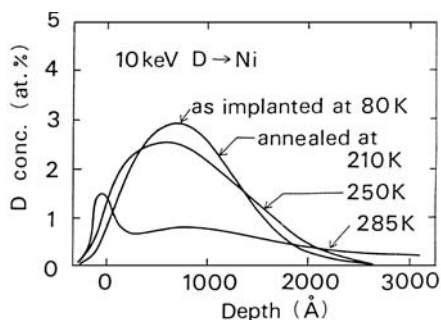


Fig. 5.50. Evolution of the depth profile of D atoms implanted at 10 keV and 80 K into Ni during linear ramping of temperature. The initial distribution reflecting the implantation range profile is shifted to a damage profile by short-range migration at 250 K and, finally, gets broadened at 285 K [5.160]

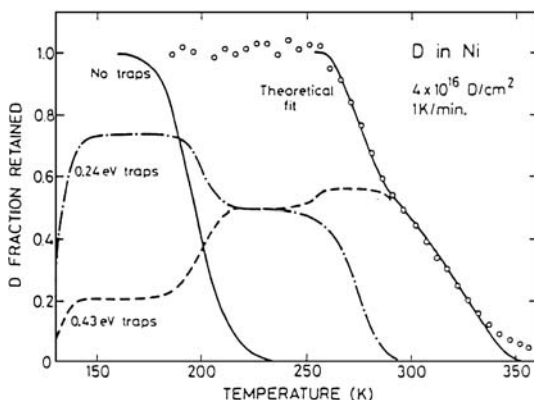


Fig. 5.51. Temperature dependence of the densities of the implanted D atoms in Ni. Experimental data (in circles) are compared with a theoretical fit assuming two binding energies (0.24 and 0.43 eV). An expectation without any traps is shown for comparison [5.157]

Very similar results were obtained for Cu [5.167]. D atoms implanted at 25 K occupy regular O sites, move to the same displaced O site as in Ni (0.1 Å towards the self-interstitial) after 75 K anneal, and assume the same delocalized state (82% dis-O and 18% dis-T) after annealing at 273 K.

A re-analysis of the data on D implanted in Pd led also to a similar delocalized configuration: 37% dis-O (0.2 Å towards the vacancy) and 63% dis-T (0.15 Å towards the vacancy) [5.157].

Ligeon et al. [5.158], *Bugeat* [5.164], and *Bugeat and Ligeon* [5.165] agree in that the D atoms in Ni, Cu, and Ag after implantation and annealing occupy near-O sites, with the displacements in Cu and Ag much smaller than in Ni.

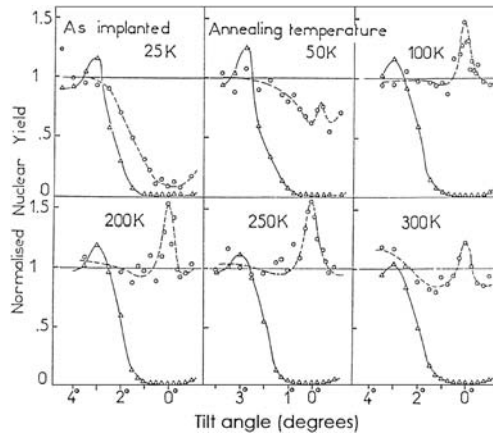


Fig. 5.52. Effects of isochronal annealing on the $\langle 100 \rangle$ channeling yield profiles of implanted D in Pt [5.158,5.164]

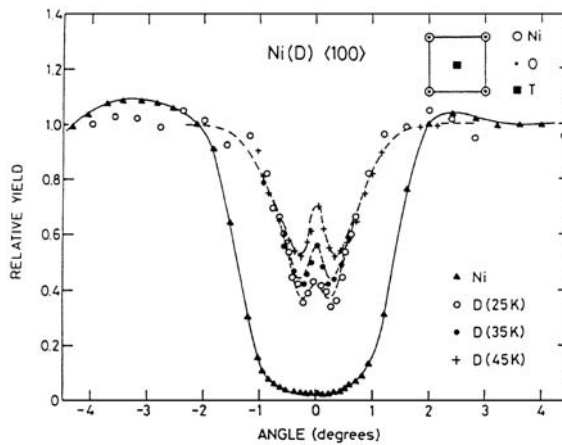


Fig. 5.53. Normalized channeling yields from implanted D and Ni after annealing at $T_a = 270$ K for 15 min. The measurements were carried out at 25, 35, and 45 K, respectively, and were reversible with respect to temperature. The increase of the central-peak intensity with temperature indicates thermal excitation to T-like sites [5.166]

The channeling profiles of D atoms in Al, on the other hand, showed a T-site occupancy from the lowest temperature of the measurement [5.168], suggesting a transition from an intrinsic site location (probably an O site) should have occurred at still lower temperatures. Although the total number of implanted D atoms is conserved up to 275 K, from ~ 175 K onwards they gradually move into “random” positions, namely, some positions unobservable by the channeling method. This indicates that large clusters of defect–D

complexes are formed as they become mobile. Above 275 K, implanted D atoms decrease in number as they move to the surface and disappear at ~ 400 K.

Among the hcp metals investigated, similar annealing stages were observed in Mg [5.169]. A transition from a T site to a displaced-T site occurs at 110 K, followed by a “random” location and a long-range migration to the surface. The configuration of the displaced-T site is such that the position is shifted by ~ 0.5 Å from a regular T site towards the $\langle 0001 \rangle$ channel center in the (0001) plane.

Lutetium, in which T-site occupancy is maintained over the entire temperature range [5.170], is believed to be a peculiar case because D atoms form stable T–M–T pairs (see Sect. 5.6.1) rather than being trapped at defects. The release temperature T_D in this case appears to correspond to the break-up of T–M–T pairs that allows the long-range migration of D atoms.

As examples of channeling profiles for in bcc metals, those for D atoms dissolved in Nb from the gas phase and ion-implanted at low temperatures are compared in Fig. 5.54 [5.158]. In contrast to T-site occupancy observed in V, Nb, and Ta for D atoms doped from the gas phase, it was found that implanted D atoms were invariably on displaced-T sites in V, Cr, Fe, Nb, Mo, Ta, and W. The displacement from a regular T site towards the nearest O site was estimated to be 0.36 Å for V [5.19], 0.2 Å for Nb [5.158, 5.171], and 0.6 Å for Mo [5.3, 5.155].

Picraux [5.155] also concluded that implanted D atoms occupy displaced-T sites in V, Mo, and W, whereas in Fe and Cr, they move from near-T sites to displaced O sites at ≥ 110 K. In Fig. 5.55 are reproduced the channeling profiles for implanted D in Fe, showing the occupancy of displaced

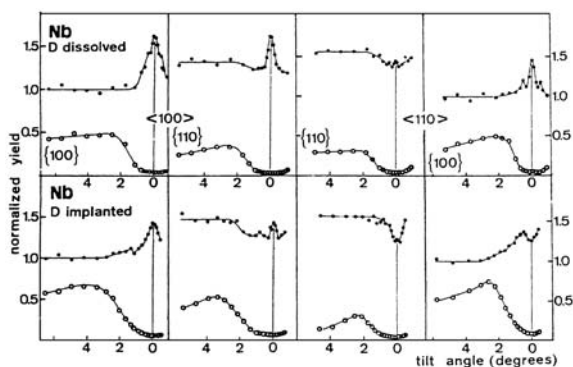


Fig. 5.54. Comparison of channeling yield profiles of D atoms implanted and dissolved from the gas phase into Nb. Nuclear-reaction yield of $D(^3\text{He}, p)\alpha$ (●) and Rutherford backscattering yield (○). The upper curves were measured on $\text{NbD}_{0.008}$ at room temperature, and the lower curves were at 15 K on D implanted at 10 keV and 15 K up to a fluence of 5×10^{15} D atoms cm^{-2} [5.158]

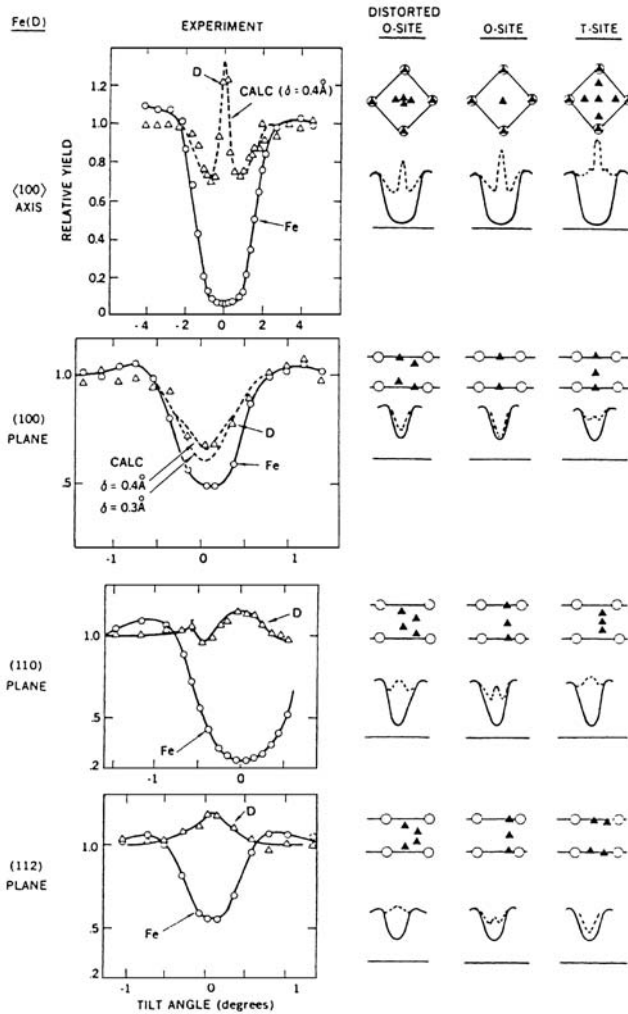


Fig. 5.55. Channeling yield profiles for implanted D atoms trapped at mono-vacancies in Fe. On the *right* are shown the atom projections and the predicted channeling yields for the three possible sites. In the distorted (displaced) O site, the D atom is assumed to be displaced by δ from a regular O site towards the nearest vacancy [5.155, 5.172]

O sites [5.155, 5.172]. The displacement from a regular O site towards the nearest-neighbor M-atom site was estimated to be 0.4 \AA for Fe [5.155] and 0.36 \AA for Cr [5.3, 5.155].

The annealing characteristics of implanted D in Fe were investigated in detail [5.172–5.174]. The fraction of D atoms retained decreased roughly in two steps: a sharp drop starting at 260 K followed by a gradual decrease

at ~ 340 K. Subsequent He-implantation experiments showed that the high-temperature tail above ~ 400 K is strongly enhanced to form another well-defined stage. The binding energies have been determined for these stages.

Based on the general consensus that the binding to self-interstitials is much weaker than vacancy-type defects – monovacancies, vacancy agglomerates (voids) and He bubbles, the sequence of reactions that take place between implanted D atoms and radiation-induced vacancies and self-interstitials can be envisaged, as shown in Fig. 5.56. D atoms implanted at low enough temperatures should occupy the intrinsic equilibrium sites, but as the temperature is raised, form complexes with self-interstitials as soon as the latter become mobile. Subsequently, these complexes dissociate and liberated self-interstitials annihilate with vacancies. In practice, the processes up to this point involving self-interstitials have never been observed clearly. Then, D atoms detrapped from Int–D complexes start migrating and form more stable complexes with vacancies. These Vac–D complexes dissociate and liberated D atoms move out of the implanted region at still higher temperatures. D atoms trapped by vacancy agglomerates (voids) and He bubbles are in many cases liberated at still higher temperatures (not shown). Analysis of the annealing kinetics was performed for D in Ni (Fig. 5.51) [5.157, 5.173] and Fe and Mo [5.175, 5.176].

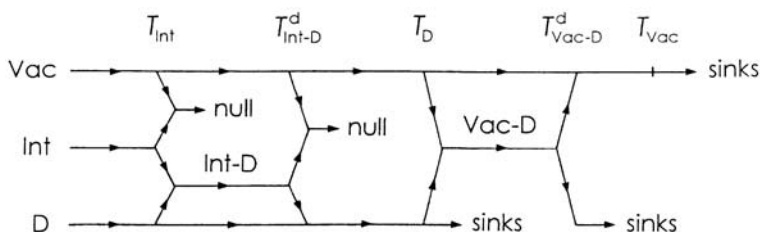


Fig. 5.56. Reaction flow diagram of monovacancies (Vac), self-interstitials (Int) and D atoms in the course of annealing after implantation. T_{Int} , T_{Vac} , and T_{D} represent, respectively, the temperatures at which a self-interstitial, a vacancy or a D atom start migrating; $T_{\text{Int-D}}^{\text{d}}$ and $T_{\text{Vac-D}}^{\text{d}}$ are the temperatures of dissociation of Int–D and Vac–D complexes

The nature of the displaced-T configuration prevalent in bcc metals deserves special consideration. *Ligeon et al.* [5.158] found that the near-surface region of Nb implanted with D atoms was elongated in the direction perpendicular to the surface, as a result of the hydrogen-induced lattice expansion of an implanted layer constrained by the unimplanted lattice below. They found that the lattice was elongated by $\sim 1 \times 10^{-2}$ after an implantation of 10^{17} D atoms cm^{-2} on the (100) plane. This reminds us of a stress-induced state observed in V, where a distribution of internal strains of $\sim 3 \times 10^{-4}$ converted the hydrogen location from a T site to a well-defined displaced T site. Essentially the same configuration was found for implanted D atoms in V [5.19].

From these observations follows the conjecture that the displaced-T configuration in implanted bcc metals may be a result of strains that build up in the implanted region, and not that of trapping by the implantation-induced defects. *Besenbacher et al.* [5.175] cautioned against literal comparison of the data obtained at high fluences ($\sim 10^{17}$ D atoms cm^{-2}) with those obtained at low fluences ($\sim 10^{15}$ D atoms cm^{-2}) [5.158]. However, even the reduction of fluence by two orders of magnitude will still produce strains of $\sim 10^{-4}$, which is exactly the magnitude that induces the site change of hydrogen in V.

Binding energies of hydrogen atoms with vacancies and voids, obtained so far by various techniques including ion implantation/channeling, positron annihilation, superabundant vacancy formation (Sect. 5.6.4), are compiled in Table 5.10. The values obtained from positron annihilation experiments were in many cases derived by less detailed analyses, and may therefore be less accurate. The appearance of two binding energies indicates the presence of different trapping configurations.

In view of its significant contribution made in clarifying the H-defect interactions, it is believed to be appropriate here to reproduce some results of the effective medium theory (EMT). The EMT is a simplified version of the electronic theory, in which the interaction energy is calculated as the energy required to embed a hydrogen atom in a homogeneous electron gas of the density corresponding to the local density at the site in question, and corrections are included using the perturbation theory. In spite of these severe approximations involved, the theory turned out to be rather useful in estimating the H-defect interaction energies. (The EMT is described in Sect. 7.2.2.)

Figure 5.57 compares the experimental Vac-H binding energies (Table 5.10) with the predictions of the EMT. The consistency between theory and experiment can be regarded to be good. The calculation was subsequently

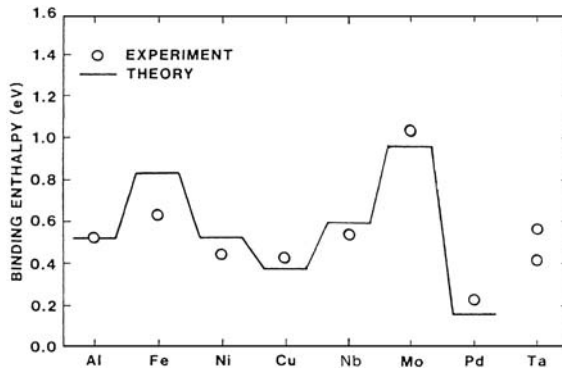


Fig. 5.57. Comparison of experimental and theoretical binding energies for hydrogen trapped by monovacancies. Experimental values are from Table 5.10 and theoretical values from effective medium theory [5.157]

extended to multiple occupancies, VacH_r , for the number of H atoms up to $r = 6$. The maximum number assumed, $r = 6$, is the number of nearest O sites around a vacancy, both in fcc and bcc lattices.

Figure 5.58 shows the binding energy as a function of occupancy calculated for three fcc metals (Pd, Cu, Ni) and three bcc metals (Nb, Mo, Fe) [5.184]. For Cu, Ni, Mo, and Fe, the binding energy decreases with increasing occupancy, whereas for Pd and Nb, the values stay nearly constant. For this general trend, a simple explanation was given by the authors: In the former group of metals having smaller lattice parameters, the extra charge density extending from nearby H atoms tends to raise the embedding energy, whereas in the latter group having rather open structures, this effect is negligibly small. A sudden drop of e_b in the former group, going from $r = 2$ to 3, can also be explained from the geometry of the problem.

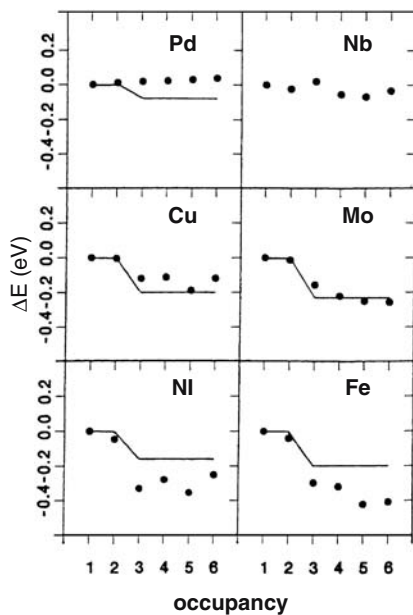


Fig. 5.58. Variation of the binding energy with occupancy of D atoms in mono-vacancies, calculated by effective medium theory. The energies are shown relative to the binding energy of the first D atom, $e_b = 0.26$ eV (Pd), 0.30 eV (Cu), 0.52 eV (Ni), 0.59 eV (Nb), 0.96 eV (Mo) and 0.83 eV (Fe). The *solid lines* are the experimental data (Table 5.10) [5.184]

The site location, determined from minimum-energy requirements, was slightly displaced from these nearest-neighbor O sites towards the vacancy at the center. Whether $r = 6$ corresponds to the real maximum occupancy was not examined in their calculation. Judging from the small variation of

e_b with the number of occupancy, the possibility of trapping more than 6 H atoms appears probable, especially for metals having large atomic volumes, such as Pd and Nb.

Figure 5.59 compares the observed binding energy of He bubbles with experimental and theoretical chemisorption energies [5.157]. The mutual agreement is reasonably good, suggesting that for H atoms bubbles/voids appear very similar to the external surface. The theory has reproduced the observation that e_b is larger for bubbles/voids than for monovacancies.

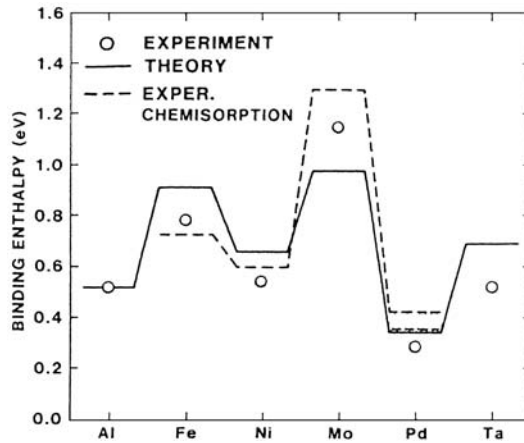


Fig. 5.59. Comparison of experimental binding energies to He bubbles with experimental and theoretical chemisorption energies. Theoretical values are from effective medium theory [5.157].

The EMT also predicted trapping of four H atoms by the side of a self-interstitial (dumbbell) in the fcc lattice, where the lattice is locally elongated [5.162].

In this way the EMT confirmed the qualitative insight that, in most metals, H atoms are attracted to any defect that has an associated region of reduced electron density.

In closing this section, a word of caution may be in order. Determination of site location from observed channeling profiles is straightforward, and may be accepted as such, but the extraction of the binding energy from annealing data should be taken with some caution. All that we know from experiments is a rather featureless annealing curve (such as the one shown in Fig. 5.51), and its analysis depends rather heavily on the prediction of the EMT, the reliability of which in turn is at best semi-quantitative. The overall reliability of the analysis is often obscured by the close interplay between theory and experiment. There is apprehension that in some cases the conclusions drawn

may not be unique. Thus the question of multiple occupancy described above will be re-examined in the next section.

5.6.4 Formation of Superabundant Vacancies

In 1993, we discovered that the lattice parameter of Ni and Pd decreased over several hours when samples were held under high temperatures and high hydrogen pressures, until it approached a value a few % smaller than the initial value [4.66, 5.185]. We inferred immediately that the phenomenon should be the result of copious vacancy formation caused by Vac-H interactions³. In the presence of interstitial H atoms, vacancies should assume the form of Vac-H clusters, the formation energy of which e_f^{cl} should be smaller than the formation energy of a vacancy e_f^{v} by the sum of binding energies, viz.

$$e_f^{\text{cl}} \approx e_f^{\text{v}} - \sum_i e_{\text{bi}}. \quad (5.43)$$

As the vacancy formation energy ranges between 1 ~ 3 eV in many metals [5.147], it can be reduced substantially by the sum of binding energies of multiply-occupied H atoms (Table 5.10). Thus, drastic enhancement of equilibrium vacancy concentrations can be expected in the presence of interstitial H atoms. Indeed, crude estimates of vacancy concentrations from the observed lattice contractions (see below) amounted to as large as ~10 at%, which is many orders of magnitude larger (in fact never attainable) in pure metals. This phenomenon has since been observed in many M-H systems, and is now called by the name of superabundant vacancy (SAV) formation.

Oates and *Wenzl* [5.186, 5.187] suggested another mechanism based on entropy effects. The loss of the configurational entropy of interstitial H atoms as their concentration approaches the stoichiometric limit should be compensated by the increase of the configurational entropy to be caused by the creation of M-atom vacancies. This mechanism may also become effective close to the stoichiometric compositions.

³ The formation of a vacancy introduces the uniform lattice contraction in addition to the formation of one extra site in the sample. Thus the formation volume of a vacancy v_f^{v} can be written as

$$v_f^{\text{v}} = v_0 + v_{\text{R}}^{\text{v}}, \quad (5.41)$$

where v_0 is the atomic volume and $v_{\text{R}}^{\text{v}} (< 0)$ is called the relaxation volume. With the formation of vacancies, the total volume increases but the lattice parameter decreases in proportion to the concentration of vacancies. The atomic volume in the presence of vacancies is given by

$$v = v_0 + x_{\text{v}} v_{\text{R}}^{\text{v}}, \quad (5.42)$$

where x_{v} is the vacancy concentration in atomic ratio.

In fact, the increase of equilibrium vacancy concentrations by interaction with impurity atoms had been recognized from early days of point-defect studies. A series of theoretical papers dealing specifically with interaction with interstitial impurities were published by two groups, a group headed by *McLellan* [5.188–5.194] and a Ukrainian group initiated by *Smirnov* [5.195–5.198].

Examples of the lattice contraction process observed under high p_H , T conditions in Ni are shown in Fig. 5.60. If we assume tentatively that the relaxation volume of Vac-H clusters can be approximated by that of a vacancy, i.e. $v_R^{cl}/v_0 \sim -0.35$ [4.45], the concentration of Vac-H clusters can be estimated as

$$x_{cl} \sim 3\Delta a/a \div (v_R^{cl}/v_0) \sim 0.3.$$

This estimate is inevitably crude, but clearly indicates the magnitude of the vacancy concentrations involved. More detailed examination of the lattice contraction process will be made later.

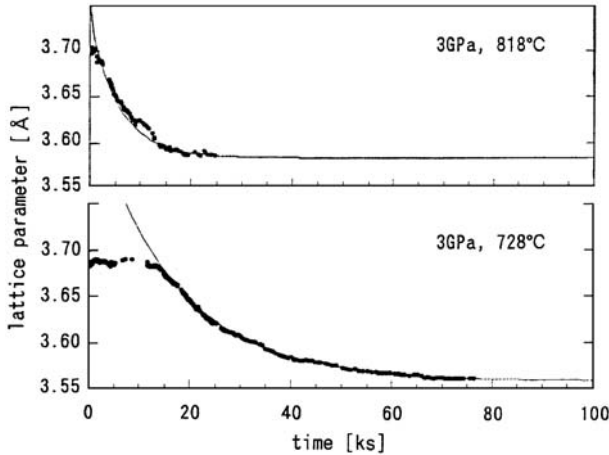


Fig. 5.60. Examples of measured lattice parameter of Ni under $p_H = 3$ GPa as a function of time. Hydrogen concentrations estimated from initial lattice parameter values are in the range $x = 0.58 \pm 0.03$. Best-fitted exponential curves are inscribed [5.199]

Evidence in support of the involvement of vacancies was provided by the appearance of superlattice lines in in situ XRD measurements on Pd–H [5.185], Mn–H [5.200] and Ni–H [5.199] alloys. In all these cases, superlattice reflections having simple-cubic indices were sometimes observed in the lattice-contracted fcc phase, as shown in Fig. 5.61 for Ni. These superlattice lines indicate the ordering of a large number of vacancies, probably in the form of $L1_2$ -type structure, $M_3\text{VacH}_4$. This structure, once formed under high p_H , T conditions, remained stable after recovery to ambient conditions.

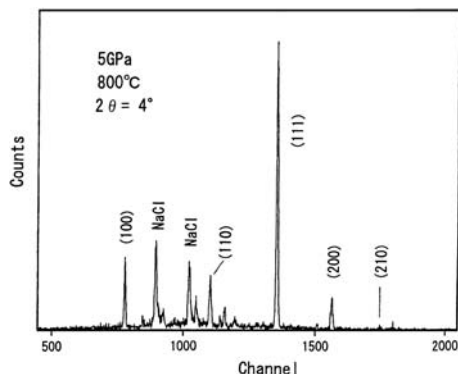


Fig. 5.61. XRD spectrum of Ni at 800°C and $p_H = 5$ GPa, showing superlattice reflections having simple-cubic indices [5.199]

Electronic calculations performed on Pd hydride showed that the total energy of this ordered defect hydride Pd_3VacH_4 is lower than that of the defect-free monohydride PdH [5.201]. A similar calculation was also made on NiH [5.202].

The first observation of a vacancy-ordered hydride structure was made earlier in the near-surface region of ion-implanted Pd hydride [5.203]. There, one of the two sublattices of the bct structure was randomly occupied by vacancies to 50%, again forming Pd_3VacH_4 . A related structure was observed in the Fe–H alloys at high p_H , T , where the superlattice diffraction lines having simple-cubic indices were observed in the bcc phase, indicating the preferential occupancy by vacancies of one of the two simple-cubic sublattices of the bcc phase, forming a L_2 structure (CsCl type) [5.204].

From the time constant of the observed lattice contraction process (~ 1 ks) and the average particle size of the sample ($\sim 30 \mu\text{m}$), the diffusivity is estimated to be of the order of $10^{-13} \text{ m}^2/\text{s}$, which compares reasonably well with the diffusivity of vacancies in Ni under corresponding p , T conditions, $D^v \sim 10^{-11} \text{ m}^2/\text{s}$ [5.147].

The formation of defect hydrides leads us to the expectation that superstoichiometric hydrides should be formed by the introduction of SAVs in monohydrides. In fact the superstoichiometric hydrides had been observed in the near-surface region of ion-implanted metals, with compositions 1.15 ± 0.07 for Ni [5.205], 1.32 ± 0.07 [5.205] and 1.6 ± 0.2 for Pd [5.206], 2.8 ± 0.4 for Ti [5.205] and 5.0 ± 0.8 for Zr [5.205]. These superstoichiometric compositions can be rationalized by assuming mono-, di-, and tri-hydrides of a defect L_{12} structure having compositions $\text{M}_3\text{VacH}_{4n}$, with $n = 1$ for Ni and Pd, $n = 2$ for Ti, and $n = 3$ for Zr. Anomalous increase of hydrogen diffusivity observed in TiH_x [5.207] and ZrH_x [5.208] close to the dihydride composition can also be considered to be the result of SAV formation (see Sect. 6.4.1).

A detailed investigation of the process of SAV formation was made on Nb–H alloys [5.209]. Niobium belongs to a group of so-called anomalous

bcc metals (Fe, V, Nb, Ta) where the vacancy migration energy is so low (~ 0.5 eV [5.147]) that the SAV formation can be studied at reasonably low temperatures. Moreover, in V, Nb and Ta, large affinities to hydrogen allow the experiments at moderate temperatures to be performed under ambient pressure. Thus very precise measurements on well-characterized samples can be made on the hydrides of these metals.

For Nb-H alloys, the SAV formation process was studied by electrical resistivity measurements [5.209] and more recently by positron annihilation spectroscopy [5.210]. The resistivity measurements were made on single-crystal specimens of prescribed hydrogen concentrations. Figure 5.62 shows the temporal variation of the resistivity at 300°C for a single-crystalline plate of $\text{NbH}_{0.21}$ [5.209]. The resistance increases in two stages. The time constant of the first process ($\tau_1 \approx 1$ ks) was found to be independent of sample thickness d , whereas that of the slow process was proportional to d^2 ; $\tau_2[\text{ks}] \approx 1.0 \times 10^3 d[\text{mm}]^2$. Thus, there are two mechanisms operating for introducing Vac-H clusters; the slow process via diffusion from the surface, and the fast process via some easy paths distributed uniformly in the samples, most probably dislocations. (In polycrystals, the formation process was dominated by the fast process, probably due to grain boundaries and higher dislocation densities.)

The resistivity increments can be converted into cluster concentrations if the resistivity per unit concentration of Vac-H clusters is known. Lacking this knowledge, we estimated the cluster concentration by approximating it by $1/2$ of the Frenkel-pair resistivity, $7 \pm 1.5 \mu\Omega \text{ cm/at\%}$ [5.147]. The results obtained

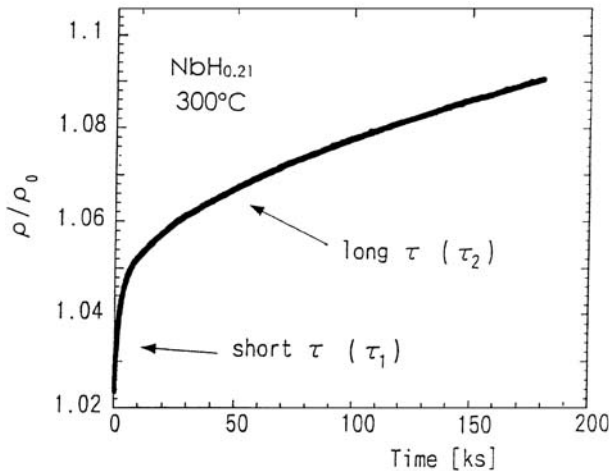


Fig. 5.62. Temporal variation of the electrical resistivity of a single-crystalline sample of $\text{NbH}_{0.21}$ at 300°C . The resistivity increases in two stages, the first stage with a short time constant (τ_1) and the slow stage with a long time constant (τ_2) [5.209]

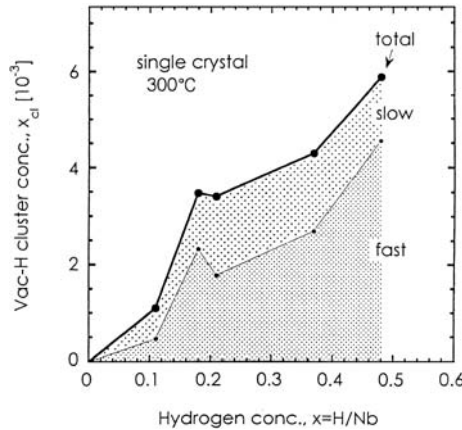


Fig. 5.63. Vacancy-hydrogen cluster concentration x_{cl} in Nb-H alloys at 300°C plotted against H concentration $x = [H]/[Nb]$. The cluster concentrations have been estimated from observed resistivity increments. The total cluster concentration and its breakdown into fast and slow components are shown [5.209]

for samples of several different H concentrations are shown in Fig. 5.63. The cluster concentration is nearly proportional to H concentration; $x_{cl} \approx 1.3 \times 10^{-2}x$.

The temperature dependence of the cluster concentration was measured between 200–300°C, with the result

$$x_{cl} \approx 2 \times 10^{\pm 1} \exp \left[\frac{-(0.3 \pm 0.1)\text{eV}}{kT} \right].$$

A reduction of the formation energy of a vacancy from the value in Nb ($e_f^v = 3.07$ eV [5.147]) is really appreciable, and its amount is consistent with the occupancy of 6 H atoms with $e_b = 0.55$ eV (Table 5.10).

From the temperature dependence of τ_2 , the diffusivity of Vac-H clusters was obtained;

$$D^{cl} = \frac{d^2}{\pi^2 \tau_2} \approx 3 \times 10^{-7} \text{e}^{-0.75\text{eV}/kT} \text{m}^2 \text{s}^{-1}.$$

Writing $D^{cl} = D_0^{cl} \exp(-e_m^{cl}/kT)$ for Vac-H clusters and $D^v = D_0^v \exp(-e_m^v/kT)$ for vacancies, with $D_0^v \approx 10^{-5} \text{m}^2 \text{s}^{-1}$, and $e_m^v = 0.55$ eV [5.147], we obtain $\Delta s_m/k = \ln(D_0^{cl}/D_0^v) = -3.5$ and $\Delta e_m = e_m^{cl} - e_m^v = 0.20$ eV. Both the reduction of D_0 and the increase of e_m in the presence of trapped H atoms can be naturally understood. The reduction of D_0 is due to additional geometrical constraints and the increase of e_m is the energy cost to displace trapped H atoms, and is comparable to the migration energy of an H atom ($e_m^H = 0.13$ eV for NbH_{0.2} [5.211]). Very similar changes of s_m and e_m were observed for the migration of Vac-H clusters in Pd-H alloys [5.212].

An important observation was made regarding the pressure dependence of the Vac-H cluster concentration, namely that its pressure dependence was very small. In terms of formation volume, the value was $v_f^{\text{cl}} = 3.7 \text{ \AA}^3$, i.e. $v_f^{\text{cl}}/v_0 = 0.18$. In comparison with the vacancy formation volume in Nb, $v_f^{\text{v}}/v_0 = 0.7$, a typical value in many metals [4.45], this value of v_f^{cl} is very small. This can be rationalized by assuming that the volume expansion caused by an H atom becomes smaller when trapped by a vacancy. Writing $v_f^{\text{cl}} = v_f^{\text{v}} + 6\Delta v_{\text{H}}$ and substituting $v_f^{\text{cl}} = 3.7 \text{ \AA}^3$ and $v_f^{\text{v}} = 14 \text{ \AA}^3$, we obtain $\Delta v_{\text{H}} = -1.7 \text{ \AA}^3/\text{H-atom}$. The H-induced volume is reduced to $\sim 40\%$ in the trapped state. The fact that Vac-H cluster concentrations of $1 \sim 10 \text{ at}\%$ were observed in many M-H alloys under hydrogen pressures of $3 \sim 5 \text{ GPa}$ indicates that the small formation volume is one of the general properties of Vac-H clusters.

Another method adopted to characterize the trapped state of hydrogen is the thermal desorption spectroscopy (TDS). An example of TDS data on Ni is shown in Fig. 5.64. After heat treatments at $p_{\text{H}} = 3 \text{ GPa}$ and $T = 800^\circ\text{C}$ for 3 hrs, three desorption peaks were observed during temperature ramping in vacuum. The lowest-temperature peak (P_0), which appeared even after brief heat treatments and disappeared gradually in several days of ageing at room temperature, is assigned to H atoms occupying regular interstitial sites. Peaks P_1 and P_2 , which appeared only after prolonged heat treatments, are assigned to H atoms trapped by vacancies. From these peak temperatures, the corresponding activation energies can be extracted using the relation [5.146]

$$\frac{e_{\text{m}}^{\text{H}}}{T_{P_0}} = \frac{e_{\text{m}}^{\text{H}} + e_{\text{b1}}}{T_{P_1}} = \frac{e_{\text{m}}^{\text{H}} + e_{\text{b2}}}{T_{P_2}} \quad (5.43)$$

This is believed to be a good approximation in the limit of slow heating rates. Substituting $e_{\text{m}}^{\text{H}} = 0.41 \text{ eV}$ [5.213] and the observed peak temperatures,

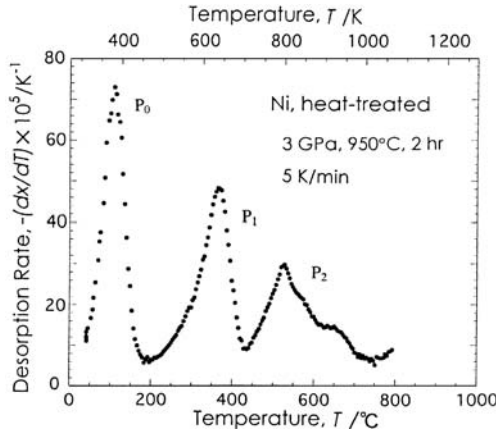


Fig. 5.64. Thermal desorption spectrum of Ni after heat treatment at 950°C , $p_{\text{H}} = 3 \text{ GPa}$ for 2 h. The heating rate was 5 K min^{-1} [5.178, 5.179]

we obtain $e_{b1} = 0.27$ eV and $e_{b2} = 0.43$ eV. These values agree excellently with those deduced from implantation/annealing experiments (Table 5.10). These binding energies are listed in Table 5.10, together with those obtained in a similar way on Cr [4.44] and Cu [5.179].

Variation of the relative magnitude of P_1 and P_2 with conditions of heat treatment is worthy of notice. Only the peak P_1 appeared when the total amount of trapped hydrogen was small (after heat treatments at relatively lower p_H , T for shorter period of time); The peak P_2 grew larger as the total amount of trapped hydrogen increased. This observation is not consistent with the multiple-occupancy model proposed from implantation/annealing data. The model would predict that the state of higher binding energy (P_2) should appear in the beginning, followed by the state of lower binding energy (P_1), which is completely the reverse of the observation. We suggested tentatively that P_1 corresponds to trapping by monovacancies and P_2 by multiple vacancies [5.179]. For vacancy concentrations of 1 ~ 10 at %, the probability of forming multiple vacancies (e.g. divacancies) cannot be ignored. Different trapping energies to be observed for multiply occupied monovacancies should correspond to substructures of the peak P_1 .

In fact, in later experiments on Ni, another peak (P_3) was observed at still higher temperatures ($T_{P3} \sim 950^\circ\text{C}$), which is only barely visible in Fig. 5.64. This high-temperature peak was found in many other metals as well, after heat treatments at intermediate temperatures or long-term ageing at room temperature, and is ascribed to desorption from H_2 bubbles.

In the case of Fe, the Arrhenius plot of the amount of hydrogen desorbed in the major stage (corresponding to P_1 in the case of Ni) after heat treatment at $p_H = 1.7$ GPa gave the activation energy of 1.0 ± 0.1 eV [5.214]. Equating this with $e_f^v + 6(e_s - e_b)$, and substituting $e_f^v = 1.89$ eV [5.147] and the heat of solution $e_s = 1.19$ eV at $p_H = 1.7$ GPa (Table 4.3), we obtain $e_b = 0.44 \pm 0.02$ eV, which is consistent with the value deduced from peak temperatures. It must be admitted, however, that some uncertainties exist regarding the implication of the amount of desorbed hydrogen. Only a part of H atoms detrapped from Vac-H clusters will be desorbed from the surface; the rest will form bubbles and be desorbed at higher temperatures.

With these results from resistometry and thermal desorption spectroscopy in mind, we shall re-examine the lattice contraction data obtained from in situ XRD at high temperatures and high hydrogen pressures. Two major drawbacks are to be recognized in the previous data analysis. First, the relaxation volume of a Vac-H cluster should be much smaller than that of a vacancy. Second, a sample in contact with fluid H_2 constitutes an open system, where the number of interstitial H atoms should change with the formation of vacancies. There, vacancies should be introduced together with H atoms, and in consequence both vacancy and H concentrations will increase with time. Thus we regard the SAV formation process as a process of gradual approach to the ultimate structure M_3VacH_4 , and the intermediate

state as a fine-scale, fluctuating mixture of original hydride MH_x and a short-range ordered phase $\text{M}_{3/4}\text{Vac}_{1/4}\text{H}$ in the ratio $(1 - \alpha) : \alpha$. Thus, the average composition becomes $\text{M}_{1-\alpha/4}\text{Vac}_{\alpha/4}\text{H}_{(1-\alpha)x+\alpha}$. In terms of Vac-H cluster concentration, this can be rewritten as $\text{M}\text{Vac}_{x_{\text{cl}}}\text{H}_{(1-3x_{\text{cl}})x+4x_{\text{cl}}}$, and a concomitant change of the atomic volume as

$$\Delta v = x_{\text{cl}} [v_{\text{R}}^{\text{cl}} + (4 - 3x)v_{\text{H}}] . \quad (5.44)$$

The atomic volume change is proportional to the cluster concentration, as expected, but the proportionality coefficient contains a term which depends on the H concentration. The relative importance of these two terms may be assessed in the Nb-H alloys. Substituting $v_{\text{R}}^{\text{cl}} = 0.18 - 1.0 = -0.82$ and $v_{\text{H}}/v_0 = 2.8/20 = 0.14$, we obtain

$$\Delta v/v_0 = -(0.26 + 0.42x)x_{\text{cl}} , \quad (5.45)$$

with the proportionality coefficient ranging between $-(0.26 \sim 0.47)$ for $x = 0 \sim 0.5$. Recognizing the general trend of small formation volume of Vac-H clusters and the near constancy of H-induced volume, variation of the proportionality coefficient from metal to metal is expected to be rather small. Incidentally, the average value of the coefficient in this range of H concentration, ≈ -0.36 , is very close to that of a vacancy. Thus, our previous estimation of Vac-H concentrations from lattice contraction data proved to be nearly appropriate numerically, although its physical basis was different.

The variation of the lattice contraction with H concentration obtained for Fe-H, Co-H and Ni-H are shown in Fig. 5.65a-c, together with the Vac-H concentration approximately estimated by $x_{\text{cl}} \approx 3\Delta a/a \div (-0.36)$. The dependence of x_{cl} on x is again approximately linear for all these systems; $x_{\text{cl}} \approx (3 \sim 5) \times 10^{-2}x$. As the data points were obtained at different p_{H} , T conditions, the observed linear dependence implies that the Vac-H concentration is primarily determined by the H concentration, nearly independent of p_{H} , T conditions adopted. The physical implication of this behavior has not been understood⁴.

One of the puzzles in the vacancy-induced lattice contraction is that it occurred only in the fcc phase. As shown in Fig. 5.66, no such contractions were observed in the hcp (dhcp) phase of the Cr-H and Mn-H alloys under comparable conditions of temperature and H concentrations. Origin of this distinctly different behavior between these close-packed structures is not easily

⁴ Our previous calculation of the equilibrium condition for the chemical reaction between vacancies and interstitial H atoms, $\text{Vac} + r\text{H} \leftrightarrow \text{VacH}_r$, led to the relation $x_{\text{cl}} \propto x^r$ [4.65]. A literal application of this relation to the observed proportionality leads to $r \approx 1$, a single occupancy, which contradicts with the observed reduction of the formation energy. The source of this apparent disparity should be sought in the approximations adopted, i.e. the Boltzmann statistics for low concentrations of vacancies and H atoms. Neither of these approximations are justified in the actual experimental conditions.

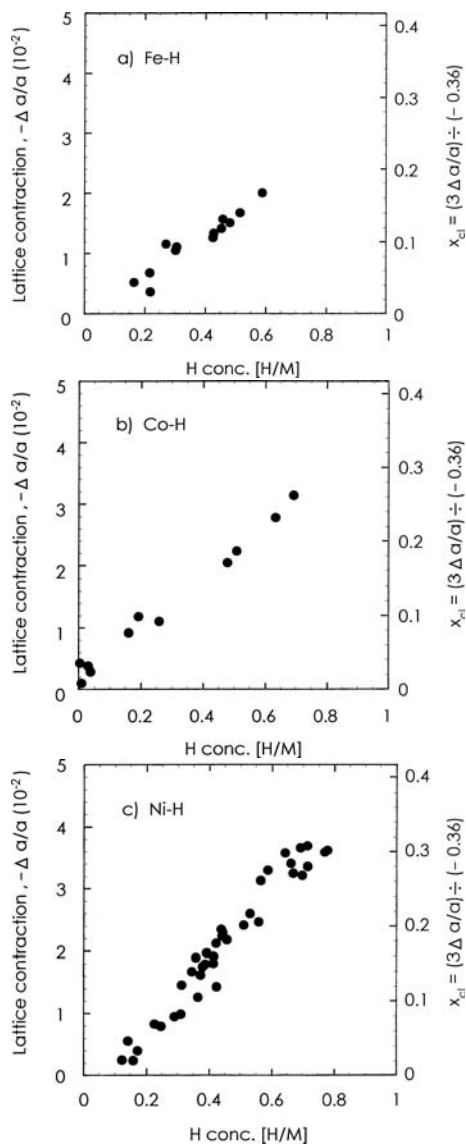


Fig. 5.65. Lattice contraction observed under high p_H , T conditions (*left scale*) plotted against H concentration. Vacancy-hydrogen cluster concentrations approximately estimated by $x_{cl} \approx 3\Delta a/a \div (-0.36)$ are also shown (*right scale*). (a) Fe-H, (b) Co-H, (c) Ni-H [5.215]

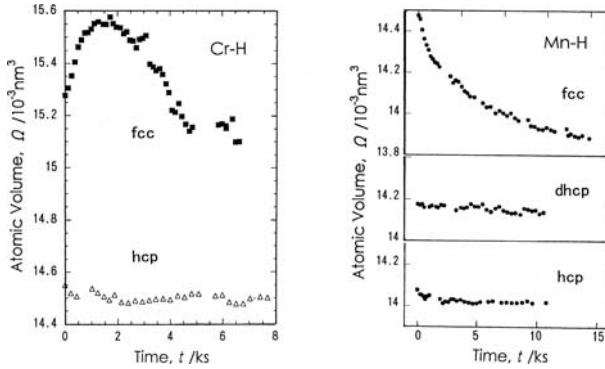


Fig. 5.66. Comparison of the temporal variation of the lattice parameter in fcc and hcp(dhcp) phases. (a) Cr-H alloys; γ (fcc) vs. ε (hcp) phases [4.44], (b) Mn-H alloys; γ (fcc) vs. ε' (dhcp) and ε (hcp) phases [5.216]

understandable, considering the similarity of the local atomic arrangements around vacancies in these structures. On the other hand, apparent absence of lattice contraction in the bcc phase of Cr-H, Fe-H, Nb-H and Mo-H alloys can be understood because vacancy concentrations involved were an order of magnitude smaller under the conditions of the experiments.

By far the most important implication in the physics of SAV formation is that the most stable structure of all M-H alloys is in fact the defect structure containing a large number of M-atom vacancies. All M-H alloys should tend to assume such defect structures, ordered or disordered depending on the temperature, as long as the kinetics allows. In practice, however, M-H alloys are in most cases prepared under conditions where M-atom vacancies cannot be introduced. Thus it can be said that most (all) phase diagrams of M-H systems reported to date are metastable ones. These metastable diagrams are certainly useful as such, but the recognition that they are metastable ones is of basic importance. The real equilibrium phase diagrams including M-atoms vacancies have not been obtained so far.

These recognitions brought us to the expectation that SAVs should be formed in the process of electrodeposition of metals from aqueous solutions. There, M and H atoms are deposited simultaneously, and in this process appropriate numbers of vacancies can be incorporated. This process is in contrast to the previous method in which high temperatures were necessary to allow introduction of SAVs by solid-state diffusion.

In order to verify this expectation, we measured the thermal desorption spectra of electrodeposited Ni and Cu, and compared them with those prepared under high p_H , T conditions [5.179]. Results are shown in Figs. 5.67 and 5.68. In both cases, the peak temperatures observed in samples prepared by the two methods are nearly the same, showing that H atoms are in the same trapped states. Very similar spectra were observed for

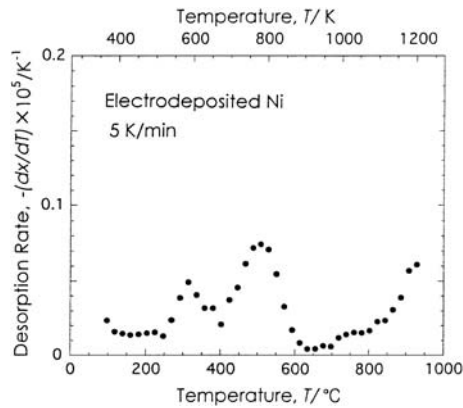


Fig. 5.67. Thermal desorption spectrum of Ni prepared by electrodeposition [5.179]. To be compared with the data obtained after high p_H - T heat treatment (Fig. 5.64)

samples manufactured more than 10 years ago. Binding energies estimated from peak temperatures are $e_{b1} = 0.28$ eV and $e_{b2} = 0.45$ eV for Ni, and $e_{b1} = 0.23 \pm 0.03$ eV and $e_{b2} = 0.37$ eV for Cu. These values agree excellently with the values deduced from other experiments. The amount of hydrogen desorbed from Vac-H clusters amounted to $x = 10^{-4} \sim 10^{-3}$.

In fact, our expectation was preceded by *Roy and Gibb* [5.217], who, trying to explain complex structural properties of electrodeposited Cr films, suggested that a defect structure containing vacancies might be formed in the electrodeposition process.

The formation of SAVs bring about some interesting phenomena, including the enhancement of M-atom diffusion and creep.

An example of enhanced interdiffusion in Cu/Ni diffusion couples is shown in Fig. 5.69 [5.218]. Concentration profiles observed after heat treatments at 800°C, 5 GPa for 30 min are shown. In comparison with the reference measurement without hydrogen (top), the enhancement of diffusion in hydrogen (bottom) is obvious. The characteristic shape of the profiles, a sudden break on the Cu side and a long tail on the Ni side, indicates that the diffusion enhancement is small on the Cu side and becomes larger at higher Ni concentrations. Analysis of these profiles showed that the interdiffusion coefficient was enhanced by 4 orders of magnitude on the Ni side and 1 order of magnitude on the Cu side. This trend clearly manifests the effect of hydrogen; the solubility in Ni is at least an order of magnitude higher than in Cu under these conditions of p_H, T .

Since the diffusion in metals proceeds by vacancy mechanism, the diffusivity of M-atoms is given by $D = x_v D^v (x_{cl} D^{cl})$ in the presence of interstitial

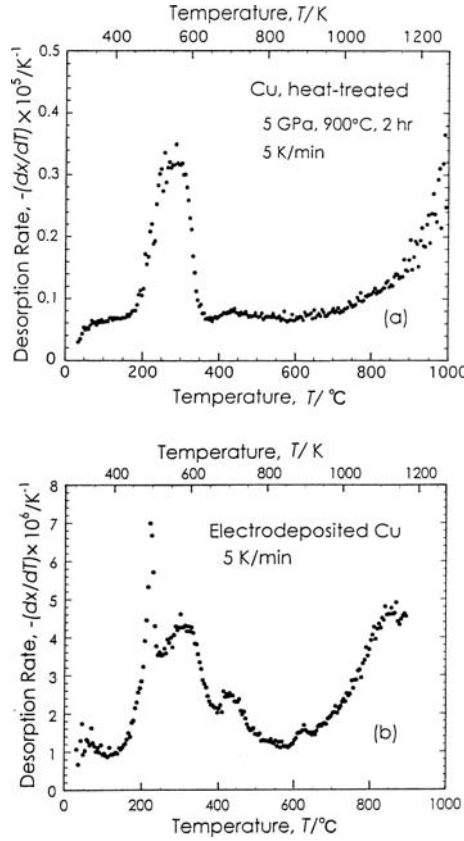


Fig. 5.68. Thermal desorption spectra of Cu samples prepared by (a) high $p_{\text{H}}-T$ heat treatment and (b) electrodeposition [5.179]

H atoms)⁵. The enhancement of x_{v} caused by hydrogen is so large that it outweighs the reduction of D^{v} . In the experiment shown above, on the Ni side, x_{cl} is enhanced by 6 orders of magnitude over x_{v} , whereas D^{cl} is reduced by 2 orders of magnitude from D^{v} , leaving the enhancement of 4 orders of magnitude of D . In short, a drastic reduction of the formation energy of vacancies caused by trapping H atoms outweighs a small increase of the migration energy, and induces enhancement of M-atom diffusion⁶.

⁵ For more detailed discussions of interdiffusion, effects of hydrogen on the thermodynamical factor, namely on the chemical potential of the diffusing entities, must be included. In the self-diffusion and impurity diffusion (interdiffusion in the low concentration limits, i.e. close to the end members), this complexity does not enter.

⁶ We note that the diffusion enhancement occurred in much shorter times than SAV concentrations to reach the equilibrium values (cf. Fig. 5.60). In fact, for

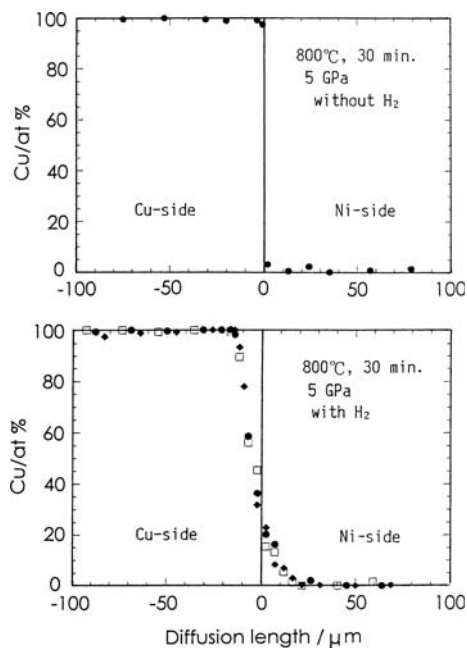


Fig. 5.69. Concentration profiles across the Cu/Ni diffusion couples observed after heat treatments at 800°C, 5 GPa for 30 min. In comparison with the reference measurement without hydrogen (*top*), the enhancement of diffusion with hydrogen (*bottom*) is obvious [5.218]

Similar enhancement of interdiffusion was observed in the phase separation process of several Pd alloys [5.222–5.227]. In Pd–Rh alloys under $p_{\text{H}} = 5$ GPa, the interdiffusion coefficient was enhanced by 5 orders of magnitude [5.227].

The effect of hydrogen on the self-diffusion was also studied in Nb, and clearly manifested H-induced diffusion enhancements [5.228, 5.382].

An interesting observation made by *Fujikawa et al.* [5.229] on electrodeposited Cu is believed to be caused by SAV formation, and is therefore worth quoting here. In the process of fabrication of Cu wiring of large-scale integrated circuits (LSIs), they discovered that an electrodeposited Cu film was more deformable than a vapor-deposited one, and amenable to subsequent high-pressure treatments to fill deep troughs (ditches) in the substrate. More

the diffusion enhancement only small concentrations of SAVs ($x_{\text{cl}} \leq 10^{-3}$) are sufficient, which can be supplied by some internal sources distributed uniformly over the samples. Investigations in pure metals have suggested dislocations and grain boundaries as possible internal sources of vacancies, and even a vacancy-interstitial pair creation in perfect crystals [5.219–5.221]. This reasoning is consistent with the result of our later experiment that the diffusion enhancement in single-crystal diffusion couples was an order of magnitude smaller.

interestingly, the deformability could be transferred from an electrodeposited film to a vapor-deposited film. These observations can only be explained in terms of enhanced creep motion of dislocations due to SAVs, which was introduced in the electrodeposition. Usually, a creep occurs at high temperatures where thermal vacancy concentrations are high ($\leq 10^{-4}$ at the melting point), but Vac-H cluster of these amounts can exist in electrodeposited Cu, as demonstrated above, and induce similar creep motion of dislocations.

It may be added in closing this section that an implication of SAVs for hydrogen embrittlement of steels has also been noted. We observed SAVs of $x_{\text{cl}} \leq 10^{-2}$ in Fe after heat treatments at $p_{\text{H}} \leq 1.7$ GPa, $T \leq 400^\circ\text{C}$, and proposed on this basis that Vac-H clusters formed in front of crack tips should play an important role in modifying the mechanical properties of the matrix [5.211]. Nagumo [5.230] was also led to the conclusion from his experiments that vacancies created by plastic deformation and stabilized by hydrogen should be playing a key role in the hydrogen embrittlement of steels. Tateyama and Ohno [5.383] suggested, on the basis of their electronic calculations, that very anisotropic agglomeration of SAVs in bcc Fe should have an important implication for the initiation of cracks.

5.7 Theory of the Atomistic State of Hydrogen in Metals

In terms of quantum mechanics, there can be two different views on the state of light particles in a periodic lattice: either localized as particles on particular interstitial sites or extended over all equivalent sites as waves, just like conduction electrons in metals. In the latter case, energy bands are formed in contrast to discrete energy levels in the former.

For interstitial hydrogen atoms, the band picture is believed to be largely irrelevant because the wave functions of hydrogen atoms are fairly well localized and the tunneling matrix elements, i.e., the overlap integrals of the wave functions on two adjacent sites, can be shown to be fairly small. In addition, in solid-solution phases, the inhomogeneous lattice distortion produced by the hydrogen atoms should make the energy states of interstitial hydrogen inequivalent, acting as a further impediment to band formation.

Let us consider the situation that exists when a single hydrogen atom is present in a crystal. Since the presence of hydrogen always causes a local (as well as uniform) expansion of the lattice, the potential acting between H and M atoms can be regarded as being generally repulsive. The outward displacements of the surrounding M atoms should make the potential around the interstitial site lower and broader and, in consequence, also lower the kinetic energy of the hydrogen atom. All this happens, however, at the expense of the elastic energy of lattice expansion, which increases nearly quadratically with the displacement of the M atoms. The situation is shown schematically in Fig. 5.70. The M lattice deforms itself spontaneously up to a certain

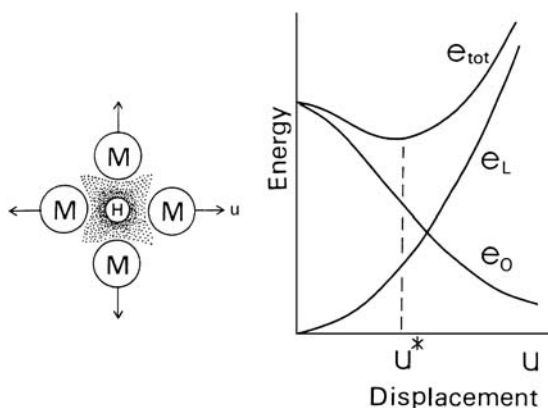


Fig. 5.70. A schematic diagram showing the physics of self-trapping effect. An interstitial H atom displaces the surrounding M atoms so as to minimize the total energy e_{tot} , which consists of the ground-state energy of the H atom, e_0 , and the energy of elastic distortion of the lattice, e_L

value that minimizes the total energy, consisting of the energy eigenvalue of the hydrogen atom and the elastic energy of the surrounding lattice. The lowering of the energy levels in the occupied site suppresses the tunneling to the surrounding sites. This mechanism of localization of a light particle is called self-trapping, or the small-polaron mechanism, after an analogous problem of the localization of an electron caused by a coupling with the lattice [5.231–5.233].

In this section, we shall try to give a consistent description of the various atomistic properties of interstitial hydrogen in the self-trapped state. This approach was initiated by *Fukai* and *Sugimoto* [5.234] and *Sugimoto* and *Fukai* [5.87, 5.235, 5.236], and has been pursued by *Puska* and *Nieminen* [5.237], and *Klamt* and *Teichler* [5.238, 5.239]. The problems to be treated by this approach include the preference of the type of interstitial sites, the energy and wave functions of the hydrogen atoms, the mechanism of the phase transition α – β in the V–H (V–D) system, the mechanism of diffusion, and the isotope dependence of these properties. The quantum character of interstitial hydrogen often manifests itself most conspicuously as a dependence of the properties on the isotopic mass: the lower the mass, the more conspicuous is the quantum character. We include here the muon (μ) as the lightest isotope of hydrogen whenever considered appropriate.

The atomic properties enumerated above are discussed in the same order below, except the diffusion process, which is the subject of the next chapter.

5.7.1 Theory of Self-Trapped States—Empirical Potential Approach

Let us consider a system which consists of one hydrogen atom and a large number of M atoms in a crystal. If the hydrogen atom can be regarded as following the motion of M atoms adiabatically, the energy of interaction between the H and M atoms, which serves as a potential for the former, is determined by the instantaneous positions of M atoms: $U(\mathbf{R}; \mathbf{r}^m + \mathbf{u}^m)$. The positions of the H atom and the m th M atom in a perfect crystal without hydrogen are written, respectively, as \mathbf{R} and \mathbf{r}^m , and \mathbf{u}^m is the displacement of the m th M atom induced by the H atom.

The energy of the hydrogen atom can be obtained by solving the Schrödinger equation,

$$[(-\hbar^2/2M)\nabla^2 + U]\Psi_\alpha = e_\alpha\Psi_\alpha, \quad (5.46)$$

for a given configuration of M atoms: $e_\alpha(\{\mathbf{u}^m\})$. The total energy of the system consists of the hydrogen energy and the elastic energy of distortion of the surrounding lattice, e_L :

$$e_{\text{tot}}(\{\mathbf{u}^m\}; \alpha) = e_\alpha(\{\mathbf{u}^m\}) + e_L(\{\mathbf{u}^m\}). \quad (5.47)$$

The configuration of the ground state ($\alpha = 0$) is obtained from the requirement that the adiabatic potential be minimum, $\partial e_{\text{tot}}(\{\mathbf{u}^m\}; 0)/\partial u_i^m = 0$, which, in the harmonic approximation, can be written in the form

$$u_i^m = \sum_{j,n} G_{ij}^{mn} F_j^n, \quad (5.48)$$

where G_{ij}^{mn} is the lattice Green's function, and F_j^n is a force exerted by the H atom on the n th M atom in the direction j , and is given by

$$F_j^n = - \int \partial U / \partial u_j^n |\Psi_0|^2 d\mathbf{R}. \quad (5.49)$$

Since the potential depends on displacements, a set of displacements $\{\mathbf{u}^m\}$ can be determined by solving (5.46–5.49) simultaneously. In this process, the energy eigenvalues and the wave function of the hydrogen atom in the ground state are also obtained; hence, the elastic energy of the lattice e_L and the components of the force-dipole tensor P_{ij} can be calculated by

$$e_L = \frac{1}{2} \sum_{n,i} u_i^n F_j^n \quad (5.50)$$

and

$$P_{ij} = \sum_n F_i^n r_j^n . \quad (5.51)$$

In solving for the excited states observed by inelastic neutron scattering, we may assume that the metal lattice remains in its ground-state configuration, and solve the Schrödinger equation by imposing the condition that the wave function is orthogonal to the ground-state function. In many cases, the condition of orthogonality is simplified by the symmetry of the site.

There remains the problem of constructing an interaction potential. Quite generally, the total energy of a metallic system can be divided into two terms: one that depends on the configuration of the constituent atoms, and the other that depends only on the total volume. In metal-hydrogen systems, as we already noted, the volume expansion due to hydrogen atoms arises almost entirely from a superposition of the local lattice distortions. Therefore, the volume-dependent term in the potential is expected to be sufficiently small.

The actual construction of the interaction potentials has been carried out either on the basis of theoretical calculations of the electronic energy as a function of atomic configuration or by taking some empirical method. The former approach, despite its obvious merits in principle, can be made computationally feasible only by taking some simplifying measures. This kind of calculation will be described in Sect. 5.7.3. Here we elucidate the calculations assuming an empirical form for the interaction potential.

Sugimoto and *Fukai* (SF) [5.235] assumed that U may be written as a sum of the central pair potentials,

$$U(\mathbf{R}; \mathbf{r}^m + \mathbf{u}^m) = \sum_m V(|\mathbf{r}^m + \mathbf{u}^m - \mathbf{R}|) . \quad (5.52)$$

In their calculation for hydrogen in the bcc metals V, Nb, and Ta, they adopted a sum of two exponential functions (a double Born-Mayer potential) for the pair potential:

$$V(R) = V_1 e^{-(R-r_t)/\rho_1} + V_2 e^{-(R-r_t)/\rho_2} , \quad (5.53)$$

where $r_t = \sqrt{5}a/4$ is the distance from a T site to a nearest M atom. The adoption of this form was motivated by the recognition that a pair potential described by a single exponential function (a Born-Mayer potential) cannot reproduce the vibrational energy and the force-dipole tensor simultaneously. The former requires a short-range potential whereas to the latter a long-range one is necessary. Thus, any appropriate potential must incorporate in it both short-range and long-range parts.

Klamt and *Teichler* (KT) [5.238] adopted a slightly modified function that allows a smooth cutoff of the long-range part:

$$V(R) = \begin{cases} V_1 e^{-(R-r_t)/\rho_1} + V_2 e^{-(R-r_t)/\rho_2} e^{-R^2/(r_0^2 - R^2)} & R < r_0 , \\ 0 & R > r_0 , \end{cases} \quad (5.54)$$

where r_0 was chosen to lie between the second- and the third-neighbor shell.

In both SF and KT, the potential parameters were determined by making a fit to the force-dipole tensor and the two fundamental vibrational excitations for protons. The values obtained are listed in Table 5.11. Note that the two range parameters (ρ_1 and ρ_2) differ by more than a factor of 10. The calculated values of the excitation energies and the force-dipole tensor are listed in Table 5.12 and compared with the experimental data fitted. The agreement can be seen to be reasonably good. (The parameters of KT appear to reproduce the isotropic force-dipole tensor better.) Electronic theories underlying the determination of the adiabatic potential will be discussed in Chap. 7.

Table 5.11. Potential adopted by *Sugimoto* and *Fukai* (SF) [5.236] and *Klamt* and *Teichler* [KT] [5.238]

Metal	V_1 [meV]	V_2 [meV]	ρ_1/a	ρ_2/a	r_0/a	Reference
V	90	400	0.025	0.333	—	SF
Nb	100	600	0.025	0.333	—	SF
	78.92	629.7	0.0208	0.91	1.104	KT
Ta	100	600	0.025	0.333	—	SF
	61.72	607.1	0.0207	0.775	1.132	KT

Table 5.12. Comparison of the calculated values of the vibrational excitation energies and the force-dipole tensor with the observed values. The calculated values are from *Sugimoto* and *Fukai* (SF) [5.236] and *Klamt* and *Teichler* (KT) [5.238], and the experimental values (Exp.) are from Tables 5.2, and 5.4

Metal	Vibrational Energies [meV]		Force-Dipole Tensor [eV]		Reference
	Δe_1^Z	Δe_1^X	$A + 2B$	$3 A - B / (A + 2B)$	
V	107	167	8.4	0.21	SF
	106	~170	7.45	0.30	Exp.
Nb	102	159	10.4	0.12	SF
	118.5	166.7	10.0	0.02	KT
Ta	107	163	10.1	≤ 0.06	Exp.
	109	168	10.9	0.15	SF
	114.0	164.0	10.2	0.00	KT
	114	154	10.1	≤ 0.06	Exp.

The purpose of the calculations of SF and KT was to demonstrate and/or examine the extent to which the adoption of an appropriate potential based on a few input data on protons can provide a general picture of hydrogen isotopes self-trapped in interstitial sites in metals. For a numerical solution of the problem, the following procedure was adopted:

- (1) One starts by assuming appropriate values for the displacements of M atoms, and calculates the potential energy U for this configuration.
- (2) Using this potential, one solves the Schrödinger equation (5.46) numerically and obtains the energy eigenvalues e_α and the ground-state wave function Ψ_0 of the interstitial hydrogen.
- (3) One calculates the forces F_j^n acting on M atoms from (5.49) and the concomitant displacements of M atoms from (5.48).
- (4) The whole procedure is to be repeated until self-consistency is attained regarding the displacements of M atoms.

Noteworthy is the fact that the crux of this kind of calculations, i.e., the solution of a Schrödinger equation for a complex potential field, was achieved by adopting the method of *Kimball* and *Shortley* [5.240]. A detailed description of the algorithm of this classic method as applied to the present problem is given by *Puska* and *Nieminen* [5.237].

a) Self-Trapped State

The self-trapping energy ΔE , which is the lowering of the total energy e_{tot} by lattice relaxation, was calculated by SF for three possible configurations, 1T, 4T, and 6T, shown in Fig. 5.71. The configuration 1T is the ordinary

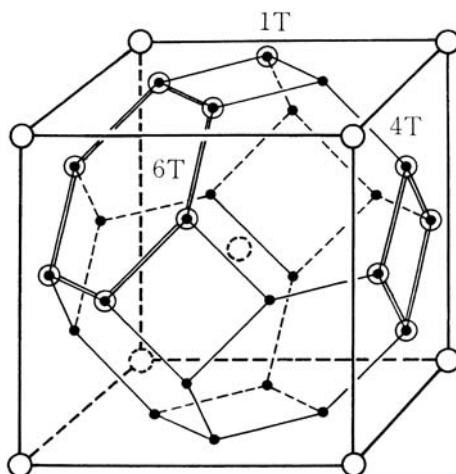


Fig. 5.71. Possible interstitial configurations in a bcc lattice having the symmetry of T-site groups

T-site occupancy; the 4T and 6T configurations are such that the symmetry around the axis passing perpendicularly through the center of these four or six T sites is conserved in the course of lattice relaxation. Note that the 4T configuration includes the O-site occupancy as a particular case; hence, we shall write it occasionally as 4T(O). As it turns out that the 6T configuration is always much higher in energy than the 1T and 4T configurations, only the latter two need be considered. (According to SF [5.235], the 6T configuration for H in Nb, for example, has $\Delta E = -0.326$ eV in comparison to -0.476 eV for the 1T and -0.417 eV for the 4T configurations.)

The self-trapping energies, the displacements of the nearest and the next-nearest M atoms, and the force-dipole tensor calculated by SF and KT for the 1T configuration are listed in Table 5.13, and those for the 4T configuration in Table 5.14. In these calculations, the directions of the coordinate axes (X, Y, Z) are chosen as shown in Fig. 5.72b. Thus, the displacements are defined as follows: For the 1T configuration, taking the origin at the T site, the position of the nearest-neighbor M atoms is written as $(a/2 + d_2, 0, a/4 + d_1)$, etc., and that of the next-nearest M atoms as $(0, a/2 + d_4, 3a/4 + d_3)$, etc. For the 4T(O) configuration, taking the origin at the center of the four

Table 5.13. Self-trapping energy, displacements of near neighbors, and force-dipole tensor for hydrogen isotopes in the 1T configuration, as calculated by *Sugimoto* and *Fukai* (SF) [5.87, 5.235, 5.236] and *Klamt* and *Teichler* (KT, given in brackets) [5.238]

Metal	Isotope	Self-Trapping Energy ΔE [meV]	Displacements (in $a/200$)				Force-Dipole Tensor	
			First Neighbor		Second Neighbor		$A + 2B$ [eV]	$3 A - B / (A + 2B)^a$
	μ		d_1	d_2	d_3	d_4		
V	H	-403	2.4	6.3	-0.3	-0.4	8.4	0.21
	D	-345	2.3	5.8	-0.2	-0.3	8.0	0.19
	T							
Nb	μ	-938(-982)	8.6	3.1	-0.3	-0.2	12.90 (12.8)	0.25(0.17)
	H	-476(-427)	2.7	6.3	0.3	0.0	10.4 (10.0)	0.12(0.02)
	D	-417(-362)	2.6	6.0	0.4	0.0	10.0 (9.7)	0.09(0.04)
	T	-390	2.5	5.8	0.4	0.0	9.7	0.08
Ta	μ	(-742)					(13.2)	(0.18)
	H	-429(-306)	2.1	5.7	0.4	0.0	10.9 (10.2)	0.15 (0.00)
	D	-375 (-257)	2.1	5.4	0.4	0.0	10.5 (9.7)	0.13 (0.04)
	T							

^aThe signs of the values calculated by SF are consistently negative, of those by KT are unknown.

Table 5.14. Self-trapping energy, displacements of near neighbors, and force-dipole tensor of hydrogen isotopes in the 4T(O) configuration, as calculated by *Sugimoto* and *Fukai* (SF) [5.87, 5.235, 5.236] and *Klamt* and *Teichler* (KT, given in brackets) [5.238]

Metal	Isotope	Self-Trapping Energy $\Delta E[\text{meV}]$	Displacements (in $a/200$)		Force-Dipole Tensor	
			First Neighbor d_1	Second Neighbor d_3	$A + 2B[\text{eV}]$	$3 A - B / (A + 2B)$
V	μ					
	H	-375	12.5	-0.6	7.5	1.06
	D					
Nb	T					
	μ	-981(-999)	14.4	0.8	(13.3)	(0.50)
	H	-423(-378)	11.6	0.9	9.4(10.3)	0.85(0.48)
	D	-357(-314)	9.6	1.4	(9.8)	(0.48)
Ta	T	-336	8.9	1.6		
	μ	(-766)			(15.0)	(0.30)
	H	-372(-253)	10.0		10.2(12.1)	0.76(0.37)
	D	(-204)			(11.6)	(0.36)
	T					

T sites (at the O site), the position of the nearest-neighbor M atoms is written as $(0, a/2 + d_1, 0)$, etc., and that of the next-nearest M atoms as $(a/2 + d_3, 0, a/2 + d_3)$, etc. An inspection of the isotope dependence of these quantities makes one realize that both the lattice distortion and the self-trapping energy become more important for lighter isotopes – only slightly in the former case but conspicuously in the latter case. A qualitative explanation for this is that the more extended wave functions of the lighter isotopes exert stronger forces on the neighboring M atoms.

The small isotope dependence of the lattice distortion is in good agreement with the experiments on the force-dipole tensor for hydrogen in the 1T configuration; cf. Table 5.2. The nearest-neighbor displacement $u_1 = 0.11 \text{ \AA}$ calculated from the tabulated values of d_1 and d_2 for H in Nb also agrees with the value 0.10 \AA obtained from the static Debye–Waller factor [5.35]. In contrast to the 1T configuration, the lattice distortion in the 4T configuration is strongly anisotropic. This stems from the fact that forces from the hydrogen atoms act almost solely on the nearest-neighbor M atoms. The calculated values of the anisotropy factor $3 | A - B | / (A + 2B)$ are in good agreement with the experimental values for H and D in V (Table 5.2) and also with the value 0.89 from high-pressure data on $\kappa\text{-NbH}_{0.75}$ [4.36]. The anisotropy factor of this magnitude is typical of heavier interstitial atoms (C, N, O)

occupying O sites in bcc metals (see, e.g., [5.241]). Another calculated feature of lattice distortion, that the dilatational force $A + 2B$ of the 4T(O) configuration is smaller than the 1T configuration, also agrees with the observation (Table 5.2).

Regarding the self-trapping energy, the values calculated by SF are in fair agreement with those of KT but much larger in magnitude than those of *Kehr* [5.242]. In the harmonic approximation adopted by *Kehr*, ΔE becomes always equal to $-2e_L$ and, in effect, underestimates the actual lowering of the energy eigenvalue caused by the self-trapping distortion of the lattice.

The potential profile and the wave function of an H atom in the ground state, self-trapped on a T site in Ta, are shown in Fig. 5.72a,b [5.236]. The maps depict the potential and the wave function on one of the cube faces of a bcc lattice, with the H atom localized on the T site labeled A in the figure. The potential field, originally having minima on T sites and maxima on O sites in an undistorted lattice, has been changed by lattice relaxation to give a fairly deep well around site A and, as a result, the wave function is fairly well localized on A.

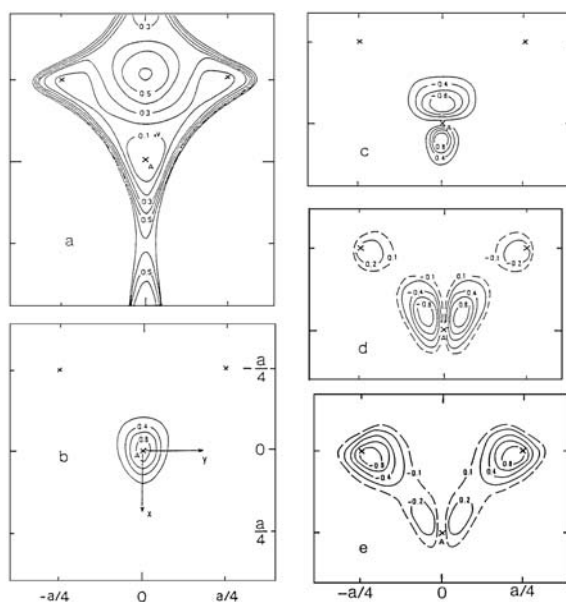


Fig. 5.72. a–e. Contour maps of the potential and the wave functions of an H atom in Ta. The H atom is self-trapped at the T site labeled A in the figure. (×: the geometrical location of T sites on the Z-X plane.) (a) The potential; (b) the wave function of the ground state, Ψ_0 ; (c) the first excited state Ψ_1^Z , having a nodal plane at $Z = 0$; and (d), (e) the excited states Ψ_1^X and Ψ_2^X , both having a nodal plane at $X = 0$ [5.236]

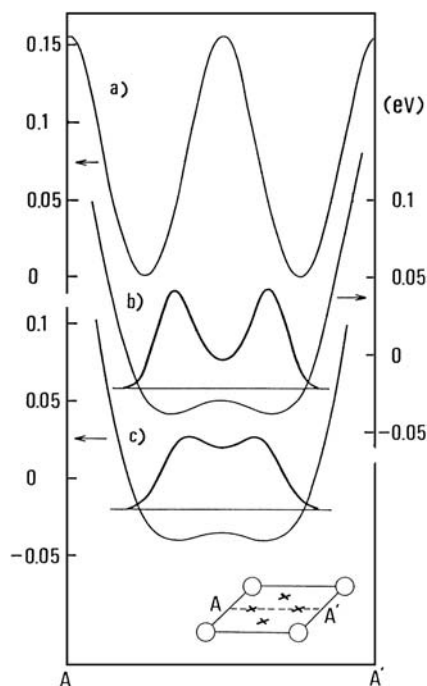


Fig. 5.73. a–c. Potential profiles and ground-state wave functions of a proton and a positive muon in the 4T configuration in Nb. Variation along the line AA' is shown in the inset. (a) Potential profile in the undistorted lattice, (b) proton, and (c) muon [5.235]

In the case of the 4T(O) configuration, the effect of lattice relaxation is more pronounced. In Fig. 5.73, the potential profiles and the ground-state wave function of an H atom and of a positive muon (μ^+) in the 4T configuration in Nb are shown [5.235]. As a result of self-trapping distortion, a potential profile along the line AA' shown in the inset is changed drastically; a local maximum originally located at the center (O site) has almost disappeared, leaving only a small hump at the bottom of the broad potential well. The wave function of the H atom is now extended over some region around the O site, having four maxima reminiscent of T sites but displaced appreciably inward from the original position of T sites. This drastic change in the potential comes mainly from the outward displacement of a pair of nearest-neighbor M atoms of the O site. The displacement lowers the repulsive potential from these neighbors so effectively that a local maximum in an undistorted lattice is gradually converted into a local minimum. For μ^+ , a hump of the potential at the center (O site) becomes even smaller due to larger displacements of the nearest-neighbor M atoms, and the wave function has a single maximum centered on the O site. This situation can legitimately

be referred to as O-site occupancy. Thus, O-site occupancy can be realized only as a result of self-trapping distortion.

It may be emphasized here that the concept of interstitial sites as geometrical points is hardly meaningful. Both the potential and the wave function vary over distances comparable to the distance between the interstitial sites; moreover, they are affected so strongly by the local lattice distortion that no prediction as to the self-trapped state could be made on the basis of the geometrical concept of interstitial sites in an undistorted lattice.

The energy difference between 1T and 4T(O) configurations (Δe_{4T-1T}) is not so large that the relative stability of these two configurations under various circumstances need to be examined. The results of the calculation of (Δe_{4T-1T}) for μ^+ , H, D, and T in the three metals V, Nb, and Ta are shown in Fig. 5.74 [5.235,5.236]. These results show that the three isotopes (H, D, T) assume the 1T configuration, in agreement with observations. Experimental determination of the μ^+ location, on the other hand, has not been conclusive. For H and D atoms, the result that Δe_{4T-1T} is smaller in V than in Nb and Ta is consistent with the realization of stress-induced 4T (dis-T) state in the α phase and the occurrence of the β phase in $VH(D)_x$ as described in the preceding chapters. The fact that the β -phase region on the phase diagram becomes narrower in the order VH_x , VD_x , and VT_x (Fig. 2.3) can also be understood from the isotope dependence of Δe_{4T-1T} .

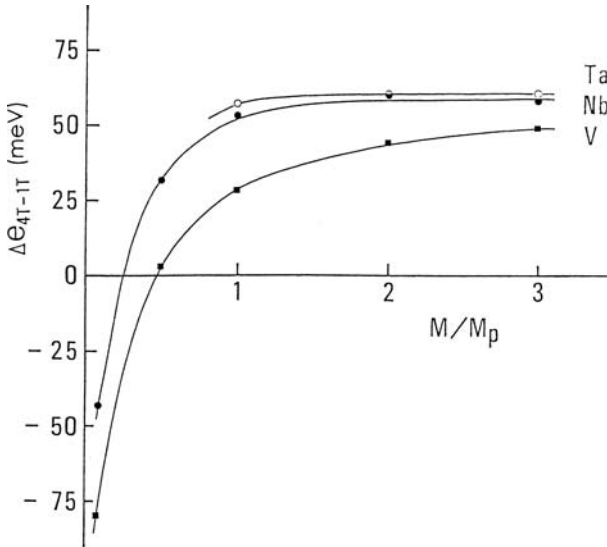


Fig. 5.74. Variation with isotope mass (in units of proton mass M_p) of the difference of self-trapping energies of 4T and 1T configurations in Group-V metals. Points for a hypothetical particle with $M/M_p = 1/2$ have been included to guide the eye [5.235,5.236]

These results on Δe_{4T-1T} provide a physical explanation for the observed size-effect in site preference. Noting that lighter isotopes appear to be larger in size owing to their more extended wave functions (larger amplitudes of the zero-point vibration), we may summarize these results by saying that the 4T(O) configuration tends to become preferable to the 1T configuration as the interstitial atom becomes larger in size or, conversely, as the lattice parameter of the host metal becomes smaller. This variation of Δe_{4T-1T} with the relative size of an interstitial atom with respect to the host lattice arises from the fact that, in more congested circumstances, it costs less energy for an interstitial atom to displace two nearest-neighbor M atoms around an O site than four M atoms around a T site. This mechanism of stabilization of O sites operates not only for hydrogen isotopes but also for larger interstitial atoms (C, N, O), which invariably enter O sites in bcc metals. This point may be noted in the calculation of *Johnson et al.* [5.234] on C in Fe.

The data for comparison with the calculated wave functions are provided by the density maps constructed from neutron diffraction data, such as those shown in Figs. 5.10, 5.11.

One of the common features of these observations is that the density distribution is nearly independent of the isotope studied, whereas the calculations of SF lead to isotope-dependent distributions, which are consistently more localized than the observed ones. It must be recognized, however, that no meaningful comparison can be made without taking band-mode vibrations into account. A dominating contribution of band-mode vibrations will make the apparent density distribution more extended in space, irrespective of the isotope (Sect. 5.4.4).

b) Excited States

For the calculation of the excitation energies observed by inelastic neutron scattering, *Sugimoto* and *Fukai* [5.87, 5.235, 5.236] assumed that a transition between the vibrational states of hydrogen atoms occurs so much faster than the motion of the surrounding lattice that M atoms are frozen in the configuration corresponding to the self-trapped state during the transition. Therefore, in order to obtain the excited states, we solve the Schrödinger equation with a known form of the potential for the ground state, imposing the condition of orthogonality of the ground-state wave function to the wave functions of the excited states. For some excited states, the condition is simplified by symmetry: from Fig. 5.72b, it may be obvious that there are three excited states whose wave functions have a node on the Z - X , Z - Y , or X - Y plane, and satisfy the symmetry condition $\Psi(Y, X, Z) = -\Psi(X, -Y, Z)$, $\Psi(X, Y, Z) = -\Psi(-X, Y, Z)$, or $\Psi(X, Y, Z) = -\Psi(Y, X, -Z)$, respectively. The wave functions of the other excited states are obtained in a more straight-forward manner by following the Schmidt orthogonalization procedure.

The contour maps of the excited-state wave functions are shown in Fig. 5.72c, d, e. The wave function Ψ_1^Z , shown in (c), has a node on the X - Y plane; thus, this state can be regarded as the excitation of motion along the Z direction, (d) and (e) show the contour maps of the wave functions Ψ_1^X and Ψ_2^X , having a node on the Z - Y plane. These states can be regarded as the excitation of motion along the X direction. These two wave functions have been orthogonalized to each other. It may be noted that Ψ_1^X has a large amplitude in the potential minimum A, whereas Ψ_2^X has a maximum amplitude near the neighboring pair of T sites. The wave functions of similar excited states, Ψ_1^Y and Ψ_2^Y , having a node on the Z - X plane are not shown. These states are degenerate in energy with Ψ_1^X and Ψ_2^X , respectively.

Considering that the wave function of the ground state Ψ_0 is strongly localized on the potential minimum A, the probability of the transition $\Psi_0 \rightarrow \Psi_2^X$ (Ψ_2^Y) is expected to be small. The two peaks observed by INS in the ratio 1: 2 should, therefore, correspond to transitions $\Psi_0 \rightarrow \Psi_1^Z$ and $\Psi_0 \rightarrow \Psi_1^X$ and Ψ_1^Y , respectively. This is the consideration that underlies the assignment of Δe_1^X (Δe_1^Y) to the experimental value of ~ 0.17 eV in the fitting procedure.

Note that the values obtained for Δe_1^Z of an H atom (Table 5.12) agree well with the experimental value of ~ 0.12 eV (Table 5.4), and that the isotope dependence of these excitation energies is also correctly reproduced.

This overall agreement with observations has a simple physical meaning. As the potential around an H atom self-trapped on a T site is essentially determined by the short-range part of the double Born-Mayer form, we may expand it to the second power of displacements from the T site, and obtain expressions for Δe_1^Z and Δe_1^X in the harmonic approximation:

$$\Delta e_1^Z = \frac{\hbar}{r_1} \sqrt{\frac{4V_1}{5M}} e^{-r_t/2\rho_1} \frac{r_t}{\rho_1} \sqrt{1 - \frac{4\rho_1}{r_t}}. \quad (5.55a)$$

$$\Delta e_1^X = \frac{\hbar}{r_1} \sqrt{\frac{8V_1}{5M}} e^{-r_t/2\rho_1} \frac{r_t}{\rho_1} \sqrt{1 - \frac{3\rho_1}{2r_t}}. \quad (5.55b)$$

In this approximation, the ratio $\Delta e_1^X/\Delta e_1^Z$ approaches $\sqrt{2}$ if the range parameter ρ_1 is much smaller than the distance r_t to the nearest-neighbor M atoms. The fact that the observed ratio of $\Delta e_1^X/\Delta e_1^Z$ (≈ 1.5) is close to $\sqrt{2}$ means that the potential is indeed sufficiently short-ranged⁷.

The observed isotope dependence of the excitation energies, $\Delta E^H/\Delta E^D \sim \sqrt{2}$ for all the observed transitions, can also be understood from (5.55a, b),

⁷ A strong correlation was found between the optic-mode excitation energy ΔE and the M-H distance R in a series of fluorite-type dihydrides where H atoms occupy T sites. Within the scatter of data points, the correlation can be represented by $\Delta E \propto R^{-3/2}$ [5.244] or $\Delta E \propto R^{-1}$ [5.245].

Fukai and Sugimoto [5.245] showed that this empirical relation could be explained, approximately, in terms of superposition of short-range, central pair potentials of the form $u(r) = V_1 e^{-r/\rho_1}$. Using harmonic approximation after expanding the sum of the four interaction potentials around a T site, we obtain

provided that the same potential can be used for both isotopes and the self-trapping distortion is nearly the same, as it really is.

It may be mentioned that second-harmonic excitation energies (Δe_2^Z) calculated by SF for D in Nb and Ta also agreed with experiments, including their small negative anharmonicities.

For higher-harmonic excitations, however, the results of SF (and KT) appear to be at variance with experiments. The observation of transitions from the excited states as high as ~ 0.8 eV [5.57] indicates that the wave functions of these excited states are fairly well localized in the same potential well as the initial ground state, whereas the calculations of SF (and KT) predict the higher-energy states to be delocalized over neighboring interstitial sites, having very small transition probabilities to the ground state. This makes one suspect that the actual depth of the potential well may be greater than that adopted by SF and KT. The fact that a calculated saddle-point energy using the SF potential fell below the observed migration energy for H in Nb in the high-temperature region also suggests the same deficiency. Indeed, the adiabatic potential for H in Nb, obtained by *Ho et al.* [5.246] from the first-principles band calculations, was found to form a potential well deep enough to accommodate at least a few excited states. It may be anticipated that a real improvement on this point would require a better treatment of the metal-metal as well as hydrogen-metal interaction potentials. The interaction between M atoms, approximately treated by SF and KT in the linearized form as the lattice Green's function, may have to be treated in a more explicit

$$\Delta E = \frac{\hbar}{R} \sqrt{\frac{4V_1}{3M}} e^{-R/2\rho_1} \frac{R}{\rho_1} \sqrt{1 - \frac{2\rho_1}{R}}, \quad (5.56)$$

where M is the proton mass. The empirical relation $\Delta E \propto R^{-1}$ indicates that the M-H distance varies in proportion to the range of the interaction potential, and therefore R/ρ_1 is independent of R . The best-fit to the experimental data leads to the following relation

$$V_1 e^{-R/\rho_1} \left(\frac{R}{\rho_1} \right)^2 \left(1 - \frac{2\rho_1}{R} \right) \approx 14.4 \text{ eV}.$$

(The term $2\rho_1/R$ in the bracket can be neglected for short-range potentials.) Assuming tentatively that this relation also holds for the T-site occupancy in bcc metals, say H in Nb, we substitute this value into (5.55) and obtain $\Delta e_1^Z = 0.118$ eV. The agreement with observation is excellent.

Thus this empirical relation and its explanation hold generally for T-site occupancies, but not for O-site occupancy. In the case of O-site occupancy in fcc and hcp monohydrides of 3d and 4d metals, no such systematic variation with atomic distance was found [5.54]. The implication is that in the region around O sites in these fcc and hcp lattices, which is much broader than around T sites, the short-range M-H interaction is not playing a decisive role in determining the overall shape of the potential.

form, at least in the neighborhood of hydrogen atoms, in order to calculate the self-trapping effect more reliably.

A step in this direction was taken by *Gillan* [5.247,5.248] and *Christodoulos* and *Gillan* [5.249,5.250]. In their series of papers, they developed a path-integral quantum simulation method and applied it to a number of properties of hydrogen isotopes in Pd and Nb, including the energy and wave functions in the self-trapped state, density distribution and diffusion. In these calculations, they adopted the M–M interaction of Finnis–Sinclair form [5.251] that reproduces the phonon dispersion relation of the host metals, and the H–M interaction of a single-exponential form fitted to the first two excitation energies. The parameters chosen were $V_1 = 676$ meV and $\rho_1/a = 0.053$ in our notation. In effect, they dropped the long-range part of the SF (and KT) potential on the ground that it is physically less-well founded.

Christodoulos and *Gillan* [5.249] demonstrated that it is straightforward, using path-integral simulation, to calculate the density distribution of H atoms with full inclusion of quantum effects. They compared their calculation on H and D in Nb with experimental structure factors, but detailed evaluation of the results was hampered by the limited accuracy of the data.

Subsequently, they performed extensive calculations on the self-trapped state of H in Nb [5.249]. The biggest technical advancement there was in their method of solving the Schrödinger equation. They realized that the Kimball–Shortley technique adopted by previous authors [5.234–5.238] was inefficient, and used instead the usual finite-difference approximation combined with the standard matrix diagonalization routines. In this way, they obtained energy eigenvalues and wave functions of as many as 42 eigenstates, and expected intensity of neutron scattering from each transition. The agreement with observation was, however, only fair. Although excitation energies of the first two fundamentals, (001) and (100)/(010) excitations, were fairly well reproduced (by fitting), as they should, the calculated scattering intensity $I(\mathbf{Q}; e_\alpha)$ agreed with observation only for the (001) excitation, and markedly deviated for (100)/(010) and (002) excitations. These results cast some doubt on the reality of the higher-energy states predicted. In fact, the failure of reproducing the observation could have been anticipated from their negligence of the long-range part of the H–M interaction potential. Their potential decays substantially at nearest-neighbor and next-nearest neighbor M-atoms, and the concomitant reduction of self-trapping distortion should affect the self-trapped state. The problem of the H–M interaction potential will be resumed in Sect. 5.7.3.

In order to examine the effects of local lattice distortion on the vibrational energies, calculations were performed by SF [5.235] by displacing the nearest-neighbor M atoms of a T site in a few simple modes. It was found that the vibrational energies are affected rather sensitively, and the displacements of M atoms caused by thermal fluctuations and/or the presence of other hydrogen atoms are large enough to account for the extra broadening of the peaks

observed in the α phase of the three metals V, Nb, and Ta (Fig. 5.23). Large-amplitude band-mode vibrations (Sect. 5.4.4) are expected to be playing an important role here.

Another effect of local lattice distortion is the Stokes shift⁸. The Stokes shift is expected between the vibrational energies to be obtained in up-scattering and down-scattering of neutrons because the energy of the excited state should be lowered by lattice relaxation, so that a downward transition of an H(D) atom from a relaxed excited state should involve a smaller energy than an upward transition from a relaxed ground state. In spite of the sensitivity of energy states to the configuration of M atoms, no such difference in energy-gain and energy-loss spectroscopies has been observed. The apparent absence of the Stokes shift requires more fundamental considerations of the mechanism of the transitions.

Klamt and *Teichler* [5.238] suggested that the degeneracy of the doublet mode (~ 0.17 eV) may be easily removed by the Jahn–Teller effect, because the doublet mode (~ 0.17 eV) is more sensitive to local lattice distortion than the singlet mode (~ 0.12 eV). This point has been pursued still further by *Klamt* [5.252]. It may be recalled in this connection that the observed peaks of the doublet mode are always much broader than the singlet and are, in fact, split by finite amounts in more recent high-resolution experiments (Figs. 5.22, 5.23).

5.7.2 Theory of β Phase of the Vanadium–Hydrogen System

One of the striking features of the vanadium–hydrogen system is that hydrogen atoms randomly distributed over T sites in the α phase move into one type of O sites (O_Z) in the low-temperature phase β and, in consequence, make the crystal structure body-centered tetragonal (bct) with $c/a \geq 1.1$. This phase transition $\alpha - \beta$ is believed to be a result of the cooperative elastic interaction, on the basis that the occupation of O_Z sites should produce an elongation of the c axis, which, in turn, should facilitate the O_Z -site occupancy of other hydrogen atoms. Here we demonstrate, according to the work of *Sugimoto* [5.88], that the theory described in the preceding section provides a natural explanation for the bcc–bct transition in the vanadium–hydrogen system.

Let us first examine the effect of uniform elongation of the c axis on the energy of a hydrogen atom self-trapped at a 1T site.

As shown in Fig. 5.75, T sites in a bct lattice are divided into two types from symmetry considerations: we call the T sites with a twofold symmetry axis in the c direction T_Z , and those with the same in the a (b) direction

⁸ The Stokes shift is a terminology borrowed from optics, where light emission occurs at a lower frequency than light emission due to the lowering of the electron energy of the excited state by electron-phonon coupling. Recently, the possibility of such effects was proposed for PdH; see Sect. 5.7.3

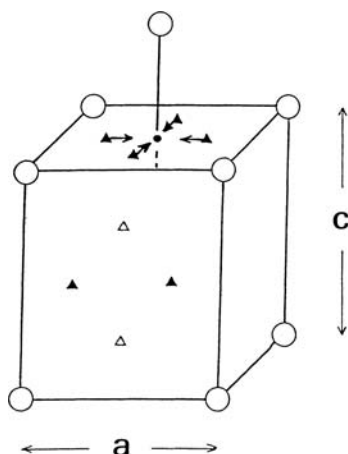


Fig. 5.75. Interstitial sites in a bcc lattice. Geometrical locations of O_Z , T_Z , and $T_{X(Y)}$ sites are denoted by ●, ▲, and △, respectively

$T_{X(Y)}$. Accordingly, $1T$ states in the bcc lattice must now be divided into $1T_Z$ and $1T_{X(Y)}$. The $4T$ state also needs to be divided into two types in the bcc lattice. We call the $4T$ state with a fourfold axis in the c direction $4T_{XY}$. Note that the $4T_{XY}$ state has the same symmetry as the state of O_Z -site occupancy. Other $4T$ states, which we label $4T_{YZ(ZX)}$ have a twofold symmetry axis along the a (b) directions.

The variation of the self-trapping energy of an H atom with elongation of the c axis, $\bar{\varepsilon}$ ($= c/a - 1$), under the condition of a constant volume is shown in Fig. 5.76. One of the interesting features is that the energies of the $1T_{X(Y)}$ and $4T_{XY}$ states decrease with increasing $\bar{\varepsilon}$, and these energies become indistinguishable at elongations larger than $\bar{\varepsilon} = 0.08$.

The physical origin of this degeneracy can be understood by examining the potential profiles and the ground-state wave function of the H atom. As shown in Fig. 5.77, the $1T_{X(Y)}$ state at $\bar{\varepsilon} = 0$ (bcc) produces by the self-trapping distortion a deep potential minimum at the position of a T site, with the ground-state wave function localized in the potential well. When the c axis is elongated uniformly under the condition of a constant volume, both the potential profile and the position of the potential minimum change drastically. With increasing $\bar{\varepsilon}$, the local minimum originally located at the T site is displaced gradually towards the geometrical position of the O_Z site. When $\bar{\varepsilon} \geq 0.08$, the potential comes to have four shallow minima symmetrically disposed around the O_Z site, and its profile looks more like a square than a parabola, as seen in Fig. 5.77. In fact, the $1T_{X(Y)}$ state is identical with the $4T_{XY}$ state at $\bar{\varepsilon} \geq 0.08$, and both can appropriately be referred to as O_Z -site occupancy.

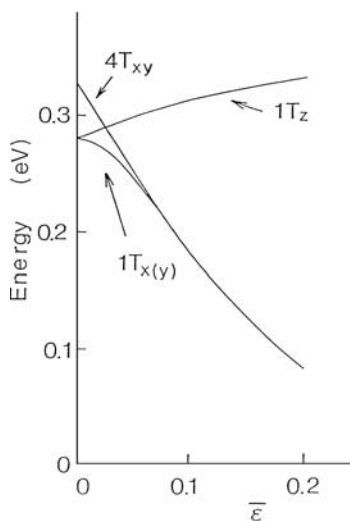


Fig. 5.76. Variation of the self-trapping energy of an H atom in the $4T_{XY}$, $1T_{X(Y)}$ and $1T_Z$ states in V with $\bar{\varepsilon}$ ($= c/a - 1$) [5.88]

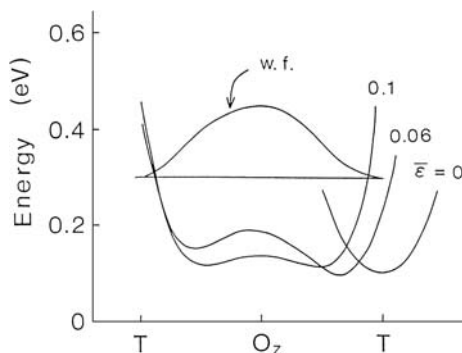


Fig. 5.77. Potential profiles along the a (b) axis for an H atom in the $1T_X$ state in V at $\bar{\varepsilon} = 0, 0.06$, and 0.1 . The ground-state wave function of the H atom for $\bar{\varepsilon} = 0.1$ is also shown [5.88]

Using this result, it is possible to understand the mechanism of the stabilization of the β phase. Considering that the lowest-energy state of H (D) atoms is the one self-trapped at $1T_{X(Y)}$ sites, the part of the energy that depends on the uniform elongation $\bar{\varepsilon}$ can be given as

$$e_{\bar{\varepsilon}} = (c_{11} - c_{12})V\bar{\varepsilon}^2/3 + ne_{1T}(\bar{\varepsilon}), \quad (5.57)$$

where $c_{11} - c_{12}$, V and e_{1T} are, respectively, the shear elastic constant, the volume of the lattice and the self-trapping energy of the $1T_{X(Y)}$ state. The variation of this energy per hydrogen atom, $e_{\bar{\varepsilon}}/n$, with $\bar{\varepsilon}$ is shown in Fig. 5.78.

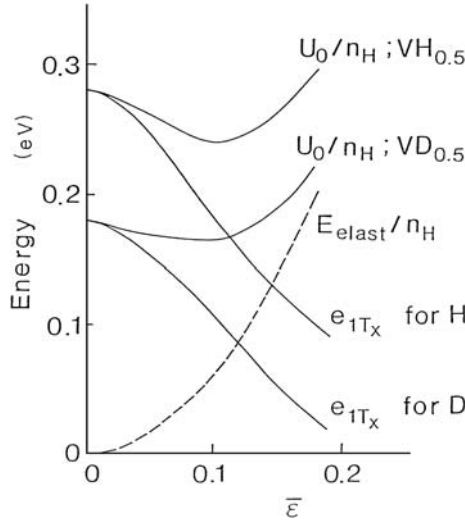


Fig. 5.78. Variation of $e_{\bar{\varepsilon}}/n$ for $\text{VH}_{0.5}$ and $\text{VD}_{0.5}$ with $\bar{\varepsilon}$. The elastic energy per H atom (e_L/n) and the self-trapping energies of H and D in the $1T_{X(Y)}$ state in V are also shown [5.88]

The volume per hydrogen atom, V/n , corresponds to that of $\text{VH(D)}_{0.5}$. The minimum of $e_{\bar{\varepsilon}}/n$ appears at $\bar{\varepsilon} \approx 0.1$ for both $\text{VH}_{0.5}$ and $\text{VD}_{0.5}$, showing that the bct structure with an axial ratio $c/a = 1.1$ is stabilized at low temperatures. The value of the spontaneous elongation obtained here agrees well with observations. We find, in addition, that the difference between the value of $e_{\bar{\varepsilon}}/n$ at $\bar{\varepsilon} = 0$ (bcc) and the minimum, $e_{\bar{\varepsilon}}/n$, depends on the isotope, being about 40 and 15 meV for $\text{VH}_{0.5}$ and $\text{VD}_{0.5}$, respectively. This is consistent with the fact that the β phase is relatively more stable in the V–H system than in the V–D system. This isotope effect comes largely from the isotope dependence of the difference in the zero-point energy of T- and O_Z -site occupancies, exactly as proposed by *Entin et al.* [5.53] for the explanation of the large isotope dependence of the α – β transition temperature.

The results of similar calculations on $\text{NbH}_{0.5}$ show that the minimum of $e_{\bar{\varepsilon}}/n$ becomes much shallower than in $\text{VH}_{0.5}$ and $\text{VD}_{0.5}$; therefore, the realization of a bct structure by O_Z -site occupancy is less favorable. This is consistent with the fact that hydrogen atoms in Nb do not occupy O_Z sites under ordinary circumstances. This difference in $\Delta e_{\bar{\varepsilon}}/n$ between Nb–H and V–H systems comes primarily from the difference in the atomic volumes; in the Nb–H system, the elastic energy [the first term of (5.57)] is larger by 30% than in the V–H system, simply because of a larger atomic volume of Nb.

We can also give a simple explanation for the observed linear concentration dependence of the axial ratio. First, the $\bar{\varepsilon}$ dependence of $e_{1T_{X(Y)}}$ (Fig. 5.78) can be regarded to be approximately linear for $\bar{\varepsilon} \geq 0.08$, $e_{1T_{X(Y)}} \approx$

$A' - B'\bar{\epsilon}$. Then the energy per hydrogen atom, $e_{\bar{\epsilon}}/n$, assumes a minimum value for the elongation of the c axis given by

$$\bar{\epsilon}^* = 3B'x/2(c_{11} - c_{12})v_0 \quad (5.58)$$

where x and v_0 are hydrogen concentration (n/N_0) and the atomic volume for pure V metal, respectively, and $B' = 1.2$ eV for $\text{VH}_{0.5}$. Provided that B' is independent of x , (5.58) predicts a linear variation of $\bar{\epsilon}^*$ with x , in agreement with observations. The calculated value of $\bar{\epsilon}^*/x \approx 0.20$ is in good agreement with the observed value (0.22).

Sugimoto and *Fukai* [5.87] also calculated the variation of the excitation energy of the $4T_{XY}$ states with axial ratio c/a and found that the excitation energies of an H atom at $c/a = 1.1$ are 50 and 262 meV, and that the outward displacement of the nearest-neighbor M atoms of the O_Z site from their original position in the bct lattice is $u_1 = 0.14$ Å. These results agree well with those from inelastic neutron scattering experiments (53.5 and 220 meV [5.57]) and X-ray reflection ($u_1 = 0.17$ Å [5.253]). It is not known, however, if the calculation can reproduce the higher excited states observed by *Hempelmann et al.* [5.59]. The calculated and the observed potential, in a and c directions are in general agreement with each other. The strong anisotropy of the potential naturally leads to a strongly anisotropic density distribution, as actually deduced from neutron diffraction (Fig. 5.13). In detail, the observed density distribution is more extended in comparison with the calculation, especially in the a - b plane [5.87]. This can be understood to some extent because the low-lying excited states, being more extended in space than the ground state, should be populated to a fairly large fraction at the temperature of the neutron diffraction measurements.

The occurrence of the displaced-T configuration for tetragonalities smaller than the β phase deserves special consideration. It implies that, whenever the displaced-T configuration is found, the original T-site occupancy in a bcc lattice is disturbed by the action of a tensile stress along one of the cube axes, whatever its cause may be. In the case of hydrogen trapped at interstitial impurities (N, O, . . .), these impurities produce a local tetragonal elongation. For D atoms implanted to high fluences in Nb (Sect. 5.6.3), lattice expansion in only the surface-normal direction is effective.

What is particularly important about the displaced-T configuration is its occurrence as a stress-induced state. From the calculation described above, it is expected that the stress-induced state should be accompanied by a local tetragonal distortion of, say, a few per cent. Since average strains actually needed to induce this configuration are much smaller ($\sim 2 \times 10^{-4}$), some mechanism based on cooperative elastic interactions must be operating to bring about this extreme stress sensitivity. This is, in a way, reminiscent of martensitic transformations, at the basis of large hysteresis and/or shape-memory effects. If we draw an analogy with magnetism, the occurrence of the stress-induced state is analogous to metamagnetism, namely, the appearance

of ferromagnetism by the action of external magnetic field, whereas the $\alpha \rightarrow \beta$ transition in the vanadium–hydrogen system is analogous to paramagnetic-to-ferromagnetic transition. More experiments are needed to elucidate the various aspects of the stress-induced change of states, before its mechanism can be discussed.

5.7.3 Theory Based on Non-Empirical Potentials

There have also been several calculations of atomistic properties based on non-empirical interaction potentials between H and M atoms. In this section, the results of such calculations are reviewed; the methods of constructing the non-empirical potentials are described and examined in more detail in Sects. 7.2–7.3.

A step towards first-principles approach was initiated by *Ho et al.* [5.246]. They performed band-theoretic calculations of the total energy of the ordered phases of NbH by displacing the hydrogen sublattice with respect to the metal sublattice in two symmetric directions. On the assumption that the interaction between hydrogen atoms is small, the potential thus obtained can be regarded as the adiabatic potential to be experienced by each hydrogen atom when it is displaced relative to the M lattice. The calculated potential profiles along two symmetry directions are shown in Fig. 5.79 [5.246]. The calculated energy levels of one-dimensional oscillators in these directions (assumed to be decoupled from each other) are also shown in the figure.

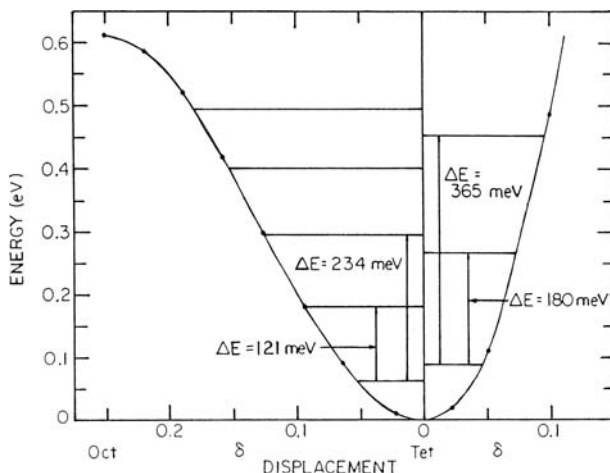


Fig. 5.79. Energy vs. displacement curves for hydrogen occupying T sites in β -NbH by energy-band calculations. On the *left* is shown the displacement in the Z direction, and on the *right*, that in the X direction in Fig. 5.72 [5.246]

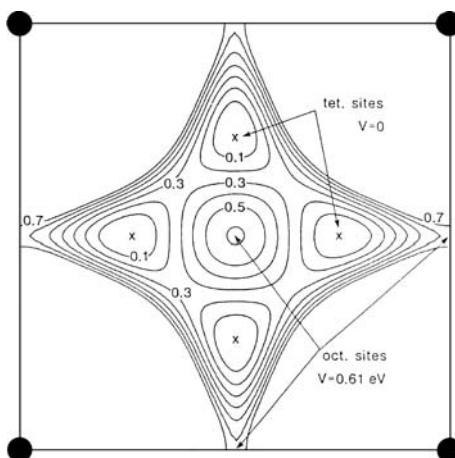


Fig. 5.80. Hydrogen potential on the (100) cubic face of Nb. Energy contours measured from the T-site position are shown at 0.1 eV intervals. No lattice relaxation was allowed for [5.255]

In their subsequent work [5.255], they calculated the hydrogen energies for 35 different points in a unit cell, and fitted the results to 24 independent Fourier components. With these Fourier components, the calculated potential could be conveniently expressed to within 1%. A contour map of the hydrogen potential on the cubic face of Nb (without lattice relaxation) is shown in Fig. 5.80. Note that the energy contours are very similar, both in shape and magnitude, to those calculated for H in Ta (with lattice relaxation) using the empirical potential of *Sugimoto* and *Fukai* (Fig. 5.72a).

The vibration energies obtained from these one-dimensional (1D) and three-dimensional (3D) potentials are listed in Table 5.15. The agreement with the observed values is excellent, both with regard to the isotope effect and the negative deviation from harmonicity. A tendency of the calculation

Table 5.15. Comparison of the calculated (calc.) and the measured (obs.) vibrational energies of hydrogen isotopes in Nb. Two sets of calculated values are given in the form 3D (1D), where 3D refers to the three-dimensional calculation [5.255] and 1D to the one-dimensional calculation [5.246]. Units are in meV

		Δe_1^Y	Δe_1^X	$2\beta^X = \Delta e_2^X - 2\Delta e_1^X$
H	Calc.	161 (180)	113 (121)	-14(-8)
	Obs.	166 ± 2	122 ± 1	-13 ± 3
D	Calc.	118 (127)	84 (87)	-5(-4)
	Obs.	121.6 ± 0.4	88.4 ± 0.3	-7 ± 4
T	Calc.	98 (104)	70 (72)	-3(-3)
	Obs.	101 ± 1	72 ± 1	-

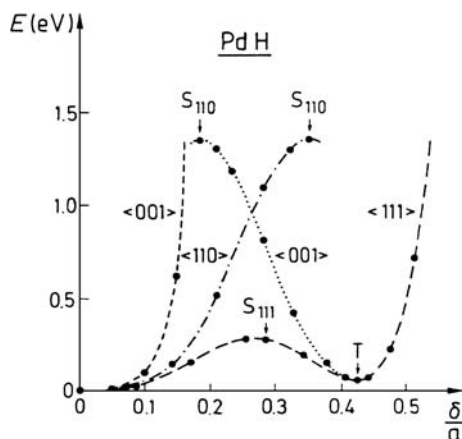


Fig. 5.81. Energy vs. displacement curves for H in PdH (fcc, $a = 4.07 \text{ \AA}$) calculated along the paths shown in Fig. 5.82. Origin is taken at O site, T signifies T site, S_{110} and S_{111} are saddle points, and • results of *ab initio* calculation [5.257]

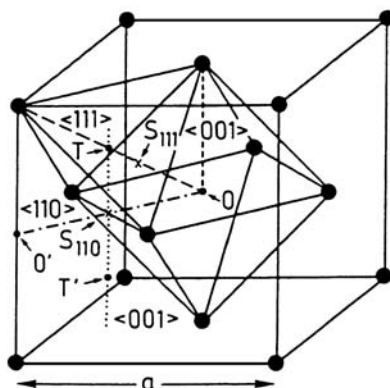


Fig. 5.82. Paths along which the energy was calculated for H in PdH. O signifies O site, T means T site, S_{110} and S_{111} are saddle points [5.257]

to slightly underestimate the vibrational energies might be ascribed to the negligence of a weak H–H repulsion.

Ho et al. [5.256] greatly advanced this approach to the quantum states of interstitial H, and *Elsässer et al.* applied it to the Pd–H system [5.257, 5.258]. They performed a series of total energy calculations for a number of superlattices Pd_nH ($n = 1, 4, 8, 16, 32$) while displacing the H sublattice in four high-symmetry directions. Figure. 5.81 shows the adiabatic potential thus obtained for PdH along the lines shown in Fig. 5.82 [5.257]. A very strong anisotropy around a minimum at O site can be noted; the potential rises steeply in the $[001]$ direction towards the nearest Pd atom, whereas

it increases very slowly in the [111] direction. In the [111] direction, the potential is connected to a second minimum at T site, nearly as deep as at O site, through a small hill at a saddle point S_{111} . They fitted the result to a finite, three-dimensional Fourier series, and solved the Schrödinger equation for H isotopes in the reciprocal space.

Table 5.16 compares the excitation energies thus obtained for the first five excited states with experimental data on a highly oriented polycrystalline foil of $\text{PdH}_{1.00}$ [5.55] and a single-crystal of $\text{PdH}_{0.85}$ [5.56]. The agreement can be deemed satisfactory.

Table 5.16. Comparison of observed and calculated vibrational excitation energies in PdH_x

Excited States	$\text{PdH}_{1.0}$ (exp.) ^a	$\text{PdH}_{0.85}$ (exp.) ^b	PdH (calc.) ^b
$e_{1,[001]} = e_{1,[010]} = e_{1,[100]}$	55.8	57	62
$e_{2,[011]} = e_{2,[101]} = e_{2,[110]}$	110.4	115.5	117
$e_{2,[C]}$	135	139 ± 2	132
$e_{2,[A]} = e_{2,[B]}$	148	135 ± 3	147
$e_{3,[111]}$	—	~ 170	164

^a[5.55], ^b[5.56].

The assignment of the transitions was confirmed later by detailed analysis of the orientation dependence of the scattering intensity [5.56]. Figure. 5.83 shows the experimental scattering intensity $S(\mathbf{Q}, \omega)$ measured at a fixed energy transfer $\hbar\omega = 115.5 \text{ eV}$, while the sample was rotated around the [110]

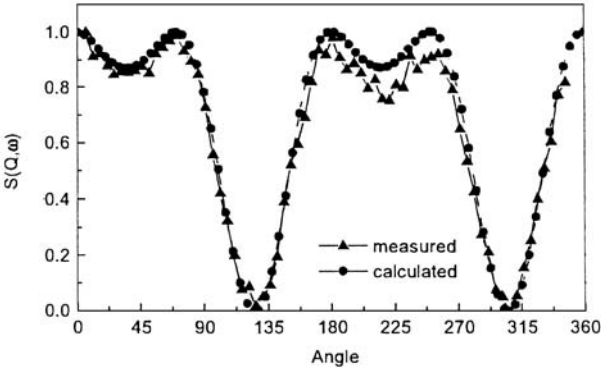


Fig. 5.83. Normalized scattering function $S(\mathbf{Q}, \omega)$ as a function of angle around the [110] axis of $\text{PdH}_{0.85}$, measured at a fixed energy transfer $\hbar\omega = 115.5 \text{ eV}$. Both experimental and theoretical results have been taken from [5.56]

axis. The agreement with the calculated result for $(000) \rightarrow (110)$ transition is remarkable, and identifies the observed transition unambiguously. Thus most of the observed features of INS spectra were explained successfully by the *ab initio* theory. The only remaining question is the origin of the high-energy shoulder above the first peak, which will be described later.

Krimmel *et al.* [5.59] proceeded further to include the effect of local lattice distortion around an H atom on its energy state. To make this calculation tractable, they approximated the adiabatic potential by a sum of central pair potentials of a simple analytic form – in fact, of two different forms (I and II) to test the sensitivity of results. The magnitude of the force-dipole tensor was $\text{Tr}\hat{P} = 9.1 \text{ eV}$ for potential I and 7.3 eV for potential II, in fair agreement with experiment $(10.0 \pm 0.5 \text{ eV})$ [4.30]. The energy of individual vibrational levels in the self-trapped state was rather strongly dependent on the choice of potential functions, but the energy difference was affected to a lesser extent due to partial cancellation. Thus it would be appropriate to accept the results with some caution, placing more emphasis on the general, qualitative aspects less affected by the uncertainties of the potential.

Some of the predictions worth quoting here include the following: First, the lattice relaxation in the excited state may take place relatively easily, and therefore the transition to the excited state in the frozen lattice in the ground-state configuration (the Frank-Condon level) may not be the only possibility. Second, a dominant relaxation should be through E-mode coupling to the tetragonal distortion of the lattice. Third, the ground-state energy of an H atom in T site is higher than in O site, but the energy difference becomes smaller by self-trapping distortion, as well as by uniform expansion of the lattice. The potential around a T site is only weakly anharmonic. This last point is believed to manifest the general characteristic of all fcc metals; the formation of dihydrides of CaF_2 structure (having larger lattice parameters than monohydrides) with equally spaced H vibration energies.

The question of high-energy shoulder in the INS spectra was resumed by Kemali *et al.* [5.56] in connection to possible lattice relaxation in the excited vibrational state. They paid attention to the fact that this shoulder, which has been observed consistently in other fcc hydrides as well, is too high in intensity and featureless in shape to be explained by multi-phonon effects, and considered suspect the original explanation in terms of H–H interactions (dispersion relation as shown in Fig. 5.16) because the line shape was always close to the Gaussian, nearly independent of H concentrations down to very low concentrations ($x = 0.002$). They suggested instead that the shoulder should be a transition to the Frank-Condon level with M atoms remaining in their ground-state positions, and the main peak the zero-phonon transition where the final state is determined after relaxing the M atoms adiabatically. The greater width of the shoulder should be an indication of a shorter lifetime of the unrelaxed state. Thus the situation realized here is intermediate between strong and weak coupling cases where both transitions should appear

with comparable intensity. It must be admitted, however, that this interpretation is not entirely consistent with their earlier calculations: the observed energy shift of ~ 23 meV is much larger than the calculated results of a few meV. Furthermore the model should be able to explain the observed Q dependence of the excitation energy of the shoulder. More work is needed before the possibility of a Frank-Condon transition be established.

A consistent description of this series of work on the Pd-H system has been given by *Ross et al.* [5.263], where several maps of proton wave functions and neutron scattering functions calculated for some excited states are presented.

This method of calculation was then applied to the self-trapped state, especially the site occupancy, of hydrogen isotopes in α -Fe (bcc) [5.261]. As regards the site occupancy in Fe, *Sugimoto* and *Fukai* [5.235] suggested the O-site occupancy based on the systematics that O sites tend to be preferred to T sites in bcc metals of smaller lattice parameters; Fe has the smallest lattice parameter (2.86 Å) of all bcc metals, much smaller than V (3.02 Å). *Puska* and *Nieminen* also predicted the O-site occupancy from their EMT calculations [5.237]. Neither of these predictions are, however, very definitive. Experimentally, the O-site occupancy was established for μ^+ and π^+ , but reliable data on H is practically non-existent. Thus *Krimmel et al.* [5.261] attempted to construct a Fe-H pair potential on the basis of their *ab initio* pseudopotential calculation on bcc FeH. The paths for which the total electronic energy was calculated are shown in Fig. 5.84, and the energy versus displacement relations are shown in Fig. 5.85. The calculated points were found to be reproduced by three different forms of central pair potentials equally well, although the resulting lattice distortion was rather different. In terms of $\text{Tr}\tilde{P}$ for T-site occupancy, the short-range potential (I) gives 4.0 eV, those containing a long-range part (II and III) give 7.0 and 9.1 eV, respectively,

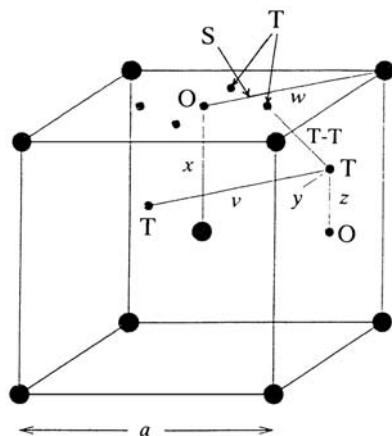


Fig. 5.84. Paths along which the total energy was calculated *ab initio* for bcc FeH [5.261]

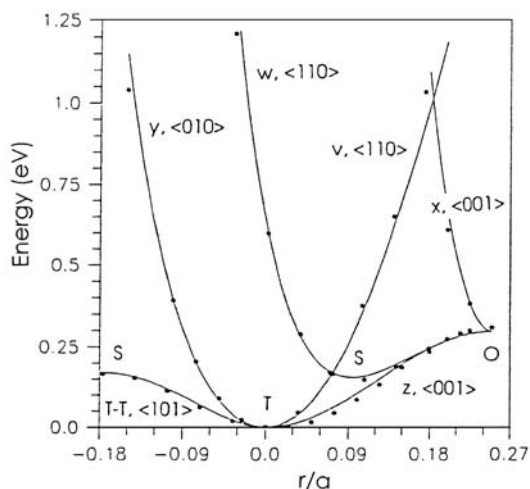


Fig. 5.85. Fitting of pair potential III to the *ab initio* calculated energy vs. displacement relation (dots) along the paths depicted in Fig. 5.84 [5.261]

and these values should be compared with the *ab initio* estimate of 10.7 eV. Thus the potential III is believed to best represent the interaction potential, the potential II to a lesser extent, and potential I totally unrealistic.

The physical significance of this procedure is worthy of notice. The H-M interaction, when approximated by central pair potentials, must contain both short-range and long-range parts in order to reproduce *ab initio* calculations. Energy values along the paths shown in Fig. 5.84 are not sensitive enough to constrain the long-range part which becomes manifest in total volume expansion. In effect, this provides a physical justification for the inclusion of a long-range part in the H-M interaction potential of SF [5.235] and KT [5.238].

The energy difference between the 4T and 1T configurations calculated for these three types of pair potentials is shown in Fig. 5.86 as a function of isotope mass. The results clearly indicate the O-site occupancy for μ^+ and π^+ , and the T-site occupancy for H, D, T. The higher-energy configuration, the O-site occupancy for H, D, T, and the T-site occupancy for μ^+ and π^+ was found to be unstable and not metastable. The breakdown of the self-trapping energy revealed that the isotope dependence of the site preference is driven by the isotope dependence of the vibrational energy. The sum of the energy of lattice distortion and concomitant change of the potential energy is found to be nearly independent of isotopes.

It should be worth pointing out that the result obtained from potential III in Fig. 5.86 in Fe is very similar to the calculation of SF on H isotopes in V (Fig. 5.74). This is a consequence of the fact that the potential III in Fe is very similar to the empirical potential of SF. This similarity between Fe and V suggests that peculiar properties of H in V, including the formation of

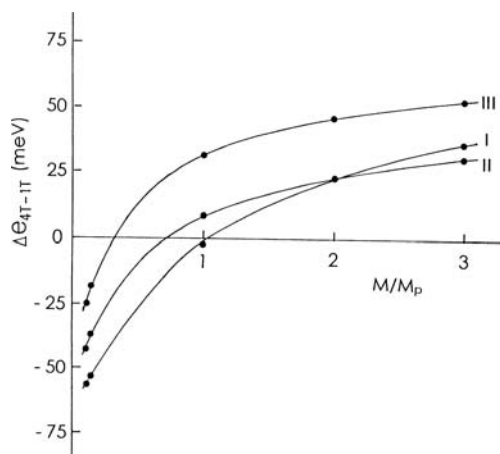


Fig. 5.86. Variation with isotope mass of the difference of self-trapping energies of 4T and 1T configurations in Fe, calculated with three different forms of pair potentials (I, II, III). Isotope mass is in units of proton mass [5.261]

stress-induced 4T-state and the occurrence of bct structure by cooperative occupation of O_Z sites, may also take place in Fe. This possibility is believed to have profound implications for the mechanism of H embrittlement of steels.

The effective medium theory (EMT) is a simplified version of the electronic theory, based on the concept of embedding an atom in a uniform sea of conduction electrons. For details of EMT, see Sects. 7.2 and 7.3. Because of this drastic simplification, theory is made applicable to a wide variety of complex problems which are otherwise hardly tractable, although its quantitative accuracy is inevitably limited (to ca. 0.2 ~ 0.5 eV in the H-M interaction potential). This theory has been very helpful in clarifying the general trend in the heat of solution and chemisorption on surface, etc., and moreover in making heuristic predictions in some cases. Thus, as described in Sects. 5.6.3–5.6.4, binding energies of H atoms to various types of defects were evaluated, and gave support to the possibility of multiple trapping by vacancies [5.184].

For Ni, a heuristic prediction on the quantum state of an H atom trapped at a monovacancy has been made based on the effective-medium theory. In Fig. 5.87 is shown a calculated contour map of the embedding energy on a cube face of the fcc unit cell containing a vacancy at the center [5.166]. The potential is, on the whole, rather flat over the vacancy region. The figure also includes the calculated D density for the ground state and the two lowest excited states, lying at energies of 4 and 14 meV. These excitation energies are comparable in magnitude to the experimental value of 3.3 meV obtained from the temperature dependence of the displaced-T component (Fig. 5.53). The physical origin of the displaced-T configuration introduced in the analysis of the channeling profiles (especially a small subpeak in the $\langle 100 \rangle$ axial scans)

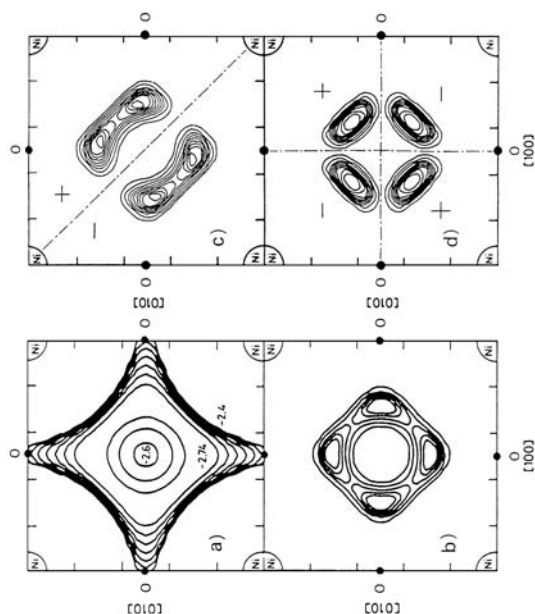


Fig. 5.87. Contour plots of the D potential (binding energy measured relative to a D atom at ∞) and D density (wave-function squared) for the ground state and the lowest two excited states of a D atom in a Ni vacancy. The contour spacing is 0.05 eV for the potential and one-sixth of the maximum in the density plots [5.166]

is thus suggested to be the admixture of these excited states. Note that such low-energy excited states can exist only in an extended potential like that of a vacancy. The excitation energy can be shown to scale roughly as $1/R_v^2$, where R_v is the average radius of the flat part of the potential – the size of the vacancy. The observation that a displaced-T fraction (a peak in the $\langle 100 \rangle$ axial scans) is much larger in Pd and Pt than in Ni and Cu is now naturally understandable: In these metals, the excitation energies become smaller because of the larger size of vacancies (lattice parameters).

The calculations of the excitation energies by means of the effective-medium theory have, however, met with varying degrees of success. For H chemisorbed on Ni (100) and (111) surfaces, the calculated excitation energies (76 and 131 meV) are in excellent agreement with the experimental values (74 and 139 meV) [5.262]. The vibrational spectrum of H in Pd was also fairly well reproduced [5.263]. However, the calculation of *Puska* and *Nieminen* [5.237] on H in Nb yielded excitation energies grossly at variance with observations: 48 and 95 meV as compared to the experimental values of 120 and 170 meV. They also calculated the self-trapping energy and the displacements of the neighboring M atoms for T- and O-site occupancies, but consistently underestimated all these quantities. Thus the application of EMT to individual microscopic properties should be made with caution.

5.8 Tunneling States

For any light particle in a crystalline lattice, there is a possibility that it may tunnel through a potential barrier between adjacent sites, and eventually propagate as a Bloch wave in an energy band of finite width. The possibility of band formation is measured by the width of the band, which is essentially determined by the degree of overlap of the wave functions of the particle on adjacent sites a and b , $\langle a|b \rangle$, or more precisely by the magnitude of the tunneling matrix element $J = \langle a|V|b \rangle$, where V is a potential intervening these two sites.

As it turned out, estimates of the tunneling matrix element (or the transfer integral) for any reasonable potential and site separation are rather small for interstitial H atoms. Values obtained by *Kehr* [5.242] for H in Pd, Nb and V ranged between 0.0065 and 130 μeV (Sect. 5.8.2), much smaller than the self-trapping energy of $\sim 0.1\text{ eV}$. Thus the band formation is strongly disrupted by the interaction with the lattice.

There remains, however, a possibility that a self-trapping distortion around a group of sites may take place in such a way as to favor the formation of localized tunneling states over these sites.

In fact, we have already seen this example in Sect. 5.7.2; the site change in VH_x from T-sites to O_Z sites in the course of lattice elongation along the c -axis. As shown in Figs. 5.75–5.77, the potential minimum, originally located at a T-site position due to self-trapping distortion, is gradually shifted inward towards the O_Z site, and at a certain elongation merges into the state of 4-fold symmetry around the O_Z site. As there are four equivalent T sites (displaced-T sites) around the O_Z site, this change of state can be viewed as the formation of a 4T tunneling state out of four dis-T states. This process has been caused by the strain-induced changes in the potential, not only in the reduction of the mutual separation but also the barrier height between the minima.

Experimentally, the formation of localized tunneling states was discovered in H(D) atoms trapped by O, N atoms in Nb, and identified as a 2T tunneling state. This system has since been studied in greater detail using various techniques and served as a prototype of the localized tunneling state. Several other examples of 2T and 4T-site tunneling systems have since been found. For a review of such tunneling systems in metals, see [5.264].

The discovery of the localized tunneling state inspired a renewed interest on the side of theoreticians in the mechanism of quantum diffusion. From the beginning of the 80's, a very peculiar diffusion behavior was reported for positive muons at low temperatures, and its explanation in terms of the tunneling motion was an important theoretical issue. The discovery and elucidation of the localized tunneling state of H, D atoms provided a firm grip on this problem, and in the mid-80's a unified picture of the tunneling process and quantum diffusion came to be established. There, the dynamics of interstitial

H isotopes in metals, in the presence of interaction with conduction electrons as well as with the lattice was described in a consistent way.

In this chapter, we start by describing the experimental information so far obtained on the localized tunneling states of H and D, including 2T and 4T configurations, and then try to explain the mechanism underlying these tunneling processes in metals.

For lighter isotopes, the positive muon and muonium (an H atom with a proton substituted by a muon), the formation of a coherent tunneling state extending over many atomic distances, and eventually the Bloch state, was observed in a number of insulators, as will be described in Appendix 6B.

5.8.1 Two-Site and Four-Site Tunneling of Hydrogen Atoms

Hydrogen atoms trapped in the vicinity of interstitial impurity atoms (O, N, C) in bcc metals serve as particularly useful cases for investigating the quantum character of the states. This is because H atoms trapped by these impurities do not precipitate to form a hydride phase but remain as such at low temperatures, thus providing rare occasions for quantum effects to appear.

As explained in Sect. 5.6.2, the configuration of the H atom trapped by interstitial impurities O, N, C is believed to be such that it occupies predominantly one of the eight equivalent pairs of (slightly displaced) T sites in the $\langle 111 \rangle$ direction from the impurity atom (Fig. 5.45).

The existence of internal excitations of hydrogen atoms in this configuration involving very small energies was first noted in specific-heat measurements at low temperatures. *Sellers et al.* [5.265,5.266] demonstrated convincingly that the specific-heat anomalies below 2 K previously observed in V, Nb, and Ta were, in fact, due to the presence of a small number of dissolved hydrogen atoms, and suggested, on the basis of strong isotope dependence of the anomalies, that some tunneling motion of hydrogen atoms might be responsible.

More critical specific-heat measurements have since been pursued, for the purpose of clarifying the nature of the quantum states of hydrogen atoms [5.267–5.269]. Figure 5.88 shows the specific heat of Nb samples doped with O or N, and H or D, and of reference samples of pure Nb and those doped with only O or H [5.269]. The results clearly demonstrate that the anomaly below 2 K is caused by hydrogen atoms trapped by O, N atoms, and furthermore, the anomaly is markedly isotope dependent. Figure 5.89 shows the dependence of the specific heat on the concentration of trapped D atoms [5.269]. The concentration dependence can be seen to be strongly nonlinear.

Wipf and *Neumaier* [5.268] succeeded in explaining these observations by a model according to which the trapped hydrogen atom is tunneling between two equivalent interstitial sites (forming a delocalized 2T configuration) whose respective energies are randomly shifted against each other due to lattice distortions originating from other complexes (O–H, etc.). Let us consider

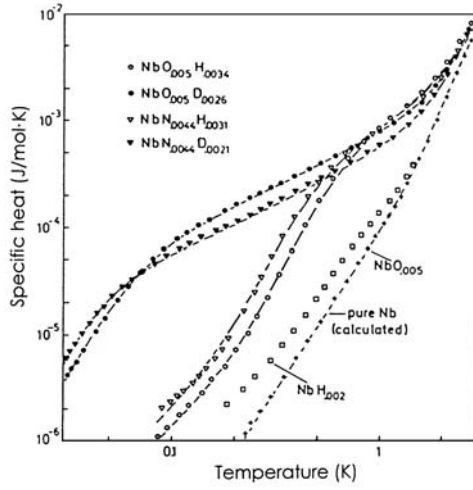


Fig. 5.88. Specific heat of superconducting Nb samples partially doped with O or N, and H or D [5.269]

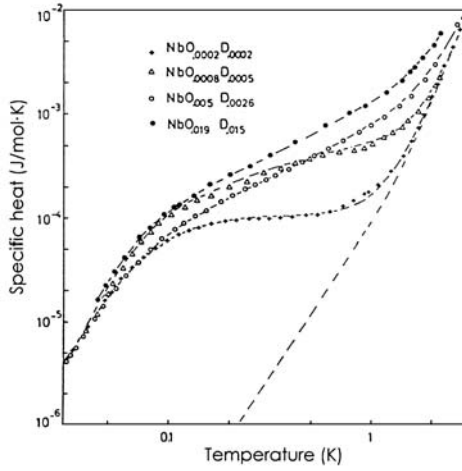


Fig. 5.89. Specific heat of superconducting NbO_xD_y samples with different concentrations of tunneling O-D complexes [5.269]

a pair of potential wells located at $\pm d/2$ on the x -axis and symmetrically disposed with respect to the y - z plane. When a particle is placed in this potential field, its ground-state wave function is an even function of x without any nodal plane, and the first excited state an odd function having a nodal plane $x = 0$.

The tunneling picture is a simple convention to describe this situation when the potential wells are fairly well isolated, and in consequence the eigenstate of a particle in each potential well can be fairly well defined. Let us assume that we know the eigenstate in one of the potential wells (in the absence of the other). The ground state of the particle is doubly degenerate when the wells are isolated from each other, but this degeneracy is gradually removed as the overlap between the ground-state wave functions on the two sites becomes larger. Writing $J = \langle a|V|b \rangle$, for the tunneling matrix element and solving the secular equation

$$\begin{vmatrix} e_0 - e & J \\ J & e_0 - e \end{vmatrix} = 0, \quad (5.59)$$

we obtain $e = e_0 \pm J$ for the energy eigenvalues of the tunnel-split states. Here, the $e_0 - J$ state corresponds to the symmetric wave function and the $e_0 + J$ state to the antisymmetric wave function.

In actual systems, some energy disorder always comes into play, and modifies the overall tunneling effects to be observed. First, the relative shift of site energies, by Δ for site a and $+\Delta$ for site b (Fig. 5.90), the situation called energy asymmetry, modifies the secular equation to

$$\begin{vmatrix} e_0 - \Delta - e & J \\ J & e_0 + \Delta - e \end{vmatrix} = 0, \quad (5.60)$$

which gives

$$e = e_0 \pm \sqrt{J^2 + \Delta^2}. \quad (5.61)$$

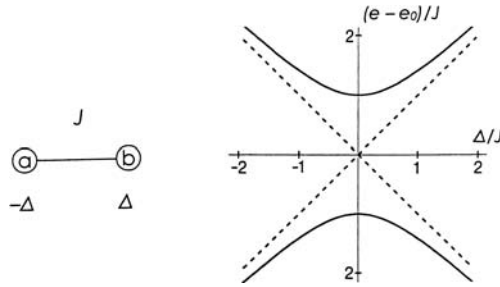


Fig. 5.90. Two-site tunneling system with tunneling matrix element J and energy disorder $\pm\Delta$. Variation of tunnel-split energies with energy disorder is also shown

Second, due to some inhomogeneities, the magnitude of the energy asymmetry is also distributed, with a distribution function approximately written in the form

$$Z(\Delta) = \frac{1}{\pi} \frac{\Delta_0}{\Delta_0^2 + \Delta^2}. \quad (5.62)$$

In the analysis of the experimental data, it is more convenient to write the relevant expressions in terms of the energy difference between the tunnel-split state $E = 2\sqrt{J^2 + \Delta^2} = \sqrt{\varepsilon_t^2 + \varepsilon^2}$, where $\varepsilon_t = 2J$ and $\varepsilon = 2\Delta$. The distribution function (5.62) is redefined as

$$Z(\varepsilon) = \frac{1}{\pi} \frac{\varepsilon_0}{\varepsilon_0^2 + \varepsilon^2} \quad (5.63)$$

with $\varepsilon_0 = 2\Delta_0$, and a distribution function for the energy differences E is derived as

$$Z(E) = \frac{2}{\pi} \frac{E}{(E^2 - \varepsilon_t^2)^{1/2}} \frac{\varepsilon_0}{\varepsilon_0^2 + E^2 - \varepsilon_t^2}, \quad (5.64)$$

which is defined for $E > \varepsilon_t$. The excess specific heat due to the complex, c_{exc} , can be written as

$$c_{\text{exc}} = k \int dE Z(E) \left(\frac{E}{kT} \right)^2 \frac{e^{-E/kT}}{(1 + e^{-E/kT})^2}. \quad (5.65)$$

By fitting this expression to the measured specific-heat data, the tunnel splitting ε_t , and the energy shift parameter ε_0 can be obtained. The quality of the fits is excellent as can be seen in Figs. 5.88, 5.89. The following tunneling energies were obtained [5.269]: $\varepsilon_t(\text{O-H}) = 0.23 \pm 0.01$ meV, $\varepsilon_t(\text{O-D}) = 0.020 \pm 0.001$ meV, $\varepsilon_t(\text{N-H}) = 0.17 \pm 0.01$ meV, $\varepsilon_t(\text{N-D}) = 0.014 \pm 0.001$ meV. These values are independent of the concentration of tunneling complexes at least up to 1 [at%]. The energy shift parameter was found to increase roughly linearly with the concentration of the complexes,

$$\varepsilon_0(\text{meV}) = (10 \pm 3) \times c_{\text{complex}}(\text{at \%}).$$

Note that in most cases ε_0 is much larger than ε_t . In fact, in their analysis, *Gutsmiedl et al.* [5.269] allowed for a distribution of ε_t , as well, i.e.,

$$Z(\varepsilon_t) = \frac{1}{\pi} \frac{\Delta\varepsilon_t}{(\Delta\varepsilon_t)^2 + (\varepsilon_t - \varepsilon_{t0})^2}, \quad (5.66)$$

and found that $\Delta\varepsilon_t$ varied in the range 5–15% of ε_{t0} according to the concentration of complexes.

A more direct observation of tunnel-split levels was made by the neutron spectroscopy of *Wipf et al.* [5.270]. By using a sample of $\text{NbO}_{0.013}\text{H}_{0.016}$, they observed at 0.09 K and 5 K weak, but well-defined, energy transfers on the tail of the elastic scattering peak. An analysis of the observed spectra based on the same model of two-site tunneling as described above led to a tunneling energy quite consistent with the one deduced from specific-heat measurements.

For the two-site tunneling systems considered, the incoherent cross sections for inelastic and elastic scattering from H atoms are written as [5.271]

$$\left(\frac{d^2\sigma}{d\Omega d(\hbar\omega)} \right)_{\text{inel}} = \frac{\sigma_{\text{inc}}}{4\pi} \frac{k_f}{k_i} e^{-2W_D} \left[\frac{1}{2} - \frac{\sin(Qd)}{2Qd} \right] \times \int_{-\infty}^{+\infty} d\varepsilon Z(\varepsilon) \frac{\varepsilon_t}{\varepsilon_t^2 + \varepsilon^2} \frac{O(\hbar\omega)}{1 + \exp(\hbar\omega/kT)}, \quad (5.67)$$

and

$$\left(\frac{d^2\sigma}{d\Omega d(\hbar\omega)} \right)_{\text{el}} = \frac{\sigma_{\text{inc}}}{4\pi} e^{-2W_D} \left[\varepsilon_0 + \varepsilon_t \left(\frac{1}{2} + \frac{\sin(Qd)}{2Qd} \right) \right] \frac{\delta(\hbar\omega)}{\varepsilon_0^2 + \varepsilon_t^2}, \quad (5.68)$$

where σ_{inc} is the incoherent cross section of H, k_i and k_f the wave vectors of the incident and scattered neutrons, $\exp(-2W_D)$ the Debye–Waller factor, and $\hbar\omega$ and $\hbar Q$ the energy and the momentum transferred during scattering. The 2T configuration is here represented by two harmonic potentials separated by a distance d . The function $O(\hbar\omega)$ describes a dynamical coupling of the tunneling system to the environment, characterized by the resonance energy E and the damping constant Γ , as

$$O(\hbar\omega) = \frac{1}{\pi} \frac{\Gamma E^2}{[(\hbar\omega)^2 - E^2]^2 + (\Gamma\hbar\omega)^2}. \quad (5.69)$$

The damping constant Γ describes the lifetime broadening; \hbar/Γ is the average lifetime during which the phase coherence of the wave function is maintained. As described below, the coherence time is limited by coupling of the tunnel-split state to other degrees of freedom, e.g. phonons and/or conduction electrons. In the limit of small Γ , the response function $O(\hbar\omega)$ becomes equivalent to δ functions located at $\pm E$.

By fitting (5.67) to experimental data, values of ε_{t0} and Γ were determined at each temperature (as well as ε_0 and $\Delta\varepsilon_t$). The quality of the fitting can be seen in Fig. 5.91, which shows the temperature dependence of the inelastic scattering of neutrons from the sample of $\text{Nb}(\text{OH})_{0.0022}$ [5.272]. At the lowest temperature, an inelastic scattering peak is observed only on the energy-loss side, whereas at higher temperatures, a peak on the energy-gain side gradually grows in intensity as more hydrogen atoms are thermally excited to the higher one of the tunnel-split states. In addition, the splitting (measured by ε_{t0}) is gradually decreased, and the width (measured by Γ) is appreciably increased as the temperature approaches the superconducting transition point of $T_c = 9.2$ K.

Similar neutron-spectroscopic measurements were also made on C–H and N–H pairs in Nb [5.273, 5.274].

The effect of conduction electrons on the tunneling state was also studied by *Wipf et al.* [5.275], who performed neutron-spectroscopic measurements on a sample of $\text{Nb}(\text{OH})_{0.0002}$ below the superconducting transition temperature in both superconducting and, by application of a magnetic field, normal-conducting states. Figure 5.92 shows four spectra taken at 0.2 and 4.3 K

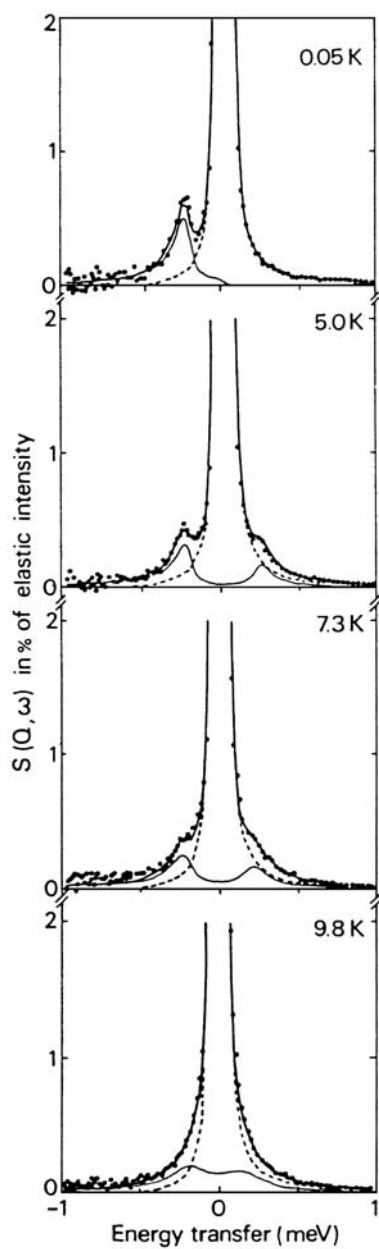


Fig. 5.91. Temperature dependence of the inelastic neutron scattering for $\text{Nb(OH)}_{0.0022}$ [5.272]

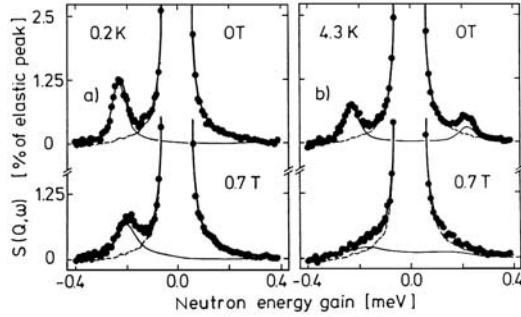


Fig. 5.92. Inelastic neutron scattering of $\text{Nb}(\text{OH})_{0.0002}$ at (a) 0.2 K and (b) 4.3 K, both in normal-conducting and superconducting state with and without application of a magnetic field, respectively [5.275]

both in the superconducting (0 T) and normal-conducting (0.7 T) state. The magnetic field, which destroys superconductivity, causes a line-shift towards lower energies and an increase of the linewidth. At 4.3 K, the data obtained in the superconducting state are practically identical to those obtained at 0.2 K (the superconducting state) except for the detailed-balance factor. In the normal-conducting state, however, the spectrum is strongly broadened, indicating the disappearance of well-defined tunneling states. Apparently, the coupling to conduction electrons tends to destroy the tunneling state.

The temperature dependence of the tunneling energy ε_t and the damping parameter Γ extracted from these results are shown in Fig. 5.93. The value of the tunnel splitting ε_t in the normal conducting state ($\varepsilon_t^N = 0.206 \pm 0.003$ meV) is reduced by about 9% compared to the value in the superconducting state ($\varepsilon_t^S = 0.226 \pm 0.004$ meV) for $T \approx 0$ K. Implications of these results will be examined in Sect. 5.8.2.

Summarizing, the results described above demonstrate the existence, below ~ 5 K, of well-defined tunneling eigenstates of hydrogen atoms delocalized in a 2T configuration near impurities O, N, C. Above ~ 5 K, the eigenstates are increasingly destroyed, and quasi-elastic neutron spectra observed at higher temperatures indicate the occurrence of local jumps between these two sites. The transition to this high-temperature regime will be described in the next section.

A process assigned to tunneling between adjacent T sites was also observed in hcp $\text{ScH}_{0.16}$, where a major fraction of H atoms occupy T–M–T type sites but a small fraction enters 2T sites (C and D in Fig.6.25). From the temperature dependence of QNS line width, the tunneling parameters $2J = 0.34$ meV and $K = 0.039$ were deduced [5.276]. Details of this experiment are described later (Sect. 6.4.1).

Meanwhile, the acoustic spectroscopy also proved to be a useful technique for investigating the tunneling state. The coupling to acoustic waves arises

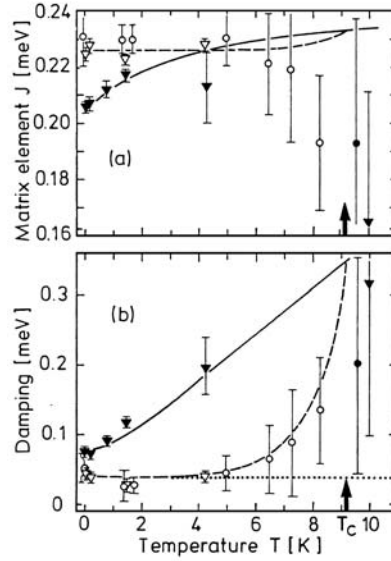


Fig. 5.93. **a** and **b.** Temperature dependence of the tunneling matrix element J , and damping Γ for $\text{Nb}(\text{OH})_x$. The *filled* and *open triangles* are the results for the normal and superconducting state, respectively, of $\text{Nb}(\text{OH})_{0.0002}$ and the *filled* and *open circles* are those for normal and superconducting state, respectively, of $\text{Nb}(\text{OH})_{0.002}$ [5.275]

from the dependence of the energy splitting on lattice strain;

$$\frac{dE}{d\varepsilon_{ij}} = \gamma_{ij}^0 \frac{\varepsilon_t}{E} + \gamma_{ij} \frac{\varepsilon}{E}, \quad (5.70)$$

where γ_{ij} 's represent the deformation potentials, $\gamma_{ij}^0 = \partial\varepsilon_t/\partial\varepsilon_{ij}$ and $\gamma_{ij} = \partial\varepsilon/\partial\varepsilon_{ij}$. The presence of two-level-systems (TLSs) thus changes the elastic constant, which is essentially the second derivative of the total energy with respect to strain, and the coupling of the TLSs with the surroundings allows a part of the acoustic energy to be transferred to the surroundings through the TLSs. The former causes velocity changes and the latter the absorption or internal friction. These acoustic interactions depend on the direction and polarization of the acoustic waves.

The effect of TLSs on acoustic-wave propagation was considered by a number of workers mainly in connection to low-temperature anomalies of amorphous materials [5.277–5.282]. Briefly, the presence of TLS causes reduction of the sound velocity by two different mechanisms; a resonant process and a relaxation process [2.278]. The relative change of the sound velocity $(\Delta c/c)_{ac}$ is expressed as

$$\left(\frac{\Delta c}{c}\right)_{\text{ac}}^{\text{res}} = -\frac{n_0 \gamma^2}{\rho v^2} \left(\frac{\varepsilon_t}{E}\right)^2 \frac{1}{E} \tanh \frac{E}{2kT} \quad (5.71)$$

for the resonant process and

$$\left(\frac{\Delta c}{c}\right)_{\text{ac}}^{\text{rel}} = -\frac{n_0 \gamma^2}{2\rho v^2} \left(\frac{\varepsilon}{E}\right)^2 \frac{1}{E} \text{sech}^2 \frac{E}{2kT} \cdot \frac{1}{1 + \omega^2 \tau^2} \quad (5.72)$$

for the relaxation process. n_0 is the concentration of the TLS, ρ is the density, γ is the deformation potential for the asymmetry energy ε for a given mode of the acoustic wave. Note that the magnitude of the former is determined by ε_t whereas the latter by ε . In the resonant process, the temperature dependence comes from the last factor describing the thermal occupation (population) of tunnel-split levels, which starts from 1 at $T = 0$ and approaches 0 for $kT \gg E$. In the relaxation process, the TLSs disturbed by acoustic waves try to recover their equilibrium population with a characteristic time τ . As it turned out, when TLSs are embedded in metallic environments, the relaxation time is determined by coupling to conduction electrons. The relaxation rate in the normal-conducting state is given by [5.280]

$$\frac{1}{\tau_N} = K \left(\frac{\varepsilon_t}{E}\right)^2 E \coth \frac{E}{2kT}, \quad (5.73)$$

and in the superconducting state by [5.281]

$$\frac{1}{\tau_S} = 4K \left(\frac{\varepsilon_t}{E}\right)^2 \frac{kT}{1 + \exp[\Delta_g(T)/kT]}. \quad (5.74)$$

K is a parameter, sometimes called Kondo parameter, which describes the strength of coupling between TLS and conduction electrons (Sect. 5.8.2). In the normal conducting state, where $\omega\tau_N \ll 1$, the temperature dependence of $(\Delta c/c)_{\text{ac}}$ comes from the factor $1/E \text{sech}^2 E/2kT$. In the superconducting state, on the other hand, the factor $1/(1 + \omega^2 \tau_S^2)$ becomes more important.

The attenuation caused by the relaxation process is given by [2.263]

$$\alpha_{\text{ac}} = \frac{n_0 \gamma^2}{\rho v^3} \left(\frac{\varepsilon}{E}\right)^2 \frac{1}{kT} \text{sech}^2 \frac{E}{2kT} \cdot \frac{\omega^2 \tau}{1 + \omega^2 \tau^2}, \quad (5.75)$$

which becomes maximum at a temperature where $\omega\tau = 1$.

The first attempt to extract a tunneling matrix element for O–H complexes in Nb from velocity changes was made by Bellessa [5.283], and a number of acoustic measurements have since been performed on (O, N)–(H, D) complexes in Nb [5.284–5.289]. Here we reproduce some results of *Morr et al.* [5.290] on N–H, D complexes in Nb to illustrate the extreme sensitivity and effectiveness of the method.

The experiments were performed on a single piece of single crystal Nb doped with 0.1 at% N and 0.3 at% H, and after extraction of the H re-charged

with 0.24 at% D. The longitudinal waves of frequencies ranging between 30–980 MHz were propagated in the [100] direction, and the velocity and attenuation were measured as a function of temperature between 0.01 and 20 K, in both normal and superconducting states. The observed change of sound velocity with temperature is shown in Fig. 5.94. Compared with the broken lines representing the case of hydrogen-free sample, the sound velocity is decreased by the presence of hydrogen. Up to 2.5 K for H and 3 K for D, the measured data are excellently described by the resonant process (5.71), yielding $\varepsilon_t(\text{N-H}) = 0.12 \pm 0.01$ meV and $\varepsilon_t(\text{N-D}) = 0.016 \pm 0.001$ meV. Above these temperatures, the data are fitted by introducing the relaxation process as well (5.72). Note that the superconducting transition temperature is $T_c = 9.2$ K.

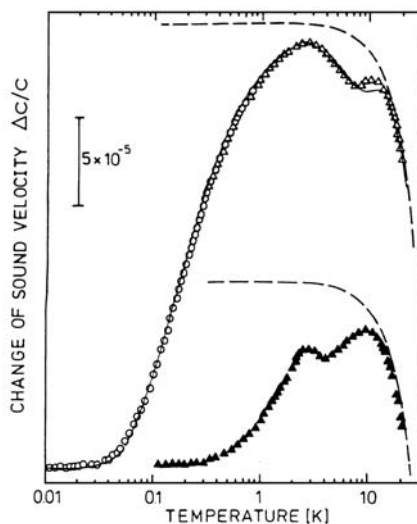


Fig. 5.94. Temperature dependence of the sound velocity of $\text{NbN}_{0.0015}\text{H}_{0.003}$ at 90 MHz (\blacktriangle) and $\text{NbN}_{0.0015}\text{D}_{0.0024}$ at 980 MHz (\circ) and 110 MHz (\triangle). *Broken lines* represent data of a hydrogen-free sample. The *solid line* is a fit including resonant and relaxation processes and the lattice anharmonicity. The data are shifted for clarity so that the sound velocities of hydrogenated and deuterized samples become equal for $T \rightarrow 0$. The material is superconducting below 9.2 K [5.290]

Figure 5.95 shows the attenuation in the normal and superconducting states of the H-doped sample, together with data for a H-free sample. In the normal state, at low temperature where the electron mean free path and hence the relaxation time τ_N becomes independent of temperature, the coupling to conduction electrons yields small, constant attenuation. In the superconducting state, this mechanism freezes out as conduction electrons condense into

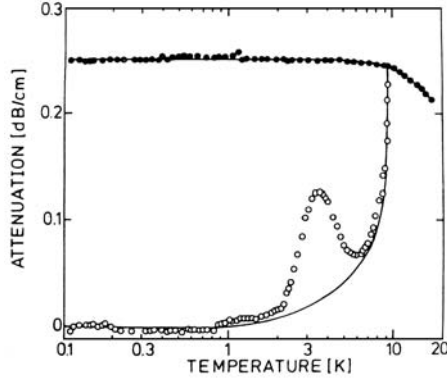


Fig. 5.95. Temperature dependence of ultrasonic attenuation in $\text{NbN}_{0.0015}\text{H}_{0.003}$ at 90 MHz: superconducting (\circ) and normal conducting (\bullet). *Solid lines* are data of a hydrogen-free sample [5.290]

Cooper pairs. Superposed on this steep decrease of the attenuation below T_c , there emerges a peak at 3.5 K in an N–H doped sample caused by the relaxation of the tunneling system in a sound field (described by (5.75)). With additional measurements at different frequencies, the coupling parameter was deduced; $K = 0.07$ for both H and D.

It may be added for clarity that under ordinary conditions of experiments, samples are in thermal equilibrium, namely in the state where thermal excitation is balanced by the relaxation process. The rate of these upward and downward transitions is connected by the ratio of populations of the particles through the detailed balance,

$$\frac{\gamma_{\uparrow}}{\gamma_{\downarrow}} = \frac{p_2}{p_1} e^{-\varepsilon_t/kT}, \quad (5.76)$$

where p_1 and p_2 are the populations of the lower and upper state, respectively, γ_{\uparrow} signifies the rate of transition from the lower to the upper state, and $1/\gamma_{\downarrow}$ is equal to the relaxation time τ , which in turn is equal to \hbar/Γ .

Up to now, that not all the acoustic properties of trapped H, D have been so well understood. Low-frequency internal friction experiments (< 100 kHz) revealed two peaks in the superconducting state, but no definitive assignment of these peaks to any specific tunneling configuration has been attained so far [5.287].

Recently, the formation of a two-site tunneling state was observed in α -Mn. Strong INS peaks were observed at 6.2 meV for H and 1.6 meV for D in Mn, and attributed to the excitation between the tunnel-split states [5.291–5.293]. Figure 5.96 shows the observed INS spectrum for α -MnH_{0.073} [5.293]. All the peaks remained observable up to 100 K. In the inset is shown the crystal structure displaying pairs of 12e sites occupied by H atoms. As is

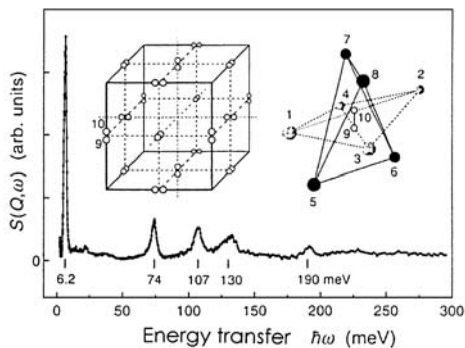


Fig. 5.96. INS spectrum of α -MnH_{0.073} measured at 23 K. H atoms occupy 12e dumbbell sites (9–10), surrounded by two distorted tetrahedra (1–4 and 5–8) [5.293]

well known, α -Mn has a peculiar cubic structure with a unit cell consisting of 58 Mn atoms. Neutron diffraction showed that H atoms form dumbbells occupying pairs of interstitial positions (12e) placed at the center of distorted tetrahedra of Mn atoms. The separation of the dumbbells was found to be $d = 0.68(3)$ Å for H and $0.70(3)$ Å for D. As this separation is too short for accommodating two H atoms, the observed dumbbells should be the superposition of density distribution of H atoms, one for each pair of 12e sites. They estimated the energy splitting using an approximate formula of *Drechsler et al.* (5.82) [5.294] by substituting the observed site separation and optical vibration frequencies $\hbar\omega_0^H = 74$ meV and $\hbar\omega_0^D = 51$ meV, and obtained 5 meV for H and 1.5 meV for D. The good agreement of these values with the observation, both in regard to their magnitude and isotope dependence, was taken to be a strong indication of the occurrence of the tunneling state in this system. The fact that the tunnel splitting in this case is an order of magnitude larger than in (O,N)–(H,D) complexes can be understood as being the consequence of much shorter distance between the potential minima (0.70 Å in comparison to ~ 1.1 Å for 2T sites in Nb). This, in turn, is the consequence of the peculiar crystal structure which produces the potential minima at such short distances.

The level splitting $\varepsilon_t = 2J$ and the coupling parameter (Kondo parameter) K obtained so far on two-site tunneling systems are listed in Table 5.17. The compilation is not exhaustive, but some general trend can be recognized. First, the tunneling matrix element for D is nearly an order of magnitude smaller than for H. Second, J decreases in the order O→N→C. As explained in Sect. 5.6.2, the local lattice distortion created by such interstitial impurity atoms should tend to reduce the 2T distance. This reduction should become smaller in the order of decreasing atomic size, O→N→C, making J to decrease in this order.

Table 5.17. Tunneling matrix element J and Kondo parameter K determined for various two-site tunneling systems

System ^a	$2J[\text{meV}]$	K	Method ^b	Reference
Nb-O-H	0.23 ± 0.01	—	SH	[5.269]
	0.230 ± 0.005	0.04	INS	[5.272]
	0.226 ± 0.004	0.05–0.06	INS	[5.275]
	0.222 ± 0.004	0.055	QNS	[5.274]
Nb-N-H	0.17 ± 0.01	—	SH	[5.269]
	0.121 ± 0.010	0.07	UA	[5.290]
	0.167 ± 0.004	0.055	QNS	[5.274]
Nb-C-H	0.162 ± 0.004	—	INS	[5.273]
Nb-O-D	0.020 ± 0.001	—	SH	[5.269]
Nb-N-D	0.014 ± 0.001	—	SH	[5.269]
	0.016 ± 0.001	0.07	UA	[5.290]
Sc-H	0.32	0.039	QNS	[5.276]
Mn-H	6.3	—	INS	[5.292]
Mn-D	1.6	—	INS	[5.292]

^aFor Nb, values refer to the superconducting state in the limit of $T \rightarrow 0$.

^bSH = Specific heat, INS = Inelastic neutron scattering, QNS = Quasielastic neutron scattering, UA = Ultrasonic absorption.

The tunneling state of H atoms trapped by substitutional Ti and Zr in Nb revealed different features. Results of specific-heat measurements by *Neumaier et al.* is shown in Fig. 5.97 [5.295] for H, D atoms trapped by Ti in Nb. In contrast to the case of (O, N)–(H, D) complexes, the excess specific heat remains high even at 50 mK. This observation was explained by the authors in terms of wide distribution of tunneling energies, analogous to amorphous metals, but later interpreted by *Cannelli et al.* [5.296] in terms of a specific property of the four-site tunneling system in the presence of distribution of asymmetry energies. *Cannelli et al.* [5.296] proposed that an H atom tunnels over the four equivalent T sites adjacent to the Ti atom, forming a four-site tunneling system.

To illustrate the energy state of the four-site tunneling system, here we consider two particular types of energy disorder shown in Fig. 5.98. In case (a), the secular equation is given by

$$\begin{vmatrix} e_0 + \Delta - e & J & 0 & J \\ J & e_0 + \Delta - e & J & 0 \\ 0 & J & e_0 - \Delta - e & J \\ J & 0 & J & e_0 - \Delta - e \end{vmatrix} = 0, \quad (5.77)$$

which gives the energy eigenvalues

$$e - e_0 = \pm J \pm \sqrt{J^2 + \Delta^2}. \quad (5.78)$$

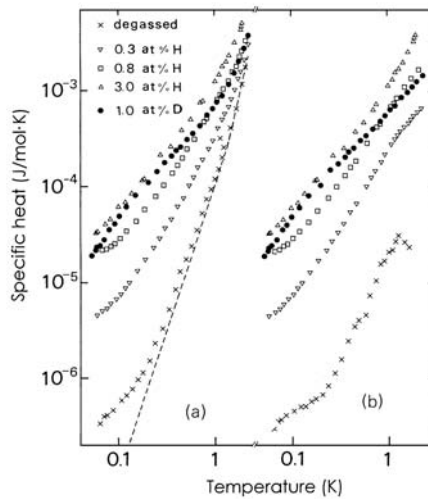


Fig. 5.97. (a) Measured and (b) excess specific heat of superconducting $\text{NbTi}_{0.05}$ doped with H or D. The *broken line* indicates the background specific heat (due to phonons and electrons) as calculated for pure Nb [5.295]

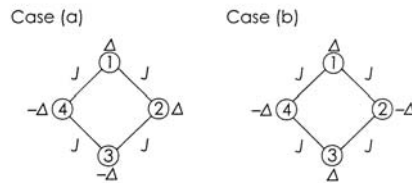


Fig. 5.98. Four-site tunneling system with two different types of energy disorder. J and Δ signify the tunneling matrix element between adjacent sites and energy disorder, respectively.

In case (b), the secular equation is

$$\begin{vmatrix} e_0 + \Delta - e & J & 0 & J \\ J & e_0 - \Delta - e & J & 0 \\ 0 & J & e_0 + \Delta - e & J \\ J & 0 & J & e_0 - \Delta - e \end{vmatrix} = 0, \quad (5.79)$$

which gives the energy eigenvalues

$$e - e_0 = \pm \Delta, \pm \sqrt{4J^2 + \Delta^2}. \quad (5.80)$$

Dependence of the energy levels on energy disorder Δ is shown in Fig. 5.99. In both cases, the splitting between the adjacent levels becomes small at small energy disorder, but in case (b), at large energy disorder as well. The

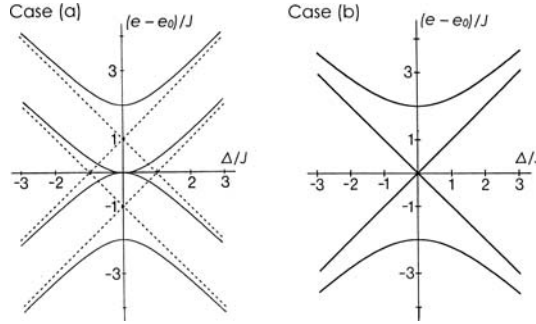


Fig. 5.99. Variation of four energy levels of four-site tunneling system with energy disorder of two different types depicted in Fig. 5.98

splitting tends to $2J^2/\Delta$ for large Δ , the condition believed to be realized in the experiment shown in Fig. 5.97. Considering the extreme sensitivity of tunneling-state formation to the presence of impurity atoms, as evidenced in (O, N)–(H, D) complexes, the fairly high impurity concentrations adopted should have induced large energy disorders. In view of this, the excess specific heat extended to very low temperatures can be interpreted naturally as being due to high strains caused by high concentrations of Ti, rather than tunneling matrix elements much smaller than in (O, N)–(H, D) complexes.

These (Ti, Zr)–(H, D) complexes in Nb have since been investigated intensively both in regard to their configuration and dynamics, and the formation of four-level system (FLS) by four-site tunneling now appears convincing. For example, recent INS experiments on $\text{Nb}_{0.999}(\text{TiH})_{0.001}$ at 1.5 K revealed two energy loss peaks at 0.2 and 0.4 meV, and a multiple splitting of an excited vibrational state [5.297]. These observations can be naturally understood by assuming tunneling states formed from states localized on more than two sites.

A large number of work performed on these systems, mostly by acoustic spectroscopy, revealed, however, that the properties of these FLSs are much more complex than TLSs. Internal friction measurements at a low frequency (70 kHz) in Nb–Ti–H alloys showed that the energy loss spectra at low temperatures change drastically with concentration of doping impurities [5.298]. In another acoustic measurement on Nb–Zr–(H, D) alloys, the energy loss peak was observed at nearly the same temperature (~ 2 K) both for H and D, whereas the intrinsic tunnel splitting is expected to be strongly isotope-dependent [5.299]. These observations indicate that the acoustic energy loss spectra of four-site tunneling systems are largely determined by the distribution of asymmetry energies, rather than intrinsic tunneling matrix elements. This makes the determination of tunneling matrix elements difficult.

Recently, an experiment was performed on a sample containing extremely dilute Zr–(H, D) complexes to avoid interactions between the impurities, and

succeeded in characterizing well-isolated FLSs, especially the dynamics of transitions between the tunnel-split states [5.300]. Theoretically, a very interesting dynamics of FLS, including long-lived oscillations of the probabilities of the site occupancy, was predicted [5.301], providing an additional incentive for investigating these systems.

Evidence of 4-site tunneling was obtained from μ SR experiments on Ti-doped Nb [5.302]. The muons implanted at low temperatures were found to undergo with increasing temperature a sequence of changes of multi-site trapping states. Below 15 K, they are trapped in 4T configuration in the Nb lattice, then between 20–50 K in 4T or 6T configuration around Ti atoms, subsequently between 80–150 K over 24T sites around Ti atoms, before they enter the state of long-range migration above 200 K. Distinction between these different states were rather clearly made by comparing the observed depolarization (relaxation) rate with calculation. Correspondence of these results with hydrogen isotopes has not been clarified so far.

Studies of FLS up to 1996 are described in a review paper of *Cannelli et al.* [5.264].

5.8.2 Theory of Tunneling States in Metals

In this section, we wish to explain the physics of how the tunneling-matrix element or the transfer integral, J , for H atoms in metals is determined. We shall start by describing the calculation of J for interstitial hydrogen atoms themselves, the so-called bare transfer integral J_0 . The real transfer integral J is obtained from J_0 by including the effect of self-trapping distortion of the lattice and screening charges.

Kehr [5.242] was the first who attempted to estimate the bare transfer integrals for H (D) atoms in a simple one-dimensional potential. He made a model calculation using a sinusoidal potential, with its period d and amplitude U_0 fitted to the lattice spacing and vibrational excitation energy $\hbar\omega_0$, and obtained an approximate analytic expression,

$$J_0 = \frac{4\pi\hbar^2}{md} \left(\frac{2md^2U_0}{\hbar^2} \right)^{3/4} \exp \left[-\frac{2}{\pi} \left(\frac{2md^2U_0}{\hbar^2} \right)^{1/2} \right]. \quad (5.81)$$

In this calculation, an approximation of a deep potential, $U_0 \gg \hbar\omega_0$, was made. The results are given in Table 5.18. The estimated values of J_0 are rather small, except for those of positive muons in V and Nb.

Another approximate formula for J_0 based on two harmonic potential wells was given by *Drechsler et al.* [5.294]

$$J_0 = \frac{1}{2} \hbar\omega_0 \exp \left[-\frac{m\omega_0 d^2}{4\hbar} \right]. \quad (5.82)$$

Estimates based on this formula are generally smaller; 1.9×10^{-3} meV for H in V and 2×10^{-4} meV for H in Nb.

Table 5.18. Estimated values of the tunneling-matrix element J_0 for μ^+ , H, and D [5.242]

Metal	J_0 [meV]		
	μ	H	D
V	69	0.13	3.1×10^{-3}
Nb	43	2.5×10^{-2}	2.9×10^{-4}
Pd	0.20	6.5×10^{-9}	1.6×10^{-13}

In order to estimate J in real systems in the frame of ordinary tunneling formalism, we have to deal with the following two problems. First, the local potential acting on an H atom is not fixed; instead it is affected by the presence of the H atom itself due to self-trapping distortion. Even in this situation, two-site tunneling states can be formed from these self-trapped states on site a and site b , as long as they are equivalent. Second, conduction electrons that screen the proton charge allow infinitesimal energy exchange between the proton and the surrounding lattice, even at very low temperatures, which eventually limits the lifetime of the otherwise coherent tunneling state.

Calculations of J_0 taking account of the self-trapping distortion of the lattice were made by *Sugimoto* and *Fukai* (SF) [5.303] and *Klamt* and *Teichler* (KT) [5.238, 5.239]. These authors calculated the tunneling-matrix element J_0 for hydrogen isotopes occupying T sites in bcc metals. The calculations were performed by the method described in Sect. 5.7.1 by solving for the minimum-energy configuration of an H atom distributed evenly over two neighboring T sites (2T configuration). The energy from the ground state to the first excited state of this configuration gives $2J_0$. The results of these calculations are listed in Table 5.19, together with the energy needed to create the 2T configuration from the 1T configuration, Δe_{2T-1T} . In comparison to Kehr's results (Table 5.18), the values of J_0 are larger by nearly two orders of magnitude, and their isotope dependence is less pronounced. These results clearly indicate that the tunneling-matrix element J_0 is extremely sensitive to the wave function of hydrogen atoms, and is, therefore, rather difficult to evaluate reliably. As it turned out, the values of J_0 obtained by SF and KT are more consistent with the experimental results described in the foregoing sections.

In order to treat the tunneling problem in general terms, let us start by writing the wave function of the state with an interstitial atom self-trapped on site a in the form

$$\chi^a = \Phi^a(\mathbf{r}; \{\mathbf{r}^i\}, \mathbf{R}) \Psi_l^a(\{\mathbf{r}^i\}) \Psi^a(\mathbf{R}, \{\mathbf{r}^i\}), \quad (5.83)$$

where Φ^a , Ψ_l^a and Ψ^a are the wave functions of conduction electrons, the lattice and the interstitial atom, respectively, with \mathbf{r} , $\{\mathbf{r}^j\}$, and \mathbf{R} representing

Table 5.19. Tunneling-matrix element J_0 and saddle-point energy e_{sp} for transitions between ground states in adjacent T sites. Calculated by *Sugimoto* and *Fukai* (SF) [5.303] and *Klamt* and *Teichler* (KT) [5.238, 5.239]

Isotope	Metal	$2J_0$ [meV]	e_{sp} [meV]	Reference
H	V	20	19	SF
	Nb	6	29	SF
		0.34	30	KT
	Ta	2	31	SF
		0.44	20.6	KT
D	V	2	24	SF
	Nb	≈ 0.3	29	SF
		0.014	27	KT
	Ta	≈ 0.2	30	SF
		0.030	16.5	KT

their coordinates. In the spirit of the Born-Oppenheimer approximation, Φ^a contains $\{\mathbf{r}^j\}$ and \mathbf{R} , and Ψ^a contains $\{\mathbf{r}^j\}$ as parameters. The many-body wave function Φ^a contains, in addition to the electron states in a perfect crystal, states describing screening charges around the interstitial. Likewise, Ψ_l^a contains, in addition to phonon states in a perfect crystal, the static distortion and disturbed phonon fields caused by the interstitial. The total wave function χ^a satisfies the Schrödinger equation

$$\mathcal{H}^a \chi^a = E^a \chi^a, \quad (5.84a)$$

and that of a self-trapped state on an adjacent site b ,

$$\mathcal{H}^b \chi^b = E^b \chi^b, \quad (5.84b)$$

For two equivalent sites, the two states are degenerate in energy: $E^a = E^b$. The presence of interactions between these two states gives rise to the energy splitting, the magnitude of which is described by a tunneling-matrix element

$$J = \langle \chi^a | \mathcal{H}' | \chi^b \rangle, \quad (5.85a)$$

$$= \langle \Psi_l^a | \Psi_l^b \rangle \langle \Phi^a \Psi^a | \mathcal{H}' | \Phi^b \Psi^b \rangle. \quad (5.85b)$$

If the electrons can follow the instantaneous positions of the interstitial, the integration over electron coordinates always gives unity, leading to the second factor of (5.85b) equal to

$$J_0 = \langle \Psi^a | \mathcal{H}' | \Psi^b \rangle, \quad (5.86)$$

the so-called bare tunneling-matrix element for the interstitial.

Actually, the motion of an interstitial is inevitably accompanied by excitations of the conduction electrons because there is a high density of states

above the Fermi surface, with infinitesimal excitation energies. The effect of this nonadiabatic response of conduction electrons can be formally written in the form of the overlap integral $\langle \Phi^a | \Phi^b \rangle$, leading to the expression

$$J = \langle \Psi_l^a | \Psi_l^b \rangle \langle \Phi^a | \Phi^b \rangle \langle \Psi^a | \mathcal{H}' | \Psi^b \rangle \quad (5.87a)$$

$$= f_l f_{el} J_0 . \quad (5.87b)$$

We shall examine these renormalization effects of the lattice and conduction electrons in this order below.

Holstein [5.232, 5.233] has shown that the effect of the lattice can be cast into the form

$$f_l = e^{-S(T)} , \quad (5.88)$$

provided that the energy of the interstitial depends linearly on the displacements of the lattice atoms, that is to say, the frequencies of phonons in the harmonic lattice are not changed by lattice distortion but only the centers of vibrations are. If the displacements of lattice atoms caused by an interstitial at \mathbf{R}^a are written as

$$\mathbf{u}_i = \sum_{\mathbf{q}} \frac{\mathbf{q}}{q} \left(\frac{\hbar}{2N_0 M \omega_{\mathbf{q}}} \right)^{1/2} e^{i\mathbf{q} \cdot \mathbf{R}^a} (b_{\mathbf{q}} + b_{-\mathbf{q}}^+) , \quad (5.89)$$

the energies of the interstitial can be written in the linear approximation as

$$e^a = e_0^a - \sum_{\mathbf{q}} A_{\mathbf{q}}^a (b_{\mathbf{q}} + b_{-\mathbf{q}}^+) , \quad (5.90)$$

where $A_{\mathbf{q}}$ represents the coupling between the interstitial and the lattice. (Hereafter, the frequencies are written in terms of angular frequencies: $\omega = 2\pi\nu$.) The function $S(T)$ is then obtained as [5.231, 5.304–5.306].

$$S(T) = \sum_{\mathbf{q}} \frac{|A_{\mathbf{q}}^a - A_{\mathbf{q}}^a|^2}{(\hbar\omega_{\mathbf{q}})^2} (\bar{n}_{\mathbf{q}} + 1/2) , \quad (5.91)$$

where $\bar{n}_{\mathbf{q}}$ is the thermal average of the phonon number

$$\bar{n}_{\mathbf{q}} = (e^{\hbar\omega_{\mathbf{q}}/kT} - 1)^{-1} . \quad (5.92)$$

The function $S(T)$ was calculated by *Teichler* [5.306] for H and D in Nb and Ta, with the results shown in Fig. 5.100. At temperatures $T < \theta_D/5$ (θ_D : Debye temperature), $S(T)$ assumes a nearly constant value $\sim S(0)$ determined by the static distortion of the lattice. The magnitude and general shape of the function $S(T)$ are expected to be similar in other metals. Thus, the lattice renormalization factor f_l is of the order of $\sim 10^{-2}$ at $T \leq \theta_D/5$ and decreases rapidly at higher temperatures.

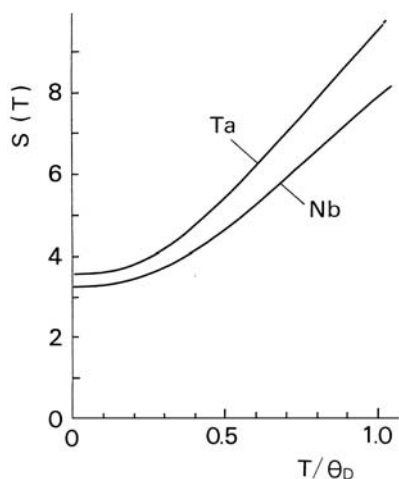


Fig. 5.100. Temperature dependence of the parameter $S(T)$ that gives the lattice renormalization factor $f_l = \exp[-S(T)]$ for H in Nb and Ta. The results also apply to D [5.306]

The effect of the nonadiabatic response of conduction electrons on the motion of a heavy charged particle in a metal was first examined by *Kondo* [5.307] and, subsequently, in a series of papers by *Kondo* [5.308–5.312], *Yamada et al.* [5.313], *Yamada* [5.314], *Kagan and Prokof'ev* [5.315], *Grabert et al.* [5.316], and *Grabert* [5.317]. A consistent description of the theory of tunneling, including both self-trapping and conduction-electron effects, was given later by *Grabert and Schober* [5.318], but here we prefer to reproduce Kondo's approach, trying to make clear the conceptual developments.

Let us consider a charged particle placed at a position \mathbf{R}^a in a uniform sea of conduction electrons. When the particle-electron interaction is treated as a perturbation, the ground-state wave function of the system is expressed, to the first order of the interaction potential V , by

$$\chi^a = N^{-1} \left(\Phi_0 - \sum_{\mathbf{k}, \mathbf{k}'} c_{\mathbf{k}\mathbf{k}'} \Phi_{\mathbf{k} \rightarrow \mathbf{k}'} \right), \quad (5.93)$$

where Φ_0 is the unperturbed, Fermi-surface (FS) state, and $\Phi_{\mathbf{k} \rightarrow \mathbf{k}'}$ is obtained from it by exciting an electron from state \mathbf{k} inside the FS to \mathbf{k}' outside. The coefficients $c_{\mathbf{k}\mathbf{k}'}$ are given in terms of the Fourier components of the potential $V_{\mathbf{k}\mathbf{k}'}$ and the electron energies $\varepsilon_{\mathbf{k}}$ and $\varepsilon_{\mathbf{k}'}$ as

$$c_{\mathbf{k}\mathbf{k}'} = V_{\mathbf{k}\mathbf{k}'} / (\varepsilon_{\mathbf{k}'} - \varepsilon_{\mathbf{k}}). \quad (5.94)$$

If the particle is in motion in a potential well $V(\mathbf{R} - \mathbf{R}^a)$, and described by the wave functions $\Psi_n^a (n = 0, 1, 2, \dots)$, the corresponding expression becomes

$$\chi^a = N^{-1} \left(\Phi_0 \Psi_0^a - \sum_{\mathbf{k}, \mathbf{k}', n} c_{\mathbf{k}\mathbf{k}'n} \Phi_{\mathbf{k} \rightarrow \mathbf{k}'} \Psi_n^a + \dots \right), \quad (5.95)$$

where

$$c_{\mathbf{k}\mathbf{k}'n} = \frac{V_{\mathbf{k}\mathbf{k}'} \langle n | e^{i(\mathbf{k}-\mathbf{k}') \cdot \mathbf{R}} | 0 \rangle}{e_n - e_0 + \varepsilon_{\mathbf{k}'} - \varepsilon_{\mathbf{k}}}, \quad (5.96)$$

$$\langle n | e^{i\boldsymbol{\kappa} \cdot \mathbf{R}^a} | 0 \rangle = \int \Psi_n^{a*}(\mathbf{R}) e^{i\boldsymbol{\kappa} \cdot \mathbf{R}} \Psi_0^a(\mathbf{R}) d\mathbf{R}, \quad (5.97)$$

and the normalization factor N is given by

$$N^2 = 1 + \sum_{\mathbf{k}, \mathbf{k}'} |c_{\mathbf{k}\mathbf{k}'n}|^2 + \dots \quad (5.98)$$

The wave function of the system χ^b for the particle in a well $V(\mathbf{R} - \mathbf{R}^b)$ can be written in a similar manner. The transfer integral is expressed, to the second order of V , by

$$\begin{aligned} \langle \chi^a | \mathcal{H}' | \chi^b \rangle &= \langle 0 | \mathcal{H}' | \tilde{0} \rangle - \langle 0 | \mathcal{H}' | \tilde{0} \rangle \sum_{\mathbf{k}, \mathbf{k}', n} \frac{|V_{\mathbf{k}\mathbf{k}'}|^2 |\langle n | e^{i\boldsymbol{\kappa} \cdot \mathbf{R}} | 0 \rangle|^2}{(e_n - e_0 + \varepsilon_{\mathbf{k}'} - \varepsilon_{\mathbf{k}})^2} \\ &+ \sum |V_{\mathbf{k}\mathbf{k}'}|^2 \frac{\langle 0 | e^{-i\boldsymbol{\kappa} \cdot \mathbf{R}} | n \rangle \langle n | \mathcal{H}' | \tilde{n}' \rangle \langle \tilde{n}' | e^{i\boldsymbol{\kappa} \cdot \mathbf{R}} | \tilde{0} \rangle}{(e_n - e_0 + \varepsilon_{\mathbf{k}'} - \varepsilon_{\mathbf{k}}) \cdot (e_{n'} - e_0 + \varepsilon_{\mathbf{k}'} - \varepsilon_{\mathbf{k}})} + \dots \end{aligned} \quad (5.99)$$

where

$$\langle n | \mathcal{H}' | \tilde{n}' \rangle = \int \Psi_n^{a*}(\mathbf{R}) \mathcal{H}' \Psi_{n'}^b(\mathbf{R}) d\mathbf{R} \quad (5.100)$$

and

$$J_0 = \langle 0 | \mathcal{H}' | \tilde{0} \rangle. \quad (5.101)$$

The abbreviation $\boldsymbol{\kappa} = \mathbf{k} - \mathbf{k}'$ has been used. Note that the relation

$$\langle \tilde{0} | e^{i\boldsymbol{\kappa} \cdot \mathbf{R}} | \tilde{0} \rangle = e^{i\boldsymbol{\kappa} \cdot \mathbf{d}} \langle 0 | e^{i\boldsymbol{\kappa} \cdot \mathbf{R}} | 0 \rangle \quad (5.102)$$

holds, where $\mathbf{d} = \mathbf{R}^b - \mathbf{R}^a$.

The summations in (5.99) are simplified by the following physical considerations [5.311, 5.314]. For sufficiently large $\varepsilon_{\mathbf{k}'} - \varepsilon_{\mathbf{k}}$, one may neglect $e_n - e_0$ and $e_{n'} - e_0$ in the denominators, and perform n and n' summations with the completeness relation. This results in the cancellation of the second and third terms. One may, thus, limit the \mathbf{k} and \mathbf{k}' summations within the region where $\varepsilon_{\mathbf{k}'} - \varepsilon_{\mathbf{k}}$ is smaller than some critical value ε_c . *Kagan* and *Prokof'ev* [5.315] took the first excitation energy $\varepsilon_c = e_1 - e_0 = \hbar\omega_0$ as this critical value. For $\varepsilon_{\mathbf{k}'} - \varepsilon_{\mathbf{k}}$ below this value, the terms with $n, n' > 1$ may be neglected. *Kondo* [5.312] showed subsequently that in order for the completeness relations to be applied, the summations must be taken at least up to the n -th term, where $n \approx \kappa d \approx k_F d$. Therefore, the maximum value for $\varepsilon_{\mathbf{k}'} - \varepsilon_{\mathbf{k}}$

should be $\varepsilon_c = k_F d \hbar \omega_0$. It must be noted that there is also a minimum value for $\varepsilon_{\mathbf{k}'} - \varepsilon_{\mathbf{k}}$ because the particle energy levels are split by the tunneling.

All in all, the transfer integral is given by

$$\langle \chi^a | \mathcal{H}' | \chi^b \rangle = J_0 f_l \left[1 + \sum_{\mathbf{k}, \mathbf{k}'} (e^{i\mathbf{k} \cdot \mathbf{d}} - 1) c_{\mathbf{k}\mathbf{k}'0}^2 + \dots \right] \quad (5.103a)$$

$$= J_0 f_l f_{el} , \quad (5.103b)$$

in which the lattice renormalization has been included, and the \mathbf{k} , \mathbf{k}' summations are limited to the region described above.

Adopting a simple form for the potential V , such that

$$V_{\mathbf{k}\mathbf{k}'} = V_0 e^{i\mathbf{k} \cdot \mathbf{R}^a} , \quad (5.104)$$

averaged over the directions of \mathbf{k} and \mathbf{k}' , and performing \mathbf{k} and \mathbf{k}' summations, we obtain the following approximate expressions for the electron renormalization factor [5.312]:

$$f_{el}^N = \begin{cases} (\bar{J}/\varepsilon_c)^K , & \bar{J} \gg kT , \\ (kT/\varepsilon_c)^K , & kT \gg \bar{J} , \end{cases} \quad (5.105a)$$

$$(5.105b)$$

where $\varepsilon_c = k_F d \hbar \omega_0$, and the superscript N stands for normal conducting state. \bar{J} is determined self-consistently in the limit of $T \rightarrow 0$ as

$$\bar{J} = J_0 f_l (\bar{J}/\varepsilon_c)^K \quad (5.106a)$$

or

$$\bar{J} = (J_0 f_l)^{1/(1-K)} \varepsilon_c^{-K/(1-K)} , \quad (5.106b)$$

and

$$K = 2V_0^2 N(E_F)^2 [1 - \sin^2 k_F d / (k_F d)^2] . \quad (5.107)$$

The response of conduction electrons becomes very different in the superconducting state, because the excitations of the electron system now have a finite low-energy cutoff corresponding to the superconducting energy gap. Thus the electron renormalization factor varies with temperature as [5.319]

$$f_{el}^S = \left[\frac{2\Delta_g(T)}{\varepsilon_c} \right]^K . \quad (5.108)$$

Several different expressions have been derived later for the electron renormalization factor f_{el} , depending on the approximation adopted. The result of *Grabert et al.* [5.318] contains a factor $[\Gamma(1-2K) \cos \pi K]^{1/2}$ on the right-hand side of (5.105) for the normal conducting state, and a factor

$[\Gamma(1-2K) \cos \pi K]^{-1/2} e^{0.1909T}$ on the right-hand side of (5.108) in the superconducting state. Both these factors approach 1 for $K \rightarrow 0$. The corresponding expressions derived by *Teichler* [5.319, 5.320] read

$$f_{el}^N = \left(\frac{2J^N}{\varepsilon_c} \right)^K, \quad (5.109)$$

$$f_{el}^S = \left[\frac{2(J^S + \Delta_g(0))}{1.1(1 - J^S/\Delta_g(0))} \frac{1}{\varepsilon_c} \right]^K \quad (5.110)$$

at $T \rightarrow 0$, with J^N and J^S standing for the tunneling matrix element in the normal and superconducting state, respectively. The expression derived by taking the ratio of (5.109) and (5.110), viz.

$$\ln \frac{J^N}{J^S} \approx K \left[\ln \frac{J^N}{J^S + \Delta_g(0)} + 1.1 \left(1 - \frac{J^S}{\Delta_g(0)} \right) \right]. \quad (5.111)$$

provides a unique possibility of determining K from the measured ratio of J^N/J^S at $T \rightarrow 0$.

The parameter K , sometimes referred to as Kondo parameter, describes the coupling between the particle and conduction electrons. For a given coupling strength $V_0 N(E_F)$, K tends to 0 for $d \rightarrow 0$ and becomes maximum for $d \rightarrow \infty$.

Yamada et al. [5.313] obtained a general expression for K in terms of S -matrices (the scattering of free electron gas), which, when a single l -th partial wave contributes dominantly, can be written in terms of phase shift δ_l as

$$K = 2(2l+1) \left\{ \frac{1}{\pi} \tan^{-1} \left[\frac{(1 - j_l^2(k_F d))^{1/2} \tan \delta_l}{(1 + j_l^2(k_F d) \tan^2 \delta_l)^{1/2}} \right] \right\}^2. \quad (5.112)$$

If, as usual, the main contribution comes from s electrons ($l = 0$), the phase shift satisfies the relation $\delta_0 \approx \pi/2$ (the Friedel sum rule) for a particle with a single positive charge, and the upper bound for the value of K is found to be 1/2. ($K = 1/2$ is realized for $\delta_0 = 1/2$ and $k_F d \rightarrow \infty$.) Estimates of K for specific metals can be obtained by substituting the phase shifts calculated by *Puska* and *Nieminen* [5.321] as a function of electron density parameter r_s . ($r_s = (3/4\pi n)^{1/3}/a_B$, where n is the electron density and a_B is the Bohr radius.) Another expression for K was obtained by *Fritzsche* [5.322] by considering the dielectric response of a homogeneous electron gas. In this formalism, K is given in terms of tunneling distance d and r_s . For a fixed value of r_s , K increases with d until it reaches a plateau for $d \geq r_s \times 1 \text{ \AA}$. The plateau value increases almost linearly with r_s [5.323]. Specifically, calculations using different forms of dielectric functions yielded $K = 0.06\text{--}0.08$ (Fe, Cr) and $0.07\text{--}0.10$ (Nb, Ta) for T-T jumps, and $K = 0.09\text{--}0.13$ (Fe, Cr) and $0.11\text{--}0.16$ (Nb, Ta) for O-O jumps [5.324], in reasonable agreement with experiments

(Table 5.17). Although detailed numerical comparison of the theory based on a homogeneous electron gas may not be very meaningful for transition metals, the small values of K obtained both from experiments and theory indicate that a coupling of hydrogen atoms to conduction electrons is weak and justify the use of the approximate expressions valid for $K \ll 1$.

In this regime of weak coupling to conduction electrons, the damping can be expressed by the following expressions

$$\Gamma^N = 2\pi K J^N \coth \left(\frac{J^N}{kT} \right) \quad (5.113)$$

for the normal conducting state [5.280], and

$$\Gamma^S = 4\pi K \frac{kT}{1 + \exp(\Delta_g(T)/kT)} \quad (5.114)$$

for the superconducting state [5.281, 5.325]. In the limit of $T \rightarrow 0$, $\Gamma^N \rightarrow 2\pi K J^N$, whereas $\Gamma^S \rightarrow 0$ because the electron bath having a finite energy gap does not allow energy exchange with the tunneling system. In both cases, Γ is proportional to the coupling strength K .

The experimental results described in Sect. 5.6.2 have demonstrated very clearly that below ~ 5 K two well-defined energy states exist for H and D trapped by interstitial impurity atoms in Nb. The energy levels are progressively broadened with rising temperature, indicating the coherent tunneling state is destroyed when the level broadening becomes comparable to the tunneling matrix element $\Gamma \approx J$. The coherent two-site tunneling state which exists below ~ 5 K turns above ~ 10 K into a state where an H atom executes incoherent hoppings between these sites. The physical implication of transition between coherent tunneling and incoherent hopping regimes will be explained in Sect. 6.6.1, in the context of the unified picture of diffusion mechanism over the whole temperature range.

Let us make a numerical comparison between the values of the tunneling-matrix element deduced from the experiments and theoretical calculations. The comparison is made most conveniently in terms of “bare” matrix element J_0 . The observed energy splitting $\varepsilon_{t0} = 2J$ divided by $f_{el}f_l$ gives $2J_0$. For superconducting Nb, the electronic renormalization factor at $T = 0$ becomes $f_{el} = [2\Delta_g(0)/k_F d\hbar_0]^K \approx (3.06/360)^{0.055} = 0.769$. [$\Delta_g(0) = 1.53$ meV, $k_F d = k_F a/2\sqrt{2} = 2.356$, $\hbar\omega_0 = (120 + 2 \times 170)/3 = 153$ meV.] Regarding the lattice renormalization factor f_l , *Teichler* [5.305] performed calculations for H and D in Nb and Ta in an isolated (free) state, and also for H and D trapped by O atom in Nb. Here we use his values for the trapped state for O, N, and C atoms. The values of $2J_0$ thus deduced are compared with the theoretical values of *Sugimoto* and *Fukai* [5.303] and *Teichler* [5.320] for H and D in Nb in the free state (Table 5.20). Considering the sensitivity of the calculations to the details of local lattice distortions and the wave functions of hydrogen atoms, the agreement can be said to be quite satisfactory.

Table 5.20. Tunneling-matrix element J_0 for H and D in Nb, existing in an isolated (free) state and states trapped by O, N, or C atoms. The experimental values of J_0 are obtained by dividing the observed values J by appropriate electronic and lattice renormalization factors (f_{el} and f_l)

Isotope (State)	$2J$ [meV]	f_{el}^c	f_l^d	$2J_0$ [meV]	
				Experimental	Calculated
H (free)	—	0.769	0.036	—	$6^e, 0.60^f$
H (O)	0.23 ± 0.01^a	(0.769)	0.034	8.8	—
H (N)	0.17 ± 0.01^a	(0.769)	(0.034)	6.5	—
H (C)	0.162 ± 0.004^b	(0.769)	(0.034)	6.2	—
D (free)	—	0.769	0.052	—	$0.3^e, 0.06^f$
D (O)	0.020 ± 0.001^a	(0.769)	0.046	0.57	—
D (N)	0.014 ± 0.001^a	(0.769)	(0.046)	0.40	—

^a*Gutsmiedl et al.* [5.269].

^b*Neumaier et al.* [5.273].

^cEstimated for pure Nb (see text).

^dFor H, D trapped by N and C, calculated values for those trapped by O are used.

^e*Sugimoto and Fukai* [5.303].

^f*Teichler* [5.300].

The real discrepancy may be even smaller as the distance between T sites becomes shorter in the trapped configuration than in the free state making the tunneling-matrix element correspondingly larger.

In fact, in addition to the coupling to conduction electrons there is another quasi-elastic (nearly energy-conserving) scattering process caused by virtual absorption and emission of phonons, often called the diphonon process. As this contribution depends on the higher power(s) of temperature and becomes extremely small at low temperatures, the omission of this effect in the foregoing discussion is perfectly justifiable. More about the diphonon process is given in Sect. 6.5.2

Appendix 5A. Formation of Entangled States of Hydrogen in Metals

The quantum entanglement, also known by the name of Einstein-Podolsky-Rosen (EPR) correlation [5.326], is a manifestation of the basic premise of quantum mechanics that any state of matter should be expressible as a linear combination of its eigenstates. More specifically, in systems composed of two (or more) indistinguishable particles the state of the system should be expressed by a linear superposition of states that satisfies the condition of

indistinguishability. Thus these particles are inherently connected with each other, even without any interactions, and form a so-called ‘entangled’ state.

The formation and destruction of the entangled state have attracted renewed interest in the last 10–20 years, the incentive being the clarification of the basic concept of quantum mechanics on one hand and its possible application to, e.g., telecommunications and quantum computers on the other [5.327–5.330].

Up to now, most of the studies have been limited to small systems well isolated from the environment so that the time for decoherence τ_{dec} is long enough to allow observation of the entangled state. In ordinary condensed matters, the disturbance from the environment is generally considered so strong that τ_{dec} becomes extremely short. Estimates based on a simple decoherence model are $\tau_{\text{dec}} \sim 10^{-(15\sim 17)} \text{ s}$ for molecules of $10 \sim 100 \text{ \AA}$ in size, and $\sim 10^{-19} \text{ s}$ for objects of 10 \AA in size, when placed in good laboratory vacuum ($10^6 \text{ particles cm}^{-3}$) [5.331]. Thus in order to investigate a few-proton entanglement in condensed matters, some experimental methods must be devised that allow to take ‘snapshots’ within the time window of 10^{-15} s (femtosecond) or less.

Recently, evidence has been obtained for the short-lived entanglement of protons in some condensed matter, including M-H systems, in an extension of work initiated by the Uppsala group [5.332]. A major technique adopted for its investigation is the neutron Compton scattering (NCS), in which the energy of incident neutrons (10–100 eV) is transferred to different nuclear species in a sample by respective recoil processes, and the intensity of scattered neutrons is measured as a function of energy transfer, measured at different scattering angles. The intensity of scattered neutrons from hydrogen isotopes (H, D) is measured relative to some heavier nuclear species coexisting in the sample. The energy transfer of $1 \sim 10 \text{ eV}$ corresponds to the reaction time of $10^{-(15\sim 16)} \text{ s}$, which determines the time window of the method. The only spectrometer available for this purpose, having a good resolution in this energy range, is the EVS spectrometer at the Rutherford-Appleton Laboratory (U.K.), where transmission of the outgoing neutrons through a foil with a sharp nuclear resonance allows the energy selection of $4.908 \pm 0.138 \text{ eV}$ for Au-foil and $6.771 \pm 0.062 \text{ eV}$ for U-foil. The coherence length set by the energy resolution (de Broglie wavelength), $l_{\text{coh}} \approx \lambda^2/\Delta\lambda$, may become comparable to the distance between adjacent protons, but in many cases such interference effects of neutron waves are not very important [5.333]. The situation is very different from thermal neutron scattering described previously (Sect. 5.4), where both the coherent length and scattering time are much longer.

The first NCS experiment for this purpose was performed on $\text{H}_2\text{O}/\text{D}_2\text{O}$ mixture [5.334], in which the ratio of scattered intensities from H and D ($A_{\text{H}}/A_{\text{D}}$) was measured as a function of isotope composition. The ratio of effective cross sections $\sigma_{\text{H}}/\sigma_{\text{D}}$ was obtained by dividing $A_{\text{H}}/A_{\text{D}}$ by the relative composition $[\text{H}]/[\text{D}]$, and the results are shown in Fig. 5A.1. Contrary to the

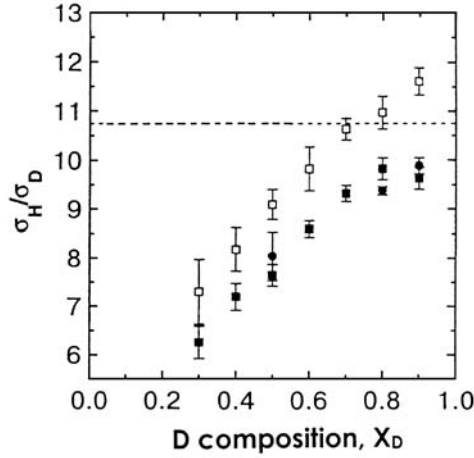


Fig. 5A.1. Dependence of the relative scattering cross section σ_H/σ_D on the D-content in H_2O/D_2O mixtures. Full (*open circles*) represent measurements with Au(U) analyzer. The *dashed line* represents the standard value $\sigma_H/\sigma_D = 10.7$ [5.334]

general expectation that σ_H/σ_D should be a constant ($=10.7$) determined by the intrinsic property of the nuclei, the result shows a striking dependence on the isotope composition: the apparent cross section of the proton is reduced with respect to that of the deuteron in H-rich samples and this reduction gradually disappears in D-rich samples. Subsequent measurements of the scattering intensity of D vs. O, σ_D/σ_O , in D_2O and 1:1 mixture of H_2O/D_2O [5.335] showed that σ_D/σ_O assumes very nearly the standard value over the time window of the measurement (Fig. 5A.2). In contrast, σ_H/σ_O in 1:1 mixture of H_2O/D_2O was found to be $\sim 50\%$ of the standard value. A similar anomaly with respect to isotope composition was found in H_2O/D_2O mixtures by a Raman scattering experiment, which observes systems within a similar time window of $\sim 10^{-15}$ s [5.336]. The authors suggested from these observations that these anomalies were associated with local quantum entanglement of protons in water.

NCS measurements on the M-H system were started with Nb hydrides, NbH_xD_y ($x + y = 0.85 \pm 0.05$) [5.337]. At this composition, the samples are predominantly in the β -phase, where H and D atoms form ordered arrays. The ratio of the cross sections of H and D to that of Nb observed at different scattering angles are shown in Fig. 5A.3. Since neutrons scattered by different angles probe the system at different time scales, the results indicate that the scattering cross section of D is independent of the scattering time τ_{sc} , whereas that of H depends strongly on τ_{sc} . The absolute values of σ_D/σ_{Nb} are close to the standard value of 1.22, whereas the values of σ_H/σ_{Nb} are generally much smaller than the standard value of 13.1 and approaches this value at low scattering angles (corresponding to long τ_{sc} s). The observed cross section

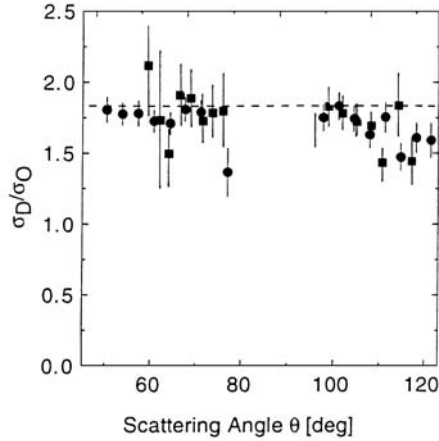


Fig. 5A.2. Relative scattering cross section σ_D/σ_O in D_2O (circles) and equimolecular mixture of H_2O/D_2O (squares) measured at different scattering angles. The dashed line represents the standard value $\sigma_D/\sigma_O = 1.80$ [5.335]

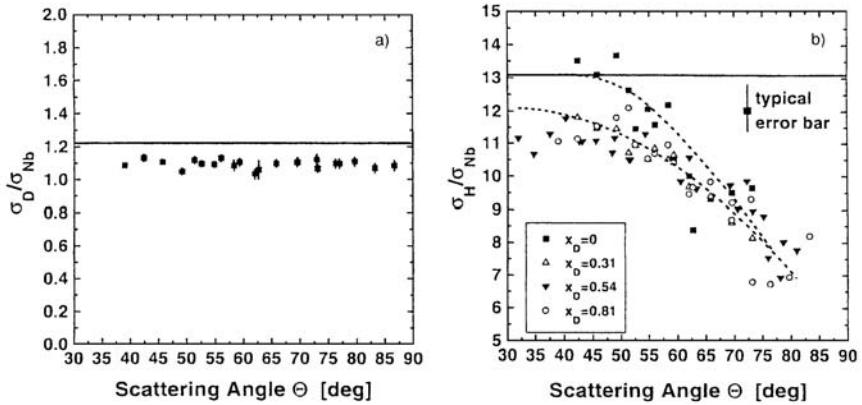


Fig. 5A.3. Dependence of the relative scattering cross section on scattering angle; (a) σ_D/σ_{Nb} in $NbD_{0.80}$, (b) σ_H/σ_{Nb} in isotope-mixed NbH_xD_y ; $x+y \approx 0.86$, $X_D = y/(x+y)$ [5.337]

ratio of protons σ_H/σ_{Nb} in $NbH_{0.85}$ as a function of scattering time τ_{sc} is shown in Fig. 5A.4, together with the data of σ_H/σ_{Pd} subsequently obtained for $PdH_{0.5}$ [5.338]. Both sets of data were obtained at room temperature. The cross section ratios have been normalized to the standard value at long scattering times. The two sets of data show closely the same behavior, as well as those obtained at 20 K (not shown). In all the cases, deviation from the expected cross section ratio starts at $\tau_{sc} \sim 0.6 \times 10^{-15}$ s.

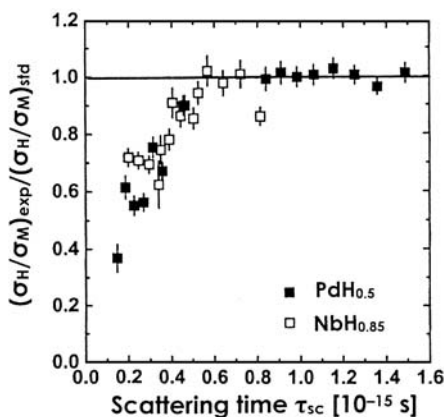


Fig. 5A.4. Dependence of the relative scattering cross section σ_H/σ_{Nb} in $NbH_{0.85}$ (*open squares*) and σ_H/σ_{Pd} in $PdH_{0.5}$ (*solid squares*) on scattering time, normalized to the standard values $\sigma_H/\sigma_{Nb} = 13.1$ and $\sigma_H/\sigma_{Pd} = 16.0$ [5.337, 5.338]

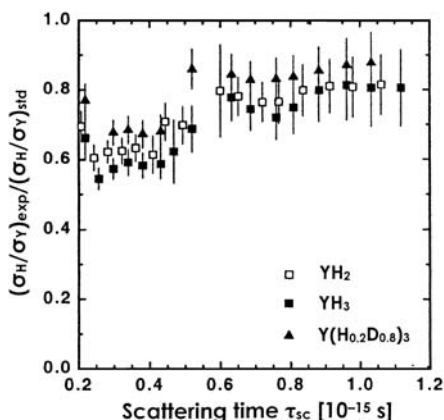


Fig. 5A.5. Dependence of the relative scattering cross section σ_H/σ_Y on scattering time, observed in YH_2 , YH_3 and $Y(H_{0.2}D_{0.8})_3$, normalized to the standard value $\sigma_H/\sigma_Y = 10.6$ [5.339]

Results obtained for Y hydrides were also similar [5.339]. Considerable reductions of σ_H were observed in YH_2 , YH_3 and $Y(H_{0.2}D_{0.8})_3$, but only minor reductions of σ_D in YD_2 and YD_3 (Fig. 5A.5).

NCS measurements were also performed on a number of other H-containing materials, including polystyrene (fully protonated and partially deuterated) [5.340], a mixture of liquid benzene (C_6H_6/C_6D_6), and a liquid mixture of acetone (CH_3COCH_3/CD_3COCD_3) [5.341]. Deviations from the classical behavior were most prominent in acetone, less pronounced but still evident in

polystyrene and benzene. The results appear to indicate that the entangled states of protons are more long-lived in water and polystyrene than in other materials.

Very recently, using a polymer film sample known as formvar ($C_8H_{14}O_2$), an important experiment was performed aiming at a direct comparison of electron Compton scattering (ECS) with NCS results [5.342]. Figure 5A.6 shows the Compton profiles derived from ECS and NCS experiments, giving confirmation that the two methods provide exactly the same information on the proton momentum distribution. Figure 5A.7 compares the ECS and NCS results for the scattering intensity ratio $R_{\text{exp}} = A_H/(A_C + A_O)$, with A_X 's denoting the area under the relevant scattering peak, as a function of momentum transfer. The standard value has been calculated from $R_{\text{st}} = N_H\sigma_H/(N_C\sigma_C + N_O\sigma_O)$, with $\sigma \propto (\text{atomic number})^2$ for ECS. Results obtained from ECS and NCS are very similar. In both cases, measured scattering intensities are smaller than standard values, and decrease with the momentum transfer.

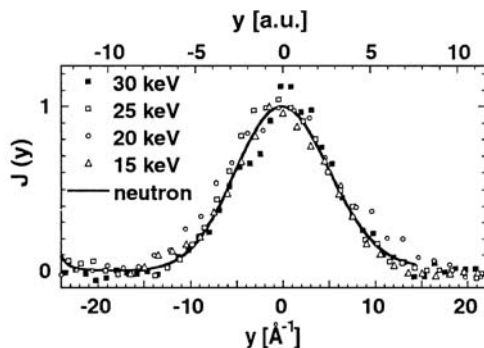


Fig. 5A.6. Compton profiles of formvar films derived from ECS experiments at different energies and from NCS experiments. The scattering intensity is plotted against the momentum of protons in the direction of momentum transfer [5.342]

Independent of this series of work, incoherent elastic neutron scattering experiments on $KHCO_3$ revealed anomalous scattering characteristics, which was suggested by the authors to be the evidence of quantum entanglement in proton dimers in the crystal [5.343, 5.344].

On the theoretical side, there are two different interpretations for the observed anomalies, in both of which the quantum entanglement of H (and D) plays a fundamental role; a model due to *Chatzidimitriou-Dreismann* [5.341, 5.342, 5.345], and *Karlsson and Lovesey* [5.333, 5.346–5.348].

In the Dreismann model, spatial quantum entanglement and decoherence – concerning protonic and electronic degrees of freedom – are considered to be crucial, and entanglements of spin states are less important. A gist of

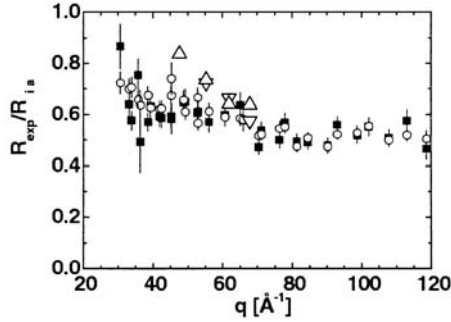


Fig. 5A.7. The ratio of measured vs. standard scattering intensities as a function of proton momentum transfer in formvar films obtained from ECS and NCS experiments. *Large triangles* from ECS on 50–100 Å films; *solid squares* and *open circles* from NCS on 0.1 mm and 0.2 mm films, respectively [5.342]

their model calculation is as follows: In the limits of incoherent and impulse approximations appropriate for the NCS experiments, a general formula for the dynamical structure factor in the van Hove theory is reduced to

$$S(\mathbf{q}, \omega) = \left\langle \delta \left(\omega - \omega_r - \mathbf{q} \cdot \hat{\mathbf{P}}/M \right) \right\rangle, \quad (5A.1)$$

where $\hbar\mathbf{q}$ and $\hbar\omega$ are the momentum and energy transfers from the neutron to the scattering nucleus respectively, $\hbar\omega_r$ is the recoil energy of the struck nucleus with mass M and its momentum operator $\hat{\mathbf{P}}$. $\langle \cdots \rangle = \Sigma W_n \langle n | \cdots | n \rangle$ is the appropriate thermodynamical and quantal average, n being the many-body quantum state. A crucial point is that the density operator involved in $\langle n | \cdots | n \rangle$ contains an intrinsic time dependence due to decoherence effects. In the position representation, the density matrix element varies with time as

$$\rho(x, x'; t) = \rho(x, x'; 0) e^{-\Lambda |x - x'|^2 t}, \quad (5A.2)$$

where Λ is usually called the localization rate, which determines the decoherence time $1/\tau_{\text{dec}} \approx \Lambda |x - x'|^2$ [5.331]. This reduction in time of the density matrix results in the reduction of the scattering intensity, i.e. the integral of $S(\mathbf{q}, \omega)$ over ω .

It has been shown that this reduction of the scattering intensity occurs only when the decoherence time is comparable to the duration of a scattering event, defined as the scattering time τ_{sc} . τ_{sc} is given approximately by

$$\tau_{\text{sc}} = 1/qv_0, \quad (5A.3)$$

where $\hbar\mathbf{q}$ is the momentum transfer and v_0 is the r.m.s. velocity of the nucleus. Physically, this implies that the scattering amplitude is affected by decoherence only when the final state of the system becomes different from

the initial state during the scattering event. For $\tau_{\text{dec}} \ll \tau_{\text{sc}}$, the effect of entanglement is obviously negligible; for $\tau_{\text{dec}} \gg \tau_{\text{sc}}$, where both initial and final state are in the same entangled state, the sum over all the states (the Tr-operation) in the calculation of scattering amplitude leads to the value equal to the dis-entangled case. A concise but self-contained description of the theory is given in [5.345].

This mechanism based on the spatial quantum entanglement and decoherence – concerning protonic and electronic degrees of freedom – is quite general, and crude estimation of the decoherence time by the theory of *Joos* and *Zeh* [5.331] for molecular-sized systems gives τ_{dec} in order-of-magnitude agreement with the values deduced from the NCS experiments. However, it is not clear from this mechanism alone why the quantum entanglement becomes manifest only for protons. The theory does not say explicitly how and what entangled states are formed. Difference of nuclear species does not affect the formation and destruction of entangled states; it affects only the scattering time through the difference of ν_0 . This rather weak variation of τ_{sc} with nuclear mass does not appear to provide a reasonable explanation for the observed strong dependence of scattering anomalies on the nuclear mass.

In the Karlsson–Lovesey model, where the exchange correlations between pairs of indistinguishable particles are playing a crucial role, the nature of entangled states is considered explicitly and various characteristics of NSC are delineated, including the isotope dependence [5.333, 5.346–5.348]. The effect of exchange-correlation is in fact well-known for thermal neutron scattering from H_2 molecules. There, a large difference of the scattering cross section from ortho and para molecules was explained in terms of correlation in the wave function of the molecule caused by two indistinguishable protons. The correlation is sufficiently long-lived due to large energy difference between ortho and para states, that it manifests itself even in slow scattering processes ($\tau_{\text{sc}} \sim 10^{-13}$ s).

This mechanism, originally proposed by *Schwinger* and *Teller* in 1937 [5.349], has been reformulated by *Karlsson* and *Lovesey* [5.333, 5.346–5.348] for application to the analysis of recent NCS experiments

Let us consider the scattering of a neutron by two indistinguishable particles α and β of spin I occupying sites 1 and 2, whose spatial and spin degrees of freedom are correlated because of their indistinguishability. The initial state before scattering is written as

$$|i\rangle = \frac{1}{\sqrt{2}} \{ \phi_1(\mathbf{R}_\alpha) \phi_2(\mathbf{R}_\beta) + \zeta \phi_1(\mathbf{R}_\beta) \phi_2(\mathbf{R}_\alpha) \} \chi_M^J(\alpha, \beta), \quad (5A.4)$$

where $\zeta = (-1)^J$, $\chi_M^J(\alpha, \beta)$ is the initial spin state with total angular momentum $J = 0, \dots, 2I$, and projection M .

In the final state after scattering, one particle remains in a state of low energy, described by $\psi(\mathbf{R})$, whereas the other flies away in the form of a plane wave. At this stage their quantum correlation is not yet broken and the

identity α or β of the struck particle will be settled only after the decoherence has occurred. Then the wave function of the final state can be written in the form

$$|f\rangle = \frac{1}{\sqrt{2}} \left\{ \exp(i\mathbf{p}' \cdot \mathbf{R}_\alpha) \psi(\mathbf{R}_\beta) + \zeta' \exp(i\mathbf{p}' \cdot \mathbf{R}_\beta) \psi(\mathbf{R}_\alpha) \right\} \chi_{M'}^{J'}(\alpha, \beta), \quad (5A.5)$$

where the spin state is $J'M'$ and $\zeta' = (-1)^{J'}$. \mathbf{p} and \mathbf{p}' are the initial and final wave vectors, respectively, of the struck particle. The neutron scattering operator has the form

$$V_{sc} = b_\alpha \exp(i\mathbf{k} \cdot \mathbf{R}_\alpha) + b_\beta \exp(i\mathbf{k} \cdot \mathbf{R}_\beta), \quad (5A.6)$$

where $\mathbf{k} = \mathbf{p} - \mathbf{p}'$ is the momentum transfer in the process. The scattering length operators have the form $b = A + B\mathbf{s} \cdot \mathbf{I}$, where \mathbf{s} is the neutron spin operator and \mathbf{I} the spin operator for the individual nuclei constituting the correlated pair.

Then, calculating $|\langle f | V_{sc} | i \rangle|^2$ and taking a ratio to the case of no correlation, we obtain the reduction of the single-particle scattering cross section

$$f_{HH} = \frac{1}{2(2I+1)} \left\{ I |T_1 + \exp(i\mathbf{q} \cdot \mathbf{d})T_2|^2 + (I+1) |T_1 - \exp(i\mathbf{q} \cdot \mathbf{d})T_2|^2 \right\}, \quad (5A.7)$$

for half-integer spins (e.g. $I = 1/2$ for protons), and

$$f_{DD} = \frac{1}{2(2I+1)} \left\{ (I+1) |T_1 + \exp(i\mathbf{q} \cdot \mathbf{d})T_2|^2 + I |T_1 - \exp(i\mathbf{q} \cdot \mathbf{d})T_2|^2 \right\}, \quad (5A.8)$$

for integer spins (e.g. $I = 1$ for deuterons). In these expressions, $\mathbf{d} = \mathbf{R}_\alpha - \mathbf{R}_\beta$ and $T_j = \int \psi^*(\mathbf{R}) \phi_j(\mathbf{R}) d\mathbf{R}$ ($j = 1, 2$).

When the correlation is lost during the scattering, the spatial part of (5A.6) becomes a simple product, resulting in $f_{HH} = f_{DD} = 1$.

This theory was applied to the quantitative analysis of NCS experiments on $\text{H}_2\text{O}/\text{D}_2\text{O}$ mixtures [5.350]. Comparison with the experiment was done in terms of relative scattering cross section σ_H/σ_D as a function of isotope composition. f_{HH} and f_{DD} were calculated by taking an average over molecular orientations, with the assumption of no shakeup effects $T_1 = T_2 = 1/\sqrt{2}$. The values obtained are $f_{HH} = 0.42$ and $f_{DD} = 0.63$ for U-foil experiments. The population of H-H, D-D and H-D pairs was estimated from isotope composition by simple probability calculations. The relative scattering cross section σ_H/σ_D calculated in this way for U-foil experiments is shown in Fig. 5A.8, together with corresponding experimental data [5.334]. Calculations were made for three different values of f_{DD} , by fixing $f_{HH} = 0.42$ and $f_{HD} = 0$. The best-fit value $f_{DD} = 0.7 \sim 0.8$ is slightly larger than the theoretical estimate, but appears quite reasonable.

The author has proceeded to estimate the decoherence time from the random spread of vibrational frequencies, and obtained $\tau_{\text{dec}} \approx 2 \times 10^{-14}$ s. This

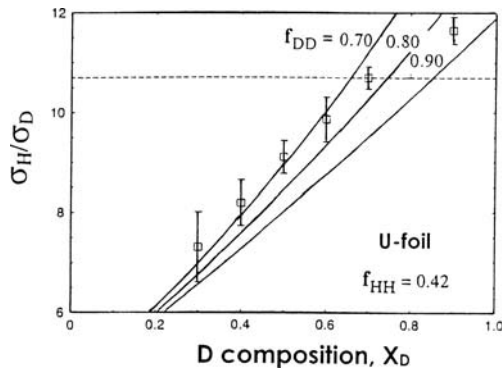


Fig. 5A.8. Dependence of the relative scattering cross section σ_H/σ_D on isotope composition in H_2O/D_2O mixtures for U-foil experiments. Theoretical curves correspond to three different choices of the reduction factor for D-D pairs (f_{DD}) [5.350] and experimental data have been taken from [5.334]

value, being longer than the range of scattering times of NCS experiments but shorter than thermal-neutron scattering experiments, is quite reasonable. In actual NCS experiments, the environment will be strongly perturbed by the recoiling particle; hence the measurement itself should have limited the decoherence time.

In the case of H in Nb, the absence of temperature dependence in the reduction of scattering intensities suggests that thermal excitation processes are not the main cause of decoherence. More probably, the short decoherence time in the metal hydrides is caused by the strong excitations along the trajectory of struck particles. If left in thermal equilibrium, forces that create and destroy entanglement would be in balance over times longer than 10^{-15} s.

Based on these results, *Karlsson* and *Lovesey* [5.347] concluded that closely lying protons in these substances are entangled in scattering over at least of the order of 10^{-15} s. The main cause of the entanglement is considered to be the indistinguishability of the particles, but may also be the consequence of the coupling of protons to other common degrees of freedom.

In $KHCO_3$, a peculiar diffuse pattern observed by thermal neutron scattering (diffraction) experiment [5.343, 5.344] was successfully explained by *Keen* and *Lovesey* [5.351] based on scattering treatments from exchange-correlated dimers. The absence of anomalies in $KDCO_3$ is also consistent with this interpretation. In this thermal-neutron experiment, where perturbations of recoil particles are negligibly small, the lower limit of the decoherence time can be set by the pertinent scattering time of 10^{-13} s. This result suggests the possibility that the intrinsic decoherence time in crystalline solids may become comparable to the period of lattice vibrations.

The views of *Karlsson et al.* on this apparently anomalous response of protons in condensed matter are fully elucidated in their recent paper [3.352]. In

spite of the apparent success in explaining various aspects of the observations, however, their theories at present cannot be taken to be well established. Especially, some arbitrariness in choosing the form of the final state (5A.5), that might affect the conclusions significantly, need more careful examinations. The above discussions regarding the decoherence time appear to be largely unaffected by these possible uncertainties, however.

As a postscript to this Appendix, it may be reminded that the very first proposition for the possibility of EPR correlation between protons in M-H systems was made by *Chatzidimitriou-Dreismann* and *Karlsson* [5.332], inspired by our diffusion data on the isotope-mixed system NbH_xD_y (Sect. 6.4.2). In their paper, it was suggested that the observed slowing-down of proton diffusion in the presence of deuterons might be explained by the breaking-up of the entangled protonic states by the presence of deuterons. Similarly, strong isotope-dependent diffusion of hydrogen on a metal surface and diffusion anomalies of protons in the presence of positive muons were viewed as indirect evidence for short-lived quantum correlations in isotopically pure systems enhancing diffusion. Nonlinearities in the ionic conductivity of water as a function of isotope composition ($[\text{H}]/[\text{D}]$ ratio) were also taken as evidence for the broken quantum correlation in mixed H/D systems.

The mechanism of these anomalies observed in isotope-mixed systems still remains unresolved. The theories described above have not reached the point to judge whether they are really the consequence of quantum entanglement between protons.

As has been emphasized repeatedly (see, e.g. [5.341]), the possible presence of quantum entanglement lasting for $\sim 10^{-15}$ s has profound implications for our basic understanding of the state and interactions of hydrogen in condensed matter.

First, it forces us to question the validity of generally accepted Born-Oppenheimer approximation in treating electronic states. In the Born-Oppenheimer approximation, the nuclei are regarded as classical mass points with specific charges, and electronic energies are calculated by fixing the nuclei at various spatial configurations. The formation of entangled states suggests that this approximation should break down in the time scale of $\sim 10^{-15}$ s.

Second, the protonic quantum entanglement being more ubiquitous than generally realized forces us to examine its implication for chemical reactions in H-containing materials. The time for chemical reactions involving the energy change of several eV is $\sim 10^{-16}$ s, which is comparable or even shorter than the observed decoherence times. Thus the quantum entanglement may affect the femtosecond dynamics of, and electron transfer in, chemical and biological reactions at large involving H atoms. Elementary jump processes of H atoms in metals may also be affected by quantum entanglement.

It must be admitted that the phenomenon of quantum entanglement in condensed matter cannot be taken to be fully established at present.

Questions have been raised from time to time both in regard to experimental and theoretical aspects of the reported NCS measurements, including the one raised by *Blostein et al.* [5.353] replied by *Abdul-Redah* and *Chatzidimitriou-Dreismann* [5.354], and another one by *Cowley* [5.355] replied by *Karlsson* and *Lovesey* [5.356]. Subsequently, *Blostein et al.* [5.357] performed neutron transmission experiments on $\text{H}_2\text{O}/\text{D}_2\text{O}$ mixtures over the same energy range of $1 \sim 100$ eV, and obtained results entirely consistent with standard cross section values to within 0.3%. The absence of any anomaly over the whole range of energy and isotope composition made them to question the validity of the previous NCS experiments. The recent observation of ECS [5.342] appears to have largely eliminated these concerns about the NCS experiments, and established at least the presence of the scattering anomaly at short times. From the occurrence of the same anomaly in both NCS and ECS, *Chatzidimitriou-Dreismann et al.* [5.342] inferred that it is of very fundamental nature, independent of the nature of interactions, either the strong interaction or the electromagnetic interaction. The ascription of this anomaly to the quantum entanglement of protons is certainly very alluring, but may not be the unique conclusion. The reality of the entangled states of hydrogen atoms in condensed matter is still under intensive scrutiny, and its implications are yet to be explored.

Recently, critical NCS experiments were performed by *Dreismann et al.* [5.379, 5.380] on the mixture of H_2 and D_2 of various proportions and on HD, in the liquid state at 20 K. No isotope exchange takes place under these conditions. The observed scattering anomaly was essentially the same in all the cases, both for H and D. The result implies that the decoherence process is intra-molecular in origin, and moreover, the exchange-correlation does not play a major role. A general theoretical framework for the correlation effects in fast scattering processes in condensed matter was also proposed [5.381].

Appendix 5B. Enhanced Electron Screening in d-d Fusion Reactions in Metals

Traditionally, nuclear physics and solid state physics have been rather separate disciplines because they deal with phenomena occurring at widely different energies, i.e. in very different time scales. Recently, however, continuing efforts to investigate nuclear reactions at low energies, and in the environment of condensed matter, revealed novel features which had remained unexplored in the long history of nuclear physics. The enhancement of d-d fusion reaction in metals is one of such discoveries. The phenomenon is not only important in its own right, but also for bringing up a specific example where a short-time response of the conduction electron system is playing a crucial role.

Nuclear fusion reactions can take place only when two nuclei come close to the touching radius R_0 , where strong attractive nuclear forces operate.⁹ In low-energy collisions, the reaction cross section is very small; it is limited by the probability of penetration of Coulomb barrier between the two nuclei. In these cases, the presence of surrounding electrons around a target is expected to increase the cross section by partial cancellation of the repulsive potential [5.358], and indeed small enhancements were observed in a number of atomic and molecular targets [5.359, 5.360]. For a D(d,p)T reaction, with which we are primarily concerned, the enhancement of $\sim 10\%$ was observed for molecular D_2 targets [5.361].

Recently, much larger enhancements of the fusion rate have come to be noted when target D nuclei are embedded in metallic environments [5.362–5.372]. For Pd, the enhancement of ~ 10 times was observed by Kasagi's group [5.366, 5.367] and nearly 100 times in the experiments of Rolfs' group using slightly different samples and measuring conditions [5.370, 5.372]. The enhancement is so large that it defies all the attempts for explanation in the existing frames of thoughts. This is the topic to be described below.

Suppose a projectile nucleus (of charge Z_1e) hits a target nucleus (of charge Z_2e) with a center-of-mass energy E , lower than the Coulomb barrier $V_0 = Z_1Z_2e^2/r_0$. The reaction cross section determined by the probability of barrier penetration is usually written in the form

$$\sigma_{\text{bare}}(E) = \frac{S(E)}{E} \exp \{-2\pi\eta(E)\} , \quad (5B.1)$$

where $S(E)$, the astrophysical S-factor, contains all the information of the nucleus, and usually depends only weakly on energy, and $\eta(E)$ is the Sommerfeld parameter

$$\eta(E) = \frac{Z_1Z_2e^2}{\hbar c} \left(\frac{\mu c^2}{2E} \right)^{1/2} , \quad (5B.2)$$

with μ being the reduced mass.

This expression must be modified when electrons surrounding the nuclei screen the Coulomb potential. The simplest way to include the screening effect in this formalism is to introduce the effective screening potential U_e that reduces the repulsive Coulomb potential uniformly. The physical implication is as follows. In the WKB approximation, the barrier penetration rate is given by the integral between the touching radius R_0 and the classical turning point $R_c = Z_1Z_2e^2/E$ where the Coulomb potential is equal to the incident energy E ,

$$\eta(E) \propto \int_{R_0}^{R_c} \sqrt{V(r) - E} dr . \quad (5B.3)$$

⁹ The touching radius R_0 of two nuclei of mass number A_1 and A_2 is given by $R_0 \approx 1.2 \times (A_1^{1/3} + A_2^{1/3})$ fm (1 fm = 10^{-15} m), which becomes $R_0 \sim 3$ fm for a d–d collision.

For energies of a few keV, the classical turning point is of the order of a few hundredth of Å, which is much shorter than the range of distribution of most of the electrons. Thus the electron screening can be expressed, to a good approximation, by a uniform shift of the potential, at least over the narrow range of the integral. As the integrand depends only on the difference $V(r) - E$, the lowering of $V(r)$ is equivalent to the increase of E , and therefore the cross section for a screened target at energy E is nearly equal to the cross section for a bare collision at energy $E + U_e$,

$$\sigma_{\text{scr}}(E) = \sigma_{\text{bare}}(E + U_e) \quad (5B.4)$$

Experiments on the D(d,p)T reaction, using molecular D₂ targets were performed down to $E = 1.6$ keV, and the screening potential of $U_e = 25 \pm 5$ eV was deduced [5.361].

Experiments on D targets embedded in metals were initiated by Kasagi's group [5.362–5.368]. They introduced D atoms by ion-implantation at 10 keV, and measured the reaction yield (protons) at different projectile energies E_p down to 3 keV. The energy dependence of the scattering cross section was expressed as enhancement from the value at $E_p = 10$ keV, from which U_e was deduced by best-fitting¹⁰.

Results obtained for several different metals are shown in Fig. 5B.1 [5.367]. The values of U_e are generally larger than in the case of atomic/molecular targets, and depend strongly on host metals. From these limited values of data they inferred, in particular, that the screening energy increases with decrease of target D density. This general trend is shown in Fig. 5B.2 for five host metals Au, Ni, Cu, Fe and Pd, including more recent data [5.367, 5.371–5.373].

More extensive measurements were made subsequently by Rolfs' group [5.371, 5.372]. In order to get insight into the screening mechanism, they performed measurements on 50 metals, 3 semi-conductors and 4 insulators. It was only in metals where reaction enhancements were observed; in semi-conductors and insulators the enhancement was below the detection limit.

In Fig. 5B.3, the values of U_e are plotted as a function of Group on the Periodic Table, and in Fig. 5B.4 the corresponding data of D concentration [5.372]. The most conspicuous feature is a dip of U_e at Group III–IV transition metals. This, however, cannot be simply ascribed to the dependence of U_e on chemical species. Much higher D concentrations in these elements than in other cases (Fig. 5B.4) may also be relevant to this systematics. At these concentrations (below D/M < 2), samples are certainly metallic, and these high D concentrations would reduce the value of U_e judging from the general

¹⁰ The actual process occurring in a sample is such that incident D⁺ ions (designated as d) gradually become lower in energy with traveling distance, before they collide with target Ds. The center-of-mass energy E is 1/2 of the energy of incident d at the point of reaction. The total reaction yield in this situation is called the thick-target yield for the initial incident energy E_p .

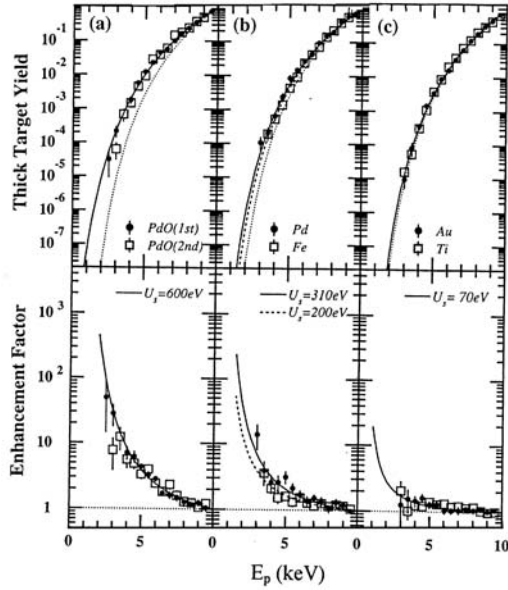


Fig. 5B.1. Relative reaction yield of protons emitted in the $D(d,p)T$ reaction in five different targets as a function of bombarding energy of deuterons E_p . *Upper section:* the observed thick-target yields normalized to the value at $E_p = 10$ keV, the calculated results from (5B.1) in *dotted curves*. *Lower section:* the enhancement of observed yield relative to the calculation from (5B.1) [5.367]

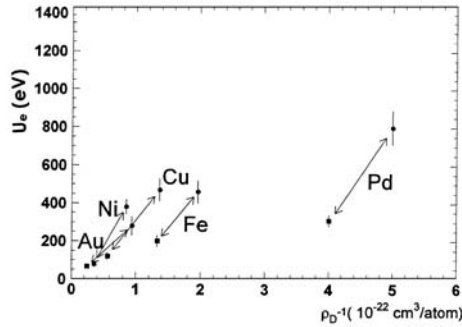


Fig. 5B.2. Screening potential plotted against the reciprocal of target D density in five host metals Au, Ni, Cu, Fe and Pd [5.367, 5.371–5.373]

trend depicted in Fig. 5B.2. Anyway, in the presence of concentration dependence of U_e , further examination of Fig. 5B.3 could be hardly meaningful. The only comment to be added is on another dip of U_e at Sn. This may be related to the fact that Sn undergoes a semiconductor-to-metal transition at

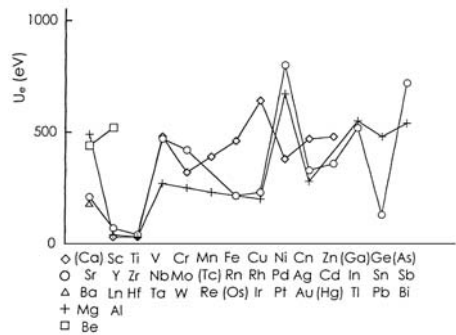


Fig. 5B.3. Screening potential plotted as a function of Group on the Periodic Table [5.372]

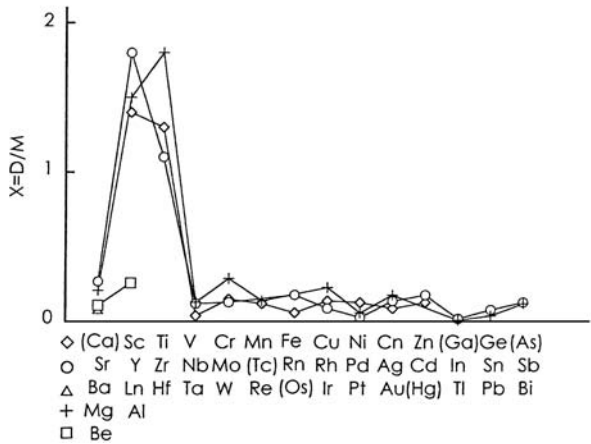


Fig. 5B.4. Target D concentrations in the experiment shown in Fig. 5B.3, in units of atomic ratio $x = D/M$ [5.372]

13.2°C. Thus at the measurement temperature of 20°C, Sn is on the verge of becoming a semi-conductor, and the screening effect can be smaller than in other metals for this reason.

There are a few points to be made regarding the experimental conditions. First, the state of implanted D atoms. Figure 5B.4 shows that, except for Group III–V transition metals and Pd, the implanted concentrations exceed the solubility limit at room temperature. Thus, in most cases, implanted D atoms remaining in the near-surface region are either in the form of Vac-D clusters or in the form of D₂ bubbles; see Sect. 5.6.3–5.6.4. As the enhancement in the latter case should be similar to molecular targets, the observed large enhancement can be expected to be the contribution of the former. In semi-conductors and insulators, the reported amount of D (0.2 ~ 0.6 in

atomic ratio) could only exist in the form of bubbles, which is consistent with the observed U_e being similar to those in atomic/molecular targets.

Second, the effect of surface states. The data shown in Figs. 5B.3 and 5B.4 are the results of their second runs [5.372] in which they cleaned the sample surface by in situ Kr sputtering at 15 keV, which removed at least 100 monolayers. This pre-treatment proved to be very effective in Al, for which their second measurement gave $U_e = 520$ eV, whereas their first measurement gave $U_e \leq 30$ eV probably due to the presence of oxide layer [5.371]. Overall, the effectiveness of Kr sputtering was not very convincing, however. In noble metals, for example, where no serious surface contamination could be expected, the results of their first measurements ($U_e = 43, 23, 61$ eV for Cu, Ag and Au, respectively) were changed to $U_e = 470, 330$ and 280 eV in the second measurements. In other cases, consistency of results of the two runs is generally better, but variable. The data shown in Fig. 5B.2 are the cases where results of the two runs agreed with each other, and are therefore probably free from surface effects, if any.

Theory of electronic screening in fusion reactions has reached a certain level for atomic/molecular targets, but remains in a rather primitive stage for metallic targets. Here we describe some theoretical treatments for atomic/molecular targets, trying to get some insight into the case of metallic targets.

In a simple atomic model of *Assenbaum et al.* [5.358], it is assumed that electrons can follow the motion of nuclei (Born-Oppenheimer approximation), and the energy gain of the electrons is transferred to the relative motion of the two nuclei, to effectively increase the value of E . As R_c is much shorter than atomic radii, during the barrier penetration the electronic state can be approximated by that of an atom with the combined nuclear charges at its center. Thus for d-D fusion reaction with atomic targets, the screening energy can be estimated by taking the difference of the binding energies of the combined He atom and original D atoms,

$$U_e \approx E_{\text{He}} - 2E_{\text{D}} . \quad (5\text{B.5})$$

There is a peculiarity in the d-D fusion reaction arising from symmetry requirements [5.374]. At large distances, the d+D wave function is an equal mixture of gerade (positive parity) and ungerade (negative parity) configurations. As parity is conserved during the collision, the combined atom configuration is an equal mixture of $\text{He}^+(1s)$ and $\text{He}^+(2p)$. For the combined atom $\text{He}^+(1s)$, the energy gain amounts to 40.7 eV, whereas for $\text{He}^+(2p)$ the gain is almost nil. In this situation, when the total reaction yield is approximately expressed by a single effective screening potential, its value becomes $U_e = 20.4$ eV.

For the molecular D_2 target, absence of the symmetry requirement allows the combined atom to assume the lowest-energy configuration, hence the screening potential can reach ~ 40 eV, if the presence of the other atom (spectator) does not alter the situation.

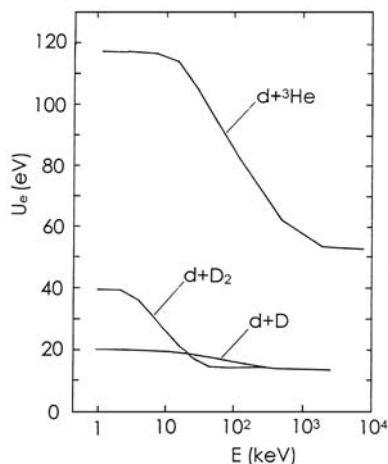


Fig. 5B.5. Scattering potential as a function of center-of-mass collision energy, calculated by the time-dependent Hartree-Fock method for d-D [5.375], d-D₂ [5.376] and d-³He [5.375] reactions

Note that the gain in the binding energy between the combined and separated atom case gives only the maximum energy which can be transferred from the electronic degrees of freedom to the relative motion of the two colliding nuclei (the adiabatic value). Attempts to go beyond this approximation were made by solving the time-dependent Schrödinger equation for electrons during the collision [5.375, 5.376]. Results of time-dependent Hartree-Fock (TDHF) calculations for d-D, d-D₂ and d-³He reactions are shown in Fig. 5B.5; the screening energy U_e as a function of center-of-mass energy E . For the atomic D target, the screening potential approaches the adiabatic value in the limit of low energy [5.375]. For the molecular D₂ target, U_e approaches the adiabatic value at low E , but decreases rather steeply between 3 ~ 30 keV [5.376]. There is, in fact, a large dependence on collision angle with respect to the molecular axis, amounting to ~10 eV; thus the average over orientations is shown in the Figure. The calculation showed, in addition, that the kinetic energy transferred to the spectator D atom is so small (~0.1 eV) that it does not move during the collision. This result disproved the assumption, frequently made, that the breaking of the molecular bond and the kinetic energy transferred to the spectator should decrease the screening energy significantly.

The result obtained for the two-electron system, the d-³He reaction, shows that U_e is much larger than the other two cases [5.375]. This is a combined effect of twice as many electrons participating in screening as well as twice as large charges on the He nucleus that attract the 1s electrons to closer distances.

Comparison between theory and experiments is made in Table 5B.1. Overall, the agreement is satisfactory. A small discrepancy in the $d + D_2$ reaction may be due in part to possible under-estimation of the experimental U_e [5.361]. Uncertainties in the bare cross section extrapolated from higher energies may lead to systematic errors of ± 10 eV.

Table 5B.1. Comparison of theoretical and experimental values of screening energy for d-D, d-D₂ and d-³He reactions

Reaction	Theory		Experiment
	Atomic Model ^a	TDHF ^b	
d + D	27	20 ^c	—
d + D ₂	—	30~40 ^d	25 ± 5 ^e
d + ³ He	110	117 ^c	120 ± 10 ^f

^aEstimated from binding energies of constituent atoms using Thomas-Fermi approximation [5.358],

^bTime-dependent Hartree-Fock calculation, for $E = 1 \sim 10$ keV, ^c[5.375], ^d[5.376], ^e[5.361], ^f[5.359]

Based on these findings on atomic and molecular targets, we shall make some speculations on the origin of large enhancements observed for metallic targets. As described in Sect. 7.1, the hydrogen-1s state is fairly well preserved for interstitial hydrogen in metals and accommodates two electrons. The resulting one extra negative charge is compensated at larger distances by the re-distribution of conduction electrons, and the depletion of anti-bonding s-d hybridized states in transition metals. Thus, the local electronic structure is more like a two-electron system, similar to d-³He. However, with the central charge of $Z_1 = 1$, the 1s wave function should be more extended than in He, and therefore the screening effect should be smaller. These considerations lead to a naïve expectation that the screening potential for D targets sitting in regular interstitial sites in metals should lie between 30 ~ 120 eV. Comparison with the observation (Fig. 5B.3) clearly shows that, except for Group III–IV transition metals, experimental values are generally larger than the upperbound set by the d-³He reaction. In the case of Pd, the observed U_e is nearly an order of magnitude larger than the upperbound.

In most of these cases the target D's are in fact trapped by radiation-induced vacancies to form, most probably, Vac-D₆ clusters (Sect. 5.6.3–5.6.4). No screening calculation for this cluster configuration has been done so far. It may be reminded in this connection that a theoretical approach regarding the M-H system as a dense plasma was made and yielded slightly larger screening for d-D reactions in Ti and Pd [5.377].

Here we wish to call attention to the time scale of the fusion reaction. For the incident energy of 1 keV, a projectile deuteron has a velocity of 3×10^5 m/s, and a time to travel a distance of 1 Å is 3×10^{-16} s. Notice that this collision time is comparable to the decoherence time of the quantum-entangled state alleged to exist in M–H alloys (Appendix 5A). If the quantum entanglement between D’s really exists, this must be considered properly in screening calculations.

It may be appropriate here, to avoid possible confusion of the readers, to briefly mention the (ir)relevance of the present observations with so-called “cold fusion”. From standard formulae, the reaction rate of two deuterons 1 Å apart can be roughly estimated at 10^{-75} s^{-1} [3.378]. Thus the probability of occurrence of a single fusion event in 1 mol of d–d pairs becomes 10^{-51} s^{-1} , and many orders of magnitude smaller for interstitial hydrogen pairs in metals (with separation > 2.1 Å; Chap. 2). Therefore, it is in no way possible, by the enhancement by 2 orders of magnitude by electron screening effects, to explain large fusion rates of $\gg 1 \text{ s}^{-1} \text{ mol}^{-1}$, alleged to be observed in most “cold fusion” experiments. Most probably, the electron screening effect and “cold fusion” are two different things.

In closing, let us briefly summarize the history of research of electron screening effects in nuclear fusion reactions. The original incentive was from astrophysics. There, fusion reactions between light nuclides have special implications because they constitute the major source of energy of Stars. Thus the determination of nuclear fusion cross sections at energies of the order of a few keV is particularly important for understanding the stellar dynamics and the consequent star neutrino flux, in addition to the operation of fusion reactors as well as for clarifying basic nuclear forces. Such determinations of the cross sections were made by extrapolation of data measured at the lowest possible laboratory energies. However, as it has come to be noted that at very low energies the experimental cross sections are larger than in bare nuclear collisions, the electron screening in atomic/molecular targets became an imminent issue. Then finally came the discovery of very strong screening taking place in metallic environments. This phenomenon not only poses a new question to nuclear fusion reactions but most probably fundamental questions regarding the state of hydrogen in metals as well – possible effects of quantum entanglement and dynamics of electrons in short times. These problems have just come to be recognized as such. For furthering research in these problems, a close collaboration of solid-state and nuclear physicists is more than ever needed.

6 Diffusion

Diffusion of hydrogen in metals has been a subject of great interest, both experimentally and theoretically. Diffusion coefficients exhibit many peculiar features, in their magnitude, their dependence on isotope mass and temperature, and these features strongly suggest that some quantum-mechanical processes are at work. Indeed, according to our present understanding, the motion of hydrogen atoms between adjacent sites is governed by quantum-mechanical tunneling (quantum diffusion) rather than thermally activated over-barrier jumps (classical diffusion), to different degrees at different temperatures.

In this chapter, we start by presenting the experimental results on diffusion coefficients and diffusion mechanisms in this order, subsequently describe theories of quantum diffusion, and finally, explain the observations in the light of these theories. The quantum-mechanical picture of interstitial hydrogen atoms presented in the preceding chapter serves as a necessary background for the present chapter.

6.1 Introduction

6.1.1 Diffusion Coefficients

Many different methods have been employed for measuring the diffusion of hydrogen isotopes in metals, giving information on either a) the chemical diffusion coefficient D^* , which describes the flow of solute atoms in the presence of concentration gradient, or b) the intrinsic (or tracer) diffusion coefficient D , which describes the random walk of individual solute atoms in the absence of concentration gradient. In other words, D^* measures the collective motion of particles as a whole, taking place under nonequilibrium conditions, whereas D measures the motion of each distinguishable particle, which occurs even under equilibrium distribution of solute atoms. Thus, it is important at the outset to make a clear distinction between these two diffusion coefficients.

Let us start by explaining the physical implication of the tracer diffusion coefficient. At finite temperatures, a solute atom will be in incessant motion by the action of fluctuating forces exerted by the surrounding atoms and, in consequence, move from one place to another in a manner which could be

described only in statistical terms. Thus we introduce the probability that a solute atom, originally at $\mathbf{R} = 0$, $t = 0$, is found in the vicinity of \mathbf{R} at time t , $G_s(\mathbf{R}, t)d\mathbf{R}$, normalized over the whole space

$$\int G_s(\mathbf{R}, t)d\mathbf{R} = 1. \quad (6.1)$$

As the motion is caused by random forces, each trajectory of many such events will be different but the probability distribution can, nevertheless, be defined as an ensemble average of such events. With the assumption that the particle loses its past memory in each step of its motion, we can write

$$G_s(\mathbf{R}, t) = \int G_s(\mathbf{R} - \mathbf{s}, t - \tau)G_s(\mathbf{s}, \tau)d\mathbf{s}. \quad (6.2)$$

Taking \mathbf{s} , τ as small increments of \mathbf{R} , t , and expanding (6.2), we obtain

$$\begin{aligned} \tau \frac{\partial G_s(\mathbf{R}, t)}{\partial t} &= \frac{1}{2} \int G_s(\mathbf{s}, \tau)(\mathbf{s} \cdot \text{grad})^2 G_s(\mathbf{R}, t)d\mathbf{s} \\ &= \frac{\overline{s^2}}{6} \nabla^2 G_s(\mathbf{R}, t), \end{aligned} \quad (6.3)$$

with the assumption that $G_s(\mathbf{R}, t)$ is an even function of \mathbf{R} . In isotropic media, (6.3) is reduced to the form of a diffusion equation, with

$$\overline{s^2} = \int s^2 G_s(\mathbf{R}, t)d\mathbf{s}, \quad (6.4)$$

$$D = \frac{\overline{s^2}}{6\tau}, \quad (6.5)$$

provided D can be regarded as constant. This last condition is well satisfied for τ 's longer than the period during which the memory of the previous motion lasts. The probability distribution is then obtained as a solution of the diffusion equation:

$$G_s(\mathbf{R}, t) = \frac{1}{(4\pi Dt)^{3/2}} e^{-R^2/4Dt}. \quad (6.6)$$

Under ordinary circumstances, the memory time can be taken to be the average time interval of elementary jumps between adjacent sites. In the specific case of H atoms in the fcc lattice, diffusing via successive jumps between adjacent O sites, the elementary jump distance is equal to $s = a/\sqrt{2}$, and (6.5) is written as

$$D = a^2/12\tau. \quad (6.5a)$$

The corresponding expression for H atoms in the bcc lattice, migrating by repetition of jumps between T sites, $s = a/2\sqrt{2}$, and hence

$$D = a^2/48\tau. \quad (6.5b)$$

These expressions provide a link between the macroscopic and microscopic descriptions of the diffusion coefficient.

When the random motion of a particle can be described classically, discussions based on the Langevin equation lead to the so-called Einstein relation

$$D = kTB, \quad (6.7)$$

where B , the mobility, is defined by

$$\mathbf{v} = B\mathbf{F}; \quad (6.8)$$

namely, it is the coefficient that gives the average velocity of the particle under the action of an average force \mathbf{F} .

Using the mobility B , the particle flow caused by the average force \mathbf{F} can be written as

$$\mathbf{J} = B\rho\mathbf{F}, \quad (6.9)$$

where ρ is the particle density per unit volume. In the case of an inhomogeneous distribution of solute atoms, a driving force arises as the gradient of the chemical potential, yielding the flow

$$\mathbf{J} = -B\rho \frac{\partial \mu}{\partial \rho} \text{grad } \rho \quad (6.10)$$

$$\equiv -D^* \text{grad } \rho. \quad (6.11)$$

D^* is called the chemical diffusion coefficient (or Fick's diffusion coefficient). In dilute regular solutions, the chemical potential can be written as

$$\mu = h + kT \ln \frac{\rho}{\rho_0 - \rho} \quad (6.12)$$

and, hence,

$$D^* \rightarrow kTB = D \quad (\rho \rightarrow 0), \quad (6.13)$$

implying that the chemical diffusion coefficient approaches the intrinsic diffusion coefficient in the low-concentration limit.

In actual systems, there always exist some correlations between atomic jumps, and the expressions given above must be corrected for this correlation effect.

In the tracer diffusion, a geometrical correlation exists between the consecutive jumps: An atom that has just jumped has a larger probability of making a reverse jump than a jump to other sites. This effect is described by introducing a tracer correlation factor f_t ($0 < f_t < 1$), in (6.5).

$$D = f_t \frac{\overline{s^2}}{6\tau}. \quad (6.14)$$

The factor f_t approaches unity in the low-concentration limit of interstitial solute atoms.

In the chemical diffusion, the correlation in the motion of indistinguishable particles is described in terms of a mobility correlation factor f_M such that

$$\mathbf{J} = f_M B \rho \mathbf{F} . \quad (6.15)$$

Thus, f_M describes the change in the total contribution to \mathbf{J} when subsequent rearrangement jumps of nearby atoms are included. The chemical diffusion coefficient now becomes

$$D^* = f_M B \rho \frac{\partial \mu}{\partial \rho} . \quad (6.16)$$

The ratio of D^* to D can be written in the form

$$\frac{D^*}{D} = \frac{1}{H_R} \frac{\rho}{kT} \frac{\partial \mu}{\partial \rho} , \quad (6.17)$$

where $H_R = f_t/f_M$ is called the Haven's ratio. The Haven's ratio is always smaller than unity because an atom that has just jumped due to the action of the potential gradient has its tendency for a jump counteracted by the enhanced probability that the atoms in front of it will move down the gradient and those behind will diffuse into the space that has been left. The second factor in (6.17), known as the thermodynamical factor f_{therm} , can be calculated if (6.12) is used for μ :

$$f_{\text{therm}} \equiv \frac{\rho}{kT} \frac{\partial \mu}{\partial \rho} = \frac{\rho_0}{\rho_0 - \rho} . \quad (6.18)$$

As H_R and f_{therm} both approach unity in the low-concentration limit of interstitial solute atoms, so does the ratio D^*/D .

At finite solute concentrations, a jumping atom may frequently find a target site blocked by the presence of other solute atoms. This effect is expressed by the site availability factor p_v , which is the probability of the target site being available. Then, the mean residence time on a site, τ , is related to the mean time between the attempted jumps, τ_0 , by

$$\tau = \tau_0 / p_v \quad (6.19)$$

In a simple model of single-site blocking, p_v for a composition $x = [\text{H}]/[\text{M}]$ can be written as

$$p_v = \begin{cases} 1 - x & \text{for O site in fcc,} \\ 1 - x/2 & \text{for T site in fcc,} \\ 1 - x/6 & \text{for T site in bcc.} \end{cases} \quad (6.20)$$

When the blocking effect extends to surrounding shells, the deviation of p_v from unity becomes larger, and may be calculated by the Monte Carlo method.

For more general implications of the diffusion coefficients and correlation effects in diffusion, including those at finite solute concentrations, see, for example, [6.1–6.9].

6.1.2 Diffusion of Interstitial Hydrogen in Metals

Interstitial hydrogen atoms in metals diffuse much faster than any other atoms in solids. Figure 6.1 compares the diffusion of H in V with diffusion of C in V and self-diffusion of V. The tracer diffusion coefficient D of H atoms is many orders of magnitude greater than the other cases, and rather close to the values typical of atomic diffusion in liquids: $D = 2.6 \times 10^{-5} \text{ cm}^2 \text{ s}^{-1}$ for molecular diffusion in water at room temperature. The difference is more pronounced at low temperatures, because the activation energy is low ($E_a \approx 45 \text{ meV}$ for H in V). The large D and small E_a are believed to arise from the small mass of hydrogen. The dependence of D on isotope mass is, in fact, distinctly different from that expected from classical, thermal activation processes, and is believed to provide a clue for understanding the quantum-mechanical character of the diffusion process. It is convenient, in this respect, that many different hydrogen isotopes are available over a wide range of mass; they include μ^+ , π^+ , H, D and T, which have $\sim 1/9$, $\sim 1/7$, 1, 2, and 3 times the proton mass (M_p), respectively. The positron, being much lighter ($\sim M_p/1800$), behaves quite differently in most cases, and requires different considerations.

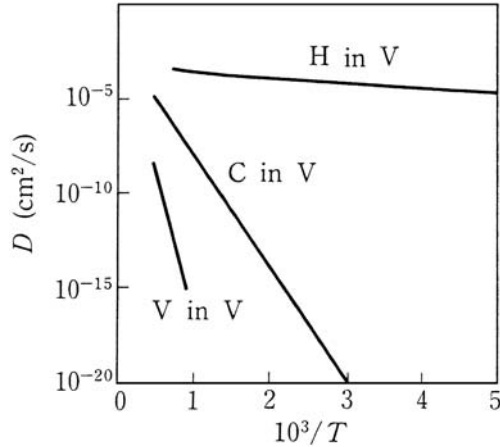


Fig. 6.1. Diffusion coefficients of H and C in V, and self-diffusion of V

A necessity for the quantum-mechanical description of the state of existence of interstitial hydrogen in metals was clearly recognized at very early stages, especially with regard to the discrete energy levels observed by inelastic neutron scattering.

Regarding diffusion, however, a physical understanding of the migration process that underlies the observed behaviors has evolved rather slowly. A theory of diffusion of light interstitials self-trapped in metals was first

formulated by *Flynn* and *Stoneham* [6.11] as an adaptation of the theory of small-polaron hopping in insulators [5.231–5.233], and has since been extended by several investigators. Among them, the most important contributions to the quantum theory of diffusion were those of *Kagan* and *Maksimov* [6.12] and *Kagan* and *Klinger* [5.304]. A line of theoretical developments before 1983 was reviewed by *Seeger* and *Teichler* [6.13], *Kehr* [5.242], and *Richter* [6.14]. In spite of these conceptual developments, the applicability of these theories for an analysis of the experimental results had been severely limited by the lack of realistic estimates of the tunneling matrix element J between neighboring interstitial configurations, before quantum-mechanical calculations such as those described in Chap. 5 were developed. Thus, *Sugimoto* and *Fukai* [5.303] were the first who made realistic calculations of J in the bcc metals, V, Nb and Ta, and suggested the occurrence of phonon-assisted tunneling in these metals at temperatures above ~ 100 K. At low temperatures, diffusion data on positive muons in Cu were found to exhibit a strong anomaly [6.15, 6.16]: the hopping rate goes through a broad minimum, and tends to increase with decreasing temperature. A similar behavior was also inferred for Al [6.17]. A theoretical interpretation of this anomaly in terms of the interaction with conduction electrons was proposed by *Kondo* [5.307–5.310], *Yamada et al.* [5.313], and *Yamada* [5.114]. In fact, the occurrence of a diffusion minimum as a consequence of interaction with phonons had already been predicted by *Kagan* and *Maksimov* [6.12] and *Kagan* and *Klinger* [5.304]; the interaction with conduction electrons only tends to suppress the otherwise very rapid diffusion at temperatures below the minimum. A similar temperature dependence of the diffusion coefficient for hydrogen isotopes H, D, T in Ta was suggested by *Fukai* [6.18], and later for the localized hopping of H trapped in 2T sites around O in Nb by *Wipf et al.* [5.275].

The quantum diffusion of hydrogen isotopes in solids has been investigated intensively in the last two decades, mainly with reference to muons, and its physics is now fairly well established. For more details, the reader is referred to the review articles [5.323, 6.19, 6.20]. The progress reports [6.21, 6.22] may also be worth reading.

Before presenting the experimental results, it may be expedient here to give a brief description of the conceptual framework for the diffusion of light interstitials in metals.

It is expected that a migration of H atoms proceeds via several different mechanisms, one of them predominating over the others in a given range of temperature. A classification of the possible mechanisms as a function of temperature is shown in Fig. 6.2.

In the low-temperature region (region I), where no phonons are available, H atoms in the self-trapped state migrate by coherent tunneling without changing the phonon state (zero-phonon process). As the coherent state is gradually damped with increasing temperature by interactions

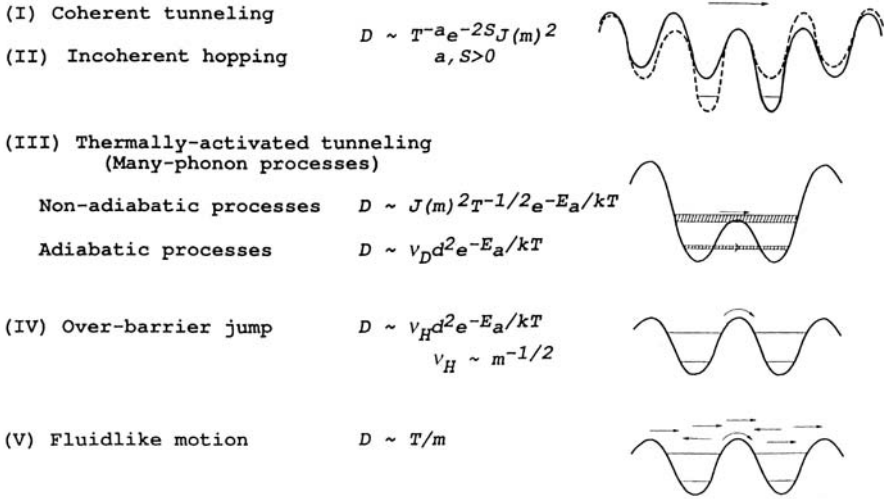


Fig. 6.2. Diffusion mechanisms of hydrogen in metals. The dominant mechanism is expected to change in the order (I) to (V) with increasing temperature, d is the jump distance, $J(m)$ the tunneling-matrix element, dependent on the isotope mass, ν_D the Debye frequency and ν_H the vibration frequency of an H atom

with conduction electrons and virtual excitation and re-emission of phonons (diphoton process), the migration process changes into incoherent hopping.

As the temperature is raised further, processes involving one phonon, a few phonons, and subsequently many more phonons may take place. The diffusion coefficient as a function of temperature decreases first as phonons tend to destroy the coherent tunneling motion (region II), but increases subsequently as more phonons become available (region III). When many phonons are available, there is a finite probability that the lattice vibration brings the energy levels of the neighboring interstitial sites into coincidence to allow the transition of an H atom to occur between these levels.

If the tunneling-matrix element J is small, the transitions occur nonadiabatically during the time of the coincidence event with a probability proportional to J^2 . If, on the other hand, J is large enough to assure successful jumps during the coincidence event, transitions are called adiabatic. This kind of process occurs more easily through excited vibrational states for which J will be larger due to more extended wave functions and, therefore, at relatively higher temperatures. The process is characterized by the fact that the frequency of attempts is nearly equal to the Debye frequency, independent of the isotope mass.

At still higher temperatures (region IV), H atoms may be regarded as classical particles, which execute the over-barrier jumps via thermal excitation.

In the highest-temperature region (region V), H atoms no longer remain within the potential wells of interstitial sites but undergo free motion like the motion of atoms in gases.

The overall temperature dependence of the diffusion coefficient is expected to look like the curve in Fig. 6.3. The figure is only schematic: it does not mean that all these five temperature regions are to be observed in a given system, nor does it mean that changes in slope should always be observed in region II. Thus, our primary concern is to ascertain the diffusion mechanism of each isotope of hydrogen in a given metal as a function of temperature.

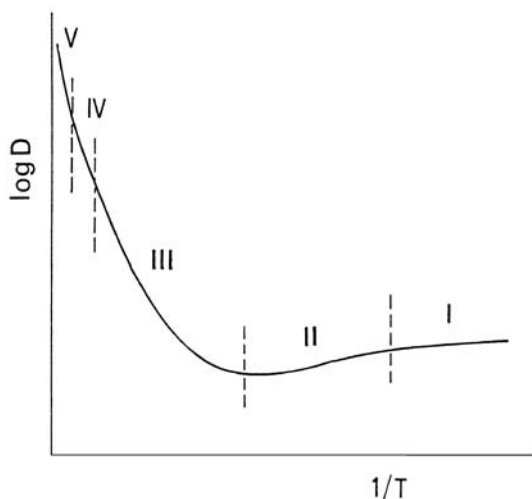


Fig. 6.3. Expected temperature dependence of the diffusion coefficient of hydrogen in metals (schematic). Temperature regions (I)–(V) are classified according to the dominant diffusion mechanism (see Fig. 6.2). Note, however, that not all these regions may be realized in real systems

The rest of this chapter is organized as follows. Sect. 6.2 deals with the experimental methods. The characteristic features of many different methods, some providing the macroscopic diffusion coefficients and others the microscopic information on the diffusion mechanisms, are described. The experimental results on the diffusion coefficient are given in Sect. 6.3, and those on diffusion mechanisms in Sect. 6.4. As our primary interest lies in elucidating the intrinsic mechanism of diffusion, some typical data are presented to illustrate the nature of elementary jumps, the effects of interactions between H atoms and jumps over inequivalent sites. For a large body of diffusion data accumulated on hydrogen in pure metals, the readers are referred to the compilations of *Fromm and Gebhardt* [2.20], *Völkl and Alefeld* [6.23, 6.24] and *Wipf* [6.25]. A gist of the theory of quantum diffusion is described in

Sect. 6.5, and interpretations of the experimental results in the light of the theory are provided in Sect. 6.6.

6.2 Experimental Methods

Experimental methods used to investigate the diffusion of hydrogen in metals are listed in Table 6.1, together with the kind of information to be derived by each method.

Table 6.1. Experimental methods for measuring the diffusion of hydrogen in metals

Method	Property Measured
1. Permeation	(Diffusivity Solubility
Absorption – Desorption	
2. Electrochemical method	Diffusivity Solubility
3. Resistivity relaxation	Diffusivity
4. Quench-recovery method	Diffusivity
5. Mechanical relaxation	
a) Gorsky effect	Diffusivity
b) Snoek effect	Jump frequency
c) Zener relaxation	Jump frequency
6. Magnetic disaccommodation	Jump frequency
7. NMR and related methods	
a) NMR	
Relaxation time	Jump frequency
Pulsed field gradient	Diffusivity
b) μ SR Jump frequency	
c) Mössbauer effect	Jump frequency
d) Perturbed angular correlation	Jump frequency
8. Quasi-elastic neutron scattering (QNS)	
$Q \sim 1/a$	Jump frequency Path
$Q \ll 1/a$	Diffusivity

Methods 1 through 5a deal with nonequilibrium distributions of hydrogen, whereas methods 5b, 7 and 8 are equilibrium measurements. (Methods 5c and 6 may be included in the latter group, although their implication is sometimes less transparent.)

Here we describe the principles of NMR and QNS in more detail, and add some supplementary remarks on other methods. A brief description of these other methods is given in [6.23].

6.2.1 Nuclear Magnetic Resonance and Related Methods

All hydrogen isotopes possess magnetic moments and are, therefore, accessible by a nuclear magnetic resonance (NMR) technique (or μ SR in the case of μ^+). In the applications to diffusion studies, two different types of experiments have been utilized: a) the measurement of the relaxation times that reflect the spectral density of the fluctuating internal fields caused by the motion of spins, and b) the pulsed-field-gradient method that measures the intrinsic diffusion coefficient D directly.

There have been a large number of papers on NMR studies of diffusion in metal hydrides. We shall limit ourselves here to those that proved particularly illuminating for investigating the mechanism of diffusion, and present a brief description of the underlying physics of the method. A number of review articles have been written on this subject, including those of *Cotts* [6.26–6.28], *Seymour* [6.29] and *Barnes* [6.30].

(a) Relaxation-Time Measurements

Three different relaxation times T_1 , $T_{1\rho}$, and T_2 are defined, and measured by pulsed-NMR techniques. The spin-lattice relaxation time T_1 and its equivalent in the rotating frame $T_{1\rho}$ characterize the energy transfer process between the spin system and the lattice, whereas the spin-spin relaxation time T_2 characterizes the energy transfer within the spin system. In μ SR, one observes the decay of the spin polarization of muons after implantation in the specimen. In NMR, both longitudinal and transverse relaxation can be measured, corresponding to T_1 ($T_{1\rho}$) and T_2 , respectively.

For H, T, and μ^+ , with their spin $I = 1/2$, the relaxation caused by the fluctuating fields results solely from the dipole-dipole interactions. For the deuteron, its spin being $I = 1$, the electric quadrupole interaction also causes the relaxation, making the situation more complicated. We shall here deal mainly with the proton, the most thoroughly investigated of all these isotopes, and refer to other isotopes when appropriate.

The expressions for the relaxation times due to the magnetic dipole-dipole interactions of a single nuclear species are given as follows:

$$1/T_1 = \frac{3}{2}\gamma_n^2\mu_n^2[J^{(1)}(\omega_0) + J^{(2)}(2\omega_0)] , \quad (6.21)$$

$$1/T_{1\rho} = \frac{3}{8}\gamma_n^2\mu_n^2[J^{(0)}(2\omega_1) + 10J^{(1)}(\omega_0) + J^{(2)}(2\omega_0)] , \quad (6.22)$$

$$1/T_2 = \frac{3}{8}\gamma_n^2\mu_n^2[J^{(0)}(0) + 10J^{(1)}(\omega_0) + J^{(2)}(2\omega_0)] , \quad (6.23)$$

where γ_n is the gyromagnetic ratio, $\mu_n = \gamma_n\hbar[I(I+1)]^{1/2}$ is the magnitude of the nuclear moment (with spin I) of the diffusing spins, $\omega_0 (= \gamma_n H_0)$ is the Larmor frequency in the static magnetic field H_0 , and $\omega_1 (= \gamma_n H_1)$ is the Larmor frequency in the r.f. magnetic field H_1 . (More precisely, H_1 should be replaced by $(H_1^2 + H_d^2)^{1/2}$, where H_d is the nonsecular part of the local dipolar field in the rotating frame.)

The spectral density function $J^{(p)}(\omega)$ is defined by

$$J^{(p)}(\omega) = \int_{-\infty}^{+\infty} G^{(p)}(t) \exp(-i\omega t) dt, \quad (6.24)$$

where $G^{(p)}(t)$ is the autocorrelation function of dipole-dipole interactions

$$G^{(p)}(t) = \sum_i \langle F_{ij}^{(p)}(t_0) F_{ij}^{(p)*}(t_0 + t) \rangle, \quad (6.25)$$

$$F_{ij}^{(p)}(t) = d_p Y_{2p}(\Omega_{ij}) / r_{ij}^3, \quad (6.26)$$

$$d_0^2 = 16\pi/5, \quad d_1^2 = 8\pi/5, \quad d_2^2 = 32\pi/5,$$

The bracket $\langle \dots \rangle$ signifies the ensemble average over all spin pairs (i, j) . The separation of the spin pair r_{ij} – both its magnitude r_{ij} and its direction Ω_{ij} relative to the applied magnetic field H_0 – varies in time with migration of spins in the crystal lattice. Y_{2p} are the normalized spherical harmonics of order $2p$.

Information on diffusion is contained in the spectral density functions $J^{(p)}(\omega)$. In ordinary NMR experiments, a magnetic field of the order of $H_1 \sim 10$ Oe and $H_0 \sim 10^3$ – 10^4 Oe is employed, so that the corresponding frequencies ω_1 and ω_0 lie in the range 10^4 – 10^8 Hz. In this range of frequencies, fluctuations caused by and/or experienced by the diffusing atoms have usually much larger spectral densities than the lattice vibrations. Thus, our problem is to extract information of the diffusion processes by investigating how $J^{(p)}(\omega)$ are determined by the atomic motion.

The first theory of the nuclear relaxation by *Bloembergen et al.* [6.31] assumed a correlation function of the form

$$G^{(p)}(t) = G^{(p)}(0) \exp(-|t|/\tau_c), \quad (6.27)$$

and, hence,

$$j^{(p)}(\omega) = G^{(p)}(0) 2\tau_c / (1 + \omega^2 \tau_c^2). \quad (6.28)$$

This expression, frequently referred to as the BPP formula, proved to give an excellent description of the dipolar relaxation in liquids, and has been used rather extensively for the relaxation in solids as well.

The correlation time τ_c of the dipole interaction is related to the mean jump time τ of the diffusing species (protons) by $\tau_c = \tau/2$ when the relaxation is solely due to interactions between protons, whereas $\tau_c = \tau$ holds for the interaction between protons and the M nuclei.

A typical example of the temperature dependence of T_1 caused by atomic diffusion is shown in Fig. 6.4 for H in $\text{TiH}_{1.70}$ [6.32]. The relaxation time goes through a minimum at a temperature where the correlation frequency $(1/\tau_c)$ comes close to the Larmor frequency: $\tau_c^{-1} \sim \omega_0$. For a quantitative

analysis, the observed relaxation rate was divided into two components, $(1/T_1)_{\text{obs}} = 1/T_{1e} + 1/T_{1d}$, where $1/T_{1e}$ is the relaxation caused by the Fermi contact interaction with conduction electrons, and $1/T_{1d}$ is the dipolar relaxation described above. The authors separated these two contributions on the basis of the temperature dependence of these terms: $T_{1e}T = \text{const}$ and $\tau_c = \tau_c^0 \exp(E_a/kT)$ in the BPP formula. The agreement of the calculated curve of T_1 with the experimental data, shown in Fig. 6.4, may appear to indicate that this way of analysis is satisfactory.

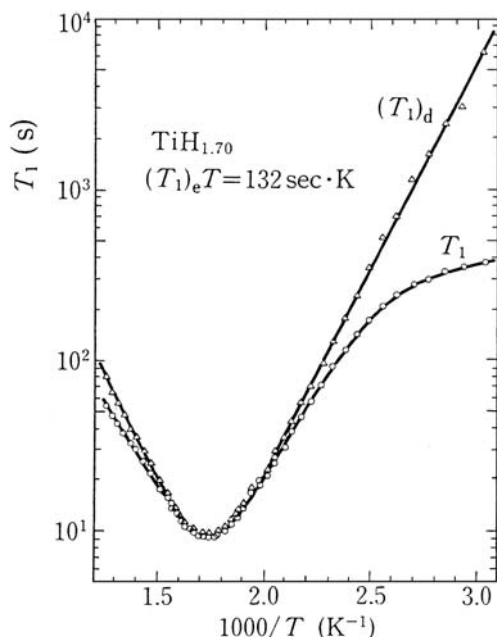


Fig. 6.4. Temperature dependence of the spin-lattice relaxation time T_1 of proton NMR in $\text{TiH}_{1.70}$. The dipolar relaxation rate $1/T_{1d}$ is deduced by subtracting the relaxation rate due to conduction electrons $1/T_{1e}$, $1/T_{1d} = 1/T_1 - 1/T_{1e}$, by using the experimental relation $T_{1e}T = 132 \text{ sK}$ [6.32]

As more NMR experiments were performed on M-H systems, it came to be recognized, however, in many cases the temperature dependence of the relaxation times cannot be reproduced by the analysis based on the BPP formula.

This recognition stimulated more realistic calculations of the spectral density functions based on the lattice-specific models of atomic jumps. These include calculations on the simple cubic (sc) lattice that are applicable to interstitial diffusion on T sites in the fcc lattice, and on the fcc lattice that are applicable to interstitial diffusion on O sites in the fcc lattice, calculations

on the bcc lattice, and on the interstitial diffusion on T and O sites in the bcc lattice. An analytical method of calculation was developed by *Fedders* and *Sankey* [6.33] and was later extended by *Barton* and *Sholl* [6.34] to allow calculations over wide temperature ranges, including the effects of spatial correlations of atomic jumps.

Comparison of the spectral density functions obtained from calculations and experiments on $\text{PdH}_{0.76}$ is made in Fig. 6.5. The “experimental” data points were obtained by *Halstead et al.* [6.35] by their iterative method of deducing a single curve of $j(\omega)$ [a reduced correlation function that approximates the functional form of all $j^{(p)}(\omega)$] from the temperature and frequency dependence of the relaxation times T_1 , $T_{1\rho}$, and T_2 . The agreement of these points with the calculated curve of *Barton* and *Sholl* [6.34] (lower graph) is almost perfect. A similar agreement was found for the sc lattice (^{19}F diffusion in PbF_2). Comparison with the BPP formula, also shown in Fig. 6.5, indicates that the asymptotic behavior at high frequencies $j(\omega) \propto \omega^{-2}$, is the same in both models. The force-fitting to the BPP formula yields the apparent τ about 1.6 times longer than the true τ in the lattice diffusion model.

The physical implications of the asymptotic behaviors of $j^{(p)}(\omega)$ at high- and low-frequency limits have been examined by *Sholl* [6.36]. He showed, in particular, that the high-frequency form is $j^{(p)}(\omega) = B_p \omega^{-2}$ for all atomic jumps, with the coefficient B_p depending on specific jump models and lattice

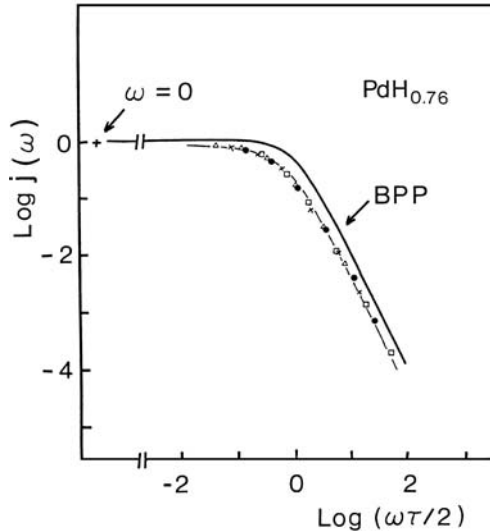


Fig. 6.5. Spectral density function of dipolar interaction for H in $\text{PdH}_{0.76}$. Data points were obtained from the measured relaxation times T_1 , $T_{1\rho}$, and T_2 by *Halstead et al.* [6.35]. The broken line is the result of a lattice-specific calculation of *Barton* and *Sholl* [6.34]. Deviation from the BPP form (the solid line) is obvious

structures. A more important conclusion reached by Sholl is that at low frequencies, where many successive jumps of spins can be approximately described by a diffusion equation, $j^{(p)}(\omega)$ takes the form

$$j^{(p)}(\omega) = j^{(p)}(0) - A_p \omega^{1/2}, \quad (6.29)$$

and $j^{(p)}(0)$ and A_p depend upon the diffusion coefficient as D^{-1} and $D^{-3/2}$, respectively. Numerical calculations show that the expression

$$j^{(p)}(\omega) = (nd_p^2/D)[0.266 - 0.056(\omega s^2/D)^{1/2} + \dots] \quad (6.30)$$

holds approximately for both sc and fcc lattices at all spin concentrations (n is the number of spins per unit volume, s the jump distance). The theory opened a new possibility of determining the diffusion coefficient from the frequency dependence of T_1 in the low-frequency regime.

The experimental verification of the theory is shown in Fig. 6.6 for H in $\text{TiH}_{1.63}$ [6.37]. Clearly, the relaxation rate $1/T_1$ at a fixed temperature (725 K) shows the expected frequency dependence,

$$T_1^{-1}(\omega) = T_1^{-1}(0) - A' \omega^{1/2}. \quad (6.31)$$

The diffusion coefficient was obtained from the value of A' by assuming nearest-neighbor jumps, and the value obtained was found to agree well with a known value of D . In this method one can circumvent the difficulty of extracting T_{1d}^{-1} from T_1^{-1} , a major source of error in the ordinary method of analysis.

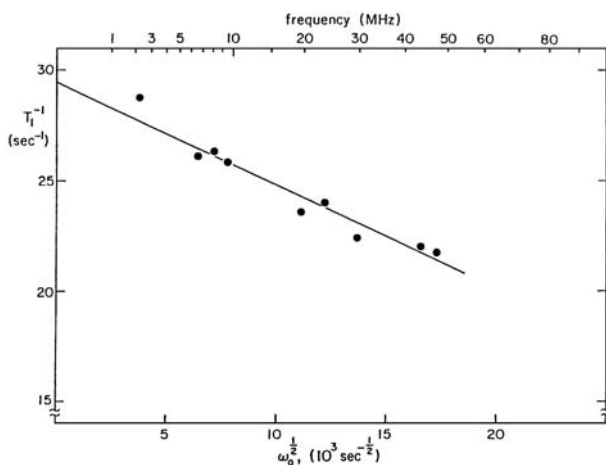


Fig. 6.6. Frequency dependence of the spin-lattice relaxation rate for proton NMR in $\text{TiH}_{1.63}$. The experimental data of *Salibi and Cotts* [6.37] show the relation $T_1^{-1}(\omega) = T_1^{-1}(0) - A' \omega^{1/2}$ predicted by *Sholl* [6.36]

(b) Pulsed-Field-Gradient Method

In this method, a pair of field-gradient pulses is applied along the direction (Z) of the static magnetic field H_0 , in an appropriate radio-frequency pulse sequence, and the rate of decrease of the spin-echo signal is measured as a function of the strength and duration of the field-gradient pulses. What one measures here is the diffusion distance of spins along the Z direction during the time between the two field-gradient pulses. Since the reduction of the spin-echo signal occurs in proportion to $\exp[-D\gamma^2(\partial H_0/\partial Z)^2 t^3/12]$, in which the measuring time t is limited by T_2 , and $\partial H_0/\partial Z \leq 250 \text{ Oe cm}^{-1}$, the capability of this technique is limited to $D \geq 4 \times 10^{-9} \text{ cm}^2 \text{ s}^{-1}$. In effect, one can measure the migration of nuclei labeled by the spin polarization over distances of $\leq 0.1 \mu\text{m}$.

(c) Muon Spin Rotation

Positive muons are created by the decay of positive pions

$$\pi^+ \rightarrow \mu^+ + \nu_\mu . \quad (6.32)$$

After a mean lifetime of $2.2 \mu\text{s}$, the muon decays into a positron and two neutrinos:

$$\mu^+ \rightarrow e^+ + \nu_\mu^- + \nu_e . \quad (6.33)$$

In muon spin rotation (μSR) experiments, spin-polarized muons are implanted into a metal specimen, and their precession frequency and/or polarization decay are measured, from which information on the local field and characteristic decay times equivalent to T_1 and T_2 in NMR can be learned. The time window of this method is limited by the muon lifetime to be 0.1 – $10 \mu\text{s}$. The muon serves as a particularly useful probe for investigating the dynamics of light particles at low temperatures, where other hydrogen isotopes become inaccessible due to limited solubilities. The implanted muon exists in a sample one at a time, which creates minimal disturbance and allows the experiment to be done in almost perfect crystals. For these reasons, the μSR has been the most effective tool for investigating the quantum diffusion.

It may be legitimate to emphasize here that all we can learn from muon spin relaxation is the average correlation time of fluctuating local field, defined by (6.24)–(6.27) as seen by diffusing muons. The information is by necessity confined in the time domain; even though the term quantum “diffusion” is commonly adopted, experimental information in the space domain is lacking. Strictly speaking, we do not know how muons are “diffusing” in space.

For details of μSR and its application to diffusion studies, see, e.g., [6.15, 6.20, 6.38–6.43]. Many conference proceedings and books have been published in this area [6.44–6.55].

(d) Perturbed Angular Correlation

In perturbed angular correlation (PAC) experiments, one measures the angular correlation of photons emitted in the γ - γ cascade decays of some probing nuclei, which carries the information on the interaction experienced by the probing nuclei in their intermediate excited state. In the experiments of *Weidinger* and his coworkers [6.56–6.58], Ta specimens were alloyed with ^{181}Hf , which acted as probes. ^{181}Hf decays first to an excited state of ^{181}Ta , which senses the presence of hydrogen atoms in its vicinity through the quadrupole interaction, and delivers this information in its subsequent γ - γ cascade decay after a mean lifetime of $25.7\text{ }\mu\text{s}$. The main idea of the experiment is to trap hydrogen at the impurity ^{181}Hf and to release it after the nuclear decay to the matrix atom ^{181}Ta . The release process during the lifetime of the excited state of ^{181}Ta is reflected on the temporal variation of the quadrupole interaction. Results obtained by this technique will be described later.

Other probe nuclei to be used for this purpose are limited to ^{111}Cd , ^{100}Rh and ^{99}Ru , produced from ^{111}In , ^{100}Pd and ^{99}Rh , respectively. A review of this method applied to hydrogen in metals was written by *Weidinger* [6.59].

(e) Mössbauer Effect

There are two different ways in which hydrogen diffusion in metals affects Mössbauer spectra: either through the fluctuating environment (isomer shifts and/or quadrupole interactions) or the fluctuating displacements of Mössbauer nuclei.

The hydrogen atoms moving in the vicinity of Mössbauer nuclei cause fluctuating displacements superposed on the lattice vibrations. The fluctuating displacements result in a partial destruction of the phase coherence of the γ -rays and consequently in the broadening (and concomitant weakening) of the Mössbauer line. Briefly, the frequency (energy) dependence of the Mössbauer absorption can be written as [6.60, 6.61]

$$I(\omega) \propto \int_{-\infty}^{+\infty} e^{-i(\omega - \omega_0)t - \Gamma_0 t/\hbar} dt \int G_s(\mathbf{R}, t) e^{i\mathbf{k}_i \cdot \mathbf{R}} d\mathbf{R}, \quad (6.34)$$

where $G_s(\mathbf{R}, t)$ is the probability that at time t the Mössbauer nucleus has moved a distance \mathbf{R} from its position at time zero, the instant when the leading edge of the γ -ray wave packet reaches the nucleus. The integral over \mathbf{R} gives the phase shift accumulated over the time $0 - t$:

$$\int G_s(\mathbf{R}, t) e^{i\mathbf{k}_i \cdot \mathbf{R}} d\mathbf{R} = \langle e^{i\phi(t)} \rangle, \quad (6.35)$$

which, when substituted into (6.34), gives the broadening of the absorption line (called the quasi-elastic broadening.)

The probability of elastic absorption of γ -rays having a natural width determined by the lifetime τ_N of the Mössbauer level $\Gamma_0 = 1/\tau_N$ is expressed in terms of a Mössbauer–Lamb factor

$$f^{\text{ML}} = f_{\text{vib}}^{\text{ML}} f_{\text{str}}^{\text{ML}}. \quad (6.36)$$

Both effects, that of the lattice vibrations $f_{\text{vib}}^{\text{ML}}$ and that of the hydrogen-induced strains $f_{\text{str}}^{\text{ML}}$, are temperature-dependent. $f_{\text{vib}}^{\text{ML}}$ shows a smooth temperature dependence which can be described by a Debye model. On the other hand, $f_{\text{str}}^{\text{ML}}$ is determined by the relative magnitude of the mean residence time of hydrogen with respect to τ_N . At low temperatures, where the mean jump time τ is longer than τ_N , $f_{\text{str}}^{\text{ML}} = 1$. As τ becomes shorter and comparable to τ_N , a certain fraction $(1 - f_{\text{str},0}^{\text{ML}})$ of the line undergoes quasi-elastic broadening, which becomes more pronounced as τ becomes shorter and shorter, and eventually leaves only the elastic part $f_{\text{str},0}^{\text{ML}}$ to be observed at $\tau \ll \tau_N$.

The reason why a part of the elastic line remains in the limit of fast diffusion is that the coherence of the γ -ray is never completely destroyed, because the motion of a Mössbauer nucleus is confined in a fairly narrow region in space (a “cage”). Thus, the magnitude of the coherent fraction $f_{\text{str},0}^{\text{ML}}$ contains information on the amplitude of the motion of a Mössbauer nucleus within the cage, while the width of the quasi-elastic component yields information on the correlation time of the cage diffusion of the Mössbauer nucleus and, hence, on the diffusion of the nearby hydrogen atoms. Analytical expressions for the quasi-elastically broadened lines have been derived for a number of model geometries of a Mössbauer probe in fcc and bcc lattices [6.61, 6.62].

An investigation of the quasi-elastic broadening due to hydrogen diffusion can be performed most conveniently by using a Mössbauer probe ^{57}Fe , which has a resonance energy of $\hbar\omega_0 = 14.4 \text{ keV}$ and a lifetime of $\tau_N = 140 \text{ ns}$, and has actually been done on TiH_x [6.61], PdH_x [6.63, 6.64], VH(D)_x [6.64, 6.65], NbH(D)_x [6.62, 6.64, 6.66–6.68] and TaH(D)_x [6.69]. In the experiments on $\text{NbH}_{0.78}$ [6.62], the jump rates of H atoms extracted from the cage motion of ^{57}Fe were found to agree reasonably well with those obtained from NMR experiments. The activation energies of the cage motion obtained from these experiments also appear to be largely consistent with the results of other experiments.

However, there is a difficulty inherent in this type of experiment using probes. What one measures is the effect of hydrogen diffusion in the close neighborhood (essentially the nearest-neighbor sites) of the probe nucleus, which is in most cases affected by the presence of the probe itself. Therefore, this type of experiment, albeit its uniqueness, should be treated with caution as a source of information on the intrinsic diffusion of hydrogen atoms. The exception is the case where the probe and matrix nuclei are of the same element (as ^{181}Ta in Ta matrix in the PAC experiment quoted above.)

The fluctuating environment of Mössbauer nuclei affects the spectrum in a different way. When the fluctuation is sufficiently rapid (the fast-diffusion

limit), a Mössbauer absorption line becomes a Lorentzian, shifted in frequency by a time-averaged value and broadened in proportion to the fluctuation rate.

This effect was observed for the 6.2 keV resonance of ^{181}Ta in $\alpha\text{-TaH}_x$ ($x \leq 0.17$) [6.70] and $\alpha\text{-TaD}_{0.02}$ [6.71]. In these cases, where the perturbation comes mainly through the isomer shift, the average shift and width of the absorption line can be written in terms of the isomer shift caused by one hydrogen atom in a nearest-neighbor site $\delta\omega$ and a correlation time of the fluctuation τ_c as

$$\bar{\omega} - \omega_0 = 4x\delta\omega, \quad (6.37)$$

$$\Gamma/\hbar = 4x(\delta\omega)^2\tau_c, \quad (6.38)$$

where $4x$ is the probability that a hydrogen atom occupies one of the 24 nearest-neighbor interstitial sites of a Ta atom (valid for $x \ll 1$), and τ_c is related to the mean residence time as $\tau_c = 12.55\tau$ for this geometry [6.72, 6.73]. An analysis of the observations in terms of this interpretation gave the hydrogen jump rates in reasonably good agreement with other experiments.

Detailed calculations of Mössbauer relaxation spectra over the whole range of hydrogen jump rates were made in [6.74].

It must be admitted, however, that a separation of this effect from the quasi-elastic broadening is not a trivial matter. The quasi-elastic broadening should always be present to some extent, whether the Mössbauer nuclei exist as constituent lattice atoms or as dilute probes. This point becomes particularly important when hydrogen jumps are fairly slow.

6.2.2 Quasi-Elastic Neutron Scattering

One of the advantages of quasi-elastic neutron scattering (QNS) experiments over the relaxation measurements described above is that they provide information on spatial as well as temporal aspects of elementary processes of diffusion. In QNS experiments, one measures the neutron scattering in the region of small energy and momentum transfers. Here, the scattering caused by the vibrational excitations can be neglected and, accordingly, the exchange of energy and momentum with hydrogen nuclei in their migration process can be measured.

Information on the self-diffusion is contained in the incoherent scattering, and most QNS measurements have been performed on protons for which $\sigma_{\text{inc}} \gg \sigma_{\text{coh}}$ (Table 5.3). The incoherent scattering function $S_{\text{inc}}(\mathbf{Q}, \omega)$ can be written as a Fourier transform of a single-particle, space-time correlation function of van Hove, $G_s(\mathbf{R}, t)$:

$$S_{\text{inc}}(\mathbf{Q}, \omega) = \frac{1}{2\pi} \int G_s(\mathbf{R}, t) e^{i(\mathbf{Q} \cdot \mathbf{R} - \omega t)} d\mathbf{R} dt. \quad (6.39)$$

In classical terms, $G_s(\mathbf{R}, t)$ is given by

$$G_s(\mathbf{R}, t) = \frac{1}{2} \sum_j \langle \delta[\mathbf{R} - \mathbf{R}^j(t) + \mathbf{R}^j(0)] \rangle, \quad (6.40)$$

which means the probability of finding a particle at \mathbf{R} after time t has elapsed since it started from the origin ($\mathbf{R} = 0$).

Usually, the correlation function is analyzed by the jump-diffusion model of *Chudley* and *Elliott* [6.75], assuming that the time spent during jumps is sufficiently short. Then, the probability of finding a diffusing atom at a site \mathbf{R} at time t , $P(\mathbf{R}, t)$, is assumed to satisfy the rate equation of the form

$$\partial P(\mathbf{R}, t) / \partial t = (1/n''\tau) \sum_{i=1}^{n''} [P(\mathbf{R} + \mathbf{s}^i, t) - P(\mathbf{R}, t)], \quad (6.41)$$

where τ is the mean residence time on a given site, and $\mathbf{R} + \mathbf{s}^i$ is the position of its nearest-neighbor site. This equation assumes that the rate of jumps to all the nearest neighbors is the same ($= 1/\tau$), and no jumps to farther neighbors are allowed. The solution of this equation for the initial condition $P(\mathbf{R}, 0) = \delta(\mathbf{R})$ can be identified as $G_s(\mathbf{R}, t)$. The scattering function is then obtained as

$$S_{\text{inc}}(\mathbf{Q}, \omega) = \frac{1}{\pi} \frac{f(\mathbf{Q})/\tau}{\omega^2 + [f(\mathbf{Q})/\tau]^2}, \quad (6.42)$$

$$f(\mathbf{Q}) = \frac{1}{n''} \sum_{i=1}^{n''} (1 - e^{-i\mathbf{Q} \cdot \mathbf{s}^i}). \quad (6.43)$$

Thus, the scattering function is a single Lorentzian with HWHM equal to $\Delta E = \hbar f(\mathbf{Q})/\tau$.

The above expressions apply to cases where the interstitial sites form a Bravais lattice, as T and O sites in the fcc lattice. In the case of a non-Bravais lattice, as T and O sites in the bcc lattice, with r inequivalent sites in a unit cell, a set of r rate equations must be solved simultaneously, leading to

$$S_{\text{inc}}(\mathbf{Q}, \omega) = \sum_{i=1}^r A_i(\mathbf{Q}) \cdot \frac{1}{\pi} \frac{f_i(\mathbf{Q})/\tau}{\omega^2 + [f_i(\mathbf{Q})/\tau]^2} \quad (6.44)$$

a sum of r Lorentzian functions having different weights and widths. For jumps between T sites in the bcc lattice, $r = 6$, and for O sites, $r = 3$.

Conclusions regarding the elementary process of diffusion can be drawn from a comparison of the scattering functions measured as a function of \mathbf{Q} for different crystal orientations with those expected for several different jump models.

A typical example is the case of H in Pd, shown in Fig. 6.7 [6.76]. From a comparison of experimental data of $f(\mathbf{Q})/\tau$ for two different directions of \mathbf{Q} ($\mathbf{Q} \parallel [100]$ and $\mathbf{Q} \parallel [110]$), it was concluded that the jumps occur between O sites in the fcc lattice with a mean residence time of $\tau = 2.8$ ps. It was

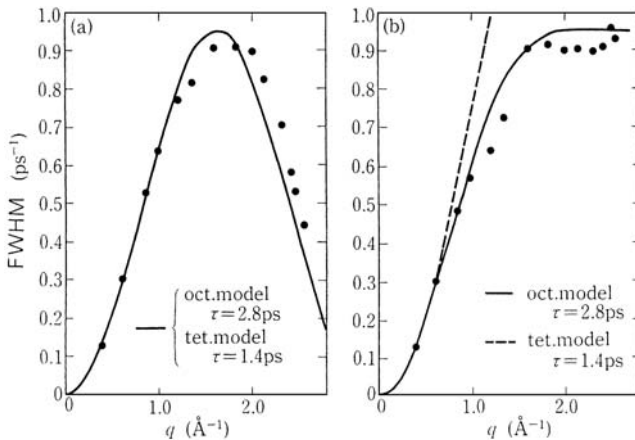


Fig. 6.7. **a** and **b.** Quasi-elastic neutron scattering due to H in Pd. **a** $q \parallel [100]$, **b** $q \parallel [100]$. Jumps occur between O sites with a mean jump time $\tau = 2.8$ ps [6.76]

also confirmed that the diffusion coefficient calculated from this value of τ , $D = a^2/12\tau$, agrees well with the values obtained from other experiments.

The above discussions on the microscopic mechanism of diffusion rely more heavily on the results at large values of $|Q|$, where the wavelength of neutrons becomes comparable to the jump distance ($sQ \sim 1$). At long wavelengths ($sQ \ll 1$), the scattering function becomes insensitive to the details of the individual jumps. In fact, it can be shown quite generally that the scattering function in this limit becomes a single Lorentzian, with a width determined by the tracer diffusion coefficient,

$$S_{\text{inc}}(\mathbf{Q}, \omega) = \frac{1}{\pi} \frac{DQ^2}{\omega^2 + (DQ^2)^2} . \quad (6.45)$$

This follows from the fact that the correlation function $G_s(\mathbf{R}, t)$ satisfies the diffusion equation for distances much larger than the jump distance ($|\mathbf{R}| \gg |s|$); or, equivalently, it follows from the relation

$$f(\mathbf{Q}) \approx s^2 Q^2 / 6 \quad (6.46)$$

for $sQ \ll 1$. Thus, the tracer diffusion coefficient can be determined by plotting the width as a function of Q^2 at small Q values. The capability of the method depends on the resolution of the spectrometers: a recent development of the high-resolution spectrometers ($\Delta E \approx 10^{-8}$ eV) allowed a determination of D as small as 5×10^{-9} cm² s⁻¹ [6.77].

For deuterons, having comparable cross sections for coherent and incoherent scatterings (Table 5.3), the quasi-elastic scattering consists of these two contributions of comparable magnitude. Whereas the incoherent scattering is, as described above, determined by the self-correlation function of

a single-particle motion, the coherent scattering is determined by the total correlation function of many particles [see (5.19)] and contains information on the collective relaxation of density fluctuations of the interacting particles. Thus, for deuterons, a double-differential cross section for quasi-elastic neutron scattering can be written as

$$\frac{\partial^2 \sigma}{\partial \Omega \partial \omega} = N_D \frac{k_i}{k_f} e^{-2W_D} \left\{ \frac{\sigma_{\text{inc}}}{4\pi} S_{\text{inc}}(\mathbf{Q}, \omega) + \frac{\sigma_{\text{coh}}}{4\pi} (1 - A_{\text{M-D}}) S_{\text{coh}}(\mathbf{Q}, \omega) \right\}, \quad (6.47)$$

where N_D is the number of D atoms, the factor $(1 - A_{\text{M-D}})$ corrects for diffuse scattering originating from M-D correlations. According to the formulation of *Sinha* and *Ross* [6.78], the coherent scattering cross section for a collection of diffusing interstitials with mutual interactions is given by [6.79]¹

$$S_{\text{coh}}(\mathbf{Q}, \omega) = S(\mathbf{Q}) \sum_{j=1}^r \frac{A_j(\mathbf{Q})}{\pi} \cdot \frac{(1 - c_r) f_j(\mathbf{Q}) / (S(\mathbf{Q}) \tau_M)}{\omega^2 + [(1 - c_r) f_j(\mathbf{Q}) / (S(\mathbf{Q}) \tau_M)]^2} \quad (6.48)$$

where $c_r = x/r$ is a filling fraction of a given interstitial sublattice, and the average mobility correlation time is defined by

$$\tau_M = \tau_0 / f_M \quad (6.49)$$

The coherent structure factor, which reflects the short-range order in the system, has been approximated by its spherical average. In Cowley's formalism of short-range order [6.80], $S(\mathbf{Q})$ can be expressed in the form

$$S_{\text{coh}}(\mathbf{Q}, \omega) = (1 - c_r) \left(1 + \sum_i Z^i \alpha^i \frac{\sin QR^i}{QR^i} \right), \quad (6.50)$$

where R^i and Z^i are the distance and coordination number of the i th shell, and the parameters α^i describe the deviations from a random mixture of vacancies and D atoms on the interstitial lattice². Equation (6.48) shows, in particular, that the coherent quasi-elastic line narrows when $S(\mathbf{Q})$ becomes a maximum, the so-called de Gennes narrowing [6.81], which implies that the spatially preferred configurations disintegrate more slowly in time. At long wavelengths, where (6.46) holds, the coherent scattering function approaches

$$S_{\text{coh}}(\mathbf{Q}, \omega) = \frac{S(\mathbf{Q})}{\pi} \frac{D^*(\mathbf{Q}) Q^2}{\omega^2 + (D^*(\mathbf{Q}) Q^2)^2}, \quad (6.51)$$

where the chemical diffusion coefficient retaining the \mathbf{Q} -dependence is written as

¹ Some confusion in [6.78, 6.79] has been corrected.

² Notice that, for $\alpha^i = 0$, the total coherent scattering intensity, i.e., (6.47) integrated over Ω and ω , correctly gives the Laue intensity as $N_D S(\mathbf{Q}) = 6N_0 c_r (1 - c_r)$.

$$\begin{aligned}
D^*(\mathbf{Q}) &= (1 - c_r) \frac{s^2}{6} \frac{1}{S(\mathbf{Q})} \frac{1}{\tau_M} \\
&= (1 - c_r) \frac{\tau_0}{\tau_M} \frac{1}{S(\mathbf{Q})} D_0 \quad (6.52a)
\end{aligned}$$

$$= p_v f_M f_{\text{therm}}(\mathbf{Q}) D_0 . \quad (6.52a)$$

The relation

$$f_{\text{therm}}(\mathbf{Q}) = 1/S(\mathbf{Q}) \quad (6.53)$$

can be rationalized by considering an ideal solution in the long-wavelength limit, where $f_{\text{therm}} = 1/(1 - c_r)$, whereas $S(0)$ becomes $(1 - c_r)$ when all α_i 's are zero in (6.50). (It will be shown in Sect. 6.4.2 that the diffusion coefficient involved here is, in fact, a little different from the chemical diffusion coefficient derived, for example, from Gorsky-effect measurements through elastic interactions, but we ignore this for the moment.)

Remembering that the tracer diffusion coefficient can be written as

$$D = p_v f_t D_0 , \quad (6.54)$$

we obtain the relation

$$D^*(\mathbf{Q}) = \frac{1}{H_R} \frac{D}{S(\mathbf{Q})} . \quad (6.55)$$

Some difficulties exist in the experimental separation of coherent and incoherent components in the quasi-elastic scattering spectra but they can be removed, in principle, by using a spin-analysis spectrometer. Some recent results of this kind of experiment performed on NbD_x will be described later.

For more details of the results of the QNS experiments, the readers are referred to the review articles of *Springer* and *Richter* [5.45], *Richter* [5.46] and *Ross* [5.47].

6.2.3 Other Methods

(a) Permeation, Absorption-Desorption, Electrochemical Method

In these methods, the temporal variation of a diffusion flow into or out of a specimen is measured after a sudden application or removal of an external driving force – a gas pressure in the permeation experiments and an electric potential in the electrochemical method. Alternatively, the same information can be obtained by measuring the phase lag in a sinusoidal modulation of pressure or voltage. One of the common difficulties of these methods is that, in many cases, the surface acts as a barrier for the flow of hydrogen, and the overall flow rate depends on the surface conditions. This difficulty can be removed, to some extent, by sputter-deposition of a Pd film in ultra-high vacuum, but not completely [6.82]. Usually, possible effects of a surface barrier are checked by performing experiments on samples of different thicknesses. For references on the technique, see, e.g., [6.83].

(b) Resistivity Relaxation

In this technique, a uni-directional flow of hydrogen is detected by measuring the temporal variation of the electrical resistance of a number of sections of a long specimen. The high sensitivity and accuracy of the resistance measurement make this technique potentially useful for low concentrations of hydrogen. It must be recognized, however, that the constancy of hydrogen-induced resistivity has been established only in a limited range of concentration and temperature (≥ 1 at.% above room temperature in V, Nb, Ta, and Pd) [6.84]. In fact, numerous experiments on substitutional impurities have established the general trend that the resistivity per impurity atom increases at low concentrations (≤ 0.01 at.%) and, as a function of temperature, goes through a maximum at around $\theta_D/5$ [6.85]. The use of resistivity for the determination of hydrogen concentrations should, therefore, be made with some caution.

It may be added here that the absence of the isotope dependence of the hydrogen-induced resistivity has been established by careful, comparative measurements of *Watanabe* and *Fukai* [6.84].

(c) Quench-Recovery Method

The application of the quench-recovery technique, widely used in the field of lattice defects, to hydrogen in metals was initiated by *Hanada et al.* [6.86]. In this method, a specimen containing hydrogen atoms in solid solution at elevated temperatures (e.g., liquid-N₂ temperatures) is quenched to low temperatures (e.g., liquid-He temperatures), and changes in the quenched-in resistivity are measured in the course of stepwise heating (isochronal annealing). As the resistivity change should be caused by the clustering of hydrogen atoms (or the precipitation of a hydride phase), it provides information on the long-range migration of hydrogen atoms. The method is particularly useful as it provides one of the rare possibilities to investigate the hydrogen diffusion at low temperatures. Some results of this type of experiment are described in Sect. 6.3.

(d) Mechanical Relaxation and Magnetic Disaccommodation

There are three major mechanisms of mechanical relaxation by which the motion of H atoms can be investigated; (i) the Gorsky effect, (ii) the Snoek effect, and (iii) the Zener relaxation. The Gorsky effect is a dilatational relaxation caused by the long-range motion of hydrogen atoms, of which the relaxation strength is proportional to $\Delta_G \propto (\lambda_1 + 2\lambda_2)^2$. The Snoek effect is a shear relaxation caused by the short-range reorientational motion, of which the relaxation strength is proportional $\Delta_R \propto (\lambda_1 - \lambda_2)^2$.

In experiments utilizing the Gorsky effect, the chemical diffusion coefficient $D^* = f_M B \rho (\partial \mu / \partial \rho)$ can be determined from the temporal variation and the factor $\partial \mu / \partial \rho$ from the magnitude of the relaxation strength. Thus, combining these results, the mobility B can also be derived. This makes the

Gorsky effect a very useful tool for investigating the hydrogen diffusion. Details of the method are described in the review article by *Völkl* [6.87].

In most cases, the Snoek effect was observed for H atoms in trapped states, forming e.g. O–H, N–H complexes in bcc metals. In pure metals, observation of the Snoek effect has not been successful because of small anisotropy of strains around hydrogen atoms. Observations of the Snoek effect in some alloys of the bcc structure have led to the conclusion that in these concentrated alloys, the hydrogen atoms occupy O sites having large values of $|\lambda_1 - \lambda_2|$.

The Zener relaxation occurs in disordered crystals due to stress-induced reorientation to change the state of atomic order. The mechanism of the Zener relaxation, which involves a multiple number of atoms, is inherently more complex than Snoek relaxation which is usually caused by single-atom jumps. A theory of Zener relaxation, specifically applied to interstitial H atoms in metals, was formulated by *Wipf* and *Kappesser* [6.88].

Other internal friction effects involving pinning or depinning of dislocation motion by the hydrogen atoms can also provide information on hydrogen diffusion. These effects are, in general, very sensitive but suffer from ambiguities in their origin, i.e., the nature of interaction between dislocations and hydrogen atoms.

For details of mechanical relaxation effects, see, e.g., [6.89, 6.90].

The temporal changes of magnetization in ferromagnetic metals occur via the motion of domain walls, which, in turn, is coupled with the distortion field of solute atoms. Thus, the magnetic after-effect provides information very similar to the Snoek effect, and proves useful in ferromagnetic metals because of its extreme sensitivity. For details, see [6.91, 6.92].

6.3 Experimental Results on Diffusion Coefficients

In this section, we present diffusion data for low concentrations of hydrogen in some selected bcc and fcc metals, for which most reliable data are available. The compilation is not exhaustive because its main purpose is to provide pertinent data for examining the diffusion mechanism in later sections. For more extensive compilations, see [2.20, 6.23–6.25].

The Arrhenius plots of the diffusion coefficient of hydrogen isotopes (H, D, and T) in some bcc metals (Fe, V, Nb, and Ta) are shown in Fig. 6.8. The data for H and D in Fe were obtained by *Nagano et al.* [6.93, 6.94] by the permeation method. For H, D, and T in V, Nb, and Ta, the data below 300°C are those reported by *Qi et al.* [6.95] obtained from Gorsky-effect measurements, and those for H above 600°C were obtained by *Eguchi* and *Morozumi* [6.96] by the absorption method. The data from quasi-elastic neutron scattering and NMR for H in V at high temperatures [6.97, 6.98] are also included (see also Fig. 6.23).

The diffusion data for fcc metals, Cu, Ni, and Pd, are shown in Fig. 6.9. The data for H, D, and T in Cu and Ni in the high-temperature region [6.99],

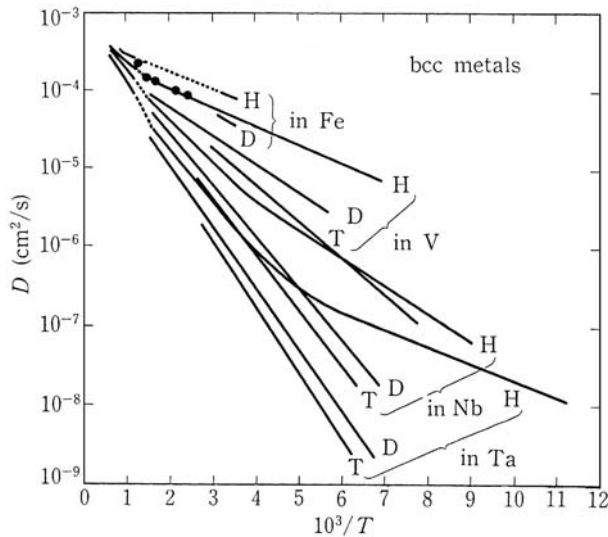


Fig. 6.8. Diffusion coefficients of hydrogen isotopes in some bcc metals, reproduced from [6.21]

those for H and D in Ni [6.100], and H in Cu [6.101] were obtained by the permeation method. The data for H and D in Ni in the low-temperature region are from absorption experiments [6.102]. For Pd, the data for H at high temperatures [6.103], H and D [6.104] and T [6.105] at intermediate temperatures were obtained by the permeation method, and those at lower temperatures from NMR [6.106].

As these experimental data in Fig. 6.8 and Fig. 6.9 are fairly well represented by straight lines on the Arrhenius plot, at least in limited temperature ranges, the diffusion coefficient can be expressed in the form $D = D_0 \exp(-E_a/kT)$. The parameters D_0 and E_a thus obtained are compiled in Tables 6.2 and 6.3 for bcc and fcc metals, respectively.

Inspection of these results shows that the diffusion behavior in bcc and fcc metals is distinctly different. First, the diffusion is generally more rapid in the bcc than in the fcc metals. This fact was demonstrated more clearly by Völkl *et al.* [6.107] from their diffusion measurements in $\text{Pd}_{0.47}\text{Cu}_{0.53}$. In this alloy, the diffusion could be measured in the quenched, metastable fcc phase over a fairly wide temperature range, which allows a comparison with the diffusion data for the stable bcc phase (Fig. 6.10). These results indicate that the magnitude of D is primarily determined by the structure of the lattice. Second, the isotope dependence is manifestly nonclassical in bcc metals, whereas in the fcc metals, its deviation from classical behavior ($D_0 \propto M^{-1/2}$, $E_a \propto M^0$) is less pronounced, though not negligibly small.

These two features can be understood qualitatively from the geometry of the lattice. The potential energy at the saddle point is considerably lower in

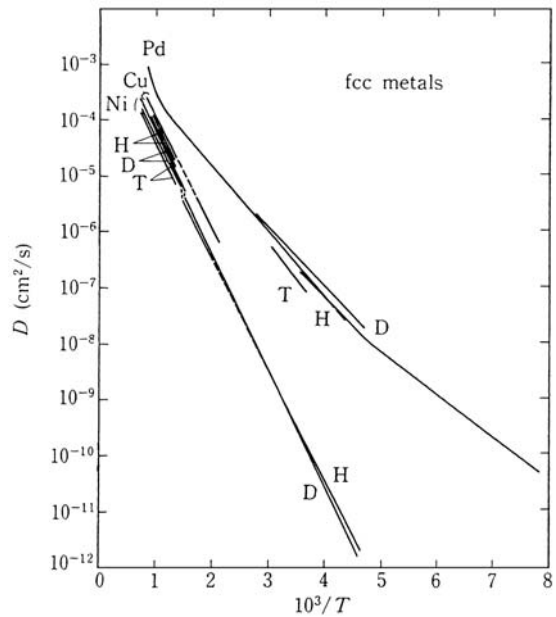


Fig. 6.9. Diffusion coefficients of hydrogen isotopes in some fcc metals, reproduced from [6.21]

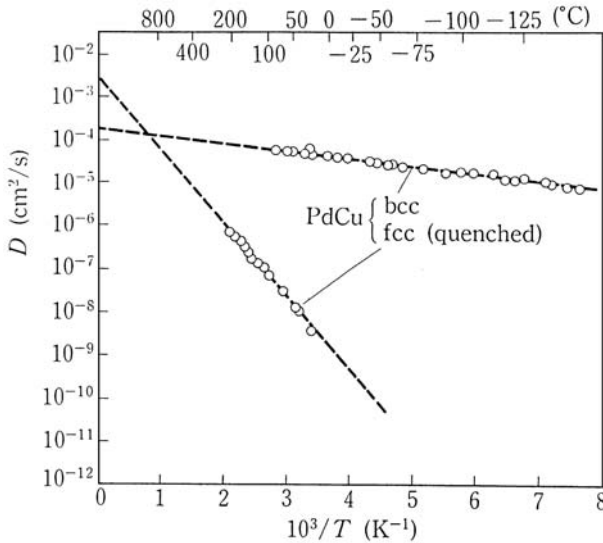
Table 6.2. Parameters of the diffusion coefficient of hydrogen isotopes in some bcc metals. (The value of D_0 for D in Fe is assumed)

Metal	Isotope	T [K]	D_0 [$10^{-4}\text{cm}^2\text{s}^{-1}$]	E_a [eV]	Method	Reference
Fe	H	290–1040	4.2	0.040	P ^a	[6.93]
	D	273–317	4.2	0.063	P	[6.94]
V	H	143–667	3.1 ± 0.8	0.045 ± 0.004	G ^b	[6.95]
		810–1380	8.9	0.113	A ^c	[6.96]
Nb	D	176–573	3.8 ± 0.8	0.073 ± 0.004	G	[6.95]
		133–353	4.9 ± 1.0	0.092 ± 0.004	G	[6.95]
	H	108–250	0.9 ± 0.2	0.068 ± 0.004	G	[6.95]
		250–560	5.0 ± 1.0	0.106 ± 0.006	G	[6.95]
Ta	D	873–1390	10	0.144	A	[6.96]
		148–560	5.2 ± 1.0	0.127 ± 0.006	G	[6.95]
		159–283	4.6 ± 1.0	0.135 ± 0.006	G	[6.95]
	H	90–190	0.028 ± 0.012	0.042 ± 0.006	G	[6.95]
		250–573	4.2 ± 1.2	0.136 ± 0.010	G	[6.95]
		986–1386	10	0.167	A	[6.96]
	D	146–573	3.8 ± 1.2	0.152 ± 0.008	G	[6.95]
		166–358	3.8 ± 1.2	0.165 ± 0.008	G	[6.95]

^aP: Permeation, ^bG: Gorsky effect, ^cA: Absorption.

Table 6.3. Parameters of the diffusion coefficient of hydrogen isotopes in some fcc metals

Metal	Isotope	T [K]	D_0 [$10^{-4}\text{cm}^2\text{s}^{-1}$]	E_a [eV]	Method	Reference
Cu	H	723–1200	11.3	0.40	P ^a	[6.99, 6.101]
	D	723–1073	7.3	0.38	P	[6.99]
	T	723–1073	6.1	0.38	P	[6.99]
Ni	H	220–330	1.8	0.40	A ^b	[6.102]
		385–620	6.7	0.41	P	[6.101]
		620–1600	6.9	0.42	P	[6.99]
	D	220–1273	4.2	0.40	P, A	[6.99, 6.100, 6.102]
Pd	T	723–1273	4.3	0.40	P	[6.99]
	H	230–760	2.9	0.230	P,NMR	[6.104, 6.106]
	D	218–333	1.7	0.206	P	[6.104]
	T	283–323	1.9	0.186	P	[6.105]

^aP: Permeation, ^bA: Absorption.**Fig. 6.10.** Diffusion coefficient of H in Pd_{0.47}Cu_{0.53}. Diffusion is much faster in the bcc (equilibrium) phase than in the fcc (quenched) phase [6.107]

the bcc than in the fcc metals because, in bcc metals, the distance between interstitial sites is generally shorter than in fcc metals, and there are no intervening M atoms in the diffusion paths. The electronic calculations described in Sect. 5.7 showed that the potential along the path connecting two T sites in the bcc lattice is rather low, whereas the potential minima on T and O sites in the fcc lattice are much deeper and isolated from each other.

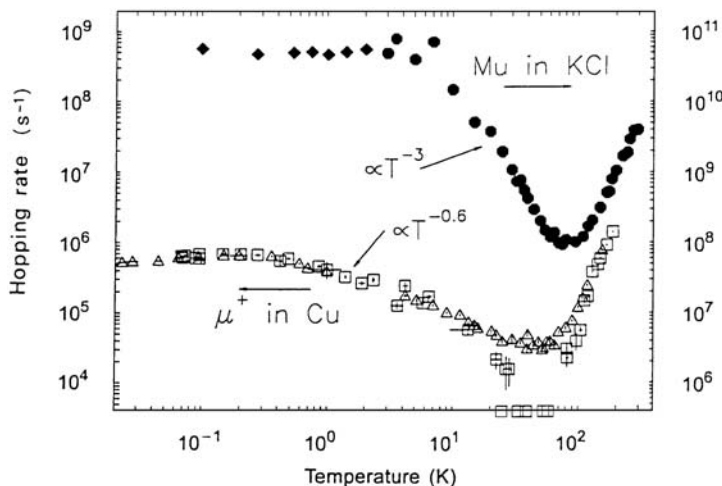


Fig. 6.11. Hopping rate of positive muons (μ^+) in Cu (*squares, left scale*) [6.108–6.110] and that of muonium (Mu) in KCl (*circles, right scale*) [6.15, 6.114]

In hcp metals, Ti, Zr, Hf, Y and Lu, measured diffusion coefficients are comparable, but slightly smaller than in fcc metals Ni and Cu [6.25]. This is also roughly understandable from the geometry of the lattice; the distance of elementary jumps (T–T or T–O–T jumps) is comparable, or even longer than in fcc metals (see Fig. 2.14).

At lower temperatures, diffusion experiments for hydrogen isotopes are severely hampered by small terminal solubilities. Therefore, it was on positive muons that first unambiguous data on jump frequencies were obtained at low temperatures. Surprisingly, the hopping rate of μ^+ in high-purity Cu was found to go through a minimum at about 50 K, and tend to level off at low temperatures [6.15, 6.16, 6.108–6.110]. Similar temperature dependence of the hopping rate was also inferred for μ^+ in Al [6.111]. Subsequent experiments performed for muonium³ in a number of insulators (e.g. NaCl [6.112], KCl [6.113, 6.114], GaAs [6.115]) showed that the minimum of jump frequencies occurs in all these cases, more conspicuously than in metals, and thus established the fact that this is one of the most characteristic features of quantum diffusion. Figure 6.11 shows the data for μ^+ in Cu and for muonium in KCl for comparison. As explained in detail in Sect. 6.6, a very fast hopping at low temperatures is due to coherent tunneling, which is gradually destroyed by interactions with surroundings, and eventually taken over by thermally activated jumps above the minimum. The temperature dependence below the minimum, $\propto T^{-0.6}$ for Cu and $\propto T^{-3}$ for KCl, is due to interactions with conduction electrons and phonons, respectively.

³ Muonium, often abbreviated as Mu, is a muon analog of an H atom, with a proton substituted with μ^+ .

For hydrogen isotopes H, D, T in bcc metals, information on low-temperature diffusion was obtained from quench-recovery and perturbed angular correlation experiments. Results of these experiments showed unambiguously that the migration of hydrogen atoms does take place at low temperatures, where no migration can be expected from extrapolation of the high-temperature data. Here we present our own critical evaluation of existing data of the quench-recovery experiments [6.18].

The most extensive quench-recovery experiments were performed by *Hanada* on H, D, and T in Ta [6.116–6.118]. In his experiment, samples doped with small amounts of hydrogen (50~3000 ppm) were quenched from liquid N₂ temperature to liquid He temperature, and the quenched-in resistivity was measured in the course of subsequent annealing. The quenched-in resistivity decreased in several stages as hydrogen atoms in different trapped states were liberated to form larger precipitates.

The rate of recovery of quenched-in resistivities is shown in Fig. 6.12. The recovery stages of D and T are brought to concur with those of H by shifting the temperature scale by 1.4 and 1.7, respectively, relative to the scale of H. Separate isothermal annealing experiments on D and T showed

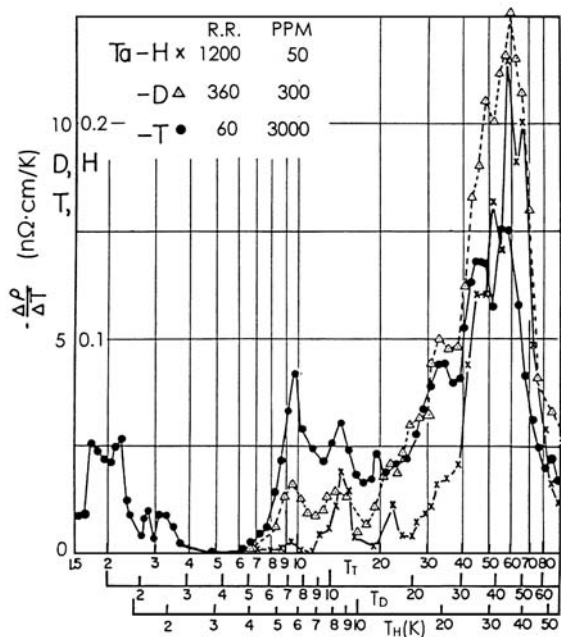


Fig. 6.12. Rate of recovery of the quenched-in resistivity for H, D, and T in Ta as a function of annealing temperature. Resistivity ratios (RR) and estimated hydrogen concentrations (in ppm) are given in the inset. The temperature scale for D and T is shifted by $\sqrt{2}$ and $\sqrt{3}$, respectively, with respect to H [6.117]

that the recovery processes were of thermal activation type, with nearly the same activation energy for the corresponding stages of these isotopes (Table 6.4). Noteworthy is the fact that, in the case of T, the recovery takes place at the lowest annealing temperature (1.5 K), with the indication of motion at even lower temperatures. The quenched-in resistivity and its recovery being smaller in the order T→D→H is an indication that hydrogen atoms are more mobile in this order, and therefore more difficult to quench to low temperatures.

Table 6.4. Observed recovery stages for D and T in Ta. The temperature of maximum recovery rate (T_{\max}) and the activation energy (E_a) are given for each stage [6.116, 6.118]

Stage	D		T	
	T_{\max} [K]	E_a [meV]	T_{\max} [K]	E_a [meV]
I	7.25	10	9.75	10
II	10.5	15	14.5	13
III	17	23	?	24
IV	~26	31	~33	31
V	~34	31	~45	45
VI	~44	58	~56	55

The Arrhenius plot of the effective diffusion coefficient D_{eff} deduced from these data is shown in Fig. 6.13, together with the data at high temperatures obtained from the Gorsky effect [6.95]. The magnitude of D_{eff} at each maximum-recovery temperature T_{\max} has been estimated approximately from the annealing time and average distance between the traps.

Obviously, D_{eff} cannot be identified with the intrinsic diffusion coefficient $D(T)$, which, in any case, should be a smooth function of temperature.

In order to extract information on $D(T)$ from D_{eff} , *Fukai* [6.18] adopted a so-called two-state model and assumed the following relation

$$D_{\text{eff}} = D(T) t_f / (t_b + t_f), \quad (6.56)$$

where t_f and t_b are the average time a hydrogen atom spends in a free (intrinsic) and bound (trapped) state, respectively. As the ratio t_f/t_b can be replaced, on the average, by the ratio of the number of hydrogen atoms in the free and the bound states, n_f/n_b , we may write

$$t_f / (t_b + t_f) \cong t_f / t_b = n_f / n_b = (n_f / n_b)_0 \exp(-e_b / kT) \quad (6.57)$$

where e_b is a binding energy of the traps activated in the stage under consideration. The implication is that the activation energy of each stage of D_{eff} is approximately equal to the sum $e_m + e_b$. Then, assuming $e_m \approx 0$

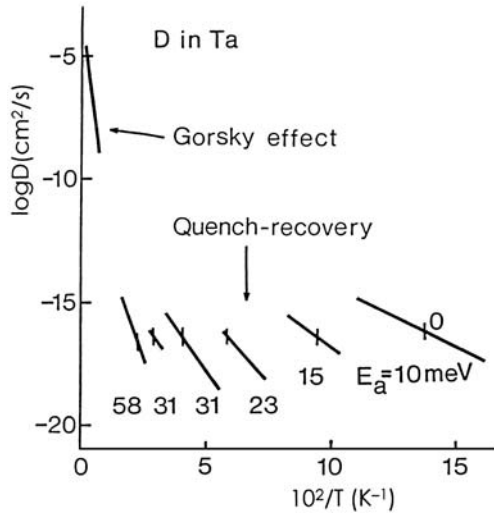


Fig. 6.13. Effective diffusion coefficients, D_{eff} , obtained from quench-recovery experiments on D in Ta. Diffusion data at high temperatures obtained from the Gorsky effect are also included [6.18]

for the lowest-temperature stage, and an appropriate set of e_b 's to smoothly join the segments of D_{eff} , the overall shape of $D(T)$ was deduced, as shown in Fig. 6.14. In this construction, the largest single source of error in determining the magnitude of $D(T)$ is the choice of $(n_f/n_b)_0$, possibly amounting to $10^{\pm 1}$. Although the detailed shape of these curves may depend, to some extent, on the assumptions made in the analysis, there is no doubt that the diffusivity at low temperatures is many orders of magnitude larger than a simple extrapolation of the high-temperature data. The general shape of these curves is, in fact, very similar to those of muons in Cu and KCl shown in Fig. 6.11, suggesting that the diffusion mechanisms in these systems are very similar. In both cases, the quantum diffusion proceeds via phonon-assisted tunneling at high temperatures (above the minimum) and coherent tunneling at low temperatures (below the minimum). Details of these mechanisms are described in Sect. 6.5.

Weidinger and Peichl applied a PAC technique for the measurements of low-temperature diffusion of H in Ta [6.56, 6.57]. As shown in Fig. 6.15, their values are larger than D_{eff} from quench-recovery experiments, but much smaller than $D(T)$ shown in Fig. 6.14. Fukai and Sugimoto [6.21, 6.22] suggested that what the PAC experiment actually measured was not a free migration but release processes of H atoms from some self-trapped configuration, probably small clusters consisting of two or three H atoms. Note that diffusivities obtained by the PAC experiments come rather close to the extrapolation of the line segments corresponding to stage I and II (Fig. 6.15).

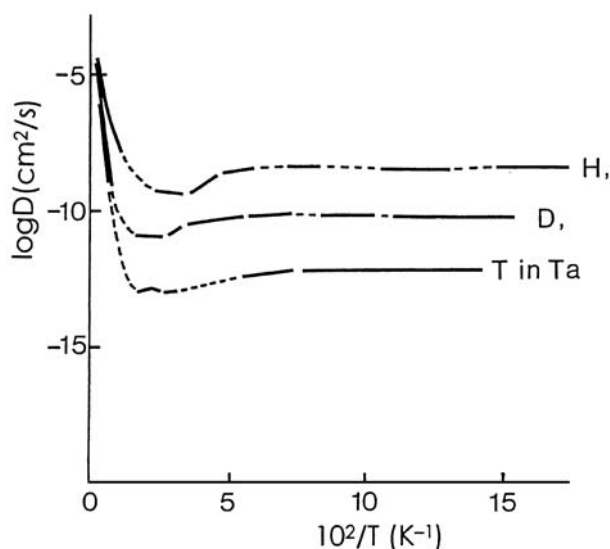


Fig. 6.14. The intrinsic diffusion coefficients $D(T)$ of H, D, T in Ta deduced from quench-recovery experiments at low temperatures, and the Gorsky effect at high temperatures [6.18]

Quench-recovery experiments were also performed on H and D in Nb [6.119–6.122]. Some of the results are shown in Fig. 6.16 [6.21]. Again, the corresponding recovery stages of H and D can be fairly well identified by shifting the temperature scale for D by 1.4. Comparison of this figure with Fig. 6.12 shows that the overall recovery processes are very similar; the corresponding stages in Nb, as indicated in Fig. 6.16, are shifted consistently to low temperatures by $\sim 15\%$ relative to those of Ta.

Staiger et al. [6.121] and *Blanz et al.* [6.122] assigned the 9 K stage of H in Nb to the motion of H atoms near dislocations, and the 21 K stage to the formation of pairs by free migration of single H atoms. However, judging from the general correspondence between the data on Nb and Ta noted above, it is believed to be more natural to regard all the recovery stages as being due to release processes from some trapped states. The diffusion coefficients they obtained are many orders of magnitude smaller than the PAC results on H in Ta, in strong dissonance with the overall similarity of diffusion behaviors in these metals.

Quench-recovery experiments performed on less pure V [6.116, 6.123] will not be described here, because recovery stages are known to be very sensitive to small amounts of impurities [6.119, 6.124].

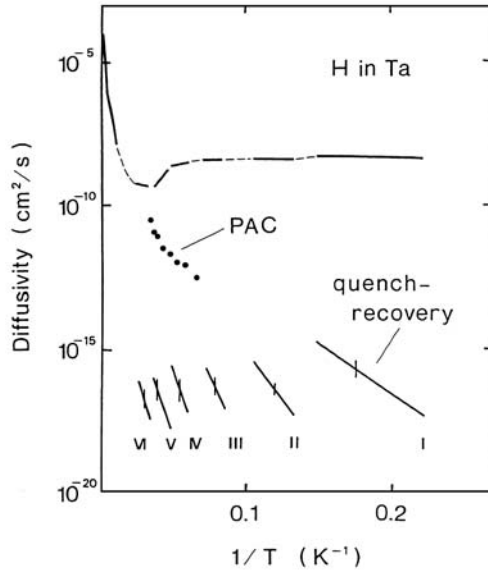


Fig. 6.15. Diffusion coefficient of H in Ta. The diffusion coefficient derived from Gorsky-effect and quench-recovery experiments (the *top curve* [6.18]), and effective diffusion coefficients obtained from PAC (data points [6.56]) and quench-recovery experiments (line segments; stage I–VI [6.18])

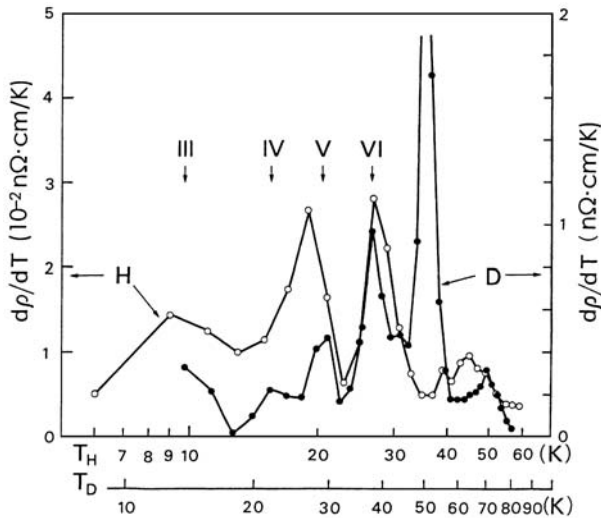


Fig. 6.16. Rate of recovery of quenched-in resistivity for H and D in Nb as a function of annealing temperature. The temperature scale for D is shifted by $\sqrt{2}$. Tentative correspondence with recovery stages in Ta (Fig. 6.12) is indicated. Experimental conditions are H; 10 ppm, isochronal annealing for 3×10^2 s in 2 K steps [6.122], and D; 380 ppm, time-linear annealing at a heating rate of 1 K min^{-1} [6.124]

6.4 Experimental Results on the Diffusion Mechanism

6.4.1 Elementary Jumps

The most fundamental information on the diffusion mechanism is on the elementary jumps – its path and frequency. Here we try to characterize the elementary jump processes in different crystal structures to help identify the underlying mechanism, to be explained in the next section.

(a) *Fcc Monohydride PdH_x*

The QNS experiment performed on PdH_x (Fig. 6.7) is a classic example in which both the jump path and frequency were determined in a single experiment [6.76]. The O–O jump was thus firmly established. From NMR, the overall concentration dependence of the prefactor D_0 was found to be proportional to $(1 - x)$, which is equal to the vacancy availability factor for O-site occupancy [6.125].

As explained in Sect. 6.2.1, NMR allows independent measurements of D and T_1 . By taking the ratio D/T_1 and comparing it with lattice-specific calculations, it is possible to identify the elementary jump process. In the case of PdH_{0.7} at room temperature, the experimental values of D/T_1 were found to be consistent with the calculation assuming jumps between neighboring O sites [6.126].

At very high temperatures ($T \geq 900$ K), the upward curvature of the diffusivity (Fig. 6.9), pointing to $D_0 \sim 0.1 \text{ cm}^2 \text{ s}^{-1}$, indicates that the average jump length is becoming longer. Substituting the Debye frequency $\nu_D = \theta_D/h = 6 \times 10^{12} \text{ s}^{-1}$ into $D_0 \sim s^2 \nu_D/6$, we obtain $s \sim 30 \text{ \AA}$, which is 12 times the O–O distance. Such a long jump length suggests the occurrence of gas-like state at these high temperatures.

In this connection, it may be mentioned that the Hall effect accompanying the flow of hydrogen in Pd was detected by *Verbruggen et al.* [6.127] in a dilute solution (≤ 0.75 at % H) at room temperature. However, the term “proton Hall effect” used by these authors is a little misleading because it was concluded that the observed effect was caused by the electron current which flowed in compensation of the proton current to maintain the charge neutrality. The effect of the Lorentz force on protons in their free flight was thought to be much smaller in comparison.

At low temperatures, the jump frequency of hydrogen isotopes in Pd₉₅Fe₅, weakly trapped by Fe atoms, was measured by magnetic after-effects [6.128]. (This alloy becomes ferromagnetic below 150 K.) As shown in Fig. 6.17, the jump frequency tends to level off at low temperatures, depending slightly on isotopes⁴. Another group of data for the Pd–H system obtained from

⁴ The high-temperature data in Fig. 6.3 of [6.128] were not correctly reproduced, and hence the pre-exponential factor $\nu_0 = 1.9 \times 10^{12} \text{ s}^{-1}$ was nearly 12 times smaller than the correct value. This error was repeated in later quotations [6.25, 6.129].

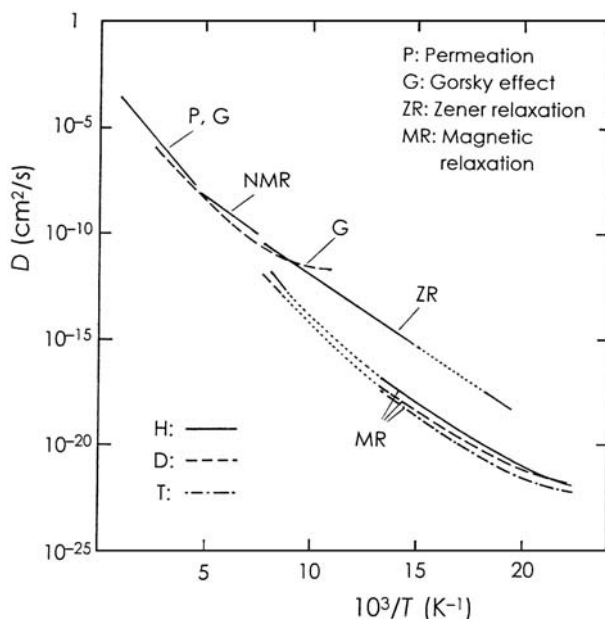


Fig. 6.17. Diffusion coefficient of hydrogen isotopes in Pd. High-temperature data for H are reproduced from [6.23]. Low-temperature data include magnetic relaxation on the dilute solid-solution (α) phase of $\text{Pd}_{95}\text{Fe}_5$ alloy [6.128], NMR and Zener relaxation in the hydride phase ($\text{H}/\text{Pd} \geq 0.7$) [6.106, 6.130], and NMR and Gorsky effect on the hydride phase ($\text{D}/\text{Pd} \geq 0.65$) [6.106, 6.131]. For the data on the hydride phase, a correction for the vacancy availability factor $(1 - x)$ has been applied

NMR [6.106] and Zener relaxation [6.130] in the hydride phase $x \geq 0.7$ show a break in the slope at 220 K, giving a lower activation energy $E_a = 0.13$ eV for the low-temperature region. This group of data give the diffusion coefficient nearly two orders of magnitude larger than those obtained in the α -phase of $\text{Pd}_{95}\text{Fe}_5$. The same discrepancy appears to exist for D between the Gorsky effect [6.131] and magnetic after-effect [6.128] data. A possible source of this big difference is not clear: It may be due to the difference of hydrogen concentration, or some problems in extracting elementary jump frequencies from the observed Zener relaxation, but most probably due to trapping by Fe atoms becoming more effective at low temperatures.

(b) *Fcc Dihydrides*

Diffusion data on fcc dihydrides obtained by Majer's group are shown in Fig. 6.18 in the form of Arrhenius plot, including the dependence on H concentration [6.132–6.138]. The dihydrides are divided into two groups; Ti, Zr, Hf hydrides on one hand and rare-earth hydrides on the other. The diffusivity

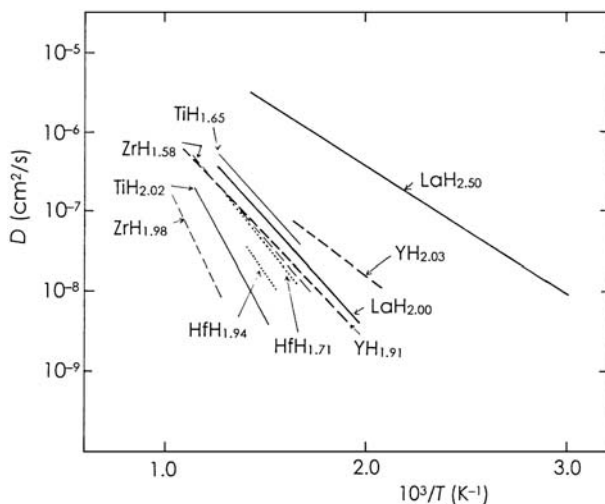


Fig. 6.18. The Arrhenius plot of diffusion coefficients of H in fcc dihydrides of Ti, Zr, Hf, Y and La obtained from NMR experiments. Data for two different compositions are shown for comparison [6.132, 6.134, 6.136–6.138]

is generally smaller in the former, and more distinctively, the concentration dependence is reversed.

The concentration dependence is more clearly seen in the QNS data of *Stuhr et al.* [6.139], compared at fixed temperatures (Fig. 6.19). Whereas the diffusivity in TiH_x and ZrH_x decreases roughly in proportion to the vacancy availability factor $(1 - x/2)$, the diffusivity in YH_x continues to increase with concentration even above $x = 2$.

Detailed inspection reveals that, in TiH_x and ZrH_x , the prefactor is nearly proportional to $(1 - x/2)$ only up to $x \approx 1.8$, with a constant activation energy of $E_a \approx 0.5 \text{ eV}$. A deviation from this behavior sets in as the stoichiometric limit is approached; the activation energy increases at $x \geq 1.8$ from $E_a \sim 0.5 \text{ eV}$ to 1.1 eV , accompanied by a drastic increase of D_0 . In fact, the activation energy changes from the low value at low temperatures to the high value at high temperatures, and the transition is shifted to lower temperatures in approaching the stoichiometric limit [6.132–6.135, 6.140]. No such anomalies were observed for the dihydrides of Y and La [6.137, 6.138].

Comparison of the jump frequency and the diffusion coefficient obtained from NMR allows one to determine the step length of elementary jumps. Figure 6.20 shows a comparison of the diffusion coefficient of H in $\text{TiH}_{1.55}$ measured by the pulsed-field-gradient technique with those predicted by the lattice-specific calculations for first-nearest-neighbor (1 n.n.) and third-nearest-neighbor (3 n.n.) jumps, using the observed mean jump time. Obviously, 1 n.n. jumps are preferred to 3 n.n. jumps [6.141]. It must be emphasized here that, to make a meaningful comparison, a rather accurate evaluation of

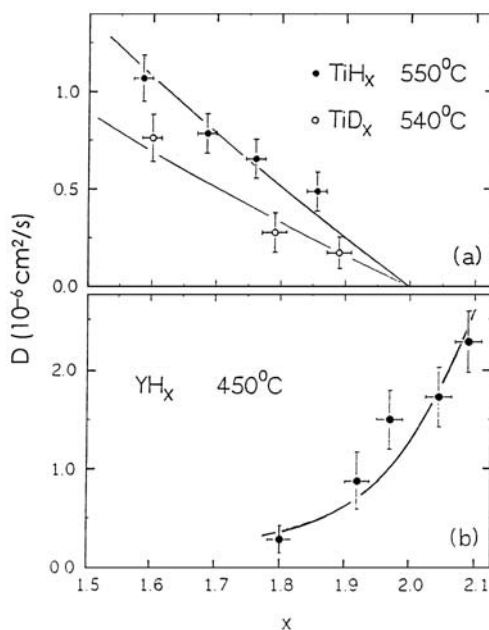


Fig. 6.19. The diffusion coefficient of TiH_x , ZrH_x and YH_x as a function of composition. Data from QNS experiments [6.139]

the mean jump time in terms of a lattice-specific formalism is indispensable. Similar experiments have since been performed on several dihydrides, TiH_x [6.132], ZrH_x [6.134, 6.135], HfH_x [6.136], YH_x [6.137], and led to the conclusion that in all these cases the nearest-neighbor T–T jumps are dominant.

In ascertaining the diffusion mechanism in the dihydrides, it is useful to recall that a large number of fluorite (CaF_2) type ionic crystals constitute a group of fast-ion conductors where the diffusivity of anions becomes very large. As the mechanism of atomic jumps should be primarily determined by the crystal structure, very similar mechanisms are expected to operate in the isomorphous dihydrides. In this group of ionic crystals, the intrinsic fast-ion phase is realized above some transition temperature, where a large number of anion Frenkel pairs (typically $\sim 5\%$) are created, and facilitate anion jumps into neighboring vacant anion sites. When extrinsic anion vacancies are introduced by doping with heterovalent cations, the fast-ion phase persists to lower temperatures.

QNS experiments performed on SrCl_2 showed that atomic jumps occur predominantly between 1 n.n. $\langle 100 \rangle$ anion sites but a small fraction of 2 n.n. $\langle 110 \rangle$ jumps also take place; the probability being 0.73 ± 0.05 and 0.27 ± 0.05 , respectively [6.142]. It was concluded from neutron scattering data that Frenkel defects in the fast-ion phase are short-lived ($\sim 10^{-12} \text{ s}$),

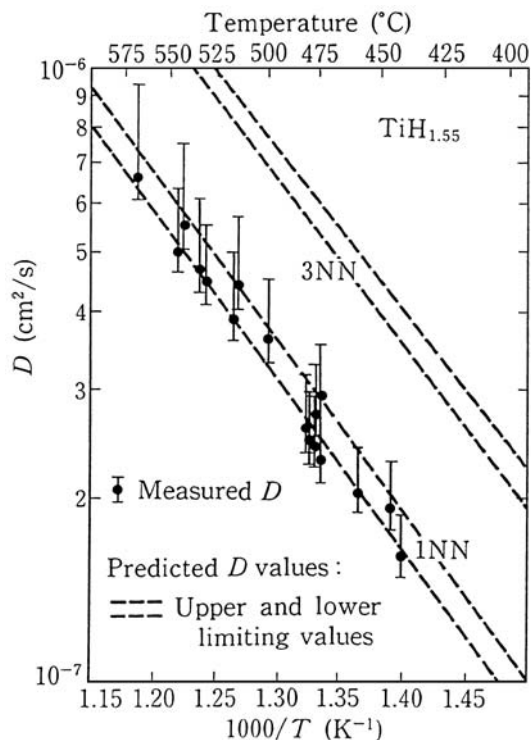


Fig. 6.20. Determination of the jump length of H in $\text{TiH}_{1.55}$ from proton NMR. The data points were obtained by the pulsed field-gradient method. Broken lines are the calculated values for 1 n.n. (nearest neighbor) and 3 n.n. jumps from the “experimental” jump frequency deduced from T_1 , data based on lattice-specific formalism. Jumps between 1 n.n.s are clearly preferred [6.141]

rather extended relaxed anion clusters [6.143]. Large-amplitude anharmonic lattice vibrations underlie these anomalous ion jumps [6.144].

These descriptions of fast-ion conductors can be directly transcribed to Ti and Zr dihydrides. At low H concentrations, where a large number of extrinsic H vacancies exist, jumps should occur via these built-in vacancies, predominantly between 1 n.n. T sites, probably with a small admixture of 2 n.n. jumps. As the stoichiometric composition is approached, intrinsic defects (Frenkel pairs) will be produced, allowing additional jumps to occur with the help of newly created vacant T sites. The energy of ~ 1 eV, nearly twice the difference of activation energies in the intrinsic and extrinsic regions, is believed to be reasonable for a hydrogen Frenkel-pair formation.

In effect, the above reasoning helps substantiating the earlier suggestion of *Bowman* and *Craft* [6.145] that the creation of H sublattice vacancies should be responsible for the observed anomalies. Judging from the concentration

and temperature dependence of the anomaly, the ring exchange mechanism suggested by *Kaess et al.* [6.132] appears less probable.

The situation is very different in rare-earth di/tri-hydrides where O sites are available without much energy costs. The fact that the diffusivity becomes larger at H concentrations $x > 2$ indicates the higher mobility of H atoms on O sites. The Arrhenius plot always forming straight lines (Fig. 6.18) is an indication that the diffusion process is dominated by a single energy barrier, regardless of whether H atoms occupy T or O sites.

A model to describe this situation was developed by *Stuhr et al.* [6.139]. Let c_T and c_O be the occupation probability of T and O sites, respectively, and ν_{TT} , ν_{TO} , ν_{OT} , and ν_{OO} represent jumps from T to T, T to O, O to T, O to O, respectively. The diffusion coefficient can be written

$$D = \frac{a^2}{4} \left\{ \frac{4c_O(1-c_O)}{x} \nu_{OO} + \frac{2c_T(1-c_T)}{x} \nu_{TT} + \frac{c_T(1-c_O)}{x} \nu_{TO} + \frac{c_O(1-c_T)}{x} \nu_{OT} \right\}. \quad (6.58)$$

The occupation probabilities are determined by the relation

$$x = 2c_T + c_O, \quad (6.59)$$

together with the condition of detailed balance

$$\frac{\nu_{TO}}{\nu_{OT}} = \frac{c_O(1-c_T)}{c_T(1-c_O)}. \quad (6.60)$$

(The last two terms in (6.58) are in fact equal from this detailed-balance condition.)

In the case of YH_x (Fig. 6.19), where the H concentrations do not differ much from $x = 2$, we may regard $c_O \ll 1$, and replace $1 - c_O$ by 1 in (6.58) and (6.60). Assuming ν_{TO}/ν_{OT} can be written in the form

$$\frac{\nu_{TO}}{\nu_{OT}} = e^{-\Delta E/kT}, \quad (6.61)$$

we obtain

$$4c_T = x + 2 + e^{-\Delta E/kT} - \sqrt{(x - 2 + e^{-\Delta E/kT})^2 + 8e^{-\Delta E/kT}}, \quad (6.62a)$$

$$2c_O = x - 2 - e^{-\Delta E/kT} + \sqrt{(x - 2 + e^{-\Delta E/kT})^2 + 8e^{-\Delta E/kT}}. \quad (6.62b)$$

If O-O jumps are so fast that only the first term in (6.58) contributes to the diffusion, the observed concentration dependence of D is reproduced reasonably well by the appropriate choice of the activation energy,

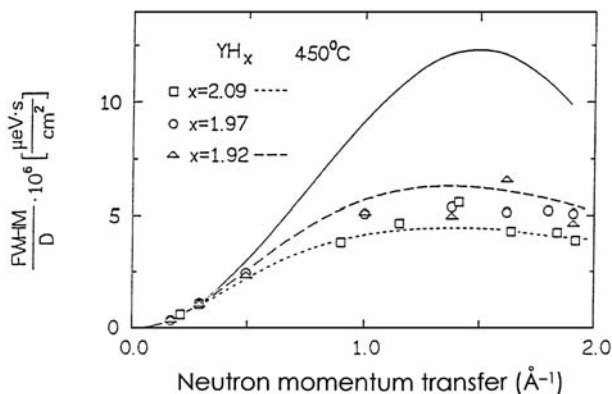


Fig. 6.21. The QNS linewidth of three YH_x samples in the dihydride phase plotted against Q . The *solid* and *broken* lines are fit curves calculated for the observed D value, assuming T-T jumps and O-site mediated jumps, respectively [6.146]

$\Delta E = 0.39 \pm 0.05$ eV (Fig. 6.19). As shown in Fig. 6.21, the form of the scattering function is also well reproduced by this model, whereas the agreement with simple T-T jumps is very poor [6.146].

Results of NMR experiments performed later by *Majer et al.* [6.137] in the same composition range ($x = 1.95 \sim 2.03$) appear to be slightly inconsistent with the QNS results. The authors admitted, however, that their NMR relaxation data were not sensitive enough to exclude a small admixture of T-O and O-O jumps claimed by the QNS data.

In the case of LaH_x (Fig. 6.18), where the diffusion data are available to much higher H concentrations, the activation energy starts decreasing especially above $x \sim 2.4$. It was suggested [6.138] that, even in this case, the mechanism was essentially the same, with the T→O excitation energy decreasing with H concentrations. However, at these high concentrations, where the contribution of thermally excited O populations should become relatively less important, it is believed to be more appropriate to take $c_O \approx x - 2$, $c_T \approx 1$. Then, (6.58) is reduced to

$$D \approx \frac{(x-2)(3-x)}{x} a^2 \nu_{OO} \quad (6.63)$$

and the activation energy should correspond to the energy barrier for O-O jumps. Qualitatively, the decrease of the activation energy can be rationalized by the increase of O-site energies in approaching the trihydride composition. Further complications were found, however, as trihydride composition was approached: The diffusivity remained high in spite of nominal lack of vacant interstitial sites, exhibited a smooth transition between high (>400 K) and low (>300 K) temperature regions, accompanied with hysteresis on temperature excursions, etc. These results appear to indicate that the diffusion bears a character of collective motion, the diffusivity depends on the M-I transition

and atomic ordering, both manifesting more clearly at high H concentrations. These point require further investigations. It may be added that NMR studies of fcc trideuteride LaD_3 were recently reported [6.147].

(c) *Hydrogen in bcc Metals*

Detailed experiments to characterize the elementary jumps of H atoms in bcc metals were made by the QNS method. *Lottner et al.* [6.97, 6.148] performed experiments on single crystals of $\text{NbH}_{0.02}$, $\text{TaH}_{0.13}$, and $\text{VH}_{0.07}$ (α phase) over a wide range of temperatures (up to around 500°C) and scattering vectors ($0.5 \leq |\mathbf{Q}| \leq 2.5 \text{\AA}^{-1}$ in several different directions), and analyzed the data in terms of the following four jump models.

Model 1. Jumps to four nearest-neighbor T sites with jump vectors of the type $\mathbf{s} = (a/4) (1,1,0)$, the jump probability to one of the nearest-neighbor sites, p_1 . The diffusion coefficient is given by $D = (a^2/12)p_1$.

Model 2. In addition to model 1, jumps to second-neighbor T sites with jump vectors of the type $(a/2) (1,0,0)$ occur with a probability p_2 ; $D = (a^2/12)(p_1 + p_2)$.

Model 3. In addition to model 1, double jumps which lead to second- and third-neighbor sites with jump vectors of the type $\mathbf{s} = (a/4) (2,1,1)$, passing through first-nearest-neighbor sites, are assumed to take place with a probability of p_2 . There are 16 possible paths of double jumps, four leading back to the original site; $D = (a^2/12)(p_1 + 8p_2)$. This model presumes that an H atom which acquired a sufficiently large energy to overcome a potential barrier for a single jump should have a finite probability of making a next jump before being self-trapped on the way. This process is expected to become more effective at high temperatures.

Model 4. Hydrogen atoms alternate between a free mobile state for a mean time τ_f , where they move quickly over T sites, and an immobile state (self-trapped, bound state) for a mean time τ_b . Writing the jump probability between T sites as p_1 , the diffusion coefficient is given by $D = (a^2/12)p_1\tau_f/(\tau_f + \tau_b)$.

From a best-fit analysis of scattering functions observed in the three specimens ($\text{VH}_{0.07}$, $\text{NbH}_{0.02}$, and $\text{TaH}_{0.13}$) for different magnitudes and orientations of \mathbf{Q} with respect to the specimens, model 1 was found to describe the room temperature results adequately. At higher temperatures, failure of model 1 became apparent. In $\text{NbH}_{0.02}$, for which the most detailed analysis of higher-temperature data was made, it was found that both models 3 and 4 could reproduce the observed results reasonably well.

Figure 6.22 shows how the Q^2 dependence of the HWHM for different sample orientations at 581 K can be reproduced by model 3. In contrast, the disagreement with predictions of models 1 and 2 is quite obvious, and disproved the validity of these models.

The temperature dependence of the parameters of models 3 and 4 is shown in Table 6.5) In model 3, the relative importance of double jumps increases

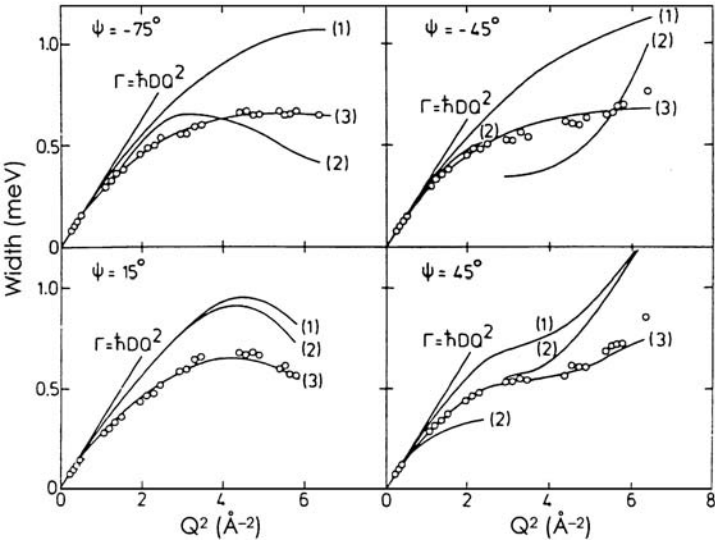


Fig. 6.22. Half-width of a Lorentzian fitted to the measured QNS spectra in NbH_{0.02} (○), and of the predictions of the models 1–3, for four different sample orientations. Data taken at 581 K [6.97]

Table 6.5. Temperature dependence of the parameters of the models 3 and 4. p_1 is the jump probability to one of the nearest-neighbor T sites, p_2 is the probability of a double jump, τ_f is the mean time in a mobile (free) state, and τ_b is the mean time in an immobile (bound) state [6.148]

$T[K]$	Model 3	Model 4	
	p_2/p_1	$\tau_f p_1$	$\tau_f/(\tau_f + \tau_b)$
293	0	3.2	0.64
431	0.4	5.5	0.66
581	1.4	6.0	0.64

with increasing temperature as expected, and at 581 K, a contribution of double jumps to the diffusion coefficient is 11 times as large as that of single jumps. In model 4, the average number of jumps in the mobile state, $\tau_f p_1$, increases with temperature, but the mean occupation of the mobile state $\tau_f/(\tau_f + \tau_b)$ stays the same. The physical implications of these results are not very clear at present.

As stated by the authors, results of QNS experiments alone do not lead to a unique picture of the diffusion mechanism. Agreement with experiments is a necessary but not a sufficient condition for the validity of a model. Thus, models 3 and 4 are equally valid, in so far as they describe the experimental results equally well. Keeping this in mind, we may summarize the conclusions

as follows: in V, Nb, and Ta, whereas jumps between neighboring T sites are dominant at room temperature, jumps to more distant sites become increasingly more important at higher temperatures.

For H in Nb, NMR experiments on $\text{NbH}_{0.03}$ also provided evidence that the jump length is slightly longer than the T–T distance. The value $D/T_1 = (1.9 \pm 0.2) \times 10^{-5} \text{ cm}^2 \text{ s}^{-2}$ determined in the temperature range 200–300 K was larger than the prediction of the lattice-specific calculation, $1.08 \times 10^{-5} \text{ cm}^2 \text{ s}^{-2}$ for jumps between the neighboring T sites [6.149]. This indicates that the actual jump distance is nearly 30% longer than the T–T distance.

Eguchi and *Morozumi* [6.96] found from absorption measurements that the diffusion coefficient of H in the high-temperature range for V (536–1108°C), Nb (599–1110°C) and Ta (713–1108°C) lies appreciably above the extrapolations of the Gorsky-effect data, showing distinctly higher slopes (Fig. 6.23).

For H in V, the diffusion coefficient obtained from the QNS data in the low- Q range [6.148] also showed an upward deviation from the Gorsky-effect data, in agreement with the absorption data.

In the high-temperature range, still another anomaly was observed in the intensity of QNS in $\text{VH}_{0.02}$. Plots of the integrated intensity against Q^2 , intended to determine the mean-square displacement $\langle u^2 \rangle$ of protons, are shown in Fig. 6.24 [6.148]. Strong deviations from straight lines at larger Q^2 are apparent, especially at 763 K. This deviation is believed to be the

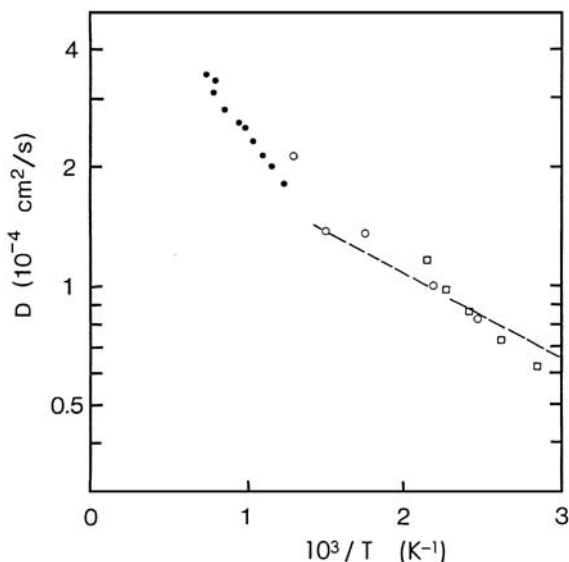


Fig. 6.23. Diffusion coefficients of H in V. The data obtained by the absorption method (●) [6.102], those obtained from QNS (○) [6.97] and NMR (□) [6.150], and a broken line extrapolated from Gorsky-effect data at lower temperatures [6.95] indicate a bend in the Arrhenius plot

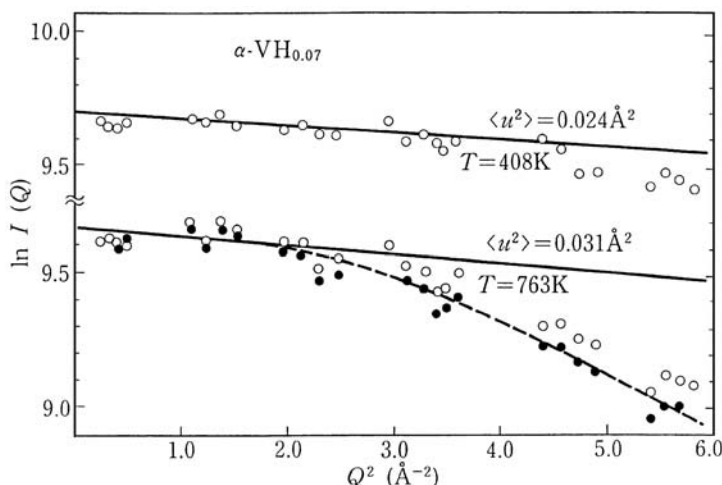


Fig. 6.24. Intensity of quasi-elastic neutron scattering, $I(Q)$, in $\alpha\text{-VH}_{0.07}$ as a function of Q^2 . Deviations from the initial slope at large values of Q indicate that the flight time is no longer negligible. The *straight lines* are drawn based on the quoted values of the mean square amplitude $\langle u^2 \rangle$ from separate experiments [6.97]

consequence of a finite flight time of protons in the migration process. If we roughly estimate the flight time by dividing the T–T distance by a thermal velocity of protons, a fraction of time spent during the flight amounts to 30% of the total time in $\text{VH}_{0.02}$ at 770 K, as compared to 10% in $\text{NbH}_{0.08}$ at 580 K. Since QNS spectra expected from protons in flight are much broader than the ordinary ones, a part of the intensity should be lost in the diffuse background if protons spend a sizeable fraction of time in flight. Although these discussions are rather qualitative in nature, we may at least conclude that we are beginning to see the gas-like diffusion of interstitial hydrogen at high temperatures.

A crude estimate of the diffusion coefficient in the gas-like state can be obtained from $D \approx \langle v^2 \rangle^{1/2} \bar{l}$, where $\langle v^2 \rangle^{1/2}$ is the mean velocity of protons, and \bar{l} is their mean free path. Assuming a thermal velocity for $T \sim 770$ K and $\bar{l} \sim a (\approx 3 \text{ \AA})$, we get $D \sim 7.5 \times 10^{-3} \text{ cm}^2 \text{ s}^{-1}$. Considering that the actual velocity should be smaller than the thermal velocity and only a fraction of H atoms should be in the gas-like state, this estimate compares reasonably well with the observed value ($D \sim 2.2 \times 10^{-4} \text{ cm}^2 \text{ s}^{-1}$).

(d) Hydrogen in hcp Metals

In hcp Sc, detailed measurements of the spin–lattice relaxation time have clarified the unique motional properties of hydrogen in the solid-solution phase, where the formation of H–M–H pairs and their alignment along the c axis are known to occur at low temperatures [6.151]. (See Sect. 5.6.1)

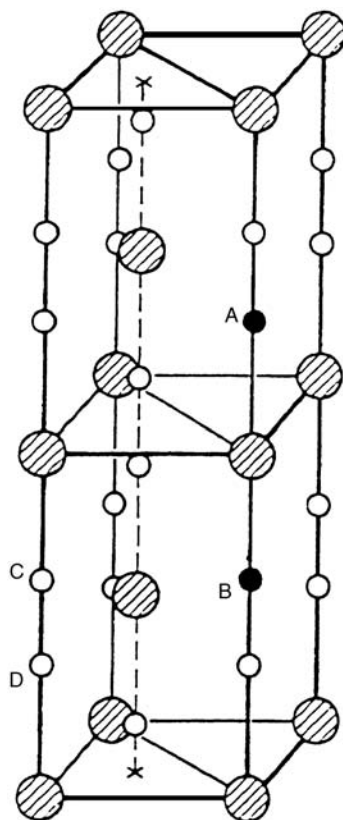


Fig. 6.25. Hexagonal close-packed metal lattice (*large hatched circles*) showing the location of T sites (*small open and closed circles*). Hydrogen atoms on sites A and B form a H–M–H pair, whereas an H atom on site D is isolated. Only one H atom can be accommodated in a closest pair of T sites, such as C and D, separated by a small distance $\sim 1 \text{ \AA}$

In the drawing of Fig. 6.25, hydrogen atoms, such as those on A and B, form H–M–H pairs, leaving others, like D, unpaired. Neutron scattering experiments on YH_x showed that even at sufficiently low temperatures, $\sim 7\%$ of the hydrogen atoms are left unpaired [5.117].

The temperature dependence of the proton relaxation rate ($1/T_1$) in $\alpha\text{-ScH}_{0.27}$ is shown in Fig. 6.26. In addition to a main relaxation peak centered around 500 K, a small additional peak is observed at low temperatures. The maximum relaxation rate of the low-temperature peak is $\sim 1.5\%$ of the main peak, nearly independent of hydrogen concentrations. The main peak is naturally explained as being due to the overall three-dimensional motion of the individual hydrogen atoms, except that the maximum relaxation rate amounts to only $\sim 75\%$ of what is expected for random jumps between the

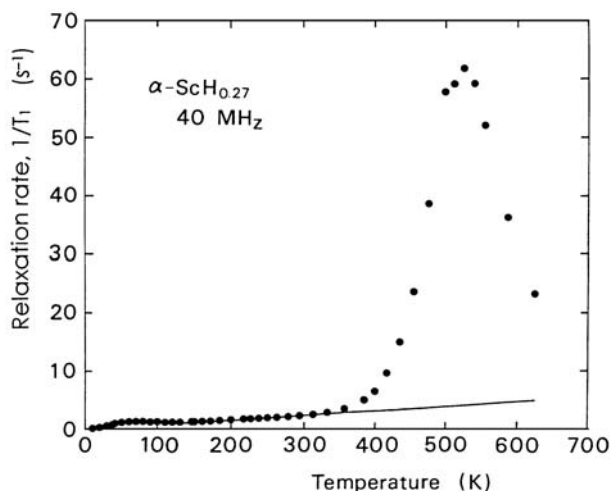


Fig. 6.26. Temperature dependence of the proton relaxation rate $1/T_1$ for α - $\text{ScH}_{0.27}$ at 40 MHz. The straight line shows the Korringa product $T_{1e}T = 123 \text{ s K}$ [6.151]

T sites. The authors showed that this discrepancy could be removed by assuming that H atoms (unpaired at high temperatures) execute a very rapid motion between the adjacent T sites (C and D in Fig. 6.25), resulting in a partial averaging-out of the dipolar interaction. The low-temperature relaxation peak was also found to be explainable in terms of these localized jumps between adjacent T sites. From the low-temperature peak it was concluded that the localized jump frequency is given by $\nu \sim 5 \times 10^{13} \exp(-50 \text{ meV}/kT) \text{ s}^{-1}$.

Direct observation of this localized hopping motion was made by QNS experiments of *Anderson et al.* on α - ScH_x [5.276]. The jump distance determined, $d \approx 1 \text{ \AA}$, is consistent with nearest-neighbor T–T distance. The quasi-elastic line width observed for $\text{ScH}_{0.16}$ (Fig. 6.27) shows a pronounced minimum, very similar to the case of $\text{Nb}(\text{OH})_x$. From the slope of the low-temperature side of the dip, the tunneling matrix element $J = 0.32 \text{ meV}$ and the coupling parameter to conduction electrons $K = 0.039$ were obtained. These values are close to the case of $\text{Nb}(\text{OH})_x$ (Sect. 5.8).

The hopping frequencies of hydrogen isotopes (including μ^+) in Sc determined by various techniques are compiled in Fig. 6.28 [6.152]. There are three different modes of hopping:

- Long-range diffusion jumps of H and D, studied by the Gorsky effect, NMR and QNS, following the Arrhenius line over 10 decades,
- Tunneling of H and D in an asymmetric T–T potential, studied by ultrasonic spectroscopy (US), showing a strong isotope dependence,
- Tunneling of H in a symmetric T–T potential, observed by the QNS experiment,

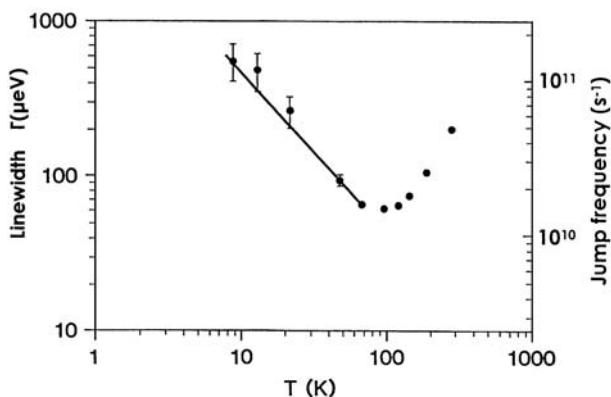


Fig. 6.27. Temperature dependence of the QNS linewidth (the hopping rate) of H in α -ScH_{0.16}. From the slope of the fit line, two parameters for the tunneling state J and K have been determined [5.276]

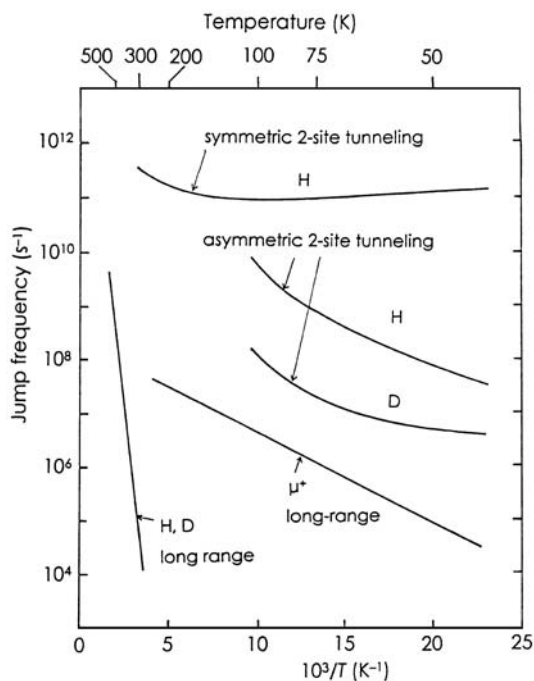


Fig. 6.28. Temperature dependence of the various hopping rates for H, D and μ^+ in Sc [6.152]. (a) long-range diffusion jumps of H and D, (b) tunneling of H and D in asymmetric T-T potential studied by ultrasonic spectroscopy (US), (c) tunneling of H in symmetric T-T potential, and (d) long-range migration of μ^+

- (d) Long-range migration of μ^+ , much faster than H isotopes, with a much smaller activation energy.

There is evidence, though not quantified, that some fraction of muons execute very rapid motion probably in a symmetric T–T potential. A fairly complete picture is thus being established for the diffusion of hydrogen isotopes in Sc, but how these mechanisms show up in particular situations appears to depend delicately on sample properties [6.153].

Yttrium is another rare-earth metal where the mechanism of H diffusion was studied rather extensively. Interestingly, the long-range migration studied by various techniques obeys the Arrhenius law over 10 decades [6.154], and coincides almost perfectly with the case of Sc. For the elementary jumps, *Anderson et al.* [6.155] analyzed their QNS results assuming T and O site occupancies, and concluded that a dynamic O-site occupation of $2 \sim 3\%$ exists at all temperatures, and thermally activated jumps from T to O site constitutes the rate-determining step.

6.4.2 Effects of Interaction Between Hydrogen Atoms

At high concentrations of hydrogen, diffusion behavior is modified by interactions between hydrogen atoms. Consequently, all the correlation factors introduced in Sect. 6.1.1 become dependent on hydrogen concentrations.

As described in the preceding section, in fcc hydrides, the concentration dependence of the pre-exponential factor is well represented by the vacancy availability factor. This implies that a single-site blocking picture is adequate for describing the effect of H–H interaction. In principle, the tracer diffusion coefficient should also include the tracer correlation factor f_t . Theoretical calculations have shown, however, that the concentration dependence of f_t is small; for an sc sublattice (applicable to the dihydride structure) f_t varies from 1 for $x = 0$ to 0.6532 for $x = 2$, and for an fcc sublattice (applicable to the monohydride structure) it varies from 1 to 0.781 [6.156–6.158]. Thus, in practice, the concentration dependence of the prefactor is dominated by p_v , and the effect of f_t is in most cases hardly discernible. In PdH_x , the experiment of *Verbruggen et al.* [6.159], showing the prefactor decreasing slightly more rapidly than p_v , may be taken to indicate the contribution of f_t . In TiH_x , QNS experiments performed on powder samples revealed a small, but significant deviation from the expectation of nearest T–T jumps [6.160]. The linewidths at large Q values were nearly 30% smaller than calculated from the observed diffusivity assuming T–T jumps. The authors suggested that this might mean either that the correlation factor f_t depends on Q or ω , or that interaction effects invalidate the simple formulation adopted for the analysis.

The interaction effect appears more explicitly in the chemical diffusion through the concentration dependence of the chemical potential. According to (6.17), the ratio of the chemical diffusion coefficient D^* to the tracer

diffusion coefficient D can be written in the form

$$\frac{D^*}{D} = \frac{f_{\text{therm}}}{(1 - x/r) H_R} . \quad (6.64)$$

Writing the chemical potential in the form,

$$\mu = \mu_0 - ux + wx^3 + kT \ln \frac{x}{r - x} , \quad (6.65)$$

by substituting (4.8) into (2.9), we obtain the expression for the thermodynamical factor

$$f_{\text{therm}} = \frac{1}{kT} \left(x \frac{\partial \mu}{\partial x} \right) = \frac{-ux + 3wx^3}{kT} + \frac{1}{1 - x/r} . \quad (6.66)$$

Recent Gorsky effect measurements on $\text{TiH}_{1.5 \sim 1.7}$ yielded D^* nearly 3.6 times the value predicted from the single-site blocking picture (the 2nd term of (6.66)) [6.161]. This is quite reasonable. If we adopt approximate values for the interaction terms $u = 0.35 \text{ eV}$ and $w = 0.5 \text{ eV}$ (Sect. 4.3), the ratio of the 1st term to the 2nd term in the temperature range of the measurement ($160 \sim 310^\circ\text{C}$) becomes 2.2, making the total value 3.2 times larger.

In bcc metals, the tracer diffusion of hydrogen at high concentrations is affected in more complex ways by interactions between hydrogen atoms.

Experiments on hydrogen in V, Nb, and Ta using the Gorsky effect [6.162], NMR [5.211, 6.150, 6.163] and QNS [6.164, 6.165] showed that both the pre-exponential factor and the activation energy of the tracer diffusion coefficient vary with hydrogen concentration, $D(x) = D_0(x) \exp[-E_a(x)/kT]$, with the variation of the latter being more pronounced. The results obtained from NMR experiments are shown in Figs. 6.29, 6.30 for $D_0(x)$ and $E_a(x)$, respectively [5.211, 6.150, 6.163].

Regarding the chemical diffusion, we must first of all recognize very peculiar effects of the long-range elastic interactions, cast in the linear term in the chemical potential. The chemical diffusion coefficient $D^* = Bx \partial \mu / \partial x$ approaches zero as $\partial \mu / \partial x$ tends to zero near the critical point. This phenomenon, known as critical slowing-down, was clearly observed in NbH_x [6.162, 6.166] and PdH_x [6.167, 6.168] near the critical point of the spinodal decomposition.

In fact, the elastic interaction is so long-ranged that it depends on the way the stress produced by the individual hydrogen atoms is relaxed on the surface. As explained in Sect. 2.3, this happens when the coherency stresses build up. In this case the chemical potential and, hence, the chemical diffusion coefficient becomes dependent on the shape of the sample, as well as on the mode of elastic distortion. The shape dependence of the chemical diffusion coefficient is clearly seen in Fig. 6.31, where the diffusivities determined by the Gorsky effect in wire and foil specimens are widely different. These results, however, give the same tracer diffusion coefficients after the correction for the factor $\partial \mu / \partial x$ has been made [6.24, 6.162].

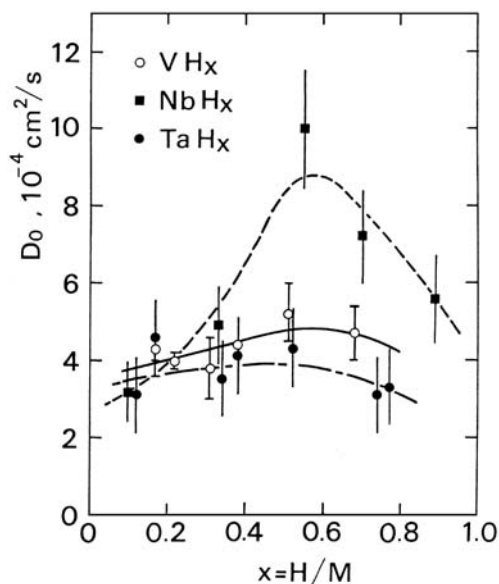


Fig. 6.29. Dependence of the pre-exponential factor for diffusion on hydrogen concentration in VH_x , NbH_x , and TaH_x [5.211]

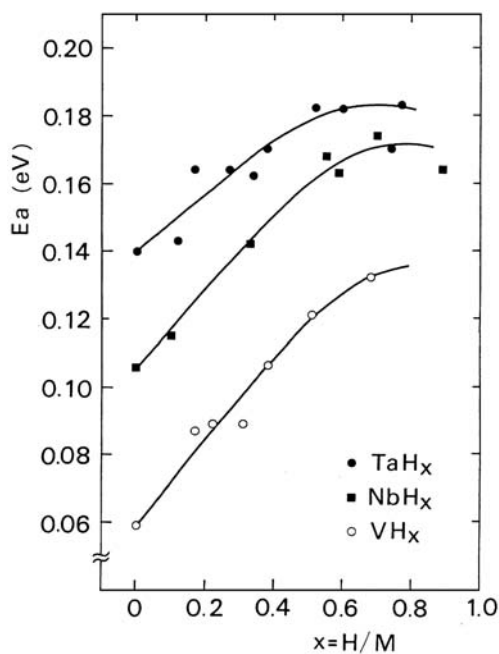


Fig. 6.30. Dependence of the activation energy for diffusion on hydrogen concentration in VH_x , NbH_x , and TaH_x [5.211]

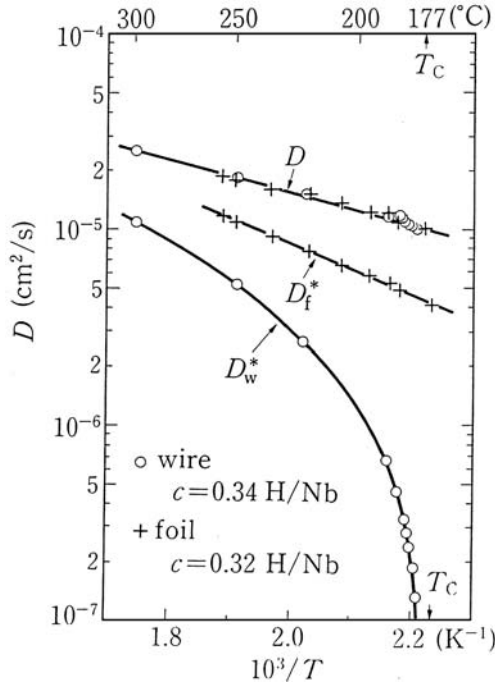


Fig. 6.31. Diffusion coefficients of H in Nb determined from the Gorsky effect. The tracer diffusion coefficient D can be determined uniquely from the chemical diffusion coefficients obtained for foil specimen (D_f^*) and wire specimen (D_w^*) by applying corrections for the chemical factor $\partial\mu/\partial c$ [6.162]

The theory of elastic interactions of *Wagner* and *Horner* [2.49] and *Wagner* [2.50] gives the expression for the diffusion coefficients that describe the diffusive decay of different modes of concentration waves in a specimen.

The effective chemical diffusion coefficient for a mode j is given by

$$D_j^* = f_M B \rho \left[\frac{\partial\mu}{\partial\rho} + \varepsilon_1 - \varepsilon_j \right], \quad (6.67)$$

where ε_1 is the energy of a macroscopic mode free of the coherency stress, given in terms of the component Λ of the force-dipole tensor as

$$\varepsilon_1 = \Lambda^2 / K_0, \quad (6.68)$$

with K_0 as the bulk modulus.

It is only when an experiment is designed to measure the concentration decay in a coherency-stress-free state that the measured diffusion coefficient coincides with the chemical diffusion coefficient. Some Gorsky-effect measurements indeed satisfied this condition [6.162, 6.164]. The neutron scattering

experiments, on the other hand, probe the short-wavelength density fluctuations (microscopic or bulk modes) that have elastic energies different from ε_1 . In elastically isotropic media, all the ε_j 's become identical and equal to

$$\varepsilon_{\text{bulk}} = \Lambda^2/c_{11} . \quad (6.69)$$

The effective diffusion coefficient to be obtained then becomes

$$D_{\text{bulk}}^* = D^* \left[1 + \frac{\varepsilon_1 - \varepsilon_{\text{bulk}}}{\partial\mu/\partial\rho} \right] \quad (6.70a)$$

$$= D^* \left[1 + \frac{\rho(\varepsilon_1 - \varepsilon_{\text{bulk}})}{f_{\text{therm}}kT} \right] . \quad (6.70b)$$

using the thermodynamical factor defined in (6.18). To illustrate the magnitude of the second term in (6.70a, 6.70b), $\rho(\varepsilon_1 - \varepsilon_{\text{bulk}})$ amounts to 0.13 eV in Nb and 0.17 eV in Ta. This is certainly a sizeable contribution and requires due consideration. This point was emphasized by *Wipf et al.* [6.169].

A comparison of the chemical diffusion coefficient and the tracer diffusion coefficient is expected to yield useful information on the collective motion. A deviation of Haven's ratio H_R from unity serves as one of its measures.

Figure 6.32 shows the concentration dependence of the thermodynamical factor f_{therm} for H in V [6.150]. The upper curve, the ratio of D^* (from the Gorsky effect) to D (from NMR), which is equal to f_{therm}/H_R [see (6.17)], was found to coincide with the values of f_{therm} deduced from the relaxation strength Λ_E of the Gorsky effect (not shown) [6.170]. The overall variation of f_{therm} deduced from these experiments and that deduced from the solubility data (the lower curve) is in reasonable agreement with each other. f_{therm} starts from unity at $x = 0$, decreases first as a consequence of attractive elastic interactions, goes through a minimum at $x = 0.2$, then backs up as mutual repulsion between hydrogen atoms overtakes. Recent measurements of the chemical diffusion of D in $\text{VD}_{0.73 \sim 0.82}$ at lower temperatures ($22 \sim 70^\circ\text{C}$) showed $D^*/D \sim 4$, roughly consistent with Fig. 6.32 [6.161]. Very similar results were also obtained for H in Nb [6.163] and Ta [6.163, 6.164]. In NbH_x the minimum value of f_{therm} approaches zero near the critical point of the spinodal decomposition.

A source of small discrepancies between the two curves of Fig. 6.32, amounting to about 30%, has not been identified yet. In any case, the discrepancy hardly exceeds the limit of the experimental errors. Thus, in spite of its potential capabilities, a comparison of chemical and tracer diffusion coefficients, as shown, cannot provide definitive information on Haven's ratio.

Hempelmann et al. [6.165] performed QNS experiments on α' - NbD_x , and determined the coefficients of the tracer and chemical diffusion, and the short-range order parameter of deuterons in a single experiment. The experimental results of quasi-elastic scattering were well described by a sum of two Lorentzians of appreciably different widths, the wider one being assigned to

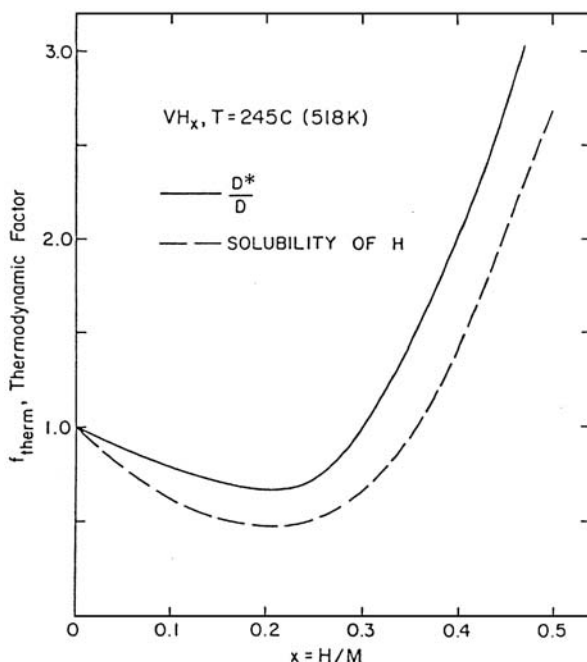


Fig. 6.32. Concentration dependence of the thermodynamical factor f_{therm} for VH_x at 581 K derived from the ratio of chemical and tracer diffusion coefficients (from Gorsky effect and NMR, respectively), and from solubility data [6.150]

the coherent scattering. A comparison of $D^*(Q)$ and $D/S(Q)$, thus derived, is made in Fig. 6.33. These two curves agree in shape with each other, and the ratio of their magnitudes was shown to be consistent with the thermodynamical factor and Haven's ratio derived by Monte Carlo calculations assuming two- and three-shell blockings. This blocking picture is consistent with the values of α^i best-fitted to the observed $S(Q)$: they were negative for the first and second shells, but very nearly zero for the third shell. More detailed discussions on the correlation effects were made by comparing the observed temperature and concentration dependence of the diffusion coefficients with Monte Carlo calculations.

Developments in QNS experiments making use of spin-polarization analysis have enabled a separate determination of coherent and incoherent scatterings (accordingly, chemical and tracer diffusion coefficients) in a single experiment. Figure 6.34 shows the separated coherent and incoherent parts of the total quasi-elastic scattering as a function of Q (varied by changing the detector angle) for α' - $\text{NbD}_{0.7}$ at 600 K [6.79]. Due to intensity reductions to $\sim 30\%$ by spin analysis, the quality of the data was not sufficiently good, but the expected qualitative features are apparent: the incoherent peak narrows as $Q \rightarrow 0$, whereas the coherent peak becomes broader and weaker in

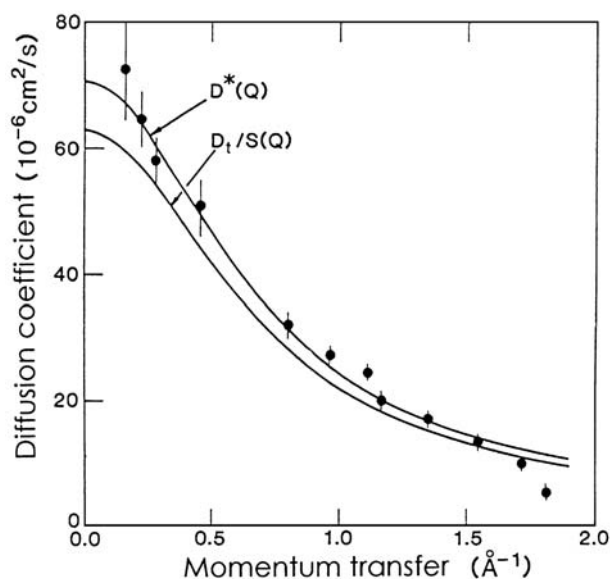


Fig. 6.33. Q -dependence of diffusion coefficients of D in $\text{NbD}_{0.83}$ at 581 K derived from simultaneous measurements of coherent and incoherent quasi-elastic neutron scatterings (left ordinate). The *upper line* represents the chemical diffusion coefficient $D^*(Q)$, the *lower line* the tracer diffusion coefficient divided by the structure factor $S(Q)$, which is obtained from the coherent intensity by simultaneous fitting [6.165]

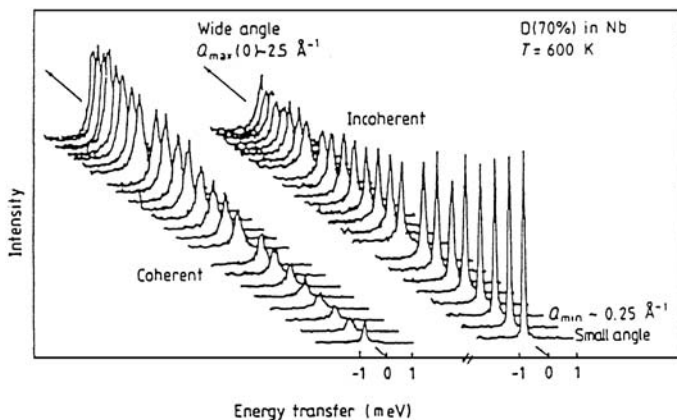


Fig. 6.34. The separated coherent and incoherent parts of the total quasi-elastic scattering as a function of detector angle [6.79]

intensity as $Q \rightarrow 0$. The authors examined the various fitting procedures to determine the parameters in the scattering functions (see (6.44, 6.48)) and found, in particular, that, within the accuracy of the experiment, there was no apparent Q -dependence of the jump times, at least not in the range $Q = 0.5\text{--}2.5 \text{ \AA}^{-1}$. From the low- Q approximation (see (6.45, 6.51)), the diffusion coefficients were obtained as $D = (1.21 \pm 0.09) \times 10^{-1} \text{ cm}^2 \text{ s}^{-1}$ and $D^* = (1.0 \pm 0.4) \times 10^{-4} \text{ cm}^2 \text{ s}^{-1}$, with $S(0) = 0.21 \pm 0.03$. Haven's ratio then becomes $H_R = 0.77 \pm 0.44$.

In the analysis of these neutron scattering experiments, effects of the elastic interactions were not taken into account. However, *Wipf et al.* [6.169] called attention to the fact that these neutron scattering experiments gave chemical diffusion coefficients consistently larger than those from Gorsky effects, and showed that this discrepancy could be removed, to a large extent, by making corrections for the elastic interaction (Sect. 6.2.2). The neutron scattering, which probes the density fluctuation and decay over the lengths of $1/Q \leq 10 \text{ \AA}$, is expected to give D_{bulk}^* larger than the true D^* to be obtained in the long-wavelength limit ($Q \rightarrow 0$). For these experiments on NbD_x , the difference estimated from (6.70) amounts to about 20%. This expected Q -dependence of the elastic-interaction effect was, indeed, found by *Cook et al.* [6.79]. The value of $D^* = (1.96 \pm 0.04) \times 10^{-4} \text{ cm}^2 \text{ s}^{-1}$ was obtained from the fit to the entire range of the Q -values ($0.5\text{--}2.5 \text{ \AA}^{-1}$), $D^* = (1.0 \pm 0.4) \times 10^{-4} \text{ cm}^2 \text{ s}^{-1}$ from their low- Q data alone, and $D^* = 0.7 \times 10^{-4} \text{ cm}^2 \text{ s}^{-1}$ from still lower- Q data of *Hempelmann et al.* [6.165]. According to (6.70), the true D^* is expected to be even smaller by about 20%.

Inclusion of elastic interactions requires reconsideration of some of the previous discussions. For example, a literal application of (6.70) leads to $\sim 20\%$ increase in Haven's ratio, much too large in comparison to the results of the Monte Carlo calculations.

The effect of elastic interactions on the coherent neutron scattering has been known for many years [6.171], but its importance in determining the chemical diffusion coefficient became manifest only after substantial developments were made in neutron scattering experiments. To proceed further, we need a theory which consistently incorporates the long-range elastic interaction in the scattering function, and helps in isolating this effect from observations, in addition to improving the experimental accuracies.

The correlated motion of hydrogens was manifested in isotope-mixture experiments on NbH_xD_y [6.172] and TaH_xD_y , [6.173]. The pulsed-field-gradient method of NMR provides a unique possibility of observing the diffusion of one particular isotope in the presence of others. The results of such experiments on NbH_xD_y , ($x + y = 0.60$) are shown in Fig. 6.35. The diffusion coefficient of H was measured in specimens having the same total concentration of $[\text{H}] + [\text{D}]$, but different isotope-mixture ratios. The purpose of this experiment was to unravel the dynamical correlation effects in the diffusion process. As the static interaction between hydrogen atoms can be regarded

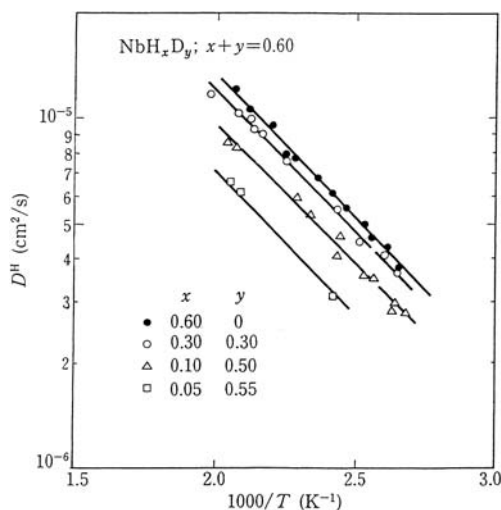


Fig. 6.35. Diffusion coefficients of H in α -NbH $_x$ D $_y$, ($x + y = 0.60$) [6.172]

as essentially the same for both isotopes, only the dynamical interaction is expected to show up, if at all. It is clearly seen in Fig. 6.35 that, as more H atoms are replaced by more slowly diffusing D atoms, the diffusion of H atoms becomes slower. Figure 6.36 shows this behavior as a variation of the activation energy E_a . (E_a was evaluated by assuming $D_0 = 2.7 \times 10^{-4} \text{ cm}^2 \text{ s}^{-1}$ in all cases; see Table 6.1). As the relative concentration of H is decreased, E_a of H atoms increases and, in the limit of low relative concentrations, appears to coincide with E_a of D atoms known from the Gorsky-effect measurements. These results provide clear evidence that the motions of H atoms are strongly correlated with each other.

Similar deceleration of diffusion by the presence of heavier isotopes was observed for μ^+ in NbH(D) $_x$ [6.174]. Figure 6.37 shows a comparison of the correlation time τ of μ^+ in NbH $_{0.92}$ and NbD $_{0.92}$ derived from the depolarization rate in μ SR, and τ of protons in NbH $_{0.92}$ derived from NMR. In the entire temperature range, the specimens are in the partially ordered phase β . It is clearly seen in Fig. 6.37 that the μ^+ diffusion is distinctly slower in NbD $_{0.92}$ than in NbH $_{0.92}$, but its activation energy is much lower than that of protons in NbH $_{0.9}$. These results demonstrate the effect of dynamical correlations on μ^+ diffusion.

Efforts to explain theoretically the isotope and concentration dependence of diffusion in the isotope-mixture systems by Monte Carlo calculations have so far been only partially successful [6.175, 6.176], probably because the site-blocking model adopted there was too simple. It remains to be seen whether the Monte Carlo calculations allowing for the blocking to second- and third-neighbor sites may explain the observed isotope-mixture effect.

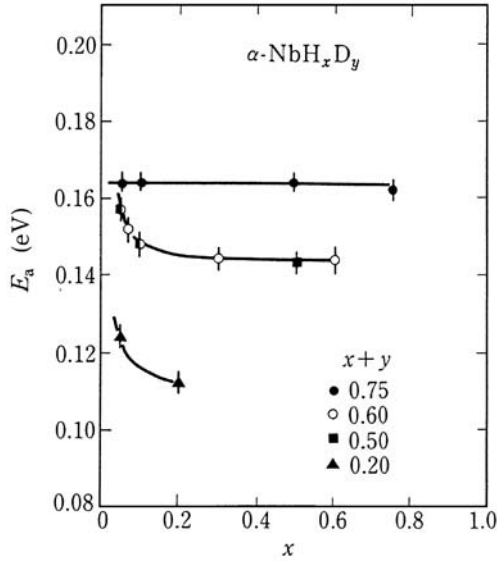


Fig. 6.36. Concentration dependence of the activation energy E_a of diffusion of H in $\alpha\text{-NbH}_x\text{D}_y$. E_a of H approaches that of D as more H atoms are replaced by D atoms [6.172]

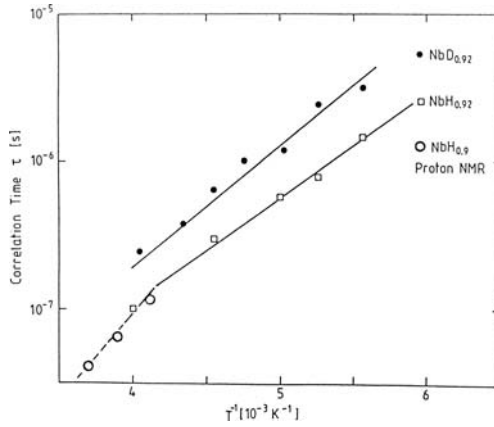


Fig. 6.37. Correlation time of fluctuating dipolar field as experienced by diffusing μ^+ in $\text{NbD}_{0.92}$ (\bullet) and $\text{NbH}_{0.92}$ (\square), and H in $\text{NbH}_{0.9}$ (\circ) [6.174]

Another aspect of diffusion which might be related to the highly correlated motion of hydrogen atoms has been noted in NMR relaxation times at high temperatures. It has been recognized for some time that, in some cases, the spin-lattice relaxation time T_1 as a function of temperature has a second minimum above a major minimum caused by hydrogen diffusion. Systems showing this high-temperature anomaly include ^1H in dihydrides of Sc, Ti, Y, Zr, and La, ^2D in diduterides of Sc and Y [6.177], ^{45}Sc in $\text{ScH}(\text{D})_2$ [6.178] and $\alpha\text{-ScH}(\text{D})_x$ [6.179], ^1H in $\alpha\text{-MH}_x$ ($M = \text{V}, \text{Nb}, \text{Ta}$) and ^1H in $\text{Nb}_{0.75}\text{V}_{0.2}\text{H}_{0.23}$ [6.180]. In none of these systems, do macroscopic diffusion coefficients of hydrogen show any anomalous variation as a function of temperature.

To account for this anomalous relaxation at high temperatures, it was suggested that a certain fraction of hydrogen atoms are in a correlated motion having a correlation time τ_L longer than those in uncorrelated motion (τ_d). The analysis based on this model led to the conclusion that at 1250 K, $\tau_L \sim 5\tau_d$ for $\text{ScH}_{1.83}$ and $\tau_L \sim 200 \tau_d$ for $\text{YD}_{1.88}$, assuming a fraction in a correlated motion of ~ 0.5 [6.177]. These values appear reasonable, lending support to this line of thought. An alternative explanation of this high-temperature anomaly in terms of formation of superabundant vacancies was also suggested [6.67]. This mechanism may not apply to cases of small hysteresis, but the possibility is believed to be worth pursuing. For a review of this high-temperature anomaly, see the paper by *Barnes* [6.179].

6.4.3 Atomic Jumps Over Inequivalent sites

(a) *Pure Metals*

Except for the case of an interstitial sublattice forming a Bravais lattice, as for O and T sites in the fcc lattice, a sequence of different types of jumps have to take place in order for a long-range diffusion to occur. The problem now is to characterize these jumps, their path and frequency, over the network of interstitial sites.

In many cases, only one of many conceivable paths is preferred to others, and only one type of jumps along the path becomes rate-determining. The Arrhenius plot forming a straight line over a wide range of temperature is an indication of such situation. In superstoichiometric fcc dihydrides, YH_x for example, it was shown that O–O jumps dominate over other possible jumps involving T sites (Sect. 6.4.1). Likewise, in $\alpha\text{-YH}_x$ having an hcp structure, combination of QNS and mechanical spectroscopy, especially the Zener relaxation in single crystals, showed that the process yielding a straight Arrhenius line over 10 decades is the jump between two adjacent chains along the c direction. Of the two jump processes observed by QNS at high temperatures, the slow one was found to extrapolate on to the low-temperature mechanical relaxation data, whereas the fast one assigned to the local jumps between adjacent T sites does not contribute to the long-range diffusion (Sect. 6.4.1) [6.154, 6.155].

In bcc metals, the long-range migration proceeds over the network of T sites shown in Fig. 5.71, where all the jumps are equivalent. However, this is only true in the absence of self-trapping distortion. In actual solid solution phases, there is a possibility that some localized ‘pocket state’ may be formed by self-trapping distortion, and make a group of sites inequivalent from others. An example is the case of 4T ring state suggested by the work of *Dosch et al.* [6.181]. Based on their detailed measurements of the scattering intensity of neutrons, they concluded that a part of the intensity was lost because the peak became too broad due to very fast motion of H atoms. The jump frequency deduced was $\sim 10^{13} \text{ s}^{-1}$, close to lattice vibration frequencies. This indicates the possibility that 4T ring states are formed by self-trapping distortion, and the long-range migration occurs via successive jumps between adjacent 4T rings. This may be the origin of the observed step length being always longer than the T–T distance.

The β_1 phase of VH_x is the case in which O_Z sites in the bcc lattice is divided into two groups O_{Z1} and O_{Z2} on alternate (101) planes, each capable of accommodating the maximum concentration of $x = 0.5$ (Sect. 2.4.3). This ordered structure gradually gets destroyed as more H atoms are thermally excited from O_{Z1} to O_{Z2} sites, and finally undergoes a transition to the disordered structure β_2 where the two sublattices are equally populated and the distinction between the two no longer exists.

The nuclear relaxation time T_1 measured in $\beta\text{-VH}_x$ as a function of temperature is shown in Fig. 6.38 for two different compositions $x = 0.546$ and 0.622 [2.120]. The presence of low-temperature humps indicates that a certain fraction of H atoms are in a more mobile state. Analysis of the data was made by assuming a spectral function of the form

$$J(\omega) = p_1 J_1(\omega, \tau_1) + p_2 J_2(\omega, \tau_2) , \quad (6.71)$$

where the subscripts 1 and 2 stand for H atoms on O_{Z1} and O_{Z2} sites, respectively. For the analysis of the major, high-temperature component, it was found necessary to allow for the explicit temperature dependence of the activation energy, viz.

$$\tau_1 = \tau_{10} \exp [\Delta E_1(T) / kT] . \quad (6.72)$$

$\Delta E_1(T)$ was then extracted from the $kT \ln \tau_1$ vs. T plot (Fig. 6.39), by subtracting $kT \ln \tau_{10}$ estimated from the low-temperature asymptotes on the graph. For the low-temperature component, on the other hand, the activation energy ΔE_2 was nearly temperature-independent. If we assume a common saddle point energy e_{sp} for all observed jumps, site energies e_1 and e_2 can be obtained from $\Delta E_1 = e_{\text{sp}} - e_1$ and $\Delta E_2 = e_{\text{sp}} - e_2$. The temperature dependence of the site energies, thus deduced, are shown in Fig. 6.40. The temperature where these energies become equal agrees with the temperature of β_1 – β_2 transition determined by other methods. The site energies at 300 K as a function of H concentration are also consistent with the structure model.

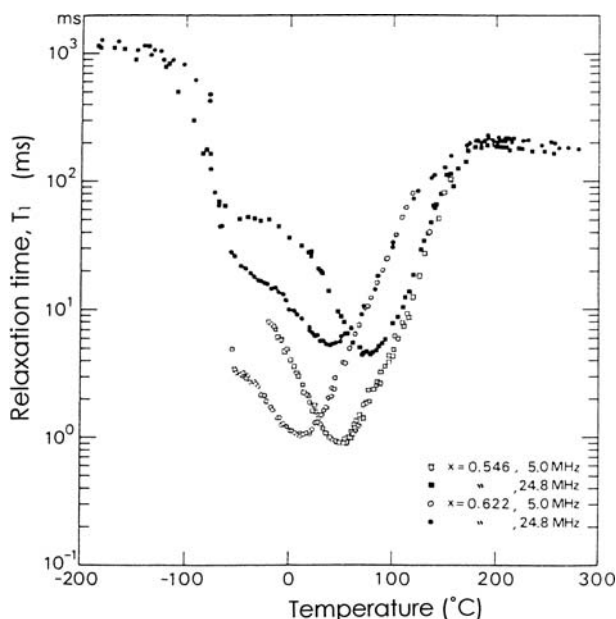


Fig. 6.38. Temperature dependence of the proton relaxation time T_1 in the β -phase of $\text{VH}_{0.546}$ and $\text{VH}_{0.622}$ measured at 5.0 and 24.8 MHz [2.120]

QNS experiments performed later on β_1 - $\text{VH}_{0.5}$ near the transition temperature [6.182] showed that the jump frequency in the O_{Z2} sublattice is at least 2 orders of magnitude larger than in the O_{Z1} sublattice. This is roughly consistent with the NMR result: the difference of sublattice energies $e_2 - e_1 \approx 0.2 \text{ eV}$ (Fig. 6.40) predicts the ratio of jump frequencies of 330 times.

(b) Pure Metals With Traps

Hydrogen in Nb coexisting with interstitial impurities O, N, C has been investigated most intensively by numerous techniques and contributed much to the understanding of the quantum character of its state and motion.

Internal friction and elastic after-effect measurements identified the configuration of H atoms trapped by O, N atoms in Nb (as shown in Fig. 5.45), and determined the frequency of re-orientational motion over a wide range of temperature. The re-orientational motion implies the jumps of an H atom over equivalent trapped sites, e.g. 8 pairs of a-a type in Fig. 5.45. The jump frequency of H and D trapped by O in Nb is shown in Fig. 6.41 as a function of temperature [6.25]. A strong curvature and a large isotope dependence were the first indication of the quantum character of diffusion, later ascribed to the phonon-assisted tunneling (Sect 6.5.3).

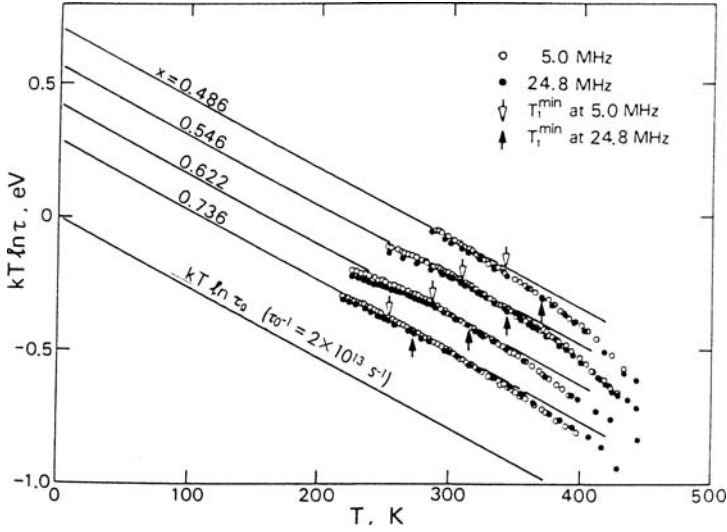


Fig. 6.39. The $kT \ln \tau_1$ vs. T plot for β - VH_x to extract the temperature dependence of the activation energy; $\tau_1 = \tau_{10} \exp [\Delta E_1(T)/kT]$. The prefactor τ_{10} , determined from the straight-line portion of the data for $x = 0.736$, is assumed to be the same for all the other cases. For clarity, the data for $x = 0.622$, 0.546 and 0.486 are shifted by 0.1 , 0.2 and 0.3 eV, respectively [2.120]

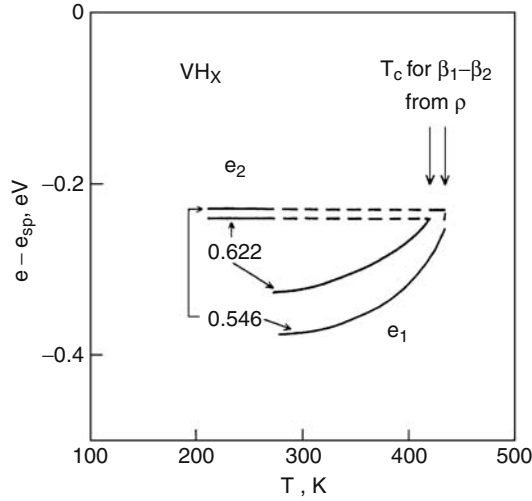


Fig. 6.40. Temperature dependence of the site energies e_1 and e_2 for $\text{VH}_{0.546}$ and $\text{VH}_{0.622}$ measured from the saddle-point energy e_{sp} . Temperatures of the β_1 - β_2 transition determined by resistivity measurements are indicated by arrows [2.120]

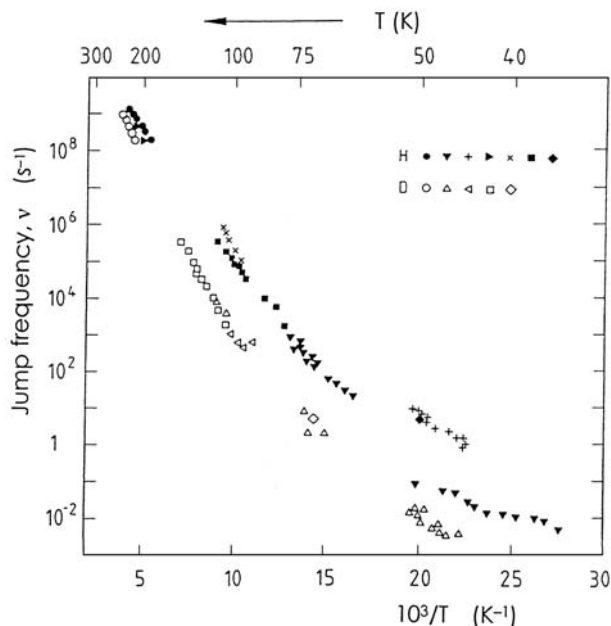


Fig. 6.41. Arrhenius plots of re-orientational motion of O–H and O–D pairs in Nb from internal friction and NMR experiments. For references, see [6.25]

For QNS, a primary effect of traps is to make a certain fraction of H atoms immobile, or equivalently, to make H atoms immobile for a certain fraction of time. An H atom alternates between mobile and immobile states at a certain rate depending on temperature. The two-state model was devised to describe this situation. (The re-orientational jumps in the trapped state are usually much slower in comparison, and therefore can be neglected.) In the two-state model, the scattering function is composed of two Lorentzians, with their widths and weight determined by the mean lifetime in the trapped (bound) state τ_b and in the free state⁵. This model was applied successfully to the analysis of QNS experiments on NbN_xH_y ($x, y = 0.37, 0.31$ and $0.70, 0.40$) over the temperature range 180–373 K, and allowed to extract various information contained; the activation energy for escape from the trap, for the migration in the free state, the effective long-range diffusivity, etc. [6.183].

At still lower temperatures, QNS experiments revealed another mode of elementary jumps, namely, local jumps within the pair of adjacent T sites (e.g. a–a in Fig. 5.45). As described in Sect. 5.8.1, the tunnel-split state formed at low temperatures over equivalent 2T sites becomes less-well defined with increasing temperature, and finally gives way to a self-trapped state. An H

⁵ τ_b is defined by the expression $\exp(-t/\tau_b)$ for the probability of finding the hydrogen in the trapped state after time t . τ_f is defined similarly.

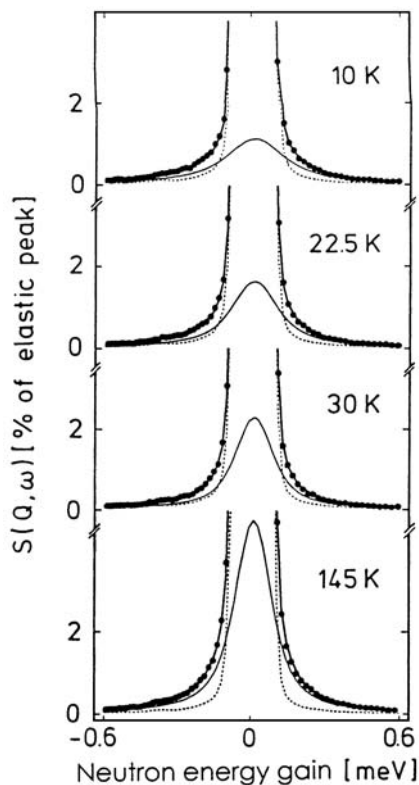


Fig. 6.42. Quasi-elastic neutron spectra of a $\text{Nb(OH)}_{0.002}$ sample at four temperatures. The spectra comprise data taken in the Q -range from 1.25 to 2.04 \AA^{-1} . The *thin* and *thick solid lines* are fit curves for the quasi-elastic and total scattering intensity. The *broken lines* indicate the resolution function [6.184]

atom is no longer extended over two T sites, but self-trapped on one of these sites.

QNS experiments by *Steinbinder et al.* [6.184] were performed above 10 K on two Nb(OH)_x samples with $x = 0.002$ and 0.011 . Examples of the observed spectra are shown in Fig. 6.42.

For a quantitative analysis, the following scattering law appropriate for atomic jumps between two sites separated by a distance \mathbf{d} may be used:

$$S(\mathbf{Q}, \omega) = \int d\varepsilon Z(\varepsilon) \left\{ \delta(\omega) \left[1 - \frac{1/2 - \sin(\mathbf{Q} \cdot \mathbf{d})/2Q \cdot \mathbf{d}}{\cosh^2(\varepsilon/2kT)} \right] + \frac{1}{\pi} \frac{\nu_1 + \nu_2}{\omega^2 + (\nu_1 + \nu_2)^2} \frac{1/2 - \sin(\mathbf{Q} \cdot \mathbf{d})/2Q \cdot \mathbf{d}}{\cosh^2(\varepsilon/2kT)} \right\}. \quad (6.73)$$

The expression has been averaged over all directions. The jump frequencies ν_1 and ν_2 on the interstitial sites 1 and 2 are related to each other by the

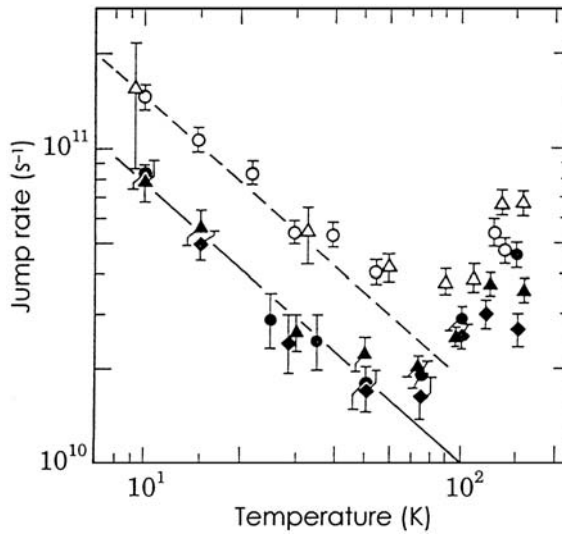


Fig. 6.43. Temperature dependence of the jump rate of H trapped by O and N in Nb. The *open symbols* refer to Nb(OH)_x (○ : $x = 0.02$, △ : $x = 0.011$), and the *solid symbols* refer to Nb(NH)_x (◆ : $x = 0.0005$, and ▲ : $x = 0.004$). The *straight lines* are the prediction from the quantum theory of diffusion (Sect. 5.8.1) [5.274]

detailed balance, $\nu_1/\nu_2 = e^{-\varepsilon/kT}$, when site 2 is higher in energy by ε than site 1. To facilitate data analysis, ε -dependence of $\nu_1 + \nu_2$ in (6.73) may be neglected, and, by putting,

$$\nu_1 + \nu_2 = 2\bar{\nu}(T), \quad (6.74)$$

the average jump rate $\bar{\nu}(T)$ can be determined by fitting (6.73) to the observed spectra. The temperature dependence of the jump rate, obtained in this way for Nb(OH)_x and Nb(NH)_x, is shown in Fig. 6.43.

The most striking feature of Fig. 6.43 is that, up to ~ 80 K, the jump rate decreases with increasing temperature, followed by a steep increase above ~ 100 K. The behavior is quite similar to the muon jumps shown in Fig. 6.11, as well as the diffusion behavior of hydrogen isotopes in Ta deduced from quench-recovery experiments (Fig. 6.14). The straight lines are the theoretical prediction for the jump frequency under the action of dragging forces exerted by conduction electrons, using the parameters determined in the low-temperature region ($2J = 0.23$ meV and $K = 0.05$ for Nb(OH)_x [6.184], and $2J = 0.167$ meV and $K = 0.055$ for Nb(NH)_x [5.274], Sect. 5.8.1).

Recently, a motion of H atoms trapped by vacancies in Nb was observed at low temperatures by motional narrowing of proton NMR [6.185]. The nature of this motion is not very clear; most probably a cluster of trapped H atoms undergoing a cage motion in a Nb vacancy.

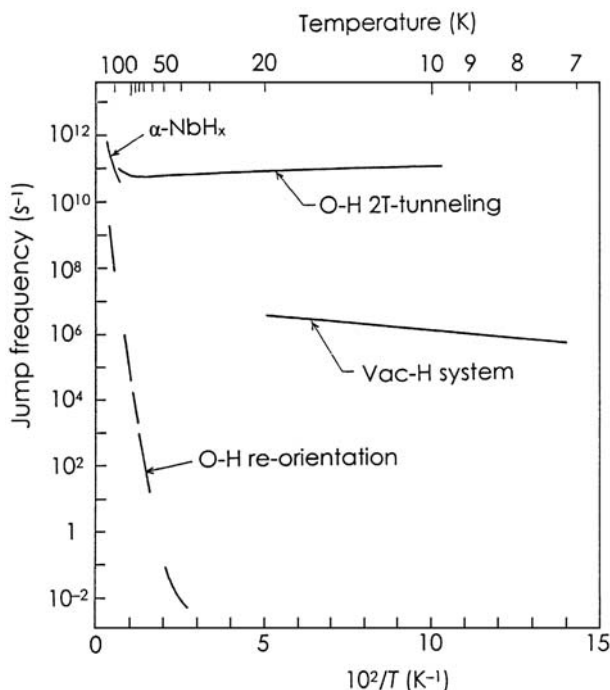


Fig. 6.44. Hopping frequencies of H in various states in Nb; long-range migration in the α -phase, tunneling in 2T sites around an O atom, reorientational jumps of OH complexes, and a cage motion in vacancies [6.185]

Figure 6.44 compares the jump frequencies of H in various states in Nb, including jumps between adjacent T sites in the long-range migration in the α -phase, localized jumps in a pair of T sites around an O atom, re-orientational jumps over equivalent O–H configurations, and a cage motion of H trapped by a vacancy. Note that the jump frequency of the long-range diffusion is similar to that of localized hopping of trapped H atoms between 2T sites, which suggests that the basic mechanism in these two cases should be the same. This mechanism will be examined in Sect. 6.5 in the context of quantum diffusion.

(c) Ordered Alloys – Intermetallic Compounds

Due to difficulties in preparing bulk specimens of intermetallic compounds, diffusion measurements in most cases have been made on powder samples by either NMR or QNS techniques, and only in a few cases on single crystals by QNS. Such experiments have been reviewed by *Richter et al.* [6.186] and *Barnes* [6.30]. Here we focus on some characteristic features revealed in representative substances, Laves phase hydrides AB_2H_x (C14 hexagonal and

C15 cubic structures) and LaNi_5H_x , both having distinctly higher diffusivities than other intermetallic hydrides.

The large diffusivity of hydrogen in the Laves structure can be understood from the connectivity of interstitial sites (T sites). In both C14 and C15 structures, three-dimensional network is formed by the stacking of polyhedra with face-sharing hexagons (see, e.g. *Yvon and Fischer* [3.61]). This structure is similar to the network of T sites in the bcc lattice (Fig. 5.71), and the distance between the adjacent T sites is also very similar ($1.1\sim 1.3$ Å as compared to 1.2 Å in Nb and Ta). In the C15 structure, all the hexagons are composed of equivalent A_2B_2 (g) sites connected by intervening AB_3 (e) sites. In the C14 structure, two distinct types of hexagons composed of different combinations of non-equivalent A_2B_2 sites exist.

Main features of H diffusion in Laves phase hydrides were already made apparent in two early papers; NMR on TiCr_2H_x by *Bowman et al.* [6.187] and QNS on $\text{Ti}_{1.2}\text{Mn}_{1.8}\text{H}_3$ by *Hempelmann et al.* [6.188].

The relaxation time measurements on TiCr_2H_x [6.187] revealed that the activation energy is relatively high ($E_a = 0.2 \sim 0.4$ eV) in the high-temperature region ($T > 180$ K), whereas it becomes low in the low-temperature region ($E_a = 0.03 \sim 0.05$ eV for $x = 0.5 \sim 0.6$, and $E_a = 0.10 \sim 0.18$ eV for $x = 2.6 \sim 2.8$). Experiments were performed on both C14 and C15 structures, but the difference between the two structures was small.

The QNS experiment on $\text{Ti}_{1.2}\text{Mn}_{1.8}\text{H}_3$ [6.188] revealed that the scattering function was composed of two Lorentzians of different widths, arising from the long-range motion of two groups of H atoms, mobile and less mobile ones. From comparison of the characteristic frequencies, the value of 90 meV was deduced for the energy difference of these two states. They noted, in addition, that a substantial part of the elastic incoherent scattering intensity was lost at large Q values (and high temperatures), which indicates the presence of rapid local motion. As the jump length of the local motion was estimated at 1.37 Å, close to the neighboring T–T distance, it was suggested that correlated (back-and-forth) jumps should be responsible.

Owing to the effort devoted to H diffusion in various Laves phase hydrides, the features of both long-range and local motions have come to be fairly well characterized.

As an example of long-range migration, the Arrhenius plot of the diffusivity in C14 and C15 ZrCr_2H_x , obtained by pulsed-field-gradient NMR, is shown in Fig. 6.45 [6.189]. The diffusivity is well represented by a sum of two exponential functions. While the high-temperature component ($D_{10} = (0.8\sim 1.3)\times 10^{-4}$ cm²s⁻¹, $E_{a1} = 146 \sim 157$ meV) stays nearly the same in the range of H concentrations investigated ($x = 0.2\sim 0.5$), the low-temperature component increases with decreasing H concentration ($E_{a2} = 21$ meV for $x = 0.2$ and $E_{a2} = 39$ meV for $x = 0.5$). From relaxation time measurements, there was no evidence for atomic motion at still lower temperatures.

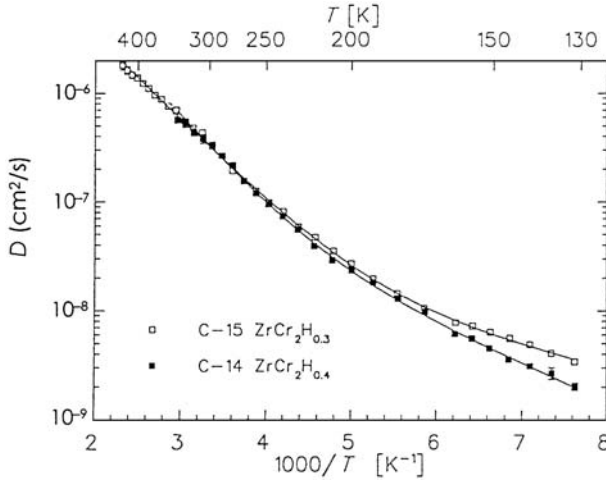


Fig. 6.45. Arrhenius plots of H diffusivity in C14-ZrCr₂H_{0.4} (■) and C15-ZrCr₂H_{0.3} (□) [6.189]

Jump lengths estimated from measured D and T_1 are compiled in Table 6.6. In all the cases, the estimated jump lengths are distinctly longer than the nearest-neighbor T–T distance. Very similar results were obtained from QNS measurements on several other C15-type hydrides; $2.36 \pm 0.07 \text{ \AA}$ in ZrV₂H_{2.9} [6.191], $2.0 \sim 2.5 \text{ \AA}$ in HfV₂H_{3.3} [6.192], $2.7 \pm 0.01 \text{ \AA}$ ($T < 394 \text{ K}$) and $3.62 \pm 0.01 \text{ \AA}$ ($T = 442 \text{ K}$) in TiCr_{1.85}H_{0.43} [6.193] and $2.4 \sim 2.6 \text{ \AA}$ in YMn₂H_{0.4~1.26} [6.194]. From these results, it may be concluded that, quite generally, the rate-determining step of long-range migration of H in C15-type hydrides is the jumps between neighboring hexagons (of A₂B₂ type (g) sites) mediated by the AB₃ type (e) site lying midway between the hexagons.

For the localized motion, the Q dependence of the elastic incoherent structure factor (EISF) observed in Ti_{1.2}Mn_{1.8}H₃ [6.188] and YMn₂H_{0.65} [6.194]

Table 6.6. Jump lengths estimated from the diffusivity D and T_1 of ¹H NMR in ZrCr₂H _{x} measured at 19.3 MHz [6.189]. The values were calculated at the temperature of T_1 minimum (T_{\min}), by adopting, approximately, the BPP model [6.31] and the result of Monte Carlo (MC) simulations on the fcc lattice [6.190]

Sample		T_{\min} (K)	Jump length, $d(\text{\AA})$	
Composition, x	Structure		BPP	MC
0.2	C15	140	1.95	1.70
0.3	C15	167	2.38	2.07
0.5	C15	170	2.46	2.14
0.4	C14	175	2.61	2.27

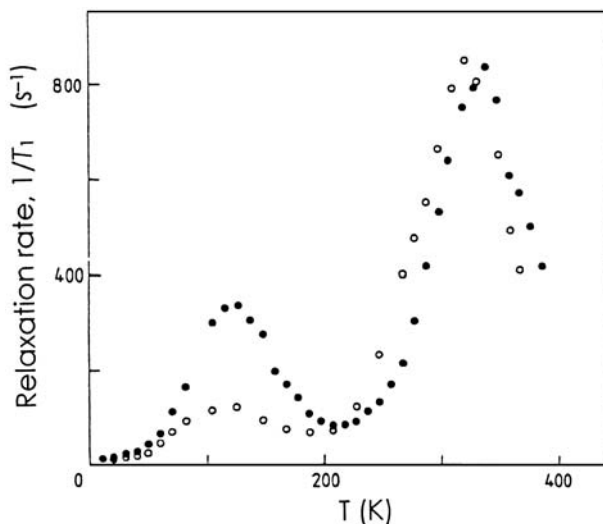


Fig. 6.46. Temperature dependence of the nuclear relaxation rate $1/T_1$ of ^{51}V measured in $\text{TaV}_2\text{H}_{0.87}$ (\circ) and $\text{TaV}_2\text{D}_{0.84}$ (\bullet) [6.195]

was found to be in favor of 2-site (back-and-forth) motion between the neighboring g sites.

Observations made on $\text{C15 TaV}_2\text{H(D)}_x$ were, however, very different. NMR experiments on $\text{TaV}_2\text{H}_{0.87}$ and $\text{TaV}_2\text{D}_{0.84}$ revealed two well-separated relaxation peaks, as shown in Fig. 6.46 [6.195]. The frequency dependence of the peak temperature indicates that both peaks are caused by some kind of atomic motion, and the magnitude of the peaks indicates that the high-temperature peak is due to long-range migration of H(D) atoms, whereas the low-temperature one is due to some motion restricted in space in which only a small fraction of internuclear interactions are modulated.

Regarding the long-range migration, subsequent ultrasonic measurements revealed that the average jump frequency can be expressed by the sum of two exponential functions for H with $1/\tau_{10} = 1 \times 10^{12} \text{ s}^{-1}$, $E_{10} = 0.27 \text{ eV}$ and $1/\tau_{20} = 1.7 \times 10^8 \text{ s}^{-1}$, $E_{20} = 0.12 \text{ eV}$, whereas it is expressed by a single exponential function for D with $1/\tau_{10} = 1.7 \times 10^{12} \text{ s}^{-1}$, $E_{10} = 0.29 \text{ eV}$ [6.196]. The situation is very similar to the case of ZrCr_2H_x described above.

Continued efforts to elucidate the nature of this low-temperature motion has finally led to the conclusion that it is a localized motion over the hexagons (six g sites) [6.197, 6.198]. Knowing that neutron diffraction experiments gave the D–D distance of 1.0 \AA in $\text{TaV}_2\text{D}_{1.3 \sim 1.65}$ [6.199], considerably shorter than the distance between the geometrical centers of their sites (1.1 \AA), *Skripov et al.* [6.198] made a detailed analysis of their EISF data, as shown in Fig. 6.47. Comparison between the 2-site and 6-site models, though delicate admittedly, is definitely in favor of the latter. (Note the data at large

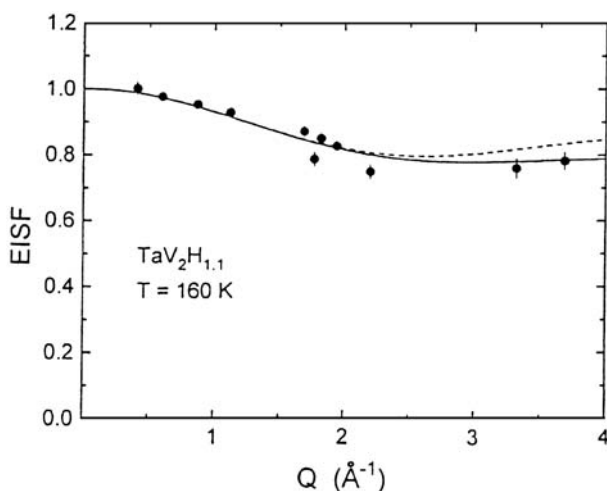


Fig. 6.47. Elastic incoherent structure factor for $\text{TaV}_2\text{H}_{1.1}$ at 160 K as a function of Q . The data are in favor of a 6-site model (*solid line*) than a 2-site model (*dashed line*) [6.198]

Q values are essential in identifying the jump mode. Analysis of EISF data comparable to this has not been made in other cases.)

The mechanism of formation of this 6-site ring state deserves special consideration. In samples used for neutron diffraction experiments, with compositions $x = 1.3 \sim 1.65$ [6.199], the average number of D atoms per hexagon is certainly less than 1, which implies that the average D–D distance measured was in fact the average distribution of single D atoms over the hexagons – the D density distribution in the pocket state. This pocket state bears a unique quantum character. The low-temperature relaxation peaks exhibit a strong isotope dependence, and more interestingly, the relaxation strength (the peak height) for D is larger than for H atoms. Qualitatively, this may be explained in terms of different spatial distribution of nuclear charges: the nuclear charge of protons, more extended in space than that of deuterons, should produce smaller electric field gradients at ^{51}V sites. These observations suggest that the 6-site ring state is in fact a coherent tunneling state, rather than a rapidly hopping state, of an H atom. The distance of 1.0 \AA is short enough to ensure sizeable tunneling effects to show up. A weak, non-Arrhenius temperature dependence of apparent jump frequencies of the low-temperature peak may also be understood along these lines of thought.

The systematics of the observed H motion in a series of Laves-phase compounds were discussed recently by *Skripov* [6.200].

In LaNi_5H_6 , the interstitial network is composed of two alternate layers; the one consisting of low-energy O sites (3f sites) and the other high-energy T sites (6m sites) lying half way between the basal planes. Detailed QNS

measurements of *Schönfeld et al.* [6.201] showed that, at 423 K, the jump frequency is $3.1 \times 10^7 \text{ s}^{-1}$ in the basal plane, $1.5 \times 10^7 \text{ s}^{-1}$ from 3f to 6m sites, $3.4 \times 10^8 \text{ s}^{-1}$ for the returning jumps, and $5.3 \times 10^{10} \text{ s}^{-1}$ within the hexagons formed by 6m sites. The energy difference between 3f and 6m sites was estimated to be 109 meV. The observed jump frequencies are correlated with the distance between the sites; 2.6~2.7 Å between 3f–3f and 3f–6m sites, and 1.5 Å between 6m sites forming hexagons. The high frequency of localized jumps within the hexagons may be taken to be an indication of the formation of a pocket state.

In this connection, it may be mentioned that the formation of localized states was clearly observed for muons in UNi_2Al_3 [6.202, 6.203] and GdNi_5 [6.204], both having a hexagonal structure similar to LaNi_5 . In both cases, a muon was found to occupy a ring state equivalent to a 6m-site hexagon in LaNi_5 . Whether the muon is in a coherent tunneling state extended over the ring, or hopping rapidly along the ring, has not been identified. In GdNi_5 , the muon hops from 6m site to 3f site with the phonon-activated tunneling process, with the activation energy of 23 meV and the tunneling matrix element of 0.11 meV [6.204].

(d) *Disordered and Amorphous Alloys*

In systems where a host metal lattice is disturbed by the presence of lattice disorder, both the energy of the equilibrium state and the saddle-point configuration for H atoms have distributed values, leading to diffusion characteristics peculiar to these systems.

One of the general features of amorphous alloys is that the hydrogen diffusivity D depends on H concentration: D is small at low concentrations, and increases with increasing concentration. For a given H concentration, the diffusivity usually follows the Arrhenius relation. Qualitatively, this can be understood as H atoms enter the most deep-lying states initially, successively filling the higher-lying states of the site-energy distribution. This situation was described quantitatively by a model proposed by *Kirchheim* [3.38] and *Kirchheim* and *Stoltz* [6.205–6.208]. They considered a distribution of site energies, but assumed a single value for the saddle-point energy between all adjacent pairs of sites. This is certainly a drastic simplification of the actual situation, but proved to be very effective in describing the observed migration processes. Later, a partial justification of this approximation was given by *Richards* and *Shinar* [6.209], who demonstrated by simulation calculations that a distribution of site energies has a much larger effect than an equivalent distribution of saddle-point energies on the temperature and frequency dependence of the NMR relaxation time T_1 . A constant saddle-point energy was also found by *McLellan* and *Yoshihara* [6.210] in their analysis of hydrogen diffusion data in V–Ti alloys.

The most comprehensive treatment of hydrogen diffusion in disordered systems that has been made is probably the one by *Brouwer et al.* [6.211] on

Nb–V alloys. They noted that the saddle-point energies in pure V and Nb, derived from the energies in equilibrium configuration and activation energies of diffusion, are closely the same, -0.26 ± 0.01 eV and so would be in Nb–V alloys. Then, the diffusion is described in terms of single-jump processes with an activation energy and a prefactor depending on the configuration of the initial and the final states. Using the site energy of each local configuration determined by other experiments and the constant saddle-point energy, the diffusion coefficient was calculated as a function of temperature over the whole composition of the alloy, yielding results in excellent agreement with experiments.

For more detailed description of diffusion in specific amorphous alloys, the reader is referred to the review article of *Richter et al.* [6.186].

6.5 Theoretical Considerations on the Diffusion Mechanism

6.5.1 Overview

In this section, a brief description is given of the theory of quantum diffusion developed in the last 20 years, with an aim to making clear the conceptual framework of the mechanisms operating at different temperatures.

The concepts involved can be most easily envisaged as an extension of the 2-site tunneling process described in Sect. 5.8.1. In a perfect crystal, many self-trapped states of hydrogen can exist at equivalent interstitial sites, and in consequence they form an energy band of width

$$W \approx 2zJ, \quad (6.75)$$

where z is the coordination number of self-trapped states and J is the tunneling matrix element between neighboring interstitial sites. This energy band is the extension of energy splitting $2J$ in the 2-site tunneling system, and is called a small polaron band.

The migration mechanism is determined by the relative importance of coherent band motion (measured by W) and damping (measured by Γ). At low temperatures where the damping is sufficiently small ($W > \Gamma$), the migration proceeds by coherent tunneling. As temperature is increased to cause overdamping ($W < \Gamma$), the migration proceeds by incoherent hopping of a localized state. In this regime, the migration process regresses into a repetition of successive 2-site hoppings. Finally, at still higher temperatures where many phonons are thermally excited to destroy the polaron band, the self-trapped state becomes only meaningful as an average of configurations fluctuating in the phonon field. The fluctuation can be so large that the coincidence probability of energy levels of self-trapped hydrogen on neighboring sites becomes large enough to allow tunneling to take place – the process called the

phonon-assisted tunneling. In contrast to the diffusivity of self-trapped H in the polaron band state, which decreases with increasing temperature as damping increases, the diffusivity of a bare H atom by the phonon-assisted tunneling increases with temperature. In the following two sections, the migration mechanisms operating in the low- and high-temperature regions are described separately.

6.5.2 Diffusion Mechanisms in the Low Temperature Region: Tunneling in the Polaron Band

In the tight-binding picture, two major quantities that characterize the energy band of self-trapped (small polaron) states of hydrogen are given by $W \approx 2zJ$ for the bandwidth, and

$$M^* = \hbar^2 / Jd^2 \quad (6.76)$$

for the effective mass defined by the energy expression $E = \hbar^2 k^2 / 2M^*$. d is the distance between neighboring interstitial sites.

Using these quantities, the thermal de Broglie wave length λ_{dB} is defined by

$$\lambda_{dB} = \frac{\hbar}{\sqrt{2\pi M^* k_B T}} = \sqrt{\frac{J}{2\pi k_B T}} d. \quad (6.77)$$

(To avoid confusion, in this section we write k_B for the Boltzmann constant.) The mean free path of diffusion l_{diff} can be defined in terms of group velocity $v_g = Jd^2 k / \hbar$ and the scattering time $t_{sc} = \hbar / \Gamma$;

$$l_{diff} = v_g t_{sc} = 2\pi k d \frac{J}{\Gamma} d. \quad (6.78)$$

The temperature dependence of l_{diff} is contained in the damping factor Γ . In the low temperature region, damping is caused by two different quasielastic (nearly energy conserving) processes; the scattering by conduction electrons and by virtual absorption and emission of phonons (the diphonon process), and is written in the form

$$\Gamma = 2\pi(K + K_{dp}) k_B T. \quad (6.79)$$

K is the electron contribution which does not depend on temperature (Sect. 5.8.2), whereas the diphonon contribution K_{dp} decreases rapidly with decreasing temperature as described later in this section. Thus in metals at low temperatures, only the electron contribution should remain effective.

The mechanism of diffusion at low temperatures is classified according to the relative magnitude of λ_{dB} , l_{diff} and d , as shown schematically in Fig. 6.48.

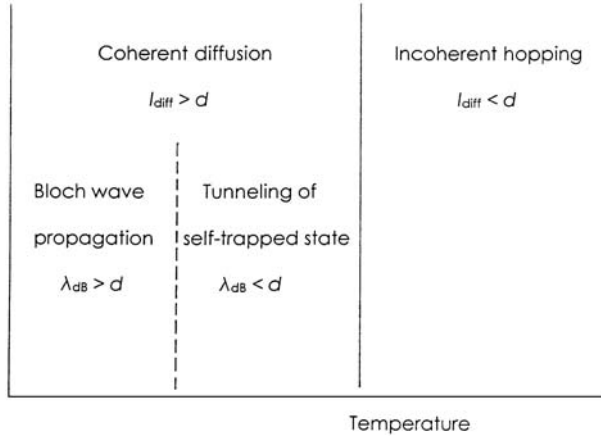


Fig. 6.48. Different regions of low-temperature quantum diffusion; after [6.212]. Diffusion mechanisms are classified according to the magnitude of the de Broglie wavelength λ_{dB} and the diffusion length l_{diff} relative to the inter-site distance d

(1) *Bloch Wave Propagation; $\lambda_{\text{dB}} > d$*

This is the condition for the self-trapped particle to propagate as Bloch waves. The state of the particle should be represented in the momentum space, and the band states are filled up from the bottom. λ_{dB} measures the extension of the wave packet which can be constructed from the band states accessible at a given temperature. At very low temperatures where only the states in a limited range of \mathbf{k} -values close to the bottom are accessible, the wave packet must delocalize due to the uncertainty principle. This condition can be rewritten in the form

$$k_{\text{B}}T < \frac{J}{2\pi} . \quad (6.80)$$

For $J = 10 \mu\text{eV}$, $T < 0.02 \text{ K}$. The formation of Bloch states occurs, if possible, at lowest temperatures. In fact, for self-trapped hydrogen in metals, it has not been observed. The only observation of Bloch wave propagation made so far is the case of muonium in KCl [6.213, 6.214], which is described in Appendix 6B.

(2) *Coherent Tunneling; $\lambda_{\text{dB}} < d < l_{\text{diff}}$*

In this regime, a particle is localized in a single site, and its states should be described by the site representation, but its migration proceeds via coherent tunneling. Since the quantity kd in (6.78) is of the order of, but smaller than 1, we may approximately take $2\pi kd \approx 1$ for simplicity, and write the condition $d < l_{\text{diff}}$ as $2\pi kdJ \approx J > \Gamma$. Then, substituting $\Gamma \approx 2\pi K k_{\text{B}}T$, we obtain the approximate expression for the temperature range

$$\frac{J}{2\pi} < k_B T < \frac{J}{2\pi K} . \quad (6.81)$$

In this range, the state extended over $\sim l_{\text{diff}}$ loses its coherence (phase memory) at average intervals of $\sim h/\Gamma$, and in each event moves an average distance of $\sim l_{\text{diff}}$. The repetition of such events leads to long-range diffusion. Thus, the expression for the diffusivity is given by

$$D \approx \frac{z}{6} \frac{l_{\text{diff}}^2}{t_{\text{sc}}} \quad (6.82a)$$

$$= \frac{z}{6} d^2 (2\pi k d)^2 \frac{J^2}{h\Gamma} \approx \frac{z}{6} d^2 \frac{J^2}{h\Gamma} . \quad (6.82b)$$

(3) *Incoherent Hopping*; $l_{\text{diff}} < d$

This condition, equivalent to $2\pi k d J \approx J < \Gamma$, implies that the tunneling state is strongly damped so that in effect the state should be described by the site representation. In terms of temperature, the above condition defines the range

$$k_B T > \frac{2\pi k d J}{2\pi K} \approx \frac{J}{2\pi K} . \quad (6.83)$$

The migration proceeds via incoherent hopping from site to site, and the diffusivity is given by

$$D = \frac{z}{6} d^2 w , \quad (6.84)$$

where

$$w = \frac{J^2}{h\Gamma} . \quad (6.85)$$

The derivation of this expression is given later.

Comparison of (6.82b) and (6.84, 6.85) shows that, although the underlying mechanisms are different, the diffusivity changes continuously over the region (2) and (3).

There is, however, a possibility that the diffusivity as a function of temperature may show a break somewhere near the boundary of region (2) and (3). This originates from the requirement that the hopping frequency cannot exceed the speed of coherent propagation; $J^2/\Gamma < J$, i.e. $J < \Gamma$. Below the temperature where $J \approx \Gamma$, the hopping frequency should level off to approach a limiting value of $w \approx J/h$. This was actually observed for muons in insulators (e.g. Fig. 6.11), but has not been observed clearly for hydrogen isotopes in metals because large damping due to conduction electrons persists to very low temperatures. We shall here limit ourselves to the cases where the condition $J < \Gamma$ is satisfied, and the self-trapped hydrogen migrates by hopping.

In order to derive a more rigorous expression for the hopping rate, we shall here reproduce the original derivation of *Kondo* [5.309], which treats the problem by a conventional stochastic theory of dissipative processes in

systems having many internal degrees of freedom and a multitude of closely spaced energy levels.

In the present problem, the transition probability from the self-trapped state a to b can be written in the form

$$w = \left\langle \sum_{\beta} \frac{2\pi}{\hbar} |\langle a\alpha | \mathcal{H}' | b\beta \rangle|^2 \delta(E_{\beta} - E_{\alpha}) \right\rangle_{\text{av}}, \quad (6.86)$$

where \mathcal{H}' represents the interaction between the states on two neighboring sites a and b, α, β stand for internal degrees of freedom (electron and lattice states) of the system with an interstitial at a and b, respectively, and $\langle \dots \rangle_{\text{av}}$ represents the thermal average in the initial state at a. E_{α} and E_{β} are energy eigenvalues of the initial and final states, respectively:

$$\mathcal{H}^a \Phi^a \Psi_l^a = E_{\alpha} \Phi^a \Psi_l^a, \quad (6.87a)$$

$$\mathcal{H}^b \Phi^b \Psi_l^b = E_{\beta} \Phi^b \Psi_l^b, \quad (6.87b)$$

and the interaction potential V is defined by

$$V = \mathcal{H}^b - \mathcal{H}^a. \quad (6.88)$$

By use of an integral form for the δ function,

$$\delta(E_{\beta} - E_{\alpha}) = \frac{1}{2\pi\hbar} \int_{-\infty}^{+\infty} e^{i(E_{\beta} - E_{\alpha})t/\hbar} dt, \quad (6.89)$$

(6.86) can be brought into the form

$$w_{\text{ab}} = \frac{J_0^2}{\hbar^2} \int_{-\infty}^{+\infty} \phi(t) dt, \quad (6.90)$$

with J_0 representing the bare matrix element defined by (6.86), and

$$\phi(t) = \left\langle e^{i\mathcal{H}^a t/\hbar} e^{-i\mathcal{H}^b t/\hbar} \right\rangle_{\text{av}}, \quad (6.91)$$

with

$$\langle \dots \rangle_{\text{av}} = \text{Tr}\{e^{-\mathcal{H}^a/kT} \dots\} / \text{Tr}\{e^{-\mathcal{H}^b/kT}\}. \quad (6.92)$$

(Hereafter, the Boltzmann constant is simply written as k .) Thus, the problem is reduced to the calculation of the function $\phi(t)$ for the given Hamiltonians \mathcal{H}^a and \mathcal{H}^b .

Let us write the Hamiltonian \mathcal{H}^a in the form

$$\mathcal{H}^a = \mathcal{H}_0 + V_{el}^a + V_l^a, \quad (6.93)$$

where

$$\mathcal{H}_0 = \sum_{\mathbf{k}, \sigma} \varepsilon_{\mathbf{k}} a_{\mathbf{k}\sigma}^+ a_{\mathbf{k}\sigma} + \sum_{\mathbf{q}} \hbar \omega_{\mathbf{q}} b_{\mathbf{q}}^+ b_{\mathbf{q}} \quad (6.94)$$

and

$$V_{el}^a = \sum_{\mathbf{k}, \mathbf{k}' \sigma} V_{\mathbf{k}\mathbf{k}'}^a a_{\mathbf{k}\sigma}^+ a_{\mathbf{k}'\sigma} , \quad (6.95)$$

$$V_l^a = \sum_{\mathbf{q}} A_{\mathbf{q}}^a (b_{\mathbf{q}} + b_{-\mathbf{q}}^+) . \quad (6.96)$$

The Hamiltonian \mathcal{H}^b is defined similarly.

Using the standard time-dependent perturbation theory, taking \mathcal{H}_0 as the unperturbed state, one can write, up to the second order of the interaction, as

$$\phi(t) = 1 - \text{P} \int \int_{t > t_1 > t_2 > 0} \langle V(t_1) V(t_2) \rangle_0 dt_1 dt_2 \quad (6.97a)$$

$$\approx \exp \left(-\text{P} \int \int_{t > t_1 > t_2 > 0} \langle V(t_1) V(t_2) \rangle_0 dt_1 dt_2 \right) , \quad (6.97b)$$

where

$$V = (V_{el}^b - V_{el}^a) + (V_l^b - V_l^a) \quad (6.98a)$$

$$= V_{el} - V_l , \quad (6.98b)$$

$$V(t) = e^{i\mathcal{H}_0 t/\hbar} V e^{-i\mathcal{H}_0 t/\hbar} \quad (6.99)$$

$$\langle \dots \rangle_0 = \text{Tr} \{ e^{-\mathcal{H}_0/kT} \dots \} / \text{Tr} \{ e^{-\mathcal{H}_0/kT} \} . \quad (6.100)$$

P denotes the omission of a term linear in t contained in the integral. Since the electron and lattice systems are independent, and their Hamiltonians (6.95, 6.96) commute, $\phi(t)$ is factorized as

$$\phi(t) = \phi_{el}(t) \phi_l(t) , \quad (6.101)$$

$$\phi_{el}(t) = \exp \left(-\text{P} \int \int_{t > t_1 > t_2 > 0} \langle V_{el}(t_1) V_{el}(t_2) \rangle_0 dt_1 dt_2 \right) \quad (6.102.a)$$

$$= e^{F_{el}(t)} , \quad (6.102.b)$$

with similar expressions for the lattice part $\phi_l(t)$.

For the lattice, calculations lead to

$$F_l(t) = \sum_{\mathbf{q}} \frac{|A_{\mathbf{q}}^b - A_{\mathbf{q}}^a|^2}{(\hbar\omega_{\mathbf{q}})^2} [(2n_{\mathbf{q}} + 1) - n_{\mathbf{q}}e^{i\omega_{\mathbf{q}}t} - (n_{\mathbf{q}} + 1)e^{-i\omega_{\mathbf{q}}t}] , \quad (6.103)$$

which, for $t \rightarrow \infty$, approaches

$$2S(T) = \sum_{\mathbf{q}} \frac{|A_{\mathbf{q}}^b - A_{\mathbf{q}}^a|^2}{(\hbar\omega_{\mathbf{q}})^2} (2n_{\mathbf{q}} + 1) , \quad (6.104)$$

because the rapidly oscillating terms are averaged out on integration over \mathbf{q} . This is exactly the expression given in the preceding section (5.91), and assumes a nearly constant value $2S(0) = \sum_{\mathbf{q}} |A_{\mathbf{q}}^b - A_{\mathbf{q}}^a|^2 / (\hbar\omega_{\mathbf{q}})^2$, below $T < \theta_D/5$.

For the electrons, calculations similar to the preceding section lead to

$$F_{el}(t) = 2 \sum_{\mathbf{k}, \mathbf{k}'} \frac{|V_{\mathbf{k}\mathbf{k}'}|^2 \cdot |e^{i(\mathbf{k}-\mathbf{k}') \cdot \mathbf{d}} - 1|^2}{(\varepsilon_{\mathbf{k}'} - \varepsilon_{\mathbf{k}})^2} (1 - e^{i(\varepsilon_{\mathbf{k}} - \varepsilon_{\mathbf{k}'})t/\hbar}) . \quad (6.105)$$

After summing over \mathbf{k}, \mathbf{k}' in the region described in Sect. 5.6.1, we obtain [5.309]

$$F_{el}(t) = 2K \ln \left[\frac{\sinh \pi k T t / \hbar}{\pi k T t / \hbar} \sqrt{1 + (\varepsilon_c t / \hbar)^2} \right] + 2iK \tan^{-1}(\varepsilon_c t / \hbar) , \quad (6.106)$$

where

$$\varepsilon_c = k_F d \hbar \omega_0 \quad (6.107)$$

and K is the parameter describing the coupling to conduction electrons, defined by (5.107). For $|t| \gg \hbar/kT$ we have

$$F_{el}(t) = -2K \ln(2\pi k T / \varepsilon_c) + 2\pi K k T |t| + i\pi K \operatorname{sgn}(t) , \quad (6.108)$$

or

$$\phi_{el}(t) = (2\pi k T / \varepsilon_c)^{2K} e^{-2\pi K k T |t|/\hbar} . \quad (6.109)$$

Note that the damping of the state is characterized by the energy

$$\Gamma = 2\pi K k T . \quad (6.110)$$

This is the quantity that has already appeared in Sect. 5.8.2.

Having obtained the functions $\phi_l(t)$ and $\phi_{el}(t)$, we can calculate the hopping rate in different temperature ranges. In the region $T < \theta_D/5$, the lattice contribution becomes nearly constant, viz., $\phi_l(t) \approx \exp[-2S(0)]$, and the hopping rate is obtained, for small K , as

$$w = \left[J_0 e^{-S(0)} \left(\frac{2\pi k T}{\varepsilon_c} \right)^K \right]^2 \frac{\cos \pi K}{\hbar \pi K k T} . \quad (6.111)$$

The expression (6.111) is certainly of the expected form, (6.85). The temperature dependence of the hopping rate predicted by (6.111), $w \propto T^{2K-1}$, is certainly one of the most characteristic features of light-particle diffusion in metals in the low-temperature region. For singly charged interstitials such as hydrogen isotopes, for which $K < 1/2$ [5.313], the hopping rate should become larger at lower temperatures.

There are two additional factors that affect diffusion in the low-temperature range, namely, the diphonon process and the effect of inhomogeneous distribution of energy levels due to static disorder in the lattice.

The importance of the diphonon process, namely, the effect of quadratic coupling of the interstitial energy to the displacements of lattice atoms, was examined by *Kagan* and *Klinger* [5.304], *Fujii* [6.215] and *Kondo* [5.311] among others. The net effect is to introduce an additional renormalization factor $(\pi T/\theta_D)^{K_{dp}}$ to the tunneling-matrix element, and replace K by $K + K_{dp}$ in the expression of the damping factor, (6.79). In contrast to K , the coupling constant K_{dp} is a function of temperature, given by

$$K_{dp} = A_{dp} T^7 \quad \text{for bcc,} \quad (6.112a)$$

$$A_{dp} T^9 \quad \text{for fcc,} \quad (6.112b)$$

and the parameter A_{dp} can be determined by the strength of the quadratic coupling.

At sufficiently low temperatures, $T \ll \theta_D$, A_{dp} quickly approaches 0, and therefore this renormalization effect becomes negligible in comparison to conduction electron effects, but K_{dp} in the damping term may become important towards the high-temperature end of the low-temperature region ($T \sim \theta_D/5$). There, the temperature dependence of the hopping rate should become steeper; $w \propto T^{2K-7}$ or T^{2K-9} .

If the energy of an interstitial on site b is displaced by ε from that of site a , we must include a factor $\exp(-i\varepsilon t/\hbar)$ in the integrand of (6.86). A general expression including this effect was derived by *Kagan* and *Prokof'ev* [5.315]. In the limit of large inhomogeneous broadening, $|\varepsilon| \gg 2\pi K kT$, the expression reduces to

$$w \approx 2 \left[J_0 e^{-S(0)} \left(\frac{\varepsilon}{\varepsilon_c} \right)^K \right]^2 \frac{2\pi K}{\varepsilon} \frac{1}{1 - e^{-\varepsilon/kT}}. \quad (6.113)$$

Comparing this with (6.111), we note that the temperature disappears both from the electron renormalization factor and the density of final states, but enters in the last factor that describes the population difference between the two sites. The last factor becomes ≈ 1 for $\varepsilon > 0$, and $\approx \exp(-|\varepsilon|/kT)$ for $\varepsilon < 0$, yielding on the average an increasing hopping rate with increasing temperature.

Sugimoto [6.216] performed a numerical calculation of the hopping rate assuming several different distributions of ε , and found that, at low temperatures $kT \ll |\varepsilon|$, the hopping rate depends on temperature approximately as

$w \propto T^{2K}$, provided that the thermal equilibrium of interstitials over sites can be attained. If not, the hopping rate becomes independent of temperature.

Sugimoto [6.217], emphasized the distinction between the local hopping rate and the long-range diffusion in the presence of energy disorder. He found that the diffusion coefficient at low temperatures becomes of a thermal-activation type, with the activation energy determined by the highest energy barrier in the most favorable path, and strongly dependent on the structure of the lattice. That is to say, the long-range diffusion is determined by the critical-percolation probability of the bond-percolation problem.

Generally speaking, the presence of energy disorder acts against the formation of a band, and tends to suppress the coherent motion. An attempt to draw a “phase diagram” of diffusion mechanisms on an ε - T plane was made by *Regelmann* and *Schimmele* [6.212].

The overall temperature dependence of the hopping rate deduced from these theoretical considerations is shown in Fig. 6.49. Results of phonon-assisted processes described in Sect. 6.5.3, giving increasing hopping rates in the high-temperature region, are also included in the figure. It may be added that, in insulators where the damping due to conduction electrons is absent ($K = 0$), the hopping rate at low temperatures can be very much higher, and reach the limiting value set by the tunneling frequency. Such an example was shown in Fig. 6.11.

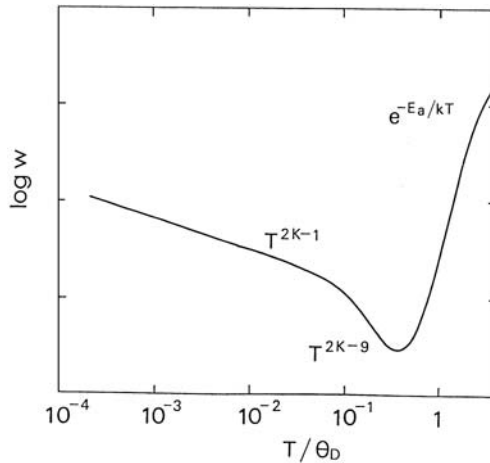


Fig. 6.49. Temperature dependence of the hopping rate (schematic)

6.5.3 Diffusion Mechanisms in the High Temperature Region: Phonon-Assisted Tunneling

As the temperature is raised above $\sim \theta_D/5$, processes involving many phonons become progressively more important.

In order to treat the phonon effects, it is more convenient to write (6.90) in the form

$$w = \frac{1}{\hbar^2} [J_0 e^{-S(T)}]^2 \int_{-\infty}^{+\infty} \phi_{el}(t) e^{f_l(t)} dt \quad (6.114)$$

$$= \frac{1}{\hbar^2} [J_0 e^{-S(T)}]^2 \int_{-\infty}^{+\infty} \phi_{el}(t) [1 + f_l(t) + \frac{1}{2}(f_l(t))^2 + \dots] dt, \quad (6.115)$$

$$f_l(t) = \sum_{\mathbf{q}} [n_{\mathbf{q}} e^{i\omega_{\mathbf{q}} t} + (n_{\mathbf{q}} + 1) e^{-i\omega_{\mathbf{q}} t}]. \quad (6.116)$$

The term in the square brackets of the integrand of (6.115) corresponds, in order, to zero-phonon, one-phonon, two-phonon processes, and so on.

The zero-phonon term has already been considered.

One-phonon processes are forbidden for jumps between equivalent sites in ideal lattices because they violate the requirement of energy conservation. However, a one-phonon process may occur between inequivalent sites, as well as between normally equivalent but energetically disturbed sites.

According to *Teichler* and *Seeger* [6.218], the one-phonon jump rate between site a and b is given by

$$w_{ab} = \frac{[J_0 e^{-S(0)}]^2}{2\pi\hbar^4 \rho v_s^5} \left\{ \frac{d^2 [\text{Tr} \{ \tilde{P}_b + \tilde{P}_a \}]^2}{216\hbar^2 v_s^2} \varepsilon^2 + \frac{[\text{Tr} \{ \tilde{P}_b - \tilde{P}_a \}]^2}{4} \right\} \frac{\varepsilon}{e^{\varepsilon/kT} - 1}, \quad (6.117)$$

where ρ is the mass density, v_s the sound velocity, d the distance, \tilde{P} the force-dipole tensor, and ε the energy difference between site a and b, respectively. The last factor becomes equal to kT for $|\varepsilon| \ll kT$, and $\varepsilon \exp(-\varepsilon/kT)$ or $|\varepsilon|$ for $kT \ll |\varepsilon|$ depending on the sign of ε . The linear T dependence characteristic of one-phonon processes can only be realized under the condition of small energy disorder: $|\varepsilon| \ll kT$. Thus, for jumps between crystallographically nonequivalent sites (e.g., between different types of sites, or between T sites or O sites in a bcc lattice), the second term in the curly bracket of

(6.117) becomes dominant, whereas for jumps between crystallographically equivalent sites (e.g., between T sites or O sites in an fcc lattice), only the first term remains. In this latter case, (6.117) is simplified to

$$w_{\text{ab}} = [J_0 e^{-S(0)}]^2 \frac{d^2 A^2 \varepsilon^2}{12\pi \hbar^6 \rho v_s^7} kT, \quad (6.118)$$

assuming $|\varepsilon| \ll kT$. Here, the component of the force-dipole tensor is written as A .

At temperatures barely above $\sim \theta_D/5$, namely, near the low-temperature end of the high-temperature region, it can be hardly expected that the condition $|\varepsilon| \ll kT \sim 5 \text{ meV}$ be satisfied for jumps between inequivalent sites. Therefore, the linear temperature dependence, if ever observed around this temperature, should be ascribed to jumps between the same type of sites; with energy disorder in an fcc lattice (the first term), but not necessarily with energy disorder in a bcc lattice (the second term). The one-phonon jumps between inequivalent sites occurring at higher temperatures will be obscured by overwhelming contributions of many-phonon processes.

A two-phonon jump is possible between equivalent sites in an ideal lattice. *Flynn* and *Stoneham* [6.11] derived an expression for this process in an isotropic Debye model, and showed that $w \propto T^7$. This temperature dependence holds for jumps between equivalent sites such as T and O sites in an fcc lattice. For jumps in a bcc lattice, where the neighboring T sites are crystallographically inequivalent though energetically equivalent, the temperature dependence becomes $w \propto T^3$ [6.215].

Parenthetically, a word of caution may be added regarding the significance of the T^7 dependence. Since the pioneering work of *Flynn* and *Stoneham* [6.11], the T^7 formula has been utilized frequently in analyzing diffusion data at low temperatures. However, no evidence has been obtained so far for the T^7 or T^3 law. It may be fair to say that the value of the T^7 formula is more historical. In view of the recent development in the theory of quantum diffusion as described here, we strongly caution against the blind application of the T^7 formula without due cognizance of its limitations (see Sect. 6.5).

At still higher temperatures, processes involving many more phonons will become more important leading to w varying more steeply with temperature. The jump rate in this region can be calculated by numerical integration of (6.90), provided we know the relevant quantities, namely, the linear-coupling parameters A_q and the phonon spectrum. Eventually, at sufficiently high temperatures, $T \gg \theta_D$, the expression for the jump rate, (6.90) is reduced to a thermal-activation type [5.231–5.233]. This can be shown as follows.

We expand $F_1(t)$ of (6.103) for short times at $\omega_D t \ll 1$ as

$$F_1(t) \approx G^2 t^2 / \hbar^2 + 4iE_a t / \hbar, \quad (6.119)$$

$$G^2 = \frac{1}{2} \sum_q |A_q^b - A_q^a|^2 (2n_q + 1), \quad (6.120)$$

$$E_a = \frac{1}{4} \sum_{\mathbf{q}} |A_{\mathbf{q}}^b - A_{\mathbf{q}}^a|^2 (\hbar \omega_{\mathbf{q}}). \quad (6.121)$$

For $kT \ll \hbar \omega_D$, the relation

$$G^2 = 4kTE_a \quad (6.122)$$

holds. We note that at $|t| = \omega_D^{-1}$, the real part of (6.19) becomes $(G/\hbar \omega_D)^2$, which is of the order of $S(T)$ and is much larger than unity. Thus, $\phi_l(t)$ decreases practically to zero when $|t|$ reaches ω_D^{-1} . The integration of (6.90) can then be performed as

$$w_{ab} = \frac{J_0^2}{\hbar^2} \int_{-\infty}^{+\infty} \phi_{el}(t) e^{-G^2 t^2 / \hbar^2 - 4iE_a t / \hbar} dt. \quad (6.123)$$

Noting further that the electronic renormalization factor should become close to unity at high temperatures, we integrate (6.123) by putting $\phi_{el}(t) = 1$, and obtain the following result:

$$w = \frac{J_0^2}{\hbar} \frac{\sqrt{\pi}}{2\sqrt{E_a kT}} e^{-E_a/kT}. \quad (6.124)$$

This is the expression often referred to as Flynn–Stoneham’s formula.

This formulation was extended by several authors to include the transitions between the excited states and/or the dependence of J on the local lattice distortion.

Kagan and *Klinger* [5.304] examined the contributions of excited states to the jump rate by using a kinetic equation for the density matrix. They considered only the transitions between the same localized vibrational states of an interstitial on two neighboring sites and expressed the jump rate as a sum of all individual contributions.

Gorham-Bergeron [6.219] took account of the transitions between different localized vibrational states in addition to those between the same vibrational states. By using a simple potential and wave functions of a harmonic oscillator for a hydrogen atom, he calculated the diffusion coefficient based on the Kubo formula, and found that the activation energy decreases slightly with increasing mass, in qualitative agreement with some experimental results on fcc metals.

As the value of J depends sensitively on the local distortion of the lattice, it is necessary for realistic calculations to drop the restriction of the Condon approximation.

Flynn and *Stoneham* [6.11] considered the case in which certain types of lattice relaxation around a moving interstitial may result in large changes of J . This effect is expected to be particularly important in those cases where intervening M atoms exist (as in the case of the O–O jump in the fcc lattice).

They included this effect approximately by assuming that J is negligibly small for lattice deformations smaller than Q_c , and is equal to J_{lim} for lattice deformations larger than Q_c . The expression thus obtained is

$$w = J_{\text{lim}}^2 / 4\hbar (E_a E_{\text{def}})^{1/2} \exp[-(E_a + E_{\text{def}})/kT] , \quad (6.125)$$

where E_{def} is the energy necessary to create the lattice deformation Q_c .

Teichler [6.220, 6.221] performed improved calculations going beyond the Condon approximation and showed that the jump frequency can be written in the form

$$w_{ij} = \frac{1}{\hbar} (\pi / 4 E_a kT)^{1/2} \langle |J_{ij}|^2 \rangle \exp[-(E^j - E^i + 4E_a)^2 / 16 E_a kT] , \quad (6.126)$$

where E^i and E^j are the energy levels of a diffusing atom on site i and j , respectively, and $\langle |J_{ij}|^2 \rangle$ means the thermal average of $|J_{ij}|^2$ over all correlated phonon modes that create fluctuations of the energies E_a , E^i , and E^j . The actual calculation was performed for hydrogen isotopes in an fcc metal Cu, assuming the O-T-O path and including the contributions of the excited states.

The basic assumption underlying the foregoing treatment has been that the transition to a neighboring site occurs with a small probability of tunneling during the time when the energy levels of the interstitial on adjacent sites are brought into coincidence by lattice vibrations. Thus, (6.124) is essentially a product of the probability of occurrence of the coincidence event and the probability of tunneling which, when treated as perturbation, is proportional to J^2 . The activation energy is the energy necessary to create the coincidence configuration. This nonadiabatic process is properly called the thermally activated tunneling.

If, on the contrary, the time required for the interstitial to adjust itself to the displacement of lattice atoms, \hbar/J , is shorter than the minimum period of lattice vibrations, ν_D^{-1} , namely, $J > \hbar\nu_D$, the transition to the neighboring site occurs adiabatically. The jump frequency is then written as

$$w \approx \nu_D e^{-E_a/kT} , \quad (6.127)$$

where again E_a is the energy necessary to bring the interstitial from self-trapped state to a coincidence, saddle-point configuration.

An expression that describes, at least approximately, the crossover from nonadiabatic to adiabatic regimes of interstitial jumps can be derived on the basis of the occurrence-probability concept. *Holstein* [5.233], and later *Emin et al.* [6.222], gave the jump rate in the form

$$w = \sum_{i,j} \langle p_{ij} P_{ij} \rangle \exp(-E^i/kT) / \sum_i \exp(-E^i/kT) , \quad (6.128)$$

where p_{ij} is the probability of occurrence of the coincidence event between the occupied level (i) on one site and another unoccupied level (j) on an

adjacent site, and P_{ij} is the transfer probability of hydrogen atom from i to j . According to the results of classical theories [6.223–6.227], P_{ij} can be written as

$$P_{ij} = \frac{1 - \exp(-\alpha_{ij})}{1 - \frac{1}{2} \exp(-\alpha_{ij})}, \quad \alpha_{ij} = \frac{2\pi}{\hbar} |J_{ij}^2 / \dot{\epsilon}_{ij}| \quad (6.129)$$

where J_{ij} and $\dot{\epsilon}_{ij}$ are, respectively, the tunneling-matrix element and the rate of change of the energy difference of the two levels, both evaluated at the coincidence. Note that $P_{ij} = 2\alpha_{ij}$ when J_{ij} is small ($\alpha_{ij} \ll 1$), and $P_{ij} = 1$ when J_{ij} is sufficiently large ($\alpha_{ij} \gg 1$). The latter case is called adiabatic, since there the interstitial adjusts adiabatically to the lattice fluctuation throughout the coincidence crossing event.

One of the important features of the adiabatic transition is that the frequency factor is nearly equal to ν_D and is independent of the mass of the interstitial. This is very different from the case of nonadiabatic transitions for which the frequency factor is much smaller than ν_D , being proportional to J^2 and, therefore, strongly dependent on the isotope mass.

As the tunneling-matrix element J between excited states is larger because of more extended wave functions, the adiabatic transition becomes more effective at high temperatures, where the interstitial can be thermally excited to higher-energy states. A large frequency factor will more than compensate for the extra Boltzmann factor describing the population in the excited states. An Arrhenius plot will show an upward bend in going from nonadiabatic jumps between ground states to adiabatic jumps between excited states.

At sufficiently high temperatures where the interstitial can be excited to energy levels close to the top of the potential barrier, the adiabatic transitions become practically the same as classical over-barrier jumps.

The limiting behavior of interstitial diffusion at high temperatures is, therefore, very simple; the jump frequency becomes nearly the same for all the isotopes and host metals (note $\theta_D = \hbar\nu_D/k = 300 \pm 100$ K for all metals of our interest). It is only when correlated successive jumps increase the effective jump distance that the diffusion coefficient can exceed the limiting value $D \sim d^2\nu_D$. Diffusion in this regime has not been studied theoretically so far.

In this and the preceding section, we have described the diffusion mechanisms of light interstitials in metals which become operative in going from low temperatures to high temperatures. Regarding the effects of conduction electrons and phonons, we followed closely the explanations of Kondo, putting more emphasis on their physics than on mathematical details. For more rigorous, consistent treatment of the problem, see [5.315–5.318, 5.323, 6.19, 6.20].

One might feel a little uneasy if one notices that the formulae of the jump rate presented here do not go over smoothly to a classical expression as $\hbar \rightarrow 0$. In fact, such a formulation has been made in terms of an extended WKB approach employing path-integral techniques. In the theory of

Hedegård [6.228], the system consisting of an interstitial and its environment (conduction electrons and phonons) is described by a density matrix, which, after integration over electron and phonon coordinates, is reduced to the density matrix for the interstitial in the form of a sum over particle histories – the path integral. This is in close analogy with a similar microscopic description of classical diffusion, namely, a random-walk model in which the particle distribution function can be written as a weighted sum over histories. In this way, the quantum description naturally goes over to a classical one in the high-temperature limit.

This alternative approach, though appealing in some respect, shall not be described any further here, simply to avoid excessive mathematical complexities. The interested reader may trace the conceptual development along this line of approach by referring to the following papers [5.247–5.250, 6.229–6.236].

6.6 Critical Analysis of the Experimental Data in Terms of the Quantum Theory of Diffusion

6.6.1 Diffusion of Positive Muons and Hydrogen Isotopes at Low Temperatures: Tunneling in the Polaron Band

The temperature dependence of the muon diffusion data for Cu [6.108–6.110] and Al [6.111] in the low-temperature region was re-evaluated by *Storchak* and *Prokof'ev* [6.20], and the following values are obtained for the strength of coupling to the conduction electrons: $K = 0.22$ for Cu and $K = 0.32$ for Al. The quality of the fit is not easy to evaluate in Al because the jump rates, being too fast for ordinary μ SR technique, has been derived by indirect methods. However, these values of K do indicate that the coupling to conduction electrons is stronger in these fcc metals than in bcc Nb. This is primarily due to the difference of local electron densities in the interstitial region.

One of the most important issues of muon diffusion at low temperatures is the effect of superconductivity. Unlike the case of H and D in metals, where the effects of superconductivity were observed only for the local tunneling process (Sect. 5.8), for muons the effects were observed for the long-range migration of polaron-band states. Indications of superconducting effects were first observed in dilute alloys of Al [6.237–6.239], and later, more unambiguously in pure Ta [6.240]. These observations provided an ultimate experimental proof of the Kondo-Yamada's theory of electron-muon coupling in metals. Details of superconducting effects on μ^+ diffusion are deferred to the following review papers [6.20, 6.241]

Let us make a critical comparison of the magnitude of the jump rates observed for μ^+ in Cu and Al, and H trapped by O in Nb. At 7 K, where the temperature ranges of the measurements barely overlap, the jump rate of μ^+ in Cu and Al is smaller by nearly 10^6 and 10^3 times, respectively, than

that of H trapped by O in Nb. By approximately evaluating the renormalization factors f_{el} and f_l , bare tunneling matrix elements J_0 can be estimated from experimental values of J at low temperatures. The results are shown in Table 6.7. Here, the lattice renormalization factor $f_l = \exp(-S(0))$ for μ^+ in Cu and Al, evaluated by *Kondo* [6.242] and *Hartmann et al.* [6.111] from high-temperature data was adopted⁶

Table 6.7. Parameters describing the tunneling motion of positive muons in Al and Cu deduced from μ SR data. Results for H in Nb are included for comparison

Isotope	Metal	$J[\mu\text{eV}]$	K	f_{el}	f_l	$J_0[\text{meV}]$
μ^+	Cu	$\sim 0.01^a$	0.22^a	0.21^b	$\approx 0.011^c$	~ 0.004
μ^+	Al	$\sim 0.3^a$	0.32^a	0.09^b	$\approx 0.11^c$	~ 0.03
H(trapped by O)	Nb	115	0.055	0.78	0.034	4.3

^aRe-evaluated by *Storchak and Prokof'ev* [6.20] from the reported data [6.108–6.111]. ^bEvaluated at 7 K, by using approximate values of $k_F d$, and $\hbar\omega_0 = 830$ and 1008 meV for μ^+ in Cu and Al (observed $\hbar\omega_0$ for H in Ni multiplied by $\sqrt{M_H/M_\mu} \approx 3$, and scaled by the lattice parameter). ^cObtained by fitting to high-temperature data; see text.

Comparison of the results shows that J_0 's in Cu and Al are much smaller than in Nb. Generally speaking, the tunneling matrix element is expected to be smaller in fcc lattices than in bcc lattices because the distance between neighboring interstitial sites (O sites in fcc and T sites in bcc) is generally larger, and a potential barrier formed by two intervening metal atoms should make the overlap of the interstitial wave function even smaller. For μ^+ in Cu, the value of J_0 , thus deduced, is in reasonable agreement with the theoretical estimate of *Teichler* [6.243] $J_0 = 0.011$ meV. The relative magnitudes of J_0 in Al and Cu are, however, not understandable simply in terms of the distance between neighboring sites, the distance in Al is, in fact, longer than in Cu by as much as 12%. Possibly, smaller ion cores of Al in comparison to Cu lead to smaller undulations of the adiabatic potential for μ^+ in Al.

We shall next examine the diffusion data of hydrogen isotopes, H, D, T in Ta, derived from quench-recovery experiments (Fig. 6.14) [6.20]. Comparison with the data on H trapped by O in Nb is particularly useful. At $T = 20$ K, near the minimum of the diffusion jumps, the jump rate of H in

⁶ The lattice renormalization factor can also be estimated from the activation energy in the high-temperature region by use of the approximate relation

$$S(0) = 5E_a/2\hbar\omega_D. \quad (6.130)$$

This can be obtained from (6.104, 6.121) by noting that $|A_q^b - A_q^a|^2 \propto q^3$ in the long-wave limit for μ^+ in an fcc lattice.

Ta calculated from the diffusion coefficient of $D \approx 10^{-8 \pm 1} \text{ cm}^2 \text{ s}^{-1}$ is $w \approx 2 \times 10^{-8 \pm 1} \text{ s}^{-1}$, which is $10^{3 \pm 1}$ times smaller than H trapped by O in Nb. Then, on the assumption that f_l [5.306] as well as f_{el} have nearly the same value in Nb and Ta, it follows that the effective J_0 of H in Ta is $10 \sim 10^2$ times smaller than H trapped by O in Nb. Considering the similarities of the state of hydrogen atoms in these two metals (see Chap. 2), such a large difference of J_0 might appear improbable. In fact, this apparent discrepancy is largely removed by taking the following two factors into account. First, a relatively higher concentration of hydrogen in the quench-recovery experiments should induce large energy disorders in the specimens. Then, the diffusion coefficient for the long-range migration, being determined by the probability of path percolation [6.217, 6.228], should become much smaller than in a perfect lattice. Even when an energy disorder is not that large, it causes the smearing of energy levels, and reduces the effective value of J_0 . Second, the distance between neighboring T sites must be shorter in the trapped configuration than that in the free state. If we take as a crude measure that the combined effect of these two factors is to reduce the effective J_0 by 1/10, the J_0 of H in the free state in Ta becomes 1/10 \sim 1 of that in Nb. This is consistent with the results of the theoretical calculation which predicts the J_0 of H in Ta to be \sim 1/3 of that in Nb (Table 5.19) [5.303].

The isotope dependence of the diffusion coefficient in Fig. 6.14, namely, that D is reduced by every two orders of magnitude in the order H, D, T, indicates that J_0 is reduced by 10 and 10^2 times in going from H to D and T. This is again in excellent agreement with the calculation (Table 5.19) [5.303].

In summary, the overall consistency of the above discussions strongly suggests that, in spite of some inherent ambiguities in the analysis of quench-recovery experiments, the diffusion data at low temperatures thus extracted are essentially correct and provide evidence for the dominance of zero-phonon tunneling processes for all hydrogen isotopes in Ta. This conclusion is particularly significant if one notices that for a given isotope of hydrogen J_0 is expected to be the smallest in Ta among all bcc transition metals. (Ta has the largest lattice parameter.) We may conclude with fair confidence that, below ~ 70 K, the diffusion of all hydrogen isotopes in bcc transition metals proceeds via zero-phonon tunneling processes, and is practically temperature-independent. Note, in particular, that this poses an intrinsic restriction on the quenchability of hydrogen atoms in the dispersed state.

Based on this picture of diffusion in the low-temperature range and the calculated values of J_0 , crude estimates of the diffusion coefficient have been made on H and D in V and Nb [6.20].

6.6.2 Diffusion of Positive Muons and Hydrogen Isotopes at High Temperatures: Phonon-Assisted Processes

The linear- T dependence characteristic of a one-phonon process has been extracted for μ^+ diffusion in Al in the range of 2–20 K [6.111]. As explained

in Sect. 6.5.3, this process is forbidden for jumps between O sites in fcc lattices. Of the two possible mechanisms, the effect of energy disorder in the lattice was discarded because of the observed insensitivity to alloying. The only possible mechanism that remains is the jump between O and T sites having an energy difference smaller than $kT \sim 1$ meV. Such a small energy difference between different types of sites is very unlikely, and could be realized in very rare cases. The linear- T dependence extracted for Al might possibly be the consequence of a force-fitting analysis of the experiment. No linear- T dependence has been observed in any other case.

The temperature dependence characteristic of two-phonon processes, $\propto T^3$ in bcc and $\propto T^7$ in fcc, has never been observed experimentally. To put it more properly, the two-phonon process, if that ever happens, has not been isolated experimentally from other many-phonon processes.

At higher temperatures, the data compiled in Fig. 6.8 and Table 6.2 show that the jump rate is described by a thermal-activation type formula, sometimes having different activation energies in different temperature ranges. Among them, the low-temperature segment for H in Ta (Fig. 6.8) can be interpreted unambiguously as being due to the non-adiabatic tunneling between the ground states. The observed activation energy $E_a = 42$ meV is in reasonable agreement with the calculated value: $E_a = 31$ meV [5.303] or 21 meV [5.237]. The observed value of the pre-exponential factor, $D_0 = 2.8 \times 10^{-6} \text{ cm}^2 \text{ s}^{-1}$, is also consistent with this interpretation. In order to show this, let us calculate the value of J_0 from the observed D_0 and compare it with theoretical values. The pre-exponential factor for the jump frequency, $w_0 = (24/a^2)D_0$ for a bcc metal, can be written as

$$w_0 = \frac{J_0^2}{2\hbar} \sqrt{\frac{\pi}{kTE_a}}. \quad (6.131)$$

Substituting appropriate values, $w_0 = 6.2 \times 10^{-10} \text{ s}^{-1}$ (from D_0), $E_a = 42$ meV, $kT = 10$ meV ($T \sim 120$ K), we obtain $J_0 = 1.0$ meV. This value is in excellent agreement with the calculated value of *Sugimoto* and *Fukai* [5.303] $J_0 = 1$ meV (Table 5.19). The value is also consistent with the one deduced from the low-temperature data in Sect. 6.1.1.

Before undertaking a more extensive comparison between experiments and theory, we must examine possible contributions of high-energy configurations in tunneling processes. There may be a multitude of configurations that cost higher energies for creation but possess larger values of J_0 .

Klamt and *Teichler* [5.237] examined this problem and found that higher-energy configurations do indeed contribute significantly to the overall tunneling process. An example of the dependence of J_0 on the increment of saddle-point (SP) energy is shown in Fig. 6.50 for the tunneling between the ground states of H on T sites in Nb and Ta. The increase of the SP energy by $\Delta e_{\text{sp}} = 10$ meV leads to the enhancement of J_0 by 7 and 4 times in Nb and Ta, respectively. They fitted this variation to a simple form:

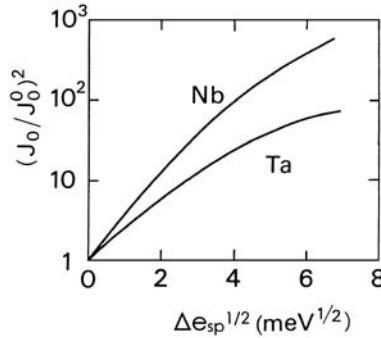


Fig. 6.50. Increase of the tunneling-matrix element between the ground states of H on adjacent T sites in Nb and Ta due to lattice activation by Δe_{sp} above the saddle-point energy [5.237]

$$J = J_0^0 \exp(g_1 \Delta e_{sp}^{1/2} - g_2 \Delta e_{sp}) , \quad (6.132)$$

and gave the coefficients g_1 and g_2 , in addition to J_0^0 , the value of J_0 for the lowest-energy SP configuration.

At high temperatures, the tunneling between the excited vibrational states may become increasingly more important. Table 6.8 lists the values calculated for the energy of excitation to the state ν , Δe_ν , the SP energy e_{sp} , the tunneling-matrix element for the transition $\nu \rightarrow \nu$ on adjacent sites via lowest-energy SP configuration, J^0 , and the parameters describing its dependence on the energy of the SP configuration, g_1 and g_2 [5.237].

Using these values, *Klamt* and *Teichler* [5.237] calculated the temperature dependence of the diffusion coefficient for H and D in Nb and Ta. The gist of their calculation lies in the consistent treatment of the transition rate encompassing the adiabatic and the nonadiabatic regions by taking into account the velocity of the coincidence configuration. The contributions of asymmetric transitions, $\nu \rightarrow \nu'$, were also included. The results of their calculation are shown in Fig. 6.51. Although the agreement with the observation is not quite satisfactory, the overall features are fairly well reproduced, especially the breaks observed for H in Nb and Ta. The lower-temperature legs in these cases come essentially from the transitions between the ground states, and the higher-temperature ones from the transitions via the excited states. The reason why the calculations tend to overestimate the diffusion coefficient is not well understood. Probably, they attached excessive weights to particular higher-energy paths having large J_0 values in taking the average over all possible paths.

A way to make an improvement on this point is to look more closely into the contributions of many different modes of lattice deformation. *Schober* and *Stoneham* [6.244] pointed out that some band-mode vibrations of H atoms (described in Sect. 5.4), with their low frequencies and their amplitudes strongly enhanced by resonant-like coupling to host vibrations, could

Table 6.8. Tunneling-matrix element for diagonal transitions J_ν (from state ν to state ν on adjacent sites) [5.239]. J_ν for configurations close to, but higher in energy by Δe_{sp} than the saddle-point configuration (with energy e_{sp}) is parametrized as $J_\nu^0 = \exp(g_1 \Delta e_{\text{sp}}^{1/2} - g_2 \Delta e_{\text{sp}})$. The activation energy for the transition $\nu \rightarrow \nu$ is given by $\Delta e_\nu + e_{\text{sp}}$

System	Transition	$\Delta e_\nu + e_{\text{sp}} [\text{meV}]$	$J_\nu^0 [\text{meV}]$	$g_1 [\text{meV}^{-1/2}]$	$g_2 [\text{meV}^{-1}]$
H in Nb	0-0	30	0.17	0.049	0.9
	1X-1X	138	16.5	0.013	0.17
	1Y-1Y	142	12.0 ^a	0.013 ^a	0.17 ^a
	2X-2X	220	50.0 ^a	0.001 ^a	0.0 ^a
D in Nb	0-0	27	0.007	0.012	0.68
	1X-1X	108	2.05	0.037	0.56
	1Y-1Y	135	1.95	0.024	0.35
	2X-2X	177	12.5	0.008	0.11
H in Ta	0-0	20.6	0.22	0.027	0.52
	1X-1X	127	9.9	0.02	0.24
	1Y-1Y	135	8.0 ^a	0.02 ^a	0.24 ^a
	2X-2X	210	50.0 ^a	0.001 ^a	0.0
D in Ta	0-0	16.5	0.015	0.031	0.8
	1X-1X	95	1.8	0.024	0.47
	1Y-1Y	121	1.0	0.018	0.34
	2X-2X	165	9.9	0.017	0.19

^aEstimated approximately.

be playing an important role in the region of non-adiabatic transitions, 50–300 K. They demonstrated this by performing a model calculation for H and D in Nb.

Such a line of study has been pursued further by *Teichler* [6.243] by examining the correlation between the vibrations of hydrogen and metal atoms and the inter-site motion of a hydrogen atom. The effects of the correlation were found to modify the tunneling-matrix element significantly, especially through virtual transitions to the higher-energy states induced by lattice vibrations.

Some of the results obtained for the effective tunneling matrix element for the transition between the ground states are listed in Table 6.9.

Let us come back to the interpretation of general diffusion behaviors in the high-temperature region. Consider first the bcc metals. One of the most conspicuous features to be noted in Fig. 6.8 is that, in the high-temperature limit, the diffusion coefficients of all isotopes in all bcc metals converge to a common value $D_0 = (4 \pm 1) \times 10^{-4} \text{cm}^2 \text{s}^{-1}$. This corresponds to $w_0 = (24/a^2)D_0 = 1 \times 10^{13} \text{s}^{-1}$, a value very close to the Debye frequency, $\nu_D = k\theta_D/h \approx 6 \times 10^{12} \text{s}^{-1}$. From this, we may readily conclude that in all the cases shown in Fig. 6.8, except the lower-temperature legs of H in Nb and

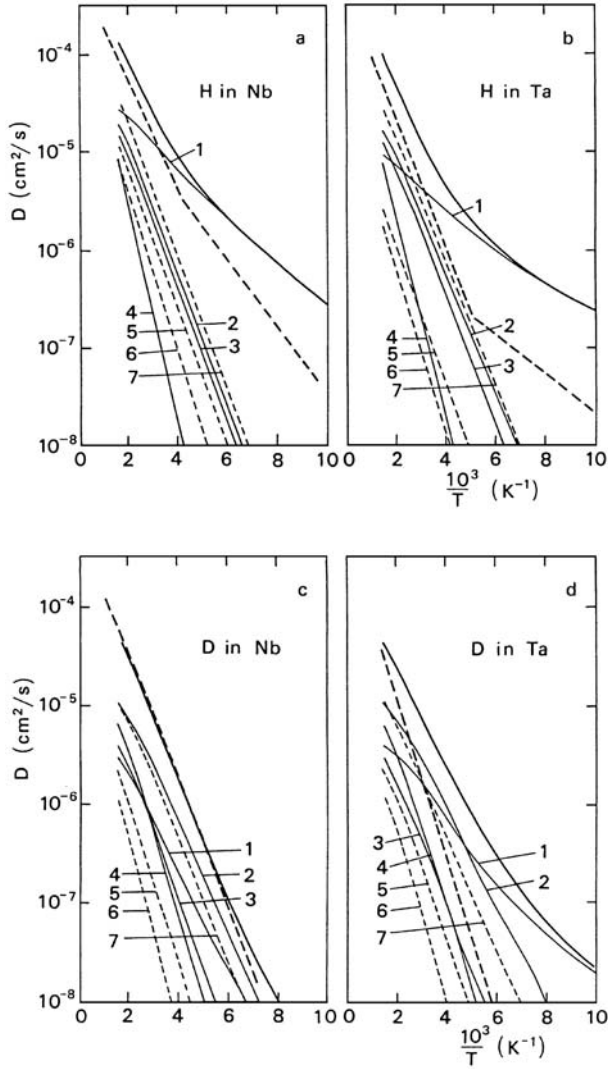


Fig. 6.51. a–d. Calculated diffusion coefficients of H and D in Nb and Ta. Partial contributions are given by *thin lines*: 1) 0–0; 2) 1X–1X; 3) 1Y–1Y; 4) 2X–2X; 5) 0–1X; 6) 0–1Y; 7) 1X–1Y. The *dashed lines* indicate the experimental data [5.237]

Ta, the diffusion proceeds via adiabatic processes. The calculation of *Klamt* and *Teichler* [5.237] showed that, in Nb and Ta, the adiabatic transitions occur between the excited states. For H in V and Fe, we infer that the adiabatic transitions occur even between the ground states. The criterion for the adiabatic transition, $J_0 > h\nu_D$, is not satisfied by $J_0 = 10$ meV for H in V calculated for the lowest-energy SP configuration [5.88], but may be easily

Table 6.9. Effects of correlated motion of H and lattice atoms on the tunneling matrix element between the ground states in adjacent sites [6.243]

Isotope	Metal	$J_0[\text{meV}]$		
		Without Correlation	With Correlation	
			$T = 0$	$T = \theta_D$
H	Nb	0.30	0.70	1.90
D	Nb	0.03	0.10	0.30
μ^+	Cu	0.011	0.015	0.027

satisfied if we allow for higher-energy SP configurations. Since the observed activation energy is higher than the calculated SP energy by as much as 25 meV, the tunneling matrix elements for such higher-energy configurations are expected to be significantly larger. In Fe, which has a lattice parameter 3% smaller than V, the tunneling-matrix element is expected to be even larger and adiabatic transitions more easily realized than in V.

Finally, it may be added for the sake of completeness that a steep rise of the Arrhenius plot towards the high-temperature end of Fig. 6.23 is believed to be the result of the occurrence of correlated jumps. This has been already described in Sect. 6.4.1.

For fcc metals, no reliable calculations of J_0 being available, only qualitative discussions could be made for interpreting the experimental results. We note, first of all, that the diffusion coefficients at high temperatures, excepting the steep rise at the highest temperatures, extrapolate to a common value, $D_0 = (4 \pm 2) \times 10^{-3} \text{ cm}^2 \text{ s}^{-1}$ (Fig. 6.9), indicating that the adiabatic transitions dominate at high temperatures. In Cu and Ni, all the Arrhenius plots for the three isotopes go straight down to low temperatures. This leads us to a picture that only the highly excited states near the top of the potential barrier having large enough values of $J_0 (\gg h\nu_D)$ contribute to the inter-site transition and other lower-lying states practically do not. In the case of H in Pd, existence of a break in the Arrhenius plot suggests that non-adiabatic transitions between the lower-energy states occur at lower temperatures, similar to the case of H in Nb and Ta.

Summing up all the discussions presented above, we may conclude that a consistent understanding is now being established for the mechanism of diffusion of hydrogen isotopes (including μ^+) in metals.

Appendix 6A. Tunneling Chemical Reaction in Solid Hydrogen

There are increasing pieces of evidence that chemical reactions involving hydrogen take place at liquid He temperatures where the rate of any thermal activation processes extrapolated from high temperatures should become extremely slow to be observable. This type of chemical reaction, briefly called tunneling reaction, is believed to have played a crucial role in the formation of light molecules, e.g. CH_4 , C_2H_4 , CHO , H_2O , NH_3 , HCHO , etc. . . . in space. The amount of these molecules in interstellar clouds, being much higher than expected from gas-phase reactions, has been shown by *Hiraoka et al.* [6.245–6.248] to be explained by tunneling reactions on the surface of interstellar dust grains.

The formation of molecules from free H atoms in solid H_2 is a prototype of such tunneling reactions. *Katunin et al.* [6.249] produced a sample of $\text{H}_2 + \text{H}$ mixture by co-deposition of molecular and atomic hydrogen on a sapphire plate, and measured the intensity of ESR signal of atomic H as a function of time. The temporal variation is just what is expected for the reaction



for which the rate equation is

$$\frac{d[\text{H}]}{dt} = -k_{\text{H}}[\text{H}]^2. \quad (6\text{A.2})$$

The reaction rate here should be determined by the diffusion of H atoms in solid H_2 .

The Arrhenius plot of the rate constant k_{H} is shown in Fig. 6A.1a. The reaction is a thermal-activation type above $T \sim 4.5 \text{ K}$ with the activation energy of $9 \pm 1 \text{ meV}$, but becomes nearly constant below this temperature.

The results of the experiments of *Miyazaki* [6.250] and *Kumada et al.* [6.251] on X-ray irradiated HD showed a very similar behavior. In these experiments, free D atoms were created by X-ray irradiation, and subsequently transformed into D_2 molecules by the transfer reaction, viz.



The rate equation takes the form

$$\frac{d[\text{D}]}{dt} = -k_{\text{D}}[\text{HD}] \cdot [\text{D}]. \quad (6\text{A.5})$$

The Arrhenius plot of the rate constant k_{D} is shown in Fig. 6A.1b. Above $\sim 5 \text{ K}$, the reaction is of thermal activation type, with the activation energy

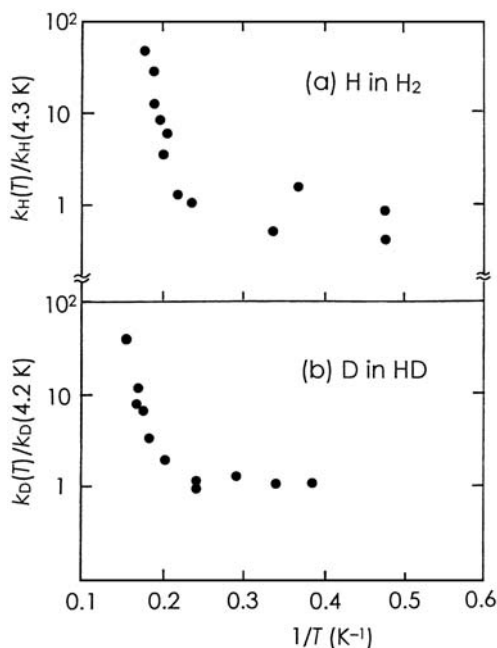
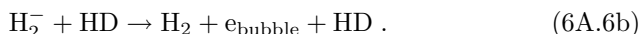


Fig. 6A.1. Arrhenius plot of the reaction rate constant for (a) H in solid H_2 [6.249] and (b) D in solid HD [6.250,6.251]. The values are normalized at liquid He temperature

of 8 ± 1 meV, whereas it becomes completely temperature-independent below 4.2 K.

These results indicate very clearly that both the migration of H in H_2 and D in HD are controlled by tunneling below $4 \sim 5$ K.

More detailed experiments were performed recently, using para- H_2 , which owing to the absence of total nuclear spin (vanishing hyperfine interactions) gives a very narrow ESR signal of H_2^- created by X-ray irradiations [6.252]. It turned out that the rate of decay of H_2^- is accelerated by the presence of HD, from which the following two-step reaction was deduced.



The radiation-induced H_2^- is transported from site to site by successive transfer of an electron, and finally annihilated by forming an electron bubble (an isolated electron) near the site of HD. The reaction $\text{H}_2^- + \text{HD} \rightarrow \text{H}_2 + \text{HD}^-$, being endothermic, cannot happen at low temperatures. Note that in reaction (6A.6a), the entity which is actually transferred is composed of an electron and a surrounding distortion field – a typical polaron.

The observed reaction rate is plotted against temperature in Fig. 6A.2. The overall shape is very similar to other known cases of quantum diffusion of hydrogen isotopes including muons (cf. Figs. 6.11, 6.14). In the low temperature section ($T < 3$ K), where the rate constant varies in proportion to temperature and its magnitude is reduced by the addition of ortho- H_2 , the rate-controlling mechanism is concluded to be the one-phonon process caused by the energy disorder introduced by impurity o- H_2 . The process between 3 \sim 5 K is due to incoherent hopping caused by a few-phonon scattering, and the process above ~ 5 K is a thermally activated process with an activation energy of ~ 8 meV. The local configuration of H_2^- was elucidated by ENDOR measurements, but estimation of tunneling parameters has not been made.

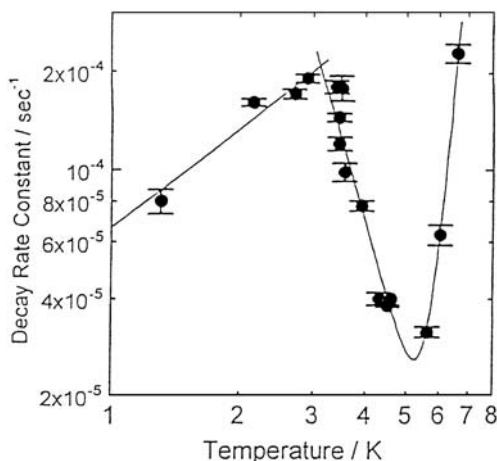


Fig. 6A.2. Temperature dependence of the decay rate constant of H_2^- in X-ray irradiated solid p- H_2 , plotted in log-log scale [6.252]

The richness of atom tunneling phenomena in wide areas of science is fully described in a recently published book “*Atom Tunneling Phenomena in Physics, Chemistry and Biology*” [6.253].

Appendix 6B. A Muonium Atom in the Bloch State

Recently, evidence for the formation of Bloch states was obtained for muonium (Mu) in KCl by *Kadono et al.* [6.213, 6.214]. There are two advantages for the choice of this system. First, rather large tunneling effects are expected in this case because in addition to low mass of μ^+ , the charge neutrality of Mu should create minimal disturbances in the surrounding lattice. Second, the application of ESR technique (MuSR) allows measurements of very short correlation times τ_C expected for large tunneling probabilities.

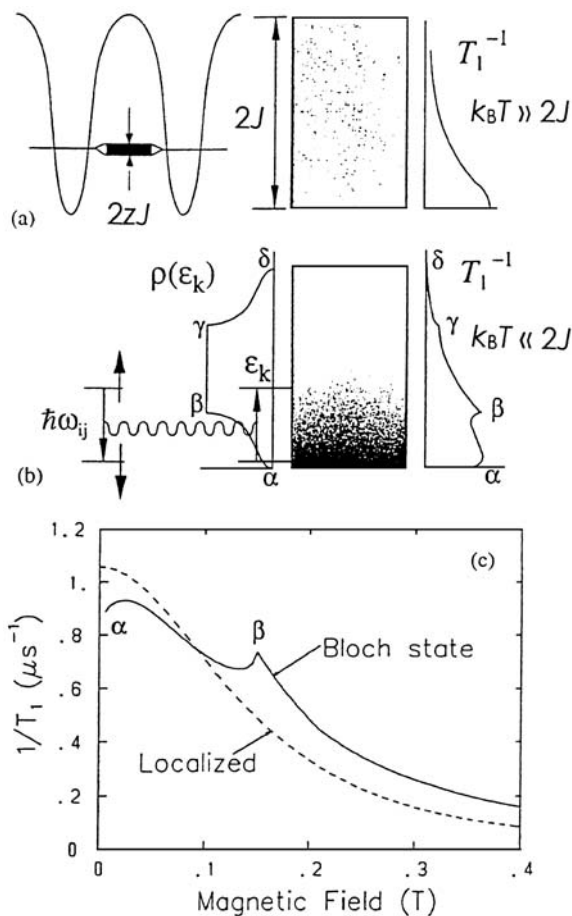


Fig. 6B.1. (a) Tunneling matrix element J of the Mu polaron state and the width of the polaron band $W = 2zJ$. When $k_B T \gg 2J$, the Mu is localized in space and the site-representation is appropriate. (b) When $k_B T \ll 2J$, the Mu is in a Bloch state, leading to the spin relaxation by transfer of the Zeeman energy $\hbar\omega_{ij}$ to Mu band energy ϵ_k . The van Hove singularities (labeled as $\alpha - \delta$) are reflected in the field dependence of the relaxation rate $1/T_1$. (c) Calculated $1/T_1$ for the Mu in the Bloch state, assuming a simple cubic band with $2J = 0.18$ K (solid curve). One can see a dip and peak corresponding to the points α and β in the Mu density of states [6.214]

In order to discuss the possibility of Bloch state formation based on MuSR experiments, it is necessary to examine closely how the “jump frequency” or the “hopping rate” is determined by relaxation time measurements.

The reported data of Fig. 6.11 [6.213] suggest that the polaron band is formed below ~ 10 K. By substituting the asymptotic value of τ_C at low

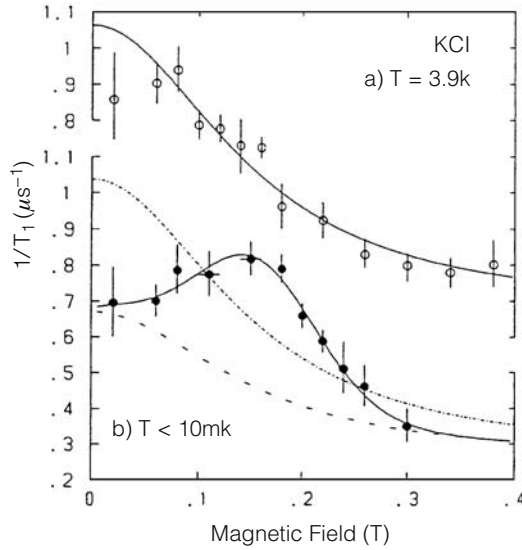


Fig. 6B.2. Muon spin relaxation rate as a function of magnetic field strength for Mu in KCl (a) at 3.9K and (b) below 10 mK. A broad peak at around 0.15 T, observed only at low temperatures, is believed to reflect the van Hove singularity of the Mu band [6.123]

temperatures into the expression due to *Kagan* and *Prokof'ev*, $\hbar/\tau_C \approx 2\sqrt{2J}$ [6.254], the tunneling matrix element is estimated at $2J \approx 22 \mu\text{eV}$ (0.26 K).

It must be noted, however, that even in the region where the hopping rate levels off, the picture of localized Mu undergoing occasional tunneling is valid as long as the temperature is high enough for Mu to occupy all the possible energy eigenstates in the Mu energy band (i.e. $k_B T \gg 2J$). When one enters the temperature region $k_B T \ll 2J$, the situation becomes completely different. The Mu begins to occupy energy eigenstates close to the bottom of the band, leading to the delocalization in space due to Heisenberg's uncertainty principle.

The longitudinal relaxation rate $1/T_1$ in MuSR is caused by fluctuating local magnetic fields $H(t)$ acting on the Mu electron,

$$T_1^{-1} = \delta_{\text{ex}}^2 \sum_{i,j} a_{ij} \int G(t) e^{i\omega_{ij}t} dt = \delta_{\text{ex}}^2 \sum_{i,j} a_{ij} C(\omega_{ij}) , \quad (6B.1)$$

where $\delta_{\text{ex}}^2 = \langle H(0) \rangle^2$, is the time correlation and $C(\omega)$ is the spectral density with ω_{ij} the Zeeman frequency corresponding to the applied field.

In the hopping regime, $G(t)$ is given to a good approximation by

$$G(t) = \frac{\langle H(t) H(0) \rangle}{\langle H(0) \rangle^2} = \exp(-t/\tau_C) , \quad (6B.2)$$

and hence,

$$C(\omega) = \frac{\tau_C}{1 + \omega_{12}^2 \tau_C^2} \equiv C_L. \quad (6B.3)$$

In the regime of Bloch states, the evolution of the initial (Bloch) states is to be described by the evolution of the density matrix of the Mu itself; hence

$$C(\omega) = \pi \rho(\hbar\omega + \varepsilon_{\mathbf{k}}) \equiv C_B(\omega), \quad (6B.4)$$

where $\rho(\varepsilon_{\mathbf{k}})$ is the density of states of Mu. The spin relaxation process occurs via exchange of Zeeman energy with Mu band energy, and therefore the relaxation rate should reflect the shape of the Mu density of states. Thus it was predicted by *Kondo* [6.255] that there is a possibility of discriminating between these two cases by measuring the relaxation rate as a function of applied magnetic field. As illustrated in Fig. 6B.1, one can expect a strong modulation of $1/T_1$ when the Zeeman frequency coincides with van Hove singularities (α to δ). The lowest Zeeman frequency ω_{12} makes the predominant contribution to (6B.1), and the lowest singularity β appears at

$$\hbar\omega_{12} \approx \frac{4}{3}J \quad (6B.5)$$

for the simple cubic lattice.

Experiments were performed taking sufficient precautions to assure good thermal contact to allow measurements below 10 mK. Results obtained at two different temperatures are shown in Fig. 6B.2. The relaxation rate as a function of magnetic field strength shows a bump at <10 mK, which is absent at 3.9 K. This is a clear signature that the Bloch state of Mu was formed at <10 mK. From the peak position, the value $2J = 19 \mu\text{eV}$ (0.22 K) was deduced. This is close to the value previously obtained from the leveling-off of the jump frequency. Although the corresponding de Broglie wavelength barely exceeds the inter-site distance, $\lambda_{\text{dB}}/d = \sqrt{J/2\pi k_B T} \approx 1.4$ at 10 mK, the experimental results clearly indicate that a transition to Bloch states is already merging.

7 Electronic Structure

In this chapter, we describe some essentials of the electronic structure underlying the thermodynamic and atomistic properties of the metal–hydrogen system. Materials have been chosen primarily for illustrative purposes. For a more comprehensive description of the electronic structure of metal hydrides, the reader is referred to the following review articles [7.1, 7.2]. The metal-insulator transition in rare-earth hydrides and the electronic structure of elemental hydrogen under high pressures, including the evidence of metalization in the liquid state, are the two subjects included anew in this second edition.

7.1 Hydrogen-Induced Changes in the Electronic Structure of Metal Hydrides

One of the common features of the electronic structure of metal hydrides is the formation of H-induced states below the d (or f) band of transition (lanthanide) metals.

As an example, a soft X-ray emission spectrum (SXS) of $\text{VD}_{0.7}$ is shown in Fig. 7.1, together with that of V metal for comparison [7.3]. It can be seen very clearly that, as hydrogen is introduced in V metal, new states are formed at ~ 6 eV below the Fermi level. On a closer look, it may be noticed that the lower-energy side of the main peak (3d band) is diminished in intensity, and the higher-energy cut-off (the Fermi level) is pushed slightly upward.

The V-L_3 spectrum shown here is that of the X-rays emitted in the electronic transition from some initial state (i) into an empty 2p core state of a V atom created by electron irradiation. As the transition probability is proportional to $|\langle i | \mathbf{r} | 2p \rangle|^2$, the V-L_3 spectrum reflects the energy distribution of the initial states having s or d character around a V atom (more heavily weighted for d electrons). Thus, the observation implies that a part of V 3d electrons are lowered in energy by the dissolved H atoms.

Many more experiments have been performed using photoelectron spectroscopy (PES), which measures the energy distribution of electrons emitted by photo-irradiation of a given energy (and polarization). The spectrum obtained by PES in most cases closely reflects the density of states of all

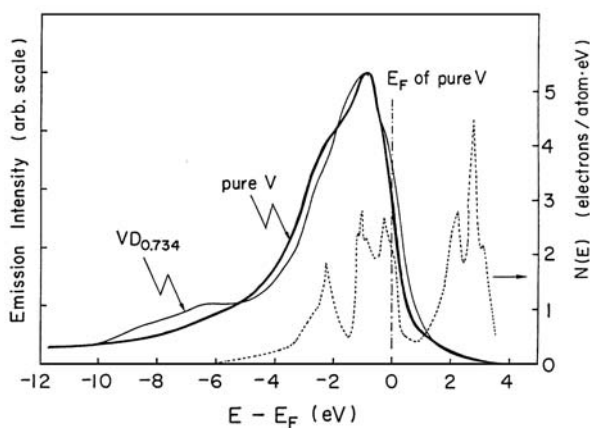


Fig. 7.1. Soft X-ray emission spectra (V- L_3) of $VD_{0.7}$ and V, including the calculated density of states of V [7.3]

conduction electrons (total DOS), and also reveals clearly the presence of H-induced states; see [7.2].

Let us explain the nature of H-induced states based on band calculations on a Pd hydride. Figure 7.2 shows the total DOS of Pd metal (without H) derived by band calculations [7.4]. Since the electronic configuration of Pd is $4d^{10}$, the Fermi energy E_F is determined as the energy where the total DOS integrated from below becomes equal to 10.

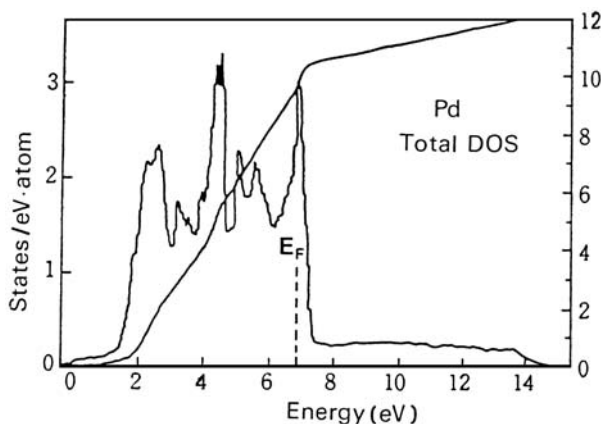


Fig. 7.2. Total density of states in Pd (*left axis*) and the integrated number of electrons (*right axis*) [7.4]

The breakdown of the total DOS into components having s, p, d characters around Pd atoms (partial DOS) is shown in Fig. 7.3 [7.5]. Obviously, electrons that form a band have predominantly d character, with a slight admixture of s, p characters. (Note that the partial DOS of s, p bands is very different from free-electron bands as a result of interference with the d band.)

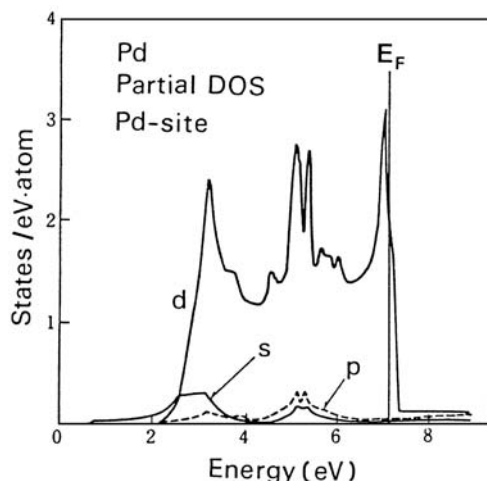


Fig. 7.3. Partial density of states in Pd of electrons having s, p, d characters around Pd atoms [7.5]

The calculated DOS of PdH is shown in Fig. 7.4a [7.4]. Comparing this with Fig. 7.3, we readily notice the formation of two groups of states: one below the d band and the other well above E_F . Figure 7.4b shows that these new states have the s symmetry around H sites [the local DOS (LDOS) around H sites]. By examining the character of wave functions, we can see that these H-induced states are, in fact, bonding and antibonding states formed by hybridization of Pd 4d and H 1s states. The energy of bonding states is lowered because the electrons feel the attractive potential of H most effectively.

Let us next examine the number of electrons accommodated in the DOS of PdH. Two electrons are accommodated in the bonding states, and a total of nearly ten are accommodated below the highest-energy subpeak in the d band. Thus, the total number of states below the subpeak is not changed by introduction of H. This is because exactly the same number of states brought in by H atoms are expelled to higher energies as antibonding states. An extra electron carried in by an H atom then enters the states near E_F .

Another approach to H-induced electronic states is to examine the local electronic structure around an H-site when only one H atom is introduced into a host metal—a single-impurity approach. Kanamori, Terakura and their collaborators have consistently pursued this line of study in a broader context of

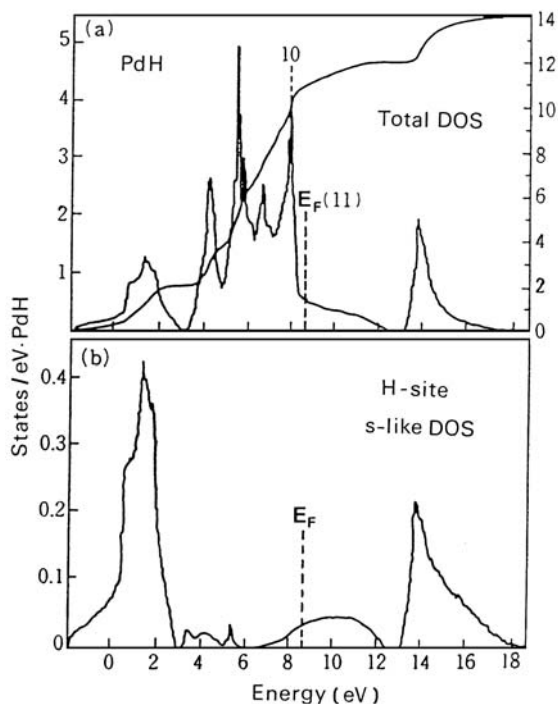


Fig. 7.4. (a) Total density of states in PdH (*left axis*) and the integrated number of electrons (*right axis*), (b) Partial density of states for electrons having s character around H atoms [7.4]

the electronic structure of nonmagnetic impurities in transition metal hosts, and have clarified, for example, the general trend of the hyperfine field as seen by impurity atoms. (For details of their calculations, see, e.g., [7.6–7.9].)

A similar single-impurity approach has also been made by Zeller, Dedrichs and their collaborators (see, e.g., [7.10–7.12]).

The calculation is based on the so-called KKR–Green’s function method. An impurity potential is incorporated in a sphere of an appropriate radius located at an interstitial site, and the response of conduction electrons of a host metal to this potential is calculated by the Green’s function method for each of the partial-wave components. The results of their calculation for H in Ni are shown in Fig. 7.5 [7.6]. The number of electrons contained in an impurity sphere (of radius 1.8 a.u.) around an O site having s and p character are shown separately as a function of energy. Due to ferromagnetism, spin-up and spin-down states are shifted in energy relative to each other. Obviously, the s-wave component plays a far more important role than p, d, ... components. The total number of electrons in the impurity sphere is equal to 2 at ~ 0.7 Ry below E_F , as a consequence of the occupation of an

H 1s orbital, but decreases continuously until it reaches a minimum (at E_{ar}) slightly below E_{F} . The energy E_{ar} is called the antiresonance energy, where the character of the wave function changes from bonding to antibonding. Such a reduction in the number of electrons around an impurity near E_{F} is a general consequence of the antiresonance (Fano) effect, which always operates in transition metals [7.13]. The total number of electrons in the impurity sphere was found to be 0.29 for up-spin and 0.22 for down-spin states, amounting to a total of 0.51. As the charge-neutrality condition requires the total number of electrons around a proton to be equal to 1, the remaining charge must reside on the surrounding M atoms.

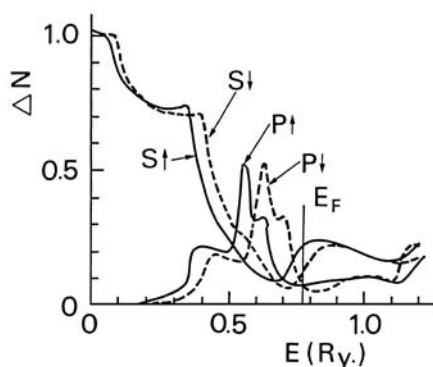


Fig. 7.5. Number of electrons contained in an H sphere in Ni, shown separately for electrons having s, p character with up and down spins [7.6]. (1 Ry = 13.6 eV)

This problem was examined further in a subsequent calculation, which allowed the perturbation potential to build up on the nearest-neighbor M atoms, as a consequence of the screening charges accumulated [7.14]. The calculation was performed self-consistently, and the charges contained in the impurity sphere (Δn_{I}) and in the six muffin-tin spheres on the nearest-neighbor M atoms ($6\Delta n_{\text{n.n.}}$) were obtained for impurities with nuclear charges $Z = 1 - 8$ (H to O) on the O site in fcc Cu. The results are listed in Table 7.1. In all cases, a major fraction of the screening charges resides on an impurity cell, but an appreciable fraction is extended to the nearest-neighbor M atoms, leaving a small fraction for further neighbors (balance).

Figure 7.6 shows the local density of states in the interstitial and in the nearest-neighbor host muffin-tin spheres for an H atom in Cu [7.14]. In addition to the H-induced states located at about -9 eV from E_{F} , the shift of the density of states on the neighboring site to lower energies can be clearly seen.

Regarding the charge transfer from M atoms to H atoms in forming metal hydrides, the so-called core shifts observed in PES spectra may be regarded as

Table 7.1. Changes in the number of electrons in the impurity sphere (Δn_I), in the six nearest-neighbor M-atom spheres ($6\Delta n_{n.n.}$), and the balance ($Z - \Delta n_I - 6\Delta n_{n.n.}$) for interstitial impurities with nuclear charge $Z = 1-8$ (H–O) occupying an O site in Cu [7.14]

	H	He	Li	Be	B	C	N	O
Z	1	2	3	4	5	6	7	8
Δn_I	0.58	1.53	2.00	2.00	2.44	3.56	4.85	6.14
$6\Delta n_{n.n.}$	0.31	0.31	0.70	1.56	2.07	2.03	1.71	1.56
Balance	0.11	0.16	0.30	0.44	0.49	0.41	0.34	0.30

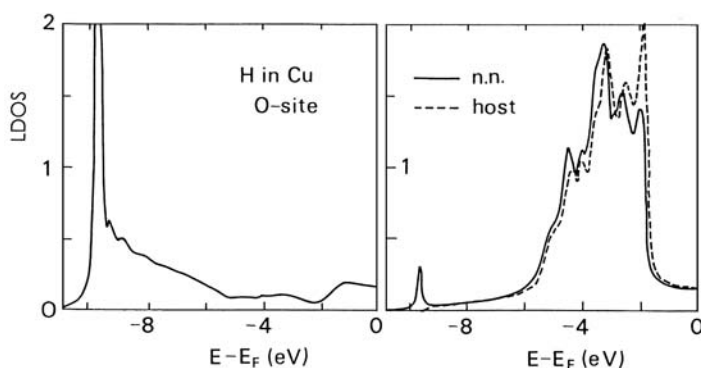


Fig. 7.6. Local electronic structure of an H atom on an O site in Cu. *Left:* local density of states (LDOS) in the impurity sphere. *Right:* LDOS in the nearest-neighbor M-atom sphere (*solid line*) as compared to that in an unperturbed host M-atom sphere [7.14]

direct evidence. In $\text{ZrH}_{1.65}$, for example, the Zr 4p level is lowered by ~ 1 eV. Similar shifts have been observed in Sc, Y, Ti, and rare-earth hydrides (see, e.g., [7.2]). These shifts, which always tend to lower the energies of core states, are a result of a stronger attractive potential of M atoms caused by charge transfer to H atoms.

In band calculations, the core shift appears in the course of attaining self-consistency. Most band calculations start from potentials constructed by a superposition of neutral atomic states, solve for conduction electrons, construct a potential anew, and repeat this process until self-consistency is achieved. The charge transfer occurs in this process and induces energy shifts of core states.

It is, however, not easy to quantify the charge transfer. In any case, the amount of charge transfer is small, of the order of $e/10$, in metallic environments. In addition, there is arbitrariness in defining the number of electrons belonging to each of the constituent atoms. It can be defined by counting the

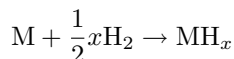
number of electrons contained in a space appropriately (but arbitrarily) allotted to each atom, or by counting the occupation number of atomic orbitals of the constituent atoms. Naturally, the numbers turn out to be different for different definitions.

If one remembers these situations, one may realize that it is almost meaningless to speak about a proton model or an anion model for interstitial hydrogen in metals.

7.2 Energies of Hydride Formation

7.2.1 Band-Theoretic Calculation

The heat of solution of hydrogen in a metal or the heat of formation of a metal hydride for the reaction



is defined by

$$\delta E = [E(\text{MH}_x) - E(\text{M})]/x - \frac{1}{2}E(\text{H}_2), \quad (7.1)$$

where $E(\text{MH}_x)$, etc., stand for the internal energy of MH_x , etc. The variation of δE across the 3d and 4d series of transition metals is shown in Fig. 7.7.

We shall explain here the origin of these general trends of δE according to *Gelatt et al.* [7.15]. They obtained the first term (δE_1) of (7.1) from band calculations for a metal hydride MH (assumed to have an NaCl structure, for the sake of simplicity) and a pure metal M , and showed that the energy change in forming a hydride can be split into three parts as

$$\begin{aligned} \delta E_1 &= E(\text{MH}) - E(\text{M}) \\ &\approx 2(\langle \varepsilon_{\text{LB}}^{\text{MH}} \rangle - \langle \varepsilon_{\text{LB}}^{\text{M}} \rangle) + n_{\text{d}}^{\text{MH}} - (\langle \varepsilon_{\text{d}}^{\text{MH}} \rangle - \langle \varepsilon_{\text{d}}^{\text{M}} \rangle) + E_{\text{F}}. \end{aligned} \quad (7.2)$$

The first term in (7.2) represents the difference in the average energy of the lowest band (LB) of the hydride, $\langle \varepsilon_{\text{LB}}^{\text{MH}} \rangle$, and the metal, $\langle \varepsilon_{\text{LB}}^{\text{M}} \rangle$, each of which contains two electrons. The second term describes the shift of the d band. The quantities $\langle \varepsilon_{\text{d}}^{\text{M}} \rangle$ and $\langle \varepsilon_{\text{d}}^{\text{MH}} \rangle$ are, respectively, the average energies of the occupied d states lying above LB in the metal and the hydride. The average energy of the 11th electron which occupies the s-d hybridized states above the top of the d band in the noble metals is included in $\langle \varepsilon_{\text{d}}^{\text{M}} \rangle$ and $\langle \varepsilon_{\text{d}}^{\text{MH}} \rangle$. The quantity n_{d}^{MH} is the number of d electrons in the hydride. If the metal has N_{M} valence electrons, n_{d}^{MH} is equal to $N_{\text{M}} - 2$. The $N_{\text{M}} + 1$ electrons per unit cell of the hydride are allocated as follows: two in the lowest band, one at the Fermi level, and n_{d}^{MH} in the d bands. Note that the value of n_{d}^{MH} is one smaller than the nominal d-electron count $N_{\text{M}} - 1$ of a pure transition metal.

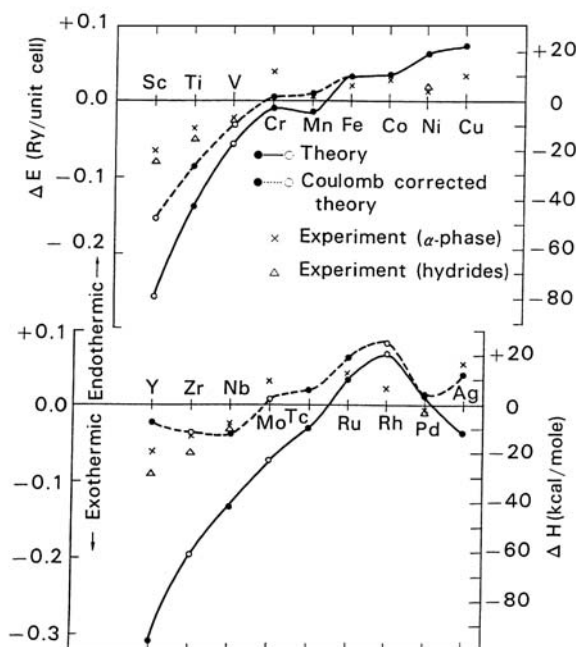


Fig. 7.7. Observed heats of solution (*crosses*) and heats of formation of hydrides (*triangles*) for 3d and 4d series of metals (*above* and *below*, respectively). Calculated values with and without Coulomb corrections are shown by *dashed* and *solid* lines, respectively [7.15] (1 Ry = 13.6 eV)

The third term approximates the contribution of the additional electron per metal atom due to the hydrogen atom, which is added on at the Fermi energy E_F .

The variation of the three terms of (7.2) across the 4d row is illustrated in Fig. 7.8. It is clear from Fig. 7.8c that the nearly linear shift in the average energy of the lowest band is the dominant and most rapidly varying contribution to δE except for noble metals. For noble metals, the rapid increase of E_F , as shown in Fig. 7.8a–d, becomes important. As seen in Fig. 7.7, the calculation (the solid curve) reproduces the gross feature of general experimental situations, namely, that with the exception of Pd and Ni, stable concentrated hydrides form only on the left-hand side of the period.

More quantitatively, however, the calculation overestimates the stability of the hydrides especially for the early transition metals. This is believed to be a result of inherent difficulty of the band calculations: In band calculations, the one-electron energy in the average potential field of other electrons is calculated neglecting the Coulomb energy between two electrons on the same atom. In the present problem, however, a Coulomb repulsion between

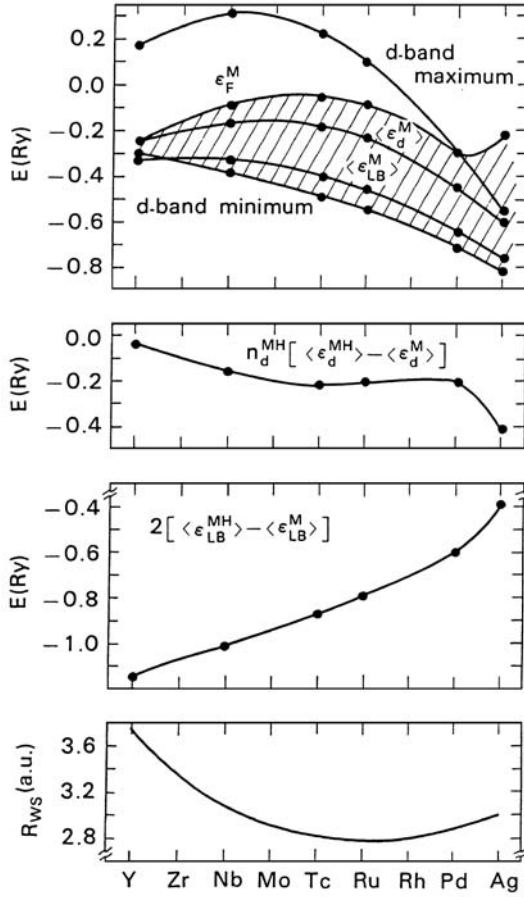


Fig. 7.8. Variation across the 4d row of (a) the *upper* and *lower* d-band edges, the average energy of the occupied d bands $\langle \epsilon_d^M \rangle$, the average energy of the lowest metal valence band $\langle \epsilon_{LB}^M \rangle$, and the metal Fermi energy E_F^M ; (b) the shift in energy of the occupied d bands; (c) the occupation-weighted shift in the average energy of the lowest band; and (d) the Wigner-Seitz radius r_s [7.15] (1 Ry = 13.6 eV)

electrons around a single H site is expected to be important. *Gelatt et al.* [7.15] included this effect in a crude approximation by recalculating the number of electrons around an H site, and obtained a better agreement with the observed values, as shown by the dashed curves in Fig. 7.7.

7.2.2 Effective-Medium Theory

Another approach to the heat of solution of hydrogen in transition metals has been made by means of the effective-medium theory, proposed by *Stott* and *Zaremba* [7.16] and *Nørskov* and *Lang* [7.17].

The basic idea behind the effective-medium theory is to replace the real host metal by a simpler host, the effective medium, for which the full quantum-mechanical calculation can be carried out in a proper self-consistent way. The embedding energy, the total energy of a combined system (M + H) minus that of the constituents (M and H), for an H atom at a position \mathbf{R} in a host metal can be written as

$$\delta E(\mathbf{R}) = \Delta E_{\text{eff}}^{\text{hom}}[\bar{n}_0(\mathbf{R})] + \Delta E^{\text{hyb}}(\mathbf{R}) + \Delta E_v(\mathbf{R}) + \Delta E_c(\mathbf{R}). \quad (7.3)$$

The dominating term $\Delta E_{\text{eff}}^{\text{hom}}(\bar{n}_0)$ is the universal embedding function characteristic of the introduced species (hydrogen), representing the interaction with the homogeneous electron gas of density (\bar{n}_0). Of the three remaining terms that describe corrections for deviations from the homogeneous electron gas, ΔE^{hyb} is important in transition metal hosts: it results from the difference between the hybridization of the hydrogen wave function with the d band of the host metal and the corresponding hybridization with the homogeneous electron gas. This term is approximately proportional to $1 - f_d$, f_d being the fraction of filling of the d band in the host. Other corrections for the interaction of hydrogen with core electrons and for inhomogeneity effects in the real metal are generally much smaller.

The embedding function $\Delta E_{\text{eff}}^{\text{hom}}(\bar{n}_0)$ is shown in Fig. 7.9 [7.18]. The increase in energy at higher electron densities is due to the progressively greater electron kinetic energy incurred by the orthogonality requirement for the wave functions.

The existence of a minimum implies that there is an optimum electron density as a consequence of chemical interactions in a broader sense of the word. (For inert atoms like He, $\Delta E_{\text{eff}}^{\text{hom}}(\bar{n}_0)$ increases monotonically with \bar{n}_0 .)

The heats of solution of hydrogen calculated by *Nørskov* [7.19] for the 3d series of metals are shown in Fig. 7.10, together with the experimental values. A remarkable agreement is seen in the trends along the series. An examination of the individual contributions of $\Delta E_{\text{eff}}^{\text{hom}}$ and ΔE^{hyb} , also included in Fig. 7.10, indicates that the trend is determined by $\Delta E_{\text{eff}}^{\text{hom}}(\bar{n}_0)$, namely by the interstitial electron density.

For most metals, the interstitial electron density lies well above the minimum of $\Delta E_{\text{eff}}^{\text{hom}}(\bar{n}_0)$, except for K and Ca, where \bar{n}_0 is so low that it comes below the minimum. The effects of local lattice relaxation through changes of \bar{n}_0 are usually small in transition metal hosts, but are expected to be important in K and Ca. Here, relaxing the nearest-neighbor M atoms towards the H atom will increase the binding. This is indeed shown to be the case by the calculations assuming local M–H distances appropriate for hydrides.

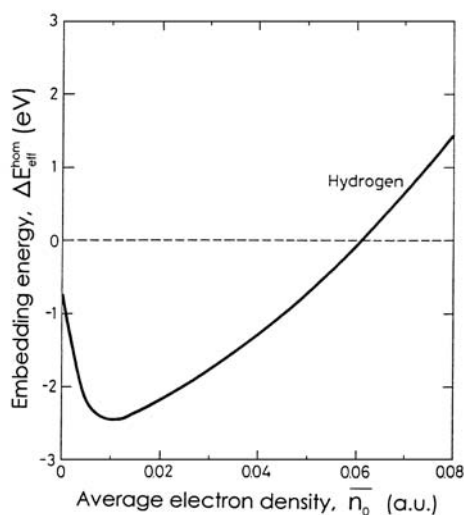


Fig. 7.9. The embedding energy $\Delta E_{\text{eff}}^{\text{hom}}$ as a function of the average electron density \bar{n}_0 in atomic units [7.18]

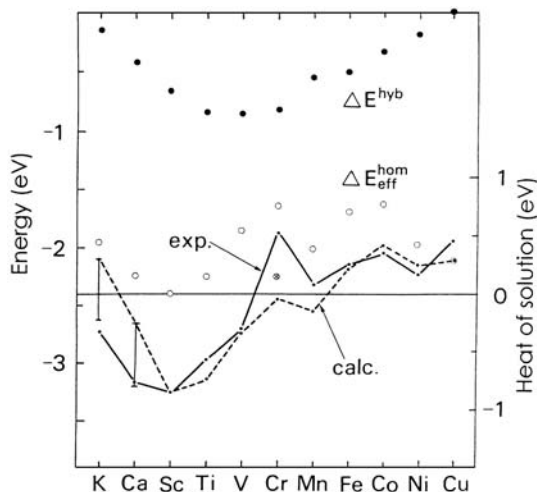


Fig. 7.10. Heats of solution of H in the metals from K to Cu. Observed values (—) are compared with calculated values (---) by the effective-medium theory; $\Delta H_s = \Delta E_{\text{eff}}^{\text{hom}} + \Delta E^{\text{hyb}} - 2.4\text{eV}$ (one-half of the binding energy of the H_2 molecule). Also shown are the individual contributions: $\Delta E_{\text{eff}}^{\text{hom}}$ (○) and ΔE^{hyb} (●). For K and Ca, the energy is also shown for a complex where the metal-H bond length has been allowed to relax. The real value is expected to lie in between these two extremes indicated by error bars. The crossed circle for Cr denotes the energy for nonmagnetic Cr [7.19]

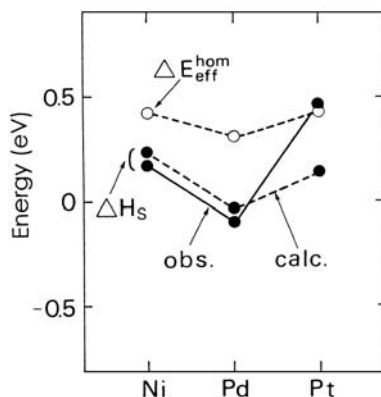


Fig. 7.11. Heats of solution of H in Ni, Pd, and Pt. The observed values (—) are compared with the calculated values (---) by the effective-medium theory. The $\Delta E_{\text{eff}}^{\text{hom}}$ contribution is also shown [7.19]

The variation of the heat of solution perpendicular to the rows is shown in Fig. 7.11 for Ni, Pd, and Pt [7.19]. The anomalous tendency of Pd to absorb hydrogen is seen to be primarily a consequence of the open Pd lattice (small \bar{n}_0).

On the whole, we may say that the effective-medium theory yields good agreement with experiments as far as the total energy is concerned – not only for the heat of solution treated here but also for the heat of adsorption [7.20] and binding energies to lattice defects described in Sect. 5.6.3.

On a closer look at Figs. 7.10, 7.11, however, we notice that the calculated heats of solution become more negative in cases where the M–H distance is small (e.g., Cr and around) or where the metal core is large (e.g., Pt). This indication of a drawback of the effective-medium theory will be discussed in Sect. 7.3.

7.3 Hydrogen–Metal Interaction Potential

In the spirit of the Born–Oppenheimer approximation, the H–M interaction potential can be described by the adiabatic potential, which can be obtained, in principle, by calculating the energies of all the electrons in the system as a function of the position of an H atom placed in a metal lattice.

This problem has been tackled by the following three methods: single-impurity calculations by the use of Green’s functions or by the effective-medium theory, and a band-theoretic calculation on stoichiometric hydrides. We describe here the principles and limitations of these calculations.

One of the most orthodox approaches to this problem is to calculate the response of conduction electrons to the introduction of one H atom by means

of the electronic Green's function. This approach was described briefly in Sect. 7.1 [7.6–7.9]. *Akai et al.* [7.9] performed calculations of the adiabatic potential for light impurities (H, He, . . . , Ne) occupying substitutional sites in Fe. For impurity atoms He, Li, and Ne, the adiabatic potential along the cube axis was found to become minimum at the substitutional site, whereas for B, C, O, F, H, and N atoms, it was found to become maximum. Therefore, the latter group of impurity atoms should occupy an off-center position when trapped in a vacancy. For H, this agrees with the conclusion of the effective-medium theory, as described in Sect. 5.7.3. For H on O and T sites in Fe, the following results were obtained [7.21]: First, the potential around an O_Z site has a broad maximum in the X – Y plane and a minimum in the Z direction, in agreement with what was obtained from a superposition of the central pair potentials of *Sugimoto* and *Fukai* [5.235]. Second, the curvature of the potential around a T site is exactly the magnitude required, based on the observed vibrational energies. These results indicate, in particular, that the short-range part of the adiabatic potential may be obtained fairly reliably by this calculation.

It must be recognized, however, that this calculation suffers from the following inherent difficulties, especially in treating interstitial impurity atoms. First, due to the short distances to the nearest M atoms, the impurity sphere must overlap the M-atom spheres, a very unfavorable situation for this calculation. Second, the relaxation of the surrounding lattice cannot easily be incorporated because it destroys the symmetry of the host Green's function. In addition, in single-impurity-type calculations, we have to deal with the small changes in the electronic structure and energies induced by only one impurity atom in a large (infinite) host metal system. In order to extract meaningful values from these small changes, we must perform large-scale calculations with high accuracies, which is no easy matter even with the Green's function method specially devised for this purpose. Calculations of the adiabatic potential for a large number of general (non-symmetrical) positions of an H atom are, therefore, almost intractable.

Qualitatively, the local electronic structure clarified by the Green's function approach provides a physical explanation for the general form of the empirical potentials described in Sect. 5.7.1. We saw in Sect. 7.1 that as a result of the hybridization of H 1s and M d states, bonding states are formed below the d band of the host metal, whereas antibonding states are distributed above the Fermi energy. Spatially, the bonding state is confined to between the H atom and the nearest-neighbor M atoms, and its wave function is strongly localized. The antibonding state, on the other hand, is slightly more extended, probably over a few atomic distances. Recognizing that electrons in the d band are the major source of attraction between M atoms [7.22], their local depletion by the formation of antibonding states should result in a local dilatation of the lattice or, equivalently, an effective repulsive interaction between H and M atoms. Thus, we may rationalize the short-range and

longer-range part in the H–M interaction as being due to the formation of bonding states and depletion of antibonding states, respectively.

Another first-principles approach to the adiabatic potential is the band-theoretic calculation for stoichiometric hydrides. The adiabatic potential can be obtained by repeating the calculation of the total electronic energy by displacing an H sublattice with respect to an M sublattice. As shown in Sect. 5.7.3, the adiabatic potential obtained for H in Nb was found to reproduce excellently the observed vibrational energies and, therefore, the short-range part of the potential [5.241]. The adiabatic potential for H can be regarded as arising from the interaction with M atoms because the interaction between H atoms was found to be fairly small. If necessary, the H–H interaction in the calculation can be made even smaller by taking a larger supercell containing a smaller number of H atoms. In comparison to single-impurity-type calculations, the accuracy required for the energy calculation is less stringent.

This type of band calculation is no doubt one of the most successful and physically most clear approaches to the adiabatic potential for H.

However, these first-principles calculations, single-impurity-type and band-theoretic-type alike, have only been performed under some simplifying conditions. The symmetry of the lattice has been fully exploited by disregarding the local lattice relaxation around H atoms. Unfortunately, this simplification is hardly justifiable in many cases.

For example, in examining the preference of interstitial sites, the energy difference involved is of the order of several tens of meV, which is comparable to the energy of lattice relaxation and zero-point vibration of an H atom. Thus, calculations of the electronic energies down to these digits under the simplifying condition of an undeformable lattice could not be physically meaningful.

In order to be able to treat the local lattice distortion, we must find some way to express the adiabatic potential obtained from first-principles calculations in a form which depends on the relative positions of H and M atoms in some simple way, for example, as a sum of the central pair potentials.

The effective-medium theory can do this job without much difficulty. In this formulation, the dominant contribution to the adiabatic potential, the embedding energy $\Delta E_{\text{eff}}^{\text{hom}}$ [the first term of (7.3)], has already been calculated (Fig. 7.9) [7.18] as a universal function of the local electronic density, which in turn can be approximated by a superposition of the atomic densities. The remaining terms of (7.3) can be calculated similarly.

The overall success of the theory in predicting the various energies (heats of solution, adsorption, and binding energies of the defects) certainly gives a measure of usefulness of the theory and suggests that it contains some essential physics in its simple form.

There are, however, several indications that the adiabatic potential constructed by the effective-medium theory is generally too soft. The calculated vibrational energies turn out to be too small (see Sect. 5.7.3); the heats of

solution are too small in more congested situations where M–H distances are smaller (see Sect. 7.2); and the displacements of the nearest-neighbor M atoms were overly underestimated [5.237].

Obviously, this is due to the inadequacy of the effective-medium theory in treating the bonding-state formation. This effect has been included in the second-order perturbation in ΔE^{hyb} , which depends on the M–H distance as $1/R^6$, but, apparently, the actual potential arising from the bonding state is more strongly repulsive at short distances.

Thus, notwithstanding all the advantages of the effective-medium theory for computational purposes, its physical foundation – its principles and limitations – needs further scrutiny.

A more orthodox method of constructing the adiabatic potential from band-theoretic calculations succeeded in reproducing the H vibration frequencies excellently, as described in Sect. 5.7.3. However, it was recognized there that such calculations have difficulties in reproducing the force-dipole tensor reliably. When cast into the form of central pair potentials, the result indicated that the potential should contain both short-range and long-range parts, of which the former determining the vibrational frequencies was derived reliably whereas the latter determining the long-range distortion was not [5.247–5.249]. This approach, which is physically better founded, should be very useful if this deficiency in the long-range component of the potential can be properly amended.

7.4 The Metal-Insulator Transition in Rare-Earth Hydrides

Rare-earth dihydride-trihydride systems are peculiar in that they exhibit a metal-insulator (M-I) transition as H concentration approaches $x = 3$. The fact was recognized from old days; one of the earliest reports by *Stalinski* [7.23] showed that in the LaH_x system, Arrhenius plots of the resistivity start to show a signature of metal to semiconductor transition above $x \sim 2.7$. Experimental results obtained before 1995 were compiled and discussed by *Vajda* [2.70]. Quantitative experiments were, however, severely hampered by disintegration of samples into fine powder upon hydrogenation. It was by technical innovation of Griessen's group [7.24, 7.25] that a wealth of information on their physical properties has been made available. In brief, they demonstrated that a film of vacuum-deposited Y and La covered with a thin overlayer of Pd can reversibly absorb/desorb hydrogen under ambient conditions, thus becomes amenable to accurate, quantitative measurements of electrical and optical properties. The film which is opaque in the metallic state at low H concentrations becomes transparent at high H concentrations when it changes into the insulating state. A great advantage of dealing with this composite film sample is that it can be taken out of a ultra-high vacuum deposition system without danger of oxidation (a severe

problem for rare-earth metals), and be placed for a whole series of *ex situ* experiments, e.g. temperature and H concentration dependence of electrical resistivity [7.24–7.30], Hall effect [7.31], photoconductivity [7.31, 7.32], optical transmission/reflectance [7.24, 7.25, 7.33–7.35], optical measurements of H diffusion [7.36–7.42], electro/thermo-migration [7.43, 7.44], etc.

Figure 7.12 shows the electrical resistivity and light transmission (measured at $\hbar\omega = 1.8\text{ eV}$) of a thin film of YH_x as a function of time after exposure to 1 atm of H_2 gas at room temperature [7.24, 7.25]. The evaporated Y film was 500 nm thick, with a protective Pd overlayer of 20 nm thick. In a few minutes, hydrogenation proceeds from hcp solid solution (α^*) phase, through fcc dihydride (β) phase to hcp trihydride (γ) phase, accompanied with large changes of the resistivity and light transmission. The resistivity decreases to $\sim 1/5$ in going from the α^* to the β phase, and subsequently increases by $\sim 10^2$ times in the γ phase. The film bears a shiny metallic luster initially, with a nearly 100% reflectivity, which changes to nearly transparent at high H concentrations close to $x \sim 3$. The observed change in the β and γ phase regions was reversible; the film hydrogenated to trihydride returned to the dihydride composition when placed in vacuum. The critical concentration for the M-I transition was located at $x = 2.86$ at room temperature, which is well within the hcp trihydride phase.

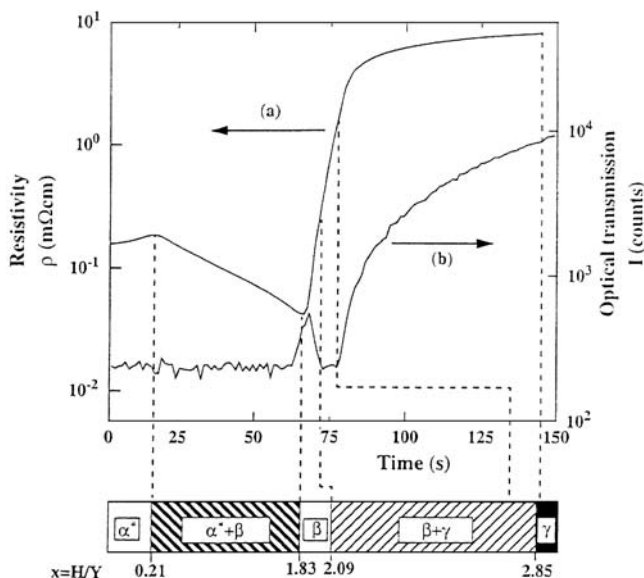


Fig. 7.12. Electrical resistivity (a) and optical transmission at $\lambda = 689\text{ nm}$ (1.8 eV) (b) of a 500 nm YH_x /20 nm Pd composite film during hydrogen absorption at room temperature. At $t = 0$, H_2 gas pressure is increased from 0 to 105 Pa, and the H concentration in the film is increased from 0 to 3, through α^* (hcp), β (fcc) and γ (hcp) phases [7.24, 7.25]

In LaH_x , the changes caused by hydrogenation were slower, but very similar [7.25]. Subsequent experiments showed that this M-I transition is a rather robust one, occurring in all lanthanide metals close to the trihydride composition, irrespective of crystal structure. In the trihydride state, they are all transparent albeit with characteristic colors: e.g. YH_3 is yellowish, LaH_3 is red, while some others are colorless. The corresponding optical band gaps are of the order of $1 \sim 2 \text{ eV}$.

There are two reasons for which this group of hydrides has attracted renewed interest in the last years. First, a possible application of such composite films has been brought up, under the eye-catching name of “switchable mirrors”, with the implication that they can be used as a reversible switching device of optical reflectivity activated by absorption/desorption of hydrogen. Second, physically more important reason is that it has provided a stringent test of various methods of electronic calculations. In spite of the apparent simplicity and robustness of the M-I transition, understanding of its mechanism in terms of electronic theories met with great difficulties. Here we trace briefly the conceptual developments made in the last years to reach to present state of understanding.

In order to illustrate the main features of the electronic structure of rare-earth dihydride-trihydride systems, the local electronic density of states for CeH_2 and CeH_3 are shown in Fig. 7.13 [7.45]. H atoms on T sites are designated as H_T and those on O sites as H_O . In the dihydride, H atoms are accommodated in T sites, and additional H atoms in the trihydride are in O sites. The Fermi level in the dihydride lies in the Ce-5d band, whereas it is located in a narrow bandgap in the trihydride. The mechanism of band formation is essentially determined by hybridization of Ce-5d and H-1s bands, as illustrated in Fig. 7.14. This mechanism is common to all rare-earth dihydride-trihydride systems, including Y hydride. (The 4f states located in the 5d band, which do not contribute to the bonding, can be disregarded for the present purpose.)

On closer examination, a number of drawbacks of electronic calculations have come to be recognized. The first obvious step for self-consistency, namely, a procedure to include the charge transfer from lanthanide to H atoms, naturally expected from large differences in the electronegativity, tended to reduce the bandgap – in some cases even led to appreciable overlaps ($\sim 1 \text{ eV}$) [7.46–7.48]. It was then discovered that, by relaxing the symmetry requirements of the crystal structure, but still within the frame of local density approximation (LDA), a small bandgap may be recovered [7.49, 7.50]. A need to include strong electron correlation was also suggested. According to the model of *Eder et al.* [7.51], the ground state of the system corresponds closely to the state of an H atom with two electrons forming a tightly bound singlet state, with the orbital of one electron primarily on an H site, and the other primarily on surrounding M sites. This lowers effectively the Coulomb repulsion between the two electrons, and shifts the H band downward. The situation is depicted in Fig. 7.15. To rationalize the expansion of the wave

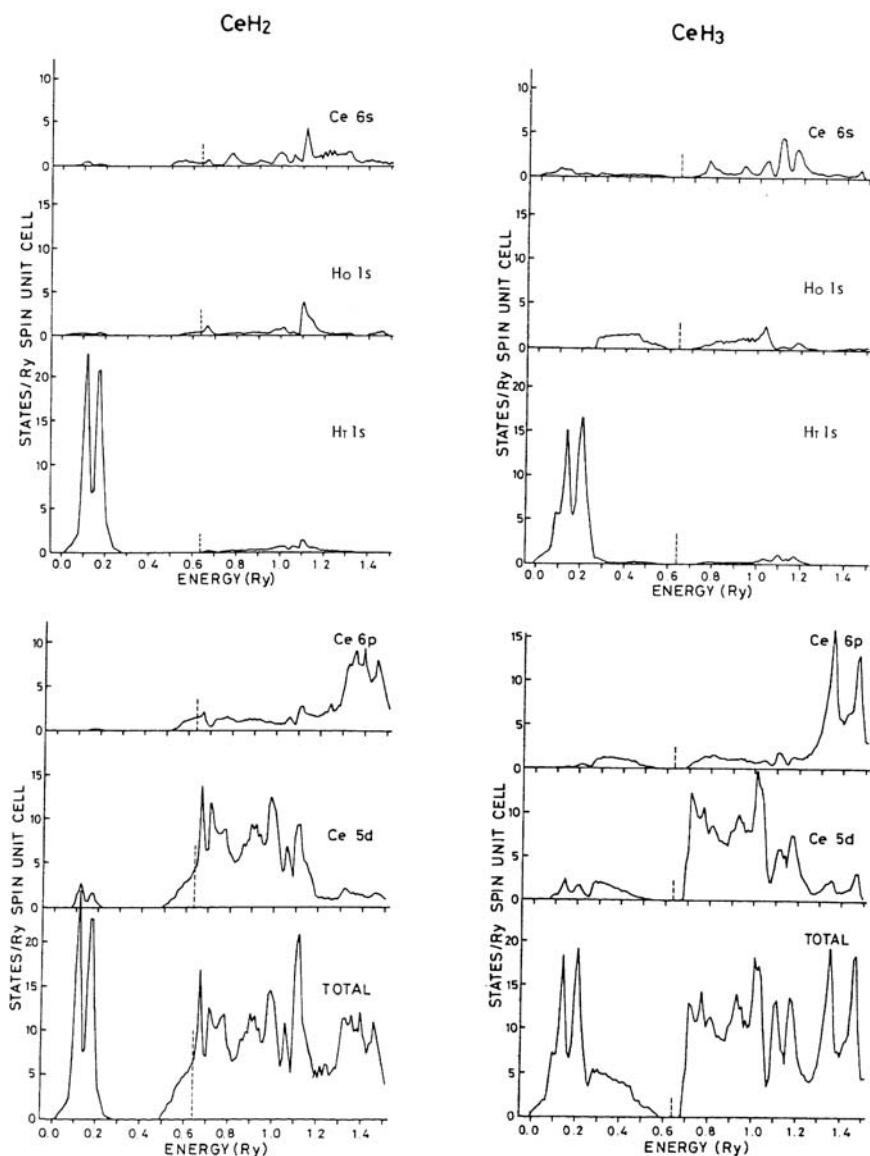


Fig. 7.13. Partial and total density of states for CeH_2 and CeH_3 . The Ce-4f orbitals have been omitted [7.45]

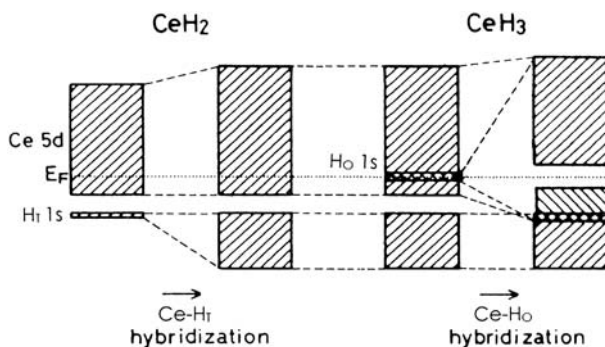


Fig. 7.14. Schematic representation of the electronic energy bands in CeH_2 and CeH_3 [7.45]

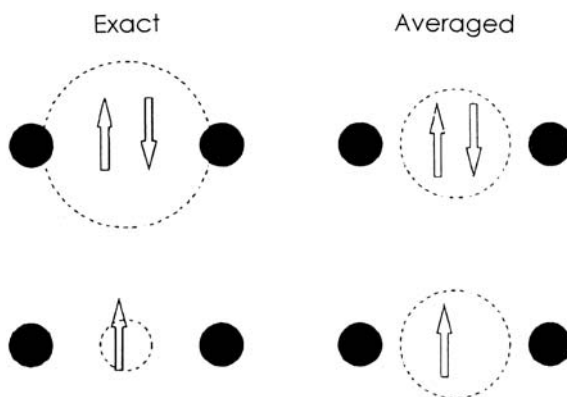


Fig. 7.15. Schematic representation of a two-electron and single-electron wave function with (left column) and without (right column) taking account of the expansion caused by double occupancy. Strong correlation model of Eder *et al.* [7.51]

function for double occupancy, it may be helpful to remember the difference of the crystal radii; 0.26 \AA for H^0 and 1.54 \AA for H^- [7.52]. The figure clearly indicates that the use of average orbitals may incur large errors. The mechanism of stabilization of a H-band formed by these two-electron singlet states is shown in Fig. 7.16. It was shown by Eder *et al.* [7.51] that in the case of Y trihydride a H-band may split off from the bottom of the Y-4d band by as much as several eV.

A better agreement with experiments was achieved by going beyond the standard density-functional formalism, adopting e.g. the GW approximation [7.53–7.55] or screened exchange approximation [7.56, 7.57]. The conclusion reached was, in essence, that the missing bandgap in LDA calculations was not so much of the effect of electron correlation as a self-energy effect. The GW method tends to narrow bands whose widths are overestimated in LDA.

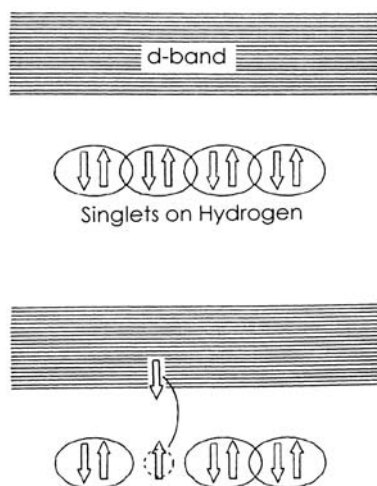


Fig. 7.16. Schematic representation of the stabilization of the local two-electron band state in the strong correlation model of *Eder et al.* [7.51]. The excitation of one electron to d-band states costs several eV

On this level, delicate structural effects (such as symmetry breaking) are no longer important.

In fact, this general trend of LDA and GW methods is well-known. What is remarkable in this instance is the magnitude of the GW correction. While the LDA itself leads to band overlap of ~ 1 eV, the GW correction opens a gap of ~ 2 eV, in reasonable agreement with observations. The question to be raised is, what particular aspect of the GW correction has brought forth this large effect. *Griessen* [7.58] presumes that a strong correlation such as the one proposed by *Eder et al.* [7.51] should be playing an important part. There is in fact a very peculiar observation of electromigration in Y trihydride that, in an Arrhenius plot, the ratio of hydrogen and electron fluxes extrapolates to unity at infinite temperature, suggesting a one-to-one correlation of hydrogen and electron hopping [7.38]. This observation was taken to be the evidence in support of strong electron correlations, i.e. each proton binding two electrons in a sort of singlet state. The importance of correlation in H 1s states in determining the general systematics of the heat of solution was noted earlier by *Gelatt et al.* [7.15] (see Sect. 7.2.1).

This expectation for the occurrence of strongly correlated H 1s states has not been supported by later band calculations, however. *van Gelderen et al.* [7.54] stated that H 1s wave functions derived by the GW method did not bear any characteristic features predicted by the strong correlation model. *Wu et al.* [7.59] arrived at similar conclusions within the weighted-density-approximation (WDA), an old method adapted for the present purpose. Their results agreed with GW calculations and showed no evidence of

strong correlation in H 1s states. They suggested on this basis that the absence of self-interaction in H 1s states might be a key for reproducing correct band structures. The reason for its absence, which is physically very important, was not clearly explained, however. Apparently, more efforts are needed before we have a clean picture of the electronic structure of this group of hydrides.

In this section, we have limited the description to very basic problems of the electronic theory. For details of the M–I transition, its temperature dependence and correlation with order–disorder transitions of H atoms on O sites, the reader is referred to the review articles of *Vajda* [2.70, 7.60].

7.5 Electronic Structure of Hydrogen Under High Pressures

A quest for metallization of hydrogen under high pressures was started in as early as 1935 when *Wigner* and *Huntington* performed a quantum mechanical calculation and predicted a transition from insulating molecular to monatomic metallic state at ~ 30 GPa [7.61]. But, as described in Chap. 4, all the effort of experimentalists for its realization has continually been defied by ever-tenacious molecular hydrogen in solid state, at least up to 316 GPa at room temperature. It was under shock compression, under high pressures and temperatures, that electrically conducting state was realized in fluid hydrogen. Here we review recent advances, both experimental and theoretical, in the study of electronic properties of hydrogen at high pressures.

7.5.1 Solid Hydrogen at Low Temperatures

Solid molecular hydrogen is a unique quantum system in the sense that the rotational state of the molecules plays the essential role in determining the phase stability. This is a result of the combined effect of the small mass of protons and open crystal structure. Thus the state of freely rotating molecules in phase I can be described by the rotational quantum number J_r . At higher pressures, the molecular rotation is expected to be gradually hindered as intermolecular distances become shorter. Indeed, the pressure-induced deviation of the axial ratio from the ideal value of hcp in phase I (Fig. 4.3) indicates the incipient admixture of high- J_r states to make the molecules gradually non-spherical [4.7].

The nature of quantum states of the high-pressure phases has been studied by infrared spectroscopy. As an example, the pressure dependence of the vibron frequency in n-H₂ is shown in Fig. 7.17. A peculiar feature is that the vibration frequency tends from normal increase to decrease with pressure, indicating the softening of the interatomic potential at high pressures. The appearance of a subsidiary vibron peak in phase II in the infrared (IR) spectra

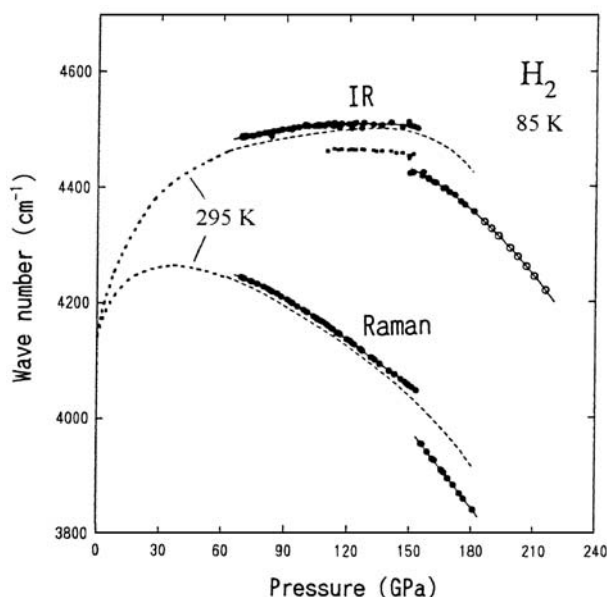


Fig. 7.17. Pressure dependence of the infrared (IR) and Raman vibron frequencies (*wave numbers*) measured at 85 K, showing the I–II and II–III phase transitions. The 295 K data in the phase I (the *dashed curve*) are given for comparison [4.2]. A linear decrease of the Raman vibron frequency in Phase III extends to still higher pressures, as was actually observed to 316 GPa by *Loubeyre et al.* [4.4]

indicates a slight symmetry-breaking distortion of the lattice, which is below the detection limit of XRD measurements [4.8, 4.9]. The II→III transition is accompanied with more distinct changes; the vibron signal jumps in frequency and its intensity is enhanced by 2~3 orders of magnitude [7.62]. These observations indicate that fairly large effective dipoles are induced on molecules as the two atom positions become inequivalent crystallographically [4.3].

An important step towards the assessment of the metallization pressure was taken by *Loubeyre et al.* [4.4]. They noted that light absorption measurements could be carried out in a diamond anvil cell above ~300 GPa because the energy gap of diamond, which is slowly varying with pressure, becomes larger than that of molecular hydrogen at these high pressures. They succeeded in determining the absorption edge of solid hydrogen at 100 K between 300 and 316 GPa until the sample became totally black at 320 GPa. The bandgap of hydrogen as a function of density is shown in Fig. 7.18. The measured exciton bandgap data extrapolate smoothly to the normal-pressure value, and are consistent with direct bandgap data of refractive index measurements [7.64–7.66]. The authors maintained that the observed absorption edge manifested the features characteristic of direct transitions, and by a linear extrapolation estimated that the direct electronic bandgap

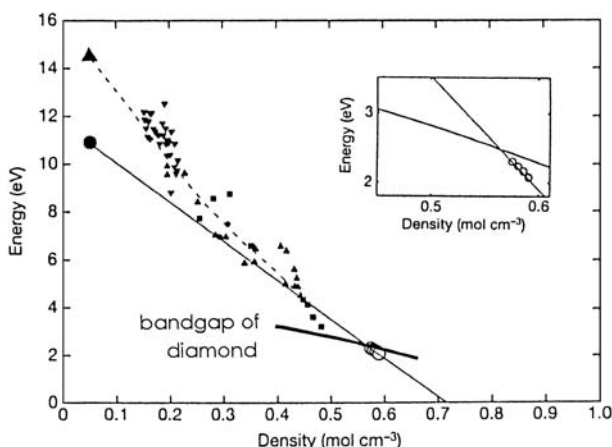


Fig. 7.18. Exciton and direct bandgaps of hydrogen as a function of density. The *large solid triangle* and *circle* are ambient-pressure data for the direct and exciton gap, respectively [7.63], the *small triangles* and *squares* the refractive index data for the direct gap [7.64–7.66], and *open circles* the exciton data from absorption measurements. The *thick solid line* gives the bandgap of diamond, below which the measurements in DACs were made as shown in more detail in the inset. The extrapolation of the exciton data gives the density of band-gap closure 0.71 g cm^{-3} [4.4]

should close at 0.71 g cm^{-3} (corresponding to $\sim 450 \text{ GPa}$) to form metallic hydrogen.

On the theoretical side, a large number of papers have been published on solid hydrogen in an effort to identify the structure of the observed high-pressure phases, and make predictions regarding the metallization to be expected at still higher pressures.

An ordinary practice of the theory is to calculate the total energy and bandgap of several candidate crystal structures, and try to find the lowest-energy structures for given p , T conditions as well as the pressure for metallization. From such calculations, a general consensus is emerging that solid hydrogen under pressure transforms from hcp to orthorhombic molecular structure, and subsequently to some monatomic structure at much higher pressures. There appears to be a good possibility that metallization occurs by band closure in the molecular state. Regarding the details of crystal structure and transition pressures, however, theoretical predictions still remain divergent.

Here we shall not retrace and evaluate these theoretical developments. Instead, we try to give an overview of the present state of the art by describing two major difficulties that have come to be realized and solved to some extent; the evaluation of the exchange-correlation effects of the electrons and proper inclusion of the vibration energy of the protons.

In most of the electronic energy calculations, which essentially solve the Schrödinger equation of the many-electron system by reducing it to an one-electron problem, the exchange–correlation effect between electrons is treated in the frame of the density-functional theory (DFT), either by the local density approximation (LDA) or its modified form called the generalized gradient approximation (GGA). There are, however, serious difficulties in the application of these methods to the hydrogen problem. As these methods are known to involve large uncertainties in the estimates of binding energies and bandgaps, it could hardly be expected that they lead to reliable predictions on the preferred structure and the pressure for metallization.

Johnson and *Ashcroft* [7.67, 7.68] critically examined the validity of the LDA and demonstrated, in particular, that a well-known underestimate of the bandgap by LDA (amounting to $2 \sim 3$ eV in 24 different semiconductors) could be largely removed by including empirical screening corrections to the exchange–correlation term. They applied this method to three different molecular structures of hydrogen at different densities, and suggested on this basis that the bandgap of a preferred orthorhombic structure ($P2_1/c$) should close before it transforms to a metallic molecular structure $Cmca$ at ~ 410 GPa.

A more orthodox approach to the evaluation of the exchange interaction was taken by *Städele et al.* [7.69, 7.70]. They developed a self-consistent, *ab initio* method of treating the exchange interaction exactly in the frame of DFT (in the first-order perturbation and linear-response regime), without inclusion of any adjustable parameters. Only the correlation energy which is typically an order of magnitude smaller had to be evaluated by the LDA. Their method, termed the exact-exchange (EXX) method, was applied to a wide class of semiconductors and yielded very good estimates of bandgaps and total energies; the bandgaps agreed with experiments to within ~ 0.2 eV. Their calculation subsequently performed on molecular hydrogen [7.71] predicted that the energetically preferred structure has $Pca2_1$ symmetry up to the density of 0.61 mol cm^{-3} ($400 \sim 450$ GPa), and a metallization via band overlap is likely to happen at ≈ 400 GPa. Note that the prediction of LDA that metallic $Cmca$ structure becoming more stable above ~ 150 GPa, which contradicts the observation, was remedied in the EXX calculation. As far as the electronic energies are concerned the EXX method is believed to be the most reliable, both in regard to the relative stability of different structures and the pressure for metallization.

In more accurate determination of the preferred structure, however, a proper evaluation of the vibration energy of the protons is needed because the electronic energies of the structures varying only in the orientational order of molecules differ by small amounts, of the order of 10 meV. The vibrational energy of the protons can easily exceed these values.

Kitamura et al. [7.72] examined this problem more carefully and found indeed that proton vibration energies are large enough to reverse the order of electronic energies for different structures and pressures. They noted that the

largest contribution to the zero-point vibration energy of protons comes from vibrons, and vibron frequencies depend sensitively on the lattice structure. They admitted, however, that their calculation of vibron frequencies also depended sensitively on the method of treating exchange-correlation effects. The vibron frequencies they predicted are smaller than experimental values by $20 \sim 30\%$.

The real significance of the calculation of *Kitamura et al.*, a major part of their paper, is in fact more profound. They treated the protons and electrons on the same quantum mechanical footing, by performing first-principles path-integral molecular dynamics (FP-PIMD) calculations to determine the quantum distribution of protons. The distribution of protons calculated for three different p , T conditions (corresponding to the three different phases) are shown in Fig. 7.19, where the projection of the equi-density surface corresponding to $1/4$ of the maximum density is plotted. The result reproduces the observed features of the high-pressure phases. In phase I, the distribution is nearly spherical, and the bond centers of the molecules lie on the hcp lattice sites. In phase II, the distribution is no longer spherical and molecules are aligned in special directions, but the bond centers do not deviate noticeably from hcp lattice sites. In phase III, the orientational order becomes even more conspicuous, and the molecular motion is strongly prohibited. The bond centers form a lattice of orthorhombic symmetry. The authors called particular

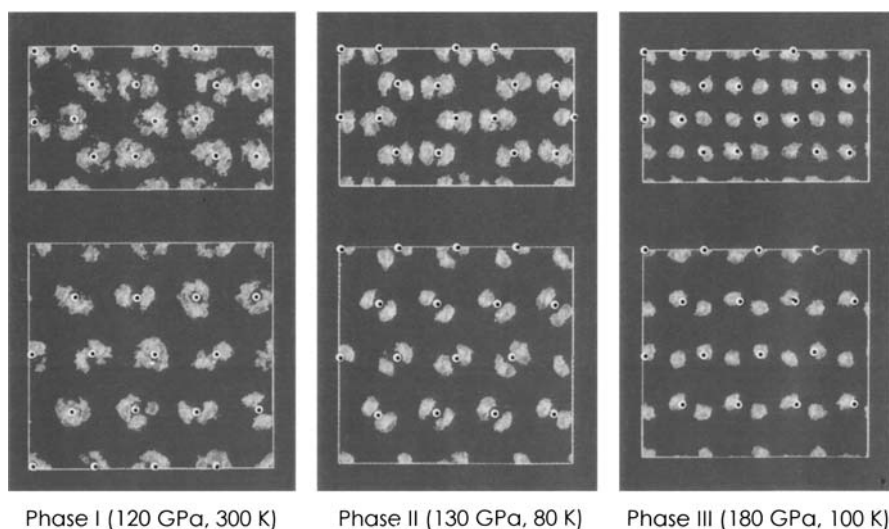


Fig. 7.19. Quantum distribution of protons in the phase I, II and III of solid H_2 . The surface of $1/4$ of the maximum density is shown, with hcp lattice sites indicated by circles. The upper figures depict the distribution projected on the plane perpendicular to the c -axis, and the lower figures are the projection on the plane containing the c -axis [7.72]

attention to the increasing orientational ordering at higher pressures as manifestation of quantum localization. In a multi-site tunneling system, depending on the shape of the potential surface, a particle may be localized on one of the potential minima leading to a structure of broken symmetry (as in phase II), or confined at a mid-point leading to a structure of higher symmetry (as in phase III). This latter is called the quantum localization, which offered an explanation for muonium in Si confined at the center of a Si cage [7.73]. As described in Sec. 5.7.2, the α - β transition in the V-H system was explained in terms of very similar change of the quantum state of H atoms.

In their MD calculation, a preferred configuration of protons for a given external parameters (p , T) emerges spontaneously. The structures deduced from their calculation are, however, not free from uncertainties arising from the adoption of LDA (or GGA) in treating the exchange-correlation effect. Throughout their calculation, they ignored the conduction band, and reached the orthorhombic structure (Cmca) in phase III. However, full-scale LDA (or GGA) calculations have shown that in this structure the band closure occurs below 50 GPa, which makes this structure metallic [7.68–7.74]. This is at variance with the observation that phase III hydrogen remains insulating to ~ 316 GPa. The prediction of the EXX method (noted above) that the structure should be Pca2₁ at these high pressures is believed to be more appropriate. Unfortunately, the combination of the EXX method for electrons and the PF-PIMD calculation for protons appears to be computationally too demanding to be effected.

7.5.2 Fluid Hydrogen at High Temperatures

What is crucial for understanding the mechanism of the observed electrical conduction under shock compression is a proper description of the state of fluid hydrogen under these conditions. Here we start by examining the implication of the Hugoniot data shown in Fig. 4.4, including possible sources of the apparent discrepancy between the two groups of data, following closely the discussions of *Nellis* [7.75].

The single-shock Hugoniot data of D₂ are replotted in Fig. 7.20 as pressure versus density compression, ρ/ρ_0 , where $\rho_0 = 0.17 \text{ g cm}^{-3}$ is the initial density at the boiling point (~ 25 K) under normal pressure [4.8–4.16]. Some theoretical predictions are also inscribed [7.76–7.79]. From this graph, the following inferences can be made regarding molecular dissociation. First, both groups of data (Group A and B of Sect. 4.1.1) agree with each other below ~ 20 GPa, and reasonably well described by a widely used SESAME model [7.76], which is in fact a semi-empirical EOS fitted to these low-pressure shock wave data. In any case, hydrogen can be regarded to be a well-behaved molecular fluid in this pressure range. Second, Group A data approach smoothly the density compression of $\rho/\rho_0 \approx 4$ at ~ 50 GPa. This is a limiting value expected for complete dissociation of diatomic gas into monatomic ideal gas [7.80]. Very similar compression behavior was observed

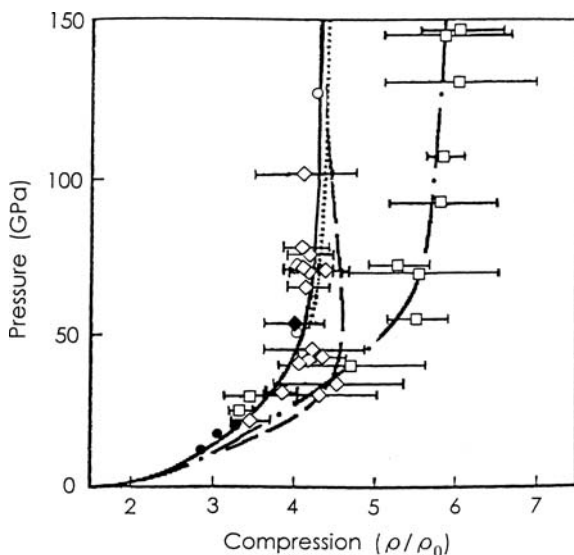


Fig. 7.20. Single-shock Hugoniot of deuterium as pressure versus compression, ρ/ρ_0 ($\rho_0 = 0.17 \text{ g cm}^{-3}$). Experiments: *solid circles* [4.8], *solid diamond* [4.10], *open diamonds* [4.13, 7.99], *open squares* [4.14, 4.15]. Theoretical models: *solid curve* [7.76], *dashed curve* [7.77], *dots* [7.78], *dot-dashed curve* [7.79]

for diatomic molecules N_2 , O_2 and CO [7.75]. Group B data, on the other hand, take rather large values $\rho/\rho_0 \sim 6$, showing a slight tendency to approach some smaller value at $>300 \text{ GPa}$. This is only possible when a majority of molecules remain intact up to very high pressures (temperatures) [7.80]. Third, the Hugoniot calculated by theoretical models based on first principles, *ab initio* methods [7.77, 7.78] and SESAME model [7.76] agree reasonably well with Group A data. All these models contain the dissociation within the formulation. Apparent agreement of the linear-mixing model of Ross [7.79] with Group B data is largely the result of empirical fitting procedure, and is therefore less meaningful physically. Fourth, evidence for nearly complete molecular dissociation at $\sim 50 \text{ GPa}$ has been provided by temperature data. Measured shock temperatures reach a plateau of $\sim 5000 \text{ K}$ near 50 GPa , indicating the occurrence of some endothermic reaction – most probably molecular dissociation [4.10]. Furthermore, Nellis [7.75] called attention to a large deviation of Group B data in the general systematics of the shock velocity versus particle velocity relation, one of the most important criteria in shock compression experiments, and suggested on this basis that some systematic errors should have been involved in the laser-driven experiments. Considering that all these highly exploratory experiments were performed under such extreme conditions, quite a respectable effort may still have to be expended before the problems have come to be completely resolved.

Based on these considerations, *Nellis* [7.75] concluded that fluid D_2 undergoes a diatomic to monatomic transition at the density of $0.6 \sim 0.7 \text{ g cm}^{-3}$, realized at $\sim 50 \text{ GPa}$ and $5000 \sim 10000 \text{ K}$ on the single-shock Hugoniot. The condition of dissociation does vary with density and temperature.

Regarding the electrical conduction, the experiments suggest that the transition to the conducting state should be continuous along the Hugoniot. As shown in Fig. 4.5, the electrical resistivity decreases continuously with pressure until it reaches a constant value ($\sim 500 \mu\Omega \text{ cm}$) above 140 GPa [4.15].

Figure 4.5 shows all the available conductivity data on H_2 and D_2 as a function of pressure [4.11, 4.15, 4.21]. The estimated temperatures are also inscribed. The conductivity does not depend on isotopes. It is primarily determined by pressure, and shows an abrupt increase between $20\text{--}80 \text{ GPa}$.

This last point parallels with the observed increase of the optical reflectivity; from 5% at 20 GPa to 60% at $\geq 55 \text{ GPa}$ characteristic of a metal [4.14]. Thus, the conductivity measurements were performed in two different regimes. To examine the conduction mechanism below $\sim 20 \text{ GPa}$, the single-shock data are replotted in the Arrhenius manner, as shown in Fig. 7.21 [4.11]. Five data points over 4 decades lie very closely on a straight line, and give the activation energy of $11.7 \pm 1.1 \text{ eV}$. The molar volume was estimated to lie between rather narrow limits, $7.17 \sim 7.83 \text{ cm}^3 \text{ mol}^{-1}$. Recognizing that this energy value agrees well with the optically determined bandgap of solid H_2 , $E_g = 12 \text{ eV}$ at $7 \text{ cm}^3 \text{ mol}^{-1}$, they proposed that fluid hydrogen could

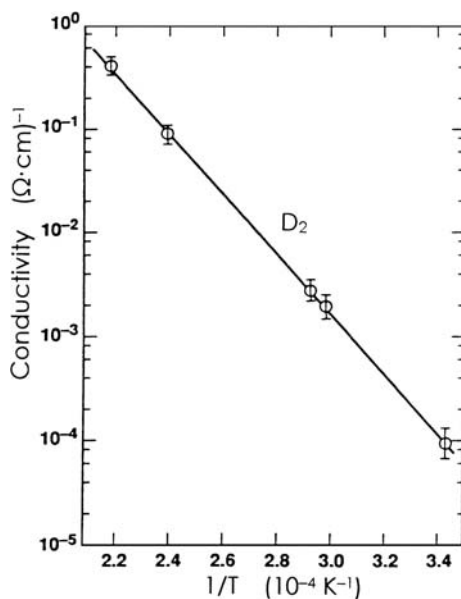


Fig. 7.21. Arrhenius plot of the electrical conductivity of shock-compressed liquid D_2 [4.11]

be regarded as a semiconductor, and the observed electrical conduction was caused by thermal excitation of carriers across the energy gap. Rather high temperatures reached by the single-shock experiments should have been a key for producing an appreciable number of carriers by excitation across this wide bandgap. In view of very similar charge distribution and similar excitation energies (ionization energy of 13.6 eV for H and a bandgap of 15 eV for solid H₂, it is expected that H and H₂ form a continuous solution having a common energy band, smeared to some extent by structural disorder and high temperatures [4.15].

In the subsequent reverberating-shock experiments above 83 GPa [4.15, 4.21], where densities are high but temperatures are rather low, a different conduction mechanism should be operating. To ascertain the conduction mechanism in this regime, it is most instructive to recall the similarities with other cases of transition to the metallic state. It appears that semiconductor-to-metal transitions are more easily realized in the fluid state than in the solid. Typical semiconductors, Si and Ge, become metals when molten. Solid I₂ at 300 K becomes metallic at 16 GPa, whereas fluid I₂ becomes metallic at only 3 GPa at 1000 K. By far the most significant is a comparison with alkali metals Rb and Cs in the fluid state [7.81]. These elements when expanded by heating above the melting point (~ 2000 K), start to form diatomic molecules, and undergo metal-to-nonmetal transition. The electrical conductivity at the transition point, called “the minimum metallic conductivity” assumes a value ≈ 2000 ($\Omega \text{ cm}$)⁻¹, which is very close to that of hydrogen (Fig. 4.5). The similarity becomes more obvious when the electrical conductivity is plotted as a function of $\rho_e^{1/3} a^*$, which is the ratio of the size of the free particles a^* (the radial extent of valence orbitals) to the average distance of the electrons $\rho_e^{-1/3}$ (assuming 1 electron per atom). This plot is shown in Fig. 7.22. In all three cases, the minimum metallic conductivity is reached at nearly the same value of $\rho_e^{1/3} a^* = 0.38$. This is a strong indication that these three elements undergo a Mott transition when the electronic charge densities of neighboring atoms come close together to produce sufficient overlap to delocalize a valence electron.

Theoretically, there have been numerous approaches to the state of fluid hydrogen and the mechanism of electrical conduction, each with different levels of approximation. The fact that the constituents – electrons and protons (deuterons) – are strongly coupled, highly correlated and form different combinations – monomers, dimers, etc. – makes the calculation extremely difficult. Empirical models based on the properties of atoms and molecules under normal conditions face difficulties when extrapolated to high p , T conditions where atoms and molecules are no longer well-defined entities. Approaches from the opposite end, an ionized plasma, have difficulties including strong correlations properly. Plasma theories unanimously predict a first-order transition from molecular to plasma state, and subsequently to another transition

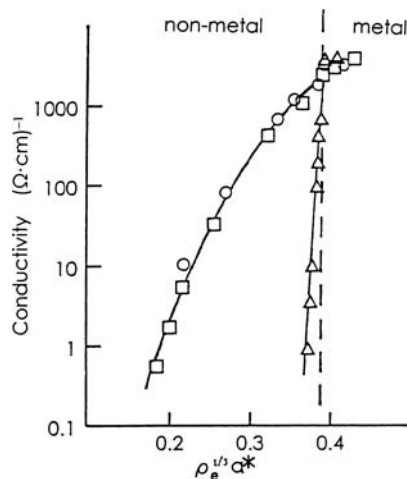


Fig. 7.22. Electrical conductivity plotted against the scaling parameter $\rho_e^{1/3} a^*$; cesium (*squares*), rubidium (*circles*), hydrogen (*triangles*). All these substances become metallic at nearly the same value of $\rho_e^{1/3} a^* = 0.38$. In terms of electron density ρ_e , the transition occurs at widely different values; $\rho_e \approx 5 \times 10^{21} \text{ cm}^{-3}$ for cesium and rubidium, and $\rho_e \approx 4 \times 10^{23} \text{ cm}^{-3}$ for hydrogen [7.81]

to more highly ionized plasma state [7.82–7.84]. These predictions do not appear to be supported by the observations.

Here, instead of critically reviewing these various calculations, I prefer to focus on the results of *Lenosky et al.* They calculated the EOS by tight-binding (TB) approximation [7.85], and then proceeded to first-principles, *ab initio* calculations without any fitting parameters [7.77]. They performed MD calculations based on density-functional theory (DFT-MD) with a modified local-density approximation (generalized gradient approximation; GGA). This calculation is believed to be physically better founded than any other calculations. They carefully examined various possible sources of error, including the limitation of GGA, and concluded that the only remaining sources are probably the neglect of nuclear zero-point motion and inaccuracies in the weak long-range interactions. They pointed out that such small errors in the total energy may incur noticeable shifts of the Hugoniot: The lowering of the total energy by 0.1 eV reduces the maximum compression by ~ 0.1 . This provides a measure of the reliability of the Hugoniot calculations.

The mechanism of electrical conduction was also examined by *Lenosky et al.* [7.86] by MD calculations based on a tight-binding (TB) model. They calculated the temperature dependence of the degree of dissociation from the change in shape of a pair distribution function, and the electrical conductivity σ using an approximate formula (in atomic units) due to *Mott* [7.87]

$$\sigma = -\frac{2\pi^2 e^2 \hbar^3}{3m^2} \bar{l} \int \{N(E)\}^2 \frac{\partial f}{\partial E} dE \quad (7.4)$$

where \bar{l} , the mean free path of an electron, is close to the average nearest-neighbor distance in the fluid, and $N(E)$ is the average number of eigenstates per unit volume and unit energy. As $\partial f/\partial E$, the derivative of the Fermi distribution function with respect to energy, is sharply peaked at the Fermi energy E_F , the principal contribution to the conductivity comes from the states near E_F . They found that monomers contribute to the density of states near the Fermi level, acting like dopant atoms in a semiconductor, and furthermore, at temperatures of 3000–15000 K and densities $\rho = 0.289$ – 0.733 g cm $^{-3}$, the conductivity calculated by eq.(7.4) is approximately proportional to the square of the monomer concentration. An example of this comparison is shown in Fig. 7.23. The limiting conductivity (the minimum metallic conductivity) is reached at a dissociation fraction of 0.374, which is close to the percolation threshold. Under the condition of the experiment (~ 3000 K and $\rho = 0.733$ g cm $^{-3}$, the minimum metallic conductivity of 3300 (Ω cm) $^{-1}$ is reached at a pressure of 132 GPa. These results are in reasonable agreement with the observation.

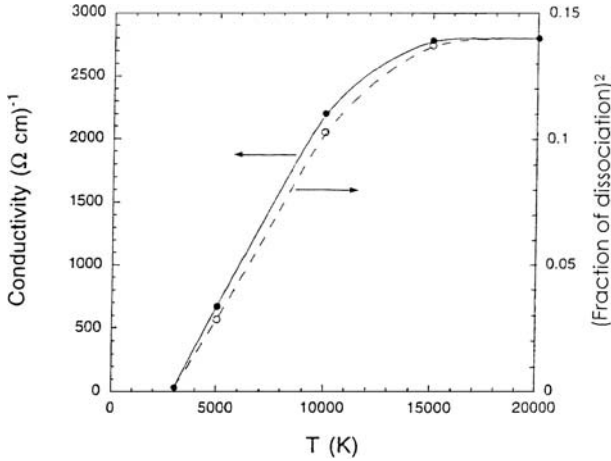


Fig. 7.23. Electrical conductivity and squared dissociated fraction of hydrogen as a function of temperature for the density $\rho = 0.335$ g cm $^{-3}$ [7.86].

It is worthy to note here that the operating mechanisms are highly transient in nature. Molecules are short-lived ($10^{-14} \sim 10^{-13}$ s), for only a few molecular vibrational periods. Therefore, although the average number of monomers participating in conduction fluctuate around a single value, the internal structure of the fluid hydrogen has a pronounced time dependent nature. Hydrogen nuclei in monomers and transient pairs are continually

exchanging in short times of $\sim 10^{-14}$ s, comparable to characteristic times for collisions, vibrations, and rotations. This is certainly a new state of matter.

7.5.3 Superconductivity

One of the important properties expected for metallic hydrogen is superconductivity.

Ashcroft, in as early as 1968 [7.88], suggested that metallic hydrogen should become superconducting with a transition temperature of ~ 50 K. In the standard weak-coupling BCS expression, T_c is given by

$$T_c = 0.85\theta_D \exp[-1/V_{\text{ep}}N(E_F)] \quad (7.5)$$

where V_{ep} stands for the matrix element of the electron-phonon interaction. θ_D of solid hydrogen was estimated at 3500 K and $V_{\text{ep}}N(E_F) \geq 0.25$.

This is in contrast to other monovalent metals (alkalis), where much smaller values of θ_D (due to larger masses) and $V_{\text{ep}}N(E_F)$ (due to the cancellation of electron-phonon and electron-electron interactions) lead to nearly vanishing transition temperatures. There is a general tendency for the electron-phonon coupling to increase as the density of the system increases. (Note that the value of r_s for metallic hydrogen is much smaller ($r_s \sim 1$) than that for alkalis; for example, $r_s = 3.94$ for Na.)

In metallic hydrogen, where high-density electrons of predominantly s character have large amplitudes at nuclear positions, the electron-phonon coupling is expected to be too strong to be described by the BCS formula, e.g. (7.5). Rather, in the strong-coupling regime, the superconducting transition temperature should be calculated by numerically solving the Eliashberg equation, or its approximate forms, such as McMillan's equation [7.89] or Leavens' formula [7.90].

The McMillan equation reads

$$T_c = \frac{\hbar\langle\omega\rangle}{1.2k} \exp \left[\frac{-1.04}{\lambda - (1 + 0.62\lambda)\mu^*} \right], \quad (7.6)$$

where $\langle\omega\rangle$ is the average phonon frequency, λ the electron-phonon coupling parameter, and μ^* the effective Coulomb interaction parameter between the electrons. (The first factor is often written as $\theta_D/1.45$.) The McMillan equation is usually said to be a good approximation for $\lambda \leq 1.25$. However, calculations of *Whitmore et al.* [7.91] showed that, for fcc metallic hydrogen in the range of λ between 0.51 and 1.26 ($r_s = 0.6 - 1.0$), the McMillan equation overestimates T_c by 40% whereas Leavens' formula overestimates it by 10%. This point has to be borne in mind when making comparisons between different calculations.

In any case, what is crucial for treating the superconductivity is a reliable calculation of the electron-phonon coupling and the phonon spectrum, especially the former. It can be naturally anticipated that estimates of the

electron–phonon coupling depend sensitively on how accurately the electron states near hydrogen nuclei are treated.

Whitmore et al. [7.91] were the first to perform a first-principles calculation on metallic hydrogen based on the nonlinear self-consistent screening of a proton by high-density electrons. They calculated the effective electron–proton potentials and proton–proton potentials for three different densities ($r_s = 0.6, 0.8, 1.0$) for fcc and bcc structures and, subsequently, the phonon spectrum in the self-consistent harmonic approximation. The function usually written as $\alpha^2 F(\omega)$, which is the average of the phonon density of states $F(\mathbf{k} - \mathbf{k}', \omega)$ weighted by the effectiveness of these phonons for causing electronic transitions $\mathbf{k} \rightarrow \mathbf{k}'$, and which essentially determines the superconductivity, is illustrated in Fig. 7.24 for the fcc structure at $r_s = 1.0$. For other densities, the shape of the function is nearly conserved, only the energy is scaled as r_s^{-2} .

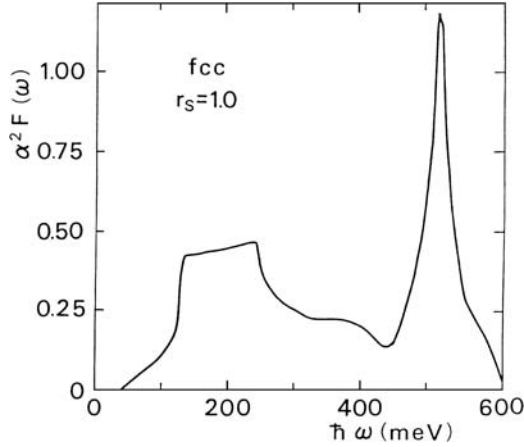


Fig. 7.24. The function $\alpha^2 F(\omega)$ obtained by first-principles calculation for fcc metallic hydrogen with $r_s = 1.0$ a.u. [7.91]

The results they obtained for the superconductivity in the fcc phase are summarized in Table 7.2. Considering the uncertainty in the values of the effective Coulomb repulsion between the electrons μ^* , which was evaluated approximately by a linear-response theory, T_c was determined for μ^* values 30% smaller and 30% larger (given in this order in parentheses). As already mentioned, the application of McMillan's and Leavens' formulae was found to overestimate T_c by 40 and 10%, respectively. In any case, the values of T_c are impressively high in the fcc phase. In contrast to these results, the T_c values obtained for the bcc phase are very low: $T_c = 0.02, 1.2$, and 10 K for $r_s = 0.6, 0.8$, and 1.0, respectively (as calculated by McMillan's equation). This lowering of T_c is a result of the reduction of λ ; $\lambda = 0.184, 0.258$, and

Table 7.2. Superconductivity of metallic hydrogen obtained by first-principles calculation for the fcc structure [7.91]. Values of T_c in parentheses are those obtained for μ^* 30% smaller and 30% larger (in this order)

r_s [a.u.]	0.6	0.8	1.0
$V_{\text{ep}}N(E_F)$	0.130	0.157	0.182
	0.5096	0.8073	1.2631
μ^*	1.04	1.21	1.36
$\hbar\langle\omega\rangle$ [eV]	1.059	0.584	0.354
T_c [K]	147	243	280
	(182, 114)	(281, 214)	(306, 260)

0.355 for $r_s = 0.6, 0.8$, and 1.0 , respectively. We shall examine this sensitivity of T_c to crystal structures later.

Another first-principles calculation was performed by *Barbee et al.* [7.92] for the distorted primitive hexagonal structure with the Wigner–Seitz radius of $r_s = 1.30$ ($p \approx 400$ GPa). The electron–phonon interaction parameter was found to be $\lambda \sim 1.5$, the average phonon energy $\hbar\langle\omega\rangle = 0.158$ eV, and the effective Coulomb repulsion $\mu^* \sim 0.10$. Then, the McMillan equation predicted $T_c = 210$ K, and the Eliashberg equation $T_c = 230$ K. By considering the uncertainties of λ and μ^* , ~ 0.02 and ~ 0.40 , respectively, the range of T_c was estimated to be 145–300 K, with a probable value of 230 K. Note that this calculation yielded T_c of the same order of magnitude as that of *Whitmore et al.* [7.91], in spite of the fact that the two calculations dealt with different crystal structures and densities.

There have been a number of other calculations on the superconductivity of metallic hydrogen based on some approximate methods.

One of them, the linear-response theory, was found to grossly underestimate T_c . This general discrepancy was clearly demonstrated by *Whitmore et al.* [7.91] by comparison of their results with those of *Caron* [7.93] by the linear-screening theory for the same structure and densities. The inadequacy of the linear-screening theory is expected to become more important at closer distances to a proton where the potential is stronger. Indeed, *Whitmore et al.* [7.91] demonstrated that the displaced electron density in the linear-screening theory is much smaller than that of the nonlinear screening theory, especially near a proton (Fig. 7.25).

Another means of calculation based on an augmented-plane-wave (APW) method appears to predict T_c close to first-principles calculations. In this method, the electronic wave function is expanded in spherical (or lattice) harmonics inside muffin-tin spheres, and connected smoothly to plane-wave states in the interstitial region. The electron–phonon coupling parameter is then evaluated in terms of phase shifts of scattered waves when the muffin tin is displaced rigidly (by using Gaspari–Gyorffy’s formula [7.94]).

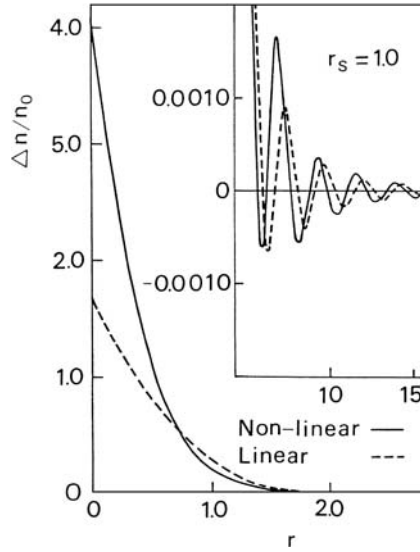


Fig. 7.25. Density of screening electrons around a proton for $r_s = 1.0$ a.u. calculated by nonlinear theory (—) and linear theory (---) [7.91]

The results obtained by *Min et al.* [7.95] for the fcc phase are given in Table 7.3. These results compare favorably with those of Table 7.2 based on first-principles calculations. Earlier calculations by the APW method also gave similar results for the fcc structure ($T_c \approx 250$ K for $r_s = 1.64$ [7.96], and $T_c = 234$ K for $r_s = 1.25$ [7.97]).

Table 7.3. Superconductivity of metallic hydrogen calculated by the APW method for the fcc structure [7.95]

r_s [a.u.]	1.0	1.1	1.2	1.3	1.4	1.5	1.6	1.7	1.8
λ	0.965	1.168	1.390	1.631	1.889	2.164	2.400	2.800	2.953
T_c [K]	243.3	267.2	276.9	276.9	270.9	261.7	248.1	242.0	225.7

Regarding the sensitivity to the crystal structure, no general consensus has been reached so far. Whereas the first-principles calculation of *Whitmore et al.* [7.91] predicted very different T_c values for the fcc and bcc phases, all other calculations seem to suggest that T_c is not very sensitive to the crystal structure. The results of APW calculations, for example, are quite insensitive to the crystal structure. *Min et al.* [7.95] stated that the values of λ and T_c for sc, bcc, and hcp structures are very similar to those for the fcc structure. *Papaconstantopoulos and Klein* [7.97] also obtained very similar values for fcc and bcc structures. Even in the liquid state, where the “lattice” vibration

is strongly damped leaving only longitudinal sound modes, T_c was estimated to be reasonably high: $T_c = 40, 141, 119$, and 87 K for $r_s = 1.20, 1.36, 1.48$, and 1.6 , respectively [7.98]. The function $\alpha^2 F(\omega)$ calculated for the liquid state is shown in Fig. 7.26 [7.98]. Furthermore, *Barbee et al.* [7.92] inferred that, even in the metallic phase with remnant molecular pairing, T_c could be high because the overall phonon spectrum appeared to be similar.

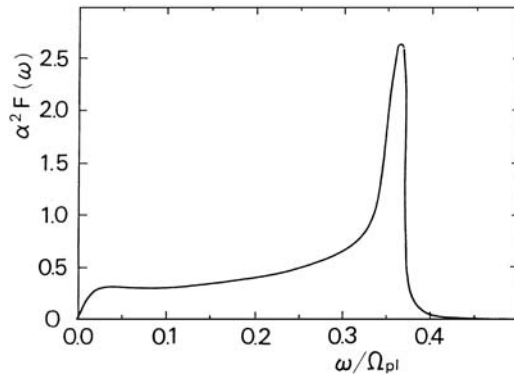


Fig. 7.26. The function $\alpha^2 F(\omega)$ calculated for metallic hydrogen in liquid state [7.98]. The frequency is expressed as a fraction of the ionic plasmon frequency $\Omega_{pl} = (4\pi n e^2 / M)^{1/2}$

If, as indicated by *Whitmore et al.* [7.91], T_c is very sensitive to the crystal structure, its realistic estimation should become extremely difficult, especially for a complex structure with remnant molecular pairing, which is the one actually realized under pressure. Thus, the sensitivity to the crystal structure remains an important consideration in the superconductivity of metallic hydrogen.

An increasing curvature of the melting curve observed at high pressures (≤ 44 GPa) [7.100, 7.101] suggested that it might tend to decrease at still higher pressures. This expectation gained additional support from recent first-principles calculations. The first-principles (GGA) MD calculations of *Bonev et al.* [7.102] demonstrated that the temperature of melting from molecular solid to molecular liquid indeed exhibits a maximum as a function of pressure, and another first-order transition from molecular to dissociated liquid takes place at still higher temperatures. The results are shown in Fig. 7.27. The melting curve is well represented by a Kechin melt equation [7.103]

$$T_m = 14.025(1 + p/0.0304)^{0.600} \exp(-7.3 \times 10^{-3} p) \quad [\text{K}],$$

where p is in units of GPa [7.102]. The extrapolation of the liquid-liquid transition line indicates a triple point at ~ 300 GPa and ~ 400 K.

An implication of this result is profound. It opens the possibility of realizing a quantum liquid state at reasonably low temperatures. There have been

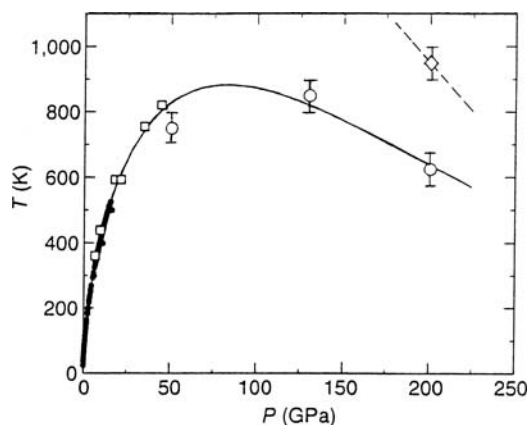


Fig. 7.27. The melting curve of H_2 . Solid circles [7.100] and open squares [7.101] are experimental data, and open circles are the results of first-principles MD calculations [7.102]. A solid curve is a Kechin equation fitted with these points. An open diamond and a slope there mark the transition from molecular to dissociated liquid derived from the first-principles MD calculations [7.102]

theoretical predictions that a dense liquid H_2 may possess unique quantum properties distinctly different from familiar liquid He, due to its composition consisting of two Fermions – protons and electrons having widely different masses [4.77, 7.104–7.106]. Thus it is suggested that a traditional classification of quantum liquid into superconductors and superfluid, characterized by dissipationless electrical currents or mass flow, may break down in this case. The liquid H_2 may undergo several phase transitions as a function of temperature and magnetic field, depending on the magnitude of the interactions between electronic and protonic vortex lines [7.106].

Even more tantalizing is the possibility that the superfluidity might show up in solid H_2 . The superfluidity in the solid state, a seemingly weird concept, has in fact been pursued theoretically for quite some time in ^4He [7.107–7.112], and appears to have been found recently below 0.23 K [7.112, 7.113]. Although the physical implication of these observations have not been elucidated yet, several views expressed on this subject are worth reading [7.115–7.117].

This problem is of particular concern to us because the solid molecular H_2 , owing to its small mass, may well exhibit similar properties.

In closing, I recall that at the time of writing of the First Edition of this book, the metallization of elemental hydrogen was an imminent goal of experimentalists. Now, after having reached this point, we have a perspective of an area wide open for exploration. No doubt hydrogen is the simplest of atoms, but it does not form the simplest of solids or liquids.

References

Chapter 1

- 1.1 N.B. Vargaftik: *Tables on the Thermophysical Properties of Liquids and Gases* (Wiley, New York 1975)
- 1.2 I.F. Silvera: *Rev. Mod. Phys.* **52**, 393(1980)
- 1.3 *Landolt-Börnstein: Numerical Data and Functional Relationships in Science and Technology, Group I, Vol. 3, Numerical Tables for Angular Correlation Computations in α -, β - and γ -Spectroscopy* (Springer, Berlin, Heidelberg 1968)
- 1.4 M. Haissinsky: *Nuclear Chemistry and Its Applications* (Addison-Wesley, Reading, MA 1964) p. 245
- 1.5 H.M. Mittelhauser, G. Thodos: *Cryogenics* **4**, 368 (1964)
- 1.6 J. van Kranendonk: *Solid Hydrogen* (Plenum, New York, London 1983) p. 6
- 1.7 P. Dehmer: *Phys. World* **3**, 27 (1995)
- 1.8 *Encyclopedie des Gaz* (Elsevier, 1976)
- 1.9 L. Pauling: *The Nature of Chemical Bonds* (Cornell University Press, N.Y. 1960) p. 93
- 1.10 R.D. Shannon, C.T. Prewitt: *Acta Crystallogr.* **B25**, 925 (1969)
- 1.11 R.D. Shannon, C.T. Prewitt: *Acta Crystallogr.* **B26**, 1046 (1970)

Chapter 2

- 2.1 G.G. Libowitz: *Solid-State Chemistry of Binary Metal Hydrides* (Benjamin, New York 1965)
- 2.2 K.M. Mackey: *Hydrogen Compounds of Metallic Elements* (Spon, London 1966)
- 2.3 W.M. Mueller, J.P. Blackledge, G.G. Libowitz (eds.): *Metal Hydrides* (Academic, New York 1968)
- 2.4 T.B. Massalski (ed.): *Binary Alloy Phase Diagrams* (American Society of Metals, Metals Park, OH 1986), vol. 1-3
- 2.5 F.A. Lewis, A. Aladjem (eds.): *Hydrogen Metal Systems I, II* (Scitec Publ., Switzerland 1996)
- 2.6 H. Frieske, E. Wicke: *Ber. Bunsenges. Phys. Chem.* **77**, 48 (1973)
- 2.7 I.S. Anderson, C.J. Carlile, D.K. Ross: *J. Phys. C* **11**, L381 (1978)
- 2.8 T.E. Ellis, C.B. Satterthwaite, M.H. Mueller, T.O. Brun: *Phys. Rev. Lett.* **42**, 457 (1979)
- 2.9 M. Hirabayashi, H. Asano: In *Metal Hydrides*, ed. by G. Bambakidis (Plenum, New York 1981) p. 53

- 2.10 T. Schober, H. Wenzl: In *Hydrogen in Metals II*, ed. by G. Alefeld, J. Völkl, Topics Appl. Phys., Vol. 29 (Springer, Berlin, Heidelberg 1978) p. 11
- 2.11 H. Zabel, J. Peisl: J. Phys. F **9**, 1461 (1979)
- 2.12 T. Kuji, T.B. Flanagan: J. Phys. F **15**, L59 (1985)
- 2.13 H. Wenzl, P. Mecking, M.E. De Prieto: Ann. de Chimie **7**, 517 (1982)
- 2.14 R. Lässer, T. Schober: J. Less-Common Met. **130**, 453 (1987)
- 2.15 Y. Fukai, Y. Endo, K. Mogi, T. Hishinuma, Y. Sakamaki, T. Yagi: to be published.
- 2.16 J.J. Reilly, R.H. Wiswall: Inorg. Chem. **9**, 1678 (1970)
- 2.17 N. Boes, H. Züchner: Z. Naturforsch. **31 A**, 754 (1976)
- 2.18 A. Sawatzky, G.A. Ledoux: In *Proc. 2nd Int'l Congress Hydrogen in Metals*, Paris, 1977, 1C8 (Pergamon, Oxford 1977)
- 2.19 T. Schober, A. Carl: J. Less-Common Met. **63**, P53 (1979)
- 2.20 E. Fromm, E. Gebhardt (eds.): *Gase and Kohlenstoff in Metallen*, Reine und angewandte Metallkunde in Einzeldarstellungen, 26. Band (Springer, Berlin, Heidelberg 1976)
- 2.21 E. Fromm, G. Hörz: Intern. Metals Rev. **25**, 269 (1980)
- 2.22 H. Wenzl: Intern. Metals Rev. **27**, 140 (1982)
- 2.23 M.L. Lieberman, P.G. Wahlbeck: J. Phys. Chem. **69**, 3514 (1965)
- 2.24 E. Veleckis, R.K. Edwards: J. Phys. Chem. **73**, 683 (1969)
- 2.25 R. Griessen, T. Riesterer: In *Hydrogen in Intermetallic Compounds I*, ed. by L. Schlapbach, Topics Appl. Phys., Vol. 63 (Springer, Berlin, Heidelberg 1988) p. 219
- 2.26 O.J. Kleppa, P. Dantzer, M.E. Melnichak: J. Chem. Phys. **61**, 4048 (1974)
- 2.27 P. Dantzer, O.J. Kleppa, M.E. Melnichak: J. Chem. Phys. **64**, 139 (1976)
- 2.28 G. Boureau, O.J. Kleppa and P. Dantzer: J. Chem. Phys. **64**, 5247 (1976)
- 2.29 G. Boureau, O.J. Kleppa: J. Chem. Phys. **65**, 3915 (1976)
- 2.30 O.J. Kleppa, R.C. Phutela: J. Chem. Phys. **76**, 1106 (1982)
- 2.31 J.W. Simons, T.B. Flanagan: J. Phys. Chem. **69**, 3581 (1965)
- 2.32 N. Boes, H. Züchner: Ber. Bunsenges. Phys. Chem. **80**, 22 (1976)
- 2.33 R. Kirchheim, R.B. McLellan: J. Electrochem. Soc. **127**, 2439 (1980)
- 2.34 J.D. Clewley, T. Curran, T.B. Flanagan, W.A. Oates: J. Chem. Soc. Faraday Trans. I **69**, 449 (1973)
- 2.35 A. Sieverts, G. Zapf: Z. Phys. Chem. **174A**, 359 (1935)
- 2.36 A. Magerl, N. Stump, H. Wipf, G. Alefeld: J. Phys. Chem. Solids **38**, 683 (1977)
- 2.37 K. Watanabe, Y. Fukai: J. Phys. Soc. Jpn. **54**, 3415 (1985)
- 2.38 D.T. Peterson, S.O. Nelson: Metall. Trans. **16A**, 367 (1985)
- 2.39 E. Wicke, J. Blaurock: Ber. Bunsenges. Phys. Chem. **85**, 1091 (1981)
- 2.40 E. Wicke, G.H. Nernst: Ber. Bunsenges. Phys. Chem. **68**, 224 (1964)
- 2.41 T.B. Flanagan, J.F. Lynch: J. Phys. Chem. **79**, 444 (1975)
- 2.42 T. Kuji, W.A. Oates: J. Less-Common Met. **102**, 251 (1984)
- 2.43 J.F. Lynch, J. Tanaka: Acta Metall. **29**, 537 (1981)
- 2.44 L.N. Yannopoulos, R.K. Edwards, P.G. Wahlbeck: J. Phys. Chem. **69**, 2510 (1965)
- 2.45 J.R. Lacher: Proc. R. Soc. London A **161**, 525 (1937)
- 2.46 J.R. Lacher: Proc. Cambridge Philos. Soc. **34**, 518 (1938)
- 2.47 G. Alefeld: Ber. Bunsenges. Phys. Chem. **76**, 335 (1972)

- 2.48 J.D. Eshelby: In *Solid State Physics*, Vol. 3, ed. by F. Seitz, D. Turnbull (Academic, New York 1956) p. 79
- 2.49 H. Wagner, H. Horner: *Adv. Phys.* **23**, 587 (1974)
- 2.50 H. Wagner: In *Hydrogen in Metals I*, ed. by G. Alefeld, J. Völkl, Topics Appl. Phys., Vol. 28 (Springer, Berlin, Heidelberg 1978) p. 5
- 2.51 R. Siemes: *Phys. Status Solidi* **42**, 105 (1970)
- 2.52 R.P. Griessen: In *Hydrogen in Disordered and Amorphous Solids*, ed. by G. Bambakidis, R.C. Bowman, Jr. (Plenum, New York 1986) p. 153
- 2.53 W.A. Oates, A.M. Stoneham: *J. Phys. F* **13**, 2427 (1983)
- 2.54 D.G. Westlake: *J. Less-Common Met.* **75**, 177 (1980)
- 2.55 K. Ghoshray, B. Bandyopadhyay, M. Sen, A. Ghoshray, N. Chatterjee: *Phys. Rev. B* **47**, 8277 (1993)
- 2.56 M. Sen, A. Ghoshray, K. Ghoshray, S. Sil, N. Chatterjee: *Phys. Rev. B* **53**, 14345 (1966)
- 2.57 V.A. Yartys, R.V. Denys, B.C. Hauback, G. Fjellvåg, I.I. Bulyk, A.B. Riabov, Ya.M. Kalychak: *J. Alloys Comp.* **330–332**, 132 (2002)
- 2.58 W.A. Oates, J.A. Lambert, P.T. Gallagher: *Trans. AIME* **245**, 47 (1969)
- 2.59 G. Boureau: *J. Phys. Chem. Solids* **42**, 743 (1981)
- 2.60 G. Boureau: *J. Phys. Chem. Solids* **45**, 973 (1984)
- 2.61 G. Boureau, J. Campserveaux: *Philos. Mag.* **36**, 9 (1977)
- 2.62 J. Kanamori, Y. Kakehashi: *J. Phys. (Paris), Colloq. C7* **38**, 274 (1977)
- 2.63 P.C. Clapp, S.C. Moss: *Phys. Rev.* **142**, 418 (1966)
- 2.64 P.C. Clapp, S.C. Moss: *Phys. Rev.* **171**, 754 (1968)
- 2.65 D.J. Picton, R.A. Bond, B.S. Bowerman, D.K. Ross, D.G. Witchell, I.S. Anderson, C.J. Carlile: *J. Less-Common Met.* **88**, 133 (1982)
- 2.66 W.A. Oates: *J. Less-Common Met.* **88**, 411 (1982)
- 2.67 H.S.U. Jo, S.C. Moss: *Solid State Commun.* **30**, 365 (1979)
- 2.68 E. Burkel, H. Behr, H. Metzger, J. Peisl: *Phys. Rev. Lett.* **46**, 1078 (1981)
- 2.69 R. Chasnov, H.K. Birnbaum, S.M. Shapiro: *Phys. Rev. B* **33**, 1732 (1986)
- 2.70 P. Vajda: In *Handbook on the Physics and Chemistry of Rare Earths*, vol. 20, ed. by K.A. Gschneidner, L. Eyring (Elsevier, 1995) p. 207
- 2.71 P. Vajda, J.N. Daou: In *Hydrogen Metal Systems I, II*, ed. by F.A. Lewis, A. Aladjem (Scitech Publ., Switzerland 1996) p. 71
- 2.72 Y. Fukai, S. Yamamoto, S. Harada, M. Kanazawa: *J. Alloys Comp.* **372**, L4 (2004)
- 2.73 T. Kuji, W.A. Oates: *J. Less-Common Met.* **102**, 273 (1984)
- 2.74 H. Zabel, H. Peisl: *Phys. Rev. Lett.* **42**, 511 (1979)
- 2.75 H. Zabel, H. Peisl: *Acta Metall.* **28**, 589 (1980)
- 2.76 Y. de Ribaupierre, F.D. Manchester: *J. Phys. C* **7**, 2126 (1974)
- 2.77 Y. de Ribaupierre, F.D. Manchester: *J. Phys. C* **7**, 2140 (1974)
- 2.78 Y. de Ribaupierre, F.D. Manchester: *J. Phys. C* **8**, 1339 (1975)
- 2.79 H. Conrad, G. Bauer, G. Alefeld, T. Springer, W. Schmatz: *Z. Physik* **266**, 239 (1974)
- 2.80 H.C. Bauer, J. Tretkowski, J. Völkl, U. Freudenberg, G. Alefeld: *Z. Phys. B* **28**, 255 (1977)
- 2.81 J. Tretkowski, J. Völkl, G. Alefeld: *Z. Phys. B* **28**, 259 (1977)
- 2.82 W. Munzing, N. Stump: *J. Appl. Cryst.* **11**, 588 (1978)
- 2.83 J. Lima-de-Faria: *Z. Kristallographie* **22**, 346 (1965)
- 2.84 J. Lima-de-Faria: *Z. Kristallographie* **22**, 359 (1965)

- 2.85 J.K. Jacobs, F.D. Manchester: J. Less-Common Met. **49**, 67 (1776)
- 2.86 O. Blaschko, R. Klemencic, P. Weinzierl, O.J. Eder: Solid State Commun. **27**, 1149 (1978)
- 2.87 O. Blaschko, R. Klemencic, P. Weinzierl, O.J. Eder, P. von Blanckenhagen: Acta Cryst. A **36**, 605 (1980)
- 2.88 H. Pinto, C. Korn, S. Goren, H. Shaked: Solid State Commun. **32**, 397 (1979)
- 2.89 P.P. Narang, G.L. Paul, K.N.R. Taylor: J. Less-Common Met. **56**, 125 (1977)
- 2.90 R.R. Arons: In *Landolt-Börnstein, NS, vol. III/12c*, ed. by K.H. Hellwege, A.M. Hellwege (Springer, Berlin 1982) p. 2645
- 2.91 R.R. Arons: In *Landolt-Börnstein, NS, vol. 19/d1*, ed. by H.P.J. Wijn (Springer, Berlin 1991) p. 391
- 2.92 C.E. Holley, Jr., R.N.R. Mulford, F.H. Ellinger, W.C. Koehler, W.H. Zachariasen: J. Phys. Chem. **59**, 1226 (1955)
- 2.93 C.G. Titcomb, A.K. Cheetham, B.E.F. Fender: J. Phys. C **7**, 2409 (1974)
- 2.94 P. Knappe, H. Müller, H.W. Mayer: J. Less-Common Met. **95**, 323 (1983)
- 2.95 G. André, O. Blaschko., W. Schwarz, J.N. Daou, P. Vajda: Phys. Rev. B **46**, 8644 (1992)
- 2.96 Q. Huang, T.J. Udovic, J.J. Rush, J. Schefer, I.S. Anderson: J. Alloys Comp. **231**, 95 (1995)
- 2.97 E. Kaldis, E. Boroch, M. Tellefsen: J. Less-Common Met. **129**, 57 (1987)
- 2.98 M. Mansmann, W.E. Wallace: J. Phys. Radium **25**, 454 (1964)
- 2.99 T.J. Udovic, Q. Huang, R.W. Erwin, B. Hjörvarsson, R.C.C. Ward: Phys. Rev. B **61**, 12701 (2000)
- 2.100 P. van Gelderen, P.J. Kelly, G. Brooks: Phys. Rev. B **63**, 100301 (2001)
- 2.101 C.B. Satterthwaite, I.L. Toepke: Phys. Rev. Lett. **25**, 741 (1970)
- 2.102 B. Stritzker, H. Wühl: In *Hydrogen in Metals II*, ed. by G. Alefeld, J. Vökl, Topics Appl. Phys., Vol. 28 (Springer, Berlin, Heidelberg 1978) p. 243
- 2.103 J.W. Ward, J.H. Haschke: In *Handbook on the Physics and Chemistry of Rare Earths*, vol. 18, ed. by K.A. Gschneidner, L. Eyring, G.R. Choppin, G.H. Lander (Elsevier, 1994) p. 293
- 2.104 W.A. Oates, T.B. Flanagan: J. Mater. Sci. **16**, 3235 (1981)
- 2.105 T.B. Flanagan: J. Less-Common Met. **63**, 209 (1979)
- 2.106 M. Koiwa, K. Shibata: J. Less-Common Met. **72**, 125 (1980)
- 2.107 O. Yoshinari, M. Koiwa: Acta Metall. **30**, 1979 (1982)
- 2.108 O. Yoshinari, M. Koiwa: Acta Metall. **30**, 1987 (1982)
- 2.109 O. Yoshinari, M. Koiwa: J. Phys. F **17**, 59 (1987)
- 2.110 R. Hanada, T. Suganuma, H. Kimura: Scripta Metall. **6**, 483 (1972)
- 2.111 T.B. Flanagan, T. Schober, H. Wenzl: Acta Metall. **33**, 685 (1985)
- 2.112 Y. Fukai, S. Kazama: Acta Metall. **25**, 59 (1977)
- 2.113 T.B. Flanagan: J. Less-Common Met. **63**, 209 (1979)
- 2.114 Y. Fukai: J. Nucl. Mater. **69/70**, 573 (1978)
- 2.115 Y. Fukai: *Physics of Diffusion Phenomena* (Asakura-Shoten, Tokyo 1988) (in Japanese)
- 2.116 J.N. Daou, J.E. Bonnet: J. Phys. Chem. Solids **35**, 59 (1974)
- 2.117 B.J. Beaudry, F.H. Spedding: Metall. Trans. **6B**, 419 (1975)
- 2.118 C.L. Jensen, M.P. Zalesky: J. Less-Common Met. **75**, 175 (1980)
- 2.119 J.N. Daou, P. Vajda, A. Lucasson, J.P. Burger: Phys. Status Solidi (a) **95**, 543 (1986)
- 2.120 J.E. Bonnet, C. Juckum, A. Lucasson: J. Phys. F **12**, 699 (1982)

- 2.121 P. Vajda, J.N. Daou, A. Lucasson, J.P. Burger: J. Phys. F **17**, 1029 (1987)
- 2.122 J.N. Daou, P. Vajda, J.P. Burger: Solid State Commun. **64**, 937 (1987)
- 2.123 J.N. Daou, P. Vajda, A. Lucasson, P. Lucasson: J. Phys. C **14**, 3155 (1981)
- 2.124 J.N. Daou, P. Vajda, A. Lucasson, P. Lucasson: Solid State Commun. **38**, 135 (1981)
- 2.125 J.N. Daou, P. Vajda, A. Lucasson, P. Lucasson: J. Phys. C **14**, 129 (1981)
- 2.126 J.N. Daou, P. Vajda: J. Phys. F **12**, L13 (1982)
- 2.127 J.E. Bonnet, J.N. Daou: J. Phys. Chem. Solids **40**, 421 (1979)
- 2.128 J.N. Daou, A. Lucasson, P. Lucasson: Solid State Commun. **19**, 895 (1976)
- 2.129 J.N. Daou, P. Vajda, A. Lucasson, P. Lucasson, J.P. Burger: Philos. Mag. A **53**, 611 (1986)
- 2.130 P. Vajda, J.N. Daou, J.P. Burger, K. Kai, K.A. Gschneidner, Jr., B.J. Beaudry: Phys. Rev. B **34**, 5154 (1986)
- 2.131 J.P. Burger, J.N. Daou, A. Lucasson, P. Lucasson, P. Vajda: Z. Phys. Chem. **143**, 111 (1985)
- 2.132 O. Blaschko, G. Krexner, J.N. Daou, P. Vajda: Phys. Rev. Lett. **55**, 2876 (1985)
- 2.133 I.S. Anderson, J.J. Rush, T. Udovic, J.M. Rowe: Phys. Rev. Lett. **57**, 2822 (1986)
- 2.134 O. Blaschko, G. Krexner, L. Pintschovius, P. Vajda, J.N. Daou: Phys. Rev. B **38**, 9612 (1988)
- 2.135 O. Blaschko, G. Krexner, J. Pleschitschnig, G. Ernst, J.N. Daou, P. Vajda: Phys. Rev. B **39**, 5605 (1989)
- 2.136 O. Blaschko, J. Pleschitschnig, P. Vajda, J.P. Burger, J.N. Daou: Phys. Rev. B **40**, 5344 (1989)
- 2.137 J.P.A. Fairclough, D.K. Ross, S.M. Bennington: Z. Phys. Chem. N.F. **179**, 281 (1993)
- 2.138 P. Vajda: Solid State Ionics **168**, 271 (2004)
- 2.139 T.R.P. Gibb, Jr., J.J. McSharry, R.W. Brandon: J. Amer. Chem. Soc. **73**, 1753 (1951)
- 2.140 Y. Fukai: J. Less-Common Met. **172–174**, 8 (1991)
- 2.141 H. Araki, M. Nakamura, S. Harada, T. Obata, N. Mikhin, V. Syvoken, M. Kubota: J. Low Temp. Phys. **134**, 1145 (2004)

Chapter 3

- 3.1 J.F. Lynch, J. Tanaka: Acta Metall. **29**, 537 (1981)
- 3.2 D.W. Jones, N. Pessall, A.D. McQuillan: Philos. Mag. **6**, 455 (1961)
- 3.3 R. Burch, N.B. Francis: J. Less-Common Met. **49**, 371 (1976)
- 3.4 D.W. Jones, A.D. McQuillan: J. Phys. Chem. Solids **23**, 1441 (1962)
- 3.5 T. Eguchi, S. Morozumi: J. Japan Inst. Metals **38**, 1025 (1974) (in Japanese)
- 3.6 J.F. Lynch, J.J. Reilly, F. Millot: J. Phys. Chem. Solids **39**, 883 (1978)
- 3.7 D.T. Peterson, S.O. Nelson: Met. Trans. **16A**, 367 (1985)
- 3.8 T. Eguchi, S. Morozumi: J. Japan Inst. Metals **38**, 1019 (1974) (in Japanese)
- 3.9 A.D. McQuillan: Proc. R. Soc. (London) A **204**, 309 (1950)
- 3.10 R.C. Phutela, O.J. Kleppa: J. Chem. Phys. **76**, 1525 (1982)
- 3.11 T.B. Flanagan, G. Gross, J.D. Clewley: *Proc. 2nd Int'l Congress Hydrogen in Metals*, Paris, 1977, 1C3 (Pergamon, Oxford 1977)

- 3.12 R. Feenstra, D.G. de Groot, R. Griessen, J.P. Burger, A. Menovski: J. Less-Common Met. **130**, 375 (1987)
- 3.13 H. Brodowsky, H. Husemann: Ber. Bunsenges. Phys. Chem. **70**, 626 (1966)
- 3.14 R. Burch, R.G. Buss: J. Chem. Soc. Faraday Trans. I **71**, 922 (1975)
- 3.15 J.D. Clewley, J.F. Lynch, T.B. Flanagan: J. Chem. Soc. Faraday Trans. I **73**, 494 (1977)
- 3.16 H. Brodowsky, E. Poeschel: Z. Phys. Chem. **44**, 143 (1965)
- 3.17 H. Brodowsky: Ber. Bunsenges. Phys. Chem. **76**, 740 (1972)
- 3.18 H. Husemann, H. Brodowski: Z. Naturforsch. **23a**, 1693 (1968)
- 3.19 Y. Sakamoto, T.B. Flanagan, T. Kuji: Z. Phys. Chem. **143**, 61 (1985)
- 3.20 M. LaPrade, K.D. Allard, J.F. Lynch, T.B. Flanagan: J. Chem. Soc. Faraday Trans. **170**, 1615 (1974)
- 3.21 K.D. Allard, A. Maeland, J.W. Simons, T.B. Flanagan: J. Phys. Chem. **72**, 136 (1968)
- 3.22 K.D. Allard, J.F. Lynch, T.B. Flanagan: Z. Phys. Chem. **93**, 15 (1974)
- 3.23 H. Buck: Ber. Kernforschungsanlage Jül-722-FF (1970)
- 3.24 M. Futran, S.G. Coates, C.K. Hall, D.O. Welch: J. Chem. Phys. **77**, 6223 (1982)
- 3.25 C.K. Hall, A.I. Shirley, P.S. Sahni: Phys. Rev. Lett. **53**, 1236 (1984)
- 3.26 I.R. MacGillivray, C.E. Soteros, C.K. Hall: Phys. Rev. B **35**, 3545 (1987)
- 3.27 W.A. Oates, T.B. Flanagan: Acta Metall. **33**, 693 (1985)
- 3.28 W.A. Oates, T.B. Flanagan: Metall. Trans. **16A**, 139 (1985)
- 3.29 D.G. Westlake, J.F. Miller: J. Less-Common Met. **65**, 139 (1979)
- 3.30 J.F. Miller, D.G. Westlake: Trans. Jpn. Inst. Metals (Suppl.) **21**, 153 (1980)
- 3.31 S.H. Lim, T.B. Flanagan, W.A. Oates: Acta Metall. **36**, 2047 (1988)
- 3.32 J.A. Pryde, I.S.T. Tsong: Trans. Faraday Soc. **65**, 2766 (1969)
- 3.33 J.A. Pryde, C.G. Titcomb: J. Phys. C **5**, 1293 (1972)
- 3.34 H.Y. Chang, C.A. Wert: Acta Metall. **21**, 1233 (1973)
- 3.35 G. Pfeiffer, H. Wipf: J. Phys. F **6**, 167 (1976)
- 3.36 S. Tanaka, H. Kimura: Trans. Jpn. Inst. Metals **20**, 647 (1979)
- 3.37 Y. Saito, Y. Fukai: J. Less-Common Met. **138**, 161 (1988)
- 3.38 R. Kirchheim: Acta Metall. **30**, 1069 (1982); **21**, 1233 (1973)
- 3.39 B. Hohler, H. Kronmüller: Z. Phys. Chem. **114**, 93 (1979)
- 3.40 G. Cannelli, R. Cantelli, M. Koiwa: Philos. Mag. A **46**, 483 (1982)
- 3.41 G. Cannelli, R. Cantelli, F. Cordero: Phys. Rev. B **32**, 3573 (1985)
- 3.42 O. Yoshinari, M. Koiwa, H. Asano, M. Hirabayashi: Trans. Jpn. Inst. Metals **19**, 171 (1978)
- 3.43 D. Richter, J. Töpler, T. Springer: J. Phys. F **6**, L93 (1976)
- 3.44 C. Baker, H.K. Birnbaum: Acta Metall. **21**, 865 (1973)
- 3.45 R.F. Mattas, H.K. Birnbaum: Acta Metall. **23**, 973 (1975)
- 3.46 P.E. Zapp, H.K. Birnbaum: Acta Metall. **28**, 1275 (1980)
- 3.47 K. Rosan, H. Wipf: Physica Stat. Solidi (a) **38**, 611 (1979)
- 3.48 G. Cannelli, R. Cantelli, F. Cordero: J. Phys. F **16**, 1153 (1986)
- 3.49 T. Matsumoto, Y. Sasaki, M. Hihara: J. Phys. Chem. Solids **36**, 215 (1975)
- 3.50 E. Yagi, S. Nakamura, F. Kano, T. Kobayashi, K. Watanabe, Y. Fukai, T. Matsumoto: Phys. Rev. B **39**, 57 (1989)
- 3.51 F.E. Wagner, G. Wortmann: In *Hydrogen in Metals I*, ed. by G. Alefeld, J. Völkl, Topics Appl. Phys., Vol. 28 (Springer, Berlin, Heidelberg 1978) p. 131
- 3.52 G. Wiesinger, G. Hilscher: In *Hydrogen in Intermetallic Compounds I*, ed. by L. Schlapbach (Springer, Berlin, Heidelberg 1988), p. 285

- 3.53 U. Gonser: In *Microscopic Methods in Metals*, ed. by U. Gonser, Topics Curr. Phys., Vol. 40 (Springer, Berlin, Heidelberg 1986), p. 409
- 3.54 F. Pröbst, F.E. Wagner, M. Karger: J. Less-Common Met. **88**, 201 (1982)
- 3.55 F.E. Wagner, M. Karger, F. Pröbst, B. Schuttler: In *Electronic Structure and Properties of Hydrogen in Metals*, ed. by P. Jena, C.B. Satterthwaite (Plenum, New York 1983), p. 581
- 3.56 R. Wordel, F.E. Wagner: J. Less-Common Met. **101**, 427 (1984)
- 3.57 M. Berneis, J. Trager, R. Wordel, M. Zelger, F.E. Wagner, T. Butz: Z. Phys. Chem. **145**, 129 (1985)
- 3.58 L. Iannarella, M. Baier, M. Zelger, F.E. Wagner: J. Less-Common Met. **130**, 173 (1987)
- 3.59 M. Amer, M. Baier, H.J. Bauer, F.E. Wagner: Z. Phys. Chem. **64**, 773 (1989)
- 3.60 B. Zhang, H.J. Bauer, M. Baier, F.E. Wagner, V.E. Antonov, T.E. Antonova: J. Less-Common Met. **172-174**, 343 (1991)
- 3.61 K. Yvon, P. Fischer: In *Hydrogen in Intermetallic Compounds I*, ed. by L. Schlapbach (Springer, Berlin, Heidelberg 1988), p. 87
- 3.62 A. Stern, A. Resnik, D. Shaltiel: J. Less-Common Met. **88**, 431 (1982)
- 3.63 M.H. Mintz, I. Javob, D. Shaltiel: In *Hydrogen in Intermetallic Compounds II*, ed. by L. Schlapbach (Springer, Berlin, Heidelberg 1992), p. 285
- 3.64 J.J. Reilly, R. Wiswall: Inorg. Chem. **13**, 218 (1974)
- 3.65 H. Wenzl, E. Lebsanft: J. Phys. F **10**, 2147 (1980)
- 3.66 L. Schlapbach (ed.): *Hydrogen in Intermetallic Compounds I*, (Springer, Berlin, Heidelberg 1988)
- 3.67 L. Schlapbach (ed.): *Hydrogen in Intermetallic Compounds II*, (Springer, Berlin, Heidelberg 1992)
- 3.68 A.J. Maeland, L.E. Tanner, G.G. Libowitz: J. Less-Common Met. **74**, 279 (1980)
- 3.69 A.J. Maeland: In *Metal Hydrides*, ed. by G. Bambakidis (Plenum, New York 1981) p. 177
- 3.70 A.J. Maeland: In *Rapidly Quenched Metals*, ed. by S. Steeb, H. Warlimont (Elsevier, Amsterdam 1985) p. 1507
- 3.71 A.J. Maeland: In *Hydrogen in Disordered and Amorphous Alloys*, ed. by G. Bambakidis, R.C. Bowman, Jr. (Plenum, New York 1986) p. 127
- 3.72 K. Aoki, M. Kamachi, and T. Masumoto: J. Non-Cryst. Solids **61/62**, 679 (1984)
- 3.73 F.H.M. Spit, J.W. Drijver, S. Radelaar: Z. Phys. Chem. **116**, 225 (1979)
- 3.74 F.H.M. Spit, J.W. Drijver, S. Radelaar: Scripta Metall. **14**, 1071 (1980)
- 3.75 K. Nakamura: Ber. Bunsenges. Phys. Chem. **89**, 191 (1985)
- 3.76 U. Stolz, U. Nagorny, R. Kirchheim: Scripta Metall. **18**, 347 (1984)
- 3.77 R. Kirchheim, F. Sommer, G. Schluckebier: Acta Metall. **30**, 1059 (1982)
- 3.78 A. Szökefalvi-Nagy, S. Filipek, R. Kirchheim: J. Phys. Chem. Solids **48**, 613 (1987)
- 3.79 S. Filipek, A.W. Szafranski, P. Duhaj: J. Less-Common Met. **101**, 299 (1984)
- 3.80 F. Jaggy, W. Kieninger, R. Kirchheim: Z. Phys. Chem. **163**, 431 (1989)
- 3.81 R. Griessen: Phys. Rev. B **27**, 7575 (1983)
- 3.82 P.M. Richards: Phys. Rev. B **30**, 5183 (1984)
- 3.83 J.J. Rush, J.M. Rowe, A.J. Maeland: J. Phys. F **10**, L283 (1980)
- 3.84 H. Kaneko, T. Kajitani, M. Hirabayashi, M. Ueno, K. Suzuki: J. Less-Common Met. **89**, 237 (1983)

- 3.85 K. Suzuki: *J. Less-Common Met.* **89**, 183 (1983)
- 3.86 K. Suzuki, N. Hayashi, J. Tomizuka, T. Fukunaga, K. Kai, N. Watanabe: *J. Non-Cryst. Solids* **61/62**, 637 (1984)
- 3.87 K. Samwar, W.L. Johnson: *Phys. Rev. B* **28**, 2907 (1983)
- 3.88 K. Kai, S. Ikeda, T. Fukunaga, N. Watanabe, K. Suzuki: *Physica B* **120**, 342 (1983)
- 3.89 B. Rodmacq, Ph. Mangin, A. Chamberod: *J. Phys. F* **15**, 2259 (1985)
- 3.90 B. Rodmacq, F. Lancon, A. Chamberod: *J. Mater. Sci. Eng.* **97**, 157 (1988)
- 3.91 T. Araki, T. Abe, K. Tanaka: *Mater. Trans. JIM* **30**, 748 (1989)
- 3.92 B. Rodmacq, M. Maret, J. Langier, L. Billard, A. Chamberod: *Phys. Rev. B* **38**, 1105 (1988)
- 3.93 B. Rodmacq, A. Chamberod: *Phys. Rev. B* **38**, 1116 (1988)
- 3.94 M. Sakata, N. Cowlan, H.A. Davies: In *Proc. Int. Conf. on Rapidly Quenched Metals*, ed. by T. Masumoto, K. Suzuki (Japan Institute of Metals, Sendai, 1982), vol.1, p. 327
- 3.95 J.H. Harris, W.A. Curtin, M.A. Tenhover: *Phys. Rev. B* **36**, 5784 (1987)
- 3.96 W.A. Curtin, J.H. Harris: *Mater. Sci. Eng.* **99**, 463 (1988)
- 3.97 H. Osterreicher, J. Clinton, H. Bitter: *Mater. Res. Bull.* **11**, 1241 (1976)
- 3.98 M. van Diepen, K.H.L. Buschow: *Solid State Commun.* **22**, 113 (1977)
- 3.99 K. Malik, W.E. Wallace: *Solid State Commun.* **24**, 283 (1977)
- 3.100 I. Jacobs, D. Shaltiel: *J. Less-Common Met.* **65**, 117 (1977)
- 3.101 L. Yeh, K. Samwar, W.L. Johnson: *Appl. Phys. Lett.* **42**, 242 (1983)
- 3.102 K. Aoki, T. Yamamoto, Y. Satoh, K. Fukamichi, T. Masumoto: *Acta Metall.* **35**, 2465 (1987)
- 3.103 K. Aoki, T. Yamamoto, T. Masumoto: *Scripta Metall.* **21**, 27 (1987)
- 3.104 K. Chattopadhyay, K. Aoki, T. Masumoto: *Scripta Metall.* **21**, 365 (1987)
- 3.105 E. Matsubara, Y. Ohzora, Y. Waseda, K. Aoki, K. Fukamichi, T. Masumoto: *Z. Naturforsch.* **42a**, 582 (1987)
- 3.106 K. Aoki, M. Nagano, A. Yanagitani, T. Masumoto: *J. Appl. Phys.* **62**, 3314 (1987)
- 3.107 K. Aoki, A. Yanagitani, X-G. Li, T. Masumoto: *Mater. Sci. Eng.* **97**, 35 (1988)
- 3.108 K. Aoki, X-G. Li, A. Yanagitani, T. Masumoto: In *Non-Equilibrium Solid Phases of Metals and Alloys* (Japan Institute of Metals, Sendai 1988) p. 101
- 3.109 A. Yanagitani, K. Aoki, T. Masumoto: In *Non-Equilibrium Solid Phases of Metals and Alloys* (Japan Institute of Metals, Sendai 1988) p. 443
- 3.110 K. Aoki, A. Yanagitani, T. Masumoto: *Appl. Phys. Lett.* **52**, 2122 (1988)
- 3.111 K. Aoki, X-G Li, K. Chattopadhyay, T. Masumoto: *Scripta Metall.* **22**, 991 (1988)
- 3.112 K. Aoki, T. Masumoto: *Sci. Rep. RITU*, **A34**, 79 (1988)
- 3.113 K. Aoki, X-G. Li, T. Masumoto: *Acta Metall. Mater.* **40**, 221 (1992)
- 3.114 K. Aoki, X-G. Li, T. Masumoto: *Acta Metall. Mater.* **40**, 1717 (1992)
- 3.115 K. Aoki, X-G. Li, T. Hirata, E. Matsubara, Y. Waseda, T. Masumoto: *Acta Metall. Mater.* **41**, 1525 (1993)
- 3.116 K. Aoki, K. Mori, H. Onodera, T. Masumoto: *J. Alloys Comp.* **253-254**, 106 (1997)
- 3.117 K. Mori, H. Onodera, K. Aoki, T. Masumoto: *J. Alloys Comp.* **270**, 35 (1998)
- 3.118 K. Aoki: *Mater. Sci. Eng. A* **304-306**, 45 (2001)

- 3.119 M. Dilixiati, K. Kanda, K. Ishihara, K. Aoki: J. Alloys Comp. **337**, 128 (2002)
- 3.120 M. Dilixiati, K. Kanda, K. Ishihara, K. Aoki: Mater. Trans. **43**, 1089 (2002)
- 3.121 K. Aoki, K. Mori, T. Masumoto: Mater. Trans. **43**, 2685 (2002)
- 3.122 K. Itoh, K. Kanda, K. Aoki, T. Fukunaga: J. Alloys Comp. **348**, 167 (2003)
- 3.123 K. Ishikawa, N. Ogasawara, K. Aoki: Philos. Mag. Lett., **84**, 207 (2004)
- 3.124 C.B. Magee: J. Less-Common Met. **72**, 273 (1980)
- 3.125 K. Aoki, X.-G. Li, T. Hirata, T. Masumoto: Appl. Phys. Lett. **61**, 2422 (1992)

Chapter 4

- 4.1 V. Diatschenko, C.W. Chu, D.H. Liebenberg, D.A. Young, M. Ross, R.L. Mills: Phys. Rev. B **32**, 381 (1985)
- 4.2 H.K. Mao, R.J. Hemley: Rev. Mod. Phys. **66**, 671 (1994)
- 4.3 I.I. Mazin, R.J. Hemley, A.F. Goncharov, M. Hanfland, H.K. Mao: Phys. Rev. Lett. **78**, 1066 (1997)
- 4.4 P. Loubeyre, F. Occelli, T. LeToullec: Nature **416**, 613 (2002)
- 4.5 C. Narayana, H. Luo, J. Orloff, A.L. Ruoff: Nature **393**, 46 (1998)
- 4.6 R.J. Hemley, H.K. Mao, L.W. Finger, A.P. Jephcoat, R.M. Hazen, C.S. Zha: Phys. Rev. B **42**, 6458 (1990)
- 4.7 P. Loubeyre, R. LeToullec, D. Hausermann, M. Hanfland, R.J. Hemley, H.K. Mao, L.W. Finger: Nature **383**, 702 (1996)
- 4.8 H. Kawamura, Y. Akahama, S. Umemoto, K. Takemura, Y. Ohishi, O. Shimomura: J. Phys.: Condens. Matter **14**, 10407 (2002) .
- 4.9 H. Kawamura, Y. Akahama, Y. Ohishi, O. Shimomura, K. Takemura: Chem. Phys. Lett, **372**, 373 (2003)
- 4.10 W.J. Nellis, A.C. Mitchell, M. van Thiel, G.J. Devine, R.J. Trainor: J. Chem. Phys. **79**, 1480 (1983)
- 4.11 W.J. Nellis, A.C. Mitchell, P.C. McCandless, D.J. Erskine, S.T. Weir: Phys. Rev. Lett. **68**, 2937 (1992)
- 4.12 R.F. Trunin: *Shock Compression of Condensed Materials* (Cambridge Press, Cambridge, 1998), p. 20
- 4.13 M.D. Knudson, D.L. Hanson, J.E. Bailey, C.A. Hall, J.R. Asay: Phys. Rev. Lett. **87**, 225501 (2001)
- 4.14 N.C. Holmes, M. Ross, W.J. Nellis: Phys. Rev. B **52**, 15835 (1995)
- 4.15 W.J. Nellis, S.T. Weir, A.C. Mitchell: Phys. Rev. B **59**, 3434 (1999)
- 4.16 L.B. DaSilva, P. Celliers, G.W. Collins, K.S. Budil, N.C. Holmes, T.W. Barbee Jr., B.A. Hammel, J.D. Kilkenny, R.J. Wallace, M. Ross, R. Cauble, A. Ng, G. Chiu: Phys. Rev. Lett. **78**, 483 (1997)
- 4.17 G.W. Collins, L.B. DaSilva, P. Celliers, D.M. Gold, M.E. Foord, R.J. Wallace, A. Ng, S.V. Weber, K.S. Budil, R. Cauble: Science **281**, 1178 (1998)
- 4.18 F.V. Grigor'ev, S.B. Komar, O.L. Mikhailova, A.P. Tolochko, V.D. Urlin: Zh. Eksp. Teor. Fiz. **16**, 286 (1972) [Sov. Phys. JETP **16**, 201 (1972)]
- 4.19 F.V. Grigor'ev, S.B. Komar, O.L. Mikhailova, A.P. Tolochko, V.D. Urlin: Zh. Eksp. Teor. Fiz. **75**, 1684 (1978) [Sov. Phys. JETP **48**, 847 (1978)]
- 4.20 P.S. Hawke, T.J. Burgess, D.E. Duerre, J.G. Huebel, R.N. Keeler, H. Klapper, W.C. Wallace: Phys. Rev. Lett. **41**, 994 (1978)

- 4.21 S.T. Weir, A.C. Mitchell, W.J. Nellis: Phys. Rev. Lett. **76**, 1860 (1996)
- 4.22 H. Hemmes, A. Driessen, R. Griessen: J. Phys. C **19**, 3571 (1986)
- 4.23 A. Michels, W. de Graaff, T. Wassenaar, J.M.H. Levelt, P. Louwerse: Physica **25**, 25 (1959)
- 4.24 R.L. Mills, D.H. Liebenberg, J.C. Bronson, L.C. Schmid: J. Chem. Phys. **66**, 3076 (1977)
- 4.25 D.S. Tsiklis, V. Ya Maslennikova, S.D. Gavrilov, A.N. Egorov, G.V. Timofeeva: Dokl. Akad. Nauk SSSR **220**, 1384 (1975)
- 4.26 M. Tkacz, A. Litwiniuk: J. Alloys Comp. **330-332**, 89 (2002)
- 4.27 H. Sugimoto, Y. Fukai: Acta Metall. **40**, 2327 (1992)
- 4.28 A. Driessen, I.F. Silvera: J. Low Temp. Phys. **54**, 361 (1984)
- 4.29 B. Baranowski, S. Majchrzak, T.B. Flanagan: J. Phys. F **1**, 258 (1971)
- 4.30 H. Peisl: In *Hydrogen in Metals I*, ed. by G. Alefeld, J. Völkl, Topics Appl. Phys. Vol. 28 (Springer, Berlin, Heidelberg 1978) p. 53
- 4.31 Y. Fukai: J. Less-Common Met. **101**, 1 (1984)
- 4.32 T. Suzuki, H. Namazue, S. Koike, H. Hayakawa: Phys. Rev. Lett. **51**, 798 (1983)
- 4.33 T. Suzuki: Trans. Jpn. Inst. Metals **26**, 601 (1985)
- 4.34 D.G. Westlake, S.T. Ockers, M.H. Mueller, K.D. Anderson: Metall. Trans. **3**, 1709 (1972)
- 4.35 H. Asano, Y. Abe, M. Hirabayashi: Acta Metall. **24**, 95 (1976)
- 4.36 A. Fukizawa, Y. Fukai: J. Phys. Soc. Jpn. **52**, 2102 (1983)
- 4.37 K. Kato, O. Yoshinari, K. Tanaka: Trans. Jpn. Inst. Metals **29**, 251 (1988)
- 4.38 S. Sato, O. Yoshinari, K. Tanaka: Z. Phys. Chem. **164**, 1025 (1989)
- 4.39 J.N. Daou, M. Chiheb, P. Lucasson: J. Less-Common Met. **79**, 65 (1981)
- 4.40 J.E. Bonnet: J. Less-Common Met. **49**, 451 (1976)
- 4.41 J.E. Bonnet, J.N. Daou: J. Phys. Chem. Solids **40**, 421 (1979)
- 4.42 C.K. Saw, B.J. Beaudry, C. Stassis: Phys. Rev. B **27**, 7013 (1983)
- 4.43 D. Khatamian, C. Stassis, B.J. Beaudry: Phys. Rev. B **23**, 624 (1981)
- 4.44 Y. Fukai, M. Mizutani: Mater. Trans. **43**, 1079 (2002)
- 4.45 P.A. Korzhavyi, I.A. Abrikosov, B. Johansson, A.V. Ruban, H.L. Skriver: Phys. Rev. B **59**, 11693 (1999)
- 4.46 M. Krukowski, B. Baranowski: Roczn. Chem. **49**, 1183 (1975)
- 4.47 I.T. Belash, B.K. Ponomarev, V.G. Thiessen, N.S. Afonikova, V.Sh. Shekhtman, E.G. Ponyatovsky: Fiz. Tverd. Tela, **20**, 442 (1978) [Sov. Phys. Solid State **20**, 244 (1978)]
- 4.48 E.G. Ponyatovsky, V.E. Antonov, I.T. Belash: In *Problems in Solid-State Physics*, ed. by A.M. Prokhorov, A.S. Prokhorov (Mir, Moscow 1984)
- 4.49 V.E. Antonov, K. Cornell, V.K. Fedotov, A.I. Kolesnikov, E.G. Ponyatovsky, V.I. Shiryayev, H. Wipf: J. Alloys Comp. **264**, 214 (1998)
- 4.50 H.K. Mao, W.A. Bassett, T. Takahashi: J. Appl. Phys. **38**, 272 (1967)
- 4.51 V.A. Somenkov, V.P. Glazkov, A.V. Irodova, S.Sh. Shil'stein: J. Less-Common Met. **129**, 171 (1987)
- 4.52 Y. Fukai, M. Mizutani: Mater. Trans. **44**, 1359 (2003)
- 4.53 T. Atou, J.V. Badding: J. Solid State Chem. **118**, 299 (1995)
- 4.54 H. Kawamura, M. Harada, Y. Akahama, K. Takemura: Solid State Commun. **130**, 59 (2004)
- 4.55 V.L. Moruzzi, J.F. Janak, A.R. Williams: *Calculated Electronic Properties of Metals* (Pergamon, Oxford 1978)

- 4.56 Y. Fukai, H. Koike, Y. Sakamaki: to be published
- 4.57 V.K. Fedotov, V.E. Antonov, A.I. Kolesnikov, A.I. Beskrovnyi, G. Grosse, F.E. Wagner: *Solid State Commun.* **107**, 787 (1998)
- 4.58 V.E. Antonov, I.T. Belash, B.K. Ponomarev, E.G. Ponyatovsky, V.G. Thiessen: *Phys. Stat. Sol. (a)* **52**, 703 (1979)
- 4.59 V.E. Antonov, T.E. Antonova, M. Baier, G. Grosse, F.E. Wagner: *J. Alloys Comp.* **239**, 198 (1996)
- 4.60 S.P. Besedin, A.P. Jephcoat: *Rev. High Pressure Sci. Technol.* **7**, **301** (1998)
- 4.61 M. Krukowski, B. Baranowski: *J. Less-Common Met.* **49**, 385 (1976)
- 4.62 V.E. Antonov, M. Baier, B. Dorner, V.K. Fedotov, G. Grosse, A.I. Kolesnikov, E.G. Ponyatovsky, G. Schneider, F.E. Wagner: *J. Phys.: Condens. Matter* **14**, 6427 (2002)
- 4.63 J.E. Shirber, B. Morosin: *Phys. Rev. B* **12**, 117 (1975)
- 4.64 E.G. Ponyatovsky, V.E. Antonov, I.T. Belash: *Sov. Phys. Usp.* **25**, 596 (1982)
- 4.65 Y. Fukai: *Z. Phys. Chem.* **164**, 165 (1989)
- 4.66 Y. Fukai, N. Ōkuma: *Jpn. J. Appl. Phys.* **32**, L1265 (1993)
- 4.67 Y. Fukai, Y. Kurokawa, H. Hiraoka: *J. Japan Inst. Metals* **61**, 663 (1997)
- 4.68 C. Elsässer, J. Zhu, S.G. Louie, M. Fähnle, C.T. Chan: *J. Phys.: Condens. Matter* **10**, 5081 (1988)
- 4.69 C. Elsässer, J. Zhu, S.G. Louie, M. Fähnle, C.T. Chan: *J. Phys.: Condens. Matter* **10**, 5113 (1988)
- 4.70 D.G. Westlake: *J. Less-Common Met.* **90**, 251 (1983)
- 4.71 D. Fruchart, F. Vaillant, E. Roudant, A. Nemoz, X.G. Tessena: *Phys. Status Solidi (a)* **65**, K19 (1981)
- 4.72 J. Osterwalder, T. Riesterer, L. Schlapbach, F. Vaillant, D. Fruchart: *Phys. Rev. B* **31**, 8311 (1985)
- 4.73 R. Griessen, R. Feenstra: *J. Phys. F* **15**, 1013 (1985)
- 4.74 Y. Syono, K. Kusaba, K. Fukuoka, Y. Fukai, K. Watanabe: *Phys. Rev. B* **29**, 6520 (1984)
- 4.75 H. Taguchi, Y. Fukai, T. Atou, K. Fukuoka, Y. Syono: *Phys. Rev. B* **49** (1994)
- 4.76 J. van Straaten, I.F. Silvera: *Phys. Rev. B* **37**, 1989 (1988)
- 4.77 E.G. Brovman, Yu. Kagan, A. Kholas: *Zh. Eksp. Teor. Fiz.* **62**, 1492 (1972) [*Sov. Phys. JETP* **35**, 783 (1972)]
- 4.78 S. Chakravarty, J.H. Rose, D. Wood, N.W. Ashcroft: *Phys. Rev. B* **24**, 1624 (1981)
- 4.79 J.V. Badding, R.J. Hemley, H.K. Mao: *Science* **253**, 421 (1991)
- 4.80 N. Hirao, E. Ohtani: Private communication (2003)
- 4.81 H.K. Mao, Y. Wu, L.C. Chen, J.F. Shu, A.P. Jephcoat: *J. Geophys. Res.* **95**, 21737 (1990)
- 4.82 G. Schneider, M. Baier, R. Wordel, F.E. Wagner, V.E. Antonov, E.G. Ponyatovsky, Yu. Kapilevskii, E. Makarov: *J. Less-Common Met.* **172**, 333 (1991)
- 4.83 I. Choe, R. Ingalis, J.M. Brown, Y. Sato-Sorensen, R. Mills: *Phys. Rev. B* **41**, 1 (1991)
- 4.84 R.G. McQueen, S.P. Marsh: *J. Appl. Phys.* **31**, 1253 (1960)
- 4.85 Y. Zhang, T. Mashimo: Private communication (2003)
- 4.86 A. Driessen, H. Hemmes, R. Griessen: *Z. Phys. Chem.* **143**, 145 (1985);
- 4.87 R. Griessen, and A. Driessen: *Phys. Rev. B* **30**, 4372 (1984)
- 4.88 V.E. Antonov, I.T. Belash, E.G. Ponyatovsky: *Dokl. Akad. Nauk SSSR* **233**, 1114 (1977)

- 4.89 B. Baranowski: In *Hydrogen in Metals II*, ed. by G. Alefeld, J. Völkl, Topics Appl. Phys. Vol. 29 (Springer, Berlin, Heidelberg 1978) p. 157
- 4.90 V.E. Antonov, I.T. Belash, E.G. Ponyatovsky: Proc. 8th AIRAPT/19th EHPRG Con/, Vol. 1 (Uppsala, Sweden, 1981) p. 80
- 4.91 V.E. Antonov, T.E. Antonova, N.A. Chirin, E.G. Ponyatovsky, M. Baier, F.E. Wagner: Scripta Mater. **34**, 1331 (1996)
- 4.92 V.E. Antonov: J. Alloys Comp. **330–332**, 110 (2002)
- 4.93 O. Shimomura, S. Yamaoka, T. Yagi, M. Wakatsuki, K. Tsuji, O. Fukunaga, H. Kawamura, K. Aoki, S. Akimoto: *Mat. Res. Soc. Symp. Proc.*, Vol. 22 (Elsevier, Amsterdam 1984) p. 171
- 4.94 S. Endo, Y. Akahama, W. Utsumi: Jpn. J. Appl. Phys. **26**, L1419 (1987)
- 4.95 Y. Fukai, T. Haraguchi, E. Hayashi, Y. Ishii, Y. Kurokawa, J. Yanagawa: Defect Diffusion Forum **194**, 1063 (2001)
- 4.96 V.P. Glazkov, A.V. Irodova, V.A. Somenkov, S.Sh. Shil'shtein, S.P. Basedin: J. Less-Common Met. **129**, 165 (1987)
- 4.97 I.O. Bashkin, E.G. Ponyatovskii, K.E. Kost: Phys. Status Solidi (b) **87**, 369 (1978)
- 4.98 R. Ahuja, B. Johansson, J.M. Mills, O. Eriksson: Appl. Phys. Lett. **71**, 3497 (1997)
- 4.99 K. Nakamura, Y. Fukai: J. Alloys Comp. **231**, 46 (1995)
- 4.100 E.G. Ponyatovsky, I.O. Bashkin, V.F. Degtyareva, Yu.A. Aksenov, V.I. Rashchupkin, D.N. Mogilyansky: J. Less-Common Met. **129**, 93 (1987)
- 4.101 I.O. Bashkin, V.Yu. Malyshev, E.G. Ponyatovsky: Z. Phys. Chem. **179**, 289 (1993)
- 4.102 I.O. Bashkin, T.I. Dyuzheva, L.M. Lityagina, V.Yu. Malyshev: Fiz. Tverd. Tela **35**, 3104 (1993) [Phys. Solid State **35**, 1528 (1993)]
- 4.103 I.O. Bashkin, A.F. Gurov, V.Yu. Malyshev, E.G. Ponyatovskii: Fiz. Tverd. Tela **34**, 1276 (1992) [Sov. Phys. Solid State **34**, 674 (1992)]
- 4.104 I.O. Bashkin, A.I. Latynin, V.Yu. Malyshev: Fiz. Tverd. Tela **37**, 2108 (1995) [Sov. Phys. Solid State **37**, 1146 (1992)]
- 4.105 Y. Fukai, K. Watanabe, A. Fukizawa: J. Less-Common Met. **88**, 27 (1982)
- 4.106 Y. Fukai, T. Matsushita, Y. Sakamaki: to be published
- 4.107 Y. Fukai, K. Nakamura, Y. Endo, N. Ōkuma: In *Advanced Materials '93, V/B: Shape Memory Materials and Hydrides*, ed. by K. Otsuka and Y. Fukai (Elsevier, Amsterdam 1994) p. 1291
- 4.108 V.E. Antonov, I.T. Belash, E.G. Ponyatovsky: Dokl. Akad. Nauk SSSR **248**, 635 (1979)
- 4.109 C.A. Snavely: Trans. Electrochem. Soc. **92**, 537 (1947)
- 4.110 R.J. Roy, T.R.P. Gibb, Jr.: J. Inorg. Nucl. Chem. **29**, 341 (1967)
- 4.111 M. Tkacz: Polish J. Chem. **71**, 1735 (1997)
- 4.112 J.F. Cannon: J. Phys. Chem. Ref. Data **3**, 781 (1974)
- 4.113 Y. Fukai, H. Ishikawa, T. Goto, J. Susaki, T. Yagi, J.L. Soubeyroux, D. Fruchart: Z. Phys. Chem. **163**, 479 (1989)
- 4.114 V.E. Antonov, T.E. Antonova, N.A. Chirin, E.G. Ponyatovsky, M. Baier, F.E. Wagner: Solid State Commun. **34**, 1331 (1996)
- 4.115 S.M. Filipek, S. Majchrzak, A.B. Sawaoka, M. Cernansky: High Pressure Research **7**, 271 (1991)
- 4.116 Y. Fukai, T. Haraguchi, H. Shinomiya, K. Mori: Scripta Mater. **46**, 679 (2002)

- 4.117 A.V. Irodova, V.P. Glazkov, V.A. Somenkov, S.Sh. Shil'shtein, V.E. Antonov, E.G. Ponyatovskii: Sov. Phys. Solid State **29**, 1562 (1987)
- 4.118 V.I. Spitsyn, E.G. Ponyatovsky, V.E. Antonov, I.T. Belash, O.A. Balakhovskii: Dokl. Akad. Nauk SSSR **247**, 1420 (1979)
- 4.119 V.I. Spitsyn, V.E. Antonov, O.A. Balakhovskii, I.T. Belash, E.G. Ponyatovsky: Dokl. Akad. Nauk SSSR **260**, 132 (1981)
- 4.120 V.P. Glazkov, A.V. Irodova, V.A. Somenkov, S.Sh. Shil'shtein, V.E. Antonov, E.G. Ponyatovskii: Sov. Phys. Solid State **26**, 1961 (1984)
- 4.121 V.E. Antonov, I.T. Belash, V.Yu. Malyshev, E.G. Ponyatovsky, N.A. Tulina: Dokl. Akad. Nauk SSSR **269**, 617 (1983)
- 4.122 V.E. Antonov, I.T. Belash, O.V. Zharikov, A.V. Palnichenko: Phys. Stat. Sol. (b) **142**, K155 (1987)
- 4.123 Y. Fukai, K. Mori, H. Shinomiya: J. Alloys Comp. **348**, 105 (2002)
- 4.124 V.E. Antonov, I.T. Belash, E.G. Ponyatovsky: Scripta Metal. **16**, 202 (1982)
- 4.125 T. Yagi, T. Hishinuma: Geophys. Res. Lett. **22**, 1933 (1995)
- 4.126 T. Okuchi: J. Phys. Condens. Matter **10**, 11595 (1998)
- 4.127 C.S. Yoo, J. Akella, A.J. Campbell, H.K. Mao, R.J. Hemley: Science **270**, 1473 (1995)
- 4.128 S.K. Saxena, L.S. Dubrovinsky, P. Häggkvist, Y. Cerenius, G. Shen, H.K. Mao: Science **269**, 1703 (1995)
- 4.129 R. Boehler: Nature **363**, 534 (1993)
- 4.130 S.K. Saxena, G. Shen, P. Lazor: Science **260**, 1312 (1993)
- 4.131 S.K. Saxena, G. Shen, P. Lazor: Science **264**, 405 (1994)
- 4.132 T. Hiroi, K. Mori, Y. Fukai: J. Alloys. Comp. in press
- 4.133 Y. Fukai, J. Yanagawa, S. Yokota: J. Alloys Comp. in press
- 4.134 V.E. Antonov, I.T. Belash, V.Yu. Malyshev, E.G. Ponyatovsky: Dokl. Akad. Nauk SSSR **272**, 1147 (1983)
- 4.135 V.K. Fedotov, V.E. Antonov, T.E. Antonova, E.L. Bokhenkov, B. Dorner, G. Grosse, F.E. Wagner: J. Alloys Comp. **291**, 1 (1999)
- 4.136 B. Baranowski, R. Wioeniewski: Bull. Acad. Polon. Sci. **14**, 273 (1966)
- 4.137 E.G. Ponyatovsky, V.E. Antonov, I.T. Belash: Dokl. Akad. Nauk SSSR **229**, 391 (1976)
- 4.138 E.G. Ponyatovsky, V.E. Antonov, I.T. Belash: Dokl. Akad. Nauk SSSR **230**, 649 (1976)
- 4.139 Y. Shizuku, S. Yamamoto, Y. Fukai: J. Alloys Comp. **336**, 159 (2002)
- 4.140 V.E. Antonov, I.T. Belash, V.M. Koltygin, E.G. Ponyatovsky: Dokl. Akad. Nauk SSSR **248**, 131 (1979)
- 4.141 V.E. Antonov, I.T. Belash, V.F. Degtyareva, E.G. Ponyatovsky: Dokl. Akad. Nauk SSSR **239**, 342 (1978)
- 4.142 E. Wicke, H. Brodowsky: In *Hydrogen in Metals II*, ed. by G. Alefeld, J. Völkl, Topics Appl. Phys. Vol. 29 (Springer, Berlin, Heidelberg 1978) p. 73
- 4.143 T.B. Massalski, H. Okamoto, P.R. Subramanian, L. Kacprzak (eds.), *Binary Alloy Phase Diagrams*, (ASM International, Materials Park, Ohio, U. S. A., 1990)
- 4.144 Y. Fukai, S. Akimoto: Proc. Jpn. Acad. **59**, 158 (1983)
- 4.145 T. Suzuki, S. Akimoto, Y. Fukai: Phys. Earth Planet. Inter. **36**, 135 (1984)
- 4.146 T. Yagi, T. Hishinuma: Geophys. Res. Lett. **22**, 1933 (1995)
- 4.147 E. Anders, R. Ganapathy, R.R. Keays, J.C. Laul, J.W. Morgan: *Proc. 2nd Lunar Sci. Conf.* 1021 (1971)

- 4.148 A.E. Ringwood: *Geochem. J.* **11**, 111 (1977)
- 4.149 Y. Fukai, T. Suzuki: *J. Geophys. Res.* **91**, 9222 (1986)
- 4.150 A.M. Dziewonski, D.L. Anderson: *Phys. Earth Planet. Inter.* **25**, 297 (1981)
- 4.151 Y. Fukai: In *High-Pressure Research: Application to Earth and Planetary Sciences*, ed. by Y. Syono, M.H. Manghnani (Terra Scientific, Tokyo/ AGU, Washington, D.C. 1992) p. 373
- 4.152 Y. Abe, T. Matsui: *J. Geophys. Res. Suppl.* **90**, C545 (1985)
- 4.153 Y. Abe, T. Matsui: *J. Geophys. Res. Suppl.* **91**, E291 (1986)
- 4.154 A.E. Ringwood: *Origin of the Earth and Moon* (Springer, New York, 1979)
- 4.155 E. Ohtani, A.E. Ringwood: *Earth Planet. Sci. Lett.* **71**, 85 (1984)
- 4.156 E. Ohtani, A.E. Ringwood, W. Hibberson: *Earth Planet. Sci. Lett.* **71**, 94 (1984)
- 4.157 Y. Fukai: *Nature* **308**, 174 (1984)
- 4.158 Y. Akahama, H. Kawamura, D. Hausermann, M. Hanfland, O. Shimomura: *Phys. Rev. Lett.* **74**, 4690 (1995)
- 4.159 D.A. Boness, J.M. Brown: *J. Geophys. Res.* **95**, 21721 (1990)
- 4.160 K. Terakura: Private communication (1983)
- 4.161 M. Nitta, S. Iino, Y. Fukai, K. Fukuoka, Y. Syono: *Phys. Rev. B* **58**, 8301 (1998)
- 4.162 T. Okuchi: *Science* **278**, 1781 (1997)
- 4.163 T. Hishinuma, T. Yagi, Uchida: *Proc. Jpn. Acad.* **70B**, 71 (1994)
- 4.164 V.N. Zharkov, T.V. Gudkova: In *High-Pressure Research: Application to Earth and Planetary Sciences*, ed. by Y. Syono, M.H. Manghnani (Terra Scientific, Tokyo/ AGU, Washington, D.C. 1992) p. 393
- 4.165 T. Palasyuk, M. Tkacz: *Solid State Commun.* **130**, 219 (2004)
- 4.166 A. Machida, T. Watanuki, A. Ohmura, K. Aoki, S. Nakano, K. Takemura: *Rev. High Press. Sci. Tech.* **14**, Special Issue (2004), p. 17. A. Ohmura, A. Machida, K. Aoki, S. Nakano, K. Takemura: *ibid.* p. 18
- 4.167 H. Kawamura, T. Moriwaki, S. Yamada, Y. Akahama, K. Takemura: *Rev. High Press. Sci. Tech.* **14**, Special Issue (2004), p. 94
- 4.168 R. Burtovyy, M. Tkacz: *Solid State Commun.* **131**, 169 (2004)

Chapter 5

- 5.1 D.V. Morgan (ed.): *Channeling* (Academic, New York 1973)
- 5.2 L.C. Feldman, J.W. Mayer, S.T. Picraux: *Materials Analysis by Ion Channeling* (Academic, New York 1982)
- 5.3 S.T. Picraux: In *Ion Beam Surface Layer Analysis*, vol. 2, ed. by O. Meyer, G. Linker, F. Kappeler (Plenum, New York 1976) p. 527
- 5.4 H.D. Carstanjen: *Phys. Status Solidi (a)* **59**, 11 (1980)
- 5.5 H.D. Carstanjen: *Z. Phys. Chem.* **165**, 141 (1989)
- 5.6 J. Lindhard: *K. Dan. Vidensk. Selsk. Mat.-Fys. Medd.* **34**, 14 (1965)
- 5.7 C. Erginsoy: *Phys. Rev. Lett.* **15**, 360 (1965)
- 5.8 H.D. Carstanjen, J. Dunstl, G. Lobl, R. Sizmann: *Phys. Status Solidi (a)* **15**, 529 (1978)
- 5.9 M. Antonini, H.D. Carstanjen: *Phys. Status Solidi (a)* **34**, K153 (1976)
- 5.10 S. Yamaguchi, K. Takahiro, S. Nagata, Y. Fujino, H. Naramoto, K. Ozawa: *J. Alloys Comp.* **231**, 132 (1995)

- 5.11 K. Ozawa, S. Yamaguchi, Y. Fujino, O. Yoshinari, M. Koiwa, M. Hirabayashi: Nucl. Instrum. Methods **149**, 405 (1978)
- 5.12 H.D. Carstanjen, R. Sizmann: Phys. Lett. **40A**, 93 (1972)
- 5.13 J. Takahashi, S. Yamaguchi, M. Koiwa, Y. Fujino, M. Hirabayashi: Radiat. Eff. **36**, 135 (1978)
- 5.14 E. Yagi, T. Kobayashi, S. Nakamura, Y. Fukai, K. Watanabe: Phys. Rev. B **31**, 1640 (1985)
- 5.15 E. Yagi, T. Kobayashi, S. Nakamura, F. Kano, K. Watanabe, Y. Fukai, S. Koike: Phys. Rev. B **33**, 5121 (1986)
- 5.16 E. Yagi, S. Nakamura, T. Kobayashi, K. Watanabe, Y. Fukai: J. Phys. Soc. Jpn. **54**, 1855 (1985)
- 5.17 E. Yagi, T. Kobayashi, S. Nakamura, Y. Fukai, K. Watanabe: J. Phys. Soc. Jpn. **52**, 3441 (1983)
- 5.18 E. Yagi, S. Nakamura, T. Kobayashi, F. Kano, K. Watanabe, Y. Fukai, T. Osaka: J. Phys. Soc. Jpn. **55**, 2671 (1986)
- 5.19 R. Danielou, J. Fontenille, E. Ligeon, Y. Fukai: J. Appl. Phys. **55**, 871 (1984)
- 5.20 A. Bontemps, J. Fontenille: Phys. Rev. B **18**, 6302 (1978)
- 5.21 H. Kanzaki: J. Phys. Chem. Solids **2**, 21 (1957)
- 5.22 G. Leibfried, N. Breuer: *Point Defects in Metals* (Springer, Berlin, Heidelberg 1978)
- 5.23 D.G. Westlake, S.T. Ockers, M.H. Mueller, K.D. Anderson: Metall. Trans. **3**, 1709 (1972)
- 5.24 H. Asano, Y. Abe and M. Hirabayashi: Acta Metall. **24**, 95 (1976)
- 5.25 M.A. Krivoglaz: *Theory of X-ray and Thermal Neutron Scattering by Real Crystals* (Plenum, New York 1969)
- 5.26 H. Trinkaus: Z. Angew. Phys. **31**, 229 (1971)
- 5.27 H. Trinkaus: Phys. Status Solidi (b) **51**, 307 (1972)
- 5.28 P.H. Dederichs: J. Phys. F **3**, 471 (1973)
- 5.29 H. Metzger, H. Peisl: J. Phys. F **8**, 391 (1978)
- 5.30 H. Pfeiffer, H. Peisl: Phys. Lett. **60A**, 363 (1977)
- 5.31 T. Suzuki: Trans. Jpn. Inst. Metals **26**, 601 (1985)
- 5.32 A. Magerl, B. Berre, G. Alefeld: Phys. Status Solidi (a) **36**, 161 (1976)
- 5.33 H. Metzger, J. Peisl, J. Wanagel: J. Phys. F **6**, 2195 (1976)
- 5.34 G. Bauer, E. Seitz, H. Horner, W. Schmatz: Solid State Commun. **17**, 161 (1975)
- 5.35 H. Dosch, F. Schmid, P. Weithoff, J. Peisl: Phys. Rev. B **46**, 55 (1992)
- 5.36 C. Elsässer, M. Fähnle, L. Schimmele, C.T. Chan, K.M. Ho: Phys. Rev. B **50**, 5155 (1994)
- 5.37 H. Trinkaus: Z. Naturforsch. **28a**, 980 (1975)
- 5.38 H. Metzger, H. Behr, J. Peisl: Z. Phys. B **46**, 295 (1982)
- 5.39 G.E. Bacon: *Neutron Diffraction*, 3rd edn. (Clarendon, Oxford 1975)
- 5.40 G.L. Squires: *Thermal Neutron Scattering* (Cambridge University Press, Cambridge 1978)
- 5.41 C.G. Windsor: *Pulsed Neutron Scattering* (Taylor and Francis, London 1981)
- 5.42 F. Reidinger, J.J. Reilly, R.W. Stoenner: Proc. 36th Annual Pittsburgh Diffraction Conf. (1978)
- 5.43 M. Hirabayashi, H. Asano: In *Metal Hydrides*, ed. by G. Bambakidis (Plenum, New York 1981) p. 53
- 5.44 I. Okada: Master's Thesis, Tohoku University, Sendai (1980) (Unpublished)

- 5.45 T. Springer, D. Richter: In *Methods of Experimental Physics, Vol. 23, Part A: Neutron Scattering*, ed. by K. Sköld, D.L. Price (Academic, New York 1986) p. 131
- 5.46 D. Richter: In *Hydrogen in Intermetallic Compounds II* (Springer, Berlin 1992) p. 97
- 5.47 D.K. Ross: In *Hydrogen in Metals III*, ed. by H. Wipf (Springer, Berlin 1997) p. 153
- 5.48 J.M. Rowe, J.J. Rush, H.G. Smith, M. Mostoller, H.E. Flotow: Phys. Rev. Lett. **33**, 1297 (1974)
- 5.49 P. Vorderwisch, S. Hautecler, W. Wegener: J. Less-Common Met. **74**, 117 (1980)
- 5.50 A. Magerl, N. Stump, W.D. Teuchert, V. Wagner, G. Alefeld: J. Phys. C **10**, 2783 (1977)
- 5.51 A. Kolesnikov, I. Natkaniec, V.E. Antonov, I.T. Belash, V.K. Fedotov, J. Krawczyk, J. Mayer, E.G. Ponyatovsky: Physica B **174**, 257 (1991)
- 5.52 J.J. Rush, J.M. Rowe, D. Richter: Z. Phys. B **55**, 283 (1984)
- 5.53 B. Dorner, I.T. Belash, E.L. Bokhenkov, E.G. Ponyatovsky, V.E. Antonov, L.N. Pronina: Solid State Commun. **69**, 121 (1989)
- 5.54 V.E. Antonov, K. Cornell, B. Dorner, V.K. Fedotov, G. Grosse, A.I. Kolesnikov, F.E. Wagner, H. Wipf: Solid State Commun. **113**, 569 (2000)
- 5.55 D.K. Ross, V.E. Antonov, E.L. Bokhenkov, A.I. Kolesnikov, E.G. Ponyatovsky, J. Tomkinson: Phys. Rev. B **58**, 2591 (1998)
- 5.56 M. Kemali, J.E. Totolici, D.K. Ross, I. Morrison: Phys. Rev. Lett. **84**, 1531 (2000)
- 5.57 S. Ikeda, N. Watanabe: J. Phys. Soc. Jpn. **56**, 565 (1987)
- 5.58 A. Magerl, J.J. Rush, J.M. Rowe: Phys. Rev. B **33**, 2093 (1986)
- 5.59 R. Hempelmann, D. Richter, D.L. Price: Phys. Rev. Lett. **58**, 1016 (1987)
- 5.60 T.J. Udovic, J.J. Rush, N.F. Berk, I.S. Anderson: Phys. Rev. B **45**, 12573 (1992)
- 5.61 O. Blaschko, J. Pleschiutchnig, L. Pintschovius, J.P. Burger, J.N. Daou, P. Vajda: Phys. Rev. B **40**, 907 (1989)
- 5.62 T.J. Udovic, J.J. Rush, I.S. Anderson, J.N. Daou, P. Vajda, O. Blaschko: Phys. Rev. B **50**, 3696 (1994)
- 5.63 V.E. Antonov, V.K. Fedotov, A.I. Harkunov, A.I. Kolesnikov, N.I. Novokhatskaya, G. Grosse, F.E. Wagner, T. Hansen, A.S. Ivanov: Phys. Rev. B **64**, 184302 (2001)
- 5.64 S. Ikeda, N. Watanabe, K. Kai: Physica **120B**, 131 (1983)
- 5.65 F.E. Wagner, G. Grosse, V.E. Antonov, V.K. Fedotov, A.I. Kolesnikov, A.S. Ivanov: ILL Exp. Rep. No. 7-02-47 (1999)
- 5.66 W. Drexel, A. Murani, D. Tocchetti, W. Kley, I. Sosnowska, D.K. Ross: J. Phys. Chem. Solids **37**, 1135 (1976)
- 5.67 A. Rahman, K. Sköld, C. Pelizzari, S.K. Sinha, H. Flotow: Phys. Rev. B **14**, 3630 (1976)
- 5.68 J.M. Rowe, J.J. Rush, J.E. Shirber, J.M. Mintz: Phys. Rev. Lett. **57**, 2955 (1986)
- 5.69 J.J. Rush, H.E. Flotow, D.W. Connor, C.L. Thaper: J. Chem. Phys. **45**, 3817 (1966)
- 5.70 D.G. Hunt, D.K. Ross: J. Less-Common Met. **49**, 169 (1976)

- 5.71 P.P. Parshin, M.G. Zemlyanov, M.E. Kost, A.Yu. Rumyantsev, N.A. Chernoplekov: *Izv. Akad. Nauk SSSR, Neorganicheskie Materialy*, **14**, 1653 (1978) [*Inorg. Mater.* **14**, 1288 (1978)]
- 5.72 J.J. Rush, N.F. Berk, A. Magerl, J.M. Rowe, J.L. Provo: *Phys. Rev. B* **37**, 7901 (1988)
- 5.73 R. Khoda-Bakhsh, D.K. Ross: *J. Phys. F* **12**, 15 (1982)
- 5.74 D. Klauder, V. Lottner, H. Scheuer: *Solid State Commun.* **32**, 617 (1979)
- 5.75 J.M. Rowe: *Solid State Commun.* **11**, 1299 (1972)
- 5.76 D. Richter: *J. Less-Common Met.* **89**, 293 (1983)
- 5.77 R. Hempelmann, D. Richter, A. Kollmar: *Z. Phys. B* **44**, 159 (1981)
- 5.78 K. Cornell, H. Wipf, V.E. Antonov, T.E. Antonova, A.I. Kolesnikov, E.G. Ponyatovsky, B. Dorner: *Polish J. Chem.* **71**, 1792 (1997)
- 5.79 R. Hempelmann, D. Richter, B. Stritzker: *J. Phys. F* **12**, 79 (1982)
- 5.80 J. Eckert, J.A. Goldstone, D. Tonks, D. Richter: *Phys. Rev. B* **27**, 1980 (1983)
- 5.81 M. Kemali, J.E. Totolici, D.K. Ross, I. Morrison: *Phys. Rev. Lett.* **84**, 1531 (2000)
- 5.82 T.J. Udovic, J.J. Rush, I.S. Anderson: *Phys. Rev. B* **50**, 15739 (1994)
- 5.83 T.J. Udovic, J.J. Rush, I.S. Anderson: *J. Phys.: Condens. Matter* **7**, 7005 (1995)
- 5.84 S.M. Bennington, D.K. Ross, M.J. Benham, A.D. Taylor, Z.A. Bowden: *Z. Phys. Chem.* **22**, 1071 (1989)
- 5.85 S.M. Bennington, D.K. Ross, M.J. Benham, A.D. Taylor, Z.A. Bowden, R. Osborn: *Phys. Lett. A* **151**, 325 (1990)
- 5.86 S.M. Bennington, D.K. Ross: *Z. Phys. Chem.* **181**, 27 (1993)
- 5.87 H. Sugimoto, Y. Fukai: *J. Phys. Soc. Jpn.* **51**, 2554 (1982)
- 5.88 H. Sugimoto: *J. Phys. Soc. Jpn.* **53**, 2592 (1984)
- 5.89 S. Ikeda, N. Furusaka, T. Fukunaga, A.D. Taylor: *J. Phys. Condens. Matter* **2**, 4675 (1990)
- 5.90 S. Ikeda: Private communication
- 5.91 S.M. Shapiro, Y. Noda, T.O. Brun, J. Miller, H. Birnbaum, T. Kajitani: *Phys. Rev. Lett.* **41**, 1051 (1978)
- 5.92 Y. Nakagawa, A.D.B. Woods: In *Lattice Dynamics*, ed. by R.W. Wallis (Pergamon, Oxford 1965) p. 39
- 5.93 J.M. Rowe, N. Vegetatos, J.J. Rush, H.E. Flotow: *Phys. Rev. B* **12**, 2959 (1975)
- 5.94 V. Lottner, H.R. Schober, W.J. Fitzgerald: *Phys. Rev. Lett.* **42**, 1162 (1979)
- 5.95 H.R. Schober, V. Lottner: *Z. Phys. Chem.* **114**, 351 (1979)
- 5.96 V. Lottner, A. Heim, T. Springer: *Z. Phys. B* **32**, 157 (1979)
- 5.97 W. Gissler, B. Jay, R. Rubin, L.A. Vinhas: *Phys. Lett.* **43A**, 279 (1973)
- 5.98 J.M. Rowe, J.J. Rush, L.A. de Graaf, C.A. Ferguson: *Phys. Rev. Lett.* **29**, 1250 (1972)
- 5.99 S. Koike, T. Suzuki: *Acta Metall.* **29**, 553 (1981)
- 5.100 T. Suzuki, H. Namazue, S. Koike, H. Hayakawa: *Phys. Rev. Lett.* **51**, 798 (1983)
- 5.101 K. Watanabe, Y. Fukai: *Z. Phys. Chem.* **163**, 175 (1989)
- 5.102 A.S. Nowick, W.R. Heller: *Adv. Phys.* **12**, 251 (1965)
- 5.103 G. Alefeld: *Ber. KFA Jülich, Jül-699-FF* (1970)
- 5.104 M. Lagos: *Surf. Sci.* **122**, L601 (1982)

- 5.105 M. Lagos, I.K. Schuller: *Surf. Sci.* **138**, L161 (1984)
- 5.106 M. Takakusaki, T. Kajitani, M. Hirabayashi: *J. Less-Common Met.* **129**, 47 (1987)
- 5.107 M. Hashimoto, Y. Sakamaki, Y. Fukai, K. Morita, J. Yuhara, M. Kato, N. Matsunami, S. Koike, E. Yagi: to be published
- 5.108 A.Yu. Chervyakov, I.R. Entin, V.A. Somenkov, S.Sh. Shil'shtein, A.A. Chertkov: *Fizika Tverdogo Tela* **13**, 2587 (1971) [*Sov. Phys.-Solid State* **13**, 2172 (1972)]
- 5.109 V.A. Somenkov, I.R. Entin, A.Yu. Chervyakov, S.Sh. Shil'shtein, A.A. Chertkov: *Fizika Tverdogo Tela* **13**, 2595 (1971) [*Sov. Phys.-Solid State* **13**, 2178 (1972)]
- 5.110 K. Watanabe, Y. Fukai: *J. Phys. Soc. Jpn.* **54**, 3415 (1985)
- 5.111 M. Sotzek, H. Sieber, H. Wipf, U. Leuthäuser: *J. Less-Common Met.* **104**, 21 (1984)
- 5.112 Z. Bieganski, B. Stalinski: *Bull. Acad. Pol. Sci.* **9**, 367 (1961)
- 5.113 J.J. Rush, H.E. Flotow: *Phys. Rev.* **48**, 3795 (1968)
- 5.114 T. Kajitani, S. Hamada, M. Hirabayashi: *Z. Phys. Chem.* **163**, 181 (1989)
- 5.115 S. Koike, H. Kojima: *Z. Phys. Chem.* **179**, 383 (1993)
- 5.116 O. Blaschko, G. Krexner, J.N. Daou, P. Vajda: *Phys. Rev. Lett.* **55**, 2876 (1985)
- 5.117 M.W. McKergow, D.K. Ross, J.E. Bonnet, I.S. Anderson, O. Schaerpf: *J. Phys. C* **20**, 1909 (1987)
- 5.118 J.E. Bonnet, D.K. Ross, D.A. Faux, I.S. Anderson: *J. Less-Common Met.* **129**, 287 (1987)
- 5.119 I.S. Anderson, N.F. Berk, J.J. Rush, T.J. Udovic: *Phys. Rev. B* **37**, 4358 (1988)
- 5.120 O. Blaschko, G. Krexner, J. Pleschiutchnig, G. Ernst, J.N. Daou, P. Vajda: *Phys. Rev. B* **39**, 5605 (1989)
- 5.121 J.P.A. Fairclough, D.K. Ross, S.M. Bennington: *Z. Phys. Chem.* **179**, 281 (1993)
- 5.122 T.H. Metzger, U. Schubert, J. Peisl: *J. Phys. F* **15**, 779 (1985)
- 5.123 P. Schiller, H. Nijman: *Phys. Status Solidi (a)* **31**, K77 (1975)
- 5.124 R. Hanada, M. Shinohara, Y. Sado, H. Kimura: *J. de Phys. C* **5**, 757 (1981)
- 5.125 P.E. Zapp, H.K. Birnbaum: *Acta Metall.* **28**, 1275 (1980)
- 5.126 For references, see, e.g., G. Cannelli, R. Cantelli, F. Cordero: *Z. Phys. Chem.* **164**, 943 (1989)
- 5.127 A. Magerl, J.J. Rush, J.M. Rowe, D. Richter, H. Wipf: *Phys. Rev. B* **27**, 927 (1983)
- 5.128 M. Heene, H. Wipf, T.J. Udovic, J.J. Rush: *J. Phys.: Condens. Matter* **12**, 6183 (2000)
- 5.129 E. Yagi, S. Nakamura, F. Kano, T. Kobayashi, K. Watanabe, Y. Fukai, T. Matsumoto: *Phys. Rev. B* **39**, 57 (1989)
- 5.130 T. Matsumoto, Y. Sasaki, M. Hihara: *J. Phys. Chem. Solids* **36**, 215 (1975)
- 5.131 D. Richter, J.J. Rush, J.M. Rowe: *Phys. Rev. B* **27**, 6227 (1983)
- 5.132 M.A. Pick, S.M. Shapiro, A.M. Stoneham: *J. Phys. F* **16**, 961 (1986)
- 5.133 C.L. Snead, J. Bethin: *Phys. Rev. B* **32**, 4254 (1985)
- 5.134 K. Kato, O. Yoshinari, K. Tanaka: *Trans. JIM* **29**, 251 (1988)
- 5.135 S. Sato, O. Yoshinari, K. Tanaka: *Z. Phys. Chem.* **164**, 1025 (1989)
- 5.136 H. Naramoto, K. Kawatsura, M. Sataka, Y. Sugizaki, K. Ozawa, S. Yamaguchi, Y. Fujino, M. Aoki: *Nucl. Instrum. Methods B* **33**, 595 (1988)

- 5.137 E. Yagi, S. Koike: J. Phys. Soc. Jpn. **67**, 340 (1998)
- 5.138 E. Yagi, S. Koike, T. Matsumoto, T. Urai, N. Tajima, K. Ogiwara: Phys. Rev. B **66**, 024206 (2002)
- 5.139 E. Yagi: ISIJ International **43**, 505 (2003)
- 5.140 E. Yagi: private communication
- 5.141 S.M. Myers, M.I. Baskes, H.K. Birnbaum, J.W. Corbett, G.G. DeLeo, S.K. Estreicher, E.E. Heller, P. Jena, N.M. Johnson, R. Kirchheim, S.J. Pearson, M.J. Stavola: Rev. Mod. Phys. **64**, 159 (1992)
- 5.142 H. Schultz: In *Point Defects and Defect Interactions in Metals*, ed. by J. Takamura, M. Doyama, M. Kiritani (University of Tokyo Press, Tokyo 1982) p. 183
- 5.143 H. Kugler, I.A. Schwirtlich, S. Takaki, K. Yamakawa, U. Ziebart, J. Petzold, H. Schultz: In *Point Defects and Defect Interactions in Metals*, ed. by J. Takamura, M. Doyama, M. Kiritani (University of Tokyo Press, Tokyo 1982) p. 520
- 5.144 P. Hautojärvi, H. Huomo, P. Saariaho, A. Vehanen, J. Yli-Kaupilla: J. Phys. F **13**, 1415 (1983)
- 5.145 P. Hautojärvi, H. Huomo, M. Puska, A. Vehanen: Phys. Rev. B **32**, 4326 (1985)
- 5.146 R.W. Balluffi: J. Nucl. Mater. **69/70**, 240 (1978)
- 5.147 P. Ehrhart, P. Jung, H. Schultz, H. Ullmaier: In *Atomic Defects in Metals*, ed. by H. Ullmaier, Landolt-Börnstein New Ser. vol. 25 (Springer, Berlin 1991)
- 5.148 S. Linderöth, H. Rajainmäki, R.M. Nieminen: Phys. Rev. B **35**, 5524 (1987)
- 5.149 S. Linderöth, H. Rajainmäki, B. Nielsen, H.E. Hansen, R.M. Nieminen, K. Petersen: Mater. Sci. Forum **15–18**, 751 (1987)
- 5.150 Cs. Szeles, A. Vértes: J. Phys. F **17**, 2031 (1987)
- 5.151 B. Lengeler, S. Mantl, W. Triftshäuser: J. Phys. F **8**, 1691 (1978)
- 5.152 W. Möller: Nucl. Instrum. Meth. **209/210**, 773 (1983)
- 5.153 S.M. Myers, W.R. Wampler, F. Besenbacher, S.L. Robinson, N.R. Moody: Mater. Sci. Eng. **69**, 397 (1985)
- 5.154 S.M. Myers, D.M. Follstaedt, F. Besenbacher: In *Surface Alloying by Ion, Electron and Laser Beams*, ed. by L.E. Rehn, S.T. Picraux, H. Wiedersich (American Society for Metals, Metals Park, OH 1987) p. 223
- 5.155 S.T. Picraux: Nucl. Instrum. Meth. **182/183**, 413 (1981)
- 5.156 F. Besenbacher, S.M. Myers, J.K. Nørskov: Nucl. Instrum. Meth. **B7/8**, 55 (1985)
- 5.157 S.M. Myers, P.M. Richards, W.R. Wampler, F. Besenbacher: J. Nucl. Mater. **165**, 9 (1989)
- 5.158 E. Ligeon, R. Danielou, J. Fontenille, E. Eymery: J. Appl. Phys. **59**, 108 (1986)
- 5.159 F. Besenbacher, J. Bøttiger, T. Laursen, W. Möller: J. Nucl. Mater. **93/94**, 617 (1980)
- 5.160 F. Besenbacher, J. Bøttiger, S.M. Myers: J. Appl. Phys. **53**, 3536 (1982)
- 5.161 F. Besenbacher, J. Bøttiger, S.M. Myers: J. Appl. Phys. **53**, 3547 (1982)
- 5.162 F. Besenbacher, H. Bogh, A.A. Pisarev, M.J. Puska, S. Holloway, J.K. Nørskov: Nucl. Instrum. Meth. **B4**, 374 (1984)
- 5.163 S.M. Myers, P. Nordlander, F. Besenbacher, J.K. Nørskov: Phys. Rev. B **33**, 851 (1986)

- 5.164 J.P. Bugeat: Thesis, Université de Grenoble (1979)
- 5.165 J.P. Bugeat, E. Ligeon: Phys. Lett. **71A**, 93 (1979)
- 5.166 F. Besenbacher, J.K. Nørskov, M.J. Puska, S. Holloway: Phys. Rev. Lett. **55**, 852 (1985)
- 5.167 F. Besenbacher, B.B. Nielsen, S.M. Myers: J. Appl. Phys. **56**, 3384 (1984)
- 5.168 J.P. Bugeat, A.C. Chami, E. Ligeon: Phys. Lett. **58A**, 127 (1976)
- 5.169 E. Ligeon, J.P. Bugeat, A.C. Chami: Nucl. Instrum. Meth. **149**, 99 (1978)
- 5.170 R. Danielou, J.N. Daou, E. Ligeon, P. Vajda: Phys. Status Solidi (a) **67**, 453 (1981)
- 5.171 F. Benyaich: Thesis, Université de Grenoble (1984)
- 5.172 S.M. Myers, S.T. Picraux, R.E. Stoltz: J. Appl. Phys. **50**, 5710 (1979)
- 5.173 S.M. Myers, F. Besenbacher, J. Bøttiger: Appl. Phys. Lett. **39**, 450 (1981)
- 5.174 S.M. Myers, D.M. Follstaedt, F. Besenbacher, J. Bøttiger: J. Appl. Phys. **53**, 8734 (1982)
- 5.175 F. Besenbacher, S.M. Myers, P. Nordlander, J.K. Nørskov: J. Appl. Phys. **61**, 1788 (1987)
- 5.176 S.M. Myers, F. Basenbacher, J.K. Nørskov: J. Appl. Phys. **58**, 1841 (1985)
- 5.177 S. Yamaguchi, K. Ozawa, O. Yoshinari, M. Koiwa, M. Hirabayashi: Nucl. Instr. Meth. **168**, 301 (1980)
- 5.178 Y. Fukai: J. Alloys Comp. **356–357**, 263 (2003)
- 5.179 Y. Fukai, M. Mizutani, S. Yokota, M. Kanazawa, Y. Miura, T. Watanabe: J. Alloys Comp. **356–357**, 270 (2003)
- 5.180 M.B. Lewis: J. Nucl. Mater. **125**, 152 (1984)
- 5.181 F. Besenbacher, B.B. Nielsen, J.K. Nørskov, S.M. Myers, P. Nordlander: J. Fusion Energy **9**, 257 (1990)
- 5.182 S.R. Lee, S.M. Myers, R.G. Spulak: (1989), unpublished, cited in [5.157]
- 5.183 H. Elefeld, A.J. van Veen: J. Nucl. Mater. **191**, 433 (1992)
- 5.184 P. Nordlander, J.K. Nørskov, F. Besenbacher, S.M. Myers: Phys. Rev. B **40**, 1990 (1989)
- 5.185 Y. Fukai, N. Ōkuma: Phys. Rev. Lett. **73**, 1640 (1994)
- 5.186 W.A. Oates, H. Wenzl: Scripta metall. Mater. **30**, 851 (1994)
- 5.187 W.A. Oates, H. Wenzl: Scripta metall. Mater. **33**, 185 (1995)
- 5.188 R.B. McLellan: J. Phys. Chem. Solids **49**, 1213 (1988)
- 5.189 R.B. McLellan: Acta metall. mater. **36**, 1923 (1988)
- 5.190 R.B. McLellan, M.L. Wasz: J. Phys. Chem. Solids **51**, 523 (1990)
- 5.191 R.B. McLellan, L. Yang: Acta metall. mater. **43**, 2463 (1995)
- 5.192 P. Maroevic, R.B. McLellan: J. Phys. Chem. Solids **58**, 403 (1997)
- 5.193 P. Maroevic, R.B. McLellan: Acta metall. mater. **46**, 5593 (1998)
- 5.194 D. Zang, P. Maroevic, R.B. McLellan: J. Phys. Chem. Solids **60**, 1649 (1999)
- 5.195 A.A. Smirnov: Metallofizika **13**, 21 (1991)
- 5.196 A.A. Smirnov: Ukr. Fiz. Zh. **37**, 1188 (1992)
- 5.197 V.N. Bugaev, V.G. Gavriljuk, Yu.N. Petrov, A.V. Tarasenko: Int. J. Hydrogen Energy **22**, 213 (1997)
- 5.198 V.A. Tatarenko, C.L. Tsynman: Solid State Ionics **101/103**, 1093 (1997)
- 5.199 Y. Fukai, Y. Shizuku, Y. Kurokawa: J. Alloys Comp. **329**, 195 (2001)
- 5.200 Y. Fukai: In *Computer Aided Innovation of New Materials, II*, ed. by M. Doyama, J. Kihara, M. Tanaka, R. Yamamoto (Elsevier, Amsterdam 1993) p. 451
- 5.201 S. Miraglia, D. Fruchart, E.K. Hlil, S.S.M. Tavares, D. dos Santos: J. Alloys Comp. **317**, 77 (2001)

- 5.202 E.K. Hlil, D. Fruchart, S. Miraglia, J. Tobola: J. Alloys Comp. **356-357**, 169 (2003)
- 5.203 S.A. Semilenov, R.V. Baranova, Yu.P. Khodyrev, R.M. Imanov: Sov. Phys. Crystallogr. **25**, 665 (1980)
- 5.204 Y. Fukai, M. Yamakata, T. Yagi: Z. Phys. Chem. **179**, 119 (1993)
- 5.205 W. Möller, F. Besenbacher, J. Böttiger: Appl. Phys. **A27**, 19 (1982)
- 5.206 S.M. Myers, P.M. Richards, D.M. Follstaed, J.E. Schirber: Phys. Rev. B **43**, 9503 (1991)
- 5.207 U. Kaess, G. Majer, M. Stoll, D.T. Peterson, R.G. Barnes: J. Alloys Comp. **259**, 74 (1997)
- 5.208 G. Mejer, W. Renz, R.G. Barnes: J. Phys. Condes. Mat. **5**, 2935 (1994)
- 5.209 H. Koike, Y. Shizuku, A. Yazaki, Y. Fukai: J. Phys.: Condens. Matter **16**, 1335 (2004)
- 5.210 J. Cizek, I. Prochazka, R. Kuzel, F. Becvar, M. Ciesler, G. Bauer, W. Anwand, R. Kirchheim, A. Pundt: J. Alloys Comp. in press
- 5.211 E.H. Sevilla, R.M. Cotts: Phys. Rev. B **37**, 6813 (1988)
- 5.212 Y. Fukai, Y. Ishii, T. Goto, K. Watanabe: J. Alloys Comp. **313**, 121 (2000)
- 5.213 J. Völkl, G. Alefeld: In *Diffusion in Solids Recent Development*, ed. by A.S. Nowick, J.J. Burton (Academic Press, New York 1975) p. 231
- 5.214 M. Iwamoto, Y. Fukai: Trans. JIM **40**, 606 (1999)
- 5.215 S. Harada, S. Yokota, Y. Ishii, Y. Shizuku, M. Kanazawa, Y. Fukai: J. Alloys Comp. in press
- 5.216 Y. Fukai, T. Haraguchi, E. Hayashi, Y. Ishii, Y. Kurokawa, J. Yanagawa: Defect Diffusion Forum **194**, 1063 (2001)
- 5.217 R.J. Roy, T.R.P. Gibb: J. Inorg. Nucl. Chem. **29**, 341 (1967)
- 5.218 E. Hayashi, Y. Kurokawa, Y. Fukai: Phys. Rev. Lett. **80**, 5588 (1998)
- 5.219 J.S. Koehler, C. Lund: In *Lattice Defects in Quenched Metals*, ed. by R.M.J. Cotterill, M. Doyama, M. Meshii (Academic Press, New York 1982) p. 1
- 5.220 T. Kino, K. Ono: In *Point Defects and Defect Interactions in Metals*, ed. by J. Takamura, M. Doyama, M. Kiritani (University of Tokyo Press, Tokyo 1982) p. 247
- 5.221 T. Kino, K. Mizuno: J. Phys. Soc. Jpn: **53**, 3290 (1984)
- 5.222 H. Noh, T.B. Flanagan, B. Corundolo, A. Craft: Scripta metal. **25**, 225 (1991)
- 5.223 H. Noh, T.B. Flanagan, M.H. Ransick: Scripta metal. **26**, 353 (1992)
- 5.224 T.B. Flanagan, H. Noh: J. Alloys Comp. **231**, 1 (1995)
- 5.225 H. Noh, T.B. Flanagan, Y. Sakamoto: J. Alloys Comp. **231**, 10 (1995)
- 5.226 H. Noh, J.D. Clewley, T.B. Flanagan, A. Craft: J. Alloys Comp. **240**, 235 (1966)
- 5.227 K. Watanabe, N. Ōkuma, Y. Fukai, Y. Sakamoto, Y. Hayashi: Scripta Mater. **34**, 551 (1996)
- 5.228 H. Yamazaki, Y. Iida, Y. Iijima, Y. Fukai: Defect Diffusion Forum, in press
- 5.229 T. Fujikawa, T. Yoshikawa, T. Ohnishi, T. Sato: Jpn. J. Appl. Phys. **40**, 2191 (2001)
- 5.230 M. Nagumo: ISIJ Int. **41**, 590 (2001)
- 5.231 J. Yamashita, T. Kurosawa: J. Phys. Chem. Solids **5**, 34 (1958)
- 5.232 T. Holstein: Ann. Phys. (NY) **8**, 325 (1959)
- 5.233 T. Holstein: Ann. Phys. (NY) **8**, 343 (1959)
- 5.234 Y. Fukai, H. Sugimoto: Trans. Jpn. Inst. Met. (Suppl.) **21**, 41 (1980)

- 5.235 H. Sugimoto, Y. Fukai: Phys. Rev. B **22**, 670 (1980)
- 5.236 H. Sugimoto, Y. Fukai: J. Phys. Soc. Jpn. **50**, 3709 (1981)
- 5.237 M.J. Puska, R.M. Nieminen: Phys. Rev. B **29**, 5382 (1984)
- 5.238 Klamt, H. Teichler: Phys. Status Solidi (b) **134**, 103 (1986)
- 5.239 A. Klamt, H. Teichler: Phys. Status Solidi (b) **134**, 533 (1986)
- 5.240 G.E. Kimball, G.H. Shortley: Phys. Rev. **45**, 815 (1934)
- 5.241 A.S. Nowick, B.S. Berry: *Anelastic Relaxation in Crystalline Solids* (Academic, New York 1972)
- 5.242 K.W. Kehr: In *Hydrogen in Metals I*, ed. by G. Alefeld, J. Völkl, Topics in Appl. Phys., Vol. 28 (Springer, Berlin, Heidelberg 1978) p. 197
- 5.243 R.A. Johnson, G.J. Dienes, A.C. Damask: Acta Metall. **12**, 1215 (1964)
- 5.244 D.K. Ross, P.F. Martin, W.A. Oates, R. Khoda-Bakhsh: Z. Phys. Chem. **114**, 341 (1979)
- 5.245 Y. Fukai, H. Sugimoto: J. Phys. F **11**, L137 (1981)
- 5.246 K.M. Ho, H.J. Tao, X.Y. Zhu: Phys. Rev. Lett. **53**, 1586 (1984)
- 5.247 M.J. Gillan: Phys. Rev. Lett. **58**, 563 (1987)
- 5.248 M.J. Gillan: Philos. Mag. A **58**, 257 (1988)
- 5.249 F. Christodoulos, M.J. Gillan: Philos. Mag. B **63**, 641 (1991)
- 5.250 F. Christodoulos, M.J. Gillan: J. Phys.: Condens. Matter **3**, 9429 (1991)
- 5.251 M.W. Finnis, J.E. Sinclair: Philos. Mag. A **50**, 45 (1984)
- 5.252 A. Klamt: J. Phys. F **16**, L1 (1986)
- 5.253 I.R. Entin, V.A. Somenkov, S.Sh. Shil'shtein: Sov. Phys.-Solid State **16**, 1569 (1975)
- 5.254 H.S.U. Jo, S.C. Moss, D.G. Westlake: J. Appl. Cryst. **13**, 486 (1980)
- 5.255 H.J. Tao, K.M. Ho, X.Y. Zhu: Phys. Rev. B **34**, 8394 (1986)
- 5.256 K.M. Ho, C. Elsässer, C.T. Chan, M. Fähnle: J. Phys.: Condens. Matter **4**, 5189 (1992)
- 5.257 C. Elsässer, K.M. Ho, C.T. Chan, M. Fähnle: Phys. Rev. B **44**, 10377 (1991)
- 5.258 C. Elsässer, K.M. Ho, C.T. Chan, M. Fähnle: J. Phys.: Condens. Matter **4**, 5207 (1992)
- 5.259 H. Krimmel, L. Schimmele, C. Elsässer, M. Fähnle: J. Phys.: Condens. Matter **6**, 7679 (1994)
- 5.260 D.K. Ross, J.E. Totolici, M. Kemali, I. Morrison, I. Ivanov, M. Johnson, C. Elsässer: In *Recent Advances in Hydrogen Chemistry*, ed. by M. Peruzzini, R. Poli (Elsevier, Amsterdam, 2001) p. 507
- 5.261 H. Krimmel, L. Schimmele, C. Elsässer, M. Fähnle: J. Phys.: Condens. Matter **6**, 7705 (1994)
- 5.262 P. Nordlander, S. Holloway, J.K. Nørskov: Surf. Sci. **136**, 59 (1984)
- 5.263 L.R. Pratt, J. Eckert: Phys. Rev. B **39**, 13170 (1989)
- 5.264 G. Cannelli, R. Cantelli, F. Cordero, F. Trequattrini: In *Tunneling Systems in Amorphous and Crystalline Solids*, ed. by P. Esquinazi (Springer, Berlin, Heidelberg 1998) p. 389
- 5.265 G.J. Sellers, M. Paalanen, A.C. Anderson: Phys. Rev. B **10**, 1912 (1974)
- 5.266 G.J. Sellers, A.C. Anderson, H.K. Birnbaum, Phys. Rev. B **10**, 2771 (1974)
- 5.267 C. Morkel, H. Wipf, K. Neumaier: Phys. Rev. Lett. **40**, 947 (1978)
- 5.268 H. Wipf, K. Neumaier: Phys. Rev. Lett. **52**, 1308 (1984)
- 5.269 P. Gutsmedl, M. Schiekhofer, K. Neumaier, H. Wipf: In *Quantum Aspects of Molecular Motions in Solids*, ed. by A. Heidemann, A. Magerl, M. Prager, D. Richter, T. Springer, Springer Proc. Phys., Vol. 17 (Springer, Berlin, Heidelberg 1987) p. 158

- 5.270 H. Wipf, A. Magerl, S.M. Shapiro, S.K. Satija, W. Thomlinson: Phys. Rev. Lett. **46**, 947 (1981)
- 5.271 Y. Imry: In *Tunneling Phenomena in Solids*, ed. by E. Burstein, S. Lundquist (Plenum, New York 1969)
- 5.272 Magerl, A.J. Dianoux, H. Wipf, K. Neumaier, I.S. Anderson: Phys. Rev. Lett. **56**, 159 (1986)
- 5.273 K. Neumaier, D. Steinbinder, H. Wipf, H. Blank, G. Kearley: Z. Phys. B **76**, 359 (1989)
- 5.274 D. Steinbinder, H. Wipf, A.J. Dianoux, A. Magerl, K. Neumaier, D. Richter, R. Hempelmann: Europhys. Lett. **16**, 211 (1991)
- 5.275 H. Wipf, D. Steinbinder, K. Neumaier, P. Gutsmedl, A. Magerl, A.J. Dianoux: Europhys. Lett. **4**, 1379 (1987)
- 5.276 I.S. Anderson, N.F. Berk, J.J. Rush, T.J. Udovic, R.G. Barnes, A. Magerl, D. Richter: Phys. Rev. Lett. **65**, 1439 (1990)
- 5.277 J. Jäckle: Z. Phys. **257**, 212 (1972)
- 5.278 J. Jäckle, L. Piché, W. Arnold, S. Hunklinger: J. Non-Cryst. Solids **20**, 365 (1976)
- 5.279 S. Hunklinger, W. Arnold: In *Physical Acoustics*, vol.12, ed. by W.P. Mason, R.N. Thurston (Academic, New York 1976) p. 155
- 5.280 B. Golding, J.E. Graebner, A.B. Kane, J.L. Black: Phys. Rev. Lett. **41**, 1487 (1978)
- 5.281 J.L. Black, P. Fulde: Phys. Rev. Lett. **43**, 453 (1979)
- 5.282 G. Weiss, S. Hunklinger, H.N. Löhneysen: Physica B&C **109/110**, 1946 (1982)
- 5.283 G. Bellessa: J. Phys. (Paris) **44**, L387 (1983)
- 5.284 D.B. Paker, G.G. Setser, A.V. Granato, H.K. Birnbaum: Phys. Rev. B **29**, 622 (1984)
- 5.285 J.L. Wang, G. Weiss, H. Wipf, A. Magerl: In *Phonon Scattering in Condensed Matter*, ed. by W. Eisinger, K. Lassmann, S. Döttinger (Springer, Berlin 1984) p. 401
- 5.286 E. Drescher-Krasicka, A.V. Granato: J. Phys. (Paris) **46**, C10 (1985)
- 5.287 G. Cannelli, R. Cantelli, F. Cordero: Phys. Rev. B **34**, 7721 (1986)
- 5.288 K.R. Maschhoff, E. Drescher-Krasicka, A.V. Granato: In *Phonon Scattering in Condensed Matter*, ed. by A.C. Anderson, J.P. Wolfe (Springer, Berlin 1987) p. 64
- 5.289 W. Morr, G. Weiss, H. Wipf: In *Quantum Aspects of Molecular Motions in Solids*, ed. by A. Heidemann, A. Magerl, H. Prager, D. Richter, T. Springer (Springer, Heidelberg 1987) p.163
- 5.290 W. Morr, A. Müller, G. Weiss, H. Wipf, B. Golding: Phys. Rev. Lett. **63**, 2084 (1989)
- 5.291 V.K. Fedotov, V.E. Antonov, K. Cornell, G. Grosse, A.I. Kolesnikov, V.V. Sikolenko, V.V. Sumin, F.E. Wagner, H. Wipf: J. Phys.: Condens. Matter **10**, 5255 (1998)
- 5.292 A.I. Kolesnikov, V.E. Antonov, S.M. Bennington, B. Dorner, V.K. Fedotov, G. Grosse, J.C. Li, S.F. Parker, F.E. Wagner: Physica B **263–264** (1999)
- 5.293 V.E. Antonov, B. Dorner, V.K. Fedotov, G. Grosse, A.S. Ivanov, A.I. Kolesnikov, V.V. Sikolenko, F.E. Wagner: J. Alloys Comp. **330–332**, 462 (2002)
- 5.294 S.L. Drechsler, G.M. Vujičić, N.M. Plakida: J. Phys. F: Met. Phys. **14**, L243 (1984)

- 5.295 K. Neumaier, H. Wipf, G. Cannelli, R. Cantelli: Phys. Rev. Lett. **49**, 1423 (1982)
- 5.296 G. Cannelli, R. Cantelli, F. Cordero: Z. Phys. Chem. **164**, 943 (1989)
- 5.297 B. Hauer, R. Hempelmann, D. Richter, T.J. Udovic, J.J. Rush, S.M. Bennington, A.J. Dianoux: Physica B **226**, 210 (1996)
- 5.298 G. Cannelli, R. Cantelli, F. Cordero, F. Trequattrini: Z. Phys. Chem. **179**, 317 (1993)
- 5.299 G. Cannelli, R. Cantelli, F. Cordero, F. Trequattrini, H. Schultz: J. Alloys Comp. **231**, 274 (1995)
- 5.300 F. Cordero, A. Paolone, R. Cantelli: J. Alloys. Comp. **356–357**, 252 (2003)
- 5.301 M. Winterstetter, M. Grifoni: Phys. Rev. B **62**, 3237 (2000)
- 5.302 H.J. Fell, R. Hempelmann, O. Hartmann, S. Harris, R. Wäppling: Ber. Bunsenges. Phys. Chem. **95**, 1091 (1991)
- 5.303 H. Sugimoto, Y. Fukai: In *Muon Spin Rotation and Associated Problems I*, ed. by T. Yamazaki, K. Nagamine (J.C. Baltzer, Basel 1984) p. 139; Hyperf. Interact. **17–19**, 139 (1984)
- 5.304 Yu. Kagan, M.I. Klinger: J. Phys. C **7**, 2791 (1974)
- 5.305 L.M. Sander, H.B. Shore: Phys. Rev. B **3**, 1472 (1971)
- 5.306 H. Teichler: J. Phys. F **16**, 1399 (1986)
- 5.307 J. Kondo: Physica B **84**, 40 (1976)
- 5.308 J. Kondo: Physica B **124**, 25 (1984)
- 5.309 J. Kondo: Physica B **125**, 279 (1984)
- 5.310 J. Kondo: Physica B **126**, 377 (1984)
- 5.311 J. Kondo: In *Muon Spin Rotation, Relaxation. Resonance*, ed. by O. Hartmann, E. Karlsson, B. Lindgren, R. Wäppling (J.C. Baltzer, Basel 1986) vol. 1, p. 117; Hyperf. Interact. **31**, 117 (1986)
- 5.312 J. Kondo: J. Phys. Soc. Jpn. **56**, 1638 (1987)
- 5.313 K. Yamada, A. Sakurai, M. Takeshige: Prog. Theor. Phys. **70**, 73 (1983)
- 5.314 K. Yamada: Prog. Theor. Phys. **72**, 195 (1984)
- 5.315 Yu. Kagan, N.V. Prokof'ev: Zh. Eksp. Theor. Fiz. **90**, 2176 (1986) [Sov. Phys. JETP **63**, 1276 (1986)]
- 5.316 H. Grabert, S. Linkwitz, S. Dattagupta, U. Weiss: Europhys. Lett. **2**, 631 (1986)
- 5.317 H. Grabert: In *Quantum Aspects of Molecular Motions in Solids*, ed. by A. Heidemann, A. Magerl, M. Prager, D. Richter, T. Springer, Springer Proc. Phys., Vol. 17 (Springer, Berlin, Heidelberg 1987) p. 130
- 5.318 H. Grabert, H.R. Schober: In *Hydrogen in Metals III*, ed. by H. Wipf, Topics Appl. Phys., Vol. 73 (Springer, Berlin, Heidelberg 1997) p. 5
- 5.319 H. Teichler: In *Quantum Aspects of Molecular Motions in Solids*, ed. by A. Heidemann, A. Magerl, M. Prager, D. Richter, T. Springer, Springer Proc. Phys., Vol. 17 (Springer, Berlin, Heidelberg 1987) p. 167
- 5.320 H. Teichler: Z. Phys. Chem. **164**, 747 (1989)
- 5.321 M.J. Puska, R.M. Nieminen: Phys. Rev. B **27**, 6121 (1983)
- 5.322 A. Fritzsche: Dr. rer. Nat. thesis, Univ. Stuttgart, 1992
- 5.323 T. Regelman, L. Schimmele, A. Seeger: Philos. Mag. **72**, 209 (1995)
- 5.324 L. Schimmele, A. Seeger: Hyperf. Interact. **85**, 45 (1994)
- 5.325 J.L. Black: In *Glassy Metals I*, ed. by H.J. Güntherodt (Springer, Berlin 1981) p. 167.
- 5.326 A. Einstein, B. Podolsky, N. Rosen: Phys. Rev. **47**, 777 (1935)

- 5.327 D. Giulini, E. Joos, C. Kiefer, J. Kupsch, I.O. Stanatescu, H.D. Zeh: *Decoherence and the Appearance of a Classical World in Quantum Theory* (Springer, Berlin 1996)
- 5.328 E.B. Karlsson, E. Brändas (eds.): *Proceedings of the Nobel Symposium 104; Modern Studies of Basic Quantum Concepts and Phenomena* [Physica Scripta T**76** (1998)]
- 5.329 Y.A. Ono, K. Fujikawa (eds.): *Foundations of Quantum Mechanics in the Light of New Technology* (World Scientific, 2002)
- 5.330 D. Bouwmeester, A. Eckert, A. Zeilinger (eds.) *The Physics of Quantum Information* (Springer, Berlin 2000)
- 5.331 E. Joos, H.D. Zeh: Z. Phys. B **59**, 223 (1985)
- 5.332 For early developments, see C.A. Chatzidimitriou-Dreismann, E.B. Karlsson: Z. Phys. Chem. **181**, 165 (1993)
- 5.333 E.B. Karlsson, S.W. Lovesey: Physica Scripta **65**, 112 (2002)
- 5.334 C.A. Chatzidimitriou-Dreismann, T. Abdul-Redah, R.M.F. Streffer, J. Mayers: Phys. Rev. Lett. **79**, 2839 (1997)
- 5.335 C.A. Chatzidimitriou-Dreismann, T. Abdul-Redah, J. Mayers: Physica B **315**, 281 (2002)
- 5.336 C.A. Chatzidimitriou-Dreismann, U.K. Krieger, A. Möller, M. Stern: Phys. Rev. Lett. **75**, 3008 (1995)
- 5.337 E.B. Karlsson, C.A. Chatzidimitriou-Dreismann, T. Abdul-Redah, R.M.F. Streffer, B. Hjörvarsson, J. Öhrmalm, J. Mayers: Europhys. Lett. **46**, 617 (1999)
- 5.338 T. Abdul-Redah, R.M.F. Streffer, C.A. Chatzidimitriou-Dreismann, B. Hjörvarsson, E.B. Karlsson: Physica B **276-278**, 824 (2000)
- 5.339 E.B. Karlsson, T. Abdul-Redah, T.J. Udovic, B. Hjörvarsson, C.A. Chatzidimitriou-Dreismann: In *Foundations of Quantum Mechanics in the Light of New Technology*, ed. by Y.A. Ono, K. Fujikawa (World Scientific, 2002) p. 295
- 5.340 C.A. Chatzidimitriou-Dreismann, T. Abdul-Redah, J. Sperling: J. Chem. Phys. **113**, 2784 (2000)
- 5.341 C.A. Chatzidimitriou-Dreismann, T. Abdul-Redah: in *Foundations of Quantum Mechanics in the Light of New Technology*, ed. by Y.A. Ono, K. Fujikawa (World Scientific, 2002) p. 299
- 5.342 C.A. Chatzidimitriou-Dreismann, M. Vos, C. Kleiner, T. Abdul-Redah: Phys. Rev. Lett. **91**, 057403 (2003)
- 5.343 F. Fillaux: Physica D **113**, 172 (1998)
- 5.344 S. Ikeda, F. Fillaux: Phys. Rev. B **59**, 4134 (1999)
- 5.345 C.A. Chatzidimitriou-Dreismann: J. Alloys Comp: **356-357**, 244 (2003)
- 5.346 E.B. Karlsson, S.W. Lovesey: Phys. Rev. A **61**, 062714 (2000)
- 5.347 E.B. Karlsson, S.W. Lovesey: in *Foundations of Quantum Mechanics in the Light of New Technology*: ed. by Y.A. Ono, K. Fujikawa (World Scientific, 2002) p. 291
- 5.348 E.B. Karlsson: Eur. Phys. J. D **22**, 393 (2003)
- 5.349 J. Schwinger, E. Teller: Phys. Rev. **52**, 296 (1937)
- 5.350 E.B. Karlsson: Phys. Rev. Lett. **90**, 095301 (2003)
- 5.351 D.A. Keen, S.W. Lovesey: J. Phys.: Condens. Matter **15**, 4937 (2003)
- 5.352 E.B. Karlsson, T. Abdul-Redah, R.M.F. Streffer, B. Hjörvarsson, J. Mayers, C.A. Chatzidimitriou-Dreismann: Phys. Rev. B **67**, 184108 (2003)

- 5.353 J.J. Blostein, J. Dawidowski, J.R. Granada: *Physica B* **304**, 357 (2001)
- 5.354 T. Abdul-Redah, C.A. Chatzidimitriou-Dreismann: *J. Alloys Comp.* **356-357**, 249 (2003)
- 5.355 R.A. Cowley: *J. Phys.: Condens. Matter* **15**, 4143 (2003)
- 5.356 E.B. Karlsson, S.W. Lovesey: to be published
- 5.357 J.J. Blostein, J. Dawidowski, S.A. Ibáñez, J.R. Granada: *Phys. Rev. Lett.* **90**, 105302 (2003)
- 5.358 H.J. Assenbaum, K. Langanke, C. Rolfs: *Z. Phys. A* **327**, 461 (1987)
- 5.359 S. Engstler, A. Krauss, K. Neldner, C. Rolfs, U. Schröder, K. Langanke: *Phys. Lett. B* **202**, 179 (1988)
- 5.360 C. Angulo, S. Engstler, G. Raimann, C. Rolfs, W.H. Schulte, E. Somorjai: *Z. Phys. A* **345**, 231 (1993)
- 5.361 U. Greife, F. Gorris, M. Junker, C. Rolfs, D. Zahnow: *Z. Phys. A* **351**, 107 (1995)
- 5.362 J. Kasagi, T. Murakami, T. Yamaji, S. Kobayashi, M. Ogawa: *J. Phys. Soc. Jpn.* **64**, 777 (1995)
- 5.363 J. Kasagi, T. Ohtsuki, K. Ishii, M. Hiraga: *J. Phys. Soc. Jpn.* **64**, 3718 (1995)
- 5.364 H. Yuki, T. Sato, T. Ohtsuki, T. Yorita, Y. Aoki, H. Yamazaki, J. Kasagi, K. Ishii: *J. Phys. Soc. Jpn.* **66**, 73 (1997)
- 5.365 H. Yuki, T. Sato, T. Ohtsuki, T. Yorita, Y. Aoki, H. Yamazaki, J. Kasagi: *J. Phys. G* **23**, 1459 (1997)
- 5.366 H. Yuki, J. Kasagi, A.G. Lipson, T. Ohtsuki, T. Baba, T. Noda, B.F. Lyakhov, N. Asami: *JETP Lett.* **68**, 823 (1998)
- 5.367 J. Kasagi, H. Yuki, T. Baba, T. Noda, T. Ohtsuki, A.G. Lipson: *J. Phys. Soc. Jpn.* **71**, 2881 (2002)
- 5.368 J. Kasagi, H. Yuki, T. Baba, T. Noda, J. Taguchi, M. Shimokawa, W. Galster: *J. Phys. Soc. Jpn.* **73**, 608 (2004)
- 5.369 K. Czerski, A. Huke, A. Biller, P. Heide, M. Hoeft, G. Ruprecht: *Europhys. Lett.* **54**, 449 (2001)
- 5.370 F. Raiola, P. Migliardi, G. Gyürky, M. Aliotta, A. Formicola, R. Bonetti, C. Brogini, L. Campajola, P. Corvisiero, H. Costantini, J. Cruz, A. D'Onofrio, Z. Fülöp, G. Gervino, L. Gialanella, A. Guglielmetti, G. Imbriani, C. Gustavino, A.P. Jesus, M. Junker, R.W. Kavanagh, P.G.P. Moroni, A. Ordine, J.V. Pinto, P. Prati, V. Roca, J.P. Ribeiro, D. Rogalla, C. Rolfs, M. Romano, F. Schümann, D. Schürmann, E. Somorjai, F. Strieder, F. Terrasi, H.P. Trautvetter, S. Zavatarelli: *Eur. Phys. J. A* **13**, 377 (2002)
- 5.371 F. Raiola, P. Migliardi, L. Gang, C. Bonomo, G. Gyürky, R. Bonetti, C. Brogini, N.E. Christensen, P. Corvisiero, J. Cruz, A. D'Onofrio, Z. Fülöp, G. Gervino, L. Gialanella, A.P. Jesus, M. Junker, K. Langanke, P. Prati, V. Roca, C. Rolfs, M. Romano, E. Somorjai, F. Strieder, A. Svane, F. Terrasi, J. Winter: *Phys. Lett. B* **547**, 193 (2002)
- 5.372 C. Rolfs: *Prog. Theor. Phys. Suppl.* **154**, 373 (2004)
- 5.373 J. Kasagi: *Prog. Theor. Phys. Suppl.* **154**, 365 (2004)
- 5.374 L. Bracci, G. Fiorentini, G. Mezzorani: *Phys. Lett. A* **146**, 128 (1990)
- 5.375 T.D. Shoppa, S.E. Koonin, K. Langanke, R. Seki: *Phys. Rev. C* **48**, 837 (1993)
- 5.376 T.D. Shoppa, M. Jeng, S.E. Koonin, K. Langanke, R. Seki: *Nucl. Phys. A* **605**, 387 (1996)
- 5.377 S. Ichimaru: *Rev. Mod. Phys.* **65**, 255 (1993)

- 5.378 S.F. Koonin, M. Nauenberg: *Nature* **339**, 690 (1989)
- 5.379 C.A. Dreismann, T. Abdul-Redah: *Physica B* **350**, 239 (2004)
- 5.380 C.A. Dreismann, T. Abdul-Redah, M. Krzystyniak: *Phys. Rev. Lett.* in press
- 5.381 C.A. Dreismann, S. Stenholm: In *Quantum Complex Systems: Decoherence, Entanglement and Information from Nano- to Macroscales*, ed. by V. Akulin, G. Kurizki, S. Pellegrin (Kluwer, 2004), in press
- 5.382 T. Iida, Y. Yamazaki, T. Kobayashi, Y. Iijima, Y. Fukai: *Acta Mater.* (2005), in press. Available on line at www.sciencedirect.com
- 5.383 Y. Tateyama, T. Ohno: *Phys. Rev. B* **67**, 174105, 1–10 (2003)

Chapter 6

- 6.1 J.R. Manning: *Diffusion Kinetics for Atoms in Crystals* (van Nostrand, Princeton 1968)
- 6.2 A.D. Le Claire: In *Physical Chemistry*, ed. by H. Eyring, D. Henderson, W. Jost (Academic, New York 1970), p. 261
- 6.3 C.P. Flynn: *Point Defects and Diffusion* (Clarendon, Oxford 1972)
- 6.4 G.E. Murch: *Atomic Diffusion Theory in Highly Defective Solids* (Trans. Tech, Aedermanns- dorf, Switzerland 1980)
- 6.5 G.E. Murch: *Phil. Mag. A* **45**, 685 (1982)
- 6.6 G.E. Murch: In *Diffusion in Crystalline Solids*, ed. by G.E. Murch, A.S. Nowick (Academic, New York 1984)
- 6.7 H. Sato: In *Nontraditional Methods in Diffusion*, ed. by G.E. Murch, H.K. Birnbaum, J.R. Cost (The Metallurgical Soc. of AIME, New York 1984) p. 203
- 6.8 S. Ishioka, M. Koiwa: *Phil. Mag. A* **52**, 267 (1985)
- 6.9 D.A. Faux, D.K. Ross: *J. Phys. C* **20**, 1441 (1970)
- 6.10 K.W. Kehr, K. Binder: In *Applications of the Monte Carlo Method in Statistical Physics*, ed. by K. Binder (Springer, Berlin 1987), p. 181
- 6.11 C.P. Flynn, A.M. Stoneham: *Phys. Rev. B.* **1**, 3966 (1970)
- 6.12 Yu. Kagan, L.A. Maksimov: *Zh. Eksp. Teor. Fiz.* **70**, 255 (1973) [*Sov. Phys. JETP* **38**, 307 (1974)]
- 6.13 A. Seeger, H. Teichler: *La Diffusion dans les Milieux Condenses—Theories et Application, I* (INSTN, Saclay, France 1976) p. 217
- 6.14 D. Richter: In *Neutron Scattering and Muon Spin Rotation*, ed. by G. Hohler (Springer, Berlin, Heidelberg 1983) p. 85
- 6.15 C.W. Clawson, K.M. Crowe, S.E. Kohn, S.S. Rosenblum, C.Y. Huang, J.L. Smith: *Physica B* **109/110**, 2164 (1982)
- 6.16 R. Kadono, J. Imazato, K. Hishiyama, K. Nagamine, T. Yamazaki, D. Richter, J.-M. Welter: In *Muon Spin Rotation and Associated Problems I*, ed. by T. Yamazaki, K. Nagamine (J.C. Baltzer, Basel 1984) p. 109, *Hyperf. Interact.* **17-19**, 109 (1984)
- 6.17 K.M. Kehr, D. Richter, J.M. Welter, O. Hartmann, E. Karlsson, L.O. Norlin, T.O. Niinikoski, A. Yaouanc: *Phys. Rev. B* **26**, 567 (1982)
- 6.18 Y. Fukai: *Jpn. J. Appl. Phys.* **23**, L596 (1984)
- 6.19 Yu. Kagan, N.V. Prokof'ev: In *Quantum Tunneling in Condensed Media*, ed. by A.J. Leggett, Yu.M. Kagan (North-Holland, Amsterdam 1992) p. 37
- 6.20 V.G. Storchak, N.V. Prokof'ev: *Rev. Mod. Phys.* **70**, 929 (1998)

- 6.21 Y. Fukai, H. Sugimoto: Adv. in Phys. **34**, 263 (1985).
- 6.22 Y. Fukai, H. Sugimoto: In *Diffusion in Solids: Unsolved Problems*, ed. by G.E. Murch (Trans Tech, Zurich 1992) p. 87
- 6.23 J. Völkl, G. Alefeld: In *Hydrogen in Metals I*, ed. by G. Alefeld, J. Völkl, Topics Appl. Phys., Vol. 28 (Springer, Berlin, Heidelberg 1978) p. 321
- 6.24 J. Völkl, G. Alefeld: In *Diffusion in Solids*, ed. by A.S. Nowick, J.J. Burton (Academic, New York 1979) p. 231
- 6.25 H. Wipf: In *Hydrogen in Metals III*, ed. by H. Wipf, Topics Appl. Phys., Vol. 73 (Springer, Berlin, Heidelberg, 1997) p. 51
- 6.26 R.M. Cotts: Ber. Bunsenges. Phys. Chem. **76**, 760 (1972)
- 6.27 R.M. Cotts: In *Hydrogen in Metals I*, ed. by G. Alefeld, J. Völkl, Topics Appl. Phys., Vol. 28 (Springer, Berlin, Heidelberg, 1978) p. 227
- 6.28 R.M. Cotts: In *Electronic Structure and Properties of Hydrogen in Metals*, ed. by P. Jena, C.B. Satterthwaite (Plenum, New York 1983) p. 451
- 6.29 E.F.W. Seymour: J. Less-Common Met. **88**, 323 (1982)
- 6.30 R.G. Barnes: In *Hydrogen in Metals III*, ed. by H. Wipf, Topics Appl. Phys., Vol. 73 (Springer, Berlin, Heidelberg, 1997) p. 93
- 6.31 N. Bloembergen, E.M. Purcell, R.V. Pound: Phys. Rev. **73**, 679 (1948)
- 6.32 C. Korn, D. Zamir: J. Phys. Chem. Solids **31**, 489 (1970)
- 6.33 P.A. Fedders, O.F. Sankey: Phys. Rev. B **18**, 5938 (1978)
- 6.34 W.A. Barton, C.A. Sholl: J. Phys. C **13**, 2579 (1980)
- 6.35 T.K. Halstead, K. Metcalfe, T.C. Jones: J. Magn. Res. **47**, 292 (1982)
- 6.36 C.A. Sholl: J. Phys. C **14**, 447 (1981)
- 6.37 N. Salibi, R.M. Cotts: Phys. Rev. B **27**, 2625 (1983)
- 6.38 A. Seeger: In *Hydrogen in Metals I*, ed. by G. Alefeld, J. Völkl, Topics Appl. Phys. Vol. 28 (Springer, Berlin, Heidelberg, 1978) p. 349
- 6.39 A. Seeger: In *Muon Spin Rotation and Associated Problems I*, ed. by T. Yamazaki, K. Nagamine (J.C. Baltzer, Basel, 1984) p. 75; Hyperfine Interact. **17-19**, 75 (1984)
- 6.40 R. Kadono: In *Perspectives in Muon Science*, ed. by T. Yamazaki, K. Nagamine (North-Holland, Amsterdam 1992), p. 113
- 6.41 R. Kadono: Z. Phys. Chem. **181**, 195 (1993)
- 6.42 R. Kadono, R.F. Kiefl: Defect Diffusion Forum **95-98**, 279 (1993)
- 6.43 R. Kadono: In *Atom Tunneling Phenomena in Physics, Chemistry and Biology*, ed. by T. Miyazaki (Springer, Berlin, Heidelberg, 2004) p. 111
- 6.44 F.N. Gygax, W. Kundig, P.F. Meier (eds.): Hyperfine Interact. **6**, 1 (1979)
- 6.45 J.H. Brewer, P.W. Percival (eds.): Hyperfine Interact. **8**, 307 (1981)
- 6.46 T. Yamazaki, K. Nagamine (eds.): *Muon Spin Rotation and Associated Problems* (P.G. Baltzer, Basel 1984), Hyperfine Interact. **17-19**, 1 (1984)
- 6.47 O. Hartmann, E. Karlsson, B. Lindgren, R. Wäppling (eds.): *Muon Spin Rotation, Relaxation and Resonance* (J.C. Baltzer, Basel 1986), Hyperfine Interact. **31-32**, 3 (1986)
- 6.48 S.F.J. Cox, G.H. Eaton, D. Herlach, V.P. Koptev (eds.): Hyperfine Interact. **64**, 613 (1990)
- 6.49 J.H. Brewer, R.F. Kiefl, P.W. Percival (eds.): Hyperfine Interact. **85-87**, 3 (1994)
- 6.50 K. Nagamine, R.M. MacRae, R. Kadono, K. Nishiyama (eds.): Hyperfine Interact. **105**, 189 (1997)
- 6.51 E. Roduner, A. Schenck, G. Solt (eds.): Physica B **289/290** (2000)

- 6.52 R.H. Heffner, D.R. Noakes, P.W. Percival (eds.): *Physica B* **326**, No.1-4 (2004)
- 6.53 J. Chappert, R.I. Grynszpan (eds.): *Muons and Pions in Materials Research* (North-Holland, Amsterdam 1984)
- 6.54 A. Schenck: *Muon Spin Rotation* (Adam Hilger, Bristol 1986)
- 6.55 E.B. Karlsson: *Solid State Phenomena, As Seen by Muons, Protons and Excited Nuclei* (Clarendon Press, Oxford 1995)
- 6.56 A. Weidinger: *J. Less-Common Met.* **103**, 285 (1984)
- 6.57 A. Weidinger, R. Peichl: *Phys. Rev. Lett.* **54**, 1683 (1985)
- 6.58 R. Peichl, P. Ziegler, A. Weidinger: *J. Less-Common Met.* **129**, 243 (1987)
- 6.59 A. Weidinger: In *Hydrogen in Intermetallic Compounds II, The Perturbed Angular Correlation Method and Its Application to Hydrogen in Metals*, ed. by L. Schlappbach (Springer, Berlin, Heidelberg, 1992) p. 259
- 6.60 M.A. Krivoglaз, S.P. Repetskii: *Fiz. Tverd. Tela* **8**, 2908 (1966) [*Sov. Phys.-Solid State* **8**, 2325 (1967)]
- 6.61 A. Bläsius, R.S. Preston, U. Gonser: *Z. Phys. Chem.* **115**, 187 (1979)
- 6.62 R. Wordel, F.J. Litterst, F.E. Wagner: *J. Phys. F* **15**, 2525 (1985)
- 6.63 F. Pröbst, F.E. Wagner, M. Karger: *J. Phys. F.* **10**, 2081 (1980)
- 6.64 F.E. Wagner, F. Pröbst, R. Wordel, M. Zelger, F.J. Litterst: *J. Less-Common Met.* **103**, 135 (1984)
- 6.65 F.E. Wagner, R. Wordel, M. Zelger: *J. Phys. F* **14**, 535 (1984)
- 6.66 R. Wordel, F.E. Wagner: *J. Less-Common Met.* **101**, 427 (1984)
- 6.67 R. Wordel, F.E. Wagner: *J. Less-Common Met.* **129**, 271 (1987)
- 6.68 R. Wordel, F.E. Wagner: *Z. Phys. Chem.* **164**, 767 (1989)
- 6.69 M. Zelger, D.C. Monitto, H.J. Rinser, F.E. Wagner: *Z. Phys. Chem.* **164**, 779 (1989)
- 6.70 A. Heidemann, G. Kaindl, D. Salomon, H. Wipf, G. Wortmann: *Phys. Rev. Lett.* **36**, 213 (1976)
- 6.71 A. Heidemann, H. Wipf, G. Wortmann: *Hyperf. Interact.* **4**, 844 (1978)
- 6.72 R.H. Swendsen, K.W. Kehr: *Solid State Commun.* **18**, 541 (1976)
- 6.73 M. Koiwa, S. Ishioka: *Solid State Commun.* **35**, 729 (1980)
- 6.74 H. Wipf, A. Heidemann: *J. Phys. F* **13**, 5757 (1980)
- 6.75 C.T. Chudley, R.J. Elliott: *Proc. Roy. Soc.* **77**, 353 (1961)
- 6.76 J.M. Rowe, J.J. Rush, L.A. de Graaf, G.A. Ferguson: *Phys. Rev. Lett.* **29**, 1250 (1972)
- 6.77 R. Hempelmann, D. Richter, R. Pugliesi, L.A. Vinhaus: *J. Phys. F* **13**, 59 (1983)
- 6.78 S.K. Sinha, D.K. Ross: *Physica B* **149**, 61 (1988)
- 6.79 J.C. Cook, D. Richter, O. Schaerpf, B.J. Benham, D.K. Ross, R. Hempelmann, I.S. Anderson, S.K. Sinha: *J. Phys: Condens. Matter* **2**, 79 (1990)
- 6.80 J.M. Cowley: *J. Appl. Phys.* **21**, 24 (1950)
- 6.81 P.G. de Gennes: *Physica* **25**, 825 (1959)
- 6.82 H. Züchner: *Hydrogen in Metals* (Japan Institute of Metals, Sendai 1980): *Trans. JIM (Suppl.)* **21**, 101 (1980)
- 6.83 R. Kirchheim, R.B. McLellan: *J. Electrochem. Soc.* **127**, 2419 (1980)
- 6.84 K. Watanabe, Y. Fukai: *J. Phys. F* **10**, 1795 (1980)
- 6.85 J. Bass: *Adv. Phys.* **21**, 431 (1972)
- 6.86 R. Hanada, T. Suganuma, H. Kimura: *Scripta Met.* **6**, 483 (1972)
- 6.87 J. Völkl: *Ber. Bunsenges. Phys. Chem.* **76**, 797 (1972)

- 6.88 H. Wipf, B. Kappesser: J. Phys. Condens Matter **8**, 7233 (1996)
- 6.89 B.S. Berry, W.C. Pritchett: In *Nontraditional Methods in Diffusion*, ed. by G.E. Murch, H.K. Birnbaum, J.R. Cost (The Metallurgical Society of AIME, New York 1984) p. 83
- 6.90 R. de Batist: *Internal Friction of Structural Defects in Crystalline Solids* (North-Holland, Amsterdam 1972)
- 6.91 H. Kronmüller: In *Hydrogen in Metals I*, ed. by G. Alefeld, J. Völkl, Topics Appl. Phys., Vol. 28 (Springer, Berlin, Heidelberg 1978) p. 291
- 6.92 B. Hohler, H. Kronmüller: Phil. Mag. A **45**, 607 (1982)
- 6.93 M. Nagano, Y. Hayashi, N. Ohtani, M. Isshiki, K. Igaki: Scripta Met., **16**, 973 (1982)
- 6.94 M. Nagano, Y. Hayashi, N. Ohtani, M. Isshiki, K. Igaki: Trans. JIM **22**, 423 (1981)
- 6.95 Zh. Qi, J. Völkl, R. Lässer, H. Wenzl: J. Phys. F **13**, 2053 (1983)
- 6.96 T. Eguchi, S. Morozumi: Nippon Kinzokugakkaishi **41**, 795 (1977) (in Japanese)
- 6.97 V. Lottner, A. Heim, T. Springer: Z. Phys. B **32**, 157 (1979)
- 6.98 D.J. Pine, R.M. Cotts: Phys. Rev. B **28**, 641 (1983)
- 6.99 L. Katz, M. Guinan, R.J. Borg: Phys. Rev. B **4**, 330 (1971)
- 6.100 W. Eichenauer, W. Loser, H. Witte: Z. Metallk. **56**, 2S7 (1965)
- 6.101 G. Perkins, D.R. Begeal: Ber. Bunsenges. Phys. Chem. **76**, 863 (1972)
- 6.102 K. Yamakawa: J. Phys. Soc. Jpn. **47**, 114 (1979)
- 6.103 V.A. Gol'tsov, V.B. Demin, V.B. Vykhodets, G.Ye. Kagan, P.V. Gel'd: *Proc. Congrès L'Hydrogène dans les Métaux* (Editions Science et Industrie, Paris 1972) p. 249
- 6.104 J. Völkl, G. Wollenweber, K.H. Klatt, G. Alefeld: Z. Naturforsch. (a) **26**, 922 (1971)
- 6.105 G. Sicking, M. Glugla, B. Huber: Ber. Bunsenges. Phys. Chem. **87**, 418 (1983)
- 6.106 R.R. Arons, H.G. Bohn, H. Lütgemeier: Solid State Commun. **14**, 1203 (1974)
- 6.107 J. Völkl, H.C. Bauer, U. Freudenberg, K. Kokkinidis, G. Lang, K.A. Steinhäuser, G. Alefeld: In *Internal Friction and Ultrasonic Attenuation in Solids*, ed. by R.R. Hasiguti, N. Mikoshiba (University of Tokyo Press, Tokyo 1977) p. 485
- 6.108 R. Kadono, J. Imazato, T. Matsuzaki, K. Nishiyama, K. Nagamine, T. Yamazaki, D. Richter, J.M. Welter: Phys. Rev. B **39**, 23 (1989)
- 6.109 G.M. Luke, J.H. Brewer, S.R. Kreitzman, D.R. Noakes, M. Celio, R. Kadono, E.J. Ansaldo: Hyperf. Interact. **64**, 721 (1990)
- 6.110 G.M. Luke, J.H. Brewer, S.R. Kreitzman, D.R. Noakes, M. Celio, R. Kadono, E.J. Ansaldo: Phys. Rev. B **43**, 3284 (1991)
- 6.111 O. Hartmann, E. Karlsson, E. Wackelgard, R. Wäppling, D. Richter, R. Hempelmann, T.G. Niinikoski: Phys. Rev. B **37**, 4425 (1988)
- 6.112 R. Kadono, R.F. Kiefl, E.J. Ansaldo, J.H. Brewer, M. Celio, S.R. Kreitzman, G.M. Luke: Phys. Rev. Lett. **64**, 665 (1990)
- 6.113 R.F. Kiefl, R. Kadono, J.H. Brewer, G.M. Luke, H.K. Yen, M. Celio, E.J. Ansaldo: Phys. Rev. Lett. **62**, 792 (1989)
- 6.114 W.A. MacFarlane, R.F. Kiefl, J.W. Schneider, K.H. Chow, G.P. Morris, T.L. Estle, B. Hitti: Hyperf. Interact. **85**, 23 (1994)

- 6.115 R. Kadono, R.F. Kiefl, J.H. Brewer, G.M. Luke, T. Pfiz, T.M. Riseman, B.J. Sternlieb: *Hyperf. Interact.* **64**, 635 (1990)
- 6.116 R. Hanada: In *Hydrogen in Metals* (Pergamon, Oxford 1978), Paper 1B7.
- 6.117 R. Hanada: *Scripta Met.* **11**, 843 (1977)
- 6.118 R. Hanada: In *Hydrogen in Metals* (Japan Institute of Metals, Sendai 1980); *Trans. JIM (Suppl.)* **21**, 185 (1980)
- 6.119 T. Ezawa, K. Yamakawa, F.E. Fujita: In *Hydrogen in Metals* (Japan Institute of Metals, Sendai 1980); *Trans. JIM (Suppl.)* **21**, 189 (1980)
- 6.120 R. Hanada: In *Hydrogen in Metals* (Pergamon, Oxford 1978) Paper 1B6.
- 6.121 W. Staiger, R. Blocher, D. Plachke, H.D. Carstanjen: *Z. Phys. Chem.* **164**, 991 (1989)
- 6.122 M. Blanz, R. Blocher, D. Plachke, R. Messer, H.D. Carstanjen, A. Seeger: *Z. Phys. Chem.* **164**, 985 (1989)
- 6.123 F. Abe, R. Hanada, H. Kimura: *Scripta Met.* **8**, 955 (1974)
- 6.124 J. Engelhard: *J. Phys. F* **9**, 2217 (1979)
- 6.125 P.P. Davies, E.F. Seymour, D. Zamir, W.D. Williams, R.M. Cottis: *J. Less-Common Met.* **49** (1976) 159
- 6.126 O.F. Sankey, P.A. Fedders: *Phys. Rev. B* **20**, 39 (1979)
- 6.127 A.H. Verbruggen, R. Griessen, J.H. Rector: *Phys. Rev. Lett.* **52**, 1625 (1984)
- 6.128 G. Higelin, H. Kronmüller, R. Lässer: *Phys. Rev. Lett.* **53**, 2117 (1984)
- 6.129 R. Lässer: *Tritium and Helium-3 in Metals* (Springer, Berlin, Heidelberg 1989)
- 6.130 F.M. Mazzolai, H. Züchner: *Z. Phys. Chem.* **124**, 59 (1981), and references cited therein.
- 6.131 B. Coluzzi, B. Sobha, A. Biscarini, F.M. Mazzolai, R.A. McNicholl: *Solid State Commun.* **83**, 643 (1992)
- 6.132 U. Kaess, G. Majer, M. Stoll, D.T. Peterson, R.G. Barnes: *J. Alloys Comp.* **259**, 74 (1997)
- 6.133 C. Korn, S.D. Goren: *Phys. Rev. B* **33**, 68 (1986)
- 6.134 G. Majer, A. Seeger, R.G. Barnes: *Z. Phys. Chem.* **181**, 187 (1993)
- 6.135 G. Majer, W. Renz, R.G. Barnes: *J. Phys. Condens Matter* **6**, 2935 (1994)
- 6.136 J. Gottwald, G. Majer, D.T. Peterson, R.G. Barnes: *J. Alloys Comp.* **365-367**, 274 (2003)
- 6.137 G. Majer, J. Gottwald, D.T. Peterson, R.G. Barnes: *J. Alloys Comp.* **330-332**, 438 (2002)
- 6.138 G. Majer, U. Kaess, R.G. Barnes: *Phys. Rev. Lett.* **83**, 340 (1999)
- 6.139 U. Stuhr, D. Steinbinder, H. Wipf, B. Frick: *Europhys. Lett.* **20**, 117 (1992)
- 6.140 H. Wipf, B. Kappesser, R. Werner: *J. Alloys Comp.* **310**, 190 (2000)
- 6.141 L.D. Bustard, R.M. Cottis, E.F.W. Seymour: *Phys. Rev. B* **22**, 12 (1980)
- 6.142 M.H. Dickens, W. Hayes, P. Schnabel, M.T. Hutchings, R.E. Lechner, B. Renker: *J. Phys. C* **16**, L1 (1983)
- 6.143 M.T. Hutchings, K. Clausen, M.H. Dickens, W. Hayes, J.K. Kjems, P.G. Schnabel, C. Smith: *J. Phys. C* **17**, 3903 (1984)
- 6.144 R. Backmann, H. Schulz: *Solid State Ionics* **9/10**, 921 (1983)
- 6.145 R.C. Bowman, Jr., B.D. Craft: *J. Phys. C* **17**, L477 (1984)
- 6.146 U. Stuhr, D. Steinbinder, H. Wipf, B. Frick: *Z. Phys. Chem.* **181**, 89 (1993)
- 6.147 B. Nowak, O.J. Žogal, R.G. Barnes: *MH2004 Conf. Abstr.* (ISBN 83-921064-0-7), (2004), p. 164
- 6.148 V. Lottner, J.W. Haus, A. Heim, K.W. Kehr: *J. Phys. Chem. Solids* **40**, 557 (1979)

- 6.149 O.F. Sankey, P.A. Fedders: Phys. Rev. B **22**, 5135 (1980)
- 6.150 J.E. Kleiner, E.H. Sevilla, K.B. Cotts: Phys. Rev. B **33**, 6662 (1986)
- 6.151 L.R. Lichty, J-W. Han, R. Ibanes-Meier, D.R. Torgeson, R.G. Barnes, E.F.W. Seymour, C.A. Sholl: Phys. Rev. B **39**, 2012 (1989)
- 6.152 F.N. Gyax, G. Solt, A. Amato, I.S. Anderson, M. Pinkpank, A. Schenck, T.J. Udovic: Phys. Rev. B **61**, 168 (2000)
- 6.153 A.V. Skripov, A.V. Soloninin, D.S. Sibirtsev, A.L. Buzlukov, A.P. Stepanov, J.J. Balbach, M.S. Conradi, R.G. Barnes, R. Hempelmann: Phys. Rev. B **66**, 054306 (2002)
- 6.154 B. Kappesser, H. Wipf, R.G. Barnes, B.J. Beaudry: J. Alloys. Comp. **253-254**, 386 (1997)
- 6.155 I.S. Anderson, D.K. Ross, J.E. Bonnet: Z. Phys. Chem. **164**, 923 (1989)
- 6.156 K. Nakazato, K. Kitahara: Prog. Theor. Phys. **64**, 2261 (1980)
- 6.157 K.W. Kehr, R. Kutner, K. Binder: Phys. Rev. B **23**, 4931 (1981)
- 6.158 R.A. Tahir-Kheli, R.J. Elliott: Phys. Rev. B **27**, 844 (1983)
- 6.159 A.H. Verbruggen, C.W. Hagen, R. Griessen: J. Phys. F **11**, 1431 (1984)
- 6.160 U. Stuhr, H. Wipf, B. Frick: J. Less-Common Met. **172-174**, 678 (1991)
- 6.161 M. Hein, A. Bals, A.F. Privalov, H. Wipf: J. Alloys Comp. **356-357**, 318 (2003)
- 6.162 H.C. Bauer, J. Völkl, J. Tretkowski, G. Alefeld: Z. Phys. B **29**, 17 (1978)
- 6.163 P.E. Mauger, W.D. Williams, R.M. Cotts: J. Phys. Chem. Solids **42**, 821 (1981)
- 6.164 U. Potzel, R. Raab, J. Völkl, H. Wipf, A. Magerl, D. Salomon, G. Wortmann: J. Less-Common Met. **101**, 343 (1984)
- 6.165 R. Hempelmann, D. Richter, D.A. Faux, D.K. Ross: Z. Phys. Chem. **159**, 175 (1988)
- 6.166 G. Alefeld, G. Schaumann, J. Tretkowski, J. Völkl: Phys. Rev. Lett. **22**, 697 (1969)
- 6.167 H. Buck, G. Alefeld: Phys. Stat. Sol. (b) **49**, 317 (1972)
- 6.168 Y. de Ribaupierre, F.D. Manchester: J. Phys. C: Solid State Phys. **7**, 2126 (1974)
- 6.169 H. Wipf, J. Völkl, G. Alefeld: Z. Phys. B **76**, 353 (1989)
- 6.170 A. Bauberger, H. Wipf: Phys. Status Solidi (a) **89**, 129 (1985)
- 6.171 H. Conrad, G. Bauer, G. Alefeld, T. Springer, W. Schmatz: Z. Phys. **266**, 239 (1974)
- 6.172 Y. Fukai, K. Kubo, S. Kazama: Z. Phys. Chem. **115**, 181 (1979)
- 6.173 S. Kazama, Y. Fukai: In *Hydrogen in Metals* (Japan Institute of Metals, Sendai 1980); Trans. JIM (Suppl.) **21**, 173 (1980)
- 6.174 D. Richter, R. Hempelmann, K.W. Kehr, O. Hartmann, E. Karlsson, L.O. Nolin, S.F.J. Cox: Hyperf. Interact. **17-19**, 261 (1984)
- 6.175 H. Sugimoto, Y. Fukai: In *Hydrogen in Metals* (Japan Institute of Metals, Sendai 1980); Trans. JIM. (Suppl.) **21**, 177 (1980)
- 6.176 R. Kutner, K.W. Kehr: Phil. Mag. A **48**, 199 (1983)
- 6.177 R.G. Barnes, F. Borsa, M. Jerosch-Herold, J.-W. Han, M. Belhoul, J. Shinar, D.R. Torgeson, D.T. Peterson, G.A. Styles, E.F.W. Seymour: J. Less-Common Met. **129**, 279 (1987)
- 6.178 R.G. Barnes, M. Jerosch-Herold, J. Shinar, F. Borsa, D.R. Torgeson, D.T. Peterson, A.J. Lucas, G.A. Styles, E.F.W. Seymour: Phys. Rev. B **35**, 890 (1987)

- 6.179 R.G. Barnes: Z. Phys. Chem. **164**, 841 (1989)
- 6.180 J.-W. Han, L.R. Lichty, D.R. Torgeson, E.F.W. Seymour, R.G. Barnes, J.L. Billeter, R.M. Cotts: Phys. Rev. B **40**, 9025 (1989)
- 6.181 H. Dosch, F. Schmid, P. Wiethoff, J. Peisl: Phys. Rev. B **46**, 55 (1992)
- 6.182 D. Richter, S. Mahling-Ennaoui, R. Hempelmann: Z. Phys. Chem. **164**, 907 (1989)
- 6.183 D. Richter, T. Springer: Phys. Rev. B **18**, 126 (1978)
- 6.184 D. Steinbinder, H. Wipf, A. Magerl, D. Richter, A.J. Dianoux, K. Neumaier: Europhys. Lett. **6**, 535 (1988)
- 6.185 T. Imai, A. Kayanuma, Y. Fukai, S. Masubuchi: J. Phys.: Condens. Matter **16**, 8191 (2004)
- 6.186 D. Richter, R. Hempelmann, R.C. Bowman: In *Hydrogen in Intermetallic Compounds II*, ed. by L. Schlapbach (Springer, Berlin, Heidelberg 1992) p. 97
- 6.187 R.C. Bowman, B.D. Craft, A. Attalla, J.R. Johnson: Int. J. Hydrogen Energy **8**, 801 (1983)
- 6.188 R. Hempelmann, D. Richter, A. Heidemann: J. Less-Common Met. **88**, 343 (1982)
- 6.189 W. Renz, G. Majer, A.V. Skripov, A. Seeger: J. Phys. Condens. Matter **6**, 6367 (1994)
- 6.190 D.A. Faux, D.K. Ross, C.A. Sholl: J. Phys. C, Solid State Phys. **19**, 415 (1986)
- 6.191 C. Schönfeld, R. Schätzler, R. Hempelmann: Ber. Bunsenges. Phys. Chem. **93**, 1326 (1989)
- 6.192 R.L. Haville, J.M. Titman, M.S. Wright, M.A. Crouch: Z. Phys. Chem. **164**, 1083 (1989)
- 6.193 S.I. Campbell, M. Kemali, D.K. Ross, D.J. Bull, J.F. Fernandez, M.R. Johnson: J. Alloys Comp. **293-295**, 351 (1999)
- 6.194 A.V. Skripov, J.C. Cook, T.J. Udovic, M.A. Gonzalez, R. Hempelmann, V.N. Kozhanov: J. Phys. Condens. Matter **15**, 3555 (2003)
- 6.195 A.V. Skripov, S.V. Rychkova, M.Yu Belyaev, A.P. Stepanov: J. Phys. Condens. Matter **2**, 7195 (1990)
- 6.196 K. Foster, R.G. Leisure, A.V. Skripov: Phys. Rev. B **64**, 214302 (2001)
- 6.197 A.V. Skripov, J.C. Cook, C. Karmonik, R. Hempelmann: J. Phys. Condens. Matter **8**, L319 (1996)
- 6.198 A.V. Skripov, J.C. Cook, C. Karmonik, R. Hempelmann: J. Alloys Comp. **253-254**, 432 (1997)
- 6.199 P. Fischer, F. Fauth, A.V. Skripov, A.A. Podlesnyak, L.N. Padurets, A.L. Shilov, B. Ouladdiaf: J. Alloys Comp. **253-254**, 282 (1997)
- 6.200 A.V. Skripov: Defect Diffusion Forum **224-225**, 75 (2003)
- 6.201 C. Schönfeld, R. Hempelmann, D. Richter, T. Springer, A.J. Dianoux, J.J. Rush, T.J. Udovic, S.M. Bennington: Phys. Rev. B **50**, 853 (1994)
- 6.202 A. Schenck, N.K. Sato, G. Solt, D. Andreica, F.N. Gygax, M. Pinkpank, A. Amato: Euro. Phys. J. B **13**, 245 (2000)
- 6.203 A. Amato, D. Andreica, F.N. Gygax, M. Pinkpank, N. K. Sato, A. Schenck, G. Solt: Physica B **289-290**, 447 (2000)
- 6.204 A.M. Mulders, P.C.M. Gubbens, C.T. Kaiser, A. Amato, F.N. Gygax, A. Schenck, P. Dalmas de Réotier, A. Yaouanc, K.H.J. Buschow, F. Kayzel, A.A. Menovsky: J. Alloys Comp. **330-332**, 454 (2002)

- 6.205 R. Kirchheim, F. Sommer, G. Schluckebier: *Acta Metall.* **30**, 1059 (1982)
- 6.206 R. Kirchheim: *J. Non-Crystalline Solids* **55**, 243 (1983)
- 6.207 R. Kirchheim, U. Stoltz: *J. Non-Crystalline Solids* **70**, 323 (1985)
- 6.208 R. Kirchheim, U. Stoltz: *Acta Metall.* **35**, 281 (1987)
- 6.209 P.M. Richards, J. Shinar: *J. Phys. F* **17**, 1659 (1987)
- 6.210 R.B. McLellan, M. Yoshihara: *J. Phys. Chem. Solids* **48**, 661 (1987)
- 6.211 R.C. Brouwer, E. Salomons, R. Griessen: *Phys. Rev. B* **38**, 10217 (1988)
- 6.212 T. Regelman, L. Schimmele: *J. Alloys Comp.* **231**, 208 (1995)
- 6.213 R. Kadono, W. Higemoto, K. Nagamine, F.L. Pratt: *Phys. Rev. Lett.* **83**, 987 (1999)
- 6.214 R. Kadono, W. Higemoto, K. Nagamine, F.L. Pratt: *Physica B* **289–290**, 459 (2000)
- 6.215 S. Fujii: *J. Phys. Soc. Jpn* **46**, 1833 (1979)
- 6.216 H. Sugimoto: *J. Phys. Soc. Jpn.* **55**, 1687 (1986)
- 6.217 H. Sugimoto: *J. Phys. Soc. Jpn.* **57**, 991 (1988)
- 6.218 H. Teichler, A. Seeger: *Phys. Lett. A* **82**, 91 (1981)
- 6.219 E. Gorham-Bergeron: *Phys. Rev. Lett.* **37**, 146 (1976)
- 6.220 H. Teichler: *Z. Phys. Chem.* **114**, 155 (1981)
- 6.221 H. Teichler: *Phys. Status Solidi (b)* **104**, 293 (1981)
- 6.222 D. Emin, M.I. Baskes, W.D. Wilson: *Phys. Rev. Lett.* **42**, 791 (1979)
- 6.223 P. Morse, E.C.G. Stuckelberg: *Ann. der Physik* **9**, 579 (1931)
- 6.224 L.R. Landau: *Z. Phys. Sowjet.* **1**, 88 (1932)
- 6.225 L.R. Landau: *Z. Phys. Sowjet.* **2**, 46 (1932)
- 6.226 C. Zener: *Proc. Roy. Soc. A* **137**, 696 (1932)
- 6.227 C. Zener: *Proc. Roy. Soc. A* **140**, 660 (1933)
- 6.228 P. Hedegård: *Phys. Rev. B* **35**, 6127 (1987)
- 6.229 A.O. Caldeira, A.J. Legett: *Ann. Phys. (NY)* **149**, 374 (1983)
- 6.230 H. Grabert, U. Weiss, P. Hanggi: *Phys. Rev. Lett.* **52**, 2193 (1984)
- 6.231 U. Weiss, H. Grabert: *Phys. Lett. A* **108**, 63 (1985)
- 6.232 M.P.A. Fischer, W. Zwerger: *Phys. Rev. B* **32**, 6190 (1985)
- 6.233 P. Hedegård, A.O. Caldeira: *Phys. Rev. B* **35**, 106 (1987)
- 6.234 P. Hedegård: *Phys. Rev. B* **35**, 533 (1987)
- 6.235 M.J. Gillan: *J. Phys. C* **20**, 3621 (1987)
- 6.236 M.J. Gillan: *J. Less-Common Met.* **172–174**, 529 (1991)
- 6.237 O. Hartmann, E. Karlsson, S. Harris, R. Wäppling, T.O. Niinikoski: *Phys. Lett. A* **142**, 504 (1989)
- 6.238 R. Kadono, R.F. Kiefl, S.R. Kreitzmann, Q. Li, T. Pfiz, T.M. Riseman, H. Zhou, R. Wäppling, S.W. Harris, O. Hartmann, E. Karlsson, R. Hempelmann, D. Richter, T.O. Niinikoski, L.P. Lee, G.M. Luke, B. Steinlieb, E.J. Ansaldo: *Hyperf. Interact.* **64**, 737 (1990)
- 6.239 E. Karlsson, R. Wäppling, S.W. Lidström, O. Hartmann, R. Kadono, R.F. Kiefl, R. Hempelmann, D. Richter: *Phys. Rev. B* **52**, 6417 (1995)
- 6.240 R. Kadono, R.F. Kiefl, J.A. Chakhalian, S.R. Dunsiger, B. Hitti, W.A. MacFarlane, J. Major, L. Schimmele, M. Matsumato, Y. Ohashi: *Phys. Rev. Lett.* **83**, 987 (1997)
- 6.241 R. Kadono: In *Atom Tunneling Phenomena in Physics, Chemistry and Biology*, ed. By T. Miyazaki (Springer, Berlin, Heidelberg 2004), p. 111
- 6.242 J. Kondo: Private communication
- 6.243 H. Teichler: *Z. Phys. Chem.* **164**, 747 (1989)

- 6.244 H.R. Schober, A.M. Stoneham: Phys. Rev. Lett. **60**, 2307 (1988)
- 6.245 K. Hiraoka, N. Ohashi, Y. Kihara, K. Yamamoto, T. Sato, A. Yamashita: Chem. Phys. Lett. **229**, 408 (1994)
- 6.246 K. Hiraoka, A. Yamashita, Y. Yachi, K. Aruga, T. Sato,: Astrophys. J. **443**, 363 (1995)
- 6.247 K. Hiraoka, T. Miyagoshi, T. Takayama, K. Yamamoto, Y. Kihara: Astrophys. J. **498**, 710 (1998)
- 6.248 K. Hiraoka: J. Mass Spectrom. Soc. Jpn: **47**, 84 (1999)
- 6.249 A.Ya. Katunin, I.I. Lukashevich, S.T. Orozmamatov, V.V. Sklyarevskii, V.V. Suraev, V.V. Filippov, V.A. Shevtsov: Pis'ma Zh. Eksp. Teor. Fiz. **34**, 375 (1981) [JETP Lett. **34**, 357 (1981)]
- 6.250 T. Miyazaki: Radiat. Phys. Chem. **37**, 635 (1991)
- 6.251 T. Kumada, K. Komaguchi, Y. Aratono, T. Miyazaki: Chem. Phys. Lett. **261**, 463 (1996)
- 6.252 T. Kumada, N. Kitagawa, S. Mori, J. Kumagai, Y. Aratono, T. Miyazaki: J. Low Temp. Phys. **114**, 413 (1999)
- 6.253 T. Miyazaki (ed.): *Atom Tunneling Phenomena in Physics, Chemistry and Biology* (Springer, Berlin, Heidelberg 2004)
- 6.254 Yu. Kagan, N.V. Prokof'ev: Phys. Lett. A **150**, 320 (1990)
- 6.255 J. Kondo: J. Phys. Soc. Jpn. **68**, 3315 (1999)

Chapter 7

- 7.1 A.C. Switendick: In *Hydrogen in Metals I*, ed. by G. Alefeld, J. Völkl, Topics Appl. Phys., Vol. 28 (Springer, Berlin, Heidelberg 1978) p. 101
- 7.2 M. Gupta, B. Schlapbach: In *Hydrogen in Intermetallic Compounds I*, ed. by B. Schlapbach, Topics Appl. Phys., Vol. 63 (Springer, Berlin, Heidelberg 1988) p. 139
- 7.3 Y. Fukai, S. Kazama, K. Tanaka, M. Matsumoto: Solid State Commun. **30**, 173 (1979)
- 7.4 D.A. Papaconstantopoulos, B.M. Klein, E.N. Economou, L.L. Boyer: Phys. Rev. B **17**, 141 (1978)
- 7.5 D.A. Papaconstantopoulos: In *Metal Hydrides*, ed. by G. Bambakidis (Plenum, New York 1981) p. 215
- 7.6 J. Kanamori: In *Hydrogen in Metals* (Japan Institute of Metals, Sendai 1980); Trans. JIM. (Suppl.) **21**, 33 (1980)
- 7.7 K. Terakura, H. Akai, M. Akai, J. Kanamori: In *Electronic Structure and Properties of Hydrogen in Metals*, ed. by P. Jena, C.B. Satterthwaite (Plenum, New York 1983) p. 413
- 7.8 J. Kanamori, H. Akai, M. Akai: In *Muon Spin Rotation and Associated Problems I*, ed. by T. Yamazaki, K. Nagamine (J.C. Baltzer, Basel 1984); Hyperf. Interact. 17-19, 287 (1984)
- 7.9 M. Akai, H. Akai, J. Kanamori: J. Phys. Soc. Jpn. **56**, 1064 (1987)
- 7.10 R. Podloucky, R. Zeller, P.H. Dederichs: Phys. Rev. B **22**, 5777 (1980)
- 7.11 M. Yussouff, R. Zeller: In *Recent Developments in Condensed Matter Physics*, Vol. 3, ed. by J.T. Devreese, L.F. Lemmens, V.E. Van Doren (Plenum, New York 1981) p. 135
- 7.12 P.J. Braspenning, R. Zeller, A. Lodder, P.H. Dederichs: Phys. Rev. B **29**, 703 (1984)

- 7.13 K. Terakura: *J. Phys. F* **7**, 1773 (1977)
- 7.14 S. Elliatioglu, H. Akai, R. Zeller, P.H. Dederichs: *Proc. 15th Annual Int'l Symp. on Electronic Structure of Metals and Alloys* (Gaussig, DDR, 1985), ed. by P. Ziesche (Dresden University, Dresden 1985) p. 99
- 7.15 C.D. Gelatt, Jr., H. Ehrenreich, J.A. Weiss: *Phys. Rev. B* **17**, 1940 (1978)
- 7.16 M.J. Stott, E. Zaremba: *Phys. Rev. B* **22**, 1564 (1980)
- 7.17 J.K. Nørskov, N.D. Lang: *Phys. Rev. B* **21**, 2136 (1980)
- 7.18 M.J. Puska, R.M. Nieminen, M. Manninen: *Phys. Rev. B* **24**, 3037 (1981)
- 7.19 J.K. Nørskov: *Phys. Rev. B* **26**, 2875 (1982)
- 7.20 J.K. Nørskov: *Phys. Rev. Lett.* **48**, 1620 (1982)
- 7.21 M. Akai, H. Akai, J. Kanamori: *J. Mag. Mag. Mater.* **31-34**, 551 (1983)
- 7.22 A.R. Williams, C.D. Gelatt, Jr., J.F. Janak: In *Theory of Alloy Phase Formation*, ed. by D.H. Bennett (The Metallurgical Soc. of AIME, New York 1979) p. 40
- 7.23 B. Stalinski: *Bull. Acad. Pol. Sci. Class III* **5**, 1001 (1957)
- 7.24 J.N. Huiberts, R. Griessen, J.H. Rector, R.J. Wijngaarden, J.P. Dekker, D.G. de Groot, N.J. Koeman: *Nature* **380**, 231 (1996)
- 7.25 J.N. Huiberts, J.H. Rector, R.J. Wijngaarden, S. Jetten, D. de Groot, B. Dam, N.J. Koeman, R. Griessen, B. Hjörvarsson, S. Olafson, Y.S. Cho: *J. Alloys Comp.* **239**, 158 (1996)
- 7.26 J.N. Huiberts, R. Griessen, R.J. Wijngaarden, M. Kremers, C. van Haesendonck: *Phys. Rev. Lett.* **79**, 3724 (1997)
- 7.27 E.S. Kooij, A.T.M. van Gogh, R. Griessen: *J. Electrochem. Soc.* **146**, 2990 (1999)
- 7.28 R.J. Wijngaarden, J.N. Huiberts, D. Nagengast, J.H. Rector, R. Griessen, M. Hanfland, F. Zontone: *J. Alloys Comp.* **308**, 44 (2000)
- 7.29 A.T.M. van Gogh, E.S. Kooij, R. Griessen: *Phys. Rev. Lett.* **83**, 4614 (1999)
- 7.30 A.T.M. van Gogh, D.G. Nagengast, E.S. Kooij, N.J. Koeman, J.H. Rector, R. Griessen, C.F.J. Flipse, R.J.J.G.A.M. Smeets: *Phys. Rev. B* **63**, 195105 (2001)
- 7.31 A.F.Th. Hoekstra, A.S. Roy, T.F. Rosenbaum, R. Griessen, R. Wijngaarden, N.J. Koeman: *Phys. Rev. Lett.* **86**, 5349 (2001)
- 7.32 A.F.Th. Hoekstra, T.F. Rosenbaum, A.S. Roy: *Rev. Sci. Instrum.* **73**, 119 (2002)
- 7.33 R. Griessen, J.N. Huiberts, M. Kremers, A.T.M. van Gogh, N.J. Koeman, J.P. Dekker, P.H.L. Notten: *J. Alloys Comp.* **253-254**, 44 (1997)
- 7.34 M. Kremers, N.J. Koeman, R. Griessen, P.H.L. Notten, R. Tolboom, P.J. Kelly, P.A. Duine: *Phys. Rev. B* **57**, 4943 (1998)
- 7.35 J.W.J. Kerssemakers, S.J. van der Molen, N.J. Koeman, R. Günther, R. Griessen: *J. Alloys Comp.* **330-332**, 342 (2001)
- 7.36 S.J. van der Molen, M.S. Welling, R. Griessen: *Phys. Rev. Lett.* **85**, 3882 (2000)
- 7.37 F.J. den Broeder, S.J. van der Molen, M. Kremers, J.N. Huiberts, D.G. Nagengast, A.T.M. van Gogh, W.H. Huisman, N.J. Koeman, B. Dam, J.H. Rector, S. Plota, M. Haaksma, R.M.N. Hanzen, R.M. Jungblut, P.A. Duine, R. Griessen: *Nature* **394**, 656 (1998)
- 7.38 S.J. van der Molen, M.S. Welling, R. Griessen: *J. Alloys Comp.* **330-332**, 426 (2001)
- 7.39 S.J. van der Molen, W.H. Huisman, R. Griessen: *J. Alloys Comp.* **330-332**, 430 (2001)

- 7.40 A. Remhof, S.J. van der Molen, A. Antosik, A. Dobrowolska, N.J. Koeman, R. Griessen: Phys. Rev. B **66**, 020101 (2002)
- 7.41 A. Remhof, R. Wijngaarden, R. Griessen: Phys. Rev. Lett. **90**, 145502 (2003)
- 7.42 A. Remhof, J.L.M. van Mechelen, N.J. Koeman, J.H. Rector, R. Wijngaarden, R. Griessen: Rev. Sci. Instrum. **74**, 445 (2003)
- 7.43 I.A.M.E. Giebels, S.J. van der Molen, R. Griessen, M. Di Vece: Appl. Phys. Lett. **80**, 1343 (2002)
- 7.44 J. Isidorsson, I.A.M.E. Giebels, M. Di Vece, R. Griessen: SPIE (2002), in press
- 7.45 A. Fujimori, F. Minami, N. Tsuda: Phys. Rev. B **22**, 3573 (1980)
- 7.46 D.K. Misemer, B.N. Harmon: Phys. Rev. B **26**, 5634 (1982)
- 7.47 J.P. Dekker, J. van Ek, A. Lodder, J.N. Huiberts: J. Phys.: Condens. Matter **5**, 4805 (1993)
- 7.48 Y. Wang, M.Y. Chou: Phys. Rev. Lett. **71**, 1226 (1993)
- 7.49 P.J. Kelly, J.P. Dekker, R. Stumpf: Phys. Rev. Lett. **78**, 1315 (1997)
- 7.50 P. van Gelderen, P.J. Kelly, G. Brocks: Phys. Rev. B **63**, 100301 (2001)
- 7.51 R. Eder, H.F. Pen, G.A. Sawatzky: Phys. Rev. B **56**, 10115 (1997)
- 7.52 D.A. McQuarrie, P.A. Rock: *General Chemistry* (Freeman, New York, 1984)
- 7.53 T. Miyake, F. Aryasetiawan, H. Kino, K. Terakura: Phys. Rev. B **61**, 16491 (2000)
- 7.54 P. van Gelderen, P.A. Bobbert, P.J. Kelly, G. Brocks: Phys. Rev. Lett. **85**, 2989 (2000)
- 7.55 P. van Gelderen, P.A. Bobbert, P.J. Kelly, G. Brocks, R. Tolboom: Phys. Rev. B **66**, 075104 (2002)
- 7.56 W. Wolf, P. Herzig: Phys. Rev. B **66**, 224112 (2002)
- 7.57 W. Wolf, P. Herzig: J. Alloys Comp. **356-357**, 73 (2003)
- 7.58 R. Griessen: Europhysics News **32**, 41 (2001)
- 7.59 Z. Wu, R.E. Cohen, D.J. Singh, R. Gupta, M. Gupta: Phys. Rev. B **69**, 085104 (2004)
- 7.60 P. Vajda: J. Alloys. Comp. **231**, 170 (1995)
- 7.61 E. Wigner, H.B. Huntington: J. Chem. Phys. **3**, 764 (1935)
- 7.62 M. Hanfland, R.J. Hemley, H.K. Mao: Phys. Rev. Lett. **70**, 3760 (1993)
- 7.63 K. Inoue, H. Kanzaki, S. Suga: Solid State Commun. **30**, 627 (1979)
- 7.64 J. van Straaten, I.F. Silvera: Phys. Rev. B **37**, 6478 (1988)
- 7.65 R.J. Hemley, M. Hanfland, H.K. Mao: Nature **350**, 488 (1991)
- 7.66 A. Garcia, M.L. Cohen, J.H. Eggert, F. Moshary, W.J. Evans, K.A. Goettel, I.F. Silvera: Phys. Rev. B **45**, 9709 (1992)
- 7.67 K.A. Johnson, N.W. Ashcroft: Phys. Rev. B **58**, 15548 (1998)
- 7.68 K.A. Johnson, N.W. Ashcroft: Nature **403**, 632 (2000)
- 7.69 M. Städele, J.A. Majewski, P. Vogl: Phys. Rev. Lett. **79**, 2089 (1997)
- 7.70 M. Städele, M. Moukara, J.A. Majewski, P. Vogl: Phys. Rev. B **59**, 10031 (1999)
- 7.71 M. Städele, R.M. Martin: Phys. Rev. Lett. **84**, 6070 (2000)
- 7.72 H. Kitamura, S. Tsuneyuki, T. Ogitsu, T. Miyake: Nature **404**, 259 (2000)
- 7.73 K. Nagao, T. Takezawa, H. Nagara: Phys. Rev. B **59**, 13741 (1999)
- 7.74 T. Miyake, T. Ogitsu, S. Tsuneyuki: Phys. Rev. Lett. **81**, 1873 (1998)
- 7.75 W.J. Nellis: Phys. Rev. Lett. **89**, 165502 (2002)
- 7.76 G.I. Kerley, in *Molecular-Based Study of Fluids*, edited by J.M. Haile and G.A. Mansoori (American Chemical Society, Washington, 1983), p. 107

- 7.77 T.J. Lenosky, S.R. Bickham, J.D. Kress, L.A. Collins: Phys. Rev. B **61**, 1 (2000)
- 7.78 B. Militzer, D.M. Ceperley: Phys. Rev. Lett. **85**, 1890 (2000)
- 7.79 M. Ross: Phys. Rev. B **58**, 669 (1998)
- 7.80 Ya.B. Zeldovich, Yu.P. Raizer: *Physics of Shock Waves and High-Temperature Hydrodynamic Phenomena* (Academic, New York, 1966), Vol.1, p. 52
- 7.81 F. Hensel, P. Edwards: Phys. World **4**, 43 (1996)
- 7.82 D. Saumon, G. Chabrier, H.M. van Horn: Astrophys. J. Suppl. **99**, 713 (1995)
- 7.83 W.R. Magro, D.M. Ceperley, C. Pierleoni, B. Bernu: Phys. Rev. Lett. **76**, 1240 (1996)
- 7.84 H. Kitamura, S. Ichimaru: J. Phys. Soc. Jpn: **67**, 950 (1998)
- 7.85 T.J. Lenosky, J.D. Kress, L.A. Collins, R. Redmer, H. Juranek: Phys. Rev. E **60**, 1665 (1999)
- 7.86 T.J. Lenosky, J.D. Kress, L.A. Collins, I. Kwon: Phys. Rev. B **55**, R11907 (1997)
- 7.87 N.F. Mott, E.A. Davis: *Electronic Processes in Non-Crystalline Materials* (Clarendon Press, Oxford, 1979), Chap. 2
- 7.88 N.W. Ashcroft: Phys. Rev. Lett. **21**, 1748 (1968)
- 7.89 W.L. McMillan: Phys. Rev. **167**, 331 (1968)
- 7.90 C.R. Leavens: Solid State Commun. **13**, 1607 (1973)
- 7.91 M.D. Whitmore, J.P. Carbotte, R.C. Shukla: Can. J. Phys. **57**, 1185 (1979)
- 7.92 T.W. Barbee, III, A. Garcia, M.L. Cohen: Nature **340**, 369 (1989)
- 7.93 L.G. Caron: Phys. Rev. B **12**, 5025 (1974)
- 7.94 G.D. Gaspari, B.L. Gyorffy: Phys. Rev. Lett. **28**, 801 (1972)
- 7.95 B.I. Min, H.J.F. Jansen, A.J. Freeman: Phys. Rev. B **30**, 5076 (1984)
- 7.96 A.C. Switendick: In *Superconductivity in d- and f-Band Metals*, ed. by D.H. Douglass (Plenum, New York 1976) p. 593
- 7.97 D. Papaconstantopoulos, B.M. Klein: Ferroelectrics **16**, 307 (1977)
- 7.98 I.E. Jaffe, N.W. Ashcroft: Phys. Rev. B **23**, 6176 (1981)
- 7.99 M.O. Knudson, D.L. Hanson, J.E. Bailey, R.W. Lemke, C.A. Hall, C. Deeney, J.R. Asay: J. Phys. A: Math. Gen. **36**, 6149 (2003)
- 7.100 F. Datchi, P. Loubeyre, R. Le Toullec: Phys. Rev. B **61**, 6535 (2000)
- 7.101 E. Gregoryanz, A.F. Goncharov, K. Matsuichi, H.K. Mao, R. Hemley: Phys. Rev. Lett. **90**, 175701 (2003)
- 7.102 S.A. Bonev, E. Schwegler, T. Ogitsu, G. Galli: Nature **431**, 669 (2004)
- 7.103 V. Kechin: Phys. Rev. B **65**, 052102 (2001)
- 7.104 N.W. Ashcroft: J. Phys.: Condens. Matter **12**, A129 (2000)
- 7.105 N.W. Ashcroft: J. Phys. A: Math. Gen. **36**, 6137 (2003)
- 7.106 E. Babaev, S. Sudbø, N.W. Ashcroft: Nature **431**, 666 (2004)
- 7.107 A.F. Andreev, I.M. Lifshitz: Sov. Phys. JETP **29**, 1107 (1969)
- 7.108 G.V. Chester: Phys. Rev. A **2**, 256 (1970)
- 7.109 A.J. Leggett: Phys. Rev. Lett. **25**, 1543 (1970)
- 7.110 K.S. Liu, M.E. Fisher: J. Low Temp. Phys. **10**, 655 (1973)
- 7.111 M. Liu: Phys. Rev. B **18**, 1165 (1978)
- 7.112 D.E. Galli, L. Reatto: J. Low Temp. Phys. **124**, 197 (2001)
- 7.113 E. Kim, M.H.W. Chan: Nature **427**, 225 (2004)
- 7.114 E. Kim, M.H.W. Chan: Published on line 3 Sept. 2004 (10.1126/science.1101501)

- 7.115 T.L. Ho: Science **305**, 1114 (2004)
- 7.116 J. Beamish: Nature **427**, 204 (2004)
- 7.117 T. Leggett: Published on line 3 Sept. 2004 (10.1126/science.1103584)

List of Symbols

\hbar	Planck's constant ($\hbar : h$ divided by 2π)
k	Boltzmann constant (k_B in Sect. 6.5.2)
N_A	Avogadro's number
m	electron mass
M	hydrogen mass
I	nuclear spin of hydrogen
μ_N	nuclear magnetic moment of hydrogen
p	pressure
p_H	hydrogen pressure
V	volume
T	temperature
T_m	melting point
T_b	boiling point
θ_D	Debye temperature
θ_E	Einstein temperature
K_0	bulk modulus
n	number of hydrogen atoms in a specimen
N_0	number of metal atoms in a specimen
N	number of interstitial sites in a specimen
$x = n/N_0 = [H]/[M]$	hydrogen-to-metal-atom ratio
$x' = n/(n + N_0)$ $= [H]/([H] + [M])$	hydrogen concentration in atomic fraction
$r = N/N_0$	number of interstitial sites per metal atom
$c = n/N = x/r$	fraction of interstitial sites filled with hydrogen atoms
N_S, N_L	number of interstitial sites in solid and liquid phases
ρ	density of hydrogen atoms per unit volume
ρ_0	maximum density of hydrogen atoms per unit volume
p_c	critical pressure of fluid hydrogen
T_c	critical temperature (of fluid hydrogen, of spinodal, or of superconductivity)
x_c	critical concentration of spinodal

E_0	ground-state energy of a hydrogen molecule
E_d	heat of dissociation of a hydrogen molecule
n_v	vibrational quantum number of a hydrogen molecule
J_r	rotational quantum number of a hydrogen molecule
E_n^v	vibrational energy of a hydrogen molecule
E_J^r	rotational energy of a hydrogen molecule
V^i, H^i, S^i, G^i	volume, enthalpy, entropy, and Gibbs free energy per mole of phase i . i stands for gas (g), fluid (f), solid solution (α), or hydride (β)
$v^i, h^i, s^i, \mu^i (i = \text{g, f})$	volume, enthalpy, entropy, and chemical potential of hydrogen per molecule
$v^i, h^i, s^i, \mu^i (i = \alpha, \beta)$	volume, enthalpy, entropy, and chemical potential of hydrogen per atom. The volume is sometimes written as v_H for the sake of clarity
$v_0^i, h_0^i, s_0^i, \mu_0^i (i = \alpha, \beta)$	volume, enthalpy, entropy, and chemical potential of a metal per atom
$\bar{v}^i = v_0^i + x_i v^i$	volume, enthalpy, entropy, and chemical potential of phase i per metal atom
$\bar{h}^i = h_0^i + x_i h^i$	
$\bar{s}^i = s_0^i + x_i s^i$	
$\bar{g}^i = \mu_0^i + x_i \mu^i$	
S^c	configurational entropy of a solid solution
S^{nc}	nonconfigurational entropy of a solid solution
$G^{\alpha\text{nc}} = G^\alpha + TS^c$	Gibbs free energy of a solid solution excluding the configurational entropy term
s^c	configurational entropy of a solid solution per hydrogen atom
$s^{\alpha\text{nc}}$	nonconfigurational entropy of a solid solution per hydrogen atom
$\mu^{\alpha\text{nc}}$	chemical potential of hydrogen in a solid solution excluding the configurational entropy term
μ_{vib}	vibrational part of the chemical potential
e_s	heat of solution (in Sect. 5.6)
$\Delta h_s, \Delta s_s$	enthalpy and entropy changes per hydrogen atom in forming a solid solution from the gas phase (of 0.1 MPa) as determined by calorimetric measurements

$\Delta H_s, \Delta S_s$	enthalpy (heat) and entropy changes per hydrogen atom in forming a solid solution from the gas phase (of 0.1 MPa) as obtained from equilibrium p - x - T measurements
ΔH_s^0 $\Delta h^{\alpha \rightarrow \beta}, \Delta s^{\alpha \rightarrow \beta}$	ΔH_s at infinite dilution enthalpy and entropy changes per hydrogen atom in forming a hydride from a solid solution
$\Delta H^{\alpha \rightarrow \beta}, \Delta S^{\alpha \rightarrow \beta}$	above quantities to be obtained from equilibrium p - x - T measurements
$\Delta H_{\text{solv}}, \Delta S_{\text{solv}}$ \bar{u}, \bar{w}	solvus enthalpy and entropy coefficients describing the concentration dependence of ΔH_s : $\Delta H_s = \Delta H_s^0 - \bar{u}x + \bar{w}x^3$. Sometimes, the term $\bar{u}x$ is written as $\bar{v}c$, where $\bar{v} = r\bar{u}$
e_b	binding energy to impurity atom, defect, etc.
y $[A_m B_n]$	alloy composition, $A_y B_{1-y}$ type of interstitial site
E	surrounded by m A-atom and n B-atom energy of an interstitial hydrogen atom as a variable; in Appendix 5B, the same letter stands for the center-of-mass energy of a projectile nucleus
$f(E)$ $D(E)$ X, Y, Z $\mathbf{R}, \mathbf{R}^j, \mathbf{R}^j(t)$	Fermi-Dirac distribution function site-energy distribution function space coordinates (for a hydrogen atom) position of a hydrogen atom, on site j , at time t
\mathbf{s}^j	a vector connecting a hydrogen site (origin) to a nearest-neighbor site (j)
\mathbf{r}^j \mathbf{u}^j \mathbf{u}_1	position of a metal atom on site j displacement of a metal atom on site j displacement of a metal atom nearest to a hydrogen atom
Z^j a $\Delta a/a$	number of atoms in the j th shell lattice parameter fractional change of the lattice parameter with hydrogen concentration $(1/a)(da/dx)$
$\Delta L/L$	fractional length change with hydrogen concentration $(1/L)(dL/dx)$
$\tilde{\lambda}_X, \tilde{\lambda}_Y, \tilde{\lambda}_Z$	strain tensors with symmetry axis along the X , Y , and Z directions, respectively. Diagonal components are written as λ_1 and λ_2 .
$\tilde{\lambda}$	isotropic strain tensor with all diagonal components equal to λ_0

$\tilde{P}_X, \tilde{P}_Y, \tilde{P}_Z$	force-dipole (stress) tensors with symmetry axis along the X , Y , and Z directions, respectively. Diagonal components are written as A and B .
\tilde{P}	isotropic force-dipole tensor with all diagonal components equal to A .
c_{11}, c_{12}, c_{44}	elastic stiffness constants
$\hbar\mathbf{Q}, \hbar\omega$	momentum and energy transferred from the wave (X-rays or neutrons) to a specimen in the course of scattering. \mathbf{Q} is called the scattering vector
W_D	Debye–Waller factor
$f_d(\mathbf{Q}), f_m(\mathbf{Q})$	scattering amplitude of a defect and a host metal atom for X-rays
$\sigma_{\text{coh}}, \sigma_{\text{inc}}$	coherent and incoherent scattering cross sections for neutrons
$S(\mathbf{Q})$	elastic scattering function
$S_{\text{coh}}(\mathbf{Q}, \omega), S_{\text{inc}}(\mathbf{Q}, \omega)$	coherent and incoherent scattering functions
$\rho(\mathbf{R})$	density distribution of interstitial hydrogen atom
$G(\mathbf{R}, t)$	Van Hove's space–time correlation function, with subscripts s and d signifying self and distinct part, respectively
$\hbar\mathbf{q}, \hbar\omega_q$	momentum and energy of a phonon of a wave vector \mathbf{q}
n_q	thermal-equilibrium number of phonons with a wave vector \mathbf{q}
$F(\mathbf{q}, \omega)$	phonon density of states
$U, U(\mathbf{R})$	adiabatic potential for a hydrogen atom
$V(\mathbf{R})$	pair potential between a hydrogen atom and a metal atom
β	anharmonicity parameter for a potential
e_{lmn}	(vibrational) energy eigenvalue of an interstitial hydrogen atom in the state (l, m, n) ; in 3 dimension
$\varepsilon_{lmn} = e_{lmn} - e_{000}$	vibrational excitation energy from the ground state $(0,0,0)$ to (l, m, n) ; in 3 dimension
e_α	(vibrational) energy eigenvalue of an interstitial hydrogen atom in state α ($\alpha = 0, 1, 2, \dots$); in 1 dimension
$\Delta e_\alpha = e_\alpha - e_0$	excitation energy of an interstitial hydrogen atom from the ground state 0 to α ; in 1 dimension
Ψ_α	wave function of a hydrogen atom in the α -th vibrational state
E_p	incident energy of a projectile in the d–d fusion reaction in metals
U_e	effective screening potential in the d–d fusion reaction in metals
T_1	spin–lattice relaxation time
$T_{1\rho}$	spin–lattice relaxation time in the rotating frame

T_2	spin-spin relaxation time
τ_c	correlation time (for dipolar interaction)
τ_N	lifetime of the nuclear level for Mössbauer effect, or perturbed angular correlation
f^{ML}	Mössbauer-Lamb factor, with contributions of lattice vibrations and strains denoted by vib and str as subscripts
$G^{(p)}(t)$	autocorrelation function of the p -th spherical harmonic component of the dipolar interaction
$J^{(p)}(\omega)$	frequency spectrum of the p -th spherical harmonic component of the dipolar interaction
D	intrinsic (tracer) diffusion coefficient
D^*	chemical diffusion coefficient
f_t	tracer correlation factor
f_M	mobility correlation factor
f_{therm}	thermodynamical factor
$H_R = f_t/f_M$	Haven's ratio
p_v	site-availability factor
$p_f(p_b)$	fractional population of hydrogen atoms in a free (bound) state: $p_f + p_b = 1$
$D_{\text{eff}} = p_f D$	effective diffusion coefficient
e_{sp}	saddle point energy
e_{m}^{H}	migration energy of a hydrogen atom, sometimes simply written as E_a
e_{m}^{v}	migration energy of a M-atom vacancy
e_{m}^{cl}	migration energy of a Vac-H cluster
e_{f}^{v}	formation energy of a M-atom vacancy
e_{f}^{cl}	formation energy of a Vac-H cluster
v_{f}^{v}	formation volume of a M-atom vacancy
v_{f}^{cl}	formation volume of a Vac-H cluster
x_v	concentration of M-atom vacancies
x_{cl}	concentration of Vac-H clusters
D^{v}	diffusivity of a M-atom vacancy
D^{cl}	diffusivity of a Vac-H cluster
τ_0	mean jump time
w	hopping rate
\mathcal{H}	total Hamiltonian of the metal-hydrogen system, comprised of a sum of an electronic part, a lattice part, and a hydrogen part, in an adiabatic approximation
\mathcal{H}^a	total Hamiltonian with a hydrogen atom on site a
χ	total wave function of the system, comprised of a product of an electronic part (Φ_{el}), a lattice part (Ψ_l), and a hydrogenic part (Ψ), in an adiabatic approximation
χ^a	total wave function with a hydrogen on site a

Φ_0	many-body wave function of electrons in the Fermi surface (FS) state
$\Phi_{\mathbf{k},\mathbf{k}'}$	wave function obtained from Φ_0 by exciting an electron from state \mathbf{k} (in FS) to \mathbf{k}' (out of FS)
$V_{\mathbf{k}\mathbf{k}'}$	Fourier component of the interaction potential causing a transition $\mathbf{k} \rightarrow \mathbf{k}'$
$\varepsilon_{\mathbf{k}}$	energy of an electron in state \mathbf{k}
E_F	Fermi energy
r_s	Wigner–Seitz radius
$N(E)$	electron density of states
$\Delta_g(T)$	superconducting energy gap
λ, μ^*	parameters describing the electron–phonon coupling and the effective Coulomb interaction in superconductivity
J	tunneling matrix element or transfer integral for a hydrogen atom between neighboring interstitial sites; $J = f_{el}f_lJ_0$
f_{el}	renormalization factor for the electrons
f_l	renormalization factor for the lattice
J_0	bare tunneling matrix element
\bar{J}	limiting value of J at $T \rightarrow 0$
Δ	level shift due to energy disorder
Γ	damping constant for a tunnel-split state
K	parameter describing the strength of coupling between a moving particle and conduction electrons
K_{dp}	parameter describing the diphonon coupling to the lattice
J^N, J^S	tunneling matrix element in the normal and superconducting state
Γ^N, Γ^S	damping constant in the normal and superconducting state
W	width of a proton band
λ_{dB}	de Broglie wavelength

List of Abbreviations

<i>a</i> -, <i>c</i> -	amorphous, crystalline
DAC	diamond-anvil cell
DOS	density of states
EOS	equation of state
ETM	early transition metals
FLS	four-level system
HDS	Huang diffuse scattering
HIA	hydrogen-induced amorphization
INS	inelastic neutron scattering
LTM	late transition metals
μSR	muon spin resonance (relaxation, rotation)
ND	neutron diffraction
NMR	nuclear magnetic resonance
n-, o-, p-	normal-, ortho-, para-
O site, T site	octahedral site, tetrahedral site
PAC	perturbed angular correlation
PES	photoelectronic spectroscopy
QNS	quasi-elastic neutron scattering
SAV	superabundant vacancy
SXS	soft-X-ray spectroscopy
TLS	two-level system
TSH	terminal solubility of hydrogen
Vac	M-atom vacancy
XRD	X-ray diffraction

Index

- absorption/desorption for diffusion
 - measurements 311, 324, 326, 328, 329, 345
- actinide metals 36
- activation of surface 12
- adiabatic potential 231–233, 249–255, 412–415
- alloy–hydrogen systems (except amorphous and ordered alloy–hydrogen systems)
 - Cu–Ni–H 226–228
 - Fe–Mn–H 106
 - Fe–Ni–Mn–H 106, 107
 - Mo–V–H 56
 - Mo–Zr–H 56
 - Nb–Au–H 68
 - Nb–Cr–H 201
 - Nb–Fe–H 319
 - Nb–Ir–H 68
 - Nb–Mo–H 56, 63, 66, 199–201
 - Nb–Pd–H 56
 - Nb–Re–H 56
 - Nb–Ru–H 68
 - Nb–Ta–H 60–63, 202
 - Nb–Ti–H 56, 60–63, 66, 67, 105, 201, 271
 - Nb–V–H 60–63, 201, 360, 373
 - Nb–Zr–H 271
 - Ni–Cu–Fe–H 68
 - Ni–Cu–H 66, 107
 - Ni–Fe–H, D 66, 68, 106–108
 - Ni–Mn–H 106
 - Ni–Pd–H 66
 - Ni–Pt–H 66
 - Ni–Ti–H 66
 - Ni–V–H 66
 - Pd–Ag–H 57–59, 107
 - Pd–Au–H 57, 58, 67, 107
 - Pd–Ce–H 57, 58
 - Pd–Co–H 57, 58, 67
 - Pd–Cu–H 57, 58, 107, 327–329
 - Pd–Fe–H 57, 58, 67, 319, 336, 337
 - Pd–Ir–H 57, 58, 67, 107
 - Pd–Mn–H 57
 - Pd–Ni–H 57, 58
 - Pd–Os–H 67
 - Pd–Pb–H 57, 58
 - Pd–Pt–H 57, 58, 67, 107
 - Pd–Rh–H 57, 58, 67, 228
 - Pd–Ru–H 67
 - Pd–Sn–H 57, 58, 67
 - Pd–U–H 58
 - Pd–V–H 57
 - Ta–Fe–H 319
 - Ti–Fe–H 319
 - Ti–Mo–H 56, 58, 59, 201
 - Ti–Nb–H 56
 - Ti–Re–H 58
 - Ti–V–H 56, 105, 201
 - V–Au–H 68
 - V–Co–H 56
 - V–Cr–H 56, 58, 59, 63, 67
 - V–Cu–H 63
 - V–Fe–H 56, 63, 67, 319
 - V–Mo–H 63, 67
 - V–Nb–H 58, 63, 67, 373
 - V–Ru–H 68
 - V–Ti–H 58, 63, 66, 67, 372
 - V–Zr–H 63, 67
- amorphous alloy – hydrogen systems
 - Hf₃Al–H 85
 - Ln₂M–H (M=Al, In) 85
 - Ln₃M–H (M=Al, Ga, In) 85
 - LnAl–H 85
 - LnM₂–H (M=Mn, Fe, Co, Ni) 85–90

- Ni-Pd-P-H 74, 76
- Ni-Ti-Zr-H 76
- Ni-Zr-H 109
- Pd-Si-Cu-H 76
- Pd-Si-H 74, 77, 109
- Ti₃M-H (M=Al, Ga, In) 85
- Ti-Cu-H 83
- Ti-Ni-H 78
- Zr₂Al-H 85
- Zr₂Pd-H 109
- Zr₃M-H (M=Al, In) 85
- Zr₃Rh-H 85, 109
- Zr-Ni-H 72, 76, 78, 81-83, 109
- amorphous alloys
 - chemical potential 75
 - measurement of 76-78
 - diffusion 372, 373
 - hydrogen-induced amorphization (HIA) 84-90
 - p*-*x*-*T* curves
 - absence of plateau 72, 77-79
 - site-energy distribution 74-76, 78-84
 - spinodal decomposition 77-79
 - thermal desorption spectroscopy (TDS) 81-83
 - thermodynamics of 74-76
- anion model 417
- Arrhenius plot
 - alternative of 46, 361-363
 - diffusion coefficient, jump frequency 307, 310, 327-330, 333-335, 337, 338, 340, 345, 349, 353, 358, 364, 367, 393
 - solubility 14, 15, 116-119
 - solvus → terminal solubility
 - terminal solubility 42, 44
- atomistic state
 - theory of β -V₂H 244-249
 - theory of self-trapped state 231-244, 373, 377, 385
- band-theoretic calculation 249-256, 401-409, 417-421
 - density of states (DOS) 402-404, 417-419
 - heat of hydride formation 36, 86, 407-412
 - hydrogen (elemental) → separate item
 - hydrogen-metal potential 231-244, 249-256, 412-415
 - rare-earth hydrides 417-421
- cancellation effect
 - hydride formation 42
 - solid solubility 20, 21
- channeling 148-152
 - D(³He, p) α reaction 149
 - H(¹¹B, α) $\alpha\alpha$ reaction 149
 - site location by 148, 198, 206-211
- collective motion 303
- correlation time 313, 358-360
- d-d fusion reaction in metals 294-302
 - enhanced electron screening 294-302
- defect strain tensor → force-dipole tensor
- density distribution (of interstitial hydrogen)
 - calculation of 237, 238, 256, 257
 - from neutron diffraction 159-164
- diffusion 303-400
 - effects of elastic interactions on 350-354
 - high concentrations 306, 337-343, 350-352
 - inhomogeneous systems 372, 373
 - near impurity atoms 362-367
- diffusion coefficient 303-306
 - bcc metals (values of) 326-328
 - chemical diffusion coefficient 305
 - fcc metals (values of) 327-329
 - Fick's diffusion coefficient → chemical diffusion coefficient
 - fundamentals of 303-306
 - Haven's ratio 306, 357
 - intrinsic diffusion coefficient 305, 312, 332-334
 - mobility 305
 - mobility correlation factor 306
 - site availability factor 306
 - thermodynamical factor 306, 324, 351, 354
 - tracer correlation factor 305
 - tracer diffusion coefficient 305

- diffusion measurements 311–326
 - absorption/desorption → separate item
 - mechanical and magnetic relaxation → separate item
 - Mössbauer effect → separate item
 - muon spin relaxation (μ SR) → separate item
 - nuclear magnetic resonance (NMR) → separate item
 - perturbed angular correlation (PAC) → separate item
 - quasi-elastic neutron scattering (QNS) → separate item
 - resistivity relaxation → separate item
- diffusion mechanism
 - adiabatic limit 385
 - coincidence event 309, 385, 386, 391
 - elementary jumps
 - in amorphous alloys 372, 373
 - in disordered alloys 372, 373
 - in ordered alloys 367–372
 - in pure metals 307, 308, 312–316, 320–322, 336, 343–350
 - in pure metals with traps 362–367
 - over inequivalent sites 360–372
 - high-temperature region – phonon-assisted processes 382–387, 389–394
 - Flynn–Stoneham formula 384
 - incoherent hopping 376–381
 - list of 375
 - occurrence probability 385, 386
 - low-temperature region – zero-phonon process 308, 309, 374–381, 387–389
 - Bloch wave propagation 375, 397–400
 - coherent diffusion 375, 376
 - effects of conduction electrons 374, 378–381, 387, 388
 - effects of diphonon coupling to the lattice 380
 - quantum diffusion 373–381
 - theoretical considerations on 373–394
 - tunneling → separate item
 - two-state model → separate item
- dihydrides 33–38, 337–343
- distribution coefficient 51
- effective-medium theory 410–412
 - calculations on trapped states 213–216, 256, 257
 - embedding energy 410
- electrical resistivity 95, 136, 325
- electrochemical method 311, 324
 - chemical potential measurements in amorphous alloys 76, 77
 - diffusion measurement 324
- electronegativity 7
- electronic structure
 - band calculation 401–409, 417–419, 423–425
 - charge transfer 7, 108, 405, 417
 - density of states (DOS) 401
 - H-induced state 401, 404, 417, 418
 - local DOS 403
 - partial DOS 403
 - total DOS 402
 - elemental hydrogen → hydrogen (elemental)
 - screening charge
 - distribution of 403–406
 - proton/anion model 417
 - wave function of 275
 - single-impurity approach 403–406
- elementary jump → diffusion mechanism
- Fe–H, D system
 - channeling 210–212
 - compression curve 112
 - diffusion coefficient 326–328
 - H-induced volume 105, 108, 112
 - implanted state 207, 211
 - phase diagram 130–132
 - solubility under high pressure 118, 132
- Fermi–Dirac distribution (of interstitial hydrogen) 64
 - amorphous alloys 74–76
 - hydrogen–solute interaction 64–68
- force-dipole tensor 152–155
 - values of 158

Gorsky effect 311, 325, 328, 351, 353

harmonic oscillator 167

hopping rate \rightarrow jump frequency

hydride 9, 30–49

enthalpy (heat) and entropy of

formation 37, 38, 42

electronic calculation 407–409

values of 38

Lima-de-Faria's notation 31

site occupancy in 28, 31

structure 30–36

thermodynamics of formation

36–42

hydrogen (elemental)

atomic jumps 396

compression curve 5, 93, 112, 426, 427

electrical resistivity 95, 428–432

electronic structure 421–437

electronic theory 423–426, 429–432

equation of state 96, 426, 427, 436, 437

fundamental properties of H, D, T
(values of) 2

melting curve 5, 92, 436, 437

metallization 95, 421–423, 428–432

molecular state 1–5, 91–104, 421–423

ortho-, para-, normal hydrogen 2–4
population of 3, 4

p - T phase diagram 5, 92

superconductivity 432–434

superfluidity 436, 437

thermodynamical quantities 96–104

calculated values of V , H , G , S
97–104

tunneling 395–397

vibron 91, 421, 422

pressure dependence of 421, 422

hydrogen effects on

amorphization 84–86

electronic structure 336, 401

melting point of metals 50–53, 124, 134

phase stability of metals 13, 50–53

hydrogen–hydrogen interaction in
metals 21–27

blocking effect 25, 53

hydrogen-induced amorphization
(HIA) 84–86

(long-range) elastic interaction
22–25, 29

coherent, incoherent strain 29, 30

short-range repulsion 25–27

hydrogen-induced volume \rightarrow volume of
hydrogen in metals

hydrogen–metal interaction potential
 \rightarrow potential field for hydrogen

hydrogen–solute (defect) interaction in
metals 63–68

blocking 63–68

effects on site occupancy 197–202

trapping \rightarrow trapped state

INS \rightarrow inelastic neutron scattering

intermetallic compounds \rightarrow ordered
alloys

internal friction \rightarrow mechanical and
magnetic relaxation

interstitial site 28, 30, 31

2T configuration 259

4T site (configuration) 234, 236,
238–240, 244–246, 271–274

6T configuration 234, 370–372

bcc lattice 31, 105

displaced-T site 187–193, 210, 258

fcc lattice 31, 105, 106

hcp lattice 31, 105

number and size of 28

octahedral (O) site 28

tetrahedral (T) site 28

ion implantation 203–216

annealing of defects 204–212

formation of defects (vacancy,
self-interstitial, He bubble)

203–208

radiation-induced defects \rightarrow trapped
state

iron–water reaction 140–145

jump frequency (rate) 311, 313–316,
320–322, 330, 341, 342, 348, 349,
364, 366, 367, 376, 390

jump length (distance) 304, 321, 322,
336, 339, 340, 342, 345, 346, 369,
374

Kanzaki force 152, 153

- lanthanide metals → rare-earth metals
- lattice distortion
 calculation of 235, 236
 effects of motion on 159
 effects on tunneling (diffusion)
 379–381, 384, 390, 391
 wave function of 277
 X-ray scattering 154–157
- magnetic disaccommodation 311, 326, 336
- mean jump time 304–306, 313, 319–321
- mean residence time → mean jump time
- mechanical and magnetic relaxation
 diffusion measurement 311, 325, 326, 336, 337, 362–364
 terminal solubility determination 43
 trapped state 66
- metal–hydrogen systems
- Ag–H, D 16, 51, 115, 116, 118, 120, 207, 298, 408, 409
- Al–μ, H, D 16, 51, 115, 116, 204, 207, 213, 215, 298, 330, 387, 388
- Au–H 16, 115, 120, 296–298
- Ba–H 38, 298
- Be–H 120, 298
- Bi–H 120, 298
- Ca–H 38, 411
- Cd–H 120, 298
- Ce–H 16, 33, 35, 38, 106, 166, 167, 173, 178, 417–419
- Co–H 16, 33, 51, 105, 106, 113, 126–128, 132, 133, 137, 173, 174, 223, 224, 298, 407, 411
- Cr–H, D 16, 33, 105, 106, 115, 116, 119, 170, 174, 204, 207, 211, 223, 224, 281, 298, 408, 411
- Cs–H 38
- Cu–μ, H, D, T 16, 33, 51, 115, 116, 120, 135, 204, 207, 208, 213–215, 225–227, 296, 297, 326–330, 387, 388, 394, 405, 406, 411
- Dy–H 33, 35, 105
- Er–H 27, 33, 35, 38, 48, 105
- Eu–H 33, 35
- Fe–H, D 16, 33, 51, 105, 108, 112, 115, 116, 118, 130–132, 174, 204, 207, 210–215, 223, 224, 254–256, 281, 296–298, 326–328, 408, 411, 413
- Gd–H 33, 35, 38
- Hf–H 16, 33, 38, 106, 298, 330, 338
- Hg–H 120
- Ho–H 27, 33, 35, 48, 105
- In–H 120, 298
- Ir–H 16, 120, 136, 298
- K–H 38, 411
- La–H, D 16, 33, 35, 38, 105, 173, 178, 338, 342, 360, 417
- Li–H 16, 38
- Lu–H, D 27, 33, 35, 48, 105, 172, 174, 196, 197, 207, 210, 330
- Mg–H, D 16, 38, 207, 210, 298
- Mn–H 33, 38, 51, 105, 106, 129, 169, 173, 174, 177, 217, 223, 224, 269–271, 298, 408, 411
- Mo–H, D 16, 33, 105, 106, 115, 116, 119, 126–128, 170, 174, 204, 207, 213–215, 298, 408, 409
- Na–H 38
- Nb–μ, H, D, T 10, 16, 21, 24, 26, 27, 29, 33, 38, 59, 60, 66, 105, 111, 112, 149, 158, 159, 162, 170, 171, 174, 177, 179, 180, 182–186, 192, 193, 198–200, 202–204, 207, 210, 212–214, 219–223, 233–244, 247, 249, 250, 258–269, 271, 274–278, 281–283, 285, 286, 293, 298, 319, 326–328, 331–337, 343–345, 351–360, 362–367, 387–393, 408, 409, 414
- Nd–H 33, 35, 38
- Ni–H, D, T 16, 24, 33, 38, 51, 105–107, 112, 113, 115, 116, 133–135, 137, 168–170, 173, 177, 203–209, 213–227, 256, 257, 296, 297, 326–329, 394, 404, 405, 408, 411, 412
- Os–H 120, 136
- Pb–H 120, 298
- Pd–H, D, T 10, 12, 13, 16, 18–21, 24, 27, 33, 38, 55–59, 67, 68, 105–107, 135, 149–151, 165, 166, 168, 169,

- 173, 175–177, 185, 186, 204, 207,
213–218, 243, 251–254, 274, 275,
286, 287, 296–298, 315, 319, 321,
322, 326–337, 350, 402–405, 408,
409, 412
- Pr–H 33, 35, 38
- Pt–H, D 16, 115, 116, 120, 136, 207,
209, 298, 412
- Rb–H 38
- Re–H 33, 105, 120, 130, 136, 172,
174, 298
- Rh–H, D 16, 33, 106, 408, 409
- Ru–H 16, 33, 120, 136, 408, 409
- Sb–H 120, 298
- Sc– μ , H, D 16, 21, 24, 27, 33, 38, 48,
105, 123, 172, 174, 196, 265, 271,
298, 347–350, 360, 408, 411
- Sm–H 33, 35, 38
- Sn–H 120, 298
- Sr–H 38, 298
- Ta–H, D, T 16, 21, 24, 26, 33,
38, 60, 105, 106, 111, 112, 151,
157, 158, 161, 168, 170, 171, 174,
177, 185, 186, 192, 193, 198, 199,
204, 205, 207, 213, 215, 233–244,
258–260, 274–278, 281, 282, 298,
318, 326–328, 331–335, 343, 345,
351, 352, 357, 360, 388–394
- Tb–H 33, 35, 105
- Tc–H 33, 105, 130, 408, 409
- Th–H 36
- Ti–H 16, 21, 24, 33, 38, 50, 105, 123,
172–174, 177, 218, 298, 313, 314,
316, 330, 338–340, 350, 351, 360,
408, 411
- Tl–H 120, 298
- Tm–H 27, 33, 35, 48, 105
- U–H 16, 51
- V–H, D, T 11, 12, 14–16, 21, 24, 26,
27, 33, 38, 45, 46, 50, 66, 67, 105,
110, 112, 125–127, 152, 153, 155,
158, 161–165, 170–174, 176, 177,
179–181, 185–193, 197, 204, 207,
210, 233–240, 242–244, 246–249,
274, 275, 298, 307, 326–328,
343, 345, 346, 351, 352, 354–356,
360–363, 401, 402, 408, 411
- W–H, D 16, 115, 116, 119, 120, 128,
204, 207, 298
- Y–H, D 16, 21, 24, 27, 33, 38, 48,
105, 172–174, 178, 179, 194–196,
287, 298, 330, 338–342, 350, 360,
408, 409, 416, 417
- Yb–H 33, 35
- Zn–H 120
- Zr–H, D 16, 33, 38, 105, 124, 172–
174, 177, 182, 204, 218, 298, 330,
338, 348, 360, 408, 409
- mobile (free) state 332, 343
- Mössbauer effect 67, 311, 318–320
- cage motion 319
- Mössbauer–Lamb factor 319
- trapped state 67, 319
- muon
 - jumps of 330, 348–350, 358, 359, 372
 - muon spin relaxation (μ SR) 274,
317, 387, 388, 397–400
 - muonium 330, 397–400
 - self-trapping energy (calculation of)
234–237, 255, 256
 - tunneling matrix element 275, 387,
388, 394
- Nb–H, D, T system
 - atomic jumps 319, 343–345,
362–367, 388, 389
 - atomistic calculations 233–244, 247,
249, 250, 275
 - channeling 149, 199, 200, 210
 - compression curve 111, 112
 - D density distribution 162
 - diffusion coefficient 326–328, 351,
352, 355–359, 364–367, 391–393
 - Gorsky effect 328, 351, 353, 354
 - H-induced volume 105
 - implanted state 207, 212
 - isotope-mixture effects 357–359
 - lattice distortion 158, 159
 - nuclear magnetic resonance (NMR)
345, 351, 352, 357–359, 364
 - phase diagram 10, 29
 - quasi-elastic neutron scattering
(QNS) 343, 344, 351, 355–357,
364–367
 - quench–recovery experiments on
334, 335

- solute-H binding energy 66
- stress-induced state 193
- superabundant vacancy (SAV)
 - formation 218–223
- terminal solubility in alloys 59, 60
- trapped states 198–202, 331–337, 362–367, 387–389
- tunneling 258–260, 389–393
- vibrational state 170, 171, 174, 177, 182–186
- X-ray diffuse scattering 158, 159
- neutron diffraction (elastic scattering) 159
 - density distribution 160–164
 - scattering cross section (table) 160
- neutron scattering
 - Compton scattering 284
 - inelastic neutron scattering (INS) 164–187, 262–266, 269, 270
 - scattering cross section (table) 160
 - tunnel-split state 262–266, 269, 270
 - vibrational state 164–187, 262–266, 269
- quasi-elastic neutron scattering (QNS) → separate item
- Ni-H, D, T system
 - calculation on defect trapping 213–216
 - channeling 206
 - compression curve 112
 - diffusion coefficient 326–329, 394
 - H-induced volume 105, 112, 113
 - implanted state 203–209
 - phase diagram 133–135
 - solubility under high pressure 117, 135
 - solute-H binding energy 66
 - superabundant vacancy (SAV)
 - formation 216–227
 - vibrational state 168–170, 173, 177
- NMR → nuclear magnetic resonance
- nuclear magnetic resonance (NMR) for diffusion measurement 311–316
- isotope-mixture experiments 357–359
- pulsed field gradient method 317, 357–359
- relaxation time (rate) 312
 - anomalous relaxation at high temperatures 360
 - inhomogeneous systems 360
- spectral density function 313, 315, 316
- Ordered alloy-hydrogen systems
 - CeRu₂-D 109
 - ErMn₂-H 109
 - GaNi₅-μ 372
 - HfV₂-H 109, 369
 - LaNi-D 109
 - LaNi₅-H, D 109, 371, 372
 - Ln₂M-H (M=Al, In) 85
 - Ln₃M-H (M=Al, Ga, In) 85
 - LnM₂-H (M=Mn, Fe, Co, Ni) 84, 85
 - LnNiIn-H, D (Ln=lanthanide) 71, 109
 - Nb₃Sn-H 109
 - Pd₃P-D 109
 - TaV₂-H, D 109, 370, 371
 - TiCr₂-H, D 109, 368
 - TiFe-H, D 70, 109
 - TiMn₂-H 368
 - UNi₂Al₃-μ 372
 - YMn₂-H 369
 - ZrCr₂-D 109, 368
 - ZrMn₂-D 109
 - ZrV₂-H, D 69, 70, 109, 369
 - Zr₂Al-H 85
 - Zr₃M-H (M=Al, In, Rh) 85
 - Zr₃V₃O-D 109
- Ordered alloys
 - diffusion 367–372
 - Laves compounds C14, C15 68, 85
 - site occupancy 68–71
 - thermal desorption spectroscopy (TDS) 70, 81
- P-tensor → force-dipole tensor
- Pd-H, D, T system
 - atomic jumps 315, 319, 321, 322, 336
 - atomistic calculation 243, 251–254, 275

- channeling 149–151
- density of states (DOS) (electronic) 402
- diffusion at high concentrations 350
- diffusion coefficient 326–329, 336, 337
- effects of alloying on 55–59
- H-induced volume 105
- implanted state 207
- nuclear magnetic resonance (NMR) 315, 329, 336
- phase diagram 10, 13
- quasi-elastic neutron scattering (QNS) 321, 322
- solute–H interactions 67, 68
- superabundant vacancy (SAV) formation 216, 218
- temperature dependence of heat of solution 18–21
- vibrational state 165, 168, 169, 173, 175–177, 185, 186
- permeation 311, 324, 326, 328, 329
- perturbed angular correlation (PAC) 311, 318, 333–335
- phase diagram
 - high pressures 5, 11, 121–135
 - tentative diagrams 137–140
 - hydrogen 5, 92
 - introduction 9–14
 - plateau 13
 - absence in amorphous alloys 72
 - pressure–composition isotherms
 - p - x - T diagram
 - p_H - T diagram 128, 129, 136
 - p - T diagram 92, 125, 126, 131, 136
 - p - x - T diagram 13, 15, 116–119, 132, 133, 135
 - x - T diagram 9–12, 29, 35, 48, 50, 124, 127, 132, 135, 137–140
- potential field for hydrogen
 - anharmonicity 175–178, 181
 - calculated results 249–256
 - empirical potential 181
 - experimental determination 179–181
 - principles and limitations 412–415
- proton model 417
- QNS → quasi-elastic neutron scattering
- quantum entanglement 283–294
- quantum diffusion → diffusion mechanism
- quasi-elastic neutron scattering (QNS) 311, 320–324, 338, 339, 341–346, 348–350, 354–357, 364–372
- Chudley–Elliot model 321
- coherent scattering 323, 354, 355
- incoherent scattering 320–323, 355
- space–time correlation function (of van Hove) 320
- spin-polarization analysis 355
- quench-recovery method for diffusion measurement 311, 325, 331–335
- rare-earth metals
 - anomalous terminal solubility 47–49
 - atomic jumps 337–343, 346–350, 360
 - dihydrides 33–35, 38, 138, 166, 167, 337–343, 360
 - H-induced volume 105, 106, 108
 - H–M–H pair 194–197, 346–350
 - metal-insulator (M-I) transition 415–421
 - phase diagram 35, 123
 - trihydrides 35, 36, 123, 138–140, 166, 167, 415–421
 - two-site tunneling 265, 348
 - vibrational state 166, 167, 173, 174, 178, 179, 194–196
- resistivity relaxation for diffusion measurement 311, 325
- self-trapped state 229–244
 - self-trapping energy 234–236, 245–248
 - theory of 231–244
- shock compression 93–95, 110, 111
- Sieverts law 14, 20, 21
 - deviation in amorphous alloys 73
- site-energy distribution 74–76
- site location 148–152, 159–165
- site occupancy
 - determination of → site location
 - effects of annealing on 205–216
 - effects of impurity atoms on 197–202

- effects of radiation-induced defects
 - on 202–216
- effects of stress on 187–193
- hydrides 30–36
- solid solution 25, 28, 173
- Snoek effect 311, 325
- solid solution 14–27, 42–49
 - configurational entropy 15–17, 25–27, 45, 49
 - enthalpy (heat) and entropy of solution 15–19
 - concentration dependence of 21, 25–27
 - effects of alloying on 55–59
 - temperature dependence of 17, 21
 - values of 16
- Sieverts law → separate item
- solubility 14
 - effects of pressure, calculated results 113–120
- space–time correlation function (of van Hove) 320
- specific heat
 - solid solution 20, 21
 - statistical thermodynamics of 19
 - stress-induced state 191, 192
 - trapped state 259, 260, 262, 271, 272
- spectral density function 313–315
- spinodal decomposition 12, 27–30
 - amorphous alloys 77–79
 - critical point 27, 28, 113–119, 131–135
 - effects of alloying on 68
 - (Maxwell's) equal-area construction 27
 - shape dependence of 29
 - under high pressure 113–119, 131–135
- stress-induced state 187–193
- superabundant vacancy (SAV) 216–229
 - effects of 226–229
 - formation by electrolysis 225, 226
 - formation under high p , T 216–218, 221–225
 - superstoichiometric hydride 218
- Ta–H, D system
 - atomic jumps 320, 343, 345, 389–391
 - atomistic calculations 233–244
 - channeling 151, 198
 - compression curve 111, 112
 - diffusion coefficient 321–328, 331–335, 343, 351, 352, 357, 388–394
 - H-induced volume 105
 - lattice distortion 158
 - nuclear magnetic resonance (NMR) 351, 352
 - perturbed angular correlation 318, 333–335
 - quasi-elastic neutron scattering (QNS) 343, 351
 - quench-recovery experiment 331–335
 - solute–H binding energy 66
 - stress-induced state 193
 - terminal solubility in alloys 60
 - tunneling 258–260, 389–393
 - vibrational state 168, 170, 171, 174, 177, 185, 186
 - X-ray diffuse scattering 157, 158
- terminal solubility 42–49
 - anomaly in rare-earth metals 35, 44, 47–49
 - effects of alloying on 59–63
 - solution thermodynamics 60–63
 - effects of ordering on 83, 84
 - effects of solute atoms on 59–63
 - experimental determination of 42, 43
 - solvus line 34, 60, 61
 - solvus enthalpy, entropy 44
- thermal desorption spectroscopy (TDS) 69, 70, 81, 82, 204, 221, 222, 226, 227
- transition metals
 - crystal structure of 32
- trapped state
 - configuration of 67, 197–202, 206–216
- impurity atoms 64–67, 197–202, 326
 - binding energy (values of) 66, 67
 - two-site tunneling 259–271, 362–367, 387–389

- mutual trapping in rare-earth metals 194–197
- statistical mechanics of 64–66
- trapping by vacancies, radiation-induced defects 202–216
 - binding energy (values of) 204
 - calculations on 213–215, 256, 257
 - superabundant vacancies → separate item
- two-state model → separate item; see also diffusion mechanism
- trihydride 33–36, 123, 138–140, 166, 167, 415–421
- tunneling 258–283
 - bare tunneling matrix element 274, 276
 - Bloch state 375, 397–400
 - chemical reaction 395–397
 - coherent tunneling 375, 376
 - damping of 263, 266, 269, 282, 374
 - effects of conduction electrons on 267, 275–283
 - effects of lattice distortion on → lattice renormalization factor
 - electron renormalization factor 278–283
 - electron–particle coupling (Kondo) parameter 267, 271, 280–283
 - four-site tunneling 271–274
 - incoherent hopping 376–381
 - lattice renormalization factor 277, 278, 283
 - migration by 330, 333, 348–350, 373–376
 - theory of 274–283
 - tunnel splitting → tunneling energy
 - tunneling energy 263, 267, 269, 272, 273, 365
 - tunneling matrix element 258, 261, 270, 271, 275, 283
 - calculated values of 274–276
 - experimental values of 262–271, 283
 - two-site tunneling 259–271
 - critical analysis 282
 - neutron scattering on 262–266, 269, 270
- two-state model 63–68, 332, 343, 361–363
- ultrasonic spectroscopy 265–269, 273, 348, 349
- V–H, D, T system
 - atomic jumps 343, 345, 346, 361–363
 - atomistic calculations 233–249, 275
 - channeling 152, 153, 187–189
 - compression curve 110, 112
 - D density distribution 161–164
 - temperature dependence of 163–165
 - diffusion coefficients 307, 326–328, 343, 345, 346, 351, 352, 354–356
 - H-induced states 401, 402
 - H-induced volume 105
 - implanted state 207, 210
 - lattice distortion 158
 - nuclear magnetic resonance (NMR) 351, 352
 - phase diagram 11, 15, 125–127
 - quasi-elastic neutron scattering (QNS) 343, 345, 346, 351
 - solute–H interaction energy 66, 67
 - stress-induced state 187–193
 - tunneling 274, 275
 - vibrational state 170–172, 174, 177, 179–181, 185, 186
 - X-ray diffuse scattering 158
- vibrational states
 - band-mode vibration 183–186, 391, 392
 - dispersion curve 165–168, 184
 - effects of pair formation on 194–196
 - effects of trapping on 194, 199
 - molecule 1–3, 421, 422
 - optic-mode vibration 165–181, 191, 194–197, 199
 - potential field for 175–181, 195
 - vibron 91, 421, 422
 - wave function of 181–183
- volume of hydrogen in metals 104–113
 - amorphous alloys (values) 109
 - empirical rule 107
 - intermetallic compounds (values) 109

- metals (values) 105, 106
- pressure dependence of 110–112
- universal compression curve in
metallic environment 112
- wave function
 - distorted lattice 377
 - screening electrons 377
 - self-trapped state 377
 - vibrational state 181–183, 237, 246
 - calculation of 231–242, 256, 257
- experimental determination of
178, 179, 181–183
- X-ray scattering
 - Bragg scattering 152
 - Huang scattering → diffuse scattering
 - diffuse scattering 156–159
 - static Debye–Waller factor 159
- Zener relaxation 311, 325, 337

Springer Series in MATERIALS SCIENCE

Editors: R. Hull R. M. Osgood, Jr. J. Parisi H. Warlimont

- | | | | |
|----|---|----|--|
| 20 | Microcluster Physics
By S. Sugano and H. Koizumi
2nd Edition | 35 | Macromolecular Science
and Engineering
New Aspects
Editor: Y. Tanabe |
| 21 | The Metal-Hydrogen System
By Y. Fukai 2nd Edition | 36 | Ceramics
Mechanical Properties,
Failure Behaviour,
Materials Selection
By D. Munz and T. Fett |
| 22 | Ion Implantation in Diamond,
Graphite and Related Materials
By M. S. Dresselhaus and R. Kalish | 37 | Technology and Applications
of Amorphous Silicon
Editor: R. A. Street |
| 23 | The Real Structure
of High-T_c Superconductors
Editor: V. Sh. Shekhtman | 38 | Fullerene Polymers
and Fullerene Polymer Composites
Editors: P. C. Eklund and A. M. Rao |
| 24 | Metal Impurities
in Silicon-Device Fabrication
By K. Graff 2nd Edition | 39 | Semiconducting Silicides
Editor: V. E. Borisenko |
| 25 | Optical Properties of Metal Clusters
By U. Kreibig and M. Vollmer | 40 | Reference Materials
in Analytical Chemistry
A Guide for Selection and Use
Editor: A. Zschunke |
| 26 | Gas Source Molecular Beam Epitaxy
Growth and Properties of Phosphorus
Containing III-V Heterostructures
By M. B. Panish and H. Temkin | 41 | Organic Electronic Materials
Conjugated Polymers and Low
Molecular Weight Organic Solids
Editors: R. Farchioni and G. Grosso |
| 27 | Physics of New Materials
Editor: F. E. Fujita 2nd Edition | 42 | Raman Scattering
in Materials Science
Editors: W. H. Weber and R. Merlin |
| 28 | Laser Ablation
Principles and Applications
Editor: J. C. Miller | 43 | The Atomistic Nature
of Crystal Growth
By B. Mutaftschiev |
| 29 | Elements of Rapid Solidification
Fundamentals and Applications
Editor: M. A. Otonari | 44 | Thermodynamic Basis
of Crystal Growth
P-T-X Phase Equilibrium
and Non-Stoichiometry
By J. Greenberg |
| 30 | Process Technology
for Semiconductor Lasers
Crystal Growth
and Microprocesses
By K. Iga and S. Kinoshita | 45 | Thermoelectrics
Basic Principles
and New Materials Developments
By G. S. Nolas, J. Sharp,
and H. J. Goldsmid |
| 31 | Nanostructures
and Quantum Effects
By H. Sakaki and H. Noge | 46 | Fundamental Aspects
of Silicon Oxidation
Editor: Y. J. Chabal |
| 32 | Nitride Semiconductors and Devices
By H. Morkoç | | |
| 33 | Supercarbon
Synthesis, Properties and Applications
Editors: S. Yoshimura and R. P. H. Chang | | |
| 34 | Computational Materials Design
Editor: T. Saito | | |
-

Springer Series in MATERIALS SCIENCE

Editors: R. Hull R. M. Osgood, Jr. J. Parisi H. Warlimont

- | | |
|---|--|
| <p>49 Alkali Halides
A Handbook of Physical Properties
By D. B. Sirdeshmukh, L. Sirdeshmukh,
and K. G. Subhadra</p> <p>50 High-Resolution Imaging
and Spectrometry of Materials
Editors: F. Ernst and M. Rühle</p> <p>51 Point Defects in Semiconductors
and Insulators
Determination of Atomic
and Electronic Structure
from Paramagnetic Hyperfine
Interactions
By J.-M. Spaeth and H. Overhof</p> <p>52 Polymer Films
with Embedded Metal Nanoparticles
By A. Heilmann</p> <p>53 Nanocrystalline Ceramics
Synthesis and Structure
By M. Winterer</p> <p>54 Electronic Structure and Magnetism
of Complex Materials
Editors: D.J. Singh and
D. A. Papaconstantopoulos</p> <p>55 Quasicrystals
An Introduction to Structure,
Physical Properties and Applications
Editors: J.-B. Suck, M. Schreiber,
and P. Häussler</p> <p>56 SiO₂ in Si Microdevices
By M. Itsumi</p> <p>57 Radiation Effects
in Advanced Semiconductor Materials
and Devices
By C. Claeys and E. Simoen</p> <p>58 Functional Thin Films
and Functional Materials
New Concepts and Technologies
Editor: D. Shi</p> <p>59 Dielectric Properties of Porous Media
By S.O. Gladkov</p> | <p>60 Organic Photovoltaics
Concepts and Realization
Editors: C. Brabec, V. Dyakonov, J. Parisi and
N. Sariciftci</p> <p>61 Fatigue in Ferroelectric Ceramics
and Related Issues
By D.C. Lupascu</p> <p>62 Epitaxy
Physical Principles
and Technical Implementation
By M.A. Herman, W. Richter, and H. Sitter</p> <p>63 Fundamentals
of Ion-Irradiated Polymers
By D. Fink</p> <p>64 Morphology Control of Materials
and Nanoparticles
Advanced Materials Processing
and Characterization
Editors: Y. Waseda and A. Muramatsu</p> <p>65 Transport Processes
in Ion-Irradiated Polymers
By D. Fink</p> <p>66 Multiphased Ceramic Materials
Processing and Potential
Editors: W.-H. Tuan and J.-K. Guo</p> <p>67 Nondestructive
Materials Characterization
With Applications to Aerospace Materials
Editors: N.G.H. Meyendorf, P.B. Nagy,
and S.I. Rokhlin</p> <p>68 Diffraction Analysis
of the Microstructure of Materials
Editors: E.J. Mittemeijer and P. Scardi</p> <p>69 Chemical-Mechanical Planarization
of Semiconductor Materials
Editor: M.R. Oliver</p> <p>70 Applications of the Isotopic Effect
in Solids
By V.G. Plekhanov</p> |
|---|--|
-